frontiers | Research Topics

DSCOVR EPIC/NISTAR: 5 years of observing earth from the first lagrangian point

Edited by
Alexei Lyapustin, Alexander Marshak and Gregory Schuster

Published in
Frontiers in Remote Sensing

frontiers | Research Topics

DSCOVR EPIC/NISTAR: 5 years of observing earth from the first lagrangian point

Edited by
Alexei Lyapustin, Alexander Marshak and Gregory Schuster

Published in
Frontiers in Remote Sensing

ISSN 1664-8714
ISBN 978-2-83250-075-0
DOI 10.3389/978-2-83250-075-0

About Frontiers

Frontiers is more than just an open access publisher of scholarly articles: it is a pioneering approach to the world of academia, radically improving the way scholarly research is managed. The grand vision of Frontiers is a world where all people have an equal opportunity to seek, share and generate knowledge. Frontiers provides immediate and permanent online open access to all its publications, but this alone is not enough to realize our grand goals.

Frontiers journal series

The Frontiers journal series is a multi-tier and interdisciplinary set of open-access, online journals, promising a paradigm shift from the current review, selection and dissemination processes in academic publishing. All Frontiers journals are driven by researchers for researchers; therefore, they constitute a service to the scholarly community. At the same time, the *Frontiers journal series* operates on a revolutionary invention, the tiered publishing system, initially addressing specific communities of scholars, and gradually climbing up to broader public understanding, thus serving the interests of the lay society, too.

Dedication to quality

Each Frontiers article is a landmark of the highest quality, thanks to genuinely collaborative interactions between authors and review editors, who include some of the world's best academicians. Research must be certified by peers before entering a stream of knowledge that may eventually reach the public - and shape society; therefore, Frontiers only applies the most rigorous and unbiased reviews. Frontiers revolutionizes research publishing by freely delivering the most outstanding research, evaluated with no bias from both the academic and social point of view. By applying the most advanced information technologies, Frontiers is catapulting scholarly publishing into a new generation.

What are Frontiers Research Topics?

Frontiers Research Topics are very popular trademarks of the *Frontiers journals series*: they are collections of at least ten articles, all centered on a particular subject. With their unique mix of varied contributions from Original Research to Review Articles, Frontiers Research Topics unify the most influential researchers, the latest key findings and historical advances in a hot research area.

Find out more on how to host your own Frontiers Research Topic or contribute to one as an author by contacting the Frontiers editorial office: frontiersin.org/about/contact

DSCOVR EPIC/NISTAR: 5 years of observing earth from the first lagrangian point

Topic editors

Alexei Lyapustin – Goddard Space Flight Center, National Aeronautics and Space Administration, United States

Alexander Marshak – Goddard Space Flight Center, National Aeronautics and Space Administration, United States

Gregory Schuster – Langley Research Center, National Aeronautics and Space Administration, United States

Citation

Lyapustin, A., Marshak, A., Schuster, G., eds. (2022). *DSCOVR EPIC/NISTAR: 5 years of observing earth from the first lagrangian point*. Lausanne: Frontiers Media SA. doi: 10.3389/978-2-83250-075-0

Table of Contents

Yaping Zhou, Yuekui Yang, Peng-Wang Zhai and Meng Gao

Effect of Scattering Angle on Earth Reflectance

Alexander Marshak, Alfonso Delgado-Bonal and Yuri Knyazikhin

Earth Imaging From the Surface of the Moon With a DSCOVR/EPIC-Type Camera

Nick Gorkavyi, Simon Carn, Matt DeLand, Yuri Knyazikhin, Nick Krotkov, Alexander Marshak, Ranga Myneni and Alexander Vasilkov

Evaluation of Version 3 Total and Tropospheric Ozone Columns From Earth Polychromatic Imaging Camera on Deep Space Climate Observatory for Studying Regional Scale Ozone Variations

Natalya A. Kramarova, Jerald R. Ziemke, Liang-Kang Huang, Jay R. Herman, Krzysztof Wargan, Colin J. Seftor, Gordon J. Labow and Luke D. Oman

Atmospheric Correction of DSCOVR EPIC: Version 2 MAIAC Algorithm

A. Lyapustin, Y. Wang, S. Go, M. Choi, S. Korkin, D. Huang, Y. Knyazikhin, K. Blank and A. Marshak

Lagrange Point Missions: The Key to next Generation Integrated Earth Observations. DSCOVR Innovation

Francisco P. J. Valero, Alexander Marshak and Patrick Minnis

Global Daytime Mean Shortwave Flux Consistency Under Varying EPIC Viewing Geometries

Wenying Su, Lusheng Liang, David P. Duda, Konstantin Khlopenkov and Mandana M. Thieman

Hourly Mapping of the Layer Height of Thick Smoke Plumes Over the Western U.S. in 2020 Severe Fire Season

Zhendong Lu, Jun Wang, Xiaoguang Xu, Xi Chen, Shobha Kondragunta, Omar Torres, Eric M. Wilcox and Jing Zeng

Vegetation Angular Signatures of Equatorial Forests From DSCOVR EPIC and Terra MISR Observations

Xiangnan Ni, Yuri Knyazikhin, Yuanheng Sun, Xiaojun She, Wei Guo, Oleg Panferov and Ranga B. Myneni

Earth Polychromatic Imaging Camera Geolocation; Strategies to Reduce Uncertainty

Karin Blank, Liang-Kang Huang, Jay Herman and Alexander Marshak

Operational Detection of Sun Glints in DSCOVR EPIC Images

Tamás Várnai, Alexander Marshak and Alexander Kostinski

Radiometric Stability Assessment of the DSCOVR EPIC Visible Bands Using MODIS, VIIRS, and Invariant Targets as Independent References

Conor Haney, David R. Doelling, Wenying Su, Rajendra Bhatt, Arun Gopalan and Benjamin Scarino

Cloud Height Daytime Variability From DSCOVR/EPIC and GOES-R/ABI Observations

A. Delgado-Bonal, A. Marshak, Y. Yang and L. Oreopoulos

Unique NISTAR-Based Climate GCM Diagnostics of the Earth's Planetary Albedo and Spectral Absorption Through Longitudinal Data Slicing

Andrew A. Lacis, Barbara E. Carlson, Gary L. Russell, Alexander Marshak and Wenying Su

Temporal Variation of the Shortwave Spherical Albedo of the Earth

A. Penttilä, K. Muinonen, O. Ihalainen, E. Uvarova, M. Vuori, G. Xu, J. Näränen, O. Wilkman, J. Peltoniemi, M. Gritsevich, H. Järvinen and A. Marshak

EPIC/DSCOVR as a Pathfinder in Cloud Remote Sensing Using Differential Oxygen Absorption Spectroscopy

Anthony B. Davis, Yuekui Yang and Alexander Marshak

The NASA EPIC/DSCOVR Ocean PAR Product

Robert Frouin, Jing Tan, Mathieu Compiègne, Didier Ramon, Marshall Sutton, Hiroshi Murakami, David Antoine, Uwe Send, Jeff Sevadjian and Vincenzo Vellucci

Unique Observational Constraints on the Seasonal and Longitudinal Variability of the Earth's Planetary Albedo and Cloud Distribution Inferred From EPIC Measurements

Barbara E. Carlson, Andrew A. Lacis, Gary L. Russell, Alexander Marshak and Wenying Su

Reduction of Spectral Radiance Reflectance During the Annular Solar Eclipse of 21 June 2020 Observed by EPIC

Guoyong Wen, Alexander Marshak, Jay Herman and Dong Wu

EDITORIAL
published: 11 August 2022
doi: 10.3389/frsen.2022.963660

Editorial: DSCOVR EPIC/NISTAR: 5 Years of Observing Earth From the First Lagrangian Point

A. Marshak[1], A. Lyapustin[1*], G. L. Schuster[2], A. Szabo[1] and R. Eckman[2]

[1] *NASA Goddard Space Flight Center, Greenbelt, MA, United States*
[2] *NASA Langley Research Center, Hampton, VA, United States*

Edited and reviewed by:
Oleg Dubovik, UMR8518 Laboratoire d'optique Atmosphèrique (LOA), France

**** Correspondence:** A. Lyapustin, alexei.i.lyapustin@nasa.gov*

***Specialty section:** This article was submitted to Satellite Missions, a section of the journal Frontiers in Remote Sensing*

***Received:** 07 June 2022*
***Accepted:** 20 June 2022*
***Published:** 11 August 2022*

***Citation:** Marshak A, Lyapustin A, Schuster GL, Szabo A and Eckman R (2022) Editorial: DSCOVR EPIC/NISTAR: 5 Years of Observing Earth From the First Lagrangian Point. Front. Remote Sens. 3:963660. doi: 10.3389/frsen.2022.963660*

Keywords: EPIC, NISTAR, aerosol, clouds, land surface properties, ozone

Editorial on the Research Topic

DSCOVR EPIC/NISTAR: 5 Years of Observing Earth From the First Lagrangian Point

The Deep Space Climate Observatory (DSCOVR) was launched in February 2015 to a Sun-Earth Lagrange-1 (L1) orbit, approximately 1.5 million kilometers from the sunlit side of the Earth. In many regards, the DSCOVR is a unique mission: for the first time, it delivers well-calibrated and multi-spectral measurements of Earth from the L1 point. This unique location allows near-hourly views of the entire illuminated disk of the Earth, multiple times a day. The moderately high observational cadence results in cloud-free views of nearly the entire Earth land surface and global ocean with significantly higher frequency than is available to the operational polar orbiters, and at a near-global scale inaccessible to geostationary sensors.

In addition to providing continuous solar wind measurements for accurate space weather forecasting, DSCOVR operates two Earth science instruments: the Earth Polychromatic Imaging Camera (EPIC) and the NIST Advanced Radiometer (NISTAR). EPIC has a 2048 × 2048 pixel CCD with sensitivity to UV, visible, and near IR (NIR) wavelengths. The filter wheel contains 10 narrow-band filters from 317.5 to 779.5 nm. The spatial resolution is about 10 km at nadir. The Earth-observing geometry of the EPIC instrument captures a nearly constant scattering angle between 168° and 178°. NISTAR measures the absolute irradiance integrated over the entire sunlit face of the Earth in four broadband channels every minute covering visible and IR wavelengths.

The unique near-backscatter view geometry of EPIC led to creation of several new Earth science products. The diurnal course of “sunlit leaf area index” SLAI is one of them (Yang et al., 2017). It characterizes the area of green leaves at a given time intercepting the direct sunlight and depends on canopy structural organization. Because sunlit and shaded leaves exhibit different photosynthetic response to incident Photosynthetically Active Radiation (400–700 nm; Mercado et al., 2009; Stenberg, 1998), SLAI is important addition to the standard total leaf area index (LAI) that has long been provided by polar orbiting sensors like MODIS or VIIRS. By virtue of

its unique view geometry, EPIC became the first sensor providing SLAI required for better characterization of ecosystem productivity and carbon/nitrogen cycles (Bonan et al., 2003; Dai et al., 2004; Mercado et al., 2009; He et al., 2013).

Other new land surface products are the Directional Area Scattering Factor (DASF), the Earth Reflector Type Index (ERTI) and Canopy Scattering Coefficient (CSC) at 443, 551, 680 and 780 nm (Knyazikhin and Myneni, 2021). DASF provides information critical to accounting for structural contributions to measurements of leaf biochemistry from remote sensing (Smolander and Stenberg, 2003; Knyazikhin et al., 2013; Stenberg et al., 2016). ERTI is an estimate of the recollision probability. This index was developed to discriminate between signals originating from clouds, cloud-free ocean, bare and vegetated land (Song et al., 2018). SCS is an estimate of the fraction of intercepted radiation that has been reflected from, or diffusively transmitted through, the vegetation (Smolander et al., 2003; Lewis and Disney, 2007). This coefficient for example is useful to detect changes in leaf chlorophyll content of equatorial forests (Sun et al., 2022). The land products use EPIC surface reflectance which is provided by MAIAC atmospheric correction algorithm along with cloud detection and aerosol retrieval (Lyapustin et al., this issue).

Even casual glimpses at EPIC images (https://epic.gsfc.nasa.gov/) reveal bright colorful spots near the image center. The analysis of observation geometry and collocated EPIC data suggests that these bright spots are caused by specular reflection from ice crystals that float inside clouds in a horizontal orientation (Marshak et al., 2017; Li J. -Z.et al., 2019; Varnai et al., 2020b). Glint studies over the ocean found that cloud glints are small but bright (Varnai et al., 2020a). Most recently (Kostinski et al., 2021) it was found that cloud glints were used to gauge the accuracy of geolocation in EPIC operational products and to examine the physical processes and instrumental considerations that affect EPIC glints caused by specular reflection from small lakes. It has been a general assumption that the ice crystals in the high-altitude ice clouds are randomly orientated. Orientation of crystals affects reflection of the incoming Sun light and its transmission to the Earth surface, and thus an improved understanding of the number, or proportion of oriented ice particles

has a potential to bring improvement in modeling of the Earth cloud radiation budget. The first operational glint product was released recently (https://epic.gsfc.nasa.gov/science/products/glint).
EPIC and NISTAR have continuously operated until 27 June 2019, when the spacecraft was placed in an extended safe hold due to degradation of gyroscopes. With development of the software patch for spacecraft attitude determination based solely on the star trackers, DSCOVR returned to full operations on 2 March 2020. Since then, DSCOVR has been able to maintain pointing accuracy similar to that with gyroscopes keeping the Earth fully in the field-of-view of EPIC. After March 2020 the range of scattering angle has substantially increased towards backscattering reaching 178°. This provided a unique opportunity to study angular variations of the Earth reflectivity in the vicinity of the exact backscattering, or hotspot (Marshak et al.). All EPIC and NISTAR observations show a strong increase of reflectance towards the hotspot. For NISTAR, which data are used to study the Earth radiation budget, this limits angular resolution of the angular distribution models to 1°–3° near the backscattering angle.
For aerosol science, a near-backscattering view geometry of EPIC has both merits and drawbacks. Increase of the land surface brightness at this geometry results in decreasing sensitivity of observations to the atmospheric aerosol variations, e.g. of the aerosol optical depth (AOD). On the other hand, the high observational cadence and near-global coverage enhances our capability for a high-quality characterization of the surface reflectance, and based on that, characterization of the high-AOD mega-events such as forest wildfires or dust storms when the surface brightness becomes less important.
Based on well-calibrated EPIC UV-vis observations, Lyapustin et al. developed an algorithm to simultaneously retrieve both AOD and spectral aerosol absorption. The latter, in turn, allows to peek into aerosol composition based on spectrally distinct absorption properties of dominant absorbers, namely black and brown carbon in biomass burning smoke, and hematite and goethite in airborne mineral dust (Go et al., 2022). The developed speciation algorithm has been integrated in MAIAC v2 EPIC algorithm. Thus, while the

fundamentals of such decomposition were developed earlier for AERONET (Holben et al., 1998; Schuster et al., 2016) and later applied for POLDER/PARASOL (Li L. et al., 2019), EPIC is becoming the first operational imager to provide such speciation information in support of both climate modeling and the air quality communities.

This special issue of Frontiers in Remote Sensing titled “DSCOVR EPIC/NISTAR: 5 years of observing Earth from the first Lagrangian point” has 23 papers that provide an integral holistic view of the Earth science from DSCOVR. Topics range from the sensors’ description, data calibration, and geolocation to the processing algorithms and official products, to the science data analysis and applications.

There are four papers on EPIC data calibration, covering EPIC geolocation strategies (Blank, et al.), raw data calibration (Cede et al.) and calibration of EPIC visible and NIR channels (Geogdzhaev et al.; Haney et al.). Eight papers describe different official EPIC products, including ocean surface photosynthetically available radiation (PAR) (Frouin et al.), total and tropospheric ozone (Kramarova et al.), aerosol height (Lu et al.), aerosol optical depth and atmospheric correction (Lyapustin et al.; Lyapustin et al.), vegetation (Ni et al.), clouds (Zhou et al.) and solar glint (Varnai et al.). Two papers discuss cloud height from EPIC: Davis et al. reviews cloud height remote sensing using atmospheric oxygen absorption spectroscopy while Delgado-Bonal et al. talks about daily variability in cloud height around the globe. Variability of the Earth’s planetary albedo is investigated in three papers by Carlson et al., Lacis et al. and Penttilä et al. If the first two deal mostly with GCM and distribution of clouds, the third one discusses a new method to derive the Earth spherical albedo from EPIC data and provides it at fine temporal resolution. Finally, Su et al. discusses the relationships between EPIC radiances and the reflected shortwave fluxes and compares EPIC- derived fluxes with those from CERES.

Phase angles between Sun illumination and EPIC observations have an important effect on estimating Earth reflectance near the backscattering (Marshak et al.). Valero et al. reviewed the history behind the current DSCOVR mission and discussed the opportunity of future Earth observations from Lagrange points while Gorkavyi et

al. highlighted Earth observations from the Moon surface with an EPIC-like instrument, as a part of the future Artemis mission. In addition, EPIC observations were used to estimate the reduction of spectral radiance during solar eclipse of 21 June 2020 (Wen et al.). Finally, Pisek et al. explores the potential of retrieving clumping vegetation index using DSCOVR EPIC data.

AUTHOR CONTRIBUTIONS

All authors listed have made a substantial, direct, and intellectual contribution to the work and approved it for publication.

PUBLISHER'S NOTE

All claims expressed in this article are solely those of the authors and do not necessarily represent those of their affiliated organizations, or those of the publisher, the editors and the reviewers. Any product that may be evaluated in this article, or claim that may be made by its manufacturer, is not guaranteed or endorsed by the publisher.

ACKNOWLEDGMENTS

We would like to acknowledge editing support of Dr. Knyazikhin. We also thank the NASA Center for Climate Simulations for providing computer resources for the EPIC and NISTAR data processing.

REFERENCES

Bonan, G. B., Levis, S., Sitch, S., Vertenstein, M., and Oleson, K. W. (2003). A Dynamic Global Vegetation Model for Use with Climate Models: Concepts and Description of Simulated Vegetation Dynamics. *Glob. Change Biol.* 9 (11), 1543–1566. doi:10.1046/j.1365-2486.2003.00681.x

Dai, Y., Dickinson, R. E., and Wang, Y.-P. (2004). A Two-Big-Leaf Model for Canopy Temperature, Photosynthesis, and Stomatal Conductance. *J. Clim.* 17 (12), 2281–2299. doi:10.1175/1520-0442(2004)017<2281:atmfct>2.0.co;2

Go, S., Lyapustin, A., Schuster, G. L., Choi, M., Ginoux, P., Chin, M., et al. (2022). Inferring Iron-Oxide Species Content in Atmospheric Mineral Dust from DSCOVR EPIC Observations. *Atmos. Chem. Phys.* 22, 1395–1423. doi:10.5194/acp-22-1395-2022

He, M., Ju, W., Zhou, Y., Chen, J., He, H., Wang, S., et al. (2013). Development of a Two-Leaf Light Use Efficiency Model for Improving the Calculation of Terrestrial Gross Primary Productivity. *Agric. For. meteorology* 173, 28–39. doi:10.1016/j.agrformet.2013.01.003

Holben, B. N., Eck, T. F., Slutsker, I., Tanré, D., Buis, J. P., Setzer, A., et al. (1998). AERONET-A Federated Instrument Network and Data Archive for Aerosol Characterization. *Remote Sens. Environ.* 66, 1–16. doi:10.1016/s0034-4257(98)00031-5

Knyazikhin, Y., and Myneni, R. B. (2021). *NASA Langley Atmospheric Science Data Center DAAC*. doi:10.5067/EPIC/DSCOVR/L2_VESDR.002Dscovr Epic Vegetation Earth System Data Record, Science Data Product Guide (Version 2)

Knyazikhin, Y., Schull, M. A., Stenberg, P., Mõttus, M., Rautiainen, M., Yang, Y., et al. (2013). Hyperspectral Remote Sensing of Foliar Nitrogen Content. *Proc. Natl. Acad. Sci. U.S.A.* 110, E185–E192. doi:10.1073/pnas.1210196109

Kostinski, A., Marshak, A., and Varnai, T. (2021). Deep Space Observations of Terrestrial Glitter. *Earth Space Sci.* 8, e2020EA001521. doi:10.1029/2020ea001521

Lewis, P., and Disney, M. (2007). Spectral Invariants and Scattering across Multiple Scales from Within-Leaf to Canopy. *Remote Sens. Environ.* 109 (2), 196–206. doi:10.1016/J.Rse.2006.12.015

Li, J.-Z., Fan, S., Kopparla, P., Liu, C., Jiang, J. H., Natraj, V., et al. (2019). Study of Terrestrial Glints Based on DSCOVR Observations. *Earth Space Sci.* 6 (1), 166–173. doi:10.1029/2018EA000509

Li, L., Dubovik, O., Derimian, Y., Schuster, G. L., Lapyonok, T., Litvinov, P., et al. (2019). Retrieval of Aerosol Components Directly from Satellite and Ground-Based Measurements. *Atmos. Chem. Phys.* 19, 13409–13443. doi:10.5194/acp-19-13409-2019

Marshak, A., Várnai, T., and Kostinski, A. (2017). Terrestrial glint seen from deep space: Oriented ice crystals detected from the lagrangian point. *Geophys. Res. Lett.* 44 (10), 5197–5202. doi:10.1002/2017GL073248

Mercado, L. M., Bellouin, N., Sitch, S., Boucher, O., Huntingford, C., Wild, M., et al. (2009). Impact of changes in diffuse radiation on the global land carbon sink. *Nature* 458, 1014–1017. doi:10.1038/nature07949

Schuster, G. L., Dubovik, O., and Arola, A. (2016). Remote sensing of soot carbon - Part 1: Distinguishing different absorbing aerosol species. *Atmos. Chem. Phys.* 16, 1565–1585. doi:10.5194/acp-16-1565-2016

Smolander, S., and Stenberg, P. (2003). A method to account for shoot scale clumping in coniferous canopy reflectance models. *Remote Sens. Environ.* 88 (4), 363–373. doi:10.1016/J.Rse.2003.06.003

Song, W., Knyazikhin, Y., Wen, G., Marshak, A., Mõttus, M., Yan, K., et al. (2018). Implications Of Whole-Disc Dscovr Epic Spectral Observations For Estimating Earth's Spectral Reflectivity Based On Low-Earth-Orbiting And Geostationary Observations. *Remote Sens.* 10 (10), 1594. doi:10.3390/rs10101594

Stenberg, P. (1998). Implications of shoot structure on the rate of photosynthesis at different levels in a coniferous canopy using a model incorporating grouping and penumbra. *Funct. Ecol.* 12 (1), 82–91. doi:10.1046/j.1365-2435.1998.00169.x

Stenberg, P., Mõttus, M., and Rautiainen, M. (2016). Photon recollision probability in modelling the radiation regime of canopies - A review. *Remote Sens. Environ.* 183, 98–108. doi:10.1016/j.rse.2016.05.013

Sun, Y., Knyazikhin, Y., She, X., Ni, X., Chen, C., Ren, H., et al. (2022). Seasonal and long-term variations in leaf area of Congolese rainforest. *Remote Sens. Environ.* 268, 112762. doi:10.1016/j.rse.2021.112762

Varnai, T., Kostinski, A. B., and Marshak, A. (2020a). Deep space observations of sun glints from marine ice clouds. *IEEE Geosci. Remote Sens. Lett.* 17 (5), 735–739. doi:10.1109/LGRS.2019.2930866

Varnai, T., Marshak, A., and Kostinski, A. B. (2020b). Deep Space Observations of Cloud Glints: Spectral and Seasonal Dependence. *IEEE Geosci. Remote Sens. Lett.* 19, 1–5. doi:10.1109/LGRS.2020.3040144

Yang, B., Knyazikhin, Y., Mõttus, M., Rautiainen, M., Stenberg, P., Yan, L., et al. (2017). Estimation of leaf area index and its sunlit portion from DSCOVR EPIC data: Theoretical basis. *Remote*

Sens. Environ. 198, 69–84. doi:10.1016/j.rse.2017.05.033

Conflict of Interest: The authors declare that the research was conducted in the absence of any commercial or financial relationships that could be construed as a potential conflict of interest.

BRIEF RESEARCH REPORT
published: 16 March 2021
doi: 10.3389/frsen.2021.652436

Exploring the Potential of DSCOVR EPIC Data to Retrieve Clumping Index in Australian Terrestrial Ecosystem Research Network Observing Sites

Jan Pisek[1*], Stefan K. Arndt[2], Angela Erb[3], Elise Pendall[4], Crystal Schaaf[3], Timothy J. Wardlaw[5], William Woodgate[6,7] and Yuri Knyazikhin[8]

[1] *Tartu Observatory, University of Tartu, Tartu, Estonia*
[2] *School of Ecosystem and Forest Science, University of Melbourne, Richmond, VIC, Australia*
[3] *School for the Environment, University of Massachusetts Boston, Boston, MA, United States*
[4] *Hawkesbury Institute for the Environment, Western Sydney University, Penrith, NSW, Australia*
[5] *School of Plant Science, University of Tasmania, Hobart, TAS, Australia*
[6] *School of Earth and Environmental Sciences, University of Queensland, Brisbane, QLD, Australia*
[7] *Land & Water, The Commonwealth Scientific and Industrial Research Organisation (CSIRO), Brisbane, QLD, Australia*
[8] *Earth and Environment Department, Boston University, Boston, MA, United States*

Edited by:
Alexei Lyapustin, National Aeronautics and Space Administration, United States

Reviewed by:
Matti Mõttus, VTT Technical Research Centre of Finland Ltd., Finland
Miguel Roman, Universities Space Research Association (USRA), United States

***Correspondence:** Jan Pisek, janpisek@gmail.com*

***Specialty section:** This article was submitted to Satellite Missions, a section of the journal Frontiers in Remote Sensing*

Received: *12 January 2021*
Accepted: *22 February 2021*
Published: *16 March 2021*

Citation: *Pisek J, Arndt SK, Erb A, Pendall E, Schaaf C, Wardlaw TJ, Woodgate W and Knyazikhin Y (2021) Exploring the Potential of DSCOVR EPIC Data to Retrieve Clumping Index in Australian Terrestrial Ecosystem Research Network Observing Sites. Front. Remote Sens. 2:652436. doi: 10.3389/frsen.2021.652436*

Vegetation foliage clumping significantly alters the radiation environment and affects vegetation growth as well as water, carbon cycles. The clumping index (CI) is useful in ecological and meteorological models because it provides new structural information in addition to the effective leaf area index. Previously generated CI maps using a diverse set of Earth Observation multi-angle datasets across a wide range of scales have all relied on the single approach of using the normalized difference hotspot and darkspot (NDHD) method. We explore an alternative approach to estimate CI from space using the unique observing configuration of the Deep Space Climate Observatory Earth Polychromatic Imaging Camera (DSCOVR EPIC) and associated products at 10 km resolution. The performance was evaluated with *in situ* measurements in five sites of the Australian Terrestrial Ecosystem Research Network comprising a diverse range of canopy structure from short and sparse to dense and tall forest. The DSCOVR EPIC data can provide meaningful CI retrievals at the given spatial resolution. Independent but comparable CI retrievals obtained with a completely different sensor and new approach were encouraging for the general validity and compatibility of the foliage clumping information retrievals from space. We also assessed the spatial representativeness of the five TERN sites with respect to a particular point in time (field campaigns) for satellite retrieval validation. Our results improve our understanding of product uncertainty both in terms of the representativeness of the field data collected over the TERN sites and its relationship to Earth Observation data at different spatial resolutions.

Keywords: clumping index, DSCOVR EPIC, TERN, validation, spatial analysis

INTRODUCTION

The clumping index (CI) quantifies the level of foliage grouping within distinct canopy structures relative to a random distribution (Nilson, 1971; Chen and Black, 1992). It provides best agreement between transmittance through clumped canopy and Beer's exponential transmission law (Nilson, 1971; Kuusk, 2018). CI equals unity with leaves completely randomly distributed. Canopy foliage is usually clumped into various sub-canopy structures such as crowns, branches, and twigs, thus clumping is defined as a situation where CI < 1. Regularly distributed foliage results in CI greater than unity. Clumping affects the interception and distribution of solar radiation within a canopy (Chen et al., 2003, 2005; Hill et al., 2011; Wei et al., 2019). In addition, the distribution of foliar nutrients and canopy evapotranspiration (ET) were found to be significantly influenced by CI (Thomas et al., 2011). Both ground and satellite ET estimates are greatly underestimated if CI is not considered (Chen et al., 2016). CI is also an important parameter for accurate canopy-level gross primary production (GPP) modeling (Ryu et al., 2011; Chen et al., 2012).

Global and regional scale CI maps have been generated from a diverse set of Earth Observation multi-angle datasets: POLarization and Directionality of the Earth's Reflectances (POLDER) data at ~6 km resolution (Chen et al., 2005); the Bidirectional Reflectance Distribution Function (BRDF) product from Moderate Resolution Imaging Spectroradiometer (MODIS) at 500 m resolution (He et al., 2012; Wei and Fang, 2016; Jiao et al., 2018), and Multi-angle Imaging SpectroRadiometer (MISR) data at 275 m resolution (Pisek et al., 2013).

All the products listed above share the common feature of estimating CI through a single approach—its empirical relationship with the normalized difference between the hotspot and darkspot (NDHD) (Chen et al., 2005; Leblanc et al., 2005a):

$$CI = A \cdot NDHD + B \qquad (1)$$

where A and B are coefficients determined by the linear regression, based on a set of model simulations made with the 4-Scale model in Chen et al. (2005). The coefficients vary with assumed crown shape and solar zenith angle [see Table 2 in Chen et al. (2005)]. The NDHD index is defined as:

$$NDHD = \frac{HS - DS}{HS + DS} \qquad (2)$$

where HS and DS mark the canopy reflectance at the hotspot and darkspot, respectively (Leblanc et al., 2001). The hotspot corresponds to the backscatter peak when the solar radiation and view directions coincide, leading to minimum shading in that view direction. The darkspot exists in the direction opposite to that of the hotspot, where the maximum shadow area can be seen leading to minimum reflectance.

This brief research report explores a new, alternative approach to NDHD how to estimate CI from Earth Observation data. The approach exploits unique observation data and products from a new satellite that is quite different from traditional polar-orbiting or geostationary satellites. The Deep Space Climate Observatory (DSCOVR) is a satellite positioned near the first Lagrange point (or L1). It offers the continuous observations of full, sunlit side of the Earth. The DSCOVR satellite carries on-board a spectroradiometer—the Earth Polychromatic Imaging Camera (EPIC). EPIC can provide spectral images of the entire sunlit face of the Earth with 10 narrow channels (from 317 to 780 nm) (Marshak et al., 2018) every 1–2 h in summer and winter, respectively.

The CI retrievals with DSCOVR/EPIC product data are validated in this study using available *in situ* measurements obtained with digital hemispherical photography (DHP), carried over select sites belonging to the Australian Terrestrial Ecosystem Research Network (TERN; Lowe et al., 2016) comprising a diverse range of canopy structure from short and sparse to dense and tall forest.

METHOD

DSCOVR EPIC Vegetation Earth System Data Record (VESDR) Product

The DSCOVR EPIC version 1 Vegetation Earth System Data Record (VESDR) provides Leaf Area Index (LAI) as well as diurnal courses of Sunlit Leaf Area Index (SLAI), Normalized Difference Vegetation Index (NDVI), Fraction of incident Photosynthetically Active Radiation (FPAR) absorbed by the vegetation and Directional Area Scattering Function (DASF). The product at 10 km sinusoidal grid with 65–110 min temporal frequency is generated from the upstream DSCOVR EPIC L2 MAIAC surface reflectance product (Lyapustin et al., 2018). With the exception of

LAI, all VESDR parameters vary with the sun-sensor geometry. The VESDR files also include Solar Zenith Angle (SZA), Solar Azimuthal Angle (SAA), View Zenith (VZA), and Azimuthal (VAA) angles at the same temporal and spatial resolutions. A quality assessment variable (QA_VESDR) is also provided. For this analysis, only the EPIC observations with best quality flags (QA_VESDR = 0) were used for the CI retrieval. It is noted that the DSCOVR EPIC VESDR product is currently released at a provisional quality level. The EPIC level 2 VESDR product and accompanying documentation are available from the NASA Langley Atmospheric Science Data Center (https://asdc.larc.nasa.gov/project/DSCOVR). The VESDR product data were downloaded through NASA's Open-source Project for a Network Data Access Protocol (OPeNDAP; https://opendap.larc.nasa.gov/opendap/).

Foliage Clumping Retrieval With DSCOVR EPIC Data

Available DSCOVR/EPIC VESDR products of sunlit leaf area index (SLAI) and leaf area index (LAI) allow to estimate sunlit fraction of leaf area (Knyazikhin et al., 2017):

$$SF = \frac{SLAI}{LAI}. \qquad (3)$$

CI provides best agreement between directional uncollated transmittance through clumped canopy, $t_0(\theta)$, and Beer's exponential transmission law, $\exp(-\tau)$, which is applicable for completely randomly distributed leaves. Here

$$\tau(\theta) = \frac{G(\theta) \cdot LAI \cdot CI(\theta)}{\cos\theta}, \qquad (4)$$

where G is the geometry factor as a function of viewing direction θ. We approximate SF based on Beer's law (Warren Wilson, 1967, Yang et al., 2017), i.e.,

$$SF = \frac{1 - \exp(-\tau)}{\tau} \qquad (5)$$

Using SF from Equation (3) allows us to solve Equation (5) for τ. Finally, CI can be then estimated from Equation (4) as:

$$CI(\theta) = \frac{\tau(\theta) \cdot \cos\theta}{G(\theta) \cdot LAI} \qquad (6)$$

The geometry factor may not be always precisely known, but G approaches a value of 0.5 around 57 degrees irrespective of orientation of canopy elements (Ross, 1981; Jupp et al., 2009; Woodgate et al., 2015). We adopt the G value of 0.5 in the CI retrieval while using VESDR products collected with the suitable sun-sensor geometry—observations with view zenith angle around 57 degrees—as an input.

Study Sites and Data for Validation

Australia's Terrestrial Ecosystem Research Network (TERN) is a distributed research infrastructure providing intensive monitoring of the physical and chemical environmental and biological components of ecosystems (Karan et al., 2016). *In-situ* measurements of CI at different heights using towers were collected at five of the TERN's SuperSites, which together offer a diverse range of canopy structure from short and sparse to dense and tall forest. Their locations and vegetation characteristics are summarized in Table 1.

Table 1. Study site characteristics.

Site code	Site name	Lat (deg)	Lon (deg)	Forest type	Overstory	Tree height (m)	LAI	References	*In-situ* data collection
CBLP	Cumberland plain	−33.62	150.72	Remnant eucalypt woodland	EMo, EF	23	1.20	Beringer et al., 2016	2019/2
TUMB	Tumbarumba	−35.66	148.15	Managed open wet schlerophyll eucalyptus forest	EDe, EDa	40	2.4	Keith et al., 2009	2019/2
VICD–Whroo	Whroo	−36.67	145.03	Box woodland	EMi, EL	15.3 ± 0.2	1.0	Beringer et al., 2016	2013/7
VICD-Wombat	Wombat	−37.42	144.09	Open eucalypt woodland	EO, ERa, ERu	25	1.75	Haverd et al., 2013	2013/7
WRRA	Warra	−43.10	146.65	Tall wet eucalypt forest	EO	55	5.84	Neyland et al., 2000	2013/8

In the column "Overstory" EMo, Eucalyptus moluccana; EF, Eucalyptus fibrosa; EDe, Eucalyptus delegatensis; EDa, Eucalyptus dalrympleana; EMi, Eucalyptus microcarpa; EL, Eucalyptus leucoxylona; EO, Eucalyptus obliqua; ERa, Eucalyptus radiata; ERu, Eucalyptus rubida.

The Cumberland Plain flux station is located in a dry sclerophyll forest in the Hawkesbury Valley in central New South Wales (site coordinates: 33.6152S, 150.7236E). The canopy is dominated by *Eucalyptus moluccana* and *Eucalyptus fibrosa*, which host an expanding population of mistletoe. Average canopy height is 23 m. The Wombat forest research site (37.42S, 144.09E) is located in the Wombat State Forest, Victoria, SE Australia. The site is a secondary regrowth Eucalypt forest that was last harvested in 1980. Dominant tree species are Messmate Stringybark (*Eucalyptus obliqua*),

Narrow Leaf Peppermint (*Eucalyptus radiata*) and Candlebark (*Eucalyptus rubida*) with an average canopy height of 25 m. The understory consists mainly of patchy grasses. The second dry sclerophyll site at Whroo (36.67 S, 145.03E) in Victoria, Australia is box ironbark woodland with lower tree height and canopy cover. The vegetation was dominated by two main Eucalypt species: Gray Box (*Eucalyptus microcarpa*) and Yellow Gum (*Eucalyptus leucoxylon*). The mean tree height at Whroo was 15.3 ± 0.2 m. The Tumbarumba flux station is located in the Bago State forest in south eastern New South Wales (35.6566S, 148.1517E). The forest is classified as wet sclerophyll, the dominant species is *Eucalyptus delegatensis*, and average tree height is 40 m. The Bago State Forest is adjacent to the south west slopes of southern New South Wales and the 48,400 ha of native forest have been managed for wood production for over 100 years. Warra Long Term Ecological Research (LTER) site (43.09S, 146.66E; Neyland et al., 2000) is located in SW Tasmania, Australia. It represented a tall *E. obliqua* wet forest with rainforest understory and a dense man-fern (*Dicksonia antarctica*) ground-layer. The forests around the Warra site had mature heights in excess of 55 m: the tallest *E. obliqua* within the LTER reaches a height of 90 m. Both Tumbarumba and Warra sites experienced bushfires in the last 2 years. Our site descriptions, *in situ* validation data, as well as the retrievals with DSCOVR EPIC data correspond to the pre-fire period.

The vertical profiles of CI (i.e., Cl for all vegetation above the given height) were obtained by climbing scaffolding/flux towers and taking leveled digital hemispherical photos (DHPs) along the climbed height. At each profile, usually several series of DHPs were acquired using a Nikon CoolPix 4500 digital camera with a Nikon FC-E8 fisheye lens under diffuse illumination conditions, following the protocol of Zhang et al. (2005). No leaves were present directly above the camera to obscure its field of view. The towers were masked from the photos before the analysis. The reference DHPs were obtained above the top of the tree canopy. Gap fraction profiles were extracted from the blue channel at view zenith angle 57° with the DHP software (v4.5; Canada Center for Remote Sensing, Ottawa, Canada). Various methods exist to estimate CI (see Gonsamo and Pellikka, 2009; Woodgate et al., 2015; Chianucci et al., 2019). The method of Leblanc et al. (2005b) was previously shown to provide reliable clumping estimates in both simulated and real canopies (Pisek et al., 2011; Leblanc and Fournier, 2014; Woodgate et al., 2017; Yan et al., 2019):

$$CI_{CLX}(\theta) = \frac{n \ln[\overline{P(\theta)}]}{\sum_{k=1}^{n} \ln[P_k(\theta)] / CI_{CCk}(\theta)} \quad (7)$$

where $CI_{CLX}(\theta)$ is CI determined with the method of Leblanc et al. (2005b), $CI_{CCk}(\theta)$ is the CI of segment k using the corrected Chen and Cihlar (1995) method by Leblanc (2002), $P_k(\theta)$ is the gap fraction of segment k, n is the total number of segments (segment size = 15°), $\overline{P(\theta)}$ is the mean gap fraction, and θ is the view zenith angle. The segment size was set to 15° as it produced the smallest error out of three segment sizes tested (15, 45, and 90°) in the mimicked virtual Eucalypt stand by Woodgate et al. (2017). Equation (7) is used to estimate CI at each climbed height.

Spatial Representativeness Assessment

An analysis of the surface heterogeneity representativeness (Román et al., 2009; Wang et al., 2017) was used in this study to determine whether direct "point-to-pixel" comparisons were appropriate for all validation sites. The method employs variograms calculated using surface albedos obtained using shortwave near nadir surface reflectances (0.25–5.0 um) generated from cloud free 30 m Landsat/Operational Land Imager (OLI) data (Román et al., 2009). To facilitate the 10 km subset, the Landsat imagery was resampled to 90 m spatial resolution. The OLI data were collected as close to the sampling date as possible. Where valid imagery was not available within a reasonable window of the sampling date, imagery from the corresponding season of a different year was used. As such, the analysis was done to illustrate the representativeness of the tower site with respect to a particular point in time.

When a measurement site is spatially representative, the overall variability between the internal (1.0 km) components (here Landsat pixel reflectances) of the measurement site and its adjacent landscape corresponding to the satellite pixel footprint should be similar in magnitude. The variogram estimator (variance of the albedo values obtained from the resampled 90 m spatial resolution Landsat imagery at the given distance) usually levels off upon reaching the variogram range indicating the distance where they are no longer spatially correlated (e.g., Figure 1B, points). The site can be simply judged to be spatially representative with respect to the given footprint when the sill value (i.e., the ordinate value of the range at

which the variogram levels off to an asymptote) is <5.0e-04 (Román et al., 2009; Wang et al., 2017).

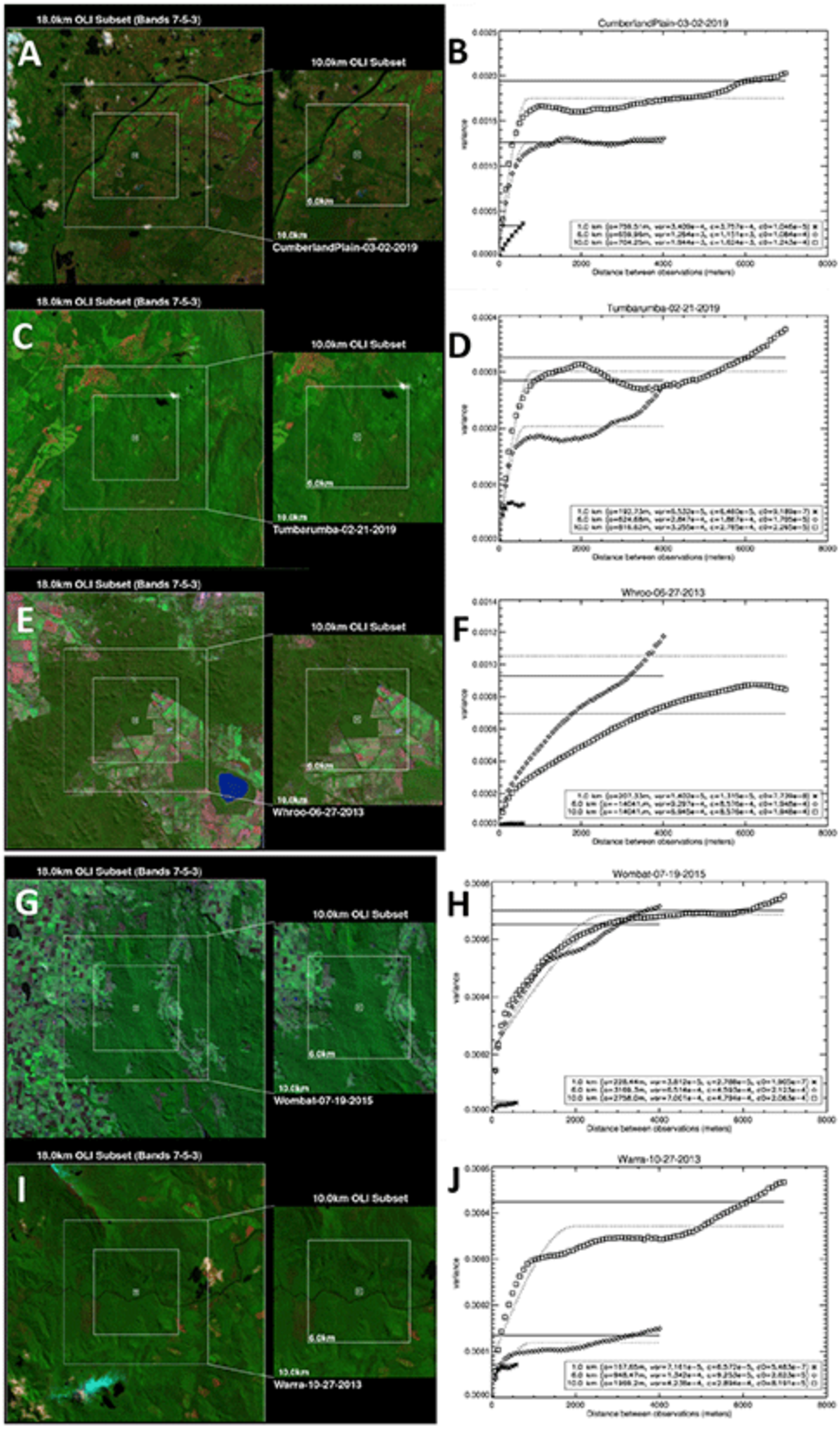
18.0km OLI Subset (Bands 7-5-3)
A
10.0km OLI Subset
6.0km
10.0km
CumberlandPlain-03-02-2019
B
CumberlandPlain-03-02-2019
variance
Distance between observations (meters)
18.0km OLI Subset (Bands 7-5-3)
C
10.0km OLI Subset
6.0km
10.0km
Tumberumba-02-21-2019
D
Tumbarumba-02-21-2019
variance
Distance between observations (meters)
18.0km OLI Subset (Bands 7-5-3)
E
10.0km OLI Subset
6.0km
10.0km
Whroo-05-27-2013
F
Whroo-05-27-2013
variance
Distance between observations (meters)
18.0km OLI Subset (Bands 7-5-3)
G
10.0km OLI Subset
6.0km
10.0km
Wombat-07-19-2015
H
Wombat-07-19-2015
variance
Distance between observations (meters)
18.0km OLI Subset (Bands 7-5-3)
I
10.0km OLI Subset
6.0km
10.0km
Warra-10-27-2013
J
Warra-10-27-2013
variance
Distance between observations (meters)

Figure 1. **(A–J)** Shortwave BRF composites centered at TERN sudy sites. Variogram estimators (points), spherical model results (dotted curves), and sample variances (solid straight lines) obtained over the sites with OLI subsets and spatial elements of 1, 6, and 10 km as a function of distance between observations. Variogram legend explanations: a–variogram range; var–sample variance; c–variogram sill; c0–nugget variance.

RESULTS

The spatial representativeness was evaluated at three different footprint sizes: 1, 6, and 10 km (Figure 1). All five sites may be considered spatially representative at the smallest 1 km pixel footprint around the time of *in situ* measurements, although the variogram curve did not reach clear asymptote at Cumberland Plain (Figure 1B). The spatial heterogeneity increased with the footprint for all sites (here indicated with an increase in sill value). Only two sites (Tumbarumba and Warra) preserved the spatial representativeness all the way to the nominal pixel resolution of 10 km for the DSCOVR EPIC VESDR product (sill value < 5.0e-04).

The landscape heterogeneity within the DSCOVR EPIC VESDR product pixel resolution also manifested itself in the agreement with the *in situ* measured values of CI over the different sites. Good agreement between the EPIC CI-derived value and *in situ* measurements (i.e., EPIC CI retrievals intersecting with the vertical profiles collected with DHP) was observed over the most homogeneous sites, Tumbarumba (Figure 2B) and Warra (Figure 2E). The EPIC CI values did not show agreement with the vertical profiles of CI at Whroo (Figure 2C) and Wombat (Figure 2D). The EPIC CI value was found to intersect the range of CI variation with height at Cumberland Plain site (Figure 2A).

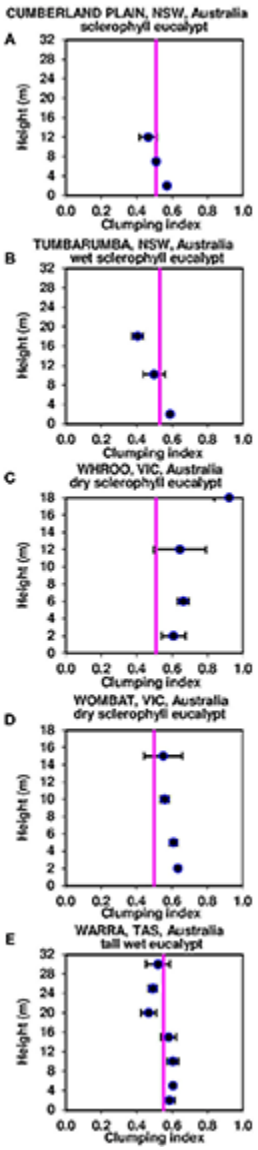

FIGURE 2. Vertical profiles of foliage clumping from *in-situ* measurements with ±1 standard deviation bars. **(A)** Cumberland Plain, **(B)** Tumbarumba, **(C)** Whroo, **(D)** Wombat, and **(E)** Warra. Clumping index values from DSCOVR EPIC data obtained around the same time of the year are marked with vertical purple line (For interpretation of the references to color in this figure legend, the reader is referred to the web version of this article).

DISCUSSION

This study explored the potential of using an alternative approach, along with unique observations and products from the Earth Polychromatic

Imaging Camera (EPIC) onboard the Deep Space Climate Observatory (DSCOVR) satellite, to estimate the clumping index (CI).

First, it must be acknowledged that our measurements are limited to single location (tower) and moment in time for a vertical profile at each site. Any factors that cause an increase in the variance of gap fraction (e.g., canopy type and size, density, disturbances) would imply that a higher number of samples is needed (Nilson et al., 2011). The relatively coarse nominal resolution of the EPIC sensor at 10 km makes the product validation with *in situ* data a particularly challenging exercise. Out of five TERN sites with available *in situ* CI measurements included in this study, only Tumbarumba and Warra may be deemed to be spatially representative of the relatively coarse EPIC nominal pixel footprint. It is encouraging that CI values obtained with EPIC data provided good agreement with the *in situ* measurements over these two sites (Figures 2B,E). It shall be noted that the spatial representativeness approach used in this study does not include land cover or vegetation type information. Many modeling studies using flux tower data will use classification layer and assess the various proportions of classes to determine whether a site is representative. Using Landsat OLI data and variograms as originally proposed by Román et al. (2009) and applied in this study may provide more detail and catch possible variation that may not be assessed with the land cover or vegetation type based evaluation. It shall be noted that our spatial representativeness evaluations may be valid only for the indicated moments in time. Although all five sites are classified as broadleaf evergreen vegetation dominated by Eucalypts, they may still experience seasonal dynamics of vegetation growth and decay (Duursma et al., 2016). The spatial representativeness of individual sites may change accordingly throughout seasons as well. Additionally, Tumbarumba and Warra sites experienced intensive bushfires in 2019 and 2020, which may have affected their current spatial representativeness as well. We recommend that future studies would follow our example and carry the spatial representativeness assessments to match the moment in time when the *in situ* measurements are collected.

The best agreement was usually not observed with the *in situ* measurements acquired close to the ground (h =2 m), but rather with those taken at a distance higher up in the canopy. Similar behavior was previously observed in case of CI estimates obtained with other EO sensors as well (Pisek et al., 2013, 2015), as satellite measurements respond primarily to

the structural effects in upper levels of canopies (Pisek et al., 2015). This feature will be further exacerbated if the observations are made under oblique angles (Biriukova et al., 2020), like in our study. Ground measurements may be also biased by any lower vegetation/understory layers that would make the foliage distribution more random. Indeed there was an understory layer present at Tumbarumba and Warra when the *in situ* measurements were taken and the comparison with DSCOVR EPIC data was done (i.e., pre-2019/2020 fire period). Lower shrubs are also present around Cumberland Plain, another site where the EPIC CI retrievals intersected with the vertical profile of CI measured along the tower height (Figure 2A). This agreement might be purely coincidental and treated with caution, since the Cumberland Plain site was the least spatially representative site at the EPIC nominal resolution. The actual EPIC measurements used in this study may in fact come even from an area twice as large due to the large oblique angles around the hinge region (Delgado-Bonal et al., 2020). The two sites from Victoria, Whroo and Wombat, were found to be spatially non-representative at the EPIC nominal resolution. EPIC CI estimates correspondingly did not match with the available *in situ* measurements (Figures 2C,D), presumably because they did not capture the variability within the greater area within the EPIC pixel footprint. The general range of the *in situ* measured CI reported in this study agreed with values reported from other Eucalyptus-dominated sites in Australia (Macfarlane et al., 2007; Woodgate et al., 2017).

Our exploratory study is very pertinent to the on-going efforts to map and incorporate clumping information in ecosystem modeling at different scales (Ryu et al., 2012; He et al., 2018). It is very encouraging we showed it is possible to obtain such good quality results using a different approach and different EO data that are very much comparable to previous efforts of mapping CI from space (Chen et al., 2005; Pisek et al., 2013; Wei and Fang, 2016; Jiao et al., 2018). This general agreement between different retrieval strategies and input data sources is important for increasing overall confidence, justification, and general validity of clumping information retrieval from space in the future.

As a part of the analysis, we also assessed the spatial representativeness of the five TERN forest ecosystem sites for validation of satellite retrievals using a different approach and extending the analysis all the way to the spatial resolution of EPIC sensor compared to Griebel et al. (2020). Our

results improve our understanding of product uncertainty both in terms of the representativeness of the field data collected over the TERN sites and its relationship to Earth Observation data at different spatial resolutions.

DATA AVAILABILITY STATEMENT

The raw data supporting the conclusions of this article will be made available by the authors, without undue reservation.

AUTHOR CONTRIBUTIONS

JP conceived the project, collected data, ran data analysis and interpretation, and led the writing of manuscript. AE carried the spatial representativeness analysis. WW helped with the field collection at Tumbarumba. SA, AE, EP, CS, TW, WW, and YK discussed the results and contributed to writing the manuscript. All authors contributed to the article and approved the submitted version.

FUNDING

This study was supported from Estonian Research Council Grants PUT232, PUT1355, and Mobilitas Pluss MOBERC11. WW was supported by an Australian Research Council DECRA Fellowship (DE190101182). The OzFlux and SuperSite network was supported by the National Collaborative Infrastructure Strategy (NCRIS) through the Terrestrial Ecosystem Research Network (TERN). YK was supported by the NASA DSCOVR project under grant 80NSSC19K0762.

ACKNOWLEDGMENTS

We thank two reviewers for the constructive comments that helped to improve the paper. We thank Marja-Liisa Plats for her assistance with figure

editing.

REFERENCES

Beringer, J., Hutley, L. B., McHugh, I., Arndt, S. K., Campbell, D., Cleugh, H. A., et al. (2016). An introduction to the Australian and New Zealand flux tower network – OzFlux. *Biogeosciences* 13, 5895–5916. doi: 10.5194/bg-13-5895-2016

Biriukova, K., Celesti, M., Evdokimov, A., Pacheco-Labrador, J., et al. (2020). Effects of varying solar-view geometry and canopy structure on solar-induced chlorophyll fluorescence and PRI. *Int. J. Appl. Earth Observ. Geoinform.* 89:102069. doi: 10.1016/j.jag.2020.102069

Chen, B., Liu, J., Chen, J. M., Croft, H., Gonsamo, A., He, L., et al. (2016). Assessment of foliage clumping effects on evapotranspiration estimates in forested ecosystems. *Agric. For. Meteorol*. 216, 82–92. doi: 10.1016/j.agrformet.2015.09.017

Chen, J., Menges, C., and Leblanc, S. (2005). Global mapping of foliage clumping index using multi-angular satellite data. *Remote Sens. Environ*. 97, 447–457. doi: 10.1016/j.rse.2005.05.003

Chen, J. M., and Black, T. A. (1992). Defining leaf area index for non-flat leaves. *Plant Cell Environ.* 15, 421–429. doi: 10.1111/j.1365-3040.1992.tb00992.x

Chen, J. M., and Cihlar, J. (1995). Plant canopy gap-size analysis theory for improving optical measurements of leaf-area index. *Appl. Opt*. 34, 6211–6222. doi: 10.1364/AO.34.006211

Chen, J. M., Ju, W. M., Cihlar, J., Price, D., Liu, J., Chen, W. J., et al. (2003). Spatial distribution of carbon sources and sinks in Canada's forests. *Tellus Series B-Chem. Phys. Meteorol.* 55, 622–641. doi: 10.3402/tellusb.v55i2.16711

Chen, J. M., Mo, G., Pisek, J., Liu, J., Deng, F., Ishizawa, M., et al. (2012). Effects of foliage clumping on the estimation of global terrestrial gross primary productivity. *Global Biogeochem. Cycles* 26:GB1019. doi: 10.1029/2010GB003996

Chianucci, F., Zou, J., Leng, P., Zhuang, Y., and Ferrara, C. (2019). A new method to estimate clumping index integrating gap fraction averaging with the analysis of gap size distribution. *Can. J. For. Res*. 49, 471–479. doi: 10.1139/cjfr-2018-0213

Delgado-Bonal, A., Marshak, A., Yang, Y., and Oreopoulos, L. (2020). Daytime variability of cloud fraction from DSCOVR/EPIC observations. *J. Geophys. Res. Atmosph.* 125:e2019JD031488. doi: 10.1029/2019JD031488

Duursma, R. A., Gimeno, T. E., Boer, M. M., Crous, K. Y., Tjoelker, M. G., and Ellsworth, D. S. (2016). Canopy leaf area of a mature evergreen Eucalyptus woodland does not respond to elevated atmospheric [CO2] but tracks water availability. *Glob. Chang. Biol*. 22, 1666–1676. doi: 10.1111/gcb.13151

Gonsamo, A., and Pellikka, P. (2009). The computation of foliage clumping index using hemispherical photography. *Agricult. Forest Meteorol.* 149, 1781–1787. doi: 10.1016/j.agrformet.2009.06.001

Griebel, A., Metzen, D., Pendall, E., Burba, G., and Metzger, S. (2020). Generating Spatially Robust Carbon Budgets From Flux Tower Observations. 47(3), e2019GL085942. doi: 10.1029/2019gl085942

Haverd, V., Raupach, M. R., Briggs, P. R., Canadell, J. G., Isaac, P., Pickett-Heaps, C., et al. (2013). Multiple observation types reduce uncertainty in Australia's terrestrial carbon and water cycles. *Biogeosciences* 10, 2011–2040. doi: 10.5194/bg-10-2011-2013

He, L., Chen, J. M., Gonsamo, A., Luo, X., Wang, R., Liu, Y., et al. (2018). Changes in the shadow: the shifting role of shaded leaves in global carbon and water cycles under climate change.

Geophys. Res. Lett. 45, 5052–5061. doi: 10.1029/2018GL077560

He, L., Chen, J. M., Pisek, J., Schaaf, C. B., and Strahler, A. H. (2012). Global clumping index map derived from the MODIS BRDF product. *Remote Sens. Environ*. 119, 118–130. doi: 10.1016/j.rse.2011.12.008

Hill, M., Román, M. O., Schaaf, C. B., Hutley, L., and Brannstrom, C. (2011). Characterizing vegetation cover in global savannas with an annual foliage clumping index derived from the MODIS BRDF product. *Remote Sens. Environ.* 115, 2008–2024. doi: 10.1016/j.rse.2011.04.003

Jiao, Z., Dong, Y., Schaaf, C. B., Chen, J. M., Román, M., Wang, Z., et al. (2018). An algorithm for the retrieval of the clumping index (CI) from the MODIS BRDF product using an adjusted version of the kernel-driven BRDF model. *Remote Sens. Environ*. 209, 594–611. doi: 10.1016/j.rse.2018.02.041

Jupp, D. L. B., Culvenor, D. S., Lovell, J. L., Newnham, G. J., Strahler, A. H., and Woodcock, C. E. (2009). Estimating forest lai profiles and structural parameters using a ground-based laser called 'echidna. *Tree Physiol*. 29, 171–181. doi: 10.1093/treephys/tpn022

Karan, M., Liddell, M., Prober, S. M., Arndt, S., Beringer, J., Boer, M., et al. (2016). The Australian supersite network: a continental, long-term terrestrial ecosystem observatory. *Sci. Total Environ*. 568, 1263–1274. doi: 10.1016/j.scitotenv.2016.05.170

Keith, H., Mackey, B. G., and Lindenmayer, D. B. (2009). Re-evaluation of forest biomass carbon stocks and lessons from the world's most carbon-dense forests. *Proc. Natl. Acad. Sci. U.S.A*. 106, 11635–11640. doi: 10.1073/pnas.0901970106

Knyazikhin, Y., Song, W., Yang, B., Park, T., and Myneni, R. B. (2017). *DSCOVR EPIC Vegetation Earth System Data Record*. Science Data Product Guide.

Kuusk, A. (2018). "Canopy radiative transfer modeling," in *Comprehensive Remote Sensing. V. 3, Terrestrial Ecosystems*, ed S. Liang (Elsevier), 9–22. doi: 10.1016/B978-0-12-409548-9.10534-2

Leblanc, S. C., and Fournier, R. A. (2014). Hemispherical photography simulations with an architectural model to assess retrieval of leaf area index. *Agricult. Forest Meteorol.* 194, 64–76. doi: 10.1016/j.agrformet.2014.03.016

Leblanc, S. G. (2002). Correction to the plant canopy gap-size analysis theory used by the Tracing Radiation and Architecture of Canopies instrument. *Appl. Opt.* 41, 7667–7670. doi: 10.1364/AO.41.007667

Leblanc, S. G., Chen, J. M., Fernandes, R., Deering, D. W., and Conley, A. (2005b). Methodology comparison for canopy structure parameters extraction from digital hemispherical photography in boreal forests. *Agric. For. Meteorol*. 129, 187–207. doi: 10.1016/j.agrformet.2004.09.006

Leblanc, S. G., Chen, J. M., White, H. P., Latifovic, R., Lacaze, R., and Roujean, J. L. (2005a). Canada-wide foliage clumping index mapping from multiangular POLDER measurements. *Can. J. Remote Sens*. 31, 364–376. doi: 10.5589/m05-020

Leblanc, S. G., Chen, J. M., White, P. H., Cihlar, J., Roujean, J.-L., and Lacaze, R. (2001). "Mapping vegetation clumping index from directional satellite measurements," in *Proceedings of the Symposium on Physical Signatures and Measurements in Remote Sensing, Aussois* (Toulouse: CNES), 450–459.

Lowe, A. J., Phinn, S., Thurgate, N., Liddell, M., Lindenmayer, D., Byrne, M., et al. (2016). *Building a New Continental, Hierarchically-Scaled Ecosystem Monitoring Network in Australia. Terrestrial Ecosystem Research Infrastructures: Challenges, New Developments and Perspectives*. Boca Raton, FL: CRC Press | Taylor & Francis Group.

Lyapustin, A., Wang, Y., Korkin, S., and Huang, D. (2018). MODIS Collection 6 MAIAC algorithm. *Atmos. Meas. Tech*. 11, 5741–5765. doi: 10.5194/amt-11-5741-2018

Macfarlane, C., Hoffman, M., Eamus, D., Kerp, N., Higginson, S., McMurtrie, R., et al. (2007). Estimation of leaf area index in eucalypt forest using digital photography. *Agricult. Forest Meteorol.* 143, 176–188. doi: 10.1016/j.agrformet.2006.10.013

Marshak, A., Herman, J., Adam, S., Karin, B., Carn, S., Cede, A., et al. (2018). Earth observations from DSCOVR EPIC instrument. *Bull. Am. Meteorol. Soc*. 99, 1829–1850. doi: 10.1175/BAMS-D-17-0223.1

Neyland, M. G., Brown, M. J., and Su, W. (2000). Assessing the representativeness of longterm ecological research sites: a case study at Warra in Tasmania. *Aust. Forest*. 63, 194–198. doi: 10.1080/00049158.2000.10674831

Nilson, T. (1971). A theoretical analysis of the frequency of gaps in plant stands. *Agric. Meteorol*. 8, 25–38. doi: 10.1016/0002-1571(71)90092-6

Nilson, T., Kuusk, A., Lang, M., Pisek, J., and Kodar, A. (2011). Simulation of statistical characteristics of gap distribution in forest stands. *Agric. For. Meteorol*. 151, 895–905. doi: 10.1016/j.agrformet.2011.02.009

Pisek, J., Govind, A., Arndt, S. K., Hocking, D., Wardlaw, T. J., Fang, H., et al. (2015). Intercomparison of clumping index estimates from POLDER, MODIS, and MISR satellite data over reference sites. *ISPRS J. Photogram. Remote Sens.* 101, 47–56. doi: 10.1016/j.isprsjprs.2014.11.004

Pisek, J., Lang, M., Nilson, T., Korhonen, L., and Karu, H. (2011). Comparison of methods for measuring gap size distribution and canopy nonrandomness at Järvselja RAMI (RAdiation transfer Model Intercomparison) test sites. *Agric. For. Meteorol*. 151, 365–377. doi: 10.1016/j.agrformet.2010.11.009

Pisek, J., Ryu, Y., Sprintsin, M., He, L., Oliphant, A. J., Korhonen, L., et al. (2013). Retrieving vegetation clumping index from Multiangle Imaging SpectroRadiometer (MISR) data at 275m resolution. *Remote Sens. Environ*. 138, 126–133. doi: 10.1016/j.rse.2013.07.014

Román, M. O., Schaaf, C. B., Woodcock, C. E., Strahler, A. H., Yang, X., Braswell, R. H., et al. (2009). The MODIS (CollectionV005) BRDF/albedo product: assessment of spatial representativeness overforested landscapes. *Remote Sens. Environ.* 113, 2476–2498. doi: 10.1016/j.rse.2009.07.009

Ross, J. (1981). *The Radiation Regime and Architecture of Plant Stands.* The Hague: Junk Publishers, 391. doi: 10.1007/978-94-009-8647-3

Ryu, Y., Baldocchi, D. D., Black, T. A., Detto, M., Law, B. E., Leuning, R., et al. (2012). On the temporal upscaling of evapotranspiration from instantaneous remote sensing measurements to 8-day mean daily-sums. *Agricult. Forest Meteorol.* 152, 212–222. doi: 10.1016/j.agrformet.2011.09.010

Ryu, Y., Baldocchi, D. D., Kobayashi, H., van Ingen, C., Li, J., Black, T. A., et al. (2011). Integration of MODIS land and atmosphere products with a coupled-process model to estimate gross primary productivity and evapotranspiration from 1 km to global scales. Global Biogeochem. *Cycles* 25. doi: 10.1029/2011GB004053

Thomas, V., Noland, T., Treitz, P., and McCaughey, J. H. (2011). Leaf area and clumping indices for a boreal mixed-wood forest: lidar, hyperspectral, and Landsat models. *Int. J. Remote Sens*. 32, 8271–8297. doi: 10.1080/01431161.2010.533211

Wang, Z., Schaaf, C. B., Sun, Q., Kim, J., Erb, A. M., Gao, F., et al. (2017). Monitoring land surface albedo and vegetation dynamics using high spatial and temporal resolution synthetic time series from Landsat and the MODIS BRDF/NBAR/albedo product. *Int. J. Appl. Earth Obs. Geoinf*. 59, 104–117. doi: 10.1016/j.jag.2017.03.008

Warren Wilson, J. (1967). Stand structure and light penetration. III. Sunlit foliage area. *J. Appl. Ecol.* 4, 159–165. doi: 10.2307/2401415

Wei, S., and Fang, H. (2016). Estimation of canopy clumping index from MISR and MODIS sensors using the normalized difference hotspot and darkspot (NDHD) method: the influence of BRDF models and solar zenith angle. *Remote Sens*. *Environ*. 187, 476–491. doi: 10.1016/j.rse.2016.10.039

Wei, S., Fang, H., Schaaf, C. B., He, L., and Chen, J. M. (2019). Global 500 m clumping index product derived from MODIS BRDF data (2001–2017). *Remote Sens. Environ*. 232:111296. doi: 10.1016/j.rse.2019.111296

Woodgate, W., Armston, J. D., Disney, M., Suarez, L., Jones, S. D., Hill, M. J., et al. (2017). Validating canopy clumping retrieval methods using hemispherical photography in a simulated Eucalypt forest. *Agricult. Forest Meteorol.* 247, 181–193. doi: 10.1016/j.agrformet.2017.07.027

Woodgate, W., Jones, S. D., Suarez, L., Hill, M. J., Armston, J. D., Wilkes, P., et al. (2015). Understanding the variability in ground-based methods for retrieving canopy openness, gap fraction, and leaf area index in diverse forest systems. *Agric. For. Meteorol*. 205, 83–95. doi: 10.1016/j.agrformet.2015.02.012

Yan, G., Hu, R., Luo, J., Weiss, M., Jiang, H., Mu, X., et al. (2019). Review of indirect optical measurements of leaf area index: recent advances, challenges, and perspectives. *Agricult. Forest Meteorol.* 265, 390–411. doi: 10.1016/j.agrformet.2018.11.033

Yang, B., Knyazikhin, Y., Mõttus, M., Rautiainen, M., Stenberg, P., Yan, L., et al. (2017). Estimation of leaf area index and its sunlit portion from DSCOVR EPIC data: Theoretical basis. *Remote Sens. Environ*, 198, 69–84. doi: 10.1016/j.rse.2017.05.033

Zhang, Y. Q., Chen, J. M., and Miller, J. R. (2005). Determining digital hemispherical photograph exposure for leaf area index estimation. *Agricult. Forest Meteorol.* 133, 166–181. doi: 10.1016/j.agrformet.2005.09.009

Conflict of Interest: The authors declare that the research was conducted in the absence of any commercial or financial relationships that could be construed as a potential conflict of interest.

ORIGINAL RESEARCH
published: 30 March 2021
doi: 10.3389/frsen.2021.645794

Retrievals of Aerosol Optical Depth and Spectral Absorption From DSCOVR EPIC

Alexei Lyapustin[1*], Sujung Go[2], Sergey Korkin[3], Yujie Wang[2], Omar Torres[1], Hiren Jethva[3] and Alexander Marshak[1]

[1] National Aeronautics and Space Administration Goddard Space Flight Center, Greenbelt, MD, United States
[2] Joint Center for Earth Systems Technology, University of Maryland Baltimore County, Baltimore, MD, United States
[3] Goddard Earth Sciences Technology and Research, Universities Space Research Association, Columbia, MD, United States

Edited by:
Yingying Ma, Wuhan University, China

Reviewed by:
Lei Li, Chinese Academy of Meteorological Sciences, China
Xiangao Xia, Institute of Atmospheric Physics (CAS), China
Weizhen Hou, Chinese Academy of Sciences, China

***Correspondence:** Alexei Lyapustin, alexei.i.lyapustin@nasa.gov*

***Specialty section:** This article was submitted to Satellite Missions, a section of the journal Frontiers in Remote Sensing*

***Received:** 24 December 2020*
***Accepted:** 01 March 2021*
***Published:** 30 March 2021*

***Citation:** Lyapustin A, Go S, Korkin S, Wang Y, Torres O, Jethva H and Marshak A (2021) Retrievals of Aerosol Optical Depth and Spectral Absorption From DSCOVR EPIC. Front. Remote Sens. 2:645794. doi: 10.3389/frsen.2021.645794*

A new algorithm is described for joint retrievals of the aerosol optical depth and spectral absorption from EPIC observations in the UV—Vis spectral range. The retrievals are illustrated on examples of the wildfire smoke

events over North America, and dust storms over greater Sahara region in 2018. An initial evaluation of single scattering albedo (SSA) at 443 nm over these regions shows a good agreement with AERONET data, generally within the uncertainty of AERONET SSA of ± 0.03. A particularly good agreement is achieved for dust with R~0.62, rmse~0.02, negligible bias, and 85% points within the expected error. This new capability is part of version 2 MAIAC EPIC algorithm. The v2 algorithm has recently completed reprocessing of the EPIC record covering the period of 2015–2020.

Keywords: EPIC, MAIAC, aerosol, biomass burning, mineral dust, spectral absorption

INTRODUCTION

Absorption is an important aerosol property determining, along with its total loading, aerosol-radiation and aerosol-cloud interactions (Boucher et al., 2013). High natural variability and lack of detailed knowledge of aerosol absorption make it one of the largest sources of uncertainty in assessments of aerosol direct radiative effects (DRE) (Samset et al., 2018; Thorsen et al., 2020) and in current climate projections (IPCC: Climate Change, 2013). Information on spectral dependence of aerosol absorption provides a pathway to the speciation of absorbing aerosol components and chemical composition analysis (e.g., Schuster et al., 2016; Li et al., 2020b). The latest climate multi-model analysis showed that uncertainties in the mineral dust iron content give rise to ~85% uncertainty of dust DRE estimates by the models (Li et al., 2020a). Composition analysis of aerosol particles and investigation of toxicity and adverse health effects of different components is a central goal of the future NASA MAIA (Multi-Angle Imager for Aerosols) mission (Diner et al., 2018).

Historically, the Total Ozone Monitoring Sensor (TOMS) and Ozone Mapping Instrument (OMI) were the first spaceborne instruments providing initially qualitative, in form of UV Aerosol Index (UVAI) (Herman et al., 1997; Torres et al., 1998), and later quantitative information on aerosol absorption for cloud-free conditions (Torres et al., 1998, 2002, 2007, 2013, 2018; Ahn et al., 2014; Jethva et al., 2014), and most recently for the characterization of aerosol above clouds (Torres et al., 2012; Jethva et al.,

2018). The UV channels of these sensors were the key for two main reasons: (i) the surface is significantly darker than in the visible range, which reduces the respective uncertainty, and (ii) higher Rayleigh and aerosol optical depth in the UV increases sensitivity to absorption via increase in the multiple scattering of light. On the other hand, the UV range adds the uncertainty due to the aerosol layer height sensitivity (Torres et al., 1998, 2013) which plays only a minor role at longer wavelengths in the visible and near-IR.

The present OMAERUV algorithm of Aura/OMI retrieves aerosol optical depth (AOD) and single scattering albedo (SSA) using two channels, i.e., 354 and 388 nm. The algorithm relies on an ancillary data on spectral dependence of absorption compiled from different sources, including lab measurements (Jethva and Torres, 2011) and seasonal/regional climatological aerosol height from CALIOP CALIPSO observations (Torres et al., 2013). Because of the aerosol height sensitivity, the product is reported for several effective heights (0, 1.5, 3, 6, and 10 km). OMAERUV is currently the baseline algorithm used to process data from several instruments having UV capability, including DSCOVR/EPIC, OMPS on SNPP platform, as well as S5p/TropOMI (Torres et al., 2020), and GEMS (Kim et al., 2020) imaging spectrometers.

The near-simultaneous multi-angle imagery (e.g., MISR) extends the range of measurements and provides an additional information on aerosol particle size, shape and absorption (Kahn et al., 2010; Kahn and Gaitley, 2015). Finally, with adding the polarization dimension, the multi-angle spectro-polarimetric missions in development, such as MAIA (Diner et al., 2018), multi-angle polarimeters on PACE (Remer et al., 2019), or EUMETSAT EPS-SG/3MI (e.g., Fougnie et al., 2020), are expected to provide the most advanced global aerosol characterization including spectral refractive index, AOD and size distribution, as demonstrated by the processing of POLDER/PARASOL observations (Chen et al., 2020) with the Generalized Retrieval of Atmosphere and Surface Properties (GRASP) (Dubovik et al., 2011) algorithm.

In this work, we present a new approach to derive AOD and spectral aerosol absorption from observations of the Earth Polychromatic Imaging Camera (EPIC) onboard the Deep Space Climate Observatory (DSCOVR) satellite located at Lagrange-1 (L1) point. Due to DSCOVR's unique orbit, EPIC continuously observes the entire sunlit side of the Earth in 10

narrowband channels (317, 325, 340, 388, 443, 551, 680, 688, 764, and 779 nm) and provides 10–12 observations for the same surface area from dawn to dusk in summer, and 6–7 images in winter (Marshak et al., 2018). Given a reliable characterization of spectral surface reflectance by MAIAC, a well-calibrated set of EPIC's visible (443 and 680 nm) and UV channels (340 and 388 nm) offers a unique opportunity to simultaneously retrieve both optical depth (AOD) and spectral absorption of aerosols.

Below, the new approach to derive AOD and spectral aerosol absorption from EPIC is presented in section MAIAC EPIC Processing Algorithm. Analysis of the global EPIC dataset for 2018 is provided for both biomass burning smoke and mineral dust in sections Retrieval Examples From EPIC and AERONET Validation. AERONET (Holben et al., 1998) validation of single scattering albedo at 443 nm (SSA_{443}) shows a good correlation and retrieval accuracy comparable with AERONET product uncertainty. This approach is a part of the v2 MAIAC EPIC atmospheric correction algorithm described in detail in a companion paper (Lyapustin et al., submitted).

MAIAC EPIC PROCESSING ALGORITHM

The current development takes advantage of the baseline EPIC MAIAC algorithm over land, which includes cloud detection, characterization of spectral regression coefficients (SRC), aerosol retrievals with regional background aerosol models, and atmospheric correction resulting in surface reflectance and parameters of spectral bidirectional reflectance distribution function (BRDF) model. Below, we provide a brief outline of the standard MAIAC algorithm relevant to sections AOD - Spectral Absorption Algorithm to Detection of Smoke and Dust that introduce the new flexible inversion algorithm.

Outline of MAIAC Algorithm

MAIAC relies on a dynamic time series analysis, which helps separate relatively static surface properties from aerosols and clouds that are changing rapidly over time. Observing the same surface area over time requires resampling data on a regular spatial grid. In v2 MAIAC, we introduced a rotated Sinusoidal projection that minimizes spatial distortions (for detail, see Lyapustin et al., submitted). The original nadir spatial

resolution of EPIC is 8 km in the Blue band (443 nm) and 16 km in other bands due to 2 × 2 onboard aggregation. To raise the probability of cloud detection and capture maximal aerosol variability, we grid EPIC data to 10 km resolution. This results in oversampling in all bands except 443 nm, but the overhead in processing is minor given current computing resources. For simplicity, the fixed grid cells are called “pixels” further on.

MAIAC cloud detection includes several steps. It starts with traditional pixel-level spectral tests, including (1) the bright cloud test based on fixed thresholds; (2) 3 × 3 standard deviation test using pixel-specific thresholds, and (3) oxygen A and B-band test for high clouds. The next level of cloud detection follows aerosol retrievals: it filters high AOD values in 25 × 25 pixels window using threshold being a function of the cloud fraction in the spatial window. The final detection of residual clouds takes place during the atmospheric correction, and is based on the known spectral BRDF for each land pixel. For instance, it filters pixels when the derived reflectance at 443 nm exceeds the BRDF model prediction by more than 0.05. The last two steps provide a significant enhancement to the cloud mask. As a result, despite the coarse spatial resolution and lack of thermal channels, the overall achieved quality of MAIAC EPIC cloud detection is satisfactory for aerosol retrieval and atmospheric correction.

Retrieving spectral regression coefficient (SRC) is a central part of MAIAC that ensures separation of the surface and atmospheric signals in the top of atmosphere (TOA) measurements, and is required for aerosol retrievals over different land surface types globally. SRC is retrieved for cloud-free pixels as a minimum value for the ratios ρ_{443}/ρ_{680}, ρ_{388}/ρ_{680}, and ρ_{340}/ρ_{388}, where surface reflectance (SR) ρ is a result of Rayleigh atmospheric correction (for detail, see Lyapustin et al., 2018). To account for the angular dependence, the ratios are characterized in 4 bins of the cosine of solar zenith angle between 0.3 and 1, for the morning and afternoon observations separately. Because of higher uncertainties of atmospheric correction at 340 nm, and large difference in reflectance at 340 and 680 nm, we use the ratio 340/388 nm which is derived from observations near the local noon. Through these three ratios, we have an assessment of SR at 340, 388, and 443 nm from the measured 680 nm for each 10 km grid cell. Figure 1 gives an example of SRC for the North American continent for August 2018.

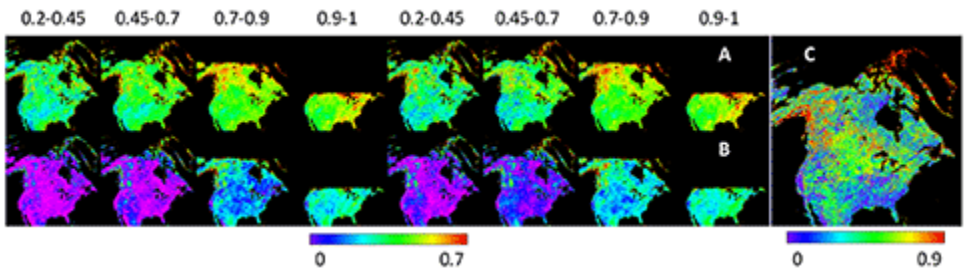

FIGURE 1. SRC of the MAIAC EPIC algorithm for August 2018 for North America and Greenland (surface reflectance ratios): **(A)** 443/680; **(B)** 388/680; **(C)** 340/388. Ratios **(A,B)** are shown for four cSZA bins labeled on the top from the morning on the left till the evening on the right. Ratio **(C)** is built from cloud-free measurements within ± 2 h from the local noon.

Following the MAIAC MODIS algorithm (Lyapustin et al., 2018), EPIC aerosol retrievals use eight prescribed regional aerosol models to represent global variability of aerosol properties over land. For cloud-free pixels, the surface reflectance at 443 nm is estimated from the red band, as described above, and AOD_{443} is derived by matching the measured TOA reflectance. Finally, for low to moderate atmospheric opacity ($AOD_{443} < 1.2$), MAIAC performs atmospheric correction and derives BRDF from the accumulated set of up to 80 previous observations at different angles.

AOD - Spectral Absorption Algorithm

With the knowledge of surface reflectance, we can use the Blue and UV channels to retrieve both AOD and spectral aerosol absorption. As mentioned before, spectral dependence of absorption carries information on particles chemical composition, including black-brown carbon partitioning for smoke, or hematite/goethite content for the mineral dust. In this work, spectral absorption is represented by a conventional power-law expression (e.g., Bond, 2001; Kirchstetter et al., 2004),

$$k_\lambda = k_0(\lambda/\lambda_0)^{-b} \text{ for } \lambda<\lambda_0, \text{ and } k_\lambda = k_0 \text{ for } \lambda\geq\lambda_0, \text{ where } \lambda_0=680nm \quad (1)$$

where k is an imaginary refractive index. In the limit of small (fine mode) particles, the spectral absorption exponent (SAE) b is related to the conventional Absorption Angstrom Exponent (AAE) that defines spectral dependence of the aerosol absorption optical depth (AAOD) as $b \sim AAE$-1. Below, the term SAE will be used to denote exponent b for convenience.

We are using Levenberg-Marquardt optimal fit algorithm (Marquardt, 1963) to derive the unknowns (AOD_{443}, k_0, b) by matching EPIC TOA reflectance at 340, 388, 443, and minimizing:

$$F^2 = \frac{1}{N}\sum\left[\frac{L_\lambda^m - L_\lambda^t}{L_\lambda^m}\right]^2 = min\{AOD_{443}, k_0, b\}, \qquad (2)$$

where L_λ^m and L_λ^t are measured and theoretical values. The retrievals are based on the look-up table (LUT) computed with combination of vector code IPOL (Emde et al., 2015; Korkin and Lyapustin, 2019) computing path reflectance and scalar code SHARM (Lyapustin and Knyazikhin, 2002; Lyapustin, 2005) generating atmospheric Green's function, transmittance, and spherical albedo.

The real refractive index (m) and size distribution for both smoke and dust models are fixed. Specifically, the smoke model uses m = 1.48 and a bimodal lognormal size distribution with r_{vf} = 0.14, σ_{vf} = 0.4, r_{vc} = 2.8, σ_{vc} = 0.6, and C_{vf}/C_{vc} = 2.5. Here, r_v, σ_v are the volumetric radius and standard deviation, and C_v is the volumetric concentration for the fine (f) and coarse (c) modes, respectively. The dust LUT uses model of randomly oriented spheroids (Dubovik et al., 2006) with m=1.56, following the dynamic model of Dubovik et al. (2002) for the Solar Village site where the relative concentration of the coarse mode dust grows rapidly with AOD.

The LUTs are generated on a 4 × 4 matrix of b = {0.1, 1.5, 3, 4} and k_0 = {0.001, 0.006, 0.011, 0.016} for smoke and k_0 = {0.0006, 0.0014, 0.0022, 0.003} for dust. For each combination of (k_0, b), the standard sub-LUT is computed for 8 AOD_{443} nodes {0.2, 0.5, 0.8, 1.2, 1.8, 2.8, 4.2, 6.}, 18 values of cosine of solar and view zenith angle from 0.15 to 1 with step 0.05, and 5 azimuths for the range 160–180° with step 5°. The sub-LUT is computed for 2 relative pressure levels, P = 1 and 0.7, for the surface height interpolation.

Calculation of TOA reflectance for each nodal combination ($k_{0,\,i}$, b_j, AOD_n) involves 4D-interpolation in view geometry and surface pressure/height. Generating output for an arbitrary set of parameters (k_0, b, AOD) involves further tri-linear interpolation over the respective nodes. The partial derivatives over these parameters are also estimated using the

neighbor nodes. Despite this rather crude estimation of partial derivatives, the algorithm generally features fast convergence on average within ~1–3% of the measurements. Overall, the developed LUT-based approach is numerically optimized and very efficient, resulting only in a fractional increase of the processing time compared to the standard MAIAC EPIC algorithm.

Finally, to account for the dependence on the aerosol plume height, we generated 2 smoke LUTs with an effective height at 1 and 4 km, generally representing the boundary layer aerosol and the long-range transport. We make separate retrievals for 2 heights and report them for the biomass burning smoke. In the v2 algorithm, the dust is represented by the boundary layer aerosol only.

The described flexible inversion algorithm is applied when AOD_{443} retrieved with the background aerosol model exceeds 0.6 or absorbing smoke or dust were detected (see section Detection of Smoke and Dust). This cut-off was introduced based on observation that our EPIC SSA_{443} retrievals are systematically biased low at lower AOD compared to those for higher AOD for the same events. A similar pattern is often observed in AERONET inversion dataset, which points to a generic nature of this artifact when, at lower AOD with higher role of uncertainties, a better fit to the measurements is often achieved at higher absorption. In certain cases, such pattern may, at least partially, be explained by aerosol humidification at high relative humidity accompanied by the increase of both AOD and SSA [e.g., Schafer et al. (2014), Figure 12].

The described approach was developed for regions with pure biomass burning or dust. A proper handling of cases with mixed dust and biomass burning, prevalent, for instance, in sub-Saharan Africa, will require further development.

Detection of Smoke and Dust

The OMI OMAERUV algorithm uses the UVAI to detect absorbing aerosols, along with the ancillary AIRS (Atmospheric Infrared Sounder) carbon monoxide (CO) serving as a tracer of carbonaceous aerosols to separate from dust. MAIAC uses a different, perhaps less flexible, approach developed for MODIS, where dust is limited to known dust source regions (see Lyapustin et al., 2018), and the smoke model is used globally

elsewhere. Because cloud edges and certain types of thin clouds often show spectral signatures similar to those of dust, such an approach was chosen in MAIAC to limit omission errors of cloud detection globally.

In v2 MAIAC EPIC algorithm, flexible inversion is performed after cloud detection and standard aerosol retrieval with associated residual cloud filtering. Designed to ensure high quality of its main product—atmospheric correction—MAIAC cloud filtering is rather conservative and often masks optically thick smoke and dust. To avoid such filtering, v2 algorithm uses AI > 4.5 for the initial identification of absorbing smoke. This AI is generated internally, while the official UVAI EPIC product is reported by the EPIC aerosol algorithm [Marshak et al., 2018; Ahn et al., in review]. While generally robust at moderate-to-high values AI > 4.5–6, AI is often low for the weakly absorbing smoke, e.g., from the Boreal forest fires or peat fires (e.g., Eck et al., 2009, 2019) with AI~1–2 where it cannot be used for reliable separation from clouds. AI can also take high values over some bright surfaces or over clouds, in particular at high sun/view zenith angles.

To overcome these issues, we developed a separate, more generic test for smoke detection. It relies on understanding that due to progressively increasing multiple scattering toward UV, aerosol absorption reduces atmospheric reflectance much stronger at 340 nm compared to 443 nm. Thus, we make three independent retrievals of AOD_{443} with the weakly absorbing background aerosol model using observed reflectance at 443 nm (τ_{443}^{443}), 388 nm (τ_{443}^{388}), and 340 nm (τ_{443}^{340}). The surface reflectance at each wavelength, required for AOD retrieval, is evaluated from 680 nm using MAIAC spectral ratios (SRC) (section Outline of MAIAC Algorithm). Note that AOD is always reported at the Blue band (443 nm, lower index) while the upper index indicates the wavelength used to derive AOD_{443} from the measurements. Spectrally increasing absorption caused by aerosol manifests in the ratios $\tau_{443}^{388}/\tau_{443}^{443}$ and $\tau_{443}^{340}/\tau_{443}^{388}$ notably below 1, while over non-absorbing clouds they are close to 1. Analysis of different smoke events shows that threshold 0.8 for both ratios detects the majority of smoke events even when the AI is low, and ensures robust separation from clouds, thus complementing the AI-based smoke detection.

We apply the described approach for dust detection in the dust regions as well, but only when the surface is sufficiently dark, or when the associated parameter *AOD uncertainty* (for definition, see Lyapustin et al.,

2018) is low (<0.1). Because most world deserts are bright and a single-band, single-angle AOD retrieval is unstable, we use the test AI > 3.5 as the baseline for dust detection.

Below, we provide examples and AERONET validation analysis for the wildfire smoke and mineral dust based on processed EPIC 2018 data over North America and Sahara/Middle East regions, respectively.

RETRIEVAL EXAMPLES FROM EPIC

Biomass Burning

With an overall increase in the wildfires over the last decades, 2018 witnessed a number of significant fire events, with the largest in August on the West Coast and central USA and in September in Alaska. In the first case, the smoke was injected above the boundary layer and was transported across the USA, reaching the East Coast.

Figure 2 shows an example of consecutive EPIC RGB images and MAIAC products from flexible retrievals, including AOD_{443}, k_0, b, and resulting single scattering albedo SSA_{443}. One can see that except extreme angles, the results are rather stable with variation of the viewing geometry. At high zenith angles, parameters b and k_0 often change in the opposite directions, b decreases and k_0 increases while keeping SSA_{443} approximately constant. The reported absorption values are typical and agree well with the range of values reported in AERONET climatological analyses (e.g., Giles et al., 2012).

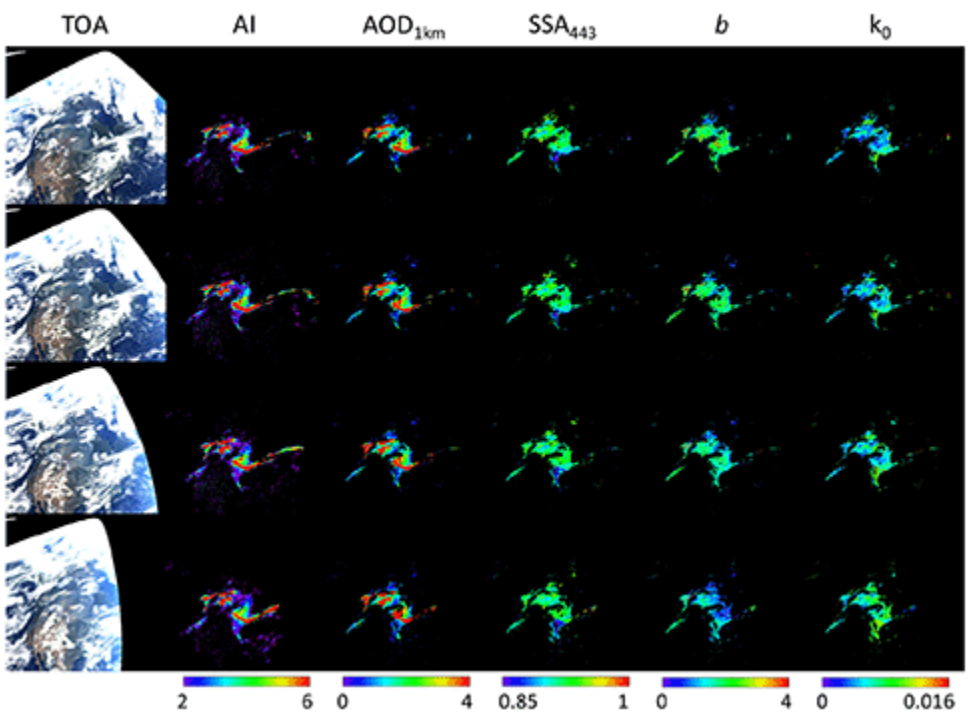

FIGURE 2. Illustration of flexible MAIAC EPIC retrievals for August 17, 2018. Shown are EPIC TOA RGB image, Aerosol Index (AI), and results of flexible retrievals for smoke at 1 km effective height.

The result in Figure 2 corresponds to aerosol in the boundary layer (mean height of 1 km). Figure 3 compares retrievals for smoke at 1 km and 4 km. The difference is significant. The higher single scattering albedo at 4 km reflects an obvious fact that it takes less absorption for the elevated smoke (with less Rayleigh atmosphere above) to create the same reduction in the reflected intensity as compared to the smoke near the surface. This is supported by a notably lower baseline absorption k_0 for smoke at 4 km, which is a proxy of spectrally neutral component of absorption, or a black carbon (e.g., Schuster et al., 2016). The observed spectral dependence (SAE, or b) for the elevated smoke may be smaller, similar, or larger than that at 1 km. For instance, $b_{4\text{km}}$ is lower for August 13, but it is slightly higher for the August 16 and 17. Analysis of all large wildfires in 2018 observed by EPIC shows that SSA_{443} is always higher for the lofted smoke, inverse being true for k_0.

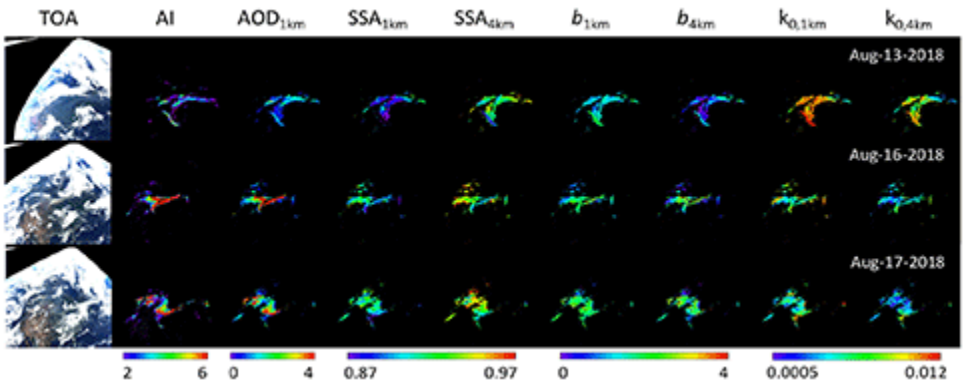

FIGURE 3. Effect of assumed smoke height (1 or 4 km) on retrieved spectral absorption.

Thus, the role of aerosol height cannot be overestimated: not only it changes the total aerosol absorption, by up to 0.02–0.05 for SSA_{443} in cases considered, but it also affects the interpretation of the results regarding aerosol chemical composition. For instance, the lower baseline absorption (k_0) and higher SAE for the lofted smoke would be interpreted as less black and more brown carbon as compared to the boundary layer smoke.

Mineral Dust

North Africa is a very active part of the world responsible for about 60% of the total global dust emissions (Tanaka and Chiba, 2006). We selected three episodes shown in Figure 4. The top row shows dust originating from the Bodélé depression on January 1, 2018. Bodélé represents a dry salt lake bed with very low hematite content or lack of thereof. It shows a very low absorption (b, k_0) and high SSA_{443}~0.94–0.96. It is interesting to note that a separate dust source is located right south of Bodélé with dust blown at a small angle (~15°) to the main Bodélé source in the South-West direction. The visual analysis shows that it has a yellow color in contrast to Bodélé's white dust. Figure 4 shows that EPIC resolves higher absorption and lower single scattering albedo (by ~0.03–0.05) from this satellite source. Such difference in absorption is distinct in the plume right at the source as well as in the "dust cloud" several hundred km downwind, which was emitted earlier.

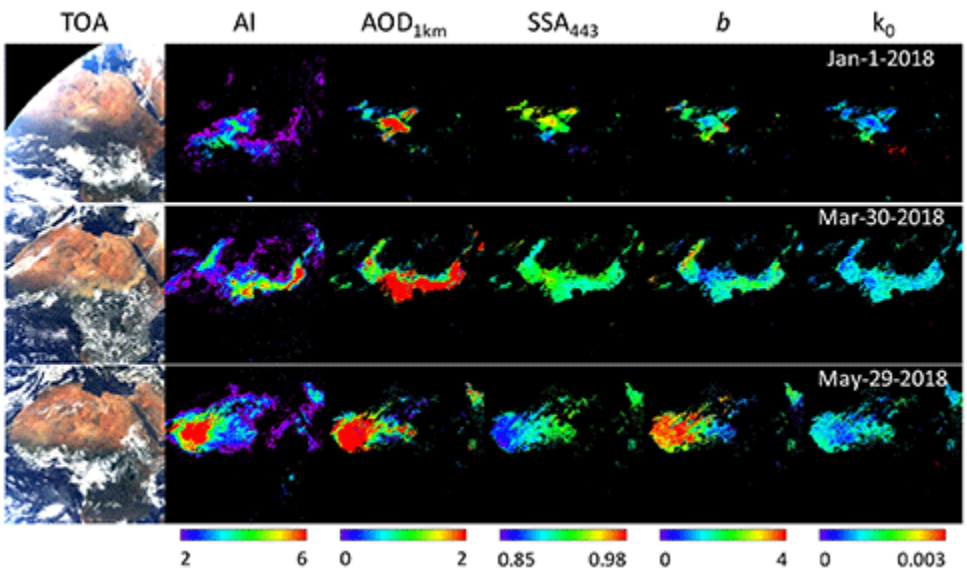

FIGURE 4. Examples of flexible MAIAC EPIC retrievals for three different dust storms over Sahara region. The columns are the same as in Figure 2.

The middle Figure 4 shows a dust mega-storm from Arabian Peninsula covering nearly the entire Sahel region for several days in late March–early May 2018. It features a moderate absorption typical for most dust emission sources in Sahara. On March 30 shown here, the Bodélé source was also active. Mixing of the respective white dust with the main dust plume shows as a well-resolved reduction in the total absorption, especially visible in lower SAE (*b*) and increased SSA.

Finally, the bottom row shows results for May 29 for the dust storm in West Africa. It is characterized by the highest spectral dependence of absorption (SAE) and lowest SSA in the Blue-UV range, indicating enhanced hematite content.

These examples show that v2 MAIAC EPIC provides a new information on spectral absorption with sufficient resolution and accuracy to differentiate sources and a change of absorption properties from the downwind mixing.

AERONET VALIDATION

To assess accuracy of the flexible retrieval algorithm, we performed validation analysis using AERONET version 3 (Giles et al., 2019) level 1.5 AOD data with improved cloud screening. MAIAC EPIC AOD_{443} data were limited to cosines of view and solar zenith angles above 0.45. We used average MAIAC AOD collocated in space and time within ± 20 km and ± 30 min for all AERONET stations, respectively.

Biomass Burning

AOD validation for North America in 2018 shows correlation coefficient $R > 0.8$ for most sites. An exception is the Rocky Mountain region and south-west USA, where the low background AOD and its low variability, exacerbated by a bright surface, result in lower *R*-values and a bias of ~0.15. This is typical for all sensors, including MODIS [e.g., see validation study by Jethva et al. (2019)]. It should be mentioned that such conditions are particularly challenging for EPIC making observations 4–16° from the retro-scattering direction where surface brightness is near its peak due to reduced shadowing. Figure 5 shows the summary validation of MAIAC EPIC AOD_{443} over North America in 2018. The first scatterplot (a) shows validation of standard MAIAC AOD (background model) for all 114 sites. The middle plot shows the same result for the reduced number of 103 sites where 11 sites with bright surface were excluded (*Bakersfield; Goldstone; KeyBiscayne; Neon_ONAQ; Railroad Valley; Sandila_NM_PSEL; TableMountain_CA; Tucson; UACJ_UNAM_ORS; White_Sands_HELSTF; Yuma*). Located in arid regions with generally low cloudiness, these 11 sites contribute disproportionate ~19% of the total matching points. With this exclusion, plot (b) shows improvement in all parameters of validation statistics. Finally, the last plot (c) shows validation of MAIAC AOD from flexible retrievals for 103 sites. In this case, we used results for the 1 km aerosol height, which are not generally representative. Nevertheless, flexible retrievals generally correct the low bias at high AOD values and raise *R* to 0.85 from 0.81.

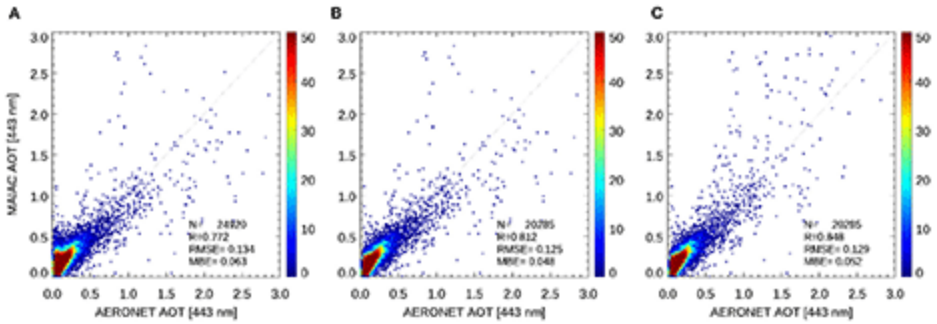

FIGURE 5. AERONET validation of MAIAC EPIC AOD_{443} over North America in 2018. **(A)** standard MAIAC AOD (background model) for all 114 sites; **(B)** is equivalent to **(A)** but for 103 sites with 11 bright sites excluded; **(C)** MAIAC AOD from flexible retrievals for 103 sites.

Validation of the single scattering albedo is shown in Figures 6, 7 for 17 AERONET/NEON sites with more or less significant statistics of at least 5 points. To enhance matchups, we extended the spatio-temporal range to ± 30 km and ± 3 h, and require at least 50% valid MAIAC retrievals in the spatial window. The results are shown in two groups, for aerosol at 1 km (Figure 6) and 4 km (Figure 7). Except *Rexburg_Idaho* and *Waskesiu* representing the boundary-layer aerosol, all other sites show a much better agreement with AERONET at 4 km, thus representing lofted smoke. While most sites indicate a general agreement with AERONET within stated uncertainty of ± 0.03, several sites, such as *Missoula, Table_Mountain, Neon_Cvalla, Waskesiu* (at 1 km) show a meaningful correlation.

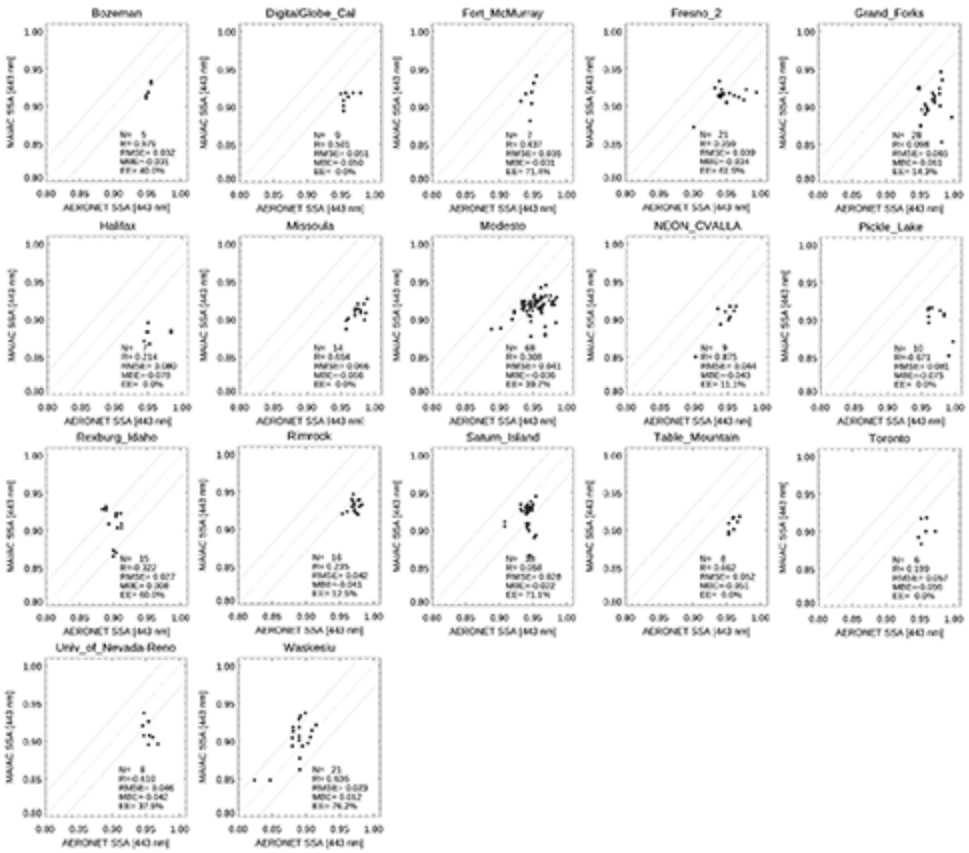

FIGURE 6. Site-level AERONET validation of MAIAC EPIC SSA_{443} over North America in 2018 for the effective aerosol height of 1 km.

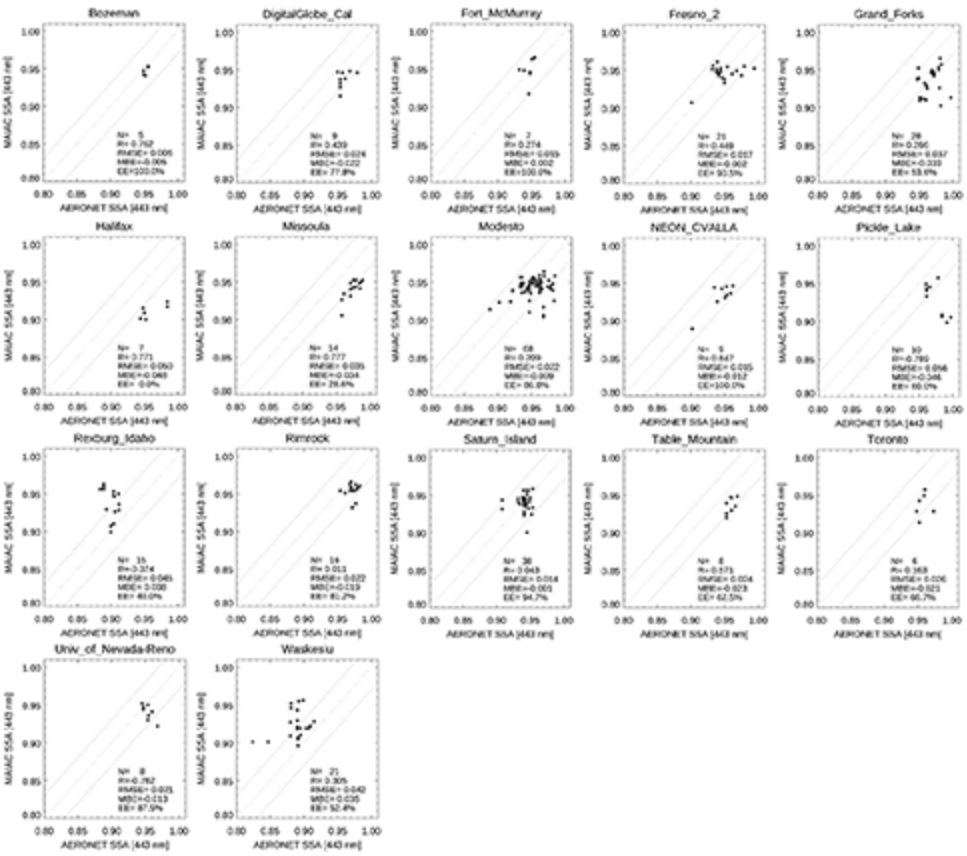

FIGURE 7. The same as Figure 6 but for the effective aerosol height of 4 km.

A summary validation (Figure 8), representing points with AOD_{443} > 0.6, once again confirms that for the most part, the smoke was lofted. 73.6% of results at 4 km fall within the expected error (EE) of ± 0.03.

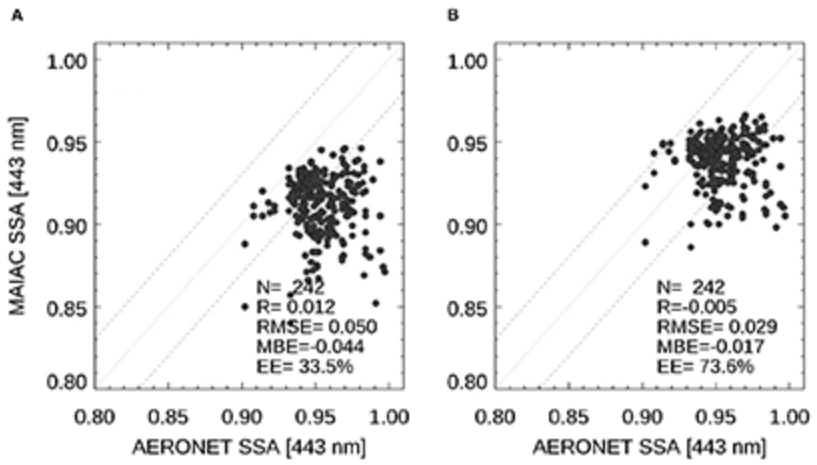

FIGURE 8. A summary AERONET validation of MAIAC EPIC SSA_{443} over North America in 2018 for the effective aerosol height of 1 km **(A)** and 4 km **(B)**.

Mineral Dust

Validation of SSA_{443} over desert dust sites from North Africa and partly, the Middle East, is shown in Figure 9. The collocation criteria were similar to the smoke case but with AERONET $AOD_{0.44} > 0.4$. Contrary to the analysis for smoke, the dust sites show a significantly better correlation with AERONET. More than half of 17 sites show a good correlation, whereas a good general agreement within EE is seen for the majority of sites. Among exceptions are *Ilorin* representing mixture of dust and biomass burning, to some extent, *Mongu* which has mostly biomass burning aerosol with some dust contribution, and *Cairo_EMA_2*, where EPIC may have an issue of unresolved sub-pixel water contribution combined with a few AERONET values anomalously low for the pure dust. As v2 MAIAC has dust at 1 km effective height only, the good overall agreement with AERONET indicates that the boundary layer dust provides a significant contribution to the measured TOA radiance, complementing that from the elevated dust layers playing an important role in the dust transport across Atlantic. We plan to optimize reporting layers for smoke and dust in the next version of algorithm based on extended EPIC data analysis.

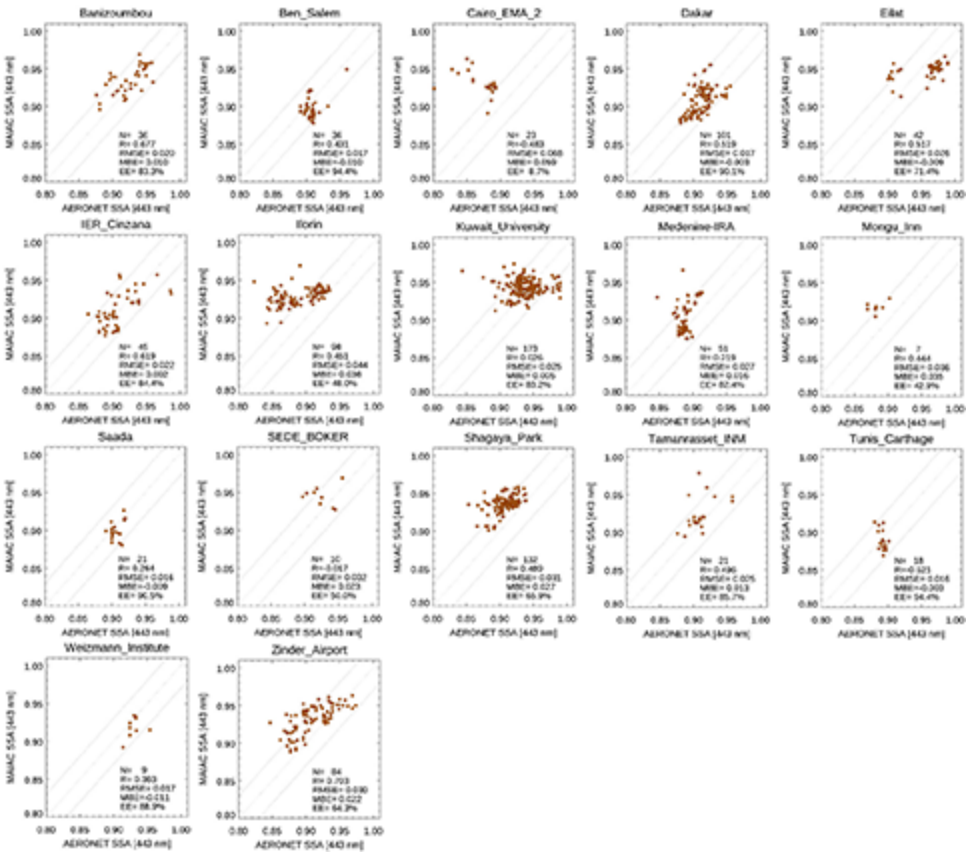

FIGURE 9. Site-level AERONET validation of MAIAC EPIC SSA_{443} over north Africa/Middle East in 2018.

Figure 10 displays the summary results. Plots (a) and (b) show comparison with AERONET SSA using thresholds AERONET $AOD_{0.44} > 0.4$ and > 0.6, respectively. Regarding SSA, Jethva et al. (2014) suggested using the term "comparison" rather than validation "*because both inversion techniques involve assumptions.*" Using higher AERONET AOD cutoff filters a number of low outliers in AERONET retrievals. This becomes obvious when we exclude 2 sites with a poorer agreement, *Cairo_EMA_2* and *Ilorin*. The resulting plot (c) shows an excellent agreement for SSA_{443} with $R = 0.62$, $rmse = 0.021$, negligible bias, and $EE = 85\%$.

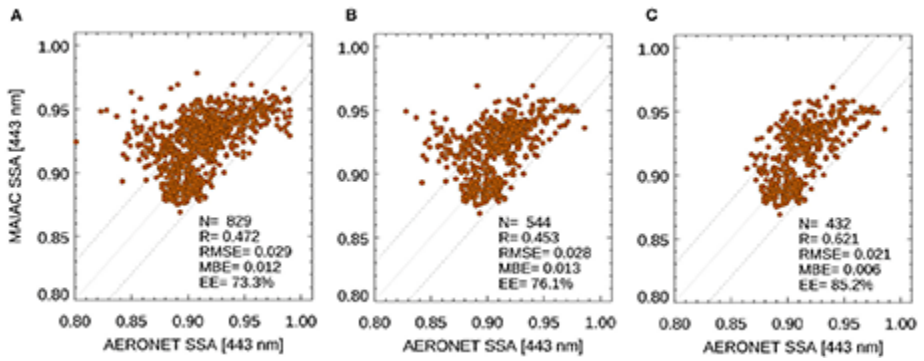

FIGURE 10. A summary AERONET validation of MAIAC EPIC SSA_{443} over North Africa/Middle East in 2018. Plots **(A,B)** represent all 17 sites with AERONET AOD_{440} > 0.4 and > 0.6, respectively. Plot **(C)** is equivalent to **(B)** but for 15 sites, with *Cairo_ENM_2* and *Ilorin* excluded.

Spectral Dependence of Absorption

Unlike the described validation of SSA_{443}, a direct comparison of spectral dependence of absorption against AERONET is associated with much higher uncertainties. First, an assessment of the AERONET inversion products (Dubovik and King, 2000) states a 30–50% accuracy for the imaginary refractive index at AOD_{440} > 0.4, with uncertainties being higher for the coarse mode dust and optically thin aerosols. Second, v2 MAIAC derives SAE (parameter *b*) from the 340–443 nm range, whereas AERONET provides refractive index for the non-overlapping range of wavelength range 440–1,020 nm. Both, Extinction and Absorption Angstrom Exponents depend on selected pair of wavelengths or spectral interval of evaluation (e.g., Moosmüller and Chakrabarty, 2011), which should hold true for the imaginary refractive index as well. Besides all that, the curvature of absorption is higher in the UV for hematite (e.g., Sokolik and Toon, 1999; Wagner et al., 2012) and in particular for brown carbon (e.g., Kirchstetter et al., 2004; Chen and Bond, 2010) as compared to the vis-NIR spectral range. For this reason, we provide only a qualitative assessment of spectral dependence of v2 MAIAC EPIC vs. AERONET. Following the idea of Figure 4 in Schuster et al. (2016), Figure 11 shows k_{440}-k_{670} plots for the North America smoke (top) and north Africa dust (bottom). For AERONET, parameter *b* was computed with Eq. (1) from the imaginary refractive index at 440 and 670 nm. In turn, EPIC values k_{440},

k_{670} were computed from (k_0, *b*). In both cases, the value of parameter b+1 is indicated by the color.

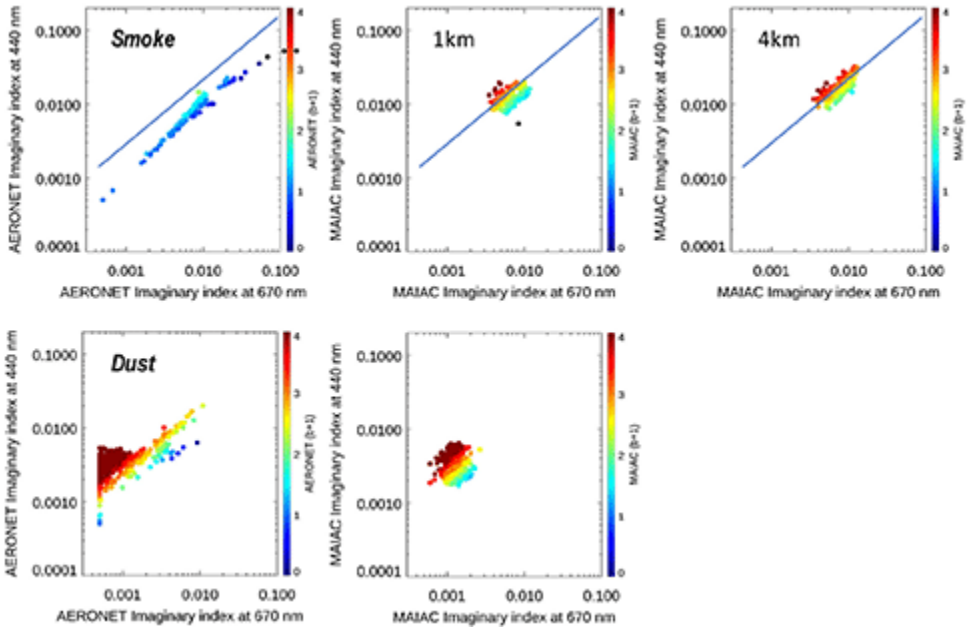

FIGURE 11. A comparison of spectral dependence of absorption between AERONET and v2 MAIAC EPIC for smoke (top) and dust (bottom). The AERONET results correspond to AOD_{440} > 0.4. The blue line on top, approximating MAIAC EPIC results, serves to illustrate the difference in absorption at 440 nm with AERONET.

For both smoke and dust cases, EPIC data occupy a much smaller range of values. The results for dust are quite similar with AERONET. EPIC shows more variation at 440 nm in comparison to 670 nm than AERONET. On the other hand, AERONET has data at k_{670} > 0.003 where EPIC has none. According to Schuster et al. (2016), data points with high absorption in the Red-NIR should represent a mixture of dust with carbonaceous aerosols.

In case of smoke, EPIC displays much higher values of SAE (*b*) than AERONET, which is expected from the properties of brown carbon where EPIC' sensitivity to parameter *b* mainly comes from the two UV channels. This is indicated by both the color of points and the offset along the y-axis, as illustrated by the blue line. Despite these expected differences, this comparison indicates an overall robust performance of the developed algorithm.

CONCLUSIONS

This paper described a new algorithm for joint retrievals of the aerosol optical depth and spectral absorption from EPIC observations in the UV–Vis spectral range. The retrievals were illustrated on examples of the wildfire smoke events in North America, and dust storms over the greater Sahara region in 2018. An initial validation of SSA_{443} over these regions shows a good agreement with AERONET data, generally within the uncertainty of the AERONET product of ± 0.03. For many AERONET sites, in particular those influenced by dust, retrieved SSA shows a good site-level regression with R~0.5–0.8. This fact is important given that it is easier to demonstrate good correlation at continental or global scales due to a significant variation of aerosol types and absorbing properties. Despite the near-backscattering EPIC view geometry, generally unfavorable for aerosol retrievals because of high surface reflectance, EPIC's high rate of observations providing good surface characterization and a well-selected combination of UV-Vis bands allowed us to achieve an overall good quality of aerosol characterization. The global validation of v2 MAIAC flexible retrieval products based on full EPIC record and comparison with other satellite datasets will be provided elsewhere.

The described flexible inversion algorithm is part of the v2 MAIAC EPIC algorithm. The v2 re-processing of the full EPIC's record 2015–2020 has recently been completed and the products will be released soon. The v2 dataset includes AOD_{443}, SSA_{443}, SAE (or b), and k_0 as part of MAIAC's standard output provided in HDF5 format. The results of flexible retrievals are reported for two aerosol effective heights (1, 4 km) for smoke and for one height (1 km) for dust. The full list of MAIAC EPIC products is given in the companion paper of this Special Issue.

Current work points to two directions of high practical value, which we plan to explore in our future research. The first one is a simultaneous evaluation of the aerosol layer height from EPIC's A and B oxygen absorption bands. Although Xu et al. (2017) developed aerosol height algorithm over the dark ocean and Xu et al. (2019) demonstrated a possibility of the wildfire smoke height retrieval over the vegetated land, systematic and reliable aerosol layer height retrieval from EPIC over land remains challenging. Such retrieval requires a good cloud detection and

knowledge of both surface reflectance and optical properties of aerosol. This information is currently provided by the v2 MAIAC algorithm. The second direction relates to the aerosol speciation of the airborne smoke and dust, based on spectral absorption. Such information would complement current datasets from the AERONET inversion products (Schuster et al., 2016) and from POLDER/PARASOL measurement record processed by the GRASP Components algorithm (Li et al., 2019).

DATA AVAILABILITY STATEMENT

The raw data supporting the conclusions of this article will be made available by the authors, without undue reservation.

AUTHOR CONTRIBUTIONS

AL and OT developed the concept. AL developed the algorithm. SK generated the look-up tables. YW performed MAIAC v2 re-processing of the EPIC data. SG conducted validation analysis. AL, OT, HJ, SG, and AM wrote the paper. All authors contributed to the article and approved the submitted version.

FUNDING

The work of AL, SG, YW, and SK was funded by the NASA DSCOVR program (manager Dr. R. Eckman) and in part by the NASA PACE program (19-PACESAT19-0039).

ACKNOWLEDGMENTS

We are grateful to the AERONET team for providing validation data and to the NASA Center for Climate Simulations providing resources for the EPIC data processing.

REFERENCES

Ahn, C., Torres, O., and Jethva, H. (2014). Assessment of OMI near-UV aerosol optical depth over land. *J. Geophys. Res. Atmos*. 119, 2457–2473. doi: 10.1002/2013JD020188

Bond, T. C. (2001). Spectral dependence of visible light absorption by carbonaceous particles emitted from coal combustion. *Geophys. Res. Let*. 28, 4075–4078. doi: 10.1029/2001GL013652

Boucher, O., Randall, D., Artaxo, P., Bretherton, C., Feingold, G., Forster, P., et al. (2013). "Clouds and aerosols," in: *Climate Change 2013: The Physical Science Basis. Contribution of Working Group I to the Fifth Assessment Report of the Intergovernmental Panel on Climate Change*. eds T. F. Stocker, D. Qin, G.-K. Plattner, M. Tignor, S. K. Allen, J. Boschung (Cambridge; New York, NY: Cambridge University Press).

Chen, C., Dubovik, O., Fuertes, D., Litvinov, P., Lapyonok, T., Lopatin, A., et al. (2020). Validation of GRASP algorithm product from POLDER/PARASOL data and assessment of multi-angular polarimetry potential for aerosol monitoring. *Earth Syst. Sci. Data* 12, 3573–3620. doi: 10.5194/essd-12-3573-2020

Chen, Y., and Bond, T. C. (2010). Light absorption by organic carbon from wood combustion. *Atmos. Chem. Phys*. 10, 1773–1787. doi: 10.5194/acp-10-1773-2010

Diner, D. J., Boland, S. W., Brauer, M., Bruegge, C., Burke, K. A., Chipman, R., et al. (2018). Advances in multiangle satellite remote sensing of speciated airborne particulate matter and association with adverse health effects: from MISR to MAIA. *J. Appl. Remote Sens*. 12:042603. doi: 10.1117/1.JRS.12.042603

Dubovik, O., Herman, M., Holdak, A., Lapyonok, T., Tanré, D., Deuzé, J. L., et al. (2011). Statistically optimized inversion algorithm for enhanced retrieval of aerosol properties from spectral multi-angle polarimetric satellite observations. *Atmos. Meas. Tech*. 4, 975–1018. doi: 10.5194/amt-4-975-2011

Dubovik, O., Holben, B., Eck, T. F., Smirnov, A., Kaufman, Y. J., King, M. D., et al. (2002). Variability of absorption and optical properties of key aerosol types observed in worldwide locations. *J. Atmos. Sci*. 59, 590–608. doi: 10.1175/1520-0469(2002)059<0590:VOAAOP>2.0.CO;2

Dubovik, O., and King, M. D. (2000). A flexible inversion algorithm for retrieval of aerosol optical properties from Sun and sky radiance measurements. *J. Geophys. Res. Atmos.* 105, 20673–20696. doi: 10.1029/2000JD900282

Dubovik, O., Sinyuk, A., Lapyonok, T., Holben, B. N., Mishchenko, M., Yang, P., et al. (2006). Application of spheroid models to account for aerosol particle nonsphericity in remote sensing of desert dust. *J. Geophys. Res. Atmos*. 111:D11208. doi: 10.1029/2005JD006619

Eck, T. F., Holben, B. N., Giles, D. M., Slutsker, I., Sinyuk, A., Schafer, J. S., et al. (2019). AERONET remotely sensed measurements and retrievals of biomass burning aerosol optical properties during the 2015 Indonesian burning season. *J. Geophys. Res. Atmos.* 124, 4722–4740. doi: 10.1029/2018JD030182

Eck, T. F., Holben, B. N., Reid, J., Sinyuk, A., Hyer, E. J., O'Neill, N. T., et al. (2009). Optical properties of boreal region biomass burning aerosols in central Alaska and seasonal variation of aerosol optical depth at an Arctic coastal site. *J. Geophys. Res. Atmos*. 114:D11201. doi: 10.1029/2008JD010870

Emde, C., Barlakas, V., Cornet, C., Evans, F., Korkin, S., Ota, Y., et al. (2015). IPRT polarized radiative transfer model intercomparison project – phase A. *J. Quant. Spectrosc. Rad. Transfer* 164, 8–36. doi: 10.1016/j.jqsrt.2015.05.007

Fougnie, B., Chimot, J., Vázquez-Navarro, M., Marbach, T., and Bojkov, B. (2020). Aerosol retrieval from space – how does geometry of acquisition impact our ability to characterize aerosol

properties. *J. Quant. Spectrosc. Rad. Transfer* 256:107304. doi: 10.1016/j.jqsrt.2020.107304

Giles, D. M., Holben, B. N., Eck, T. F., Sinyuk, A., Smirnov, A., Slutsker, I., et al. (2012). Analysis of AERONET aerosol absorption properties and characteristics from representative aerosol source locations. *J. Geophys. Res. Atmos*. 117:17203. doi: 10.1029/2012JD018127

Giles, D. M., Sinyuk, A., Sorokin, M. G., Schafer, J. S., Smirnov, A., Slutsker, I., et al. (2019). Advancements in the Aerosol Robotic Network (AERONET) Version 3 database – automated near-real-time quality control algorithm with improved cloud screening for Sun photometer aerosol optical depth (AOD) measurements. *Atmos. Meas. Tech*. 12, 169–209. doi: 10.5194/amt-12-169-2019

Herman, J. R., Bhartia, P. K., Torres, O., Hsu, C., Seftor, C., and Celarier, E. (1997). Global distribution of UV-absorbing aerosols from Nimbus 7/TOMS data. *J. Geophys. Res. Atmos.* 102, 16911–16922. doi: 10.1029/96JD03680

Holben, B. N., Eck, T. F., Slutsker, I., Tanr,é, D, Buis, J. P., Setzer, A., et al. (1998). AERONET - A federated instrument network and data archive for aerosol characterization. *Rem. Sens. Environ*. 66, 1–16. doi: 10.1016/S0034-4257(98)00031-5

IPCC: Climate Change (2013). "The physical science basis," *Contribution of Working Group I to the Fifth Assessment Report of the Intergovernmental Panel on Climate Change.* eds T. F. Stocker, D. Qin, G. K. Plattner, M. Tignor, S. K. Allen, J. Boschung (Cambridge; New York, NY: Cambridge University Press).

Jethva, H., and Torres, O. (2011). Satellite-based evidence of wavelength-dependent aerosol absorption in biomass burning smoke inferred from ozone monitoring instrument. *Atmos. Chem. Phys.* 11, 10541–10551. doi: 10.5194/acp-11-10541-2011

Jethva, H., Torres, O., and Ahn, C. (2014). Global assessment of OMI aerosol single-scattering albedo using ground-based AERONET inversion. *J. Geophys. Res. Atmos.* 119, 9020–9040. doi: 10.1002/2014JD021672

Jethva, H., Torres, O., and Ahn, C. (2018). A 12-year long global record of optical depth of absorbing aerosols above the clouds derived from the OMI/OMACA algorithm. *Atmos. Meas. Tech*. 11, 5837–5864. doi: 10.5194/amt-11-5837-2018

Jethva, H., Torres, O., and Yoshida, Y. (2019). Accuracy assessment of MODIS land aerosol optical thickness algorithms using AERONET measurements over North America. *Atmos. Meas. Tech*. 12, 4291–4307. doi: 10.5194/amt-12-4291-2019

Kahn, R. A., and Gaitley, B. J. (2015). An analysis of global aerosol type as retrieved by MISR. *J. Geophys. Res. Atmos*. 120, 4248–4281. doi: 10.1002/2015JD023322

Kahn, R. A., Gaitley, B. J., Garay, M. J., Diner, D. J., Eck, T. F., Smirnov, A., et al. (2010). Multiangle imaging spectroradiometer global aerosol product assessment by comparison with the aerosol robotic network. *J. Geophys. Res. Atmos.* 115:D23. doi: 10.1029/2010JD014601

Kim, J., Jeong, U., Ahn, M.-H., Kim, J. H., Park, R. J., Lee, H., et al. (2020). New era of air quality monitoring from space: Geostationary Environment Monitoring Spectrometer (GEMS). *Bull. Am. Meteorol. Soc.* 101, E1–E22. doi: 10.1175/BAMS-D-18-0013.1

Kirchstetter, T., Novakov, T., and Hobbs, P. (2004). Evidence that spectral dependence of light absorption by aerosols is affected by organic carbon. *J. Geophys. Res. Atmos*. 109:D21208. doi: 10.1029/2004JD004999

Korkin, S., and Lyapustin, A. (2019). Matrix exponential in C/C++ version of vector radiative transfer code IPOL. *J. Quant. Spectrosc. Radiat. Transfer* 227, 106–110. doi: 10.1016/j.jqsrt.2019.02.009

Li, L., Che, H., Derimian, Y., Dubovik, O., Schuster, G. L., Chen, C., et al. (2020b). Retrievals of fine mode light-absorbing carbonaceous aerosols from POLDER/PARASOL observations over East and South Asia. *Remote Sensing Environ*. 247:111913. doi: 10.1016/j.rse.2020.111913

Li, L., Dubovik, O., Derimian, Y., Schuster, G. L., Lapyonok, T., Litvinov, P., et al. (2019). Retrieval of aerosol components directly from satellite and ground-based measurements. *Atmos. Chem. Phys*. 19, 13409–13443. doi: 10.5194/acp-19-13409-2019

Li, L., Mahowald, N. M., Miller, R. L., Pérez García-Pando, C., Klose, M., Hamilton, D. S., et al. (2020a). Quantifying the range of the dust direct radiative effect due to source mineralogy uncertainty. *Atmos. Chem. Phys. Discuss*. doi: 10.5194/acp-2020-547

Lyapustin, A., and Knyazikhin, Y. (2002). Green's function method in the radiative transfer problem. II: spatially heterogeneous anisotropic surface. *Appl. Optics*. 41, 5600–5606. doi: 10.1364/AO.41.005600

Lyapustin, A., Wang, Y., Korkin, S., and Huang, D. (2018). MODIS collection 6 MAIAC algorithm. *Atmos. Meas. Tech*. 11, 5741–5765. doi: 10.5194/amt-11-5741-2018

Lyapustin, A. I. (2005). Radiative transfer code SHARM for atmospheric and terrestrial applications. *Appl. Optics*. 44, 7764–7772. doi: 10.1364/AO.44.007764

Marquardt, D. R. (1963). An algorithm for the least-squares estimation of nonlinear parameters. *SIAM J. Appl. Math*. 11, 431–441. doi: 10.1137/0111030

Marshak, A., Herman, J., Szabo, A., Blank, K., Carn, S., Cede, A., et al. (2018). Earth observations from DSCOVR/EPIC instrument. *Bull. Amer. Meteor. Soc*. 99, 1829–1850. doi: 10.1175/BAMS-D-17-0223.1

Moosmüller, H., and Chakrabarty, R. K. (2011). Technical note: simple analytical relationships between Ångström coefficients of aerosol extinction, scattering, absorption, and single scattering albedo. *Atmos. Chem. Phys*. 11, 10677–10680. doi: 10.5194/acp-11-10677-2011

Remer, L. A., Knobelspiesse, K., Zhai, P.-W., Xu, F., Kalashnikova, O. V., Chowdhary, J., et al. (2019). Retrieving aerosol characteristics from the PACE mission, part 2: multi-angle and polarimetry. *Front. Earth Sci*. 7:94. doi: 10.3389/fenvs.2019.00094

Samset, B., Sand, M., Smith, C. J., Bauer, S. E., Forster, P. M., Fuglestvedt, J. S., et al. (2018). Climate impacts from a removal of anthropogenic aerosol emissions. *Geophys. Res. Lett.* 45, 1020–1029. doi: 10.1002/2017GL076079

Schafer, J., Eck, T., Holben, B., Thornhill, K., Anderson, B., Sinyuk, A., et al. (2014). Intercomparison of aerosol single-scattering albedo derived from AERONET surface radiometers and LARGE *in situ* aircraft profiles during the 2011 DRAGON-MD and DISCOVER-AQ experiments. *J. Geophys. Res. Atmos*. 119, 7439–7452. doi: 10.1002/2013JD021166

Schuster, G., Dubovik, O., and Arola, A. (2016). Remote sensing of soot carbon – part 1: distinguishing different absorbing aerosol species. *Atmos. Chem. Phys*. 16, 1565–1585. doi: 10.5194/acp-16-1565-2016

Sokolik, I., and Toon, O. (1999). Incorporation of mineralogical composition into models of the radiative properties of mineral aerosol from UV to IR wavelengths. *J. Geophys. Res. Atmos.* 104, 9423–9444. doi: 10.1029/1998JD200048

Tanaka, T. Y., and Chiba, M. (2006). A numerical study of the contributions of dust source regions to the global dust budget. *Glob. Planet. Change* 52, 88–104. doi: 10.1016/j.gloplacha.2006.02.002

Thorsen, T. J., Winker, D. M., and Ferrare, R. A. (2020). Uncertainty in observational estimates of the aerosol direct radiative effect and forcing. *J. Climate*. 34, 195–214. doi: 10.1175/JCLI-D-19-1009.1

Torres, O., Ahn, C., and Chen, Z. (2013). Improvements to the OMI near-UV aerosol algorithm using A-train CALIOP and AIRS observations. *Atmos. Meas. Tech*. 6, 3257–3270. doi: 10.5194/amt-6-3257-2013

Torres, O., Bhartia, P. K., Herman, J. R., Ahmad, Z., and Gleason, J. (1998). Derivation of aerosol properties from satellite measurements of backscattered ultraviolet radiation: theoretical basis. *J. Geophys. Res. Atmos.* 103, 17099–17110. doi: 10.1029/98JD00900

Torres, O., Bhartia, P. K., Jethva, H., and Ahn, C. (2018). Impact of the ozone monitoring instrument row anomaly on the long-term record of aerosol products. *Atmos. Meas. Tech.* 11, 2701–2715. doi: 10.5194/amt-11-2701-2018

Torres, O., Herman, J. R., Bhartia, P. K., and Sinyuk, A. (2002). Aerosol properties from EP-TOMS near UV observations. *Adv. Space Res*. 29, 1771–1780. doi: 10.1016/S0273-1177(02)00109-6

Torres, O., Jethva, H., Ahn, C., Jaross, G., and Loyola, D. G. (2020). TROPOMI aerosol products: evaluation and observations of synoptic-scale carbonaceous aerosol plumes during 2018–2020. *Atmos. Meas. Tech*. 13, 6789–6806. doi: 10.5194/amt-13-6789-2020

Torres, O., Jethva, H., and Bhartia, P. K. (2012). Retrieval of aerosol optical depth above clouds from OMI observations: sensitivity analysis and case studies. *Journal. Atm. Sci*. 69, 1037–1053. doi: 10.1175/JAS-D-11-0130.1

Torres, O., Tanskanen, A., Veihelman, B., Ahn, C., Braak, R., Bhartia, P. K., et al. (2007). Aerosols and surface UV products from OMI Observations: an overview. *J. Geophys. Res. Atmos.* 112:D24S47. doi: 10.1029/2007JD008809

Wagner, R., Ajtai, T., Kandler, K., Lieke, K., Linke, C., Müller, T., et al. (2012). Complex refractive indices of Saharan dust samples at visible and near UV wavelengths: a laboratory study. *Atmos. Chem. Phys*. 12, 2491–2512. doi: 10.5194/acp-12-2491-2012

Xu, X., Wang, J., Wang, Y., Zeng, J., Torres, O., Reid, J. S., et al. (2019). Detecting layer height of smoke aerosols over vegetated land and water surfaces via oxygen absorption bands: hourly results from EPIC/DSCOVR in deep space. *Atmos. Meas. Tech*. 12, 3269–3288. doi: 10.5194/amt-12-3269-2019

Xu, X., Wang, J., Wang, Y., Zeng, J., Torres, O., Yang, Y., et al. (2017). Passive remote sensing of altitude and optical depth of dust plumes using the oxygen A and B bands: first results from EPIC/DSCOVR at lagrange-1 point. *Geophys. Res. Lett*. 44, 7544–7554. doi: 10.1002/2017GL073939

Conflict of Interest: The authors declare that the research was conducted in the absence of any commercial or financial relationships that could be construed as a potential conflict of interest.

ORIGINAL RESEARCH
published: 21 May 2021
doi: 10.3389/frsen.2021.671933

Calibration of the DSCOVR EPIC Visible and NIR Channels using Multiple LEO Radiometers

Igor V. Geogdzhayev[1,2], Alexander Marshak[3] and Mikhail Alexandrov[1,2]*

[1] *Department of Applied Physics and Applied Mathematics, Columbia University, New York, NY, United States*
[2] *NASA Goddard Institute for Space Studies, New York, NY, United States*
[3] *NASA Goddard Space Flight Center, Greenbelt, MD, United States*

Edited by:
Oleg Dubovik, CNRS, UMR8518 Laboratoire d'optique atmosphèrique (LOA), France

Reviewed by:
Jeffrey Czapla-Myers, University of Arizona, United States
David Doelling, National Aeronautics and Space Administration (NASA), United States

**** Correspondence:*** *Igor Geogdzhayev, igor.v.geogdzhayev@nasa.gov*

Specialty section: *This article was submitted to Satellite Missions, a section of the journal Frontiers in Remote Sensing*

Received: *24 February 2021*
Accepted: *10 May 2021*
Published: *21 May 2021*

Citation: *Geogdzhayev IV, Marshak A and Alexandrov M (2021) Calibration of the DSCOVR EPIC Visible and NIR Channels using Multiple LEO Radiometers. Front. Remote Sens. 2:671933. doi: 10.3389/frsen.2021.671933*

The first five years of operation of the Deep Space Climate Observatory (DSCOVR) Earth Polychromatic Imaging Camera (EPIC) at the Lagrange one point have produced results that uniquely complement the data from currently operating low orbit Earth-observing instruments. In this paper we describe an updated unified approach to EPIC calibration. In this approach, calibration coefficients and their trends were obtained by comparing EPIC observations to the measurements from polar orbiting radiometers. In this study L1B reflectances from Moderate Resolution Imaging Spectroradiometer (MODIS) onboard the Aqua and Terra satellites, Multi-angle Imaging Spectroradiometer (MISR) onboard Terra and Visible Infrared Imaging Radiometer (VIIRS) onboard the Suomi National Polar-orbiting Partnership (Suomi NPP) spacecraft were used to infer calibration coefficients for four EPIC visible and near-infrared channels: 443 nm, 551 nm, 680 nm, and 780 nm. EPIC Version three measurements made between June 2015 and August 2020 were used for comparison. The calibration procedure identifies the most homogeneous low Earth orbit radiometer scenes matching scattering angles that are temporarily and spatially collocated with EPIC observations. These scenes are used to determine reflectance to count (R/C) ratios in spectrally analogous channels. Seasonal average R/C ratios were analyzed to obtain EPIC calibration gains and trends. The trends for the full dataset period are not statistically significant except in the 443 nm channel. No significant changes in calibration were found after the instrument's exit from safe hold in March 2020. The R/C ratios were also used to determine the differences in EPIC gains resulting from separate calibrations: against MODIS Aqua or Terra, as well as against forward or aftward MISR cameras. Statistical tests indicate that the differences between the two datasets are not significant except in the 780 nm channels where Aqua-derived coefficients may be around 2% lower compared to Terra. The dependence of EPIC calibration gains on the instrument scattering angle and on DSCOVR-Earth distance were investigated. Lastly, model Low Earth Orbit (LEO) reflectances calculated to match the EPIC viewing geometry were employed to study how EPIC calibration coefficients depend on EPIC-LEO viewing geometry differences. The effect of LEO and EPIC angular mismatch on calibration was shown to be small.

Keywords: deep space climate observatory/earth polychromatic imaging camera, calibration, moderate resolution imaging spectroradiometer,

multi-angle imaging spectroradiometer, visible infrared imaging radiometer

INTRODUCTION

The Deep Space Climate Observatory (DSCOVR) spacecraft actively maintains itself in a Lissajous orbit around the Lagrange point L1 between the Sun and the Earth at about 1.5 million kilometers from Earth (Marshak et al., 2018). From this position the DSCOVR Earth Polychromatic Imaging Camera (EPIC) views the entire sunlit Earth's hemisphere in ten narrow spectral channels ranging from UV to near IR 10 (in winter) to 22 (in summer) times a day. The Earth-observing geometry of the EPIC instrument is close to backscattering: the scattering angle varies between 168 and 178°. EPIC's viewing geometry differs significantly from instruments on sun-synchronous orbits for which only a small portion of Earth views occurs in the backscattering region. For comparison, depending on the season, latitude and scan view angle, the scattering angle for MODIS is typically in a wide range between 110 and 175°. The Suomi-NPP VIIRS instrument, due to its wider scan, covers an even larger range of angles, including the whole backscattering region. The near-backscattering EPIC observations are a direct consequence of its position at L1.

We previously reported Geogdzhayev and Marshak, (2018) EPIC calibration coefficients based on comparisons with MODIS. Since then, Version 3 EPIC L1b data has become available. Compared to Version 2, significant improvements were made in geolocation and flatfield correction (Kostinski et al., 2021). A number of L2 products were developed from EPIC observations. In this paper we describe an improved, more robust version of the intercalibration algorithm and apply it to data from four low Earth orbit (LEO) radiometers. In addition, we analyze trends and sources of variability in the derived calibration.

Thanks to its unique vantage point and spatial and temporal Earth coverage, EPIC remote sensing observations have been used in such applications as the retrieval of aerosol, cloud, sulfur dioxide and ozone amounts and vegetation properties Marshak et al., (2018), as well as ocean color products (Gao et al., 2019). In addition, EPIC data have been employed to observe volcanic clouds Carn et al. (2016, 2018), analyze the global distribution of erythemal irradiance Herman et al. (2020); Herman et al. (2018a), and observe solar eclipse irradiance changes (Herman at al., 2018b).

EPIC observations in the backscattering region have been used to observe and characterize the glint caused by oriented ice crystals in clouds Varnai et al. (2020); Marshak et al. (2017), retrieve cloud properties Yang et al. (2013); Yang et al. (2019); Yin et al. (2020), ozone Herman et al. (2018a) and vegetation properties (Marshak et al., 2017; Yang et al., 2017). More EPIC-related research papers may be found here: https://epic.gsfc.nasa.gov/science/pubs.

Most of the above applications rely on radiometric calibration of the EPIC measurements. The lack of in-flight calibration capabilities necessitates a comparison of EPIC Earth observations with well-calibrated measurements from radiometers in polar and geostationary orbits. In addition, the images of the Moon regularly observed by the instrument may also be employed for calibration.

In this study we employ EPIC measurements combined with collocated Level 1b TOA reflectances from the Moderate Resolution Imaging Spectroradiometer King et al. (2003) on-board the Aqua and Terra satellites, the Multi-angle Imaging Spectroradiometer Diner et al. (2005) on-board Terra and the Visible Infrared Imaging Radiometer Suite Cao et al. (2014), which is part of the Suomi National Polar-orbiting Partnership (NPP), to derive the calibration coefficients in four EPIC visible and near-infrared (NIR) channels. These instruments were chosen for comparison because of their well-established calibration record and wide use in the remote sensing applications. Contemporaneous data from these instruments are available for the entire period of the DSCOVR mission. Using these data, we derive calibration gains for the latest Version 3 release of the EPIC data.

DATA

Version 3 data EPIC L1B data were obtained from the NASA EOSDIS OpeNDAP data server at https://opendap.larc.nasa.gov/opendap/. The EPIC sampling size at nadir (at the center of the image) is about 8 km × 8 km (10 km × 10 km when the EPIC point spread function is applied) and increases toward the edges. The radiometric resolution of the EPIC data is 12 bits per pixel. To reduce the amount of data transmitted from DSCOVR, for all but the blue channel (443 nm), four pixels are averaged on-board the spacecraft resulting in an effective spatial resolution at nadir of approximately 18 km.

We use MODIS Aqua and Terra L1B Collection 6.1 1 km reflectances obtained from the Level-1 and Atmosphere Archive and Distribution System (LAADS) Distributed Active Archive Center (DAAC). Note that the MODIS reflectance, as well as the EPIC one, is the true TOA reflectance multiplied by the solar zenith angle (MODIS Characterization Support Team, 2006). We will refer to this quantity simply as "reflectance" and will use it for all radiometers. MODIS also has a radiometric resolution of 12 bits per pixel and calibration design requirements of 2% for reflectance and 5% for radiance in the solar bands (Toller et al., 2013). MODIS instruments have a cross-track swath width of 2,330 km. The equator crossing times are 10:30 AM and 1:30 PM for MODIS Terra and Aqua, respectively. We note here that while we used publicly available MODIS L1B data obtained from LAADS DAAC, additional calibration for Terra and Aqua is performed in MODIS Land discipline processing. This additional calibration includes polarization correction of Terra data based on Ocean Biology Processing Group Kwiatkowska et al. (2008), de-trending for both Terra and Aqua, and gain adjustment for Terra (cross-calibration to Aqua). These coefficients come from the Multi-Angle Implementation of Atmospheric Correction (MAIAC) group's calibration over deserts sites (Lyapustin et al., 2014). This additional calibration was not used in this study.

The MISR ellipsoid-projected L1B2 radiance product (MI1B2E) data were obtained from the Atmospheric Science Data Center (ASDC) DAAC. MISR uses 14-bit quantization and has an instrument specification for radiometric accuracy of 3% at maximum signal (Bruegge et al., 2002). The global mode data are provided at 1.1 km spatial resolution for all nine cameras in blue (446 nm), green (558 nm), and NIR (866 nm) channels and for the nadir camera in the red (672 nm) channel. The off-nadir red channel data provided at 275 m resolution were downsampled to 1.1 km to match the other channels/cameras. MISR is onboard the Terra satellite and thus has identical equator crossing time as MODIS Terra. Among the LEO instruments considered in this paper it has the narrowest swath of 360 km in the cross-track direction.

The VIIRS Level 1 data were downloaded from the Level-1 and Atmosphere Archive and Distribution System (LAADS) DAAC. The moderate resolution (750 m) channels M3 (448 nm), M4 (555 nm), M5 (672 nm) and M7 (865 nm) were used in this study. VIIRS radiometric accuracy requirement is 2% in reflectance of a typical scene radiance (JPSS

Level 1 Requirements Document, 2016). The VIIRS daytime equator crossing time is similar to MODIS Aqua, at 1:30 PM. The instrument is on a higher orbit compared to Terra and Aqua satellites and has a wide swath of 3,060 km, sufficient to eliminate data gaps from adjacent orbits in the tropics.

The matching of EPIC channels to those of the LEO instruments is summarized in Table 1. The table also includes the position and bandwidth of the channels.

TABLE 1 | EPIC-MODIS-MISR-VIIRS channel correspondence. Midpoint wavelengths are band-averaged values. For simplicity, for the rest of the paper we will call the EPIC NIR channel 780 nm.

EPIC channel (full width in nm)	MODIS channel Midpoint (bandwidth)	MISR channel Midpoint (bandwidth)	VIIRS channel Midpoint (bandwidth)
443 ± 1 nm (3 ± 0.6)	3 466 nm (19 nm)	Blue 446 nm (42 nm)	M3 448 nm (20 nm)
551 ± 1 nm (3 ± 0.6)	4 554 nm (20 nm)	Green 558 nm (29 nm)	M4 555 nm (20 nm)
680 ± 0.2 nm (3 ± 0.6)	1 646 nm (48 nm)	Red 672 nm (22 nm)	M5 672 nm (20 nm)
779.5 ± 0.3 nm (2 ± 0.4)	2 857 nm (38 nm)	NIR 866 nm (40 nm)	M7 865 nm (39 nm)

Figure 1 compares the normalized filter functions of the four instruments to the corresponding EPIC channels. The curves for the matching channels are marked by the same color. As one can see from the figure, EPIC channels are significantly narrower compared to the channels of LEO radiometers. The best spectral match is for the overlapping green channels, while the largest spectral difference, of about 80 nm, is observed between the NIR channels. The central wavelength of the EPIC NIR channel is significantly shorter compared to the LEO radiometers. While the locations of the green and NIR spectral channels are similar among the LEO radiometers, there are differences in positions of the blue channels. Compared to MISR and VIIRS the red channel of MODIS is shifted toward the shorter wavelengths. We note that the spectral channels used for intercomparison in this study are not exhaustive. Other MODIS and VIIRS channels, such as VIIRS M6 (745 nm) and MODIS Band 15 (748 nm) ocean color bands in near IR, may be employed for this purpose.

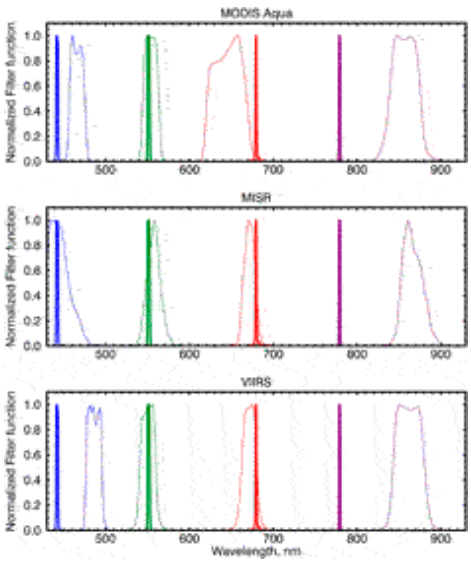

FIGURE 1 | MODIS **(upper panel)**, MISR **(middle panel)**, VIIRS **(lower panel)** spectral response functions normalized to the maximum value for the channels used in this study are shown by wide curves. Repeated on each panel are the corresponding EPIC channels (narrow curves).

METHODS

The first step for the derivation of EPIC calibration coefficients is to identify favorable LEO scenes. This process is illustrated by Figure 2 for MODIS (upper panel), MISR (middle panel) and VIIRS (lower panel). All EPIC observations are made in the backscattering region, while for the LEO instruments only a small fraction of the pixels have similar viewing geometry. We therefore begin by selecting pixels that match the EPIC scattering angle to within 1.5°. LEO radiometer pixels that satisfy this criterion form a ring on the Earth surface, shown as white areas in Figure 2. Compared to the EPIC Version 2 calibration approach Geogdzhayev and Marshak, (2018), the angular match threshold was relaxed to increase the number of matching fully filled scenes away from the ring borders. Due to the relatively narrow width of the MISR cross-track swath, matching areas are often found on the edge of the scan, as illustrated in the middle panel of Figure 2, where the dark area in the upper right part of the image is outside of the MISR swath. To mitigate this effect, the scattering angle matching threshold was relaxed to 3°. We ran tests using MODIS data to evaluate the effect of such a change and did not find it to be significant. Among the selected pixels, we retain those taken within 7 min of the EPIC image. These

pixels are shown as dots in the white areas of the images of Figure 2. There are time lags in the data acquisition between different EPIC spectral channels associated with the rotation of the filter wheels: ~3 min difference between blue (443 nm) and green (551 nm), and ~4 min between blue and red (680 nm) (Marshak and Knyazikhin, 2017). Therefore, the temporal collocation is done separately for each spectral channel. The solar zenith angle (SZA) of all matching pixels is limited to 60° to exclude scenes with low illumination and scenes where the curvature of the Earth may complicate the comparison. Pixels within 40° of the glint angle over ocean are excluded as well. For each EPIC pixel that matches the above criteria we identify LEO radiometer pixels that fall within an approximately 25 km radius. Scenes are retained for further analysis if at least 2/3 of the 25 km neighborhood is covered with valid LEO radiometer pixels (one such scene is represented by a gray circle on each of the upper and lower panels of Figure 2). This requirement was introduced in the current version of the algorithm and serves to exclude sparsely populated scenes that can have more variability, thus introducing more noise in comparisons. For each matching scene we calculate the mean and relative standard deviation (defined as the ratio of the standard deviation to the mean) for the matching LEO radiometer pixels within the 25 km radius. We also calculate the standard deviation for the 5 × 5 EPIC pixel neighborhood. The values of the relative standard deviation are used to select the most homogeneous scenes.

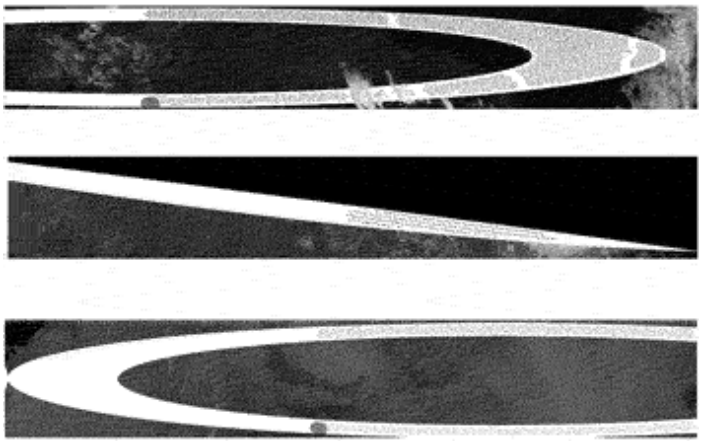

FIGURE 2 | Examples of matching EPIC-LEO instrument scenes. Top, middle and lower panels show selected areas of MODIS, MISR and VIIRS images (green channel reflectances), respectively. MODIS image is approximately 400 km in the cross-track dimension and 2,000 km long and is centered on 24.5°S and 51.1°E. MISR image is approximately 250 km in the cross-track dimension and 1,750 km long and cetered at 17.1°S and 141.61°E. VIIRS image is approximately 330 km in the cross-track dimension and 2,200 km long and cetered at 27.5°N and 43.9°E Areas of matching scattering angles are shown in white. Black dots on white are EPIC pixels that are temporarily and spatially collocated with LEO instrument pixels. Gray circles on the upper lower panel shows the 25 km vicinity of single EPIC pixels. Cross-track direction is approximately vertical. Dark upper-right region in the middle panel is outside of the MISR swath. White streaks on top of the lower panel are due to VIIRS bow-tie effect.

The differences in the position and spectral width of the corresponding EPIC and LEO radiometer channels illustrated in Figure 1 may cause discrepancy when a scene is observed by the two orbit types (Chander, 2013). This discrepancy is generally a function of the scene's spectral signature and may result in both noise and systematic errors of calibration. As in the previous V2 calibration procedure, in this work we compensate for these differences by employing spectral band adjustment factors (SBAFs), which convert MODIS, MISR and VIIRS TOA reflectance values to equivalent EPIC reflectances for various surface types. These factors, in the form of linear regression coefficients, were obtained from the database available at https://cloudsgate2.larc.nasa.gov/cgi-bin/site/showdoc?mnemonic = SBAF; they are based on the analysis of the SCIAMACHY hyperspectral data for various surface targets and account for the differences in radiometer's spectral response functions (Scarino et al., 2016).

In addition, we used the same source to identify the range of reflectance values for each scene type. LEO radiometer's pixels were adjusted if their

reflectance was within this range using the SBAFs for the appropriate land cover type. For scenes with reflectance higher than 0.6 we used the deep convection cloud spectral corrections. Land cover types were taken from a data set developed by Channan et al. (2014). The dataset is a .5 x .5-degree reprojected version of the Global Mosaics of the standard MODIS land cover type data product (MCD12Q1) in the IGBP Land Cover Type Classification. Separate adjustment factors were used for each of the four LEO instruments.

The EPIC calibration coefficients may be derived from the matching scenes using two methods (Geogdzhayev and Marshak, 2018). The first one involves calculating the linear regression between EPIC counts/sec and LEO reflectances for the most homogeneous scenes. The second involves finding the mean reflectance/count (R/C) ratio for bright homogeneous scenes (LEO reflectance greater than 0.6). The two approaches possess a certain degree of independence since the regression method uses darker pixels in addition to the bright ones. A linear regression also produces the intercept values; their closeness to zero may be used as an indication of the quality of fit. The ratio method can be used on a smaller dataset to derive, for example, seasonal gains, or to investigate the sensitivity of calibration to various parameters. Since these topics will mostly be the focus of this study, here we will be using the ratio method.

Specifically, to derive calibration gains we employ the ratios of LEO instrument reflectance to EPIC count for all available matching scenes where the reflectance is greater than 0.6 and relative standard deviation is less than 10%. These scenes are binned according to the relative standard deviation of the MODIS reflectance and the mean R/C ratio is calculated for each bin. The mean bin values are then extrapolated to the ideal case of a completely uniform scene (zero standard deviation) using a linear regression. The extrapolated value is then taken to be the calibration coefficient.

The following list summarizes the conditions used to match pixels between EPIC and LEO instruments: 1) scattering angle is within 1.5° of the EPIC scattering angle 2) temporal collocation with EPIC image is less than 7 min for each EPIC channel 3) glint angle is greater than 40° 4) at least 2/3 of the 25 km-neighborhood of the EPIC pixel is covered with LEO radiometer measurements 5) LEO radiometer reflectance is greater than 0.6 6) relative standard deviation in the neighborhood is less than 10%.

RESULTS

Calibration Gains and Trends

Figure 3 presents a summary of the calibration datasets as timeseries of seasonal mean R/C ratio for the four channels. The top, middle and lower panels show the combined MODIS Aqua and Terra data, MISR, and VIIRS NPP data, respectively. The gap in data in June 2019–February 2020 corresponds to the period when EPIC was is safe mode. The average number of points per year that went into the calculation of the curves on Figure 3 are 6,000 for MODIS, 70,000 for MISR and 20,000 for VIIRS. The higher value for MISR is due to the relaxed scattering angle match condition. The higher resolution and wider swath of VIIRS resulted in more matches compared to MODIS. The corresponding calibration gain values and their relative differences are given in Table 2. The values in Table 2 are based on the data for the time period to 06/2019, when EPIC was put in safehold. Encouragingly, MODIS results agree to within 1.4%, 0%, 1.2%, 2.6% with the corresponding values for each channel derived by an independent method by Doelling et al. (2019), also see (Haney et al., 2016). VIIRS results agree to within 0.4% with corresponding values from the same source. We found that the relative difference between calibration gains derived from MISR and VIIRS is less than 2% in all channels (last column in Table 2), while the MODIS-VIIRS difference is within 4.3%. These differences are in line with the reported values for the radiometric accuracy of the instruments.

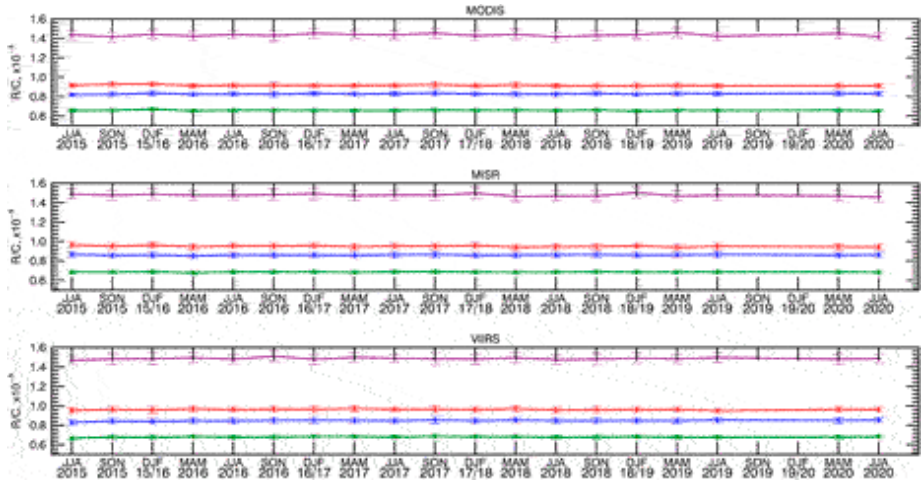

FIGURE 3 | Time series of seasonal mean R/C ratios for combined MODIS Aqua and Terra instruments **(upper panel)**, MISR **(middle panel)** and VIIRS **(lower panel)**. Here and in the following R/C figures blue green, red and magenta lines represent 443, 551,680 and 780 nm EPIC channels. Whiskers represent the standard deviation of R/C ratios within each three-month period.

TABLE 2 | EPIC calibration gains derived from several LEO instruments and their relative differences.

	EPIC gains ($x10^{-5}$) vs			Relative difference	
	MODIS	MISR	VIIRS	MODIS-VIIRS	MISR-VIIRS
443 nm	0.8330	0.8686	0.8528	−2.3%	1.9%
551 nm	0.6617	0.6882	0.6842	−3.3%	0.6%
680 nm	0.9238	0.9565	0.9658	−4.3%	1%
780 nm	1.4538	1.4834	1.4887	−2.3%	0.36%

MODIS channel 2 may saturate over bright deep convective clouds (Doelling et al., 2019). In this study we considered MODIS L1B data marked to be within the valid range (integer values [0, 32,767]). The saturated pixels (with value 65,533) were excluded. To investigate whether possible saturation of MODIS band 2 affected our results, we recalculated the 780 nm calibration gain while additionally restricting MODIS reflectances to values smaller than some threshold. Across all threshold values down to 0.7, we found that the effect on the calibration was limited to about 0.5%.

We used the seasonal mean R/C values summarized in Figure 3 to estimate calibration gain trends for the whole period of EPIC data. The results are listed in Table 3. As can be seen from the table, EPIC calibration values are stable. We used a standard double-sided test with a 95% confidence threshold (corresponding to a "*p*-value" of 0.05) to evaluate the statistical significance of the trends. We found the calculated trend values to not be statistically significant (with corresponding *p*-values greater than 0.05), except in the blue channel for VIIRS data. To test how the resumption of operations in March 2020 affected the calibration, we used the trend values from Table 3 together with their confidence intervals to find the expected range of R/C values for the two 3 month periods after the gap (the last two points of the curves in Figure 3). We found that the actual values are well within the expected range for all instruments. We conclude that the safe hold incident did not noticeably affect the calibration.

TABLE 3 | Absolute and relative EPIC calibration gains trends derived from several LEO instruments and their statistical significance.

	EPIC channels (nm)	Absolute linear trend per year	Relative linear trend per year	Significant? (p-value)	Relative RMSE (%)
MODIS	443	1.19E-08	0.14%	No (p = 0.12)	0.52
	551	−9.99E-09	−0.15%	No (p = 1.86)	0.59
	680	2.22E-08	−0.24%	No (p = 1.99)	0.45
	780	4.09E-09	0.03%	No (p = 0.85)	0.88
MISR	443	5.96E-09	0.07%	No (p = 0.3)	0.39
	551	4.16E-10	0.01%	No (p = 0.92)	0.34
	680	−2.69E-08	−0.28%	No (p = 1.99)	0.56
	780	−3.00E-08	−0.20%	No (p = 1.89)	0.72
VIIRS	443	2.31E-08	0.27%	Yes (p = 0.006)	0.52
	551	8.83E-09	0.13%	No (p = 0.24)	0.64
	680	−3.93E-09	−0.04%	No (p = 1.34)	0.54
	780	2.48E-09	0.02%	No (p = 0.88)	0.64

Next, we normalized the time series for MODIS, MISR and VIIRS to the second three-month period (September-October-November of 2015) and combined them into one time series by taking the arithmetic average of the three curves as illustrated in Figure 4, since the first three-month period (June-July-August 2015) contains fewer EPIC data points leading to more variability in the calculated values. Using this combined time-series we calculated the "overall" MODIS + MISR + VIIRS trends. The values are shown on the inserts in Figure 4. We found a small statistically significant trend of 0.16%/year in the 443 nm channel, while trends in other channels were not significant. The differences between the normalized curves (gray lines) appear to be greater in the red and NIR channels compared to the blue and green channels. It can be seen from the last column of Table 3 that relative RMSE values are higher in the NIR channels compared to the visible channels for all LEO instruments, possibly due to bigger spectral separation (see Figure 1). This may have contributed to the larger differences for the 780 nm curves. In addition, the observed offsets between individual instrument curves may partly be an artifact of random differences between the instruments at the point of normalization. This, however, does not have any effect on the trend calculations.

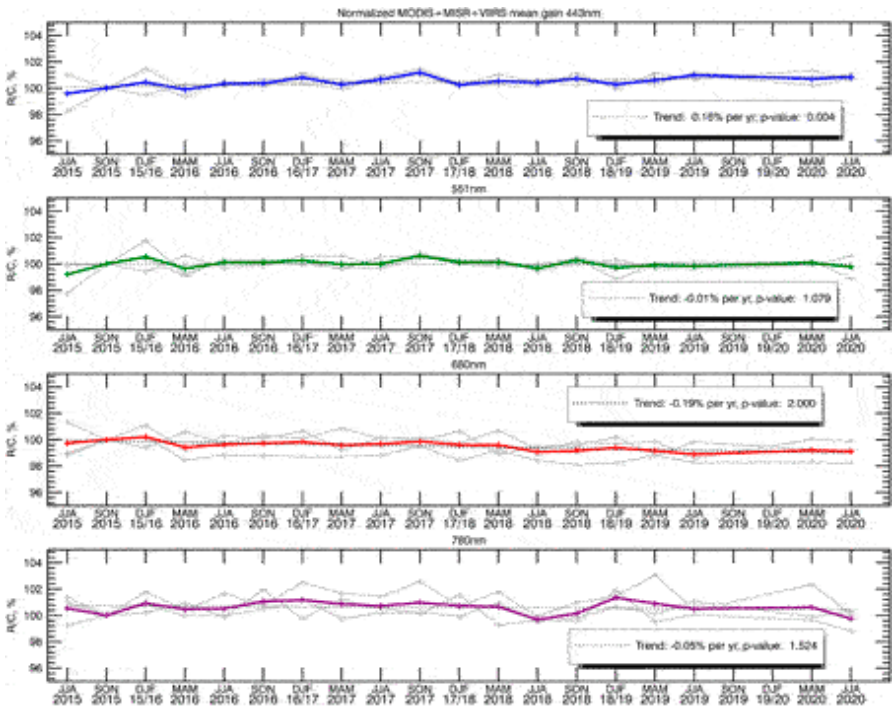

FIGURE 4 | Average MODIS + MISR + VIIRS seasonal mean R/C values normalized to one on SON 2015 (colored curves). Solid gray curves are for individual LEO instruments, dotted line is linear trend.

Variability due to Orbital Motion

The DSCOVR satellite's orbital motion around L1 point means that EPIC's scattering angle fluctuates by as much as 10° in the time frame of about 1.5°months (top panel of Figure 5). In addition, the instrument's distance to Earth can change by as much 200,000 km in about 3°months (top panel of Figure 6). This behavior differs a lot form the very regular orbits of instruments in sun-synchronous or geostationary orbits. In this section we estimate how much variability in EPIC calibration is caused by the DSCOVR orbital motion. This is useful for algorithm validation and provides reference values for EPIC-LEO intercalibration and trend analysis. Detrended R/C ratios derived from MODIS were binned and averaged according to the EPIC scattering angle and according to the EPIC-Earth distance. The results are displayed on the lower panels of Figures 5, 6. The dependance of the R/C ratios on the scattering angle is essentially flat with some increase observed for the largest angles in the 443 and 680 nm channels. RMSE values over the four bins used is about 1%. We conclude that the changes in scattering angle are not a significant source of variability of the calibration gains. The

changes in the DSCOVR-Earth distance have an even smaller effect on the variability of calibration values, as can be seen from the lower panel of Figure 6. The corresponding RSME values are on the order of 0.5% for the binned R/C mean values. As expected, this value is small, because EPIC counts for identical scenes should not depend on the distance from Earth.

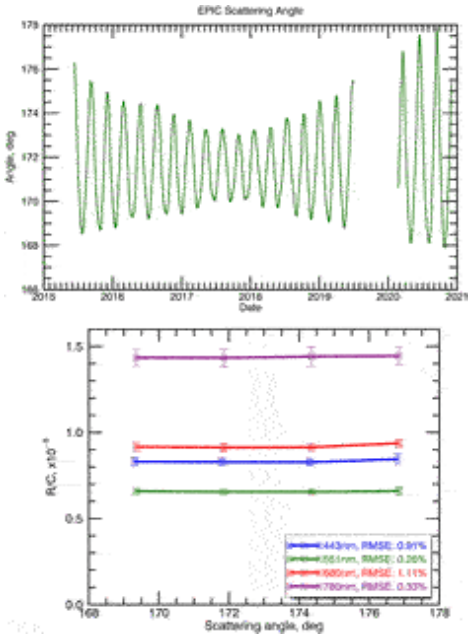

FIGURE 5 | Top panel: EPIC scattering angle vs. time. Lower panel: mean R/C ratio vs. scattering angle. Whiskers represent the standard deviation of the values within each bin. Based on MODIS data.

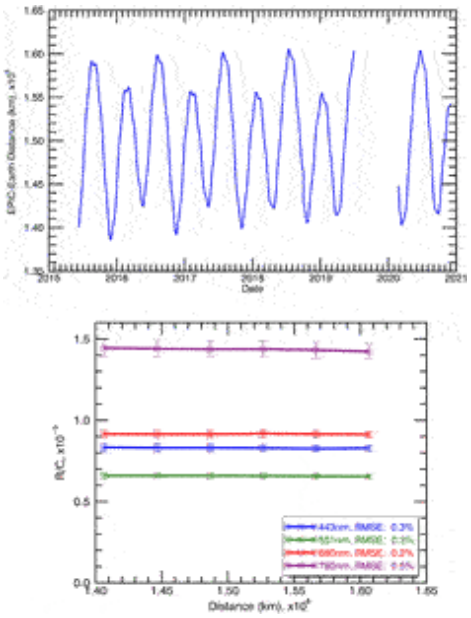

FIGURE 6 | Top panel: EPIC-Earth distance vs. time. Lower panel: mean R/C ratio vs. EPIC-Earth distance. Whiskers represent the standard deviation of the values within each bin. Based on MODIS data.

Aqua- and Terra-Derived Calibration

In the preceding sections, data from MODIS Aqua and Terra were combined into one dataset. While the two instruments are very similar and follow the same calibration approach, the Aqua and Terra satellites have different equator crossing times and thus, generally speaking, different observational geometries. It is therefore of interest to investigate the differences that may occur if the two instruments are used separately. Figure 7 presents the time-series of R/C ratios derived from MODIS Terra (blue curve) and MODIS Aqua (red curve), while Table 4 lists the relevant statistics. We found that MODIS Aqua R/C values have higher variability compared to MODIS Terra (third and second columns of Table 4, respectively). Assuming that seasonal mean R/C values are statistically independent samples, we can apply the Kolmogorov-Smirnov (KS) test to the two datasets. The test reveals that the Terra and Aqua values for 443, 551 and 680 nm channels are not significantly different (the fifth column of Table 4). However, a significant statistical difference exists between Aqua- and Terra-derived 780 nm values, with Aqua values being systematically lower by about 2% compared to Terra. This is consistent with the higher (2.6%, see *Calibration Gains and Trends* above) difference in the calibration gains in this channel reported here

and by Doelling et al. (2019), since they used MODIS Aqua data only. In addition, the Aqua 780 nm R/C ratios appear to be somewhat higher during the period from the middle of 2017 to the middle of 2018 than during other periods (Figure 7). We cannot establish with confidence the cause of these differences. We plan to investigate them further using the additional MODIS calibration from MODIS Land discipline processing, mentioned in *Data*, which does not have trends or biases between the two MODIS sensors. Please refer to *Modeling Earth Polychromatic Imaging Camera Reflectances* below for additional modeling analysis and further discussion.

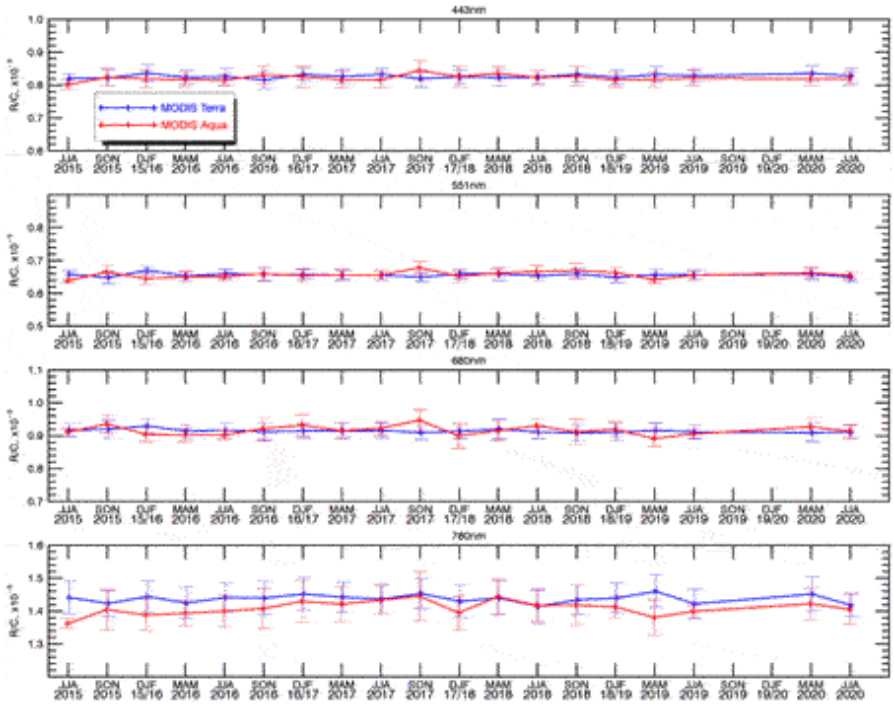

FIGURE 7 | Time series of MODIS Aqua (red) and Terra (blue) derived seasonal mean R/C ratios.

TABLE 4 | Statistics of EPIC R/C ratios derived from Terra and Aqua MODIS data.

EPIC channel (nm)	Terra RMSE (%)	Aqua RMSE (%)	Relative Terra-Aqua difference	Kolmogorov-Smirnov test significant?	Relative RMSE difference (%)
443	0.68	1.06	0.61%	No (p = 0.05)	1.5
551	0.75	1.41	−0.13%	No (p = 0.25)	1.9
680	0.53	1.51	−0.19%	No (p = 0.25)	1.75
780	0.86	1.47	1.96%	Yes (p = 0.0005)	2.53

Multi-Angle Imaging Spectroradiometer Camera-Specific Calibration Analysis

MISR on board Terra spacecraft has a nadir, 4 forward, and 4 aftward looking cameras. Figure 8 shows the distribution of EPIC-matching pixels over MISR cameras. Over 80% of EPIC matches are viewed through the two cameras closest to nadir (Af and Aa). The number of matching pixels viewed through each of these cameras (around 40%) is similar across the four channels. Some variation may be due to time delays between EPIC image acquisition in different spectral channels. We can compare the calibration gains derived separately for the two cameras. The results of an analysis analogous to the previous section are summarized in Figure 9. We found the relative difference between the MISR aftward (Aa) and forward (Af) cameras to be 0.03, −0.02, −1.53, and −0.85% for the 443, 551, 680 and 780 nm channels, respectively. The corresponding relative RMSE differences were 1, 1, 1.7, and 1.4%. Using the Kolmogorov-Smirnov test, we determined that the differences between EPIC R/C values derived from the two MISR cameras' data are not statistically significant in the blue and green channels (*p*-values of 0.5 and 0.3, respectively) and are significant in the red and NIR channels (*p*-values of 0 and 0.004, respectively).

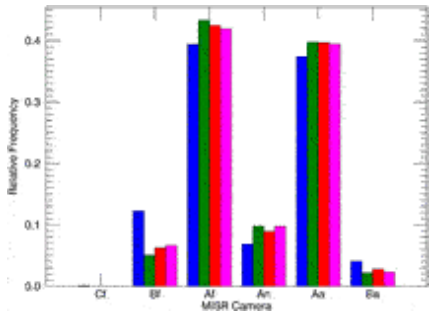

FIGURE 8 | Distribution of EPIC-matching scenes over MISR cameras. Blue, green, red, and magenta bars represent 443, 551, 680 and 780 nm channels.

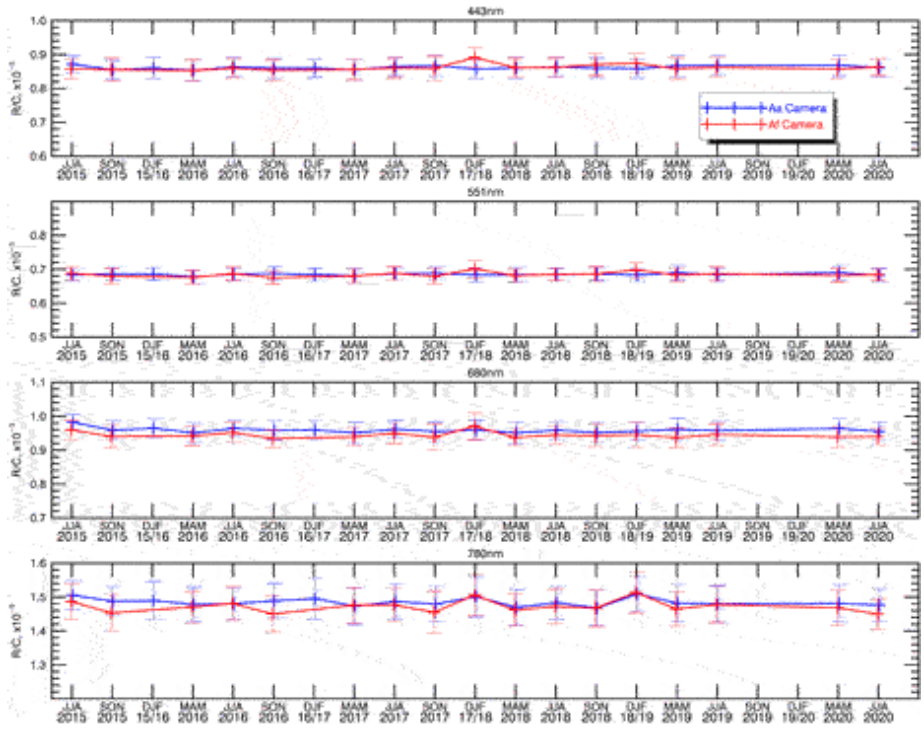

FIGURE 9 | Time series of seasonal mean R/C ratios derived from MISR Af (red) and Aa (blue) cameras.

Modeling Earth Polychromatic Imaging Camera Reflectances

EPIC and the LEO instruments view a collocated scene at the same scattering angle in the backscattering region, but may have different viewing and azimuth angles. In this section we conduct a model study to investigate how the differences in viewing geometry affect EPIC calibration coefficients. Such a study is also relevant for the evaluation of the range of any potential systematic differences due to viewing geometry between MODIS Aqua and MODIS Terra, which have different equator crossing times. For this purpose, we calculated reflectance look-up tables (LUT) for water clouds of various brightness. A LUT was calculated for each of the four channels, on a grid of 35 values of cosine of the solar zenith angle (in increments of 0.015), 150 values of cosine of the viewing angle, 181 values of azimuth angle (in increments of 1°), and 19 values of droplet number density, selected to cover the observed range of TOA reflectance. Using the actual geometries of matching EPIC and MODIS scenes, we then calculated what EPIC and MODIS would see, had they flown over such clouds. Specifically, we used the measured MODIS reflectance and viewing geometry (for the actual

pixels used for calibration) to look up the cloudy scene that matches the observed MODIS reflectance. Using that scene, we then determined the reflectance that EPIC would measure using its viewing geometry angles for this scene. Thus, we created a set of synthetic (modeled) EPIC reflectances which may be used in place of MODIS reflectances for "calibration." The procedure is illustrated schematically in Figure 10. The background contour plot shows calculated reflectance field as a function of relative azimuth and view angles for a specific solar zenith angle. Each pair of connected circles and crosses represents MODIS and EPIC positions for a single matching scene. The scenes were randomly selected from the available pool. The calculated reflectance field is selected from the look-up table to match the observed MODIS reflectance for the actual MODIS viewing geometry for each scene. The scene marked by the green line illustrates a situation where MODIS and EPIC would register similar reflectance (same background shade at the ends). For the scene marked by the blue line, EPIC reflectance will be lower than the reflectance registered by MODIS (different background shades at the ends). Repeating this procedure for all available matching scenes allowed us to create a synthetic dataset for this idealized case where both instruments observed scenes of plane-parallel water clouds. If we replace the actual MODIS-observed reflectances with the modeled EPIC ones we can eliminate the influence of the imperfect viewing geometry match between the instruments. In this way we can investigate how calibration gains would change if MODIS were always in the line of sight of EPIC (perfect viewing geometry match). Using only MODIS Terra data, we found the relative differences of mean R/C ratios to be 0.28, 0.1, 0.1, and 0.5% for the 443, 551, 680, and 780 nm channels respectively. For MODIS Aqua the corresponding values were -1.2, −0.02, 0.4, and −2.27%. It can be seen that in this highly idealized case, the average effects of the imperfect viewing geometry match are generally small, except for Aqua in the 780 nm channel. In addition, most of the time, the effects described above influence Aqua and Terra values in opposite directions, so that the results for the combined Aqua + Terra dataset (0.02, 0.09, 0.13, and 0.18% difference, respectively) are very close. It may therefore be advantageous to combine MODIS Terra and MODIS Aqua data for the purpose of EPIC calibration.

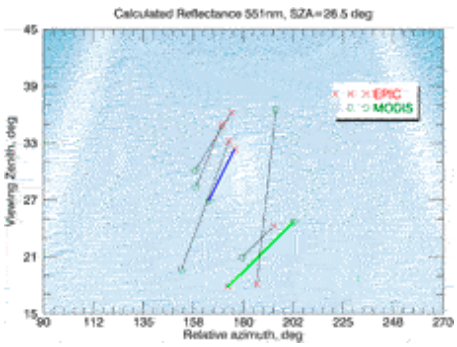

FIGURE 10 | A schematic representation of modeling EPIC reflectances. The background contour plot shows calculated reflectance field as a function of relative azimuth and view angles for a specific solar zenith angle. Each pair of connected circles and crosses represents MODIS and EPIC positions for a single matching scene. The scene marked by the green line illustrates a situation where MODIS and EPIC would register similar reflectance (same background shade at the ends). For the scene marked by the blue line EPIC reflectance will be lower than the reflectance registered by MODIS (different background shades at the ends).

We also looked at the ratio of modeled EPIC to measured MODIS reflectance as a function of scattering angle. The results are presented in Figure 11. As can be seen from the figure, in this idealized case, MODIS Terra and Aqua may exhibit biases of up to several percent for the largest scattering angles. This is consistent with measured data in Figure 5, where small increases in the last scattering angle bin may be observed. As can be seen from Figure 10, reflectance gradients are larger in the region close to the exact backscattering. In this region viewing geometry mismatch may result in larger EPIC-LEO reflectance differences. Since the resumption of operations in February 2020, the DSCOVR satellite operates without a gyroscope and relies on its startracker for angular rate information. The satellite is allowed to operate closer to exact backscattering, approaching it every three months to within 2° to conserve fuel for station-keeping. Our results suggest that caution should be exercised when data from such periods are used for calibration purposes. Note however, that, as mentioned above, the biases point in the opposite directions for MODIS Terra and MODIS Aqua and tend to cancel when the data is combined.

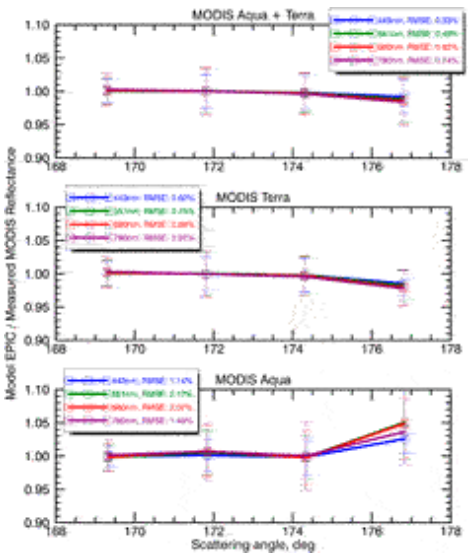

FIGURE 11 | Modeled EPIC to measured MODIS reflectance ratios as a function of scattering angle. **Top panel:** combined Aqua and Terra data, middle panel: MODIS Terra data, **lower panel:** MODIS Aqua data.

DISCUSSION

We applied the EPIC VIS-NIR calibration algorithm to the full duration of the data record. We assembled database of EPIC-matching data files from MODIS Aqua and Terra, MISR and VIIRS NPP, thus producing uniform EPIC calibration data records against four major LEO radiometers. Calibration gains for data until June 2019 were found to be in excellent agreement with independent published values (Doelling et al., 2019). No significant changes in calibration were observed after the instrument's exit from safe hold in March 2020. Analysis of seasonal mean R/C ratios revealed that the trends for the full dataset period are not statistically significant except in the 443 nm channel. We conducted an investigation of how DSCOVR's varying Sun-Earth-Vehicle angle and the distance from Earth could affect the calibration gains. We found that such changes result in less than 1 and 0.5% RMSE variability, respectively. Using MODIS Aqua and MODIS Terra as two independent datasets we analyzed the consistency of the retrieved time series of EPIC calibration gains. Statistical tests indicate that the differences between the two datasets are not significant except in the 780 nm channels, where Aqua-derived coefficients may be around 2% lower compared to Terra-derived ones. Similar consistency analysis was performed using two MISR cameras separately. We found that the gains derived from

the forward- and aftward-looking cameras agreed to within 1.5% of each other. These analyses increase our confidence in the robustness of the developed algorithm as applied to multiple LEO radiometers.

DATA AVAILABILITY STATEMENT

Publicly available datasets were analyzed in this study. This data can be found here: DSCOVR EPIC L1B data: https://opendap.larc.nasa.gov/opendap/ MODIS Aqua and Terra L1B data: https://ladsweb.modaps.eosdis.nasa.gov/archive/allData/61/MOD021KM/https://ladsweb.modaps.eosdis.nasa.gov/archive/allData/61/MYD021KM/ MISR L1B data: https://asdc.larc.nasa.gov/data/MISR/MI1B2E.003/ VIIRS L1B data: https://ladsweb.modaps.eosdis.nasa.gov/archive/allData/5000/NPP_VMAES_L1/ MISR Ellipsoid-projected L1B2 data: https://asdc.larc.nasa.gov/MISR/MI1B2E.003 VIIRS L1 data: https://ladsweb.modaps.eosdis.nasa.gov/archive/allData/5000/NPP_VMAES_L1/.

AUTHOR CONTRIBUTIONS

IG developed the calibration algorithm and performed the data analysis. AM helped in the algorithm development and participated in data analysis. MA provided radiative transfer calculations for the modeling of EPIC reflectances.

FUNDING

This research was funded by NASA Grant 80NSSC19K0761 “Calibration of the DSCOVR EPIC visible and NIR channels using multiple satellite data.”

ACKNOWLEDGMENTS

We thank two reviewers and the editor of this paper for their insightful comments, which resulted in a much improved manuscript. The MODIS Terra and Aqua data and VIIRS data were acquired from the Level-1 and Atmosphere Archive and Distribution System (LAADS) Distributed Active Archive Center (DAAC), located in the Goddard Space Flight Center in Greenbelt, Maryland (https://ladsweb.nascom.nasa.gov/). The DSCOVR EPIC and MISR data were obtained from the NASA Langley Research Center Atmospheric Science Data Center.

REFERENCES

Bruegge, C. J., Chrien, N. L., Ando, R. R., Diner, D. J., Abdou, W. A., Helmlinger, M. C., et al. (2002). Early Validation of the Multi-Angle Imaging SpectroRadiometer (MISR) Radiometric Scale. *IEEE Trans. Geosci. Remote Sensing* 40, 1477–1492. doi:10.1109/TGRS.2002.801583

Cao, C., De Luccia, F. J., Xiong, X., Wolfe, R., and Weng, F. (2014). Early On-Orbit Performance of the Visible Infrared Imaging Radiometer Suite Onboard the Suomi National Polar-Orbiting Partnership (S-NPP) Satellite. *IEEE Trans. Geosci. Remote Sensing* 52, 1142–1156. doi:10.1109/TGRS.2013.2247768

Carn, S. A., Clarisse, L., and Prata, A. J. (2016). Multi-decadal Satellite Measurements of Global Volcanic Degassing. *J. Volcanology Geothermal Res.* 311, 99–134. doi:10.1016/j.jvolgeores.2016.01.002

Carn, S. A., Krotkov, N. A., Fisher, B. L., Li, C., and Prata, A. J. (2018). First Observations of Volcanic Eruption Clouds from the L1 Earth-Sun Lagrange Point by DSCOVR/EPIC. *Geophys. Res. Lett.* 45. doi:10.1029/2018GL079808

Channan, S., Collins, K., and Emanuel, W. R. (2014). *Global Mosaics of the Standard MODIS Land Cover Type Data*. College Park, Maryland, USA: University of Maryland and the Pacific Northwest National Laboratory.

Diner, D. J., Braswell, B. H., Davies, R., Gobron, N., Hu, J., Jin, Y., et al. (2005). The Value of Multiangle Measurements for Retrieving Structurally and Radiatively Consistent Properties of Clouds, Aerosols, and Surfaces. *Remote Sensing Environ.* 97, 495–518. doi:10.1016/j.rse.2005.06.006

Doelling, D., Haney, C., Bhatt, R., Scarino, B., and Gopalan, A. (2019). The Inter-calibration of the DSCOVR EPIC Imager with Aqua-MODIS and NPP-VIIRS. *Remote Sensing* 11, 1609. doi:10.3390/rs11131609

Gao, B.-C., Li, R.-R., and Yang, Y. (2019). Remote Sensing of Daytime Water Leaving Reflectances of Oceans and Large Inland Lakes from EPIC Onboard the DSCOVR Spacecraft at Lagrange-1 Point. *Sensors* 19 (5), 1243. doi:10.3390/s19051243

Geogdzhayev, I. V., and Marshak, A. (2018). Calibration of the DSCOVR EPIC Visible and NIR Channels Using MODIS Terra and Aqua Data and EPIC Lunar Observations. *Atmos. Meas. Tech.* 11, 359–368. doi:10.5194/amt-11-359-2018

Haney, C., Doelling, D., Minnis, P., Bhatt, R., Scarino, B., and Gopalan, A. (2016). "The calibration of the DSCOVR EPIC multiple visible channel instrument using MODIS and VIIRS as a reference," in *Proc. SPIE 9972, Earth Observing Systems XXI, 99720P*, *(September 19, 2016)* (SPIE Optical Engineering + Applications). doi:10.1117/12.2238010

Herman, J., Cede, A., Huang, L., Ziemke, J., Torres, O., Krotkov, N., et al. (2020). Global Distribution and 14-year Changes in Erythemal Irradiance, UV Atmospheric Transmission, and Total Column Ozone For2005-2018 Estimated from OMI and EPIC Observations. *Atmos. Chem. Phys.* 20, 8351–8380. doi:10.5194/acp-20-8351-2020

Herman, J., Huang, L., McPeters, R., Ziemke, J., Cede, A., and Blank, K. (2018a). Synoptic Ozone, Cloud Reflectivity, and Erythemal Irradiance from Sunrise to sunset for the Whole Earth as Viewed by the DSCOVR Spacecraft from the Earth-Sun Lagrange 1 Orbit. *Atmos. Meas. Tech.* 11, 177–194. doi:10.5194/amt-11-177-2018

Herman, J., Wen, G., Marshak, A., Blank, K., Huang, L., Cede, A., et al. (2018b). Reduction in 317-780 Nm Radiance Reflected from the Sunlit Earth during the Eclipse of 21 August 2017. *Atmos. Meas. Tech.* 11, 4373–4388. doi:10.5194/amt-11-4373-2018

JPSS Level 1 Requirements Document (2016). *Joint Polar Satellite System (JPSS) Level 1 Requirements Document, JPSS-REQ-1001*. https://www.jpss.noaa.gov/assets/pdfs/technical_documents/level_1_requirements.pdf.Final Version: 2.0.

King, M. D., Menzel, W. P., Kaufman, Y. J., Tanré, D., Bo-Cai Gao, B. C., Platnick, S., et al. (2003). Cloud and Aerosol Properties, Precipitable Water, and Profiles of Temperature and Water Vapor from MODIS. *IEEE Trans. Geosci. Remote Sensing* 41, 442–458. doi:10.1109/tgrs.2002.808226

Kostinski, A., Marshak, A., and Várnai, T. (2021). Deep Space Observations of Terrestrial Glitter. *Earth Space Sci.* 8, e2020EA001521. doi:10.1029/2020EA001521

Kwiatkowska, E. J., Franz, B. A., Meister, G., McClain, C. R., and Xiong, X. (2008). Cross Calibration of Ocean-Color Bands from Moderate Resolution Imaging Spectroradiometer on Terra Platform. *Appl. Opt.* 47, 6796–6810. doi:10.1364/ao.47.006796

Lyapustin, A., Wang, Y., Xiong, X., Meister, G., Platnick, S., Levy, R., et al. (2014). Scientific Impact of MODIS C5 Calibration Degradation and C6+ Improvements. *Atmos. Meas. Tech.* 7, 4353–4365. doi:10.5194/amt-7-4353-2014

Marshak, A., Herman, J., Adam, S., Karin, B., Carn, S., Cede, A., et al. (2018). Earth Observations from DSCOVR EPIC Instrument. *Bull. Am. Meteorol. Soc.* 99, 1829–1850. doi:10.1175/BAMS-D-17-0223.1

Marshak, A., and Knyazikhin, Y. (2017). The Spectral Invariant Approximation within Canopy Radiative Transfer to Support the Use of the EPIC/DSCOVR Oxygen B-Band for Monitoring Vegetation. *J. Quant. Spectrosc. Radiat. Trans.* 191, 5197–5202. doi:10.1016/j.jqsrt.2017.01.015

Marshak, A., Várnai, T., and Kostinski, A. (2017). Terrestrial Glint Seen from Deep Space: Oriented Ice Crystals Detected from the Lagrangian point. *Geophys. Res. Lett.* 44. doi:10.1002/2017GL073248

MODIS Characterization Support Team (2006). *MODIS Level 1B Product User's Guide*. https://mcst.gsfc.nasa.gov/sites/mcst.gsfc/files/file_attachments/M1054.pdf.

Scarino, B. R., Doelling, D. R., Minnis, P., Gopalan, A., Chee, T., Bhatt, R., et al. (2016). A Web-Based Tool for Calculating Spectral Band Difference Adjustment Factors Derived from SCIAMACHY Hyperspectral Data. *IEEE Trans. Geosci. Remote Sensing* 54 (5), 2529–2542. doi:10.1109/tgrs.2015.2502904

Toller, G., Xiong, X., Sun, J., Wenny, B. N., Geng, X., Kuyper, J., et al. (2013). James Kuyper, Amit Angal, Hongda Chen, Sriharsha Madhavan, Aisheng Wu,Terra and Aqua Moderate-Resolution Imaging Spectroradiometer Collection 6 Level 1B Algorithm. *J. Appl. Remote Sens* 7 (1), 073557. doi:10.1117/1.JRS.7.073557

Varnai, T., Marshak, A., and Kostinski, A. B. (2020). *Deep Space Observations of Cloud Glints: Spectral and Seasonal Dependence*. IEEE Geoscience and Remote Sensing Letters, 1–5. doi:10.1109/LGRS.2020.3040144

Yang, B., Knyazikhin, Y., Mõttus, M., Rautiainen, M., Stenberg, P., Yan, L., et al. (2017). Estimation of Leaf Area index and its Sunlit Portion from DSCOVR EPIC Data: Theoretical Basis. *Remote Sensing Environ.* 198, 69–84. doi:10.1016/j.rse.2017.05.033

Yang, Y., Marshak, A., Mao, J., Lyapustin, A., and Herman, J. (2013). A Method of Retrieving Cloud Top Height and Cloud Geometrical Thickness with Oxygen A and B Bands for the Deep Space Climate Observatory (DSCOVR) Mission: Radiative Transfer Simulations. *J. Quantitative Spectrosc. Radiative Transfer* 122, 141–149. doi:10.1016/j.jqsrt.2012.09.017

Yang, Y., Meyer, K., Wind, G., Zhou, Y., Marshak, A., Platnick, S., et al. (2019). Cloud Products from the Earth Polychromatic Imaging Camera (EPIC): Algorithms and Initial Evaluation. *Atmos. Meas. Tech.* 12, 2019–2031. doi:10.5194/amt-12-2019-2019

Yin, B., Min, Q., Morgan, E., Yang, Y., Marshak, A., and Davis, A. (2020). Cloud Top Pressure Retrieval with DSCOVR-EPIC Oxygen A and B Bands Observation. *Atmos. Meas. Tech.* 13, 1–18. doi:10.5194/amt-13-5259-2020

Conflict of Interest: The authors declare that the research was conducted in the absence of any commercial or financial relationships that could be construed as a potential conflict of interest.

ORIGINAL RESEARCH
published: 09 July 2021
doi: 10.3389/frsen.2021.702275

Raw EPIC Data Calibration

Alexander Cede[1,2,3*], Liang Kang Huang[2,4], Gavin McCauley[1], Jay Herman[2,5], Karin Blank[2], Matthew Kowalewski[2] and Alexander Marshak[2]

[1] *SciGlob Instruments & Services LLC, Elkridge, MD, United States*
[2] *Goddard Space Flight Center, NASA, Greenbelt, MD, United States*
[3] *LuftBlick, Innsbruck, Austria*
[4] *Science Systems and Applications, Inc., Lanham, MD, United States*
[5] *Joint Center for Earth Systems Technology, Baltimore, MD, United States*

Edited by:
Yongxiang Hu, National Aeronautics and Space Administration, United States

Reviewed by:
Daniel Perez Ramirez, University of Granada, Spain
Rong Wang, Fudan University, China

**** Correspondence:** Alexander Cede, alexander@sciglob.com*

***Specialty section:** This article was submitted to Satellite Missions, a section of the journal Frontiers in Remote Sensing*

***Received:** 29 April 2021*
***Accepted:** 23 June 2021*
***Published:** 09 July 2021*

***Citation:** Cede A, Kang Huang L, McCauley G, Herman J, Blank K, Kowalewski M and Marshak A (2021) Raw EPIC Data Calibration. Front. Remote Sens. 2:702275. doi: 10.3389/frsen.2021.702275*

Earth Polychromatic Imaging Camera (EPIC) raw level-0 (L0) data in one channel is a 12-bit 2,048 × 2,048 pixels image array plus auxiliary data such

as telemetry, temperature, etc. The EPIC L1a processor applies a series of correction steps on the L0 data to convert them into corrected count rates (level-1a or L1a data): Dark correction, Enhanced pixel detection, Read wave correction, Latency correction, Non-linearity correction, Temperature correction, Conversion to count rates, Flat fielding, and Stray light correction. L1a images should have all instrumental effects removed and only need to be multiplied by one single number for each wavelength to convert counts to radiances, which are the basis for all higher-level EPIC products, such as ozone and sulfur dioxide total column amounts, vegetation index, cloud, aerosol, ocean surface, and vegetation properties, etc. This paper gives an overview of the mathematics and the pre-launch and on-orbit calibration behind each correction step.

Keywords: Satellite remote sensing, Earth observation, Lagrange 1 point, instrument calibration, flat field correction, stray light correction

INTRODUCTION

The Earth Polychromatic Imaging Camera (EPIC) operates aboard the Deep Space Climate Observatory (DSCOVR) satellite that is orbiting the Sun at the Lagrange-1 point, L_1, about 1.5 million kilometers away from Earth (Marshak et al., 2018). It measures the solar radiance backscattered from the sunlit portion of the Earth using 10 narrow-band wavelength filters, from the ultraviolet (UV) to the near-infrared (NIR). The science products (L2 data, see also Table 1) derived from these observations include total column ozone (Herman et al., 2018; Yang and Liu, 2019; Herman et al., 2020) and sulfur dioxide (SO_2) (Carn et al., 2018), aerosol information (Christian et al., 2019; Sasi et al., 2020; Xu et al., 2019; Torres et al., 2020; Lyapustin et al., 2021), cloud (Meyer et al., 2016; Molina García et al., 2018; Davis et al., 2018; Yang et al., 2019, Yin et al., 2020; Zhou et al., 2020) and vegetation (Marshak and Knyazikhin, 2017; Weber et al., 2020; Pisek et al., 2021) properties, reflectivity (Song et al., 2018; Yang et al., 2018; Wen et al., 2019), and atmospheric correction (Herman et al., 2020; Lyapustin et al., 2021). The sequence from raw data to final products is a 3-step process:

- **L0 to L1a**: L0 data in each channel are converted into corrected count rates (level-1a or L1a data). L1a images should have all instrumental effects removed so that the resulting data images are proportional to the absolute radiances.

• **L1a to L1b**: The latitude, longitude, sun, and view angles are calculated for the L1a image in its original orientation. For level-1b (L1b), the images are reprojected into a common grid, which fixes offsets due to variation in attitude, rotational offsets due to time, and orients the images so that north is up.

• **L1b to L2**: A calibration factor is derived to convert the corrected count rates in either L1a or L1b into radiances (Geogdzhaev and Marshak, 2018; Herman et al., 2018; Doelling et al., 2019). The L1b images from one or more channels are converted into level-2 (L2) data through application of a specific algorithm for each output science product.

TABLE 1 | Specifications of the EPIC filters. Filter wheel 1 with filters 1–5 is closer to the primary mirror, filter wheel 2 with filters 6 to 10 is closer to the detector. The center wavelengths are given in nm-air and the resolutions are given as the full width half maximum (FWHM) of the filter function. The exposure time is the one used in regular operation and is never changed. For the meaning of the stray light fraction see *Stray Light Correction*. The primary science purpose indicates for which science L2 product the respective channel is used.

Filter (Filter wheel)	Center Wavelength [nm]	Resolution FWHM [nm]	Exposure Time [ms]	Stray light fraction [%]	Primary science purpose
1 (1)	317.4	1.1	654	13	O_3, SO_2
2 (1)	324.9	1.0	442	12	O_3, SO_2
3 (1)	339.8	2.7	67	12	O_3, SO_2, Aerosols, Reflectivity
4 (1)	387.8	2.6	87	14	Aerosols, Reflectivity
5 (1)	442.3	2.7	28	14	Aerosols, Reflectivity, Vegetation
6 (2)	551.5	3.0	70	13	Aerosols, Reflectivity, Vegetation
7 (2)	687.5	0.9	75	18	Clouds, O_2 B-Band
8 (2)	679.7	1.7	32	20	Aerosols, Reflectivity, Vegetation, Clouds
9 (2)	763.7	1.0	101	19	Clouds, O_2 A-Band
10 (2)	779.2	1.8	49	18	Aerosols, Reflectivity, Vegetation, Clouds

This paper gives an overview of the mathematics and the pre-launch and on-orbit calibration behind the first of the steps above that is the basis for all further processes. *Instrument Overview* gives a short overview of the instrument design and performance. The different calibration periods are listed in *Calibration Periods*. *L1a Processing Steps* goes through each of the

steps to convert the L0 data in L1a data. *Pixel Size on Ground* and *Uncertainty* discuss the EPIC pixel size on the ground and L1a data uncertainty, respectively. Conclusions are given in *Conclusions*.

INSTRUMENT OVERVIEW

The EPIC instrument is described in detail in the DSCOVR Overview report (Atmospheric Science Data Center, 2016; also https://epic.gsfc.nasa.gov/about/epic). Here we will provide a brief overview of the optical elements that are relevant for this paper. The optical path of EPIC is shown in Figure 1.

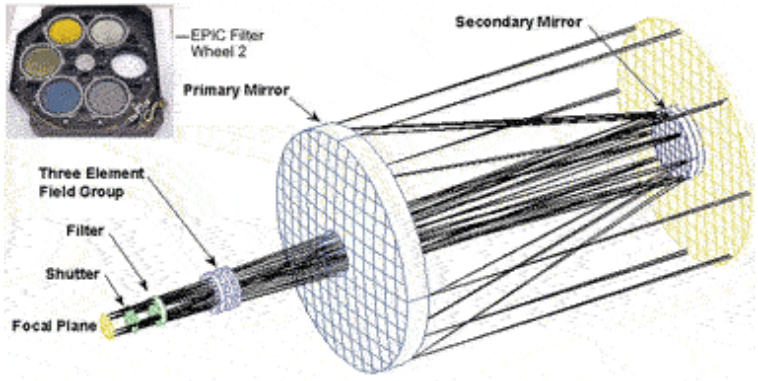

FIGURE 1 | EPIC light path. The picture at the top left shows one of the filter wheels with six positions.

As light enters the front end of the 286 cm focal length Cassegrain telescope, it is reflected by the 30.5 cm diameter primary mirror onto the 9.5 cm diameter secondary mirror. Light reflected by the secondary mirror passes through the center of the primary mirror, where it enters the camera assembly. A three-element fused silica field lens group is designed to correct the inherent optical aberrations of the Cassegrain telescope such as coma, astigmatism, and field curvature. EPIC houses two filter wheels, each with six openings of 4 cm diameter, of which five are equipped with an optical filter and one position is left open (Figure 1). Each filter is a combination of a narrow band interference filter with a broadband blocking filter. The next element in the EPIC camera assembly is a 3-slit rotating shutter wheel to control the length of the exposure, i.e., the duration in which the detector actively collects photons of light. The filter specifications and the mission invariant exposure times for each channel used in orbit are given in Table 1.

In the focal plane of the beam is the EPIC detector, a thinned, backside-illuminated hafnium coated silicon wafer CCD with an anti-reflection coating. It contains 2,048 × 2,048 square pixels of 15 microns pitch, resulting in a total imaging area of slightly more than 3 × 3 cm^2. In angular measurements, the pixel instantaneous field of view (iFOV) is 1.078 arcsecs. Therefore, the total field of regard (FOR) of the EPIC telescope is 0.607°, limited by the horizontal and vertical edges of the CCD (see Figure 2, where the gray areas in the corners of each panel show the region outside the FOV).

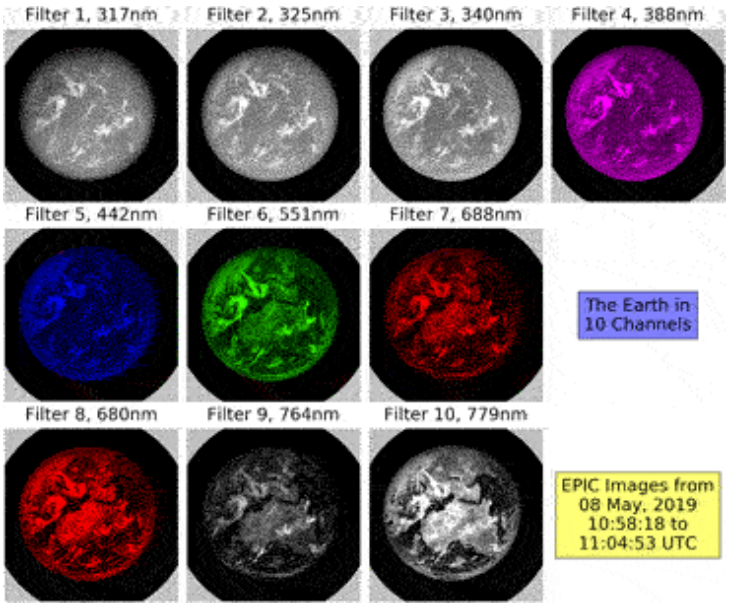

FIGURE 2 | EPIC L1a images for each channel taken on May 8, 2019 around 11 UTC. One such full set of 10 images is taken by EPIC approximately every 65 min during the Northern Hemisphere summer and every 110 min during the Northern Hemisphere winter. The gray areas in the corners of each panel show the regions outside of the FOV of the telescope. Areas with no signal are plotted in black color. Higher signal intensity is plotted in shades of white for the UV filters 1 to 3 and the NIR filters 9 and 10 and for the visible filters in that color our eye would see if we placed the respective filter in front of it. The contrast between dark and bright areas in the images is smallest for the UV channels due to strong Rayleigh scattering, and increases with wavelength. The filter pairs 7–8 and 9–10 are relatively close in wavelength, but one channel in each pair is strongly absorbed by molecular oxygen (filters 7 and 9), which causes a much darker image of the Earth compared to the other filter in the pair.

The EPIC CCD can be drained (readout) from two opposite corners. In regular operation, the same corner is always used. If the readout through that corner fails, EPIC could switch to the readout from the other corner. While

the entire EPIC calibration has been done for both readout modes, all results shown in this paper refer to the regular readout mode.

EPIC is read in a so-called "over-scanned" mode. This means although there are 2,048 × 2,048 pixels, 2,056 readings in both row and column direction are done. Therefore, the pixels from the first eight rows and columns do not include those photons that have been accumulated during the exposure time, but instead, only the photons caused by thermal electrons during the readout process. The pixels in these rows and columns are called "oversampled pixels" and are used in the dark correction (*Dark Correction*).

CALIBRATION PERIODS

Most of the information used for the EPIC raw data calibration was obtained during calibration periods that are listed in this section. The first version of full calibration for EPIC L1a processing was finished before the launch of DSCOVR. The necessary measurements were obtained during two dedicated pre-launch calibration campaigns (*Calibration Period "CalLM"* and *Calibration Period "CalGSFC"*). This first calibration version was then modified based on information obtained during two on-orbit calibration campaigns (*Calibration Period "CalDark"* and *Calibration Period "CalMoon"*). Finally, the operational EPIC images are used to determine if the instrumental characteristics are changing with time. The observed small changes have been used to modify the calibrations.

Calibration Period "CalLM"

The first calibration period "CalLM" took place at the Lockheed Martin Advanced Technology Center, Palo Alto, CA. Preparatory measurements were taken in air and with the detector at room temperature during July and August 2011. Final measurements were obtained at flight conditions in the vacuum chamber with a cooled detector from 15–20 Sept 2011. More than 3,000 images were taken in total. The calibration setup for CalLM is described in detail by Cede et al. (2011). The light from a 1500W xenon lamp entered the vacuum chamber through a window into an integrating sphere. After exiting the sphere, the light passed a focusing lens and a selected "target" on the 6-position aperture wheel (most targets were holes of different diameters). Then it entered a Dobsonian collimator, which produced an extended beam with a divergence determined by the target. The beam was then reflected by the steering mirror and entered EPIC. This setup allowed

EPIC to be illuminated with beams of different divergence, from point sources used for stray light calibration to extended sources that overfilled the instrument's total FOV.

Calibration Period "CalGSFC"

The second pre-launch calibration period "CalGSFC" took place in February 2014 at NASA/Goddard Space Flight Center, Greenbelt, MD. In this period, measurements were taken in the vacuum chamber at flight conditions for 7 days with over 600 images in total. The focus was to repeat the original calibration sequences that did not give conclusive results in the 2011 tests during CalLM, namely the non-linearity and flat field calibration. In this calibration EPIC was illuminated by a beam reflected from a diffuser plate that overfilled the instrument's FOV.

Calibration Period "CalDark"

The period from DSCOVR's launch on February 11, 2015 to reaching its orbital location at the Earth-Sun Lagrange-1 point on June 7, 2015 was used for extensive dark count measurements with the closed telescope door and closed shutter and is called "CalDark". More than 1,000 dark images were taken to complement the pre-launch dark count calibration.

Calibration Period "CalMoon"

At the beginning of the mission, EPIC was pointed towards the fully illuminated Moon instead of the Earth on several occasions in between regular operations ("lunar observations"). They were usually taken at times where the angular distance between Earth and Moon as seen from EPIC was at a maximum, which corresponds approximately to half-moon phases on Earth. The longest of these periods is called "CalMoon" and lasted from August 15–19, 2015, where the lunar surface was "moved" over 36 positions across the detector. Images for 5 filters were taken at each position. Additional shorter periods with lunar observations have been and continue to be inserted in the regular EPIC observations schedule (26 of such periods as of March 2021). The objectives of the lunar observations are to test the stray light and flat field calibrations, and to check the radiometric stability of EPIC over time.

L1A PROCESSING STEPS

Any measurement device has imperfections, so does EPIC. For example, the radiometric sensitivity and the dark counts vary across the detector, stray light affects the pixels in different ways, the readout mechanism has a latency, etc. In processing the raw L0 data to L1a data we try to correct for all such imperfections in the best possible way. This is done in several processing steps.

If everything was done "perfectly", then each of the more than four million EPIC pixels would give exactly the same L1a output, if it was receiving the same input, and consequently the entire image only would need to be multiplied by one single number to convert from corrected count rates to radiances. Apart from the L1a data array, the L1a output also includes a so-called "pixel type array" of the same dimension as the image itself. The pixel types give information about whether the specific pixel is outside the EPIC FOV, is oversampled, is on or off "target" (i.e., inside or outside the disk of the Earth or the Moon), or is saturated or enhanced (see *Enhanced Pixel Detection*).

Some of the L1a corrections have less impact on the data than others. For those, the data would only differ from the "correct" data by a small amount if the correction was not applied. In order to get an overview of the magnitude (or impact) of each correction step, we decided to introduce "impact levels", which allow a quick qualitative assessment of the impact each correction has on the data. Here we define four impact levels: "**small**" (impact is below 0.4%), "**moderate**" (between 0.4 and 2%), "**significant**" (between 2 and 10%), and "**large**" (above 10%). Note that these percentage limits have been chosen, since the magnitudes of the different corrections clustered approximately into groups limited by these numbers. Corrections may have a moderate impact on the image as a whole, but a significant impact on a subgroup of pixels that are especially affected by the respective effect. The nine processing steps are listed below, with the impact given in parenthesis. If two impact levels are given (e.g., significant to large), then the first one is for the average impact and the second one for the impact on the subgroup of more affected pixels:

- Step 1-Dark correction (**moderate** to **large**)
- Step 2-Enhanced pixel detection (**small** to **large**)
- Step 3-Read wave correction (**small**)
- Step 4-Latency correction (**moderate** to **significant**)

- Step 5-Non-linearity correction (**small**)
- Step 6-Temperature correction (**small**)
- Step 7-Conversion to count rates (**small**)
- Step 8-Flat fielding (**significant** to **large**)
- Step 9-stray light correction (**significant** to **large**)

In this section, we describe each correction step separately. Since it would go beyond the limits of this paper to describe each correction step in full detail, we focus on those corrections with more significant effects on the data, i.e., dark-count, flat-field, and stray light corrections.

Dark Correction

The first correction applied on the 12-bit digital resolution EPIC raw data is the dark correction. A rather "safe" way to perform dark correction on the data would be to add a dark measurement (i.e., a measurement with closed shutter) after every single regular measurement using the same exposure time (Table 1). In this way, the dark count would be measured with exactly the same conditions (e.g., electronic state and temperature of the detector) and, therefore, any possible systematic errors in the dark correction could be avoided. However, the download rate for DSCOVR is limited so that such a technique cannot be applied. Due to this limit, the operational EPIC images for all filters, except the 443 nm blue filter number 5, are reduced on the spacecraft from the original size of 2,048 × 2,048 pixels to 1,024 × 1,024 pixels by averaging each group of 2 × 2 pixels. This was the only way to keep the EPIC image sequence in the range of one set of 10 images every 65 min in the Northern Hemisphere summer and 110 min in winter. The difference is caused by the number of hours a single S-band receiving antenna located at Wallops Island, Virginia, United States is in view. As a consequence, the strategy for the dark correction was the following:

- Develop a model that determines the EPIC dark count at pixel i, DC_i, based on two input variables, exposure time, t_{EXP}, and detector temperature, T_{CCD}, which are both transmitted in the auxiliary data.
- Adjust the modeled dark count to the electronic conditions at the measurement time using the oversampled pixels.

- Check the dark count behavior over time taking a daily dark measurement at 1,000 ms exposure time.

From the analysis of the data from CalLM, CalGSFC, and CalDark we developed the dark count model for dark count DC_i at the ith pixel given in Eq. 1.

$$DC_i(t_{EXP}, T_{CCD}, t_{IM}) = DO_{OV}(T_{CCD}) + DO_{Ci} + DO_{Ti} \cdot \exp[k_O \cdot (T_{CCD} - T_{REF})] + DS_i \cdot \exp[k_{si} \cdot (T_{CCD} - T_{REF})] \cdot t_{EXP} + DO_T(t_{IM}) \quad (1)$$

T_{REF} is the reference temperature. It was originally set to −40.0°C, since this was the temperature the EPIC detector was expected to have in operation. After the CalDark period it was changed to −20.8°C, since this temperature was then effectively observed in the first months on orbit (Figure 3).

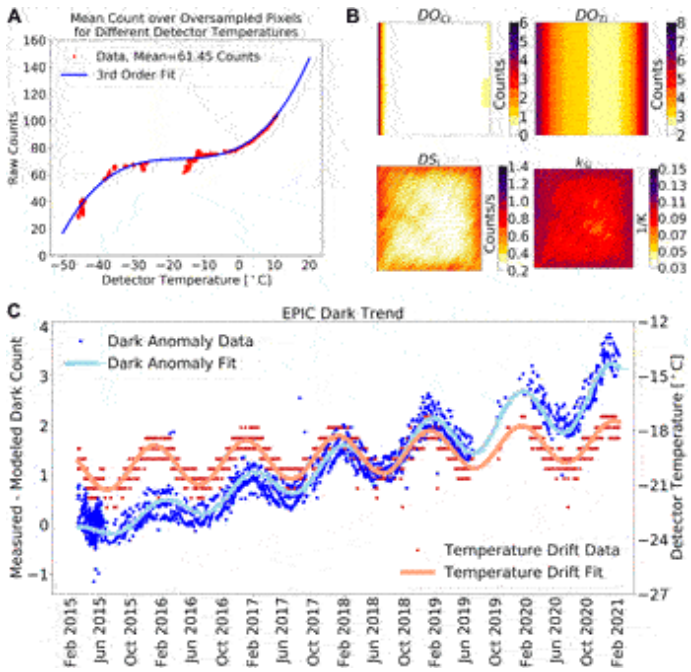

FIGURE 3 | (A) DO_0 as a function of T_{CCD} measured during CalLM. **(B)** Dark model parameters DO_{Ci}, DO_{Ti}, DS_i and k_{Si} from Eq. 1. **(C)** EPIC dark trend. The apparent noise in the dark anomalies (blue dots) is mostly caused by the low resolution of 0.6 K for the detector temperature readings (red dots). Both data sets are fitted with formula $\mathbf{y = a_0 + a_1 \cdot t + (a_3 + a_5 \cdot t) \cdot \sin[2 \cdot \pi \cdot (t - a_2)/a_4]}$, where t is the time in days since January 1, 2017 0:00 UTC. The obtained fitting parameters for the Dark Anomaly Fit (blue line) are : a_0 = 0.71 counts, a_1 = 0.49 counts/year, a_2 = 71 days, a_3 = 0.30 counts, a_4 = 359 days, a_5 = 0.07 counts/year. For the Temperature Drift Fit (red line): a_0 = −19.69°C, a_1 = 0.28 K/y, a_2 = 94 days, a_3 = 1.13 K, a_4 = 368 days, a_5 = −0.02 K/y.

The DO-terms represent the dark offset and are independent of t_{EXP}. The dark slope DS depends linearly on t_{EXP}. t_{IM} is the time since January 1, 2017 0:00 UTC.

DO_{OV} is the average dark count over the oversampled pixels (Figure 3). It is mostly a function of T_{CCD}, but also depends on the electronic state of the detector system at the measurement time. This term does not need to be taken from the calibration, since it can be calculated for each operational measurement.

All 2,048 × 2,048 arrays DO_{Ci}, DO_{Ti}, DS_i, and k_{Si} from Eq. 1 are shown in Figure 3. DO_{Ci} gives the difference between the dark offset at each pixel and the value DO_{OV} at standard conditions. As seen in Figure 3, DO_{Ci}

increases towards the left edge of the detector, probably due to a temperature increase in this direction, and also shows a separation into four regions covering a quarter of the CCD each, which we believe is due to some characteristic of the readout electronics. The temperature dependence of the dark offset uses calibration parameters DO_{Ti} and k_O. DO_{Ti} is mostly a function of the CCD columns (Figure 3) with k_O determined to be 0.166/K.

The dark slope DS uses calibration parameters DS_i and k_{Si}. DS_i is characterized by an increase at the readout corners due to elevated temperature and also shows a rather small number of hot pixels. Using as a criterion for a hot pixel to exceed the expected value by more than 10 counts at the reference temperature, then EPIC has 210 hot pixels, which is 0.005% of the total pixels. Since they are singular isolated pixels, they are not visible in Figure 3.

In the first calibration versions, the "trend term" DO_T in Eq. 1 was not included in the dark model. It was added in 2017 when we discovered some pattern of the true dark count drifting away from the dark model as shown in Figure 3. This effect is clearly temperature-related but is obviously not correctly captured by the T_{CCD}-dependent terms in Eq. 1, although they have been determined over a wide range of temperatures as seen in Figure 3. It turned out that adjusting the dark model with a modified T_{CCD}-dependence was not possible, since the relation between the temperature and the observed dark count bias does not "fit" in the dark model framework. The seasonal temperature cycle of ±1.1 K is rather constant over time, while the seasonal cycle in the dark count bias changes from ±0.16 counts in 2015 to >±0.5 counts in 2020. Furthermore, the seasonal temperature cycle relates to the seasonal dark anomaly cycle on average by ~0.3 counts/K, while the upwards trend in the temperature of ~0.3 K/year causes an upwards trend of the dark count bias of ~0.5 counts/year, i.e., a much higher relation of ~1.7 counts/°C. Due to this discrepancy, we decided to define DO_T as a function of the image acquisition time t_{IM} with seasonal variation and a linear drift as shown in Figure 3. With this addition the dark model again well represents the true EPIC dark counts over its time in orbit.

Enhanced Pixel Detection

This L1a processing step only affects the pixel type array and does not change the L1a data array itself. The raw EPIC data can be saturated or

enhanced. The invariant EPIC exposure times (Table 1) were selected on the first day of operation so that saturation rarely occurs, but it can still happen when a pixel views a highly reflective ice cloud high up in the atmosphere.

Enhanced pixels are pixels with physically impossible values that exceed the values of the neighbor pixels by a too large amount. This can be understood when looking at Figure 8, which shows the EPIC point spread function (more in *Stray Light Correction*). For example, based on this function it is not possible that the value in a pixel is five times larger than the average value over the adjacent pixels. We believe this enhancement is mostly caused by issues in the readout electronics. Nearly all EPIC images show a small percentage of enhanced pixels. Their number varies between just a few such pixels up to around 1,000 of them in a single image of four million pixels. An algorithm to detect enhanced pixels was developed. It is based on a comparison of the value in a pixel relative to the average value over its eight neighbor pixels. It then marks enhanced pixels in the pixel type array so that they can be ignored for science data products.

Read-Wave Correction

EPIC's read-out electronics add a small sinusoidal wave to the image, called the "Read-wave". This wave is a function of the image column and has a rather constant period between 10 and 11 pixels but varies from image to image in amplitude (between 0 and 0.6 counts) and phase. Both amplitude and phase are approximately constant for all rows. An example of such a read wave is shown in Figure 4. We developed an algorithm to determine the amplitude and phase of the wave for each measurement. It is based on fitting a sinusoidal wave into those rows of the image, which get no direct light input, i.e., the ones below and above the Earth's disk, and then subtracting this wave from the entire image.

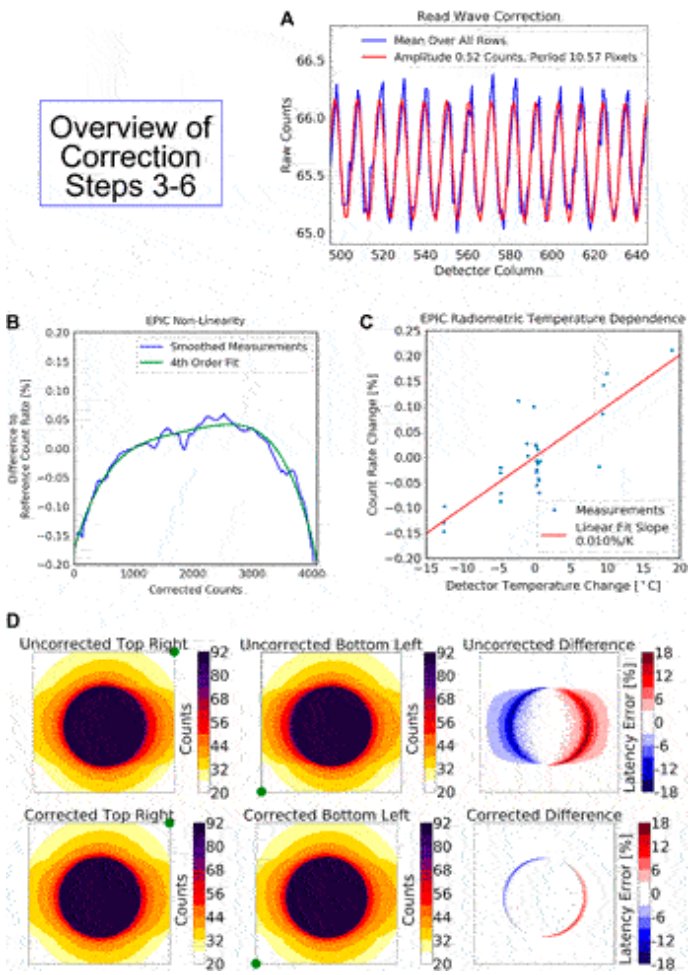

FIGURE 4 | (A) Example for read wave for a dark count measurement. The blue line shows the average of the counts over all CCD rows between columns 495 and 645. The red line is a fitted sinusoidal wave, which is subtracted from the image for the read wave correction. **(B)** Measured (blue) and fitted (green) non-linearity of EPIC based on laboratory measurements during CalGSFC. **(C)** Measured and linearly fitted radiometric temperature sensitivity of EPIC based on laboratory measurements during CalGSFC. **(D)** Illustration of EPIC latency effect using measurements from CalLM. The exactly identical illumination, a circular illumination with a radius of 560 pixels, has been measured with two readout modes. One drains the image at the top right corner (see green dots), the other at the bottom left corner. The latency effect adds a positive bias to the data read just after the target, i.e., at the right side of the detector in the top left panel and at the left side in the top center panel. The top right panel shows the percentage difference of the panels (Top Right Corner minus Bottom Left Corner) before applying the latency correction. The bottom panels show the same images after the latency correction has been applied.

Latency Correction

Just like many imaging devices with a CCD, EPIC suffers from a so-called "latency effect". That is, pixels with a low signal level are significantly

biased high when they are read after a large number of pixels with a high signal level. This can cause an overestimation of as much as 12% in the signal from a low signal clear scene on Earth that is adjacent to a high signal extended region of clouds that is read just before it. The consequences of this bias have been analyzed for other satellite instruments (Várnai and Marshak, 2009).

The EPIC detector has two readout amplifiers located at opposite corners of the array, which allowed us to characterize the latency effect and develop a correction method for it. The method determines the additional charge Δ_i, which is accumulated in the readout electronics and added to the "true" signal C_i, which is the proper charge originating from the measured photons. We assume $\Delta_i = 0$ for the first pixel $i = 1$ to be read, and for each subsequent pixel i+1, Δ_{i+1} is given by Eq. 2:

$$\Delta_{i+1} = \Delta_i \cdot (1 - k_D) + C_i \cdot k_G \qquad (2)$$

k_G and k_D are the latent charge gain and decay constants, respectively, and have been determined to $k_G = 8.6 \times 10^{-6}$ and $k_D = 3.7 \times 10^{-3}$ for the regular readout mode based on measurements during CalLM. The effect is illustrated in Figure 4. Use of Eq. 2 reduces latency errors by a factor of 3.

Non-Linearity Correction

EPIC readout electronics underestimate very small (<500 counts) and very high signal levels (>3,500 counts) by up to 0.2% (Figure 4). This is a relatively small non-linearity effect and was characterized during CalGSFC.

Temperature Correction

EPIC shows a small radiometric temperature sensitivity of 0.01%/K (Figure 4), which is corrected in this step by using the onboard reading of the detector temperature. It was calibrated during CalGSFC, where images from a constant light source were taken over a temperature range from −40 to −10°C.

Conversion to Count Rates

The exposure time of an EPIC image is controlled by the shutter, which is a rotating disk with three open sectors of different angular width that moves in and out of the light path to unblock the incoming beam (Atmospheric

Science DataCenter, 2016). The shutter is slightly non-linear, meaning that different pixels are exposed to light for a different amount of time. However, this shutter effect is only significant when the smallest sector (exposure times <10 ms) is used. For this reason, the filter bandwidths were decreased during refurbishment of EPIC to increase the exposure time to more than 20 ms so as to never use the smallest slit (Table 1). In this conversion step the data are divided by the invariant exposure time given in Table 1 to convert from "corrected counts" to "corrected count rates" (counts/s).

Flat Fielding

When EPIC is illuminated by a uniform input (i.e., each pixel receives exactly the same signal), the recorded image lacks uniformity for several possible reasons:

- Pixel response non-uniformity (PRNU): this is caused by small variations in the sensitivity of each pixel. It is independent of wavelength, has a very small spatial extent (i.e., changes from pixel to pixel), and a magnitude in the order of a few percent.
- Etaloning (ETAL): this is caused by optical interference effects from thickness variations in the depletion region of the CCD. It only affects longer wavelengths above 600 nm (hence only for EPIC filters 7–10), has a wider spatial extent than PRNU, and a magnitude of tens of percent.
- Surface inhomogeneity (INHOMO): this is caused by inhomogeneities on the detector surface, especially from the hafnium coating. It manifests as a localized reduction or enhancement of the sensitivity for a group of pixels with a magnitude of tens of percent. It has the same distribution, but different magnitudes for different channels, usually a stronger effect in the UV than in the visible, since hafnium is nearly transparent in the visible and NIR. Therefore, it manifests most in filters 1–4. The affected regions can have very different spatial extensions. Some features affect only a few pixels, while others spread over hundreds of pixels.
- Vignetting (VIGN): this is the reduction of the instrument sensitivity towards the periphery of the field of view. VIGN varies smoothly across the CCD and might be different for different

filters. Based on optical modeling EPIC should not have strong VIGN, at most in the order of a few percent. It affects all EPIC channels in the same way, but it is best seen in filters 5 and 6, since the other filters are dominated by either ETAL (filters 7–10) or INHOMO (filters 1 to 4) as those effects have a much larger magnitude.

Due to the combination of the above described effects, the sensitivity of each EPIC pixel is different and a homogenous (or flat) illumination produces not at all a homogenous (or flat) image. Once the sensitivity across the detector, called the "flat-field response", is known, the image can be divided by it, which is called "flat-field correction". In the remainder of this section we describe how the EPIC flat-field response was determined.

In both pre-launch calibration campaigns CalLM and CalGSFC we attempted to produce an illumination as uniform as possible across the CCD. In CalLM the beam reaching EPIC was the output of a Dobson collimator telescope. In CalGSFC, EPIC was looking onto a large diffuser plate that was illuminated by a high-power tungsten halogen lamp. However, both inputs were far from being "flat" and showed gradients up to 30%. This forced us to accept some compromises for the pre-launch flat-field calibration.

We split the PRNU from the other effects described above, since it does not really need a flat input as long as the signal varies smoothly across the detector. It can be derived by comparing the value at a single pixel to the average value of the surrounding pixels. The final PRNU array is shown in Figure 5. It is applied separately from the other flat-field effects in the L1a data correction. We do not expect the PRNU to change over the mission lifetime.

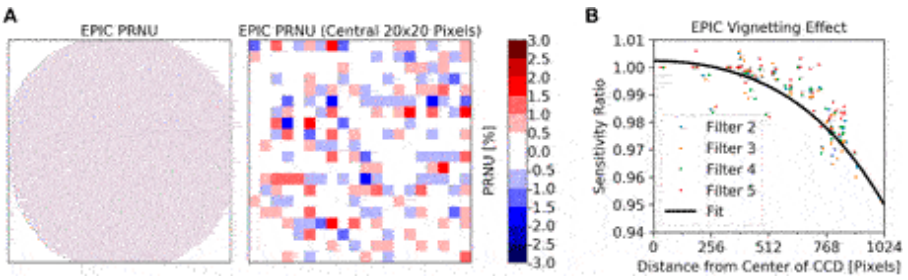

FIGURE 5 | (A) EPIC Pixel response non uniformity as determined during CalGSFC. 61% of the pixels inside the telescopes's FOV have an absolute value of the PRNU below 0.5%, 30% between 0.5 and 1.0%, 8% between 1.0 and 1.5%, 1% between 1.5 and 2.0 and 0.1% above 2.0%. **(B)** EPIC VIGN effect estimated from lunar observations during CalMoon. Each dot is the result of a single lunar image for the respective filter. The black line is a polynomial fit in all the data.

Instead of getting the absolute numbers for ETAL, INHOMO, and VIGN, we derived the combined result from these three effects relative to the 552 nm green filter 6, for which no flat field correction other than the PRNU was assumed or needed. The reason we picked filter 6 is that it is not affected by ETAL and we also observed very little INHOMO, as described in the next paragraph. In this way, it was possible to cancel out that part of the inhomogeneity of the input beam, which affects all filters in the same way.

The actual flat field maps are shown in Figure 6. We can observe that filters 1 to 4 are dominated by INHOMO, seen as regional depressions or enhancements across the detector. Filters 5 and 6 show much less INHOMO, with filter 6 even less than filter 5, which is the reason it was selected as the reference filter. Hence, they are dominated by VIGN. Finally, filters 7 to 10 are dominated by ETAL, seen as a pronounced variation over the entire detector. Overall, the flat-field correction for EPIC is on the order of ±25%. The magnitude of INHOMO was significantly different between CalLM and CalGSFC. We believe this is partly caused by the uncertainty in the laboratory measurements itself, but also originates from changes on the detector surface over pre-launch time from 2011–2014. We used the results from CalGSFC for the final pre-launch flat field correction, as they were closer to the launch date (2015). Due to these difficulties in the flat field calibration and the resulting large uncertainty, the plan was to re-evaluate and possibly modify the flat-field correction using in-flight data.

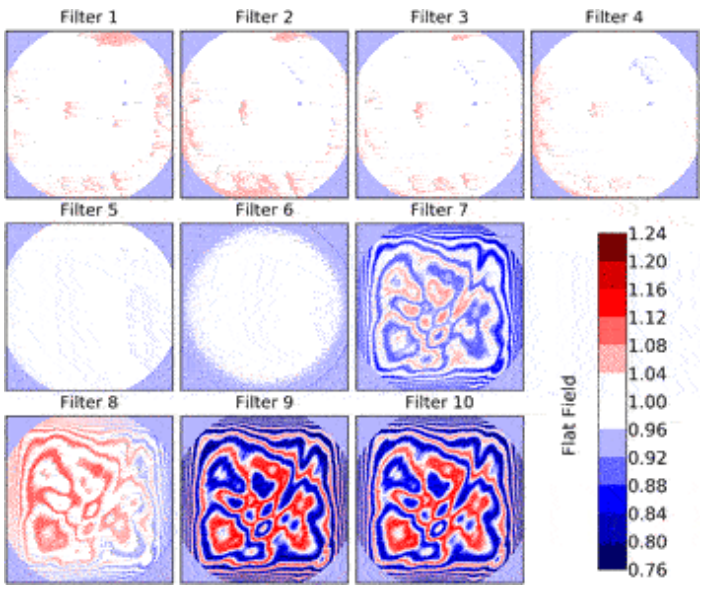

FIGURE 6 | EPIC flat field maps without PRNU from the actual calibration version 18. Filters one to four are dominated by INHOMO, filters 5 and 6 by VIGN, and filters 7 to 10 by ETAL. The flat field correction consists of dividing the data in each filter by the arrays shown in this figure.

A first in-orbit modification of the flat-field calibration was performed in Fall 2016 using the fact that the telescope rotates about its optical axis with a six-months period. The idea was that when we average all the images of one filter over a long period, we should obtain a rather smooth image, since all features caused by the atmosphere and the ground should average out as they are "moving" across the detector. We saw that this assumption holds for small features, i.e., the resulting averaged image is rather smooth, but there are still systematic effects that cause an inhomogeneous result. For example, ocean glint, which creates an enhancement at the specular reflection angle near the center of the Earth (Várnai et al., 2020), and also the high albedo regions of Greenland and Antarctica, which cause higher backscattered signal away from the center of the image as they are at high latitudes. Therefore, we again fixed the flat field in filter 6 and only looked at the differences from it with this technique. The in-flight version of the flat field correction differed on average from the 1st version by <0.03% for filters 1–5, and in the range of 0.3–0.5% for filters 7, 9, and 10. However, in all filters there were extreme values, where the flat field changed for certain pixels by 34–53% in filters 1–5, and 9–15% for filters 7, 9, and 10. The technique did not seem to improve the flat field for filter 8 and therefore that channel was

left unchanged. As a result of this improvement, L2 data such as the total ozone columns gave smoother and more consistent results (see Figure 7, left and middle panel).

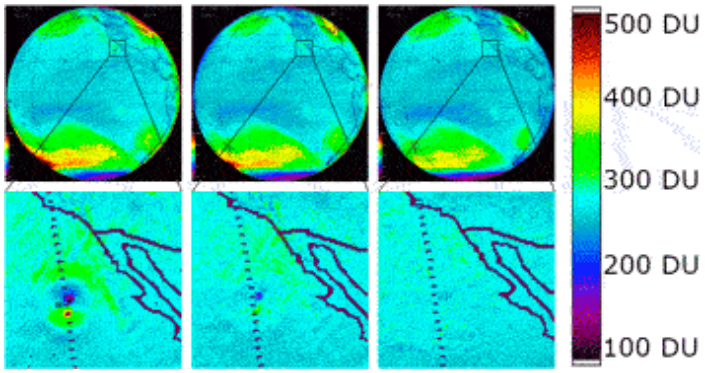

FIGURE 7 | EPIC total ozone columns in Dobson Units (DU) on October 17, 2015 at 20:14 UTC using flat field calibration from pre-launch **(left panels)**, the update from Fall 2016 **(middle panels)** and the actual latest version **(right panels)**. The bottom row is a zoom into the region indicated by the black lines. The very low ozone values below 200 DU in a region of the bottom left panel are not real, as we know from other data, and are a consequence of the imperfect initial flat field correction. This artifact is not seen in the bottom right panel anymore, where the latest flat field correction is used.

The next improvement was to compare EPIC measured radiances for filters 1–4 with synthesized radiance images based on the NASA Ozone Mapping and Profiler Suite (OMPS) satellite (National Oceanic and Atmospheric Administration, 2021), while EPIC blue channel 5 was compared with the Ozone Monitoring Instrument (OMI) (Goddard Space Flight Center, 2021). For every EPIC radiance image, OMPS Nadir Mapper (NM) radiance spectra measured on the same day was convoluted with EPIC bandpass function and interpolated to the given EPIC channel wavelength. Then, the OMPS radiance measurements at EPIC wavelength were interpolated to each EPIC pixel geographic location. All of the nearly 6,000 synthesized images and as well as EPIC measured images from the first 18 months of the EPIC mission were averaged, respectively. Ratios of the averaged EPIC radiance image to the averaged OMPS radiance image were computed. The synthesized radiance images were corrected by accounting for the differences in the solar incidence angles and the satellite observation angles using the TOMRAD atmospheric radiative transfer model (Bhartia and Wellemeyer, 2002) and OMPS NM ozone retrieval results (ozone and surface reflectivity, etc.), which were also averaged and synthesized in

parallel with the synthesizing of radiance images. Ratios of the averaged EPIC radiance image to the resulting OMPS (and OMI) radiance image were computed. This technique eliminates some large geophysical features mentioned above and characterizes pixel-to-pixel variations very well. However, we found the resulting flatfield still had significant offsets changing from the CCD-center to the edge. We believe this is because the spherical geometry approximation in TOMRAD causes increased uncertainties at large solar/viewing zenith angles. Also, the forward model does not simulate the ocean Sun glint. These two errors are circularly symmetric. Therefore, a polar coordinate system was set at the CCD center, and circles of CCD pixels were selected from the ratios and fitted with piecewise linear functions of the polar angle to determine a reference background. Pixels with large deviations from a fitted background were removed from the circle, and the raw ratios of the remaining pixels in the circle were fitted again. Two iterations of this fitting were performed. This procedure was repeatedly applied with 1-pixel radius increments from the center to the edge, where a sufficient (3,000) number of EPIC images were accumulated. Finally, the raw ratios were normalized with the resulting reference background for the flat field correction.

A further step to improve the flat-field correction was to estimate the magnitude of VIGN from the lunar measurements during CalMoon. After correcting for the slightly changing distances for Sun-Moon-EPIC, a given face of the Moon can be considered a stable light source. The obtained results for the EPIC sensitivity decrease towards the edge of the FOV and are shown in Figure 5. Since the scatter in the results was significantly larger than potential differences among the filters, we used a polynomial fit to the average over all filters as the final function for VIGN. The lunar calibration measurements are periodically repeated over the life of the mission.

The in-flight modifications described above further improved the quality of the L2 data like total ozone columns (Figure 7, right panel). The modification is on the order of up to 4% of radiance to optical speckle-like features in broad regions, and up to 60% for some bad pixels, which lead to corrections in the retrieved ozone from tens DU to hundreds DU. The estimated uncertainty in the flat field correction (pixel-to-pixel sensitivity changes) is 0.5%.

Stray Light Correction

Light entering EPIC from a specific direction does not only end up at the CCD location defined by geometric optics, the "core region" that consists of the corresponding pixel and its neighbor pixels. A fraction of the light is distributed over the entire detector as stray light. The fraction of the total signal ending up outside the core region, the "stray light fraction", is rather large for EPIC, between 12 and 20% depending on the filter (Table 1). If not corrected, the stray light would severely reduce the quality of the scientific data products, particularly those depending on the ratio of light from different wavelength channels. Therefore, a stray light correction method based on the knowledge of the instrument's point spread function (PSF) was developed. The method follows the principle described in Zong et al. (2006) used for a different purpose. To our knowledge this is the first time that such a technique has been applied to a 2-dimensional detector. Our novel approach is described in this section.

As mentioned in *Calibration Periods*, different targets were used during CalLM to create different illuminations for EPIC. For example, one target produced the circular image seen in Figure 4. Another target produced a quasi-parallel beam with divergence of $\pm 5 \times 10^{-5}$ degrees, which is only one third of the angular extension of one pixel, 3×10^{-4} degrees. When this "sub-pixel-illumination" was positioned to reach the CCD right in the center of a pixel, the obtained signal is considered to be the PSF of EPIC (Figure 8). Within the measurement uncertainty, the shape of the PSF for EPIC in the core region was found independent of the filter and the position on the detector.

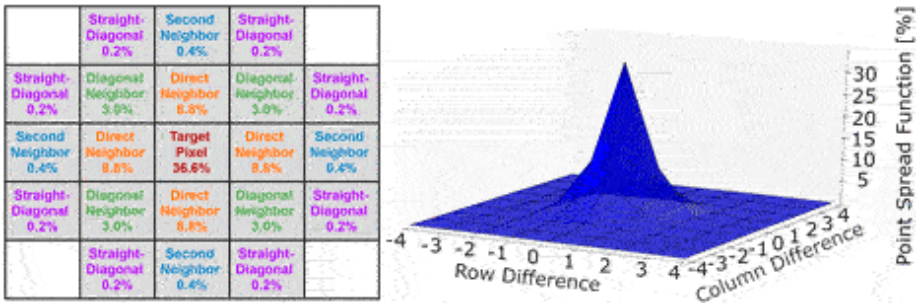

FIGURE 8 | EPIC PSF in the core region measured during CalLM for filter 6 using sub-pixel-illumination. The data are normalized to the sum of the signal over the entire detector. The individual values are listed in the left panel. For filter 6, 87% of the signal ends up in the core region, i.e., the center pixel and the next neighbor pixels (cells with gray background), while 13% of the signal is stray light and spreads over the remaining part of the CCD. For other filters the shape of the PSF in the core region is the same, but the normalized values are different due to a different stray light fraction (Table 1).

When using the sub-pixel illumination, the signal outside the core region basically disappears in the measurement noise, i.e., the exact structure of the stray light cannot be determined. It was also not possible to increase the exposure time and saturate the center pixel to such an extent that this structure was seen. To solve this problem another target was used, which produces a beam with divergence of $\pm 3 \times 10^{-3}$ degrees or 3,600 times more energy than the sub-pixel illumination. This results in a "small circular image" with a radius of 20 pixels. Both unsaturated and saturated measurements with this target were taken and then merged to produce final images (Figures 9, 10). As in Figure 8, the data are normalized to the sum of the corrected signal over the entire detector. Several common features can be seen in the figures, but not all of them are related to stray light. For example, we believe that the enhancement of entire rows in the saturated regions is due to a not fully removed readout latency effect.

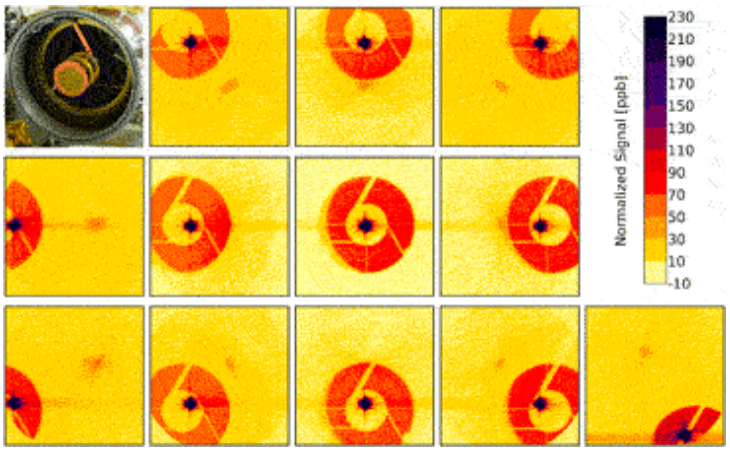

FIGURE 9 | EPIC PSF in parts per billion (ppb) measured during CalLM for filter 8 using the small circular illumination directed at different positions on the detector. The top left panel shows the entrance of EPIC with the support structure of the secondary mirror.

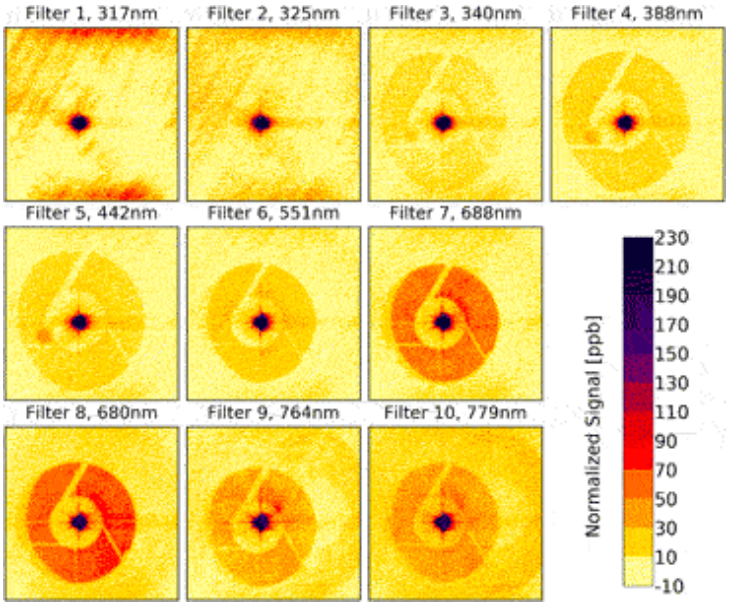

FIGURE 10 | EPIC PSF measured during CalLM using the small circular illumination directed at the center of the detector for all filters.

The most obvious feature of EPIC stray light is a ghost image, in which the support structure of the secondary mirror can be seen. Based on optical modeling, we think this ghost image is mainly caused by reflections between the detector and the parallel filters, which are significant, although all of these optical elements have proper anti-reflection coatings applied. Since

filter wheel 1 is farther away from the detector, the diameter of the ghost image is larger for filters 1 to 5 than for filters 6 to 10 (Figure 10).

Based on these measurements we developed a PSF-model for EPIC. For this model the PSF was divided into eight different "regions": the core region with the 21 pixels shown in Figure 8, the near field, transition and interpolation regions, extending to a distance of ~200 pixels around the center pixel (violet and dark red colors in the figures), the ghost image region (mostly orange colors in Figure 9), the regions inside and outside of the ghost (mostly yellow) and the region outside the telescope (the gray corners of Figure 2). The PSF-model consists of a set of filter-dependent parameters for each region, e.g., the stray light level in the transition region or the diameter of the ghost image region, etc. Details such as the arms of the support structure of the secondary mirror were omitted in the model (see also Figure 11). The PSF-model allows us to calculate an estimation of the EPIC PSF for each of the 10 filters for any of the more than four million pixels on the CCD.

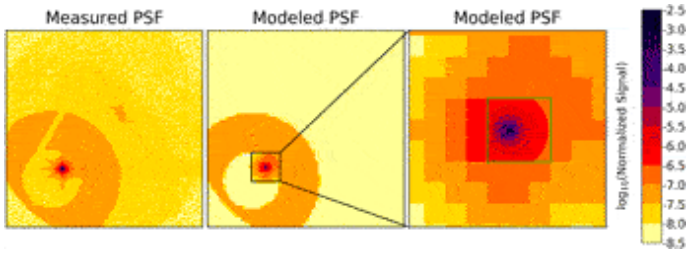

FIGURE 11 | Measured **(left panel)** and modeled partially binned PSF **(middle and right panels)** for filter 8 at target pixel (1400,600) in logarithmic scale. The right panel is a zoom into the middle panel for the region of rows 1,250–1,550 and columns 450−750. The area inside the green frame in the right panel is the central part of 96x96 pixels around the target pixel, which is resolved in full resolution. Outside the green frame are the 32x32 "super-pixels".

The next step in the stray light correction method described by Zong et al. (2006) is to build the so-called stray light distribution matrix D, which is basically the combination of all the PSFs. One column of D is the PSF with the core region replaced by zeros for the respective pixel as a column vector, i.e., with dimension (2,048 * 2,048 = 4194304,1) instead of (2,048, 2,048). The unitary matrix I is added to D. The result, I + D, is a diagonally dominant matrix with ones in the main diagonal and very small numbers

elsewhere (values as shown in Figures 9, 10). I + D is inverted to obtain the stray light correction matrix C (Eq. 3).

$$C = (I + D)^{-1} = I - D + \tfrac{1}{2} \cdot D^2 - \ldots \sim I - D^* \qquad (3)$$

D* is an approximation for the combined D-terms in Eq. 3 as is described below. C is then applied to the measured data (as a column vector) to correct for the stray light. The problem we faced is that for a 2D-detector like EPIC matrices D and C have a huge dimension (4194304, 4194304). Such a matrix would occupy >70 TB of disk space (for each filter) if stored in single precision. While it is in theory possible to create D using our PSF-model, it is completely impractical to invert D even with the most advanced computer system. And even if we were able to perform this inversion, applying matrix C to an image would also take far too much time to be executed for routine operation. Therefore, we made two simplifications:

First, we applied "partial binning" on the PSFs. The central part of 96 × 96 pixels around the target pixel is saved in full resolution, but all the pixels outside this central part are binned into "super-pixels" with a size of 32 × 32 pixels each. An example for this binned PSF is shown in Figure 11. The specific numbers for the configuration of the central part and the binning were a compromise between reducing the size of matrix C as much as possible and still maintaining a good measure of the stray light correction. This compromise was obtained by testing different configurations. The lower physical limit for the central part was about 90 × 90 pixels, since this covers the near field of the PSF (Figure 10), which has the strongest gradient. Any smaller size for the central region would have altered the results significantly. Since the width of the super-pixels must be an integer fraction of the pixel number in one dimension, 2,048, and the width of the central region must be a multiple of the width of the super-pixels (both for numerical reasons), the minimum possible size for the central region was then given by 96 × 96, as 96 is three times 32 or six times 16. Since we did not see a large difference between 32 × 32 and 16 × 16 super-pixels, we chose 32 × 32 as it significantly reduces the size of matrix C.

With these settings, the partially binned PSF has a total of 13,303 entries (9,216 pixels in the central part and in addition 4,087 super-pixels), which means the final stray light correction matrix C occupies ~208 GB of disk space per filter in single precision. Despite this simplification, the operational stray light correction would still take a long time (roughly 52 min

per image) when executed on a desktop computer. Instead, the operational EPIC data processing is done on a supercomputer at the NASA Center for Climate Simulation (NCCS) (National Aeronautics and Space Administration, 2021), where the processing can be done in less than 30 s per image.

The second simplification is that we approximate the inversion in Eq. 3 with only the first term of a Taylor series expansion, which can directly be obtained from the PSF-model. In order to compensate for the underestimation caused by the approximation $I - D$, we created a modified distribution matrix D* (Eq. 3). D* was obtained by testing the stray light correction on pre-launch and post-launch data with a known signal input.

Examples of such test images are shown in Figure 12. For the left panel in this figure, another target used during CalLM, the "bar target", is measured. This target consists of rectangular areas with gaps in between. Knowing that the signal outside and in between the openings must be zero, we could fine-tune our PSF-model. These images were especially useful to test the performance of the stray light correction in the regions near the central pixel (the near field, transition, and interpolation regions), which is something that cannot really be verified after launch.

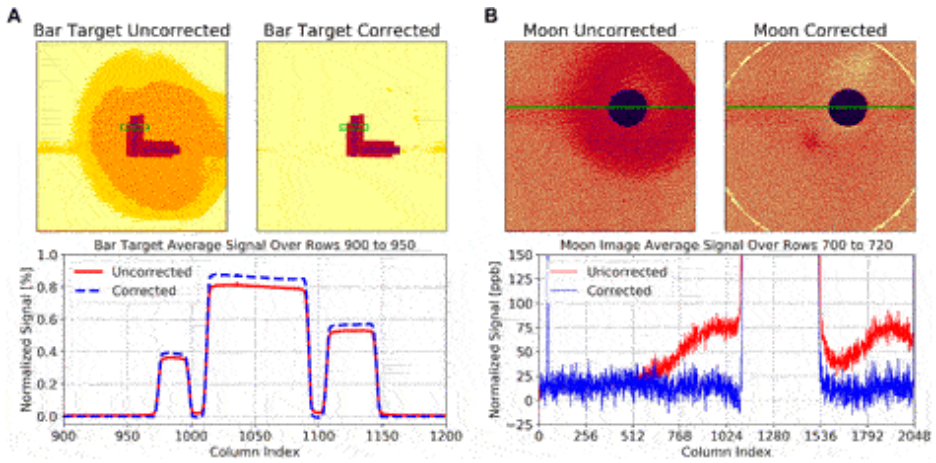

FIGURE 12 | (All pseudo-color images are in logarithmic scales and use the same color bar as in Figure 11): **(A)** Bar target measurement for filter 8 from CalLM before stray light correction ("Uncorrected") and after stray light correction ("Corrected"). The bottom panel shows the average over rows 900–950 as a function of the column index, which is indicated by the green area in the full images. The stray light reduces the signal at the maxima and fills the gaps in between the maxima (red solid line). After the correction (dashed blue line) the signal at the maxima is "restored" and the signal in the gaps caused by the stray light is "cleared". **(B)** Lunar image for filter 8 from CalMoon before stray light correction and after stray light correction. The bottom panel shows the average over rows 700–720 as a function of the column index, which is indicated by the green line in the images. Before the correction (red line) the signal outside the lunar surface is enhanced, mostly due to the ghost image, while after the correction (dashed blue line) it is approximately zero.

The right panel in Figure 12 shows a lunar image taken during CalMoon. While we could not use the region on the moon itself to test the stray light correction, since we do not know the exact structure of the lunar surface, we could make use of the fact that outside the moon the signal must be basically zero and that the signal drops sharply to zero at the edge of the lunar disk since the moon has no atmosphere.

One check for the quality of the stray light correction that can be done for the operational data is simply to look at the region outside the target (Earth or Moon), which should give a signal as close to zero as possible. We have analyzed the ratio R of the mean signal outside the Earth $\langle S_{OUT} \rangle$ over the mean signal on the Earth $\langle S_{ON} \rangle$ for the first year of EPIC data in orbit, $R = \langle S_{OUT} \rangle / \langle S_{ON} \rangle$. For eight of the filters, R ranged from 0.8–2.7% before stray light correction was applied, and from −0.1%–+0.4% after the correction, which proves excellent performance of the stray light correction algorithm of a factor of 7 or higher. An exception is filter 9, where the

numbers are 3.5 and 1.0%, respectively, hence, still an improvement by a factor 3.5, but not of the same quality as for the other filters.

Another way to test the quality of the stray light correction is described in Geogdzhaev and Marshak (2018), where absolute calibration constants for EPIC filters 5, 6, 8, and 10 are found through comparison with data from the Moderate Resolution Imaging Spectroradiometers (MODIS) onboard the Terra and Aqua satellites. The authors applied their technique separately for dark scenes and bright scenes. When EPIC L1a calibration, especially the stray light correction, was done correctly, the two methods should give approximately the same calibration constants. Their analysis showed that the agreement between the calibration based on the dark and bright scenes respectively increased by a factor of 1.7–3.3 after EPIC stray light correction was applied.

Figure 13 shows the stray light error (SLE) for the same images as shown in Figure 2, i.e., from May 8, 2019 around 11:00 UTC. Here we define the SLE as the percent difference between the data before and after the stray light correction. The median of the SLE-distribution for the pixels on the Earth's disk ("pixels on Earth") ranges from −2% for filters 1 to 5 down to −4% for filter 8. This is because stray light causes a fraction of the energy from the pixels on Earth to spread to the pixels outside the Earth's disk ("pixels outside Earth"). For the pixels outside Earth, the SLE goes towards infinity since the corrected data are close to zero. Bright scenes (clouds, ice or high surface albedo like over Africa for the higher filters) have a negative SLE, which ranges from −6% for filters 1–6 down to −10% for filter 8 (this is based on the 1-percentile of the SLE-distribution for pixels on Earth). Dark scenes (clear sky and low surface albedo) have a positive SLE, which can exceed the scale of Figure 13 substantially with values above 50% and even up to 100% for filter 8 (this is based on the 99-percentile of the SLE-distribution for pixels on Earth).

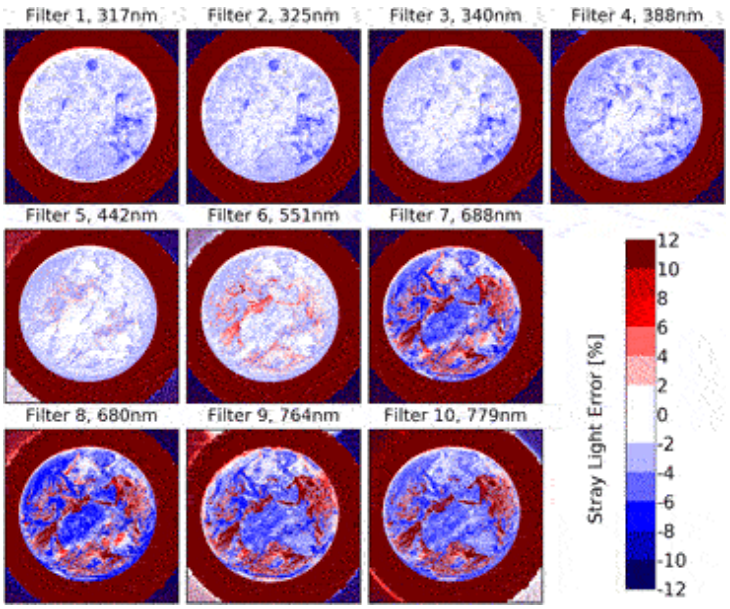

FIGURE 13 | Stray light error for the EPIC images from Figure 2 (May 8, 2019 around 11:00 UTC).

PIXEL SIZE ON GROUND

An important question for the data user is where does the light come from as measured by one EPIC pixel? This is often referred to as the "footprint" of a satellite pixel. The answer to this question is strongly related to the PSF, which describes how the light originating from a point source is distributed over the CCD. The core part of the EPIC PSF (Figure 8) can be approximated by a 2-dimensional super Gaussian function with exponent 1.63 ± 0.11 and FWHM of 1.29 ± 0.11 pixels. The angular FOV of a pixel is given by the core PSF "mirrored on the center point" and convoluted over the extension of the pixel. It describes the angles where light originates that ends up on a given pixel. The FWHM of the EPIC FOV, which is obviously a 2D super-Gaussian just like the PSF, is 1.73 arcsecs. The geographic footprint finally is the projection of the angular FOV on the Earth's surface, i.e., one needs to include the distances, angles, etc., included in the telemetry. The blue lines in Figure 14 show the footprint for the "standard case" of normal incidence on the ground (satellite viewing zenith angle VZA = 0°) and the average Earth-Lagrange 1 distance. For this situation, the footprint is approximately circular with a FWHM of 12.5 km, a 50% energy contour line with a diameter of 13.2 km (i.e., 50% of the energy measured in the pixel is from within this circle) and a 90% energy contour line with diameter of

24.9 km. The footprint increases with the distance of EPIC from the Earth and also changes in size and shape for other places on the Earth with VZA > 0°.

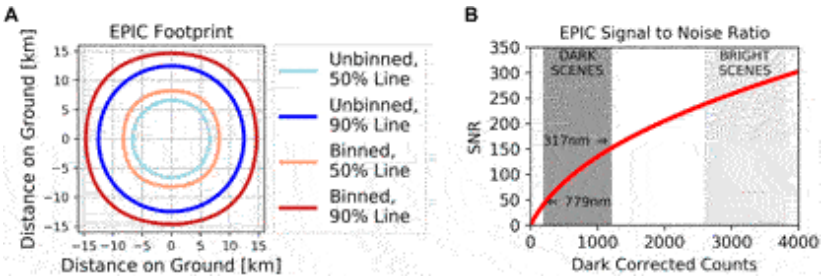

FIGURE 14 | (A) Energy contours of the EPIC footprint for a pixel at 0° satellite zenith angle and average Earth-Lagrange 1 distance. The blue lines represent the unbinned case, the red lines the case of 2 × 2 binned pixels. The light colors give the 50% level, i.e., 50% of the energy reaching the pixel comes from inside this region. The dark colors give the 90% level. **(B)** EPIC SNR for the operational readout mode at typical CCD temperatures. The SNR of dark scenes is smaller in the visible than in the UV due to the larger contrast between dark and bright scenes (see also Figure 2).

As already mentioned in *Dark Correction*, the images from all filters except the blue filter 5 are "binned", i.e., the averages over groups of 2 × 2 pixels are formed. The FOV for one of these binned pixels increases to 2.41 arcsecs, since the convolution is done over a larger area than in the unbinned case. This also changes the native footprint of the L1a data for these filters (red lines in Figure 14). The "binned" footprint is not circular anymore and has a FWHM of 17.5 km, a 50% energy contour line with a diameter of 16.4 km and a 90% energy contour line with diameter of 29.2 km.

UNCERTAINTY

A complete uncertainty analysis for EPIC L1a data has not been made, since this is outside of the available resources. However, we can determine the read noise and the gain of EPIC, which allows us to estimate the signal to noise ratio (SNR) of an EPIC measurement:

$$SNR = CC/\mathrm{sqrt}(N_{READ}{}^2 + GAIN \cdot CC) \qquad (4)$$

CC are the dark corrected counts ranging from 0 to about 4,000. CC can be approximated by multiplying the L1a data (count rates) with the exposure times given in Table 1. N_{READ} is the read noise, which is 3.9 counts for the

operational EPIC readout mode. GAIN = 0.04 on average (it changes with the CCD temperature). The SNR is shown in Figure 14. It ranges from 50:1–150:1 for dark scenes (lower values for higher wavelengths and higher values for short wavelengths that have significant Rayleigh scattering) and from 250:1 to 300:1 for bright scenes containing clouds or snow/ice. A measure of the success of the corrections is that features as small as 10 km can be discerned (Nile river banks) in the 443 nm blue channel and that the very sensitive algorithm for ozone retrieval is successful (Kramarova et al., 2021 submitted).

For the binned images (all filters but filter 5), the SNR is the double of the numbers shown in Figure 14 and listed in the previous paragraph for L1a data.

CONCLUSION

We believe that within the available possibilities from pre-launch and on-orbit calibration activities, an adequate EPIC raw data calibration has been obtained. The produced L1a data are corrected for all known instrumental effects and only need to be multiplied by a single number for each filter to obtain absolute calibrated radiances from the count rate. Before in-flight data were available, it was decided that no attempt would be made to determine the conversion from count rates to radiances for two reasons. First, the laboratory setup to produce an absolutely calibrated, homogenous, extended light source is a rather difficult task and would have exceeded the possibilities with respect to budget and schedule. Second, it is unlikely that the absolute calibration values obtained during pre-launch would have been applicable to the operation on orbit, as many factors, such as launch stress or the different environment and instrument illumination in space, usually modify the calibration significantly (see, e.g., Kabir et al., (2020). Therefore, the EPIC L1a data are given as corrected count rates and the 10 numbers needed to convert to radiances are determined by comparison to other satellites in a later processing step.

Several of the corrections described in *L1a Processing Steps* follow well-established procedures for instrument calibration. However, for some of the steps, we needed to develop rather novel techniques that have not been previously used to our knowledge.

- A readout latency correction method was determined. This was possible since the EPIC detector can be drained (read) from

different CCD corners and the necessary measurements were made before launch (*Latency Correction*).

• The flat-field corrections, which turned out to be the most critical part with respect to producing reliable L1a data, needed to be adjusted on-orbit relative to their pre-launch values. This was done through comparison with other satellites and by applying a statistical analysis of all the EPIC images taken over a long period (*Flat Fielding*).

• A novel stray light correction method was developed based on partially binned PSFs to handle the huge dimensions of the matrices involved (*Stray Light Correction*).

Since its launch in 2015, EPIC has been monitored for possible calibration changes, e.g., the dark count evolution (*Dark Correction*), the number of hot pixels (*Enhanced Pixel Detection*), or the radiometric stability from periodic lunar observations. The overall conclusion is that the observed instrumental changes are small, which we attribute to the benevolent conditions for the Lagrange 1 orbit. EPIC does not undergo periodic variations of extremely hot and cold temperatures like satellites in Earth orbits (low Earth orbits or geostationary orbits), which periodically move from sun to shadow, for low Earth orbits every ~50 min. Furthermore, it is in a much more constant radiation environment compared to the instrument in LEOs, which cross the South Atlantic Anomaly (SAO) at least once per day [see, e.g., Li et al. (2020)]. Since the same side of the DSCOVR satellite always points to the Sun, the shielded effect from charged particles originating from the solar wind is much better than the charged particle effect in the SAO. We believe that apart from the excellent Earth-observing situation from Lagrange 1, the observations discussed in this document are another positive aspect of this orbit, which should be considered when possible future missions are discussed.

DATA AVAILABILITY STATEMENT

The raw data supporting the conclusions of this article will be made available by the authors, without undue reservation.

AUTHOR CONTRIBUTIONS

All authors have contributed to conception and design of the study and manuscript revision, and have read, and approved the submitted version.

FUNDING

The work was supported through different grants by the NASA DSCOVR program managed by R. S. Eckman, specifically grants NNX15AB57G, NNX15AN07G, NNX17AC97G, 80NSSC18K0992, and 80NSSC19K0769.

ACKNOWLEDGMENTS

The authors and the DSCOVR project would like to thank the EPIC refurbishment and calibration efforts of the Lockheed-Martin team headed by Joseph Mobilia. Resources supporting this work were provided by the NASA High-End Computing (HEC) Program through the NASA Center for Climate Simulation (NCCS) at Goddard Space Flight Center.

REFERENCES

Atmospheric Science DataCenter (2016). Deep Space Climate Observatory, Earth Science Instrument Overview. Report available under (Accessed February 18, 2021).

Bhartia, P., and Wellemeyer, C. (2002). "TOMS-V8 Total O_3 Algorithm," in *OMI Algorithm Theoretical Basis Document* , (Greenbelt, MD, USA: NASA Goddard Space Flight Center). Vol. II, 15–31.

Carn, S. A., Krotkov, N. A., Fisher, B. L., Li, C., and Prata, A. J. (2018). First Observations of Volcanic Eruption Clouds from the L1 Earth-Sun Lagrange Point by DSCOVR/EPIC. *Geophys. Res. Lett.* 45 (20), 11456–11464. doi:10.1029/2018GL079808

Cede, A., Mobilia, J., Demroff, H., Sawyer, K., Hertzberg, E., and Herman, J. (2011). *Stray Light in EPIC*. San Francisco, CA, USA: AGU Fall Meeting. December 5-9, 2011.

Christian, K., Wang, J., Ge, C., Peterson, D., Hyer, E., Yorks, J., et al. (2019). Radiative Forcing and Stratospheric Warming of Pyrocumulonimbus Smoke Aerosols: First Modeling Results with Multisensor (EPIC, CALIPSO, and CATS) Views from Space. *Geophys. Res. Lett.* 46, 10061–10071. doi:10.1029/2019GL082360

Davis, A. B., Ferlay, N., Libois, Q., Marshak, A., Yang, Y., and Min, Q. (2018). Cloud Information Content in EPIC/DSCOVR's Oxygen A- and B-Band Channels: A Physics-Based Approach. *J. Quant. Spectrosc. Radiat. Transfer* 220, 84–96. doi:10.1016/j.jqsrt.2018.09.006

Doelling, D., Haney, C., Bhatt, R., Scarino, B., and Gopalan, A. (2019). The Inter-calibration of the DSCOVR EPIC Imager with Aqua-MODIS and NPP-VIIRS. *Remote Sens.* 11, 1609. doi:10.3390/rs11131609

Geogdzhaev, I. V., and Marshak, A. (2018). Calibration of the DSCOVR EPIC Visible and NIR Channels Using MODIS Terra and Aqua Data and EPIC Lunar Observations. *Atmos. Meas. Tech.* 11, 359–368. doi:10.5194/amt-11-359-2018

Goddard Space Flight Center (2021). *Aura | Ozone Monitoring Instrument*. Available at: (Accessed March 31, 2021).

Herman, J., Huang, L., McPeters, R., Ziemke, J., Cede, A., and Blank, K. (2018). Synoptic Ozone, Cloud Reflectivity, and Erythemal Irradiance from Sunrise to sunset for the Whole Earth as Viewed by the DSCOVR Spacecraft from the Earth-Sun Lagrange 1 Orbit. *Atmos. Meas. Tech.* 11, 177–194. doi:10.5194/amt-11-177-2018

Herman, J., Cede, A., Huang, L., Ziemke, J., Torres, O., Krotkov, N., et al. (2020). Global Distribution and 14-year Changes in Erythemal Irradiance, UV Atmospheric Transmission, and Total Column

Ozone For2005-2018 Estimated from OMI and EPIC Observations. *Atmos. Chem. Phys.* 20, 8351–8380. doi:10.5194/acp-20-8351-2020

Kabir, S., Leigh, L., and Helder, D. (2020). Vicarious Methodologies to Assess and Improve the Quality of the Optical Remote Sensing Images: A Critical Review. *Remote Sens.* 12, 4029. doi:10.3390/rs12244029

Kramarova, N., Ziemke, J., Huang, L. K., and Herman, J. (2021). Evaluation of Version 3 Total and Tropospheric Ozone Columns from EPIC on DSCOVR for Studying Regional Scale Ozone Variations. *Front. Remote Sens* . (submitted June 2021).

Li, C., Krotkov, N. A., Leonard, P. J. T., Carn, S., Joiner, J., Spurr, R. J. D., et al. (2020). Version 2 Ozone Monitoring Instrument SO2 Product (OMSO2 V2): New Anthropogenic SO2 Vertical Column Density Dataset. *Atmos. Meas. Tech.* 13 (11), 6175–6191. doi:10.5194/amt-13-6175-2020

Lyapustin, A., Go, S., Korkin, S., Wang, Y., Torres, O., Jethva, H., et al. (2021). Retrievals of Aerosol Optical Depth and Spectral Absorption from DSCOVR EPIC. *Front. Remote Sens.* 2. doi:10.3389/frsen.2021.645794

Marshak, A., and Knyazikhin, Y. (2017). The Spectral Invariant Approximation within Canopy Radiative Transfer to Support the Use of the EPIC/DSCOVR Oxygen B-Band for Monitoring Vegetation. *J. Quant. Spectrosc. Radiat. Transfer* 191, 7–12. doi:10.1016/j.jqsrt.2017.01.015

Marshak, A., Herman, J., Adam, S., Karin, B., Carn, S., Cede, A., et al. (2018). Earth Observations from DSCOVR/EPIC Instrument. *Bull. Am. Meteorol. Soc.* 99 (9), 1829–1850. doi:10.1175/BAMS-D-17-0223.1

Meyer, K., Yang, Y., and Platnick, S. (2016). Uncertainties in Cloud Phase and Optical Thickness Retrievals from the Earth Polychromatic Imaging Camera (EPIC). *Atmos. Meas. Tech.* 9, 1785–1797. doi:10.5194/amt-9-1785-2016

Molina García, V., Sasi, S., Efremenko, D. S., Doicu, A., and Loyola, D. (2018). Radiative Transfer Models for Retrieval of Cloud Parameters from EPIC/DSCOVR Measurements. *J. Quant. Spectrosc. Radiat. Transf.* 123, 228–240. doi:10.1016/j.jqsrt.2018.03.014

National AeronauticsSpace Administration (2021). *NASA Center for Climate Simulation: High Performance Computing for Science*. Available at: (Accessed March 18, 2021).

National OceanicAtmospheric Administration (2021). *Joint Polar Satellite System: Ozone Mapping and Profiler Suite*. Available at: (Accessed March 5, 2021).

Pisek, J., Arndt, S. K., Erb, A., Pendall, E., Schaaf, C., Wardlaw, T. I., et al. (2021). Exploring the Potential of DSCOVR EPIC Data to Retrieve Clumping Index in Australian Terrestrial Ecosystem Research Network Observing Sites. *Front. Remote Sens.* 2. doi:10.3389/frsen.2021.652436

Sasi, S., Natraj, V., Molina-Garcia, V., Efremenko, D. S., Loyola, D., and Doicu, A. (2020). Model Selection in Atmospheric Remote Sensing with an Application to Aerosol Retrieval from DSCOVR/EPIC, Part 1: Theory. *Remote Sens.* 12, 22. doi:10.3390/rs12223724

Song, W., Knyazikhin, Y., Wen, G., Marshak, A., Mõttus, M., Yan, G., et al. (2018). Implications of Whole-Disc DSCOVR EPIC Spectral Observations for Estimating Earth's Spectral Reflectivity Based on Low-Earth-Orbiting and Geostationary Observations. *Remote Sens.* 10, 1594. doi:10.3390/rs10101594

Torres, O., Bhartia, P. K., Taha, G., Jethva, H., Das, S., Colarco, P., et al. (2020). Stratospheric Injection of Massive Smoke Plume from Canadian Boreal Fires in 2017 as Seen by DSCOVR-EPIC, CALIOP and OMPS-LP Observations. *JGR Atmospheres* 125 (10), e2020JD032579. doi:10.1029/2020JD032579

Várnai, T., and Marshak, A. (2009). MODIS Observations of Enhanced clear Sky Reflectance Near Clouds. *Geophys. Res. Lett.* 36 (6). doi:10.1029/2008gl037089

Várnai, T., Kostinski, A., and Marshak, A. (2020). Deep Space Observations of Sun Glints from marine Ice Clouds. *IEEE Remote Sens. Lett.* 17 (5), 735–739. doi:10.1109/LGRS.2019.2930866

Weber, M., Hao, D., Asrar, G. R., Zhou, Y., Li, X., and Chen, M. (2020). Exploring the Use of DSCOVR/EPIC Satellite Observations to Monitor Vegetation Phenology. *Remote Sensing* 12, 2384.

doi:10.3390/rs12152384

Wen, G., Marshak, A., Song, W., Knyazikhin, Y., Mõttus, M., and Wu, D. (2019). A Relationship between Blue and Near-IR Global Spectral Reflectance and the Response of Global Average Reflectance to Change in Cloud Cover Observed from EPIC on DSCOVR. *Earth Space Sci.* 6, 1416–1429. doi:10.1029/2019EA000664

Xu, X., Wang, J., Wang, Y., Zeng, J., Torres, O., Reid, J., et al. (2019). Detecting Layer Height of Smoke Aerosols over Vegetated Land and Water Surfaces via Oxygen Absorption Bands: Hourly Results from EPIC/DSCOVR in Deep Space. *Atmos. Meas. Tech.* 12, 3269–3288. doi:10.5194/amt-12-3269-2019

Yang, K., and Liu, X. (2019). Ozone Profile Climatology for Remote Sensing Retrieval Algorithms. *Atmos. Meas. Tech.* 12, 4745–4778. doi:10.5194/amt-12-4745-2019

Yang, W., Marshak, A., Varnai, T., and Knyazikhin, Y. (2018). EPIC Spectral Observations of the Variability in Earth's Global Reflectance. *Remote Sens* 10 (2), 254. doi:10.3390/rs10020254

Yang, Y., Meyer, K., Wind, G., Zhou, Y., Marshak, A., Platnick, S., et al. (2019). Cloud Products from the Earth Polychromatic Imaging Camera (EPIC) Observations: Algorithm Description and Initial Evaluation. *Atmos. Meas. Tech.* 12, 2019–2031.[1]. doi:10.5194/amt-12-2019-2019

Yin, B., Min, Q., Morgan, E., Yang, Y., Marshak, A., and Davis, A. (2020). Cloud Top Pressure Retrieval with DSCOVR-EPIC Oxygen A and B Bands Observation. *Atmos. Meas. Tech.* 13, 1–18. doi:10.5194/amt-13-1-202010.5194/amt-13-5259-2020

Zhou, Y., Yang, Y., Gao, M., and Zhai, P-W. (2020). Cloud Detection over Snow and Ice with Oxygen A- and B-Band Observations from the Earth Polychromatic Imaging Camera (EPIC). *Atmos. Meas. Tech.* 13 (3), 1575–1591. doi:10.5194/amt-13-1575-2020

Zong, Y., Brown, S. W., Johnson, B. C., Lykke, K. R., and Ohno, Y. (2006). Simple Spectral Stray Light Correction Method for Array Spectroradiometers. *Appl. Opt.* 45 (6), 1111–1119. doi:10.1364/ao.45.001111

Conflict of Interest: AC is co-owner of SciGlob Instruments & Services LLC and LuftBlick. GM was employed by SciGlob Instruments & Services LLC. LH was employed by Science Systems and Applications, Inc.The remaining authors declare that the research was conducted in the absence of any commercial or financial relationships that could be construed as a potential conflict of interest.

ORIGINAL RESEARCH
published: 15 July 2021
doi: 10.3389/frsen.2021.690010

Cloud Detection Over Sunglint Regions With Observations From the Earth Polychromatic Imaging Camera

Yaping Zhou[1,2*], Yuekui Yang[1], Peng-Wang Zhai[3] and Meng Gao[1,4]

[1] *NASA Goddard Space Flight Center, Greenbelt, MD, United States*
[2] *JCET/University of Maryland Baltimore County, Baltimore, MD, United States*
[3] *JCET/Department of Physics, University of Maryland Baltimore County, Baltimore, MD, United States*
[4] *SSAI/NASA Goddard Space Flight Center, Ocean Ecology Laboratory, Greenbelt, MD, United States*

Edited by:
Gregory Schuster, National Aeronautics and Space Administration, United States

Reviewed by:
Weizhen Hou, Aerospace Information Research Institute (CAS), China
Yuri Knyazikhin, Boston University, United States

**** Correspondence:** Yaping Zhou, yaping.zhou-1@nasa.gov*

***Specialty section:** This article was submitted to Satellite Missions, a section of the journal Frontiers in Remote Sensing*

***Received:** 01 April 2021*
***Accepted:** 09 June 2021*
***Published:** 15 July 2021*

***Citation:** Zhou Y, Yang Y, Zhai P-W and Gao M (2021) Cloud Detection Over Sunglint Regions With Observations From the Earth Polychromatic Imaging Camera. Front. Remote Sens. 2:690010. doi: 10.3389/frsen.2021.690010*

With the ability to observe the entire sunlit side of the Earth, EPIC data have become an important resource for studying cloud daily variability. Inaccurate cloud masking is a great source of uncertainty. One main region that is prone to error in cloud masking is the sunglint area over ocean surfaces. Cloud detection over these regions is challenging for the EPIC instrument because of its limited spectral channels. Clear sky ocean surface reflectance from visible channels over sunglint is much larger than that over the non-glint areas and can exceed reflectance from thin clouds. This paper presents an improved EPIC ocean cloud masking algorithm (Version 3). Over sunglint regions (glint angle ≤25°), the algorithm utilizes EPIC's oxygen (O_2) A-band ratio (764/780 nm) in addition to the 780 nm reflectance observations in masking tests. Outside the sunglint regions, a dynamic reflectance threshold for the Rayleigh corrected 780 nm reflectance is applied. The thresholds are derived as a function of glint angle. When compared with co-located data from the geosynchronous Earth orbit (GEO) and the low Earth orbit (LEO) observations, the consistency of the new ocean cloud mask algorithm has increased by 4~10% and 4~6% in the glint center and granule edges respectively. The false positive rate is reduced by 10~17%. Overall global ocean cloud detection consistency increases by 2%. This algorithm, along with other improvements to the EPIC cloud masks, has been implemented in the EPIC cloud products Version 3. This algorithm will improve the cloud daily variability analysis by removing the artificial peak at local noon time in the glint center latitudes and reducing biases in the early morning and late afternoon cloud fraction over ocean surfaces.

Keywords: EPIC, cloud detection, sunglint, oxygen A-band, ocean surface reflectance

INTRODUCTION

When the geometric configuration of Sun, surface, and viewing angles form a mirroring path, the specular reflection, or sunglint, creates a bright spot on the remote sensing imagery. Ocean surface reflectance in the visible spectrum over sunglint is much larger than that from other areas. If the ocean surface were perfectly smooth, sunglint would appear in remote sensing images as the mirror image of the Sun, occupying a relatively small portion of the images. In reality, because of the wave and ocean currents, the ocean surface is tilting toward different directions, causing the sunlight to scatter

and resulting in a large area of glint zone. The size of the glint zone in the satellite imagery depends on the ocean surface roughness, which in turn can be parameterized in terms of the vector wind field. The classical work by Cox and Munk (1954a), Cox and Munk (1954b) use sea surface wind speed and direction 10 m above the ocean surface to parameterize the distribution probability of the orientation of sea surface facets, which is widely used in radiative transfer models to estimate glint distribution and intensity.

The large reflectance in the glint region poses significant problems in the remote sensing of some atmospheric and ocean constituents. For example, remote sensing of atmospheric aerosol over ocean relies on separating the total sensor reflectance originated from surface and atmospheric molecular and aerosol backscattering. While surface reflectance over ocean can be estimated with auxiliary wind information, aerosol retrieval is normally avoided near and in the sunglint region (glint angle <40°) because of the large uncertainties (Levy et al., 2005). Likewise, sunglint is a serious confounding factor for remote sensing of water column properties and benthos as the total signal is dominated by the sunglint which makes the retrieval of water-leaving radiance very difficult (e.g., Khattak et al., 1991; Hagolle et al., 2004; Ottaviani et al., 2008; Kay et al., 2009; Jackson and Alpers, 2010; Harmel and Chami, 2013).

Outside the sunglint regions, cloud detection over ocean surfaces is considered relatively easy due to the sharp contrast between bright cloud objects and the generally dark ocean surface in the visible spectral channels. A single reflectance test at 0.86 μm can detect over 95% of daytime clouds over water when compared to the full set of Moderate Resolution Imaging Spectroradiometer (MODIS) cloud mask tests (Zhou et al., 2003). The MODIS cloud mask algorithm utilizes a varying reflectance threshold for the 0.86 μm channel in sunglint regions, where they are split into three sections according to the sunglint angle Θ_{glint}. For Θ_{glint} from 0 to 10°, the mid-point threshold is constant at 0.105, for Θ_{glint} from 10° to 20° the threshold varies linearly from 0.105 to 0.075, and for Θ_{glint} from 20° to 36°, it varies linearly from 0.075 to 0.055 (Frey et al., 2008; Ackerman et al., 2010). Additional spectral tests in thermal and near infrared channels are useful in delineating between clear sky and some optically thin clouds.

The Earth Polychromatic Imaging Camera (EPIC) on board the Deep Space Climate Observatory (DSCOVR) launched in 2015 has 10 narrow spectral channels in the ultraviolet (UV) and visible/near-infrared (Vis/NIR)

(317–780 nm) spectral regions. The DSCOVR satellite, which is located in the first Lagrangian (L1) point of the Earth–Sun orbit, approximately 1.5 million kilometers away, allows the EPIC instrument to take continuous measurements of the entire sunlit side of the Earth from the nearly backscattering direction (scattering angles between 168.5 and 175.5□) every 1~2 h (Marshak et al., 2018; Yang et al., 2019). The geometric configuration of EPIC leads to a large sunglint zone close to the center of each 2024x2024 CCD pixel granule (e.g., Figure 1A).

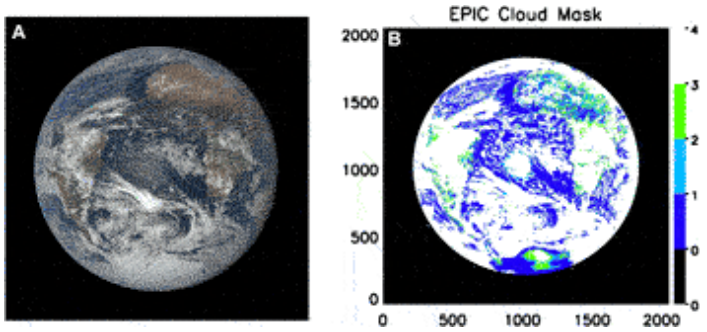

FIGURE 1 | (A) Example of EPIC RGB image for the granule at 13:31 UTC on January 1, 2016. **(B)** Cloud mask for this granule from Version 2 (old) cloud mask algorithm. Notice the enhanced glint reflectance in the center of the granule in **(A)** and corresponding false positives of cloud identification in the glint region in **(B)**. Blue, light blue, green, and white colors indicate four levels of cloud mask output: confident clear, uncertain clear, uncertain cloud and confident cloud, respectively.

A suit of cloud products, including cloud mask (CM), cloud effective pressure (CEP), cloud effective height (CEH), and cloud optical depth (COD), have been developed with observations from the EPIC's 10 spectral channels (Yang et al., 2019). EPIC possesses two oxygen (O_2) band pairs each with an absorption channel and a non-absorption reference channel. The A-band absorption channel is centered at 764 nm with a full width at half maximum (FWHM) of 1.02 nm, and its reference channel is centered at 780 nm with a FWHM of 1.8 nm. The B-band's absorption channel is centered at 688 nm with a FWHM of 0.84 nm, and its reference channel is centered at 680 nm with a FWHM of 1.6 nm (Marshak et al., 2018). Oxygen absorption has been applied to remote sensing of cloud and aerosol extensively (e.g., Fischer and Grassl, 1991; Stammes et al., 2008; Wang et al., 2008; Ferlay et al., 2010; Ding et al., 2016; Richardson et al., 2020). The EPIC's two O_2 band pairs (R_{764}/R_{780} and R_{688}/R_{680}) are used for the

retrieval of CEP (Yang et al., 2013; Davis et al., 2018a; Yang et al.,2019; Yin et al., 2020) and for cloud masking over snow and ice (Zhou et al., 2020). The retrieval is based on the principle that the O_2 absorption bands are sensitive to the presence of clouds, especially high and thick clouds that reduce the absorbing air mass that light travels through while the reference channel does not. An increase in the ratio of the bidirectional reflectance functions (BRFs) between the absorbing and reference channel can not only indicate the presence of cloud but also be used to retrieve the effective cloud height (Yang et al., 2013; Yang et al., 2019). Zhou et al. (2020) further improved the O_2 band ratio-based cloud mask algorithm over snow and ice by developing a dynamically varying threshold with surface altitude and Solar/view zenith angles.

Over ocean, the Version 2 (old) EPIC cloud mask algorithm uses the Rayleigh corrected reflectance of 680 and 780 nm channels with fixed thresholds (Yang et al., 2019). The Rayleigh correction partially mitigated the angle effect. EPIC cloudmask algorithm generates four levels of clear and cloud confidences similar to those of official MODIS cloud mask (Table 1). The global mean cloud fraction over ocean derived from EPIC is within 3% of those computed from collocated LEO/GEO composites. The pixel level accuracy of EPIC cloud mask product is about 88% (Yang et al., 2019). Though the performance is reasonable, further inspection reveals that over sunglint regions near the center of the granules, the algorithm nearly always identifies pixels as cloudy regardless of whether or not clouds are present (Figure 1). This increases the cloud fraction around local noon time over the ocean at latitudes where sunglint occurs. In addition, we also noticed that the cloud mask for ocean pixels near the edge of the granules is biased toward cloudy, which is due to enhanced reflectance in the large solar/view zenith angles near the edge. This bias can lead to an overestimation of cloud fraction close to the edge of the images, including high-latitude regions. It is worth noting that the biases in the cloud mask affect the EPIC downstream products as well. For example, the EPIC COD retrieval procedure (Meyer et al., 2016), which adopts a single channel retrieval approach similar to what Yang et al. (2008) describes, uses cloud mask as part of the input.

TABLE 1 | Cloud mask classification from EPIC and GEO/LEO. CldHC, CldLC, ClrLC, ClrHC stand for cloud with high confidence, cloud with low confidence, clear with low confidence, and clear with low confidence, respectively.

Scene classification	CM values	EPIC CM	GEO/LEO CM
Cloud	4	CldHC	*cloud fraction* > 95%
	3	CldLC	50% < *cloud fraction* < 95%
Clear	2	ClrLC	5% < *cloud fraction* < 50%
	1	ClrHC	*cloud fraction* < 5%

This study aims to improve the EPIC cloud mask over the sunglint region and granule edges over ocean based on the radiative transfer simulations and collocated observations from GEO/LEO platforms. A new application of the A-band ratio in the glint region will be investigated. The remainder of the paper is organized as follows: First, we introduce the data and radiative transfer model (RTM) used and the sensitivity studies conducted. Then we will describe EPIC's sunglint distribution and impact. Next we will describe the new ocean cloud mask algorithm including the threshold derivation and algorithm evaluation. Then we will discuss impact of the new algorithm on cloud diurnal cycle and zonal mean oceanic cloud fraction. *Summary and discussion* will be provided in the end.

DATA AND RADIATIVE TRANSFER MODEL SIMULATIONS

Data

The primary data used in the study are the EPIC level 1B calibrated reflectance and the EPIC level 2 standard cloud products (Yang et al., 2019). In addition, the study uses the composite cloud product developed by the Clouds and the Earth's Radiant Energy System (CERES) team at the NASA Langley Research Center as reference for comparison with the EPIC cloud detection results. The composite is created by projecting the geosynchronous Earth orbit (GEO) and low Earth orbit (LEO) satellite retrievals to the EPIC grid at each EPIC observing time (Khlopenkov et al., 2017; Su et al., 2018). The procedure ensures that every EPIC image/pixel has a corresponding GEO/LEO composite image/pixel with approximately the same size and observing time. The LEO satellites include NASA Terra and Aqua MODIS

and NOAA AVHRR, while geosynchronous satellite imagers include the Geostationary Operational Environmental Satellites (GOES) operated by NOAA, Meteosat satellites by EUMETSAT, and Multifunctional Transport Satellites (MTSAT) and Himawari-8 satellites operated by the Japan Meteorological Agency (JMA). The time differences between the GEO/LEO and the EPIC observations are included in the product files. To limit uncertainties, we only use pixels where the GEO/LEO and EPIC observations are within 5 min of each other. Compared to EPIC, the GEO/LEO sensors are usually better equipped for cloud detection because more spectral channels are available in these instruments. The cloud retrievals in the composite data follow Minnis et al. (2011). Because of EPIC's large pixel size, one EPIC pixel corresponds to many GEO/LEO pixels each with its own cloud mask and optical properties retrievals; hence a composite pixel reports a cloud fraction based on cloud masks of the GEO/LEO pixels within it.

Radiative Transfer Model Simulations

An EPIC simulator (Gao et al., 2019) has been developed based upon an RTM (Zhai et al., 2009; Zhai et al., 2010) that solves multiple scattering of monochromatic light in the atmosphere and surface systems. The model setup is described in Gao et al. (2019), Zhou et al. (2020). The EPIC simulator is used to generate the oxygen A-band and B-band reflectance over ocean surface. Gas absorptions due to ozone, oxygen, water vapor, nitrogen dioxide, methane, and carbon dioxide are incorporated in all EPIC bands. The gas absorption cross sections are computed from the HITRAN line database (Rothman et al., 2013) using the Atmospheric Radiative Transfer Simulator (ARTS) (Buehler et al., 2011). Line broadening caused by pressure and the temperature dependencies of line absorption parameters are considered. In the O_2 A- and B-bands, radiances from line-by-line radiative transfer simulations are conducted and then convolved with the EPIC instrument response functions. The model atmosphere uses Standard US atmosphere profile from Intercomparison of Radiation Codes in Climate Models (ICRCCM) project (Barker et al., 2003) and assumes a one-layer cloud with a molecular layer both above and beneath. The O_2 absorption within clouds is considered by assuming a fixed O_2 molecule vertical profile.

The cloud is assumed to be liquid droplets following a gamma size distribution with an effective radius of 10 μm and an effective variance of

0.1. The cloud layer has varied optical thickness ranging from 0.2 to 30 and cloud top height (CTOP) from 1.0 to 15 km above the ground. The cloud geometrical thickness (CGT) varies from 0.5 to 4 km. The model simulates a variety of cases with 17 solar zenith angles (SZAs) ranging from 0 to 80□, 18 view zenith angles (VZAs) from 0 to 85□, and 37 relative azimuth angles (RAZMs) from 0 to 180□, all with an increment of 5□. The lower boundary is an ocean surface with the surface roughness characterized by the Cox Munk model (Cox and Munk, 1954a; Cox and Munk, 1954b). A fixed surface wind speed of 6 m/s is used (Gao et al., 2019). The model simulated reflectance under similar sun-view geometry to the EPIC observations are used for developing thresholds for cloud detection.

GLINT DISTRIBUTIONS AND IMPACT

The sunglint region of an image can be roughly estimated by the glint angle (Θ_{glint}), which denotes the angle between the reflection received by satellite sensor and the angle of specular reflection. The glint angle is defined as

$$\Theta_{glint} = \cos^{-1}\left(\cos\theta_s\cos\theta_v + \sin\theta_s\sin\theta_v\cos\phi\right) \qquad (1)$$

where θ_S, θ_V, and Φ are the solar zenith, the satellite zenith and the relative azimuth angles (between the Sun and the satellite), respectively. Glint contamination are normally considered within [0°, 30°] or [0°, 40°] depending on applications.

Figure 2 shows glint covered area from a single granule (Figure 2A), an entire day (Figure 2B) to an entire year (Figure 2C). Based on the sunglint contamination on cloud mask, we define our glint region in this study as a region with glint angle less than 30°. Figure 2 shows that sunglint covers a large fraction of a granule in the granule center if the region happens to be ocean. At any given day, the glint center moves from east to west and creates a zonal band of about 30° in the meridional direction where the glint is centered (Figure 2B). June 21 and December 21 represent the north (south) most position of the Sun (and glint center latitude) respectively. The glint center is located near the equator on March 21. Because sunglint appears in the entire oceanic part of the latitudinal band, if included, it is sufficiently large to affect the oceanic cloud fraction diurnal cycle analysis, and possibly mean cloud fraction in those latitudes due to the bias in the Version 2 cloud mask. This issue has been noticed by the community. For example, in the

analysis of Delgado-Bonal et al. (2020), the time period with sun-glint is excluded. Lastly, the glint center migrates between 23°S–23°N each year and creates a total glint contamination region spanning from -38° to 38° (Figure 2C). Figure 2D shows the percentage of ocean area in each latitude which ranges from around 50% in 40°N to more than 95% in 40°S. The glint effect of the mean zonal cloud fraction is expected to be larger in southern hemisphere, with a larger percentage of ocean coverage.

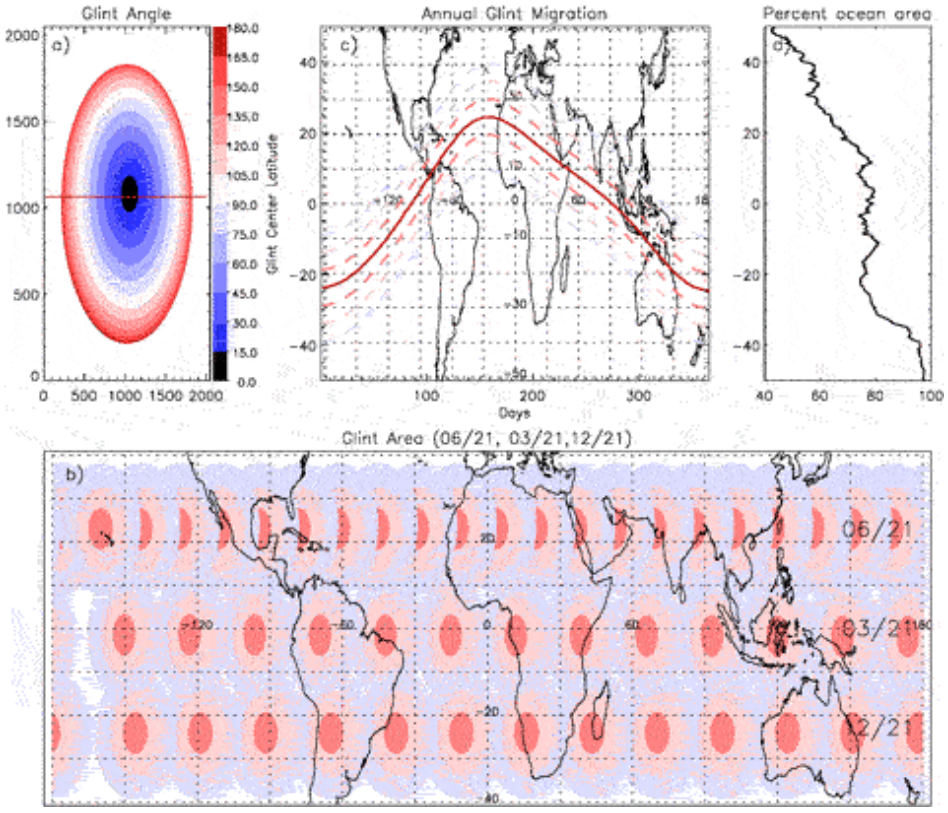

FIGURE 2 | (A) Glint angles for a single granule from September 24, 2017, 04 UTC. The thick red line in the middle is the location of the simulations shown in Figures 3, 4. **(B)** Glint areas (within 30° of glint angle) in all granules drawn from left to right as the day progresses on June 21, March 21, and December 21, 2016 in the top, middle and low rows, respectively; pink, light pink, and pale represent areas within 10, 20 and 30 degrees of glint angle. **(C)** Glint migration during a year. Red, pink, light pink and light purple colors mark the boundaries of 0° and 10°, 20°, 30° of glint angles. **(D)** Ocean area percentage at each latitude.

It is important to correct the cloud mask bias in the sunglint area. The simulation of Gao et al. (2019) shows that while clear sky ocean reflectance increases over sunglint regions, the presence of thin clouds dims the glint reflectance. While this makes single reflectance threshold tests difficult, they

also find that the cloudy sky A-band ratio is usually higher than that of clear sky in the glint region, making it a potential test for cloud mask in the glint region. In the following section, we will further investigate the behavior of A-band ratio in the glint region and try to incorporate it in the ocean cloud mask algorithm.

OCEAN CLOUD MASK ALGORITHM DEVELOPMENT

Sensitivity Study

To demonstrate the effect of sunglint on reflectance over the ocean, the reflectance at 780 nm R_{780} from the EPIC simulator along a horizontal line passing the center of one granule from September 24, 2017 (Figure 2A) is shown (Figure 3). Hypothetical ocean surface is assumed everywhere. The clear sky R_{780} is smaller than those of cloudy sky outside the sunglint zone, but increases toward the center and surpasses the cloudy sky R_{780} for thin clouds with optical thickness less 3. The cloudy sky R_{780} generally increases with cloud optical depth (COD), even at the glint center except when clouds are very thin (COD <1). The R_{780} of cloudy sky is always larger than that of clear sky outside the sunglint zone, and is insensitive to cloud height (figure now shown), which makes it a good candidate for cloud detection for ocean surface outside sunglint zone. Inside the sunglint zone, however, R_{780} for cloudy sky can be larger or smaller than that of clear sky depending on cloud optical thickness, hence a single R_{780} test cannot always separate clear and cloudy pixels.

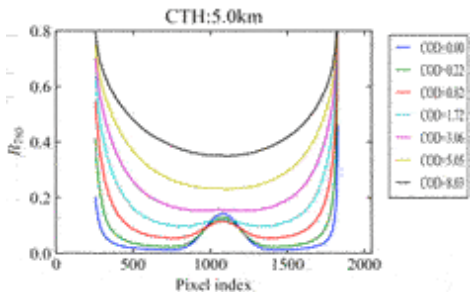

FIGURE 3 | Model simulations of reflectance at 780 nm for clear sky and cloud with different optical thickness along the horizonal line passing the granule center in Figure 2A. Clear sky is in color blue.

The ratio of A-band behaves quite differently than the 780 nm channel. In the center of glint, A-band ratio of clear skies is always smaller than those of cloudy skies, regardless of cloud optical thickness and cloud height (Figure 4). The separation between clear sky and cloudy sky A-band ratio increases with cloud height and optical thickness. For low cloud at 2.5 km, a clear separation between cloudy sky and clear sky in A-band ratio would require a cloud optical thickness greater 2, while for clouds with height greater than 5 km, a thin cloud with optical thickness greater than 0.82 is sufficient to separate the two. This is due to the greater sensitivity of the absorbing channel to the cloud height and optical depth as discussed in Zhou et al. (2020). Exact conditions (combination of COD and height) of clouds that can be detected would depend on the measurement uncertainty, which is estimated to be around 1% after considering the cancelation of calibration errors in the two bands (Davis et al., 2018b). The clear sky A-band ratio in the glint center is around 0.38; hence a difference between cloudy sky and clear sky A-band ratio larger than 0.04 would be above the 1% uncertainty range. It is found that 82% of the pixels at the glint center ($\Theta_{glint} < 20°$) with a cloud at 2.5 km and COD of 1.72 can satisfy this condition. Outside the sunglint region, the clear sky A-band ratio can be higher or lower than cloudy sky depending on the cloud height and COD. This renders the A-band ratio test only good for the sunglint region where the surface reflectance is high. To summarize, the EPIC R_{780} can serve as a good test for cloud detection outside the sunglint region; inside the sunglint, the EPIC O_2 A-band ratio can be used to separate clear and cloudy pixels when R_{780} fails for thin clouds.

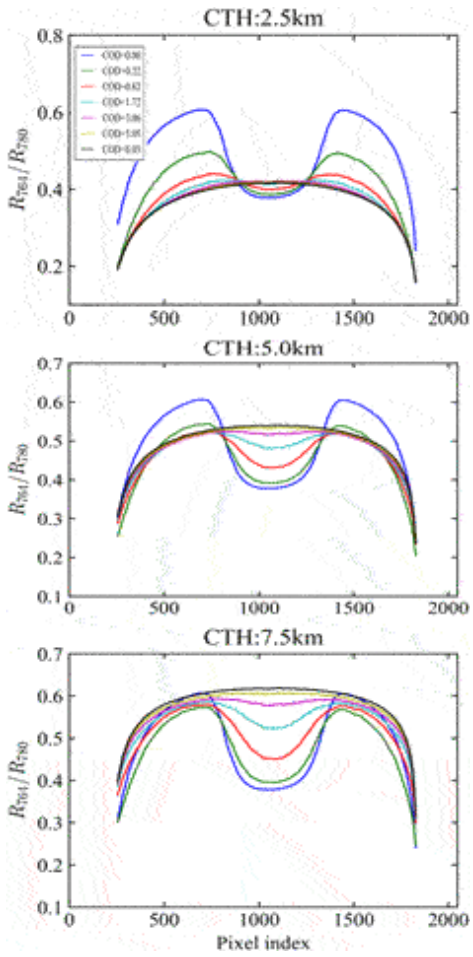

FIGURE 4 | Model simulations of A-band ratio (R_{764}/R_{780}) for clear sky (blue curve, COD = 0) and cloudy sky with different cloud optical thickness (COD) (see color legend) and cloud top height (CTH) at **(A)** 2.5 km, **(B)** 5 km, and **(C)** 7.5 km along a horizonal line passing the granule center in Figure 2A.

To derive stable thresholds for the EPIC instrument, additional investigation is necessary to examine the clear and cloudy sky data under all possible EPIC Sun-view geometry. For this purpose, we selected one EPIC granule from each month in 2016 and extracted the Sun-view geometry for all the pixels in this dataset. This creates a representative dataset for the EPIC Sun-view geometries. The EPIC simulator results are then interpolated into all the Sun-view angles in this dataset. Figure 5 shows that the EPIC R_{780} and A-band ratio as a function of Θ_{glint}. The sawtooth appearance in the figure is due to the Sun-view angle spread and corresponding R_{780} for a given Θ_{glint}. As shown in the figure, there is a well-defined curve of R_{780}

and A-band ratio as a function of Θ_{glint} from clear sky simulations for most of the ocean areas. The clear sky R_{780} increases at the glint center (Θ_{glint} < 30°) and spreads slightly that overlaps with thin clouds (COD <1.7) (Figure 5A). It remains quite flat, though not completely constant, at the Θ_{glint} range of 40°~120° before rising sharply again at Θ_{glint} > 150° with an even larger spread. Importantly, the A-band ratio for clear skies is consistently lower than that of thin clouds in the glint region (Figure 5B). The curves show that it is possible to define tabulated baseline thresholds in 1° intervals for cloud detection by combining the R_{780} and A-band ratio tests.

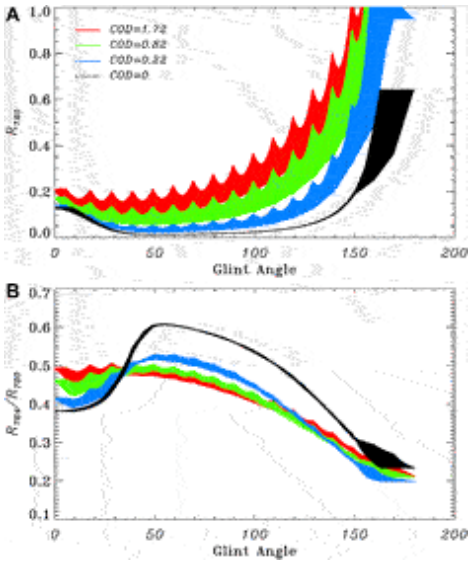

FIGURE 5 | Ensembles of simulated **(A)** 780 nm reflectance and **(B)** A-band ratio with geometries from 12 EPIC granules (one per month) in 2016. Black, blue, green and red shows simulations from COD = 0.0, 0.22, 0.82, 1.72, respectively. Cloud top height is 5 km and geometric thickness is 3 km.

R_{780} and A-Band Ratios From EPIC Observations

In this section we examine the observed Rayleigh corrected R_{780} (R'_{780}) and A-band ratio as a function of Θ_{glint} (Figure 6). Choosing Rayleigh corrected reflectance is to minimize the known angle effect. The separation of clear sky and cloudy sky is based on the results derived from the collocated GEO/LEO cloud fraction (Su et al., 2018). The upper bounds of the model-simulated clear sky of R'_{780} and A-band ratio are plotted for comparison. We notice that the upper bounds of the model derived clear sky

R'_{780} and A-band ratio (solid lines) represent the lower and upper bounds of their observed counterparts, respectively. The observed clear sky R'_{780} distribution shows a high concentration of low values in the middle range of the glint angles, but increases toward both ends, similar to what is shown in Figure 5. There is more spread (toward higher values) in the clear sky R'_{780} distribution than that of the simulation, possibly due to cloud contamination in the GEO/LEO dataset (also notice that the clear sky category we define for GEO/LEO may contain some cloud, see Table 1). The spread is larger with larger Θ_{glint} due to larger pixel size; hence more likely cloud contamination. The cloudy sky R_{780} is generally higher than those for the clear sky at the same Θ_{glint} except at very small Θ_{glint} (<25°), where a large portion of the clear sky and cloudy sky R'_{780} are in the same range. The model simulated R_{780} envelops the observed reflectance in both clear sky and cloudy sky plots outside the glint region, which makes it a good candidate as a cloud masking test. On the other hand, the model simulated clear sky A-band ratio curve falls between observed cloudy sky A-band ratios, indicating that it is not an ideal test beyond the glint region. As expected, the large spread of the observed clear sky A-band ratio narrows towards the glint center where most clear sky values are under the simulated curve. Inside the glint region, however, the cloudy sky A-band ratio is mostly higher than that of the clear sky, which indicates that the A-band ratio can be used as a test in the glint region.

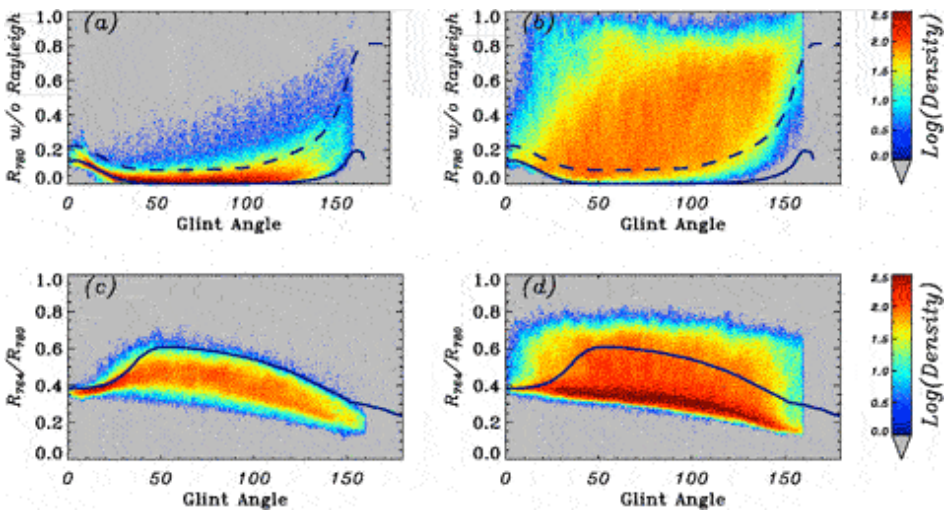

FIGURE 6 | Observed Rayleigh corrected EPIC 780 nm reflectance **(A,B)** and A-band ratio **(C,D)** as a function of glint angles from January and July 2017 for clear sky **(A,C)** and cloudy sky **(B,D)**. The solid black lines represent the upper bounds of the model simulated clear sky Rayleigh corrected R_{780} in each 1-degree glint angle bins. Dash lines represent the adjusted Rayleigh corrected R_{780} thresholds.

Based on these observations, we designed the cloud mask ocean algorithm as follows:

For $\Theta_{glint} < 25°$,

$R'_{780} > R_0$ => cloud

$R'_{780} < R_0$ and $R_{764}/R_{780} > A_0$ => cloud

For $\Theta_{glint} > 25°$,

$R'_{780} > R_0$ => cloud

where the R_0 and A_0 values are the thresholds for Rayleigh corrected R_{780} and R_{764}/R_{780}, respectively, which are a function of Θ_{glint}. The values of R_0 and A_0 are modified from the model simulations (dashed curves in Figure 6). These adjustments are necessary as model derived values represent theoretical lower and upper bounds of clear sky values.

New Algorithm Evaluation

Case Study

The improvement of the new algorithm can be easily examined visually, as more than 2/3 of the granules have sunglint in the ocean. Figure 7 shows the new cloud mask for the granule at 13:31 UTC on January 1, 2016 shown in Figure 1. The new cloud mask algorithm eliminates the obvious overestimate of clouds in the glint center while keeping small cloud features in the glint intact. It is also noticeable that the old cloud mask overestimates cloud coverage in most of the edge areas of the granule (Figure 2B), especially on the right side, and the new algorithm has mitigated this issue as well.

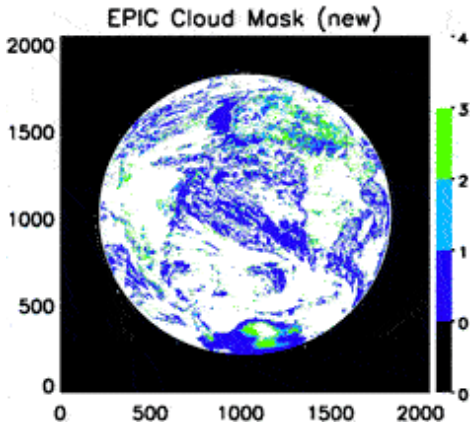

FIGURE 7 | New cloud mask for the granule at 13:31 UTC on January 1, 2016 shown in Figure 1. The new algorithm shows mostly clear sky with small features of cloud consistent with the cloud pattern outside the sunglint region.

Monthly Statistics

To quantitatively evaluate the new cloud mask, we conducted a comparison with the CM from the Langley LEO/GEO composite product introduced in *Data and RTM simulations*. As in Zhou et al. (2020), we divide the GEO/LEO cloud fraction into four categories to match with the four confidence levels of CM in EPIC (Table 1).

In addition, we define the accuracy, probability of correct detection rate (POCD) and probability of false detection rate (POFD) as:

$$Accuracy = (a + b)/(a + b + c + d) \quad (2)$$

$$POCD = a/(a + c) \quad (3)$$

$$POFD = d/(b + d) \quad (4)$$

where a is the number of pixels that both algorithms identify as cloudy (including high and low confidence), b is the number of pixels that both identify as clear (including high and low confidence), c is the number of pixels that EPIC identifies as clear while GEO/LEO identifies as cloudy, and d is the number of pixels that EPIC identifies as cloudy while GEO/LEO identifies as clear. We note that the cloud detection in GEO/LEO is by no means the truth, hence the "accuracy" here should be interpreted as consistency with GEO/LEO rather than true accuracy. The same should be applied to POCD and POFD as they are relevant to GEO/LEO's cloud detection.

Figure 8 shows the matchups between EPIC cloud mask in 1 (blue), 2 (cyan), 3 (yellow), 4 (red) with the GEO/LEO cloud fraction with <5%, 5–50%, 50–95% and >95% categories. It is obvious that the old algorithm overestimates the cloud in the glint center, evidenced by a red bar in the first group where GEO/LEO has low cloud fraction (<5%) and virtually no blue bar in high cloud fractions (>95%) categories. The new algorithm increases the blue bar (high confident clear sky) in the clear region without overestimating clear sky in the cloudy region. Similarly in the high Θ_{glint} region (toward granule edge), the new algorithm was able to detect more clear sky (blue bar) in the clear region without overestimating clear sky in the cloudy region. Improvement is evident for the new algorithm, where most of the pixels with <5% cloud fraction have CM = 1 or 2 (high and low confidence clear, respectively), while pixels with >95% cloud fraction more likely have CM values of four and 3 (high and low confidence cloudy, respectively). In the glint center, the overall consistency increases from 81.9 to 86.9% and POFD decreases from 17.3 to 7.3%. In the large glint angle region, the consistency increases from 80.3 to 86.6% and POFD decreases from 20.7 to 9.5%. For the entire global ocean, the improvement in the glint center and granule edge leads to an improvement of consistency from 86.6 to 88.7% and false detection rate from 10.2 to 6.7%. The improvements in other months are similar to that of January and July 2017 (Table 2). Based on these results, the new ocean cloud mask algorithm increases the detection consistency in the glint center and granule edges by 4~10% and 4~6%, respectively, with a reduction of false cloud detection rate by 10~17%. Overall global ocean cloud detection consistency increases by approximately 2%.

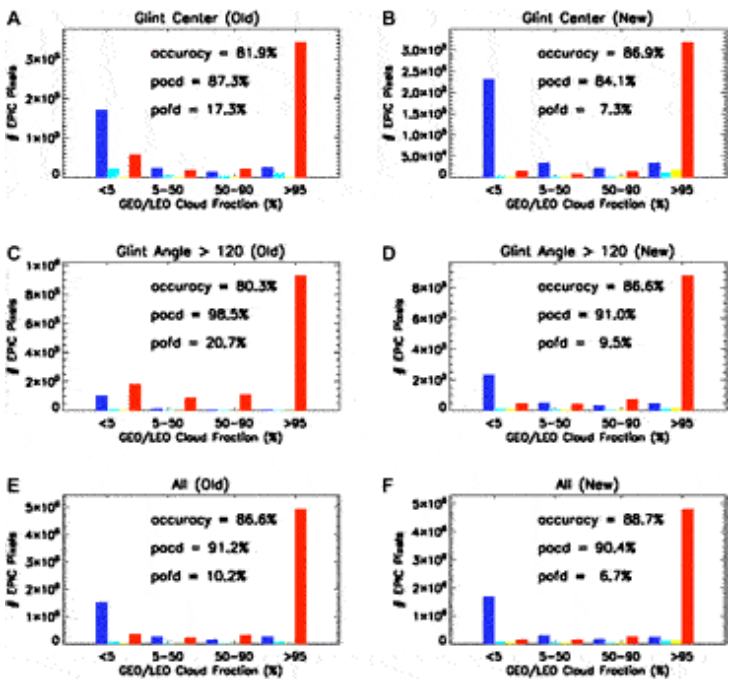

FIGURE 8 | Number of pixels in each pixel-by-pixel matchup category between the cloud mask from EPIC and cloud fraction from GEO/LEO composite over ocean surfaces for January and July 2017 at glint center ($\Theta_{glint} < 25°$) **(A,B)**; large glint angles ($\Theta_{glint} > 120°$) **(C,D)**, and all glint angles **(E,F)**. Left is from Version 2 EPIC cloud mask algorithm and the right is from the new algorithm. Blue, cyan, yellow, and red bars are for EPIC cloud mask equals to 1, 2, 3, 4, respectively. POCD: probability of correct detection; POFD: probability of false detection.

TABLE 2 | Comparison of EPIC ocean cloud mask performance between the Version 2 algorithm and the new algorithm at glint center ($\Theta_{glint} < 25°$), large glint angles ($\Theta_{glint} > 120°$), and all glint angles of four additional months.

Month	Region	Glint center ($\Theta_{glint} < 25°$)		Large glint angles ($\Theta_{glint} > 120°$)		All angles	
		v1	New	v1	New	v1	New
2016.01	Accuracy	77.0	86.7	83.5	88.2	87.2	89.4
	POCD	93.6	85.0	98.8	92.0	91.5	90.9
	POFD	24.8	7.2	17.0	7.4	8.6	5.4
2017.03	Accuracy	76.4	88.3	84.4	91.7	88.5	90.9
	POCD	92.9	93.0	99.1	94.3	91.3	91.4
	POFD	25.9	12.0	16.5	5.3	8.2	5.0
2017.09	Accuracy	85.5	91.8	84.9	91.1	88.6	90.8
	PCD	95.2	93.6	99.0	93.3	91.5	91.3
	POFD	13.9	5.0	15.8	5.0	7.4	4.3
2017.12	Accuracy	82.5	86.3	83.7	89.6	89.9	90.5
	POCD	93.9	86.0	99.2	93.9	92.9	92.3
	POFD	15.6	4.8	17.1	7.3	7.4	4.8

Systematic retrieval bias can often be revealed through examining the retrieved parameters as a function of independent variables such as viewing geometry (Zhou et al., 2020). During the evaluation of the EPIC cloud products, we notice that the EPIC clear and cloud detection rates vary with view zenith angle. Here the clear (cloud) detection rates are computed as the number of matched clear (cloudy) pixels divided by total clear (cloudy) pixels.

$$\text{Cloud\_detection\_rate} = a/(a+c) \quad (5)$$

$$\text{Clear\_detection\_rate} = b/(b+d) \quad (6)$$

Figure 9 shows the comparison of the clear/cloud detection rates between the old and new algorithms. It is quite obvious that the old algorithm significantly underestimates clear sky pixels in the glint center ($\Theta_{glint} < 30°$) and large glint angles ($\Theta_{glint} > 100°$) while detecting clouds at nearly 100% (Figure 9A). The new algorithm has a nearly constant clear and cloud detection rate of more than 90% (Figure 9B). Cloud detection rate decreases slightly when Θ_{glint} reaches zero. Pixels with $\Theta_{glint} > 160^{o}$ appear at the very edge of the granule and retrieval uncertainty is large due to much larger pixel size and other factors such as the curvature of the Earth not considered in the RTM. Cloud fraction from the new algorithm is closer to the cloud fraction from GEO/LEO composites, while the old algorithm shows much larger cloud fraction at glint center and high glint angles (Figure 9C). Similarly, the systematic bias as a function of view zenith angle from the old algorithm is significantly reduced (Figures 9D–F). These results show that the new algorithm largely eliminates systematic bias in the old algorithm as a function of the viewing geometry.

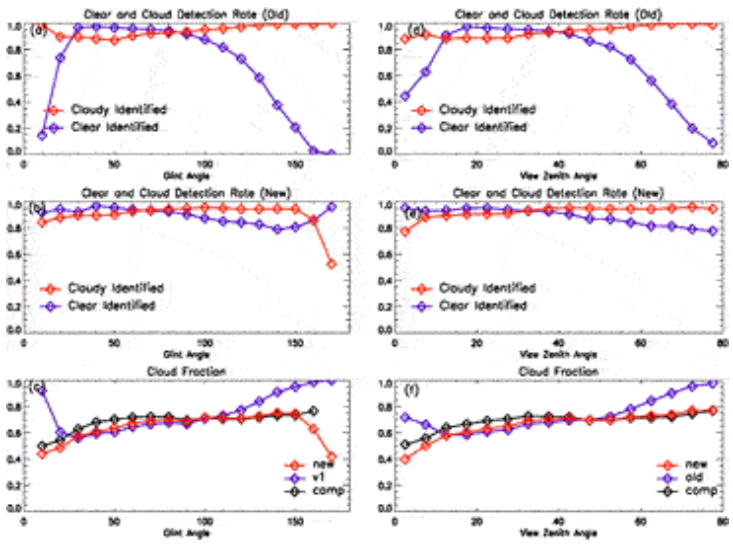

FIGURE 9 | Comparison of cloud (red) and clear (blue) detection rates as a function of glint angle from Version 2 algorithm **(A)** and the new algorithm **(B)**. **(C)** cloud fraction as a function of glint angle from GEO/LEO composite (black line), Version 2 algorithm (blue) and the new algorithm (red). **(E–F)** are similar as **(A–C)** except as a function of view zenith angles. Data are from January and July of 2017.

IMPACT ON CLOUD DIURNAL CYCLE AND ZONAL MEAN CLOUD FRACTION STUDIES

As mentioned in *Glint distributions and impact*, sunglint affects a zonal band of 30° in any given time of the year in tropical regions from 38°S to 38°N. Since sunglint appears near the centers of the granules which correspond to local noon time, it is likely that tropical oceanic cloud diurnal cycle analysis is affected if sunglint is not properly treated. In addition, a fixed threshold would misidentify pixels near granule edges to be cloudy because of high reflectance in those areas.

In Figure 10 we examine the latitudinal distributions of daytime cycles of cloud fraction over oceans in January and July. Note the complete diurnal cycle is not available from EPIC since it only measures the sunlit side of the Earth. The daytime cycle is computed by first converting the cloud mask retrievals from universal time (UTC) to local time according to their longitudes and then sorting the pixels according to their local solar time and latitude bins. Mean cloud fraction is then computed based on cloud mask results for each of these bins. Because the length of daytime differs with latitude, the figures are bell-shaped toward the winter hemisphere (shorter daytime in the winter hemisphere). One feature of the old latitudinal

distribution of daytime cloud cycles is the circle-shaped high values in the midst of low cloud fraction near 20°S in January and 20°N in July at local noon, corresponding to glint center latitude in these two months (Figures 10A,E). The new algorithm has largely eliminated this artificial noon peak in the daytime cloud fraction (Figures 10B,F). In addition, the old cloud mask has produced near 100% cloud fraction in the beginning and ending hours of the daylight time even in dry subtropical latitudes, which is due to high-reflectance at large zenith angles. This problem is largely mitigated in the new algorithm. The difference maps clearly show reduced cloud fraction in the glint center and daytime edge hours (Figures 10C,G). This is especially significant in the glint center latitudes (Figures 10D,H), because 1) the noon peak disappears, and 2) even though diurnal cycle still features as higher cloud fraction in the morning and afternoon with minimum in local noon, the range of daytime cloud variation is greatly reduced.

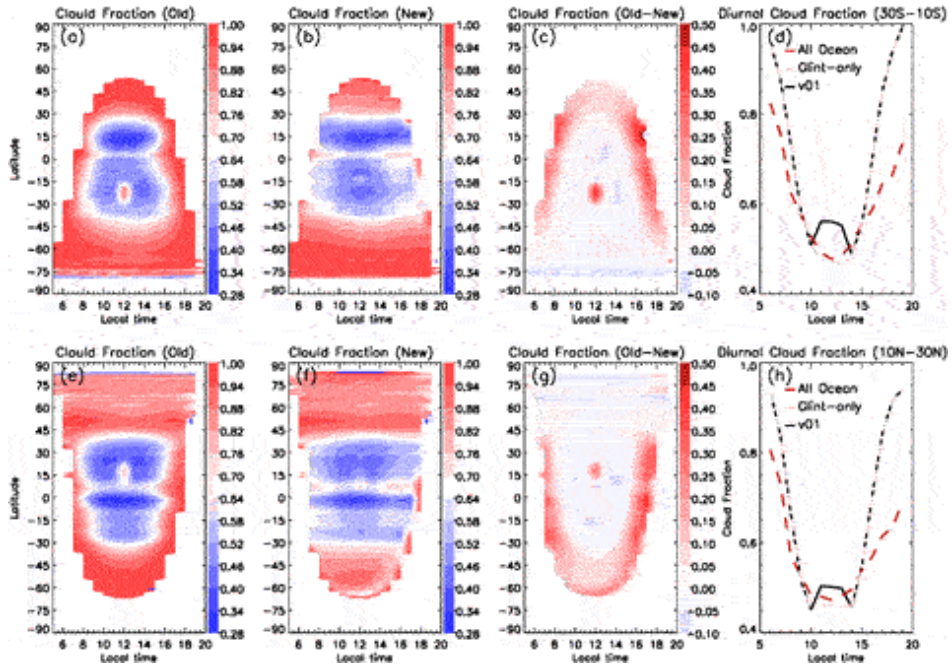

FIGURE 10 | Zonal mean oceanic cloud fraction as a function of latitude and local time from the old algorithm **(A,E)**, the new algorithm **(B,F)** and the difference (old–new) **(C,G)** in January (top) and July (bottom) in 2016. **(D,H)** show daytime cycle of cloud fractions from glint center latitudes (10°S–30°S) in January and (10°N–30°N) in July, respectively.

Because of the reduction in cloud fraction in the glint center and granule edge, some reduction in the zonal mean oceanic cloud fraction is expected. Figure 11 shows that the reduction appears for different latitudes in different

seasons. In January, glint related reduction of about 10% appears around 25°S and up to 10% north of 15°N (Figure 11A). In July, the opposite is observed even though glint related reduction is smaller near 25°N (Figure 11C). In March and September, the Sun is near the equator; therefore, major reductions of cloud fraction occur in the latitudinal zone of 15°S–15°N, and high latitudes in each hemisphere also incur less reduction.

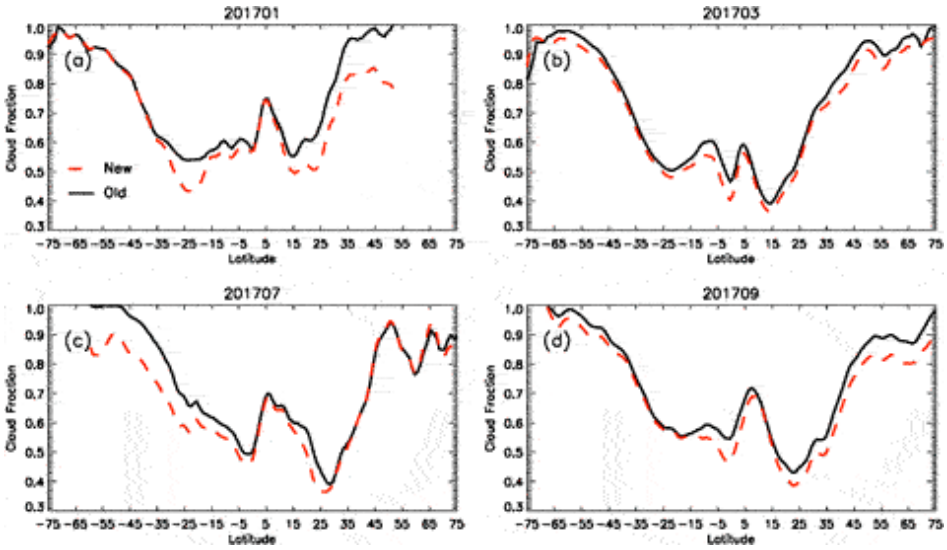

FIGURE 11 | Zonal mean oceanic cloud fraction with latitude from old cloud mask algorithm (black) and new algorithm (red) in January, March, July, and September 2017.

SUMMARY AND DISCUSSION

Even though the old EPIC cloud mask algorithm attempts to reduce the sun-view geometry impact by applying the Rayleigh correction procedure, it is shown that fixed thresholds with the visible and near infrared channels lead to biases in the EPIC cloud mask product. Because of EPIC's unique orbit, each EPIC granule over the ocean consists of a large area near the granule center that is affected by the sunglint. The glint affected area covers a latitudinal band of about 30° at any given time and migrates between 38°S and 38°N as the direct Sun position moves with the season. The old EPIC cloud mask tends to miss-identify the clear sunglint pixels as cloud due to its fixed reflectance threshold, therefore creating an artificial cloud fraction peak in local noon time. In addition, pixels with large Sun and view zenith angle at the granule edge tend to be miss-identified as clouds because of enhanced Rayleigh scattering.

A new ocean cloud mask algorithm is developed, which consists of two tests. The first test is based on the Rayleigh corrected 780 nm reflectance. A dynamic threshold dataset is developed as a function of glint angle to account for the enhanced reflectance in the glint region at the granule center and large glint angle region at the granule edge. The second test is based on the O_2 A-band ratio, which is applied to regions where glint angles are smaller than 25^o. Inside the sunglint region, the cloudy sky 780 nm reflectance can be smaller than that of the clear sky when clouds are thin. A unique property of A-band ratio is that the clear sky A-band ratio is lower than that of the cloudy A-band ratio in the glint center; thus, a supplemental A-band ratio test in the Sun glint regions can make up the reflectance test. The consistency of the new ocean cloud mask algorithm, as compared with GEO/LEO cloud detection, has increased by 4~10% and 4~6%, in the glint center and granule edges respectively. The false cloud detection rate is reduced by 10~17% and the overall global ocean cloud detection consistency is increases by approximately 2%. The new algorithm has largely eliminated the systematic biases dependent on glint-angle and view zenith angles found in the old algorithm.

The new ocean cloud mask algorithm can help studies on the diurnal cycles of cloud fraction over ocean by reducing the artificial peak at local noon time in the glint center latitudes and by reducing early morning and late afternoon cloud fraction biases.

DATA AVAILABILITY STATEMENT

The datasets presented in this study can be found in online repositories. The names of the repository/repositories and accession number(s) can be found below:
https://asdc.larc.nasa.gov/project/DSCOVR/DSCOVR_EPIC_L2_CLOUD_03.

AUTHOR CONTRIBUTIONS

YZ designed the new improvements of the ocean cloud mask algorithm, conducted the analysis and drafted the paper. YY led the development of the EPIC cloud algorithm, contributed to the design, testing and implementation of the new improvements to the operational algorithm. MG and P-WZ conducted the EPIC simulations and analysis. All authors contributed to the writing of the manuscripts.

REFERENCES

Ackerman, S., Strabala, K., Menzel, P., Frey, R., Moeller, C., and Gumley, L. (2010). "Discriminating clear-sky from Cloud with MODIS Algorithm Theoretical Basis Document (MOD35)," in *MODIS Cloud Mask Team, Cooperative Institute for Meteorological Satellite Studies* (Madison: University of Wisconsin).

Barker, H. W., Stephens, G. L., Partain, P. T., Bergman, J. W., Bonnel, B., Campana, K., et al. (2003). Assessing 1D Atmospheric Solar Radiative Transfer Models: Interpretation and Handling of Unresolved Clouds. *J. Clim.* 16, 2676–2699. doi:10.1175/1520-0442(2003)016<2676:adasrt>2.0.co;2

Buehler, S. A., Eriksson, P., and Lemke, O. (2011). Absorption Lookup Tables in the Radiative Transfer Model ARTS. *J. Quantitative Spectrosc. Radiative Transfer* 112 (10), 1559–1567. doi:10.1016/j.jqsrt.2011.03.008

Cox, C., and Munk, W. (1954a). Measurement of the Roughness of the Sea Surface from Photographs of the Sun's Glitter. *J. Opt. Soc. Am.* 44, 838–850. doi:10.1364/josa.44.000838

Cox, C., and Munk, W. (1954b). Statistics of the Sea Surface Derived from Sun Glitter. *J. Mar. Res.* 13, 198–227.

Davis, A. B., Ferlay, N., Libois, Q., Marshak, A., Yang, Y., and Min, Q. (2018b). Cloud Information Content in EPIC/DSCOVR's Oxygen A- and B-Band Channels: A Physics-Based Approach. *J. Quantitative Spectrosc. Radiative Transfer* 220, 84–96. doi:10.1016/j.jqsrt.2018.09.006

Davis, A. B., Merlin, G., Cornet, C., Labonnote, L. C., Riédi, J., Ferlay, N., et al. (2018a). Cloud Information Content in EPIC/DSCOVR's Oxygen A- and B-Band Channels: An Optimal Estimation Approach. *J. Quantitative Spectrosc. Radiative Transfer* 216, 6–16. doi:10.1016/j.jqsrt.2018.05.007

Delgado-Bonal, A., Marshak, A., Yang, Y., and Oreopoulos, L. (2020). Daytime Variability of Cloud Fraction from DSCOVR/EPIC Observations. *J. Geophys. Res. Atmos.* 125 (10). doi:10.1029/2019JD031488

Ding, S., Wang, J., and Xu, X. (2016). Polarimetric Remote Sensing in Oxygen A and B Bands: Sensitivity Study and Information Content Analysis for Vertical Profile of Aerosols. *Atmos. Meas. Tech.* 9, 2077–2092. doi:10.5194/amt-9-2077-2016

Ferlay, N., Thieuleux, F., Cornet, C., Davis, A. B., Dubuisson, P., Ducos, F., et al. (2010). Toward New Inferences about Cloud Structures from Multidirectional Measurements in the Oxygen A Band: Middle-Of-Cloud Pressure and Cloud Geometrical Thickness from POLDER-3/PARASOL. *J. Appl. Meteorol. Climatol.* 49, 2492–2507. doi:10.1175/2010JAMC2550.1

Fischer, J., and Grassl, H. (1991). Detection of Cloud-Top Height from Backscattered Radiances within the Oxygen A Band. Part 1: Theoretical Study. *J. Appl. Meteorol.* 30, 1245–1259. doi:10.1175/1520-0450(1991)030<1245:docthf>2.0.co;2

Frey, R. A., Ackerman, S. A., Liu, Y., Strabala, K. I., Zhang, H., Key, J. R., et al. (2008). Cloud Detection with MODIS. Part I: Improvements in the MODIS Cloud Mask for Collection 5. *J. Atmos. Oceanic Technol.* 25, 1057–1072. doi:10.1175/2008JTECHA1052.1

Gao, M., Zhai, P.-W., Yang, Y., and Hu, Y. (2019). Cloud Remote Sensing with EPIC/DSCOVR Observations: a Sensitivity Study with Radiative Transfer Simulations. *J. Quantitative Spectrosc. Radiative Transfer* 230, 56–60. doi:10.1016/j.jqsrt.2019.03.022

Hagolle, O., Nicolas, J.-M., Fougnie, B., Cabot, F., and Henry, P. (2004). Absolute Calibration of VEGETATION Derived from an Interband Method Based on the Sun Glint over Ocean. *IEEE Trans. Geosci. Remote Sensing* 42 (7), 1472–1481. doi:10.1109/TGRS.2004.826805

Harmel, T., and Chami, M. (2013). Estimation of the Sunglint Radiance Field from Optical Satellite Imagery over Open Ocean: Multidirectional Approach and Polarization Aspects. *J. Geophys. Res. Oceans* 118, 76–90. doi:10.1029/2012JC008221

Jackson, C. R., and Alpers, W. (2010). The Role of the Critical Angle in Brightness Reversals on Sunglint Images of the Sea Surface. *J. Geophys. Res.* 115, C09019. doi:10.1029/2009JC006037

Kay, S., Hedley, J., and Lavender, S. (2009). Sun Glint Correction of High and Low Spatial Resolution Images of Aquatic Scenes: a Review of Methods for Visible and Near-Infrared Wavelengths. *Remote Sensing* 1, 697–730. doi:10.3390/rs1040697

Khattak, S., Vaughan, R., and Cracknell, A. (1991). Sunglint and its Observation in AVHRR Data. *Remote Sensing Environ.* 37 (2), 101–116. doi:10.1016/0034-4257(91)90022-X

Khlopenkov, K. V., Su, W., Duda, D. P., Minnis, P., Bedka, K. M., and Thieman, M. (2017). "Development of Multi-Sensor Global Cloud and Radiance Composites for Earth Radiation Budget Monitoring from DSCOVR," in *Proceedings Volume 10424, Remote Sensing of Clouds and the Atmosphere XXII* (Warsaw, Poland: SPIE Remote Sensing), 104240K. doi:10.1117/12.2278645

Levy, R. C., Remer, L. A., Martins, J. V., Kaufman, Y. J., Plana-Fattori, A., Redemann, J., et al. (2005). Evaluation of the MODIS Aerosol Retrievals over Ocean and Land during CLAMS. *J. Atmos. Sci.* 62, 974–992. doi:10.1175/JAS3391.1

Marshak, A., Herman, J., Adam, S., Karin, B., Carn, S., Cede, A., et al. (2018). Earth Observations from DSCOVR EPIC Instrument. *Bull. Amer. Meteorol. Soc.* 99 (9), 1829–1850. doi:10.1175/BAMS-D-17-0223.1

Meyer, K., Yang, Y., and Platnick, S. (2016). Uncertainties in Cloud Phase and Optical Thickness Retrievals from the Earth Polychromatic Imaging Camera (EPIC). *Atmos. Meas. Tech.* 9, 1785–1797. doi:10.5194/amt-9-1785-2016

Minnis, P., Sun-Mack, S., Young, D. F., Heck, P. W., Garber, D. P., Chen, Y., et al. (2011). CERES Edition-2 Cloud Property Retrievals Using TRMM VIRS and Terra and Aqua MODIS Data-Part I: Algorithms. *IEEE Trans. Geosci. Remote Sensing* 49, 4374–4400. doi:10.1109/TGRS.2011.2144601

Ottaviani, M., Spurr, R., Stamnes, K., Li, W., Su, W., and Wiscombe, W. (2008). Improving the Description of Sunglint for Accurate Prediction of Remotely Sensed Radiances. *J. Quantitative Spectrosc. Radiative Transfer* 109, 2364–2375. doi:10.1016/j.jqsrt.2008.05.012

Richardson, M., Lebsock, M. D., McDuffie, J., and Stephens, G. L. (2020). A New Orbiting Carbon Observatory 2 Cloud Flagging Method and Rapid Retrieval of marine Boundary Layer Cloud Properties. *Atmos. Meas. Tech.* 13, 4947–4961. doi:10.5194/amt-13-4947-2020

Rothman, L. S., Gordon, I. E., Babikov, Y., Barbe, A., Chris Benner, D., Bernath, P. F., et al. (2013). The Hitran2012 Molecular Spectroscopic Database. *J. Quantitative Spectrosc. Radiative Transfer* 130, 4–50. doi:10.1016/j.jqsrt.2013.07.002

Stammes, P., Sneep, M., de Haan, J. F., Veefkind, J. P., Wang, P., and Levelt, P. F. (2008). Effective Cloud Fractions from the Ozone Monitoring Instrument: Theoretical Framework and Validation. *J. Geophys. Res.* 113, D16S38. doi:10.1029/2007JD008820

Su, W., Liang, L., Doelling, D. R., Minnis, P., Duda, D. P., Khlopenkov, K., et al. (2018). Determining the Shortwave Radiative Flux from Earth Polychromatic Imaging Camera. *J. Geophys. Res. Atmos.* 123, 11479–11491. doi:10.1029/2018JD029390

Wang, P., Stammes, P., van der A, R., Pinardi, G., and van Roozendael, M. (2008). FRESCO+: an Improved O2 A-Band Cloud Retrieval Algorithm for Tropospheric Trace Gas Retrievals. *Atmos. Chem. Phys.* 8, 6565–6576. doi:10.5194/acp-8-6565-2008

Yang, Y., Marshak, A., Chiu, J. C., Wiscombe, W. J., Palm, S. P., Davis, A. B., et al. (2008). Retrievals of Thick Cloud Optical Depth from the Geoscience Laser Altimeter System (GLAS) by Calibration of Solar Background Signal. *J. Atmos. Sci.* 65 (11), 3513–3526. doi:10.1175/2008JAS2744.1

Yang, Y., Marshak, A., Mao, J., Lyapustin, A., and Herman, J. (2013). A Method of Retrieving Cloud Top Height and Cloud Geometrical Thickness with Oxygen A and B Bands for the Deep Space Climate Observatory (DSCOVR) Mission: Radiative Transfer Simulations. *J. Quantitative Spectrosc. Radiative Transfer* 122, 141–149. doi:10.1016/j.jqsrt.2012.09.017

Yang, Y., Meyer, K., Wind, G., Zhou, Y., Marshak, A., Platnick, S., et al. (2019). Cloud Products from the Earth Polychromatic Imaging Camera (EPIC): Algorithms and Initial Evaluation. *Atmos. Meas. Tech.* 12, 2019–2031. doi:10.5194/amt-12-2019-2019

Yin, B., Min, Q., Morgan, E., Yang, Y., Marshak, A., and Davis, A. B. (2020). Cloud-top Pressure Retrieval with DSCOVR EPIC Oxygen A- and B-Band Observations. *Atmos. Meas. Tech.* 13, 5259–5275. doi:10.5194/amt-13-5259-2020

Zhai, P.-W., Hu, Y., Chowdhary, J., Trepte, C. R., Lucker, P. L., and Josset, D. B. (2010). A Vector Radiative Transfer Model for Coupled Atmosphere and Ocean Systems with a Rough Interface. *J. Quantitative Spectrosc. Radiative Transfer* 111, 1025–1040. doi:10.1016/j.jqsrt.2009.12.005

Zhai, P.-W., Hu, Y., Trepte, C. R., and Lucker, P. L. (2009). A Vector Radiative Transfer Model for Coupled Atmosphere and Ocean Systems Based on Successive Order of Scattering Method. *Opt. Express* 17, 2057–2079. doi:10.1364/oe.17.002057

Zhou, Y., Yang, Y., Gao, M., and Zhai, P.-W. (2020). Cloud Detection over Snow and Ice with Oxygen A- and B-Band Observations from the Earth Polychromatic Imaging Camera (EPIC). *Atmos. Meas. Tech.* 13, 1575–1591. doi:10.5194/amt-13-1575-2020

Zhou, Y., Yeh, P.-S., Wiscombe, W. J., and Tsay, S.-C. (2003). Cloud Context-Base Onboard Data Compression. *Proc. IGARSS* 6, 3598–3600.

Conflict of Interest: The authors declare that the research was conducted in the absence of any commercial or financial relationships that could be construed as a potential conflict of interest.

ORIGINAL RESEARCH
published: 17 August 2021
doi: 10.3389/frsen.2021.719610

Effect of Scattering Angle on Earth Reflectance

Alexander Marshak[1*], Alfonso Delgado-Bonal[2] and Yuri Knyazikhin[3]

[1] *Earth Sciences Division, NASA Goddard Space Flight Center, Greenbelt, MD, United States*
[2] *Universities Space Research Association, Columbia, MD, United States*
[3] *Earth and Environment Department, Boston University, Boston, MA, United States*

Edited by:
Pavel Lytvynov, Generalized Retrieval of Atmosphere and Surface Properties (GRASP), France

Reviewed by:
Victor Tishkovets, National Academy of Sciences of Ukraine, Ukraine
Crystal Schaaf, University of Massachusetts Boston, United States

**** Correspondence:*** *Alexander Marshak, alexander.marshak@nasa.gov*

Specialty section: *This article was submitted to Satellite Missions, a section of the journal Frontiers in Remote Sensing*

Received: *02 June 2021*
Accepted: *30 July 2021*
Published: *17 August 2021*

Citation: *Marshak A, Delgado-Bonal A and Knyazikhin Y (2021) Effect of Scattering Angle on Earth Reflectance. Front. Remote Sens. 2:719610. doi: 10.3389/frsen.2021.719610*

After March 2020 the range of scattering angle for DSCOVR EPIC and NISTAR has been substantially increased with its upper bound reaching 178°. This provides a unique opportunity to observe bi-directional effects of

reflectance near backscattering directions. The dependence of the top-of-atmosphere (TOA) reflectance on scattering angle is shown separately for ocean and land areas, for cloudy and clear pixels, while cloudy pixels are also separated into liquid and ice clouds. A strong increase of TOA reflectance towards backscattering direction is reported for all components (except cloudless areas over ocean). The observed increase of reflectance is confirmed by cloud and vegetation models. The strongest correlation between TOA reflectance and scattering angle was found near IR where contribution from vegetation dominates. Surface Bidirectional Reflectance Factor (BRF) acquired by DSCOVR EPIC and Terra MISR sensors over the Amazon basin is used to demonstrate the bi-directional effects of solar zenith and scattering angles on variation of reflected radiation from rainforest.

Keywords: radiative transfer, scattering angle, clouds, ocean, vegetation

INTRODUCTION

The Deep Space Climate Observatory (DSCOVR) was launched in February 2015 to a Sun-Earth Lagrange-1 (L_1) orbit, approximately 1.5 million kilometers from Earth towards the Sun (Marshak et al., 2018). In addition to continuous solar wind measurements for accurate space weather forecasting, it observes the full, sunlit disk of Earth from a unique vantage point with the two instruments: the Earth Polychromatic Imaging Camera (EPIC) and the NIST (National Institute of Standards and Technology) Advanced Radiometer (NISTAR). The Earth-observing geometry of the EPIC instrument is characterized by a scattering angle between 168° and 178°. The left panel in Figure 1 displays a time series of the scattering angle[1] from June 2015.

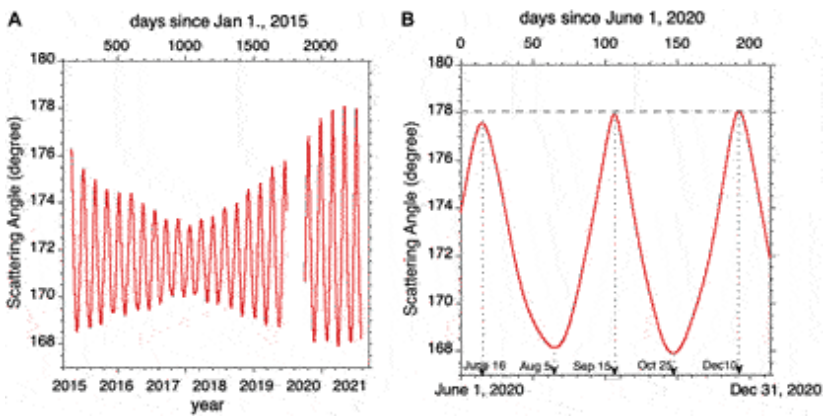

FIGURE 1 | Time series of the scattering angle between solar beam and sensor directions. **(A)** Scattering angle is plotted versus UTC since June 12, 2015, the first day DSCOVR became operational. **(B)** Zoom. Scattering angle is plotted for days between June 1 and December 31, 2020. Horizontal dash line indicates scattering angle of 178°; in December 10 scattering angle is 178.05° (SEV = 1.95°).

EPIC and NISTAR have continuously operated until June 27, 2019, when the spacecraft was placed in an extended safe hold due to degradation of the inertial navigation unit (gyros). Since then, a software patch was developed and uploaded to the spacecraft that relies only on the star tracker for spacecraft attitude determination. DSCOVR returned to full operations on March 2, 2020. Since then, DSCOVR has been able to maintain a ~0.02° pointing accuracy, similar to the pre-gyro-failure operations, that keeps Earth fully in the field-of-view of EPIC. Both EPIC and NISTAR calibrations performed since March 2020, show no change in the performance or calibration constants of the instruments.

As Figure 1 shows, after March 2020 the range of scattering angle has substantially increased towards backscattering reaching 178° (see the right panel). This provides a unique opportunity to study angular variations of the Earth reflectivity in the vicinity of the backscattering direction.

It is well-known that radiation reflected from rough surface exhibits a sharp increase in the backscattering direction (e.g., Hapke, 1963; Lumme and Bowell E, 1981; Kuusk, 1991). Therefore one should expect an enhance reflection near backscattering in the Earth observations from the DSCOVR platform.

This paper studies the effect of scattering angles near the backscattering directions on Earth reflectivity using EPIC and NISTAR data with emphases on understanding mechanisms contributing to this phenomenon. After

description of the data used in the paper (*Data Used*), we focus on the EPIC observed radiance emanating from ocean and land, clear, and cloudy skies; in addition, ice and water clouds are treated separately (*EPIC Observations*). In *Simulations* EPIC cloud and vegetation reflectances are simulated with models. A special attention is paid to Amazonian forests where EPIC results near backscattering are complemented with Multi-Angle Imaging SpectroRadiometer (MISR) observations (*Forest BRF*). Finally, *NISTAR Observations* discusses NISTAR data near backscattering and *Summary* summarizes the results.

DATA USED

EPIC provides 10 narrow band spectral images at 317, 325, 340, 388, 443, 551, 680, 688, 764, and 780 nm of the entire sunlit face of Earth using a 2048 x 2048 pixel CCD (Marshak et al., 2018). The sampling size is about 8 km at nadir (near the center of the image), which effectively increases to 10 km when EPIC's point spread function is included. The pixel size increases as the reciprocal of cosine of latitude. To reduce transmission time for EPIC data for maximizing time cadence, the images of all wavelength channels, except 443 nm, have been reduced to 1024 x 1024 pixels.

We use DSCOVR EPIC L1B data product that provides radiance data every 65–110 min (NASA/LARC/SD/ASDC-L1B, 2018c). The radiance data are in engineering units of counts per second. The EPIC team provides a calibration factor to convert measurements given in counts per second into the TOA reflectance (Geogdzhayev and Marshak, 2018; Geodzhayev et al., 2021).

We also use surface Bidirectional Reflectance Factor (BRF) derived from DSCOVR EPIC (NASA/LARC/SD/ASDC-MAIAC, 2018b) and MISR onboard low-earth-orbiting Terra satellite (NASA/LARC/SD/ASDC-MISR, 1999). BRF describes surface reflective properties in the absence of atmosphere and is defined as the ratio of the surface-reflected radiance to radiance reflected from an ideal Lambertian surface into the same beam geometry and illuminated by the same mono-directional beam (Martonchik et al., 2000; Schaepman-Strub et al., 2006). The MISR sensor views the Earth's surface with nine cameras simultaneously. MISR has a ground track repeat cycle every 16 days and achieves global coverage every 9 days. In an equatorial zone it can measure surface reflected radiation over a wide range

of the phase angle (Bi et al., 2015). Unlike DSCOVR EPIC, the Terra MISR samples reflectance over a 360 km wide swath at 10:30 am local solar time.

NISTAR measures the outgoing radiation from the Earth integrated over the entire face of Earth in four broadband channels: total radiation (Band A, 0.2–100 μm), total solar reflected (Band B, 0.2–4 μm), NIR solar reflected (Band C, 0.7–4 μm) and photodiode (0.2–1.1 μm). These measurements provide data for estimating planet's energy budget (Trenberth et al., 2009; Su et al., 2020).

EPIC OBSERVATIONS

To study the effect of scattering angle on the reflection from sunlit Earth, we first focus on the EPIC 780 nm band in the year of 2020. Figure 2 shows the total reflectance at 780 nm between September 17 and December 10 when scattering angle first drops from 178° to 168° and then increases back to 178°. We use here only 2 months of data in order to limit the effect of seasonality on total reflectance. Left panel shows global average TOA reflectance together with averages over ocean and land. Middle and right panels illustrate mean TOA reflectances accumulated over ocean and land under clear sky and cloudy conditions. The increase of both clear and cloudy reflectances with scattering angle (especially for large angles close to the backscattering direction) is clearly seen.

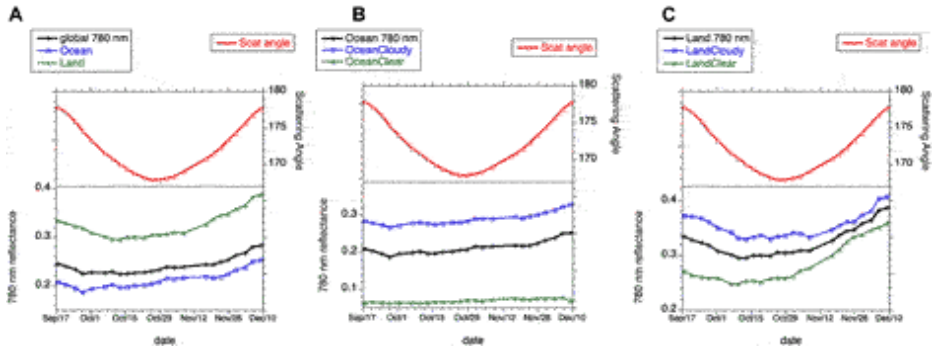

FIGURE 2 | Time series of scattering angle and top-of-atmosphere (TOA) reflectance at 780 nm between September 17 and December 10, 2020. To reduce noise, 3 days averages are used here. **(A)** Global TOA reflectance and its components accumulated over ocean and land; **(B)** TOA reflectance accumulated over cloudy and clear sky pixels over ocean. **(C)** TOA reflectance accumulated over cloudy and clear sky pixels over land.

To better illustrate the dependence of TOA reflectance on scattering angles, Figure 3 provides scatter plots of reflectances vs. scattering angles for

the whole year 2020. With exception of cloud-free regions over ocean (lower dots in the middle panel), a positive correlation between TOA reflectance and scattering angle is clearly seen. The strongest correlation is over land that includes both cloudy and clear pixels. These observations suggest that radiation reflected from clouds and land exhibits a strong sensitivity towards scattering angle near backscattering directions.

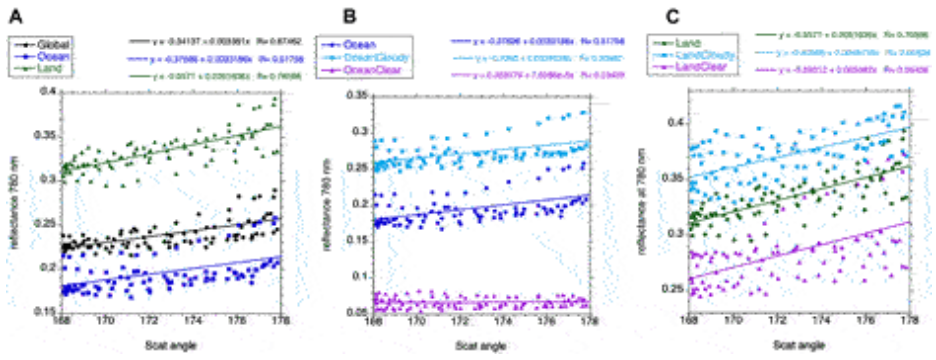

FIGURE 3 | Scatter plots of reflectance at 780 nm vs. scattering angle for the whole 2020 (from February 26 to December 20, 2020). **(A)** Global reflectance together with ocean and land reflectances; **(B)** Ocean reflectance together with ocean cloudy and ocean clear reflectances; **(C)** Land reflectance together with land cloudy and land clear reflectances.

Such correlations are also valid for all EPIC visible spectral bands. Figure 4 (see also Table 1) illustrates scatter plots of TOA reflectance vs. scattering angle for four different wavelengths, 443, 551, 680, and 780 nm, corresponding to the 168° to 178° peak-to-peak amplitude of the scattering angle between October 25 and December 14, 2020 (for clarity, see the right panel in Figure 2). As expected, the correlation over land is much stronger than that over ocean for all spectral bands. Table 1 provides the values of slopes of reflectance versus scattering angle relationships for land and ocean separately for all visible and NIR EPIC bands from October 25 to December 14. The highest value (0.0088) corresponds to the reflection from land at 780 nm.

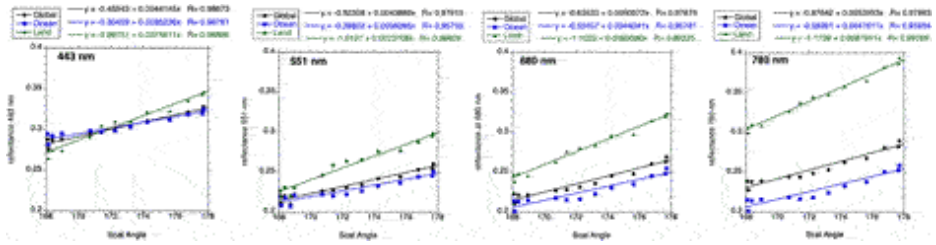

FIGURE 4 | Scatter plots of spectral reflectance vs. scattering angle for the last increase of scattering angle in 2020 (from October 25 to December 14). Global reflectance together with ocean and land reflectances. **(A)** 443 nm; **(B)** 551 nm; **(C)** 680 nm; **(D)** 780 nm.

TABLE 1 | Slope of correlation between reflectance and scattering angle from October 22 to December 14, 2020 for Earth global, ocean, and land.

	Global	Ocean	Land	
443	44	35	75	(x 10^{-4})
551	44	36	74	(x 10^{-4})
680	51	44	80	(x 10^{-4})
688	32	28	50	(x 10^{-4})
764	19	17	31	(x 10^{-4})
780	54	48	88	(x 10^{-4})

First column is wavelength in nm.

It is also of interest to study variations in TOA reflectance of ice and liquid clouds separately[2] as viewing direction approaches the backscattering direction. Figure 5 illustrates TOA reflectance for the whole year 2020. Total fraction of cloudy pixels is about 60%, of which liquid clouds account for about 47% (13% over land and 34% over ocean) and ice clouds for 13% (9.3% over land and 3.4% over ocean). Liquid clouds dominate over ocean while ice clouds over land. The trend towards the backscattering direction in reflectance from cloudy pixels is very similar to the global one shown on Figure 5.

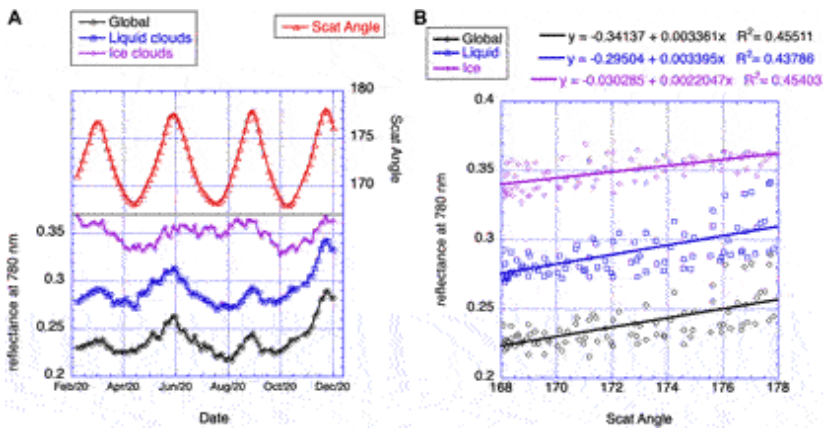

FIGURE 5 | Liquid and ice clouds. **(A)** Scattering angle and 780 nm reflectance from ice and water clouds between February 26 and December 20, 2020 (liquid–46.9%, ice–12.6%). **(B)** Scatter plot of liquid and ice reflectance vs scattering angle for 10 months of the year 2020 (from February 26 to December 20).

As we see from the right panel in Figure 5 and Table 2, the slope of the "reflectance-versus-scattering angle" dependence for ice clouds (0.0022) is lower than for liquid ones (0.0034). More than that, in the left panel of Figure 5 we can see the lack of correlation for ice clouds in summer 2020 (June-September) while there is still a good correlation in spring and fall 2020. This is related to seasonal behavior of ice clouds, at least in 2020: there are less ice clouds in September than in July; thus, in September, when scattering angle riches its maximum of 178°, a smaller number of ice clouds leads to a smaller than expected reflectance from ice clouds.

TABLE 2 | Slope of correlation between reflectance and scattering angle for 780 nm from February 26 to December 20, 2020 for Earth global, ocean, and land.

	Global	Ocean	Land	
Ice	22	18	46	(x 10^{-4})
Liquid	34	34	47	(x 10^{-4})
Clouds	30	30	45	(x 10^{-4})
Clear	13	01	51	(x 10^{-4})
Ocean	33	**	**	(x 10^{-4})
Land	52	**	**	(x 10^{-4})

The main contribution to global reflectance comes from an area around the center of sunlit Earth, which is located in an equatorial zone. Contributions from other areas decline as the square of cosine of latitude since the amount of radiant energy reflected from an area dS varies with solar (SZA) and view (VZA) zenith angles as $BRFcos(SZA)cos(VZA)dS$. Ocean and forests are dominant types of the Earth's surface in the equatorial zone (Figure 6). Ocean acts as an absorber of solar radiation at the EPIC spectral bands and its contribution to Earth reflectance is small. Therefore, clouds and cloud-free forests are reflectors that control the sensitivity of TOA reflectance to the phase angle. We will focus on analyses of radiation reflected by clouds and forests. We start with cloud and vegetation radiative transfer models to understand features of reflectance in near backscattering directions.

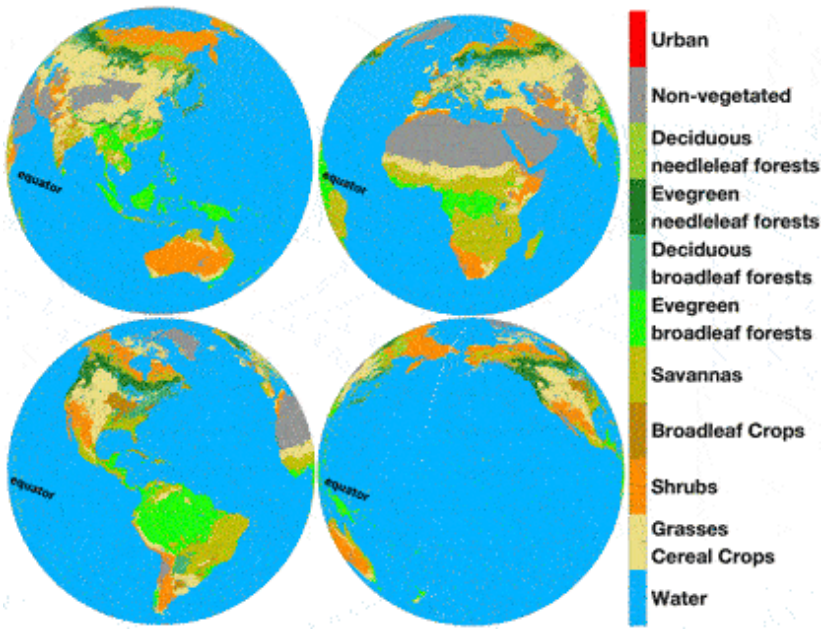

FIGURE 6 | DSCOVR EPIC 10 km land cover map (NASA/LARC/SD/ASDC-VESDR, 2018a) on orthographic projection. Ocean and rainforests are dominant types of the Earth's surface in equatorial zone. Amazonian rainforests are shown in South America as evergreen broadleaf forest.

SIMULATIONS

Cloud Model

Here we use a one-dimensional radiative transfer model (Stamnes et al., 1988) to simulate reflectance near backscattering directions. Figure 7 shows TOA reflectance as a function of scattering angle for water and ice clouds for two cloud optical depths and three SZAs. We clearly see that reflectance increases between 170 and 178 degrees of scattering angle in all cases. The increase is substantial: 5–15% for water clouds and 10–25% for ice clouds.

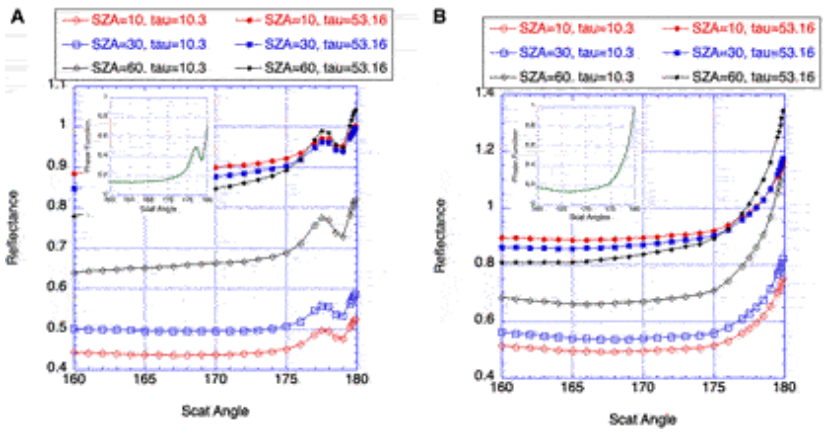

FIGURE 7 | Reflectance from water **(A)** and ice **(B)** clouds for optical depths 10.3 and 53.16; SZAs are 10°, 30°, and 60°. For water clouds Mie scattering phase function was used with r_e = 10 μm and λ = 0.87 μm; for ice clouds MODIS band-2 (λ = 0.87 μm) C5 ice phase function was used with r_e = 30 μm. Both liquid and ice phase functions are shown as inserts.

Vegetation Model

In vegetation canopies finite size of scatters (leaves, needles, etc.) can cast shadows. A satellite-borne sensor sees minimal shadows if the Sun is behind the sensor. This makes the forest looking very bright in satellite images. With a change in view direction more shaded leaves appear in the sensor field of view and the radiance of the forest reflected radiation is consequently decreased. This mechanism causes a sharp peak in retro-solar direction. This phenomenon is known as "the hotspot effect" (Ross and Marshak, 1988; Knyazikhin and Marshak, 1991; Kuusk, 1991; Gerstl, 1999). Its shape and magnitude depend on canopy structural organization.

Figure 8 shows forest BRF at the NIR spectral band simulated with the stochastic radiative transfer equation (Huang et al., 2008; Yang et al., 2018) as functions of VZA (left panel) and phase angle (right panel) for three values of the SZA. It illustrates important features in relation between BRF and sun-sensor geometry, namely, a sharp increase in BRF as scattering

direction approaches the direction to the Sun and a rise in magnitude of BRF and its rate with respect to the phase angle, $\partial(BRF)/\partial(SEV)$, as SZA increases. Thus, an increase in SZA and/or decrease in phase angle enhances the hotspot effect in the canopy BRF.

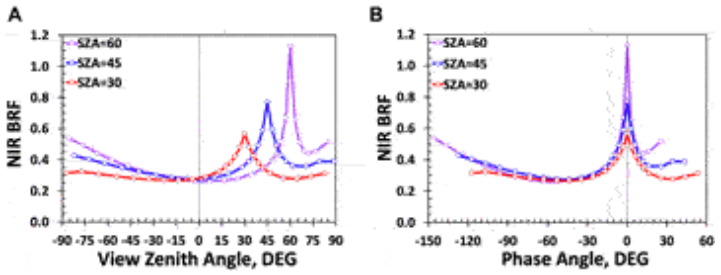

FIGURE 8 | Bidirectional Reflectance Factor (BRF) of forest at the NIR spectral band in the principal plane as a function of VZA **(A)** and phase angle **(B)**. Phase angle (or SEV) = VZA-SZA for SZA of 30°, 45°, and 60°. (Values of VZA with the sign "minus" are for azimuthal plane $\varphi = \pi$.) The BRF was simulated with the stochastic radiative transfer equation model (Huang et al., 2008; Yang et al., 2018). Leaf area index was five.

FOREST BRF

Let us check how much vegetated areas increase surface BRF as observational direction approaches sun direction. As an example, we consider the Amazon basins. The Amazonian forests represent the largest equatorial rainforest on Earth (Figure 6). The rainforests play a uniquely important role in carbon and water cycles across regional to global scales as it contains nearly 50% of the tropical forest carbon stocks and is the most productive and biodiverse of terrestrial ecosystems (Saatchi et al., 2011). It was found that the green vegetation contributes significantly to the NIR global average reflectance when the South America appears in the EPIC's field of view (Wen et al., 2019) suggesting a significant contribution from the equatorial forests. The left panel in Figure 9 demonstrates BRF of Amazonian forests derived from Terra MISR data acquired on August 28, 2016, at 10:30 local solar time. One can clearly see a sharp increase in BRF as scattering direction approaches the direction to the Sun, as theory predicts (cf. Figure 8).

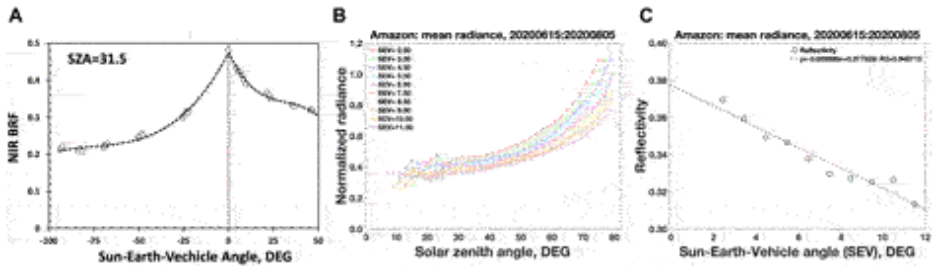

FIGURE 9 | Reflective properties of Amazonian forests. Reflectance of other equatorial forests show similar behavior (not shown here). **(A)** NIR BRF of an area of 70 by 256 km in Amazonian rainforests obtained from MISR data acquired on August 28, 2016 at 10:30 am (1502:29 UTC). The MISR sensor can see this area at phase angles up to 4°. **(B)** Two-months average normalized radiance over Amazonian forests derived from DSCOVR EPIC MAIAC BRF acquired between June 15 and August 08, 2020, as a function of SZA for 10 values of SEV. **(C)** Two-months average scattering function as a function of SEV accumulated over the same area and time interval as in the middle panel.

Terra MISR surface product provides BRFs over a 360 km wide swath at 10:30 local solar time and achieves global coverage every 9 days. This obviously is not sufficient for temporal analyses of Earth reflectivity. Therefore, we use DSCOVR EPIC BRF (NASA/LARC/SD/ASDC-MAIAC, 2018d) which provides global coverage at about hourly frequency (Lyapustin et al., 2018). We use two variables to characterize angular variation of forest reflectance. The first one is the temporal average normalized radiance estimated as

$$J(SZA, SEV) = \frac{\sum BRF\left(SZA, VZA_{xy}\right)\cos\left(VZA_{xy}\right)}{\sum \cos\left(VZA_{xy}\right)} \qquad (1)$$

The integration is performed over pixels (x,y) in the Amazonian forests with given values of SZA and SEV accumulated over a given time interval. The middle panel in Figure 9 shows normalized radiance for the period of June 15 to August 8, 2020. As theory predicts, the normalized radiance and its rate of variation with respect to phase angle, $\partial J/\partial(SEV)$, increases with SZA. For a given sun position in the sky, its value increases as phase angle (or SEV) approaches to zero. All data shown in Figure 9 are expresses in term of SZA and SEV.

The surface scattering function, P, is the fraction of the total radiant energy incident on the surface that is scattered towards the sensor. It depends on scattering angle and exhibits strong diurnal variations. The right panel in

Figure 9 shows two-month average scattering function of Amazonian forests estimated as

$$P(SEV) = \frac{\sum BRF(SZA_{xy}, VZA_{xy})\cos(SZA_{xy})\cos(VZA_{xy})}{\sum \cos(SZA_{xy})} \quad (2)$$

Here the integration is performed over pixels (x,y) in the Amazonian forests with a given phase angle. As expected from theory, it is a decreasing function with respect to phase angle (or SEV). Thus, anisotropy of forest reflected radiation can explain increase in Earth scattering at least when equatorial forests appear in the EPIC image.

NISTAR OBSERVATIONS

NISTAR measures the outgoing radiation from the Earth integrated over the entire face of Earth in four broadband channels: total radiation (Band A, 0.2–100 μm), total solar reflected (Band B, 0.2–4 μm), NIR solar reflected (Band C, 0.7–4 μm) and photodiode (0.2–1.1 μm). In addition to EPIC observations, it is of interest to see how scattering angles affect NISTAR measurements.

Figure 10 shows NISTAR band A and B radiance and scattering angle for 2020. A strong positive correlation (R~0.98) between the scattering angle and NISTAR data is clearly seen. This is especially pronounced for the time interval between November 15 and December 20, 2020 with maximum around December 10 when scattering angle reaches its maximum of 178.1°. The left panel that illustrates radiances plotted vs. scattering angles confirms it with high correlation which is slightly higher for the B-band radiance. It is also true for C-band radiance (not shown here) though with a bit lower correlation coefficient (0.90 for band C vs. 0.98 for band B). This is understandable since the increase of radiation near backscattering is higher in visible than in NIR (Platnick et al., 2017).

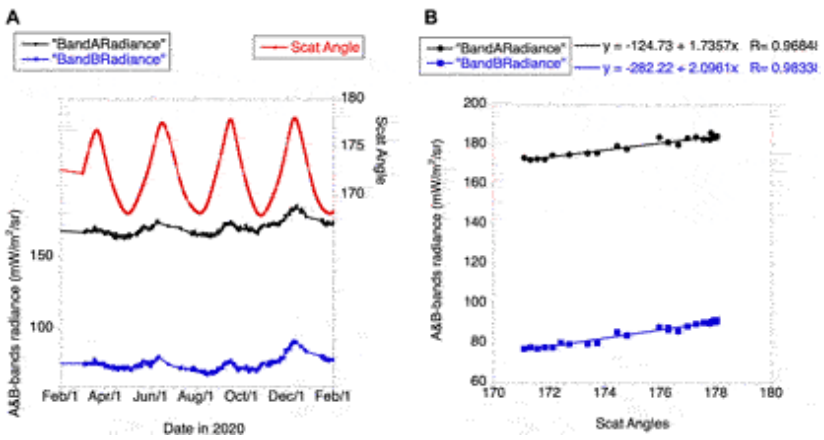

FIGURE 10 | NISTAR band A and B radiance and scattering angle. **(A)** Band A and B radiance and scattering angle for the time period February 26, 2020 to February 1, 2021. **(B)** Band A and B radiance vs. scattering angle for the time period November 15–December 20, 2020.

SUMMARY

DSCOVR EPIC and NISTAR observations from the Lagrange L_1 point (about 1.5 mln km from Earth) provide a unique opportunity to study the effect of scattering angle on TOA reflectance near backscattering. This effect was studied for ocean and land areas, for cloudy and clear pixels, for liquid and ice clouds separately. All EPIC observations, except over ocean under clear sky conditions, show a strong increase of reflectance towards backscattering direction. The increase is well confirmed with cloud and vegetation models. The strongest increase is observed over land at the NIR band (780 nm). The Amazonian basin is taken as an example of a possible mechanism causing variation of BRF with solar zenith and scattering angles. NISTAR observations also demonstrate an increase with scattering angle for all bands but the strongest one is for B-band radiance (0.2–4 μm).

To summarize, measurements of Earth reflectance near the backscattering direction show a strong sensitivity towards scattering angle, especially for scattering angles above 175°. Any angular distribution model with a bin size bigger than 1°–3° near backscattering may lead to substantial errors.

DATA AVAILABILITY STATEMENT

Publicly available datasets were analyzed in this study. This data can be found in the article/supplementary material, further inquiries can be directed to the corresponding author.

AUTHOR CONTRIBUTIONS

All authors contributed to the article. AD-B and YK conducted an analysis of EPIC and NISTAR data. YK focused on vegetation while AM on clouds. AM wrote the very first version of the paper; it was later modified by all co-authors.

FUNDING

This work was supported by NASA DSCOVR program. YK is supported by the NASA DSCOVR project under grant 80NSSC19K0762 and Jet Propulsion Laboratory under contract 1625837.

PUBLISHER'S NOTE

All claims expressed in this article are solely those of the authors and do not necessarily represent those of their affiliated organizations, or those of the publisher, the editors and the reviewers. Any product that may be evaluated in this article, or claim that may be made by its manufacturer, is not guaranteed or endorsed by the publisher.

ACKNOWLEDGMENTS

We are grateful to the DSCOVR science team for providing data and to the NASA Center for Climate Simulations providing resources for the EPIC data processing.

FOOTNOTES

[1]We will be using "scattering angle" here which goes from 0° (forward scattering) to 180° (backward scattering). We will be also using Sun Earth Vehicle (SEV) angle (a.k.a. Phase angle) = 180°–scattering angle.

[2]A threshold of 4,500 m was used to separate ice and liquid clouds.

REFERENCES

Bi, J., Knyazikhin, Y., Choi, S., Park, T., Barichivich, J., Ciais, P., et al. (2015). Sunlight Mediated Seasonality in Canopy Structure and Photosynthetic Activity of Amazonian Rainforests. *Environ. Res. Lett.* 10, 064014. doi:10.1088/1748-9326/10/6/064014

Geogdzhayev, I. V., Marshak, A., and Alexandrov, M. (2021). Calibration of the DSCOVR EPIC Visible and NIR Channels Using Multiple LEO Radiometers. *Front. Remote Sens* 2. doi:10.3389/frsen.2021.671933

Geogdzhayev, I. V., and Marshak, A. (2018). Calibration of the DSCOVR EPIC Visible and NIR Channels Using MODIS Terra and Aqua Data and EPIC Lunar Observations. *Atmos. Meas. Tech.* 11, 359–368. doi:10.5194/amt-11-359-2018

Gerstl, S. A. W. (1999). Building a Global Hotspot Ecology with Triana Data. *Remote Sens. Earth Science, Ocean, Sea Ice Appl.* 3868, 184–194. doi:10.1117/12.373094

Hapke, B. W. (1963). A Theoretical Photometric Function for the Lunar Surface. *J. Geophys. Res.* 68, 4571–4586. doi:10.1029/JZ068i015p04571

Huang, D., Knyazikhin, Y., Wang, W., Deering, D., Stenberg, P., Shabanov, N., et al. (2008). Stochastic Transport Theory for Investigating the Three-Dimensional Canopy Structure from Space Measurements. *Remote Sensing Environ.* 112, 35–50. doi:10.1016/j.rse.2006.05.026

Knyazikhin, Y., and Marshak, A. (1991). "Fundamental Equations of Radiative Transfer in Leaf Canopies, and Iterative Methods for Their Solution," in *Photon-vegetation Interactions: Applications in Plant Physiology and Optical Remote Sensing* ed . Editors R. B. Myneni, and J. Ross (Berlin Heidelberg: Springer-Verlag), 9–43. doi:10.1007/978-3-642-75389-3_2

Kuusk, A. (1991). "The Hot Spot Effect in Plant Canopy Reflectance," in *Photon-vegetation Interactions: Applications in Plant Physiology and Optical Remote Sensing* ed . Editors R. B. Myneni, and J. Ross (Berlin Heidelberg: Springer-Verlag), 139–159. doi:10.1007/978-3-642-75389-3_5

Lumme, K., and Bowell, E. (1981). Radiative Transfer in the Surfaces of Atmosphereless Bodies. I - Theory. II - Interpretation of Phase Curves. *I. Theor. Astron J.* 86, 1694–1704. doi:10.1086/113054

Lyapustin, A., Wang, Y., Korkin, S., and Huang, D. (2018). MODIS Collection 6 MAIAC Algorithm. *Atmos. Meas. Tech.* 11, 5741–5765. doi:10.5194/amt-11-5741-2018

Marshak, A., Herman, J., Adam, S., Karin, B., Carn, S., Cede, A., et al. (2018). Earth Observations from DSCOVR EPIC Instrument. *Bull. Amer. Meteorol. Soc. (Bams)* 99, 1829–1850. doi:10.1175/BAMS-D-17-0223.1

NASA/LARC/SD/ASDC (1999). *MISR Level 2 Surface parameters V003*. NASA Langley Atmospheric Science Data Center DAAC. Available at: https://doi.org/10.5067/TERRA/MISR/MIL2ASLS_L2.003-23.

NASA/LARC/SD/ASDC (2018a). *DSCOVR EPIC Level 2 Vegetation Earth System Data Record (VESDR), Version 1*. NASA Langley Atmospheric Science Data Center DAAC. Available at: https://doi.org/10.5067/EPIC/DSCOVR/L2_VESDR.001.

NASA/LARC/SD/ASDC(2018b). *DSCOVR EPIC L2 Multi-Angle Implementation of Atmospheric Correction (MAIAC) Version 02*. NASA Langley Atmospheric Science Data Center DAAC. Available at: https://doi.org/10.5067/EPIC/DSCOVR/L2_MAIAC.002.

NASA/LARC/SD/ASDC (2018c). *DSCOVR EPIC Level 1B Version 3*. NASA Langley Atmospheric Science Data Center DAAC. Available at: https://doi.org/10.5067/EPIC/DSCOVR/L1B.003.

NASA/LARC/SD/ASDC (2018d). *Multi-Angle Implementation of Atmospheric Correction (MAIAC) Atmospheric Correction data product*. NASA Langley Atmospheric Science Data Center DAAC. Available at: https://doi.org/10.5067/EPIC/DSCOVR/L2_MAIAC.001.

Martonchik, J. V., Bruegge, C. J., and Strahler, A. H. (2000). A Review of Reflectance Nomenclature Used in Remote Sensing. *Remote Sensing Rev.* 19, 9–20. doi:10.1080/02757250009532407

Platnick, S., Meyer, K. G., King, M. D., Wind, G., Amarasinghe, N., Marchant, B., et al. (2017). The MODIS Cloud Optical and Microphysical Products: Collection 6 Updates and Examples from Terra and Aqua. *IEEE Trans. Geosc. Rem. Sens.* 55, 1. doi:10.1109/tgrs.2016.2610522

Ross, J. K., and Marshak, A. L. (1988). Calculation of Canopy Bidirectional Reflectance Using the Monte Carlo Method. *Remote Sensing Environ.* 24, 213–225. doi:10.1016/0034-4257(88)90026-0

Saatchi, S. S., Harris, N. L., Brown, S., Lefsky, M., Mitchard, E. T. A., Salas, W., et al. (2011). Benchmark Map of forest Carbon Stocks in Tropical Regions across Three Continents. *Proc. Natl. Acad. Sci.* 108, 9899–9904. doi:10.1073/pnas.1019576108

Schaepman-Strub, G., Schaepman, M. E., Painter, T. H., Dangel, S., and Martonchik, J. V. (2006). Reflectance Quantities in Optical Remote Sensing-Definitions and Case Studies. *Remote Sensing Environ.* 103 (1), 27–42. doi:10.1016/j.rse.2006.03.002

Stamnes, K., Tsay, S.-C., Wiscombe, W., and Jayaweera, K. (1988). Numerically Stable Algorithm for Discrete-Ordinate-Method Radiative Transfer in Multiple Scattering and Emitting Layered media. *Appl. Opt.* 27, 2502–2509. doi:10.1364/ao.27.002502

Su, W., Minnis, P., Liang, L., Duda, D. P., Khlopenkov, K., Thieman, M. M., et al. (2020). Determining the Daytime Earth Radiative Flux from National Institute of Standards and Technology Advanced Radiometer (NISTAR) Measurements. *Atmos. Meas. Tech.* 13, 429–443. doi:10.5194/amt-13-429-2020

Trenberth, K. E., Fasullo, J. T., and Kiehl, J. (2009). Earth's Global Energy Budget. *Bull. Amer. Meteorol. Soc.* 90, 311–324. doi:10.1175/2008BAMS2634.1

Wen, G., Marshak, A., Song, W., Knyazikhin, Y., Mõttus, M., and Wu, D. (2019). A Relationship between Blue and Near-IR Global Spectral Reflectance and the Response of Global Average Reflectance to Change in Cloud Cover Observed from EPIC. *Earth Space Sci.* 6, 1416–1429. doi:10.1029/2019ea000664

Yang, B., Knyazikhin, Y., Xie, D., Zhao, H., Zhang, J., and Wu, Y. (2018). Influence of Leaf Specular Reflection on Canopy Radiative Regime Using an Improved Version of the Stochastic Radiative Transfer Model. *Remote Sensing* 10, 1632. doi:10.3390/rs10101632

Conflict of Interest: The authors declare that the research was conducted in the absence of any commercial or financial relationships that could be construed as a potential conflict of interest.

ORIGINAL RESEARCH
published: 25 August 2021
doi: 10.3389/frsen.2021.724074

Earth Imaging From the Surface of the Moon With a DSCOVR/EPIC-Type Camera

Nick Gorkavyi[1*], Simon Carn[2], Matt DeLand[1], Yuri Knyazikhin[3], Nick Krotkov[4], Alexander Marshak[4], Ranga Myneni[3] and Alexander Vasilkov[1]

[1] *Science Systems and Applications, Lanham, MD, United States*
[2] *Department of Geological and Mining Engineering and Sciences, Michigan Technological University, Houghton, MI, United States*
[3] *Earth and Environment Department, Boston University, Boston, MA, United States*
[4] *NASA Goddard Space Flight Center, Greenbelt, MD, United States*

Edited by:
Hartmut Boesch, University of Leicester, United Kingdom

Reviewed by:
Hartwig Deneke, Leibniz Institute for Tropospheric Research (LG), Germany
Zhenzhu Wang, Aiofm (CAS), China

**** Correspondence:** Nick Gorkavyi, nick.gorkavyi@ssaihq.com*

***Specialty section:** This article was submitted to Satellite Missions, a section of the journal Frontiers in Remote Sensing*

***Received:** 11 June 2021*
***Accepted:** 12 August 2021*
***Published:** 25 August 2021*

***Citation:** Gorkavyi N, Carn S, DeLand M, Knyazikhin Y, Krotkov N, Marshak A, Myneni R and Vasilkov A (2021) Earth Imaging From the Surface of the Moon With a DSCOVR/EPIC-Type Camera. Front. Remote Sens. 2:724074. doi: 10.3389/frsen.2021.724074*

The Earth Polychromatic Imaging Camera (EPIC) on the Deep Space Climate Observatory (DSCOVR) satellite observes the entire Sun-illuminated Earth from sunrise to sunset from the L1 Sun-Earth Lagrange point. The L1 location, however, confines the observed phase angles to ~2°–12°, a nearly backscattering direction, precluding any information on the bidirectional surface reflectance factor (BRF) or cloud/aerosol phase function. Deploying an analog of EPIC on the Moon's surface would offer a unique opportunity to image the full range of Earth phases, including observing ocean/cloud glint reflection for different phase angles; monitoring of transient volcanic clouds; detection of circum-polar mesospheric and stratospheric clouds; estimating the surface BRF and full phase-angle integrated albedo; and monitoring of vegetation characteristics for different phase angles.

Keywords: DISCOVR EPIC, Moon, phase function, clouds, vegetation

INTRODUCTION

Numerous Low Earth Orbit (LEO) and Geosynchronous Equatorial Orbit (GEO) Earth-observing satellites provide a broad spectral range of viable data; however, it is obtained at the expense of limited geographical (GEO) or temporal (LEO) coverage. Satellites from near-polar Sun-synchronous LEOs have limited observation capabilities at polar latitudes greater than 80° North and South. These polar regions are not observable from geostationary satellites located above the equator. Although current Earth-observing satellites can produce high-resolution views, LEO sensors can only scan a small portion of the surface at a given time, while GEO sensors can provide temporally continuous, though lower-resolution observations of a significant, though incomplete and fixed portion of the Earth's disk. The Earth Polychromatic Imaging Camera (EPIC) on the Deep Space Climate Observatory (DSCOVR) clearly stands apart, observing the entire Sun-illuminated Earth from the L1 Sun-Earth Lagrange point (Marshak et al., 2018). EPIC has an aperture diameter of 30.5 cm, a focal ratio of 9.38, a field of view of 0.61°, and a spatial resolution of ~10 km/pixel. The camera produces 2048 × 2048 pixel images in 10 narrowband channels (317.5, 325, 340, 388, 443, 551, 680, 688, 764, and 779.5 nm). The L1 location, however, restricts phase angles to ~2°–12° (a nearly backscattering direction), depriving the observer of any information on bidirectional surface reflectance factors (BRFs) or on cloud/aerosol phase functions. A compact,

lightweight, autonomous EPIC-type camera on the Moon's surface offers a unique opportunity to overcome these limitations and advance Earth science in novel and potentially unanticipated ways (Marshak et al., 2020). An EPIC-Moon camera would work in synergy with the DSCOVR/EPIC instrument, increasing the efficiency of both sensors. Earth science goals of EPIC-Moon are to extend and improve the current DSCOVR/EPIC Earth imaging by extending spectral coverage, increasing spatial resolution and image cadence, and expanding coverage of circumpolar regions. Assuming the EPIC-Moon camera produces 2048 × 2048 pixel images, the spatial resolution would be ~7 km/pixel for full Earth disk images or ~2 km/pixel for a DSCOVR/EPIC-like field of view of ~0.6°. DSCOVR/EPIC obtains images of the entire sunlit Earth disk every ~60–100 min. Increasing the EPIC-Moon frame rate to obtain images every ~10–15 min will allow much better tracking, for example, of drifting volcanic ash and SO_2 clouds, which can move at speeds of ~100 km/h or more (see *Volcanic SO2 and Ash Clouds*).

The acquired data will enable retrievals of aerosol scattering phase functions and Earth surface properties. The recent Earth Science Decadal Survey prioritized aerosols, clouds, convection, precipitation, terrestrial vegetation and surface albedo studies in connection with climate change (National Academies of Sciences, 2018). As stated in IPCC AR5 Chapter 7: "Clouds and aerosols continue to contribute the largest uncertainty to estimates and interpretations of the Earth's changing energy budget" (IPCC, 2014). In this paper we analyze the features and potential benefits of an EPIC-like camera located on the Moon (or in lunar orbit).

Note that in the coming years, lunar bases are planned for deployment on the Moon and in lunar orbit, which will be equipped with small telescopes for astronomical observations, for observing the Moon and for laser communication with the Earth. The concept presented here will be useful for assessing the principal possibilities of observing the Earth using telescopes located on the Moon. We do not consider sensors on the Moon as an alternative to sensors located in LEO, GEO, and L1 orbit, but observations from the Moon have a few useful and novel features that are important to discuss and consider in future projects.

PHASE ANGLES OF OBSERVATION FROM L1 AND FROM THE MOON

Here, we compare the phase angles of observation of DSCOVR/EPIC with a sensor placed on the lunar surface. Figure 1A shows the Sun-Earth-Vehicle (SEV) angle, which is close to the phase observation angle, for the first 3 months (or 90 days) of 2021.

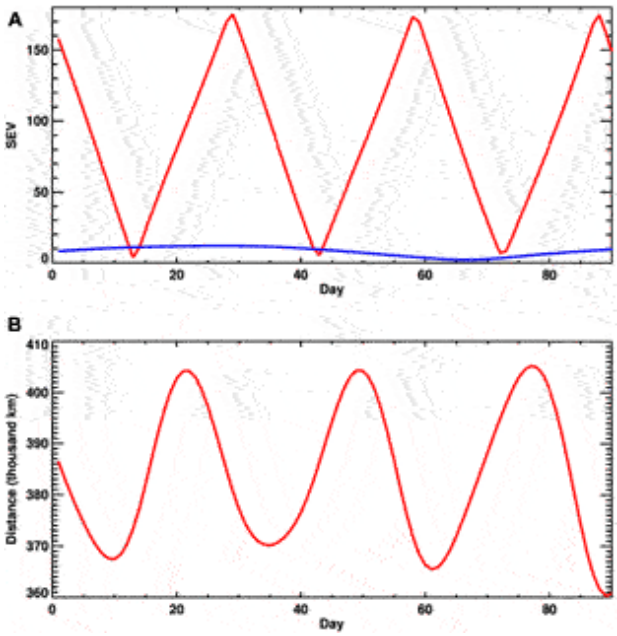

FIGURE 1 | (A) Sun-Earth-Vehicle (SEV) angle for any sunlit Earth object observed from the Moon during the first 3 months of 2021 (red line, data from Espenak, 2021), compared to DSCOVR/EPIC's SEV (blue line, see https://epic.gsfc.nasa.gov/); **(B)** Distance between the Moon and Earth during the same period (Espenak, 2021).

The SEV angle for DSCOVR/EPIC varies from 11.91° (01/27/2021) to 2.09° (03/07/2021); this allows us to estimate the approximate period of SEV change as ~80 days. During this time, DSCOVR/EPIC's distance from Earth varied from 1.54 million km (01/01/2021) to 1.39 million km (02/03/2021). Figure 1A shows the SEV angle for the Sun-Earth-Moon (or lunar sensor), which varies from about 0° to 180° during the lunar month. Figure 1B shows the distance between the Moon's and the Earth's centers, which changes in 90 days from 360×10^3 to 405×10^3 km. Therefore, on average, the camera on the Moon is 4 times closer to the Earth than a sensor at the L1 point. The location of Earth and Moon for phase angles of about 0°, 90°, and 180° is shown in Figure 2, along with an assumed view of the Earth from the surface of the Moon. The view of the Earth will be approximately the same from any point in the visible hemisphere of the Moon (from where the Earth is

visible). The location of the sensor on the lunar surface is an essential observation factor in terms of solar illumination. A sensor located in the equatorial or mid-latitudes of the Moon will be illuminated by the Sun for only half of the lunar month, remaining in shadow for the second half of the month. This imposes certain constraints on the energy sources for the sensor, as well as on its temperature parameters and calibration.

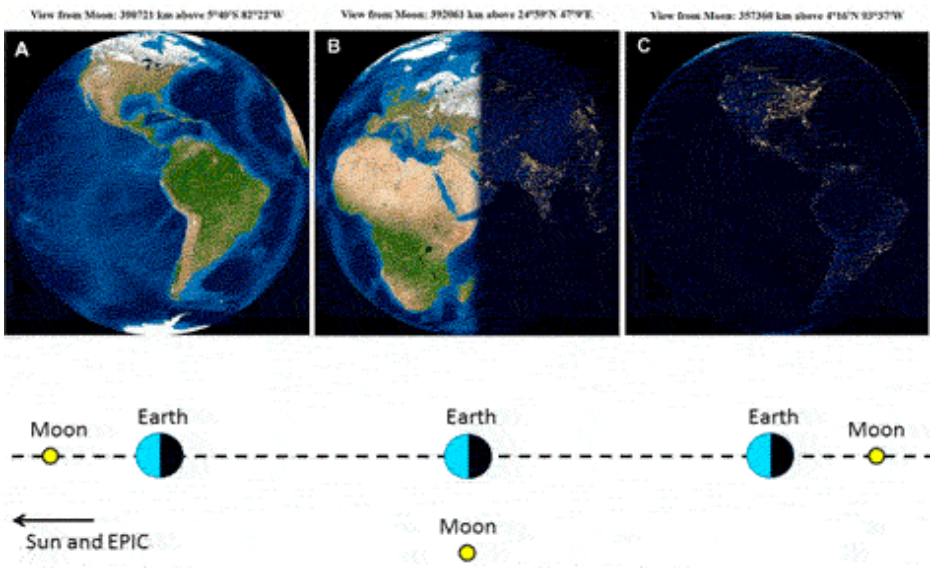

FIGURE 2 | View of the Earth from the Moon at three points of the lunar orbit with phase angles of **(A)** 0°, **(B)** 90°, and **(C)** 180°. The image of the Earth shown here and in Figure 3 was obtained by J. Walker based on MODIS/TERRA and Suomi/NPP images (Walker, 2021).

Scientific equipment could be located at high latitudes on the Moon, for example, in the region of the South Pole, which is an attractive location for a lunar base. There are areas on the rim of Shackleton crater where the Sun illuminates the lunar surface more than 90% of the time. The view of the Earth from the South Pole of the Moon is shown in Figure 3A. Note that the Earth is inverted with the North Pole towards the Moon's horizon. The elevation of the Sun above the Moon's horizon will change. For ~10% of the time, the Sun will be located below the horizon (possible positions of the Sun are shown by dashed circles). Interestingly, lunar eclipses that occur on Earth between 2 and 5 times a year are solar eclipses from the point of view of an observer on the Moon. Unlike an ordinary short-term solar eclipse on Earth, a solar eclipse on the Moon can last up to 108 min. This provides a unique opportunity to make observations without the influence of the atmosphere,

for example, to observe phenomena such as the solar corona and its dynamics for an hour and a half, the red ring glow of the Earth's atmosphere, as well as relativistic displacements of the position of stars near the Sun. Figure 3B shows the assumed view of a solar eclipse from the South Pole of the Moon.

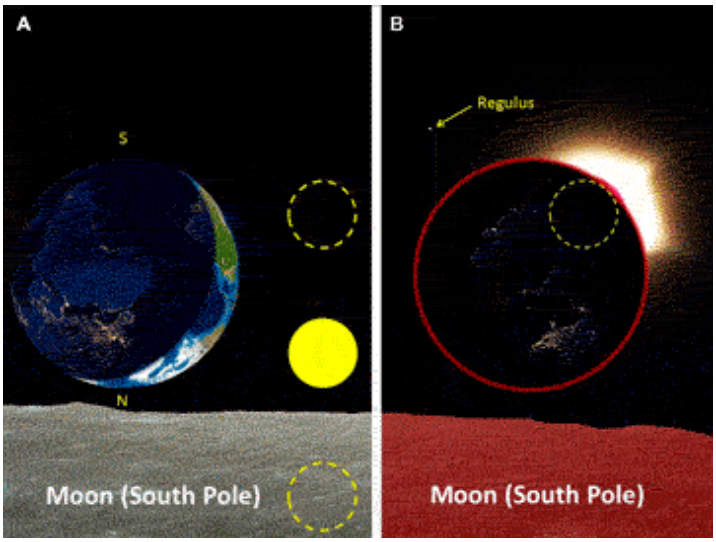

FIGURE 3 | The expected view of the Earth and the Sun from the Moon's South Pole. The picture uses a photo of the lunar surface obtained during the Apollo expedition. Images of the Earth were taken from the Earth and Moon viewer (Walker, 2021). **(A)** The position of the Sun above (or below) the horizon can vary (shown by dashed circles). If the Sun sets behind the disk of the Earth, then a solar eclipse occurs on the Moon–see **(B)**. During a solar eclipse the Earth's atmosphere will glow with red light, and the Sun's corona will glow with white light. Stars will be visible near the Sun's corona. Image **(B)** uses a photograph of the solar corona during an actual solar eclipse on August 21, 2017, where the star Regulus (constellation Leo) is visible (photo by N. Gorkavyi).

The proximity to the Earth and wide variations in phase angle accessible by a Moon-based camera offer significant advantages for Earth observation, which we will discuss in the following sections.

SOLAR GLINTS

At least 10% of DSCOVR/EPIC images of Earth contain intensely bright flashes of light over land, not seen by other satellites. The physical origin of these flashes is specular reflection from horizontally floating ice crystals in clouds. The cloud ice crystal glints are also observed over oceans together with glints from the ocean surface. Figure 4 provides three examples of such flashes.

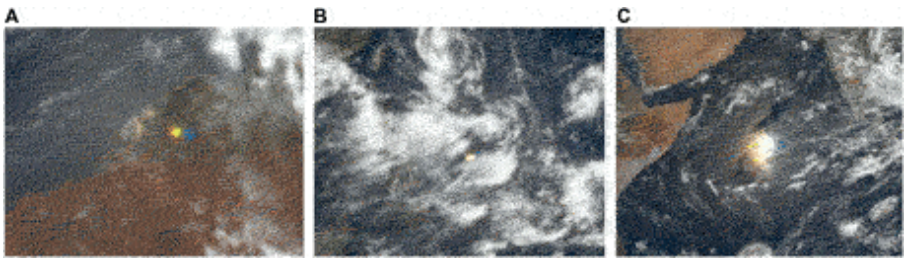

FIGURE 4 | Three examples of glints captured by DSCOVR/EPIC in 2018. The Sun-Earth-Vehicle (SEV) angle is around 9°. Note that the filter wheel used to select EPIC wavelengths causes a time lag between the component images in these red-green-blue (RGB) composites: ~3 min between blue (443 nm) and green (551 nm); ~4 min between blue and red (680 nm). **(A)** Terrestrial glint over Australia from cloud ice crystals on February 13, 2018 (see https://epic.gsfc.nasa.gov/?date=2018-02-13); **(B)** Terrestrial glint over the Pacific Ocean from marine cloud ice crystals on June 15, 2018 (see https://epic.gsfc.nasa.gov/?date=2018-06-15); **(C)** Ocean surface glint on September 17, 2018 (see https://epic.gsfc.nasa.gov/?date=2018-09-17).

In order to test the hypothesis that the detected bright flashes over land (see A panel) are caused by specular reflection from horizontally oriented crystals in ice clouds, the measured latitudes of the detected bright colorful flashes were compared with the theoretical ones that permit specular reflection for a given time of year and color (Marshak et al., 2017). The almost complete coincidence of the measured latitudes for all three colors with the theoretical curve constituted compelling evidence for the specular reflection hypothesis. As a result, it was shown that tiny hexagonal platelets of ice, floating in the air in nearly perfect horizontal alignment, are likely responsible for the glints observed by EPIC over land. Varnai et al. (2020) also demonstrated EPIC's ability to distinguish ocean surface glints (C panel) from marine ice cloud glints (B panel). Indeed, EPIC's observations in oxygen absorption bands (A-band over ocean) help to uniquely distinguish between ocean surface and high ice clouds. In addition to solar glints from ocean surface and cloud ice, bright reflections of sunlight were also observed from high mountains in the Andes that are likely caused by calm small lakes (Kostinski et al., 2021).

However, the Sun-Earth-satellite geometry of DSCOVR observations is not a particularly favorable one for glint detection. Specular reflection tends to be much stronger for oblique illumination and at grazing angles (Williams and Gaidos, 2008; Robinson et al., 2010). Thus, one expects that in observations at "crescent or half-moon" phases from the Moon, glints will contribute more to the overall planetary radiances-especially when

accounting for the decrease in the diffuse radiance when only a portion of the planet's sunlit side is visible. As a function of phase angle, Earth imaging from the Moon will provide ocean/cloud glint reflection for different phase angles than available from GEO, LEO, and L1.

Motivated by EPIC observations of solar glints off the terrestrial atmosphere, it is also important to explore the impact of starlight glints on the detection and characterization of exoplanets. This idea goes back to 1993 when Carl Sagan and colleagues (see p. 715 in Sagan et al., 1993) used the Galileo spacecraft's fly-by observation of Earth as an exoplanet control experiment. Based solely on observations of specular reflection, they deduced that Earth was covered in part by liquid oceans. Their conclusions were based entirely on several Galileo images collected on Dec. 12, 1990 while Galileo was on its way to Jupiter, crossing a line between Sun and Earth. In Sagan et al. (1993) they wrote "*The Galileo mission constitutes an apparently unique control experiment on the ability of fly-by spacecraft to detect life* …." In addition, on p. 718 it was noted that "… *close examination of the images shows a region of specular reflection in ocean but not on land*." Note that the fraction of oriented ice crystals might be negligible (Breon and Dubrulle, 2004); hence the effect of glints on cloud brightness is small. The sun-glint in EPOXI [two missions: *Deep Impact Extended Investigation* (DIXI) and *Extrasolar Planet Observation and Characterization* (EPOCh)] was relatively minor (though the image was intrinsically blurry; Livengood et al., 2011). However, if some preliminary estimates of the frequency and brightness of solar glints from EPIC are confirmed, specular reflection observations from the Moon's surface could have a longer-term consequence for exoplanet science.

VOLCANIC SO_2 AND ASH CLOUDS

Volcanic eruptions periodically emit large quantities of sulfur dioxide (SO_2) and aerosol into the free troposphere and stratosphere, with potential impacts on climate, the environment and aviation. After emission, volcanic SO_2 converts to liquid sulfate aerosol particles (on timescales of days to months), which can impact climate through the direct aerosol effect on solar radiation. Young volcanic eruption clouds (within a few hours of emission) also contain volcanic ash particles which can be a significant hazard to aviation. Timely monitoring of volcanic SO_2 and ash emissions is therefore critical for aviation safety and for assessing the impacts of volcanic eruptions on

climate. Volcanic SO_2 and ash emissions have been measured using UV satellite instruments on LEO platforms for several decades (Carn et al., 2016), but these observations have low (~daily) temporal resolution. GEO instruments can measure SO_2 and volcanic ash in the IR with high cadence, providing critical data for operational detection of volcanic eruptions (e.g., Pavolonis et al., 2018), but are unable to detect volcanic clouds at latitudes above ~70–80° and retrievals become noisy (with lower sensitivity) towards the edge of the GEO field-of-view. LEO satellites provide coverage of the polar regions, but with relatively low cadence and without a synoptic, hemispheric imaging capability.

DSCOVR/EPIC is able to detect volcanic SO_2 and ash emissions (Carn et al., 2018) and has now demonstrated the value of observations from L1 for observing high-latitude volcanic eruptions. A major eruption of Raikoke volcano (Kuril Islands, Russia) in June 2019 emitted SO_2 and ash clouds that initially drifted north to high latitudes and were measured with hourly cadence by EPIC (Figure 5). EPIC was able to map the extensive Raikoke volcanic SO_2 clouds in single images with no temporal gaps, in contrast to LEO instruments, elucidating the dynamics of SO_2 transport. Such high-latitude eruptions occur quite frequently in active volcanic regions such as Kamchatka, the Kuril Islands, Alaska and the Aleutian Islands, and Iceland. In addition to Raikoke, notable high-latitude volcanic eruptions include Kasatochi (Aleutian Islands, United States) in 2008, Sarychev Peak (Kuril Islands, Russia) in 2009, Holuhraun (Iceland) in 2014–15 and Alaid (Kuril Islands, Russia) in 1981. Each of these eruptions produced extensive SO_2 clouds that drifted over the Arctic region. The Southern Hemisphere has fewer active volcanoes at high latitudes, but nevertheless, significant eruptions such as Cerro Hudson (Chile) in 1991 and Cordon Caulle (Chile) in 2011 produced volcanic clouds that drifted south around Antarctica. Hence there is a need for improved observations of volcanic clouds at high latitudes, given the importance of the polar regions in the context of climate change. An EPIC-like instrument on the Moon would provide synoptic imaging of the polar regions with higher spatial resolution and higher cadence than provided by DSCOVR/EPIC at L1.

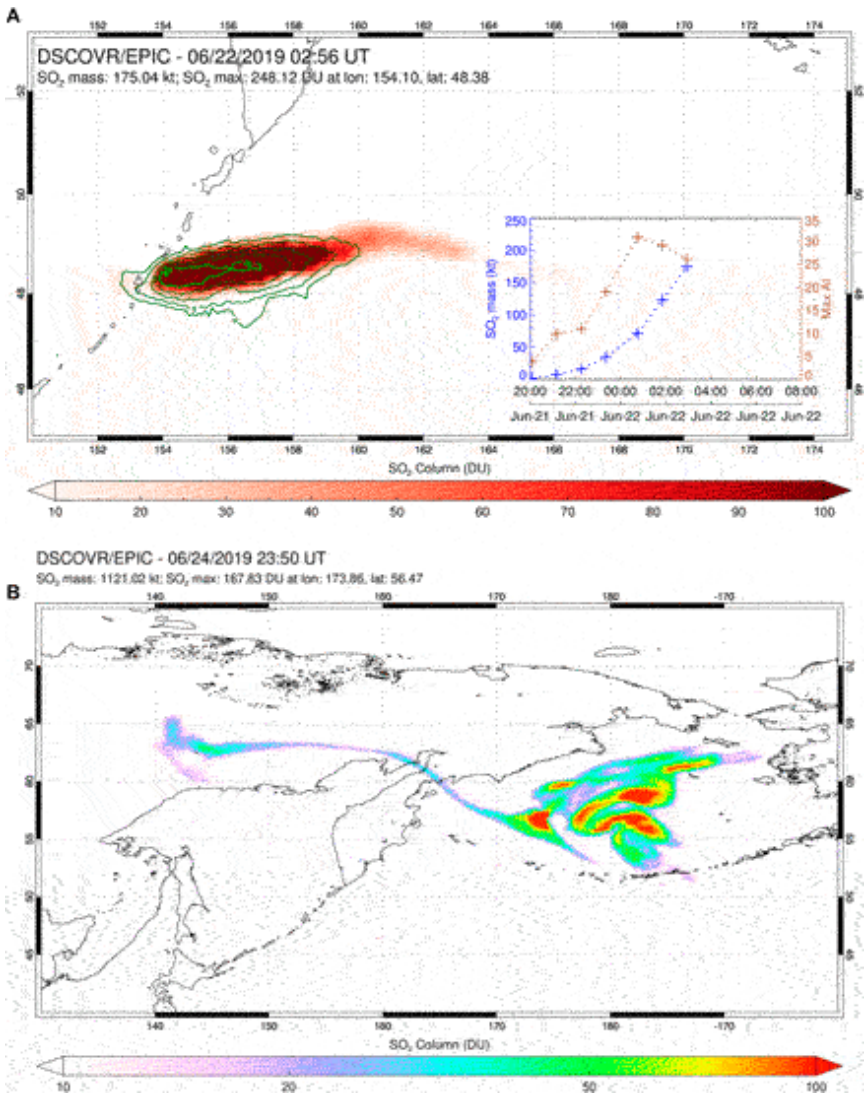

FIGURE 5 | (A) EPIC SO_2 and UV Aerosol Index (UVAI; *green contours*) measurements during the eruption of Raikoke volcano (Kuril Islands, Russia; *triangle*) on June 22, 2019 at 02:56 UT. The UVAI is used to detect volcanic ash. Inset lower right shows a time-series of volcanic SO_2 mass and UVAI derived from EPIC measurements with hourly cadence during the eruption. **(B)** EPIC SO_2 retrieval for the high-latitude Raikoke volcanic cloud on June 24 at 23:50 UTC. EPIC was able to capture this extensive, high-latitude volcanic cloud in single synoptic images with hourly cadence, whereas such latitudes are towards the edge of the geostationary (GEO) field-of-view and can only be covered by multiple overpasses of polar-orbiting (LEO) instruments (with inter-orbit gaps of ~100 min).

In addition to improved cadence and spatial resolution of volcanic SO_2 and ash measurements, EPIC-Moon observations would offer advantages over DSCOVR/EPIC for volcanic aerosol detection and retrieval. Aerosol

particles in volcanic clouds include liquid sulfate aerosol, which are spherical, plus volcanic ash particles (glass shards and crystal fragments) which can have highly irregular shapes. Ash particle phase functions depend on effective particle size but are typically strongly forward scattering at UV wavelengths (Krotkov et al., 1997; Krotkov et al., 1999), which is a limitation for observations of volcanic ash from L1 (in the backscattering direction). Due to changes in the phase function with particle size, the ability to discriminate between ash particle sizes in a volcanic cloud increases if observations at different scattering angles are available.

Studies of particle shape effects on the phase function indicate that, at UV wavelengths, particle non-sphericity leads to increased scattering at side-scattering angles (120–140°) and decreases at backscattering angles (Krotkov et al., 1997; Krotkov et al., 1999). If ash particles are assumed to be spherical, UV retrievals of ash optical depth will be underestimated at backscattering angles (i.e., EPIC observations from L1) and overestimated at side-scattering angles. Scattering angles near 150° are optimal for optical depth retrievals independent of particle shape. Hence the larger range of phase angles accessible from EPIC-Moon observations could potentially improve the accuracy of UV volcanic ash retrievals.

POLAR MESOSPHERIC CLOUDS AND POLAR STRATOSPHERIC CLOUDS

Numerous phenomena in the Earth's middle and upper atmosphere occur in layers that are typically limited in vertical extent but cover extensive horizontal areas. Examples include polar stratospheric clouds (PSCs) and polar mesospheric clouds (PMCs). Localized injections into the stratosphere from below, such as ash plumes from volcanic eruptions or smoke from pyrocumulonimbus (pyroCb) wildfire events, can also be transported by strong winds to spread globally and last for months. Measurements with limb viewing geometry are valuable in studying these phenomena because the long line-of-sight through the atmosphere can enhance an otherwise faint signal. Examples of limb observations for each type of event have been published recently (Tsuda et al., 2018; Bourassa et al., 2019; DeLand et al., 2020; DeLand and Gorkavyi, 2020; Torres et al., 2020; Gorkavyi et al., 2021). The source material for these clouds and plumes are primarily composed of relatively small particles (tens of nm to few hundred nm in radius), with varying composition (PMC = water ice, PSC = nitric acid trihydrate, volcano = ash, and sulfate, pyroCb = smoke). The small size of

these particles means that the intensity of observed reflected light (near-UV, visible, near-IR) will be governed by Mie theory, and thus will vary significantly as a function of scattering angle. The periodic variation of observing phase angle shown in Figure 1A for a lunar sensor would be quite valuable for these atmospheric measurements. The resulting variation in phase function (and thus observed signal) can be used to help distinguish between different assumptions about particle size distribution and composition, which also affect the phase function.

MONITORING VEGETATION

Natural terrestrial surfaces scatter shortwave radiation into an angular reflectance pattern or Bidirectional Reflectance Factor (BRF). In vegetation canopies, the finite size of scatterers (e.g., leaves, coniferous shoots, etc.) can cast shadows. This causes the canopy "hot spot" effect, i.e., a sharp increase in canopy reflected radiation as the scattering direction approaches the direction to the Sun (Figure 6) (Ross and Marshak, 1988; Knyazikhin and Marshak, 1991; Kuusk, 1991; Myneni et al., 1991; Qin et al., 1996; Gerstl, 1999). The hot spot phenomenon is strongly correlated with canopy architectural parameters such as foliage size and shape, crown geometry and within-crown foliage arrangement, foliage grouping, leaf area index and its sunlit fraction (Ross and Marshak, 1991; Qin et al., 1996; Goel et al., 1997; Knyazikhin et al., 1998; Qin et al., 2002; Schull et al., 2011; Yang et al., 2017; Pisek et al., 2021). Angular signatures that include the hot spot region are critical for monitoring phenological changes in dense vegetation such as equatorial forests (Bi et al., 2015).

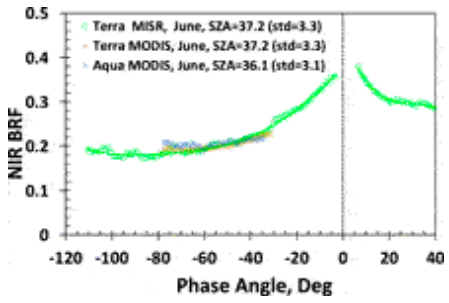

FIGURE 6 | Near-infrared BRF of Amazonian forests confined between 0° to 10°S and 60°W to 70°W from Terra MISR, Terra MODIS, and Aqua MODIS sensors for the period between June 25 and July 10 accumulated over a 7-years period from 2001 to 2008. The MISR sensor views the Earth's surface with nine cameras simultaneously, as opposed to the two MODIS sensors, which are capable of only one view each. The MISR observing geometry allows for measurements of angular signatures over a wider range of phase angles.

Sensors onboard Earth-orbiting satellites sample reflectance over swaths at a specific local solar time, or over a specific area of the sunlit Earth. Such intrinsic sampling limits makes observations of the hot spot rare in occurrence. For example, the cross-track MODIS scanners on the Terra and Aqua near-polar Sun-synchronous orbits can observe about 30–35% of equatorial Amazonian rainforests along the hotspot directions around the Equinoxes. No such observations are available from May to July and November to December (Figure 7). The Multiangle Imaging Spectroradiometer (MISR) on the Terra satellite views the Earth's surface with nine cameras simultaneously, as opposed to the two MODIS sensors, which are capable of only one view each. The MISR observing strategy allows for a better angular variation of surface BRFs in the equatorial zone (Figure 7). However, spatially and temporally varying phase angles could be far from zero, making global observation of the hot spot phenomenon impossible. A spectroradiometer on the Moon's surface offers a unique opportunity to provide observations of every region of the Earth from sunrise to sunset at a full range of phase angles. Here, we discuss an application of surface reflectance data at a full range of phase angles to monitor phenological changes in equatorial forests.

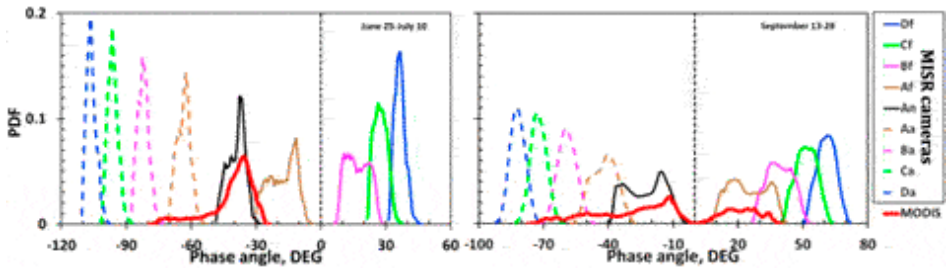

FIGURE 7 | Probability density function (pdf) of the phase angle during 25 June to 10 July and 13–28 September periods over Amazonian rainforests (0°–10°S and 60°W to 70°W) for Terra MODIS and MISR sun-sensor geometries derived from MODIS and MISR data acquired from June 2000 to May 2008. MISR instrument uses nine cameras to view the Earth's surface in the forward and backward directions along the spacecraft's flight track with nominal viewing zenith angles relative to the surface reference ellipsoid of 0.0° (camera An), 26.1° (Af and Aa), 46.5° (Bf and Ba), 60.0° (Cf and Ca), and 70.5° (Df and Da). The 360 km swath width covers the globe in 9 days. MODIS is a single view sensor that scans the Earth's surface across the spacecraft flight track. It has a viewing swath width of 2,330 km and views the entire surface of the Earth every 1–2 days. From Song et al., 2018.

Tropical forests account for approximately one-third of Earth's terrestrial gross primary productivity and one-half of Earth's carbon stored in terrestrial vegetation (Lewis et al., 2009; Pan et al., 2011; Lewis et al., 2015; Hubau et al., 2020). They play an essential role in surface energy partitioning and the Earth's carbon cycle and consequently impact regional climate (Cook et al., 2020; Forzieri et al., 2020). Because of its large geographical extent, any perturbations within this system can have significant impacts on climate and on the carbon and water cycles. Monitoring the spatial patterns, intra-annual seasonality and their controls, inter-annual variability and long-term trends in the structure and functioning of rainforests is crucial to our understanding of how these biodiverse and productive ecosystems will respond to future climate change, disturbances and human appropriation (Cox et al., 2004; Cox et al., 2013; Guimberteau et al., 2017).

Monitoring of dense vegetation such as equatorial rainforests is a challenge for optical remote sensing because reflection of solar radiation saturates and becomes weakly sensitive to vegetation changes. At the same time, satellite data are strongly influenced by changing sun-sensor geometry. This makes it difficult to discriminate between vegetation changes and sun-sensor geometry effects. Commonly used approaches for interpretation of satellite data from single-viewing sensors consider the viewing and solar zenith angle (SZA) dependence of reflected radiation as a source of noise or error, requiring a correction or normalization to a "standard" sun-sensor

geometry. Figure 6 shows the BRF in the NIR spectral band from single-angle Terra and Aqua MODIS sensors acquired over Amazonian rainforests. Their values are almost constant: they vary between 0.18 and 0.23 with mean, standard deviation and coefficient of variation of 0.2, 0.08 and 4%, respectively. Most surface BRF models would interpret such observations as radiation scattered by Lambertian surfaces. Transformation of such data to a fixed, standard sun-sensor geometry therefore invokes statistical assumptions that may not apply to specific scenes. The lack of information on the angular variation of forest-reflected radiation introduces model uncertainties that in turn may have significant impacts on interpretation of satellite data. For example, studies of Amazon forest seasonality based on analyses of data from single-viewing sensors disagree on whether there is more greenness in the dry season than in the wet season: the observed variations in the forest BRF were explained by an increase in the leaf area, an artifact of sun-sensor geometry and changes in leaf age through the leaf flush (Huete et al., 2006; Myneni et al., 2007; Brando et al., 2010; Samanta et al., 2012; Morton et al., 2016; Saleska et al., 2016). Conflicting conclusions among these studies arise from different interpretations of surface reflectance data acquired under saturation conditions (Bi et al., 2015).

Figure 8 shows seasonal changes in NIR BRF of Amazonian forests. The seasonal cycle consists of a short dry season from June to October, and a long wet season thereafter. There are several noteworthy features in the variation of angular signatures. First, a distinct decrease in reflected NIR radiation in all viewing directions from the early (October) to middle (March) part of the wet season with no change in the overall shape of the angular signatures. The SZA is almost the same. The observed downward shift under similar illumination conditions can only result from a change in canopy properties (Bi et al., 2015). Second, the shape of the BRF changes from the beginning (June) to late (October) dry season. Illumination conditions are different in these months. A higher or equal reflectance at lower SZA relative to that at higher SZA always indicates an increase in leaf area and foliage scattering properties (Bi et al., 2015). Moreover, the intersection point of BRFs acquired in these months deviates significantly from that predicted by the reciprocity theorem for identical canopies under different illumination conditions, suggesting that Amazonian forests cannot be similar at the beginning and end of dry seasons (Bi et al., 2015). These examples illustrate that the availability of BRFs over equatorial forests at a

full range of the phase angle under different illumination conditions will make monitoring their changes more reliable.

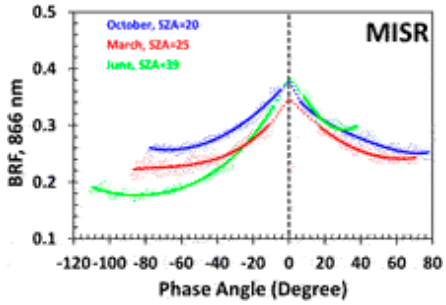

FIGURE 8 | Angular signatures of NIR reflectance of Amazonian forests in March (5 Mar to 20 Mar), June (25 Jun to 10 Jul), and October (15 Oct to 30 Oct) derived from MISR data.

Improved measurements of albedo of the components of Earth's land surface–snow, ice, vegetation, and soil are among the priority targeted observables that were ranked in the Earth Science Decadal Survey as most important or very important (National Academies of Sciences, 2018, p. 229). Spectral albedo (or directional hemispherical reflectance in remote sensing nomenclature) is the integral of the cosine weighted BRF over scattering directions. Measurements of radiation scattered by the land surface in all directions are therefore required to perform the integration. An EPIC-like camera on the Moon's surface can provide frequent observations of every region of the Earth in the full range of scattering directions. The availability of such data will undoubtedly advance our ability to model evapotranspiration, snowmelt, and retrospective reconstruction of the snow water equivalent, which are critical for accurate description of the surface radiation balance (National Academies of Sciences, 2018, p. 227).

LUNAR ENVIRONMENT

Forward scattering conditions create advantages for observing the lunar dust cloud. The lunar dust exosphere is an important factor for the long-term residence of astronauts on the Moon, as well as for the functioning of scientific equipment on the lunar surface and orbiters (Elphic et al., 2014; Richard et al., 2018). Telescopic limb observations of the scattering of sunlight (or starlight) from the lunar dust cloud would help construct a 3D model of the lunar dust exosphere (Richard et al., 2018). We believe that preliminary information regarding the effectiveness of observing the Earth

from the lunar surface can be obtained by analyzing photographs of the Earth obtained using the navigation cameras of the lunar rover VIPER (Colaprete et al., 2021). In addition, analysis of photographs from VIPER cameras taken under conditions of forward scattering of both sunlight and reflected light of the Earth can provide useful information for comparison with models of lunar dust (Richard et al., 2018). A similar program was implemented for the Cosmic Background Explorer (COBE) data and the model of the zodiacal dust cloud (Gorkavyi et al., 2000). Observations from the Moon will help improve existing models of the zodiacal cloud, which is important for astronomical observations, e.g., by the James Webb Space Telescope (JWST) in particular. Even a small meteoroid with a mass of 5 kg can excavate a ~10 m crater, ejecting 75 tons of lunar regolith and rock on ballistic trajectories above the Moon (Dunbar, 2021). However, "*The lunar impact rate is very uncertain because observations for objects in this mass range are embarrassingly few*" (Speyerer et al., 2016). Accurate assessment of the meteorite hazard is required for the effective and safe implementation of the Artemis program (Elphic et al., 2014). Using the Earth's atmosphere as a detector, EPIC-Moon imaging of the night-side and limb of the Earth will detect atmospheric impacts (either by a flash or from dispersion of meteoritic dust clouds; see Gorkavyi et al., 2013) from potentially threatening small (<10 m) asteroids in the vicinity of Earth, thus improving the current highly uncertain estimates.

CONCLUSION

Deploying an analog of DSCOVR/EPIC on the Moon's surface would offer a unique opportunity to image the full range of Earth phases, potentially advancing Earth science in many ways:

1) observing ocean/cloud glint reflection for different phase angles;

2) comprehensive whole-globe monitoring of transient volcanic and aerosol clouds (smoke, dust), including the strategically important (for climate studies) polar regions not covered by GEO missions;

3) detecting of polar mesospheric and stratospheric clouds *via* whole-Earth limb imaging;

4) estimating surface BRF and full phase-angle integrated albedo;

5) monitoring and quantifying changes in vegetated land;

6) simultaneous imaging of the day and night parts (i.e., the twilight zone) during crescent phases of the Earth and shadowed parts illuminated by the Moon.

DATA AVAILABILITY STATEMENT

The original contributions presented in the study are included in the article/supplementary material, further inquiries can be directed to the corresponding author.

AUTHOR CONTRIBUTIONS

NG, SC, MD, YK, AM, and RM developed computer codes and algorithms, analyzed the results and wrote the manuscript. NK, AM, and AV set the task of developing, supported the development of the algorithm, analyzed the results and wrote the manuscript.

FUNDING

YK is supported by the NASA DSCOVR project under grant 80NSSC19K0762 and Jet Propulsion Laboratory under contract 1625837. SC is supported by the NASA DSCOVR Science Team under grant 80NSSC19K0771. NG, MD, and AV are supported by NASA contract NNG17HP01C.

PUBLISHER'S NOTE

ACKNOWLEDGMENTS

The authors thank the EPIC teams for providing the DSCOVR/EPIC data.

REFERENCES

Bi, J., Knyazikhin, Y., Choi, S., Park, T., Barichivich, J., Ciais, P., et al. (2015). Sunlight mediated seasonality in canopy structure and photosynthetic activity of Amazonian rainforests. *Environ. Res. Lett.* 10, 064014. doi:10.1088/1748-9326/10/6/064014

Bourassa, A. E., Rieger, L. A., Zawada, D. J., Khaykin, S., Thomason, L. W., and Degenstein, D. A. (2019). Satellite limb observations of unprecedented forest fire aerosol in the stratosphere. *J. Geophys. Res. Atmos.* 124, 9510–9519. doi:10.1029/2019JD030607

Brando, P. M., Goetz, S. J., Baccini, A., Nepstad, D. C., Beck, P. S. A., and Christman, M. C. (2010). Seasonal and interannual variability of climate and vegetation indices across the Amazon. *Proc. Natl. Acad. Sci.* 107, 14685–14690. doi:10.1073/pnas.0908741107

Bréon, F.-M., and Dubrulle, B. (2004). Horizontally oriented plates in clouds. *J. Atm. Sci.* 61, 2888–2898. doi:10.1175/JAS-3309.1

Carn, S. A., Clarisse, L., and Prata, A. J. (2016). Multi-decadal satellite measurements of global volcanic degassing. *J. Volcanology Geothermal Res.* 311, 99–134. doi:10.1016/j.jvolgeores.2016.01.002

Carn, S. A., Krotkov, N. A., Fisher, B. L., Li, C., and Prata, A. J. (2018). First Observations of Volcanic Eruption Clouds from the L1 Earth-Sun Lagrange Point by DSCOVR/EPIC. *Geophys. Res. Lett.* 45, 11456–11464. doi:10.1029/2018GL079808

Colaprete, A., Elphic, R. C., Shirley, M., Ennico-Smith, K., Lim, D. S. S., Zacny, K., et al. (2021). The Volatiles Investigating Polar Exploration Rover (VIPER) Mission. 15-19 March, 2021. LPI Contribution No. 2548, id.1523, https://ui.adsabs.harvard.edu/#abs/2021LPI.52.1523C/abstract. *52nd Lunar and Planetary Science Conference*.

Cook, K. H., Liu, Y., and Vizy, E. K. (2020). Congo Basin drying associated with poleward shifts of the African thermal lows. *Clim. Dyn.* 54, 863–883. doi:10.1007/s00382-019-05033-3

Cox, P. M., Betts, R. A., Collins, M., Harris, P. P., Huntingford, C., and Jones, C. D. (2004). Amazonian forest dieback under climate-carbon cycle projections for the 21st century. *Theor. Appl. Climatol* 78, 137–156. doi:10.1007/s00704-004-0049-4

Cox, P. M., Pearson, D., Booth, B. B., Friedlingstein, P., Huntingford, C., Jones, C. D., et al. (2013). Sensitivity of tropical carbon to climate change constrained by carbon dioxide variability. *Nature* 494, 341–344. doi:10.1038/nature11882

DeLand, M. T., Bhartia, P. K., Kramarova, N., and Chen, Z. (2020). OMPS LP observations of PSC variability during the NH 2019-2020 season. *Geophys. Res. Lett.* 47, e2020GL090216. doi:10.1029/2020gl090216

DeLand, M. T., and Gorkavyi, N. (2021). PMC observations from the OMPS Limb Profiler. *J. Atmos. Solar-Terrestrial Phys.* 213, 105505. doi:10.1016/j.jastp.2020.105505

Dunbar, B. (2021). *About Lunar Impact Monitoring*. Huntsville, AL: NASA. https://www.nasa.gov/centers/marshall/news/lunar/overview.html.

Elphic, R. C., Delory, G. T., Delory, G. T., Hine, B. P., Mahaffy, P. R., Horanyi, M., et al. (2014). The Lunar Atmosphere and Dust Environment Explorer Mission. *Space Sci. Rev.* 185, 3–25. doi:10.1007/s11214-014-0113-z

Espenak, F. (2021). *Geocentric Ephemeris for the Sun, Moon and Planets*. http://astropixels.com/ephemeris/moon/moon2021.html.

Forzieri, G., Miralles, D. G., Ciais, P., Alkama, R., Ryu, Y., Duveiller, G., et al. (2020). Increased control of vegetation on global terrestrial energy fluxes. *Nat. Clim. Chang.* 10, 356–362. doi:10.1038/s41558-020-0717-0

Gerstl, S. A. W. (1999). Building a global hotspot ecology with Triana data. *Remote Sensing Earth Sci. Ocean, Sea Ice Appl.* 3868, 184–194. doi:10.1117/12.373094

Goel, N. S., Qin, W., and Wang, B. (1997). On the estimation of leaf size and crown geometry for tree canopies from hotspot observations. *J. Geophys. Res.* 102, 29543–29554. doi:10.1029/97JD01110

Gorkavyi, N., Krotkov, N., Li, C., Lait, L., Colarco, P., Carn, S., et al. (2021). Tracking aerosols and SO2 clouds from the Raikoke eruption: 3D view from satellite observations. *Atmos. Meas. Tech.* , 58. amt-2021. doi:10.5194/amt-02-58

Gorkavyi, N., Ozernoy, L. M., Mather, J. C., and Taidakova, T. A. (2000). "The NGST and the zodiacal light in the Solar system," in *NGST Science and Technology Exposition* ed . Editors E. P. Smith, and K. S. Long (San Francisco: ASP Series), 207, 462–467.

Gorkavyi, N., Rault, D. F., Newman, P. A., Da Silva, A. M., and Dudorov, A. E. (2013). New stratospheric dust belt due to the Chelyabinsk bolide. *Geophys. Res. Lett.* 40, 4728–4733. doi:10.1002/grl.50788

Guimberteau, M., Ciais, P., Ducharne, A., Boisier, J. P., Dutra Aguiar, A. P., Biemans, H., et al. (2017). Impacts of future deforestation and climate change on the hydrology of the Amazon Basin: a multi-model analysis with a new set of land-cover change scenarios. *Hydrol. Earth Syst. Sci.* 21, 1455–1475. doi:10.5194/hess-21-1455-2017

Hubau, W., Lewis, S. L., Phillips, O. L., Affum-Baffoe, K., Beeckman, H., Cuní-Sanchez, A., et al. (2020). Asynchronous carbon sink saturation in African and Amazonian tropical forests. *Nature* 579, 80–87. doi:10.1038/s41586-020-2035-0

Huete, A. R., Didan, K., Shimabukuro, Y. E., Ratana, P., Saleska, S. R., Hutyra, L. R., et al. (2006). Amazon rainforests green-up with sunlight in dry season. *Geophys. Res. Lett.* 33, L06405. doi:10.1029/2005GL025583

IPCC (2014). *Fifth Assessment Report (AR5)*. https://www.ipcc.ch/assessment-report/ar5/.

Knyazikhin, Y., and Marshak, A. (1991). "Fundamental Equations of Radiative Transfer in Leaf Canopies, and Iterative Methods for Their Solution," in *Photon-vegetation interactions: applications in plant physiology and optical remote sensing* ed . Editors R. B. Myneni, and J. Ross (Berlin Heidelberg: Springer-Verlag), 9–43. doi:10.1007/978-3-642-75389-3_2

Knyazikhin, Y., Martonchik, J. V., Myneni, R. B., Diner, D. J., and Running, S. W. (1998). Synergistic algorithm for estimating vegetation canopy leaf area index and fraction of absorbed photosynthetically active radiation from MODIS and MISR data. *J. Geophys. Res.* 103, 32257–32275. doi:10.1029/98JD02462

Kostinski, A., Marshak, A., and Várnai, T. (2021). Deep space observations of terrestrial glitter. *Earth Space Sci.* 8, e2020EA001521. doi:10.1029/2020EA001521

Krotkov, N. A., Flittner, D. E., Krueger, A. J., Kostinski, A., Riley, C., Rose, W., et al. (1999). Effect of particle non-sphericity on satellite monitoring of drifting volcanic ash clouds. *J. Quantitative Spectrosc. Radiative Transfer* 63, 613–630. doi:10.1016/S0022-4073(99)00041-2

Krotkov, N. A., Krueger, A. J., and Bhartia, P. K. (1997). Ultraviolet optical model of volcanic clouds for remote sensing of ash and sulfur dioxide. *J. Geophys. Res.* 102 (D18), 21891–21904. doi:10.1029/97JD01690

Kuusk, A. (1991). "The Hot Spot Effect in Plant Canopy reflectance," in *Photon-vegetation interactions: applications in plant physiology and optical remote sensing* ed . Editors R. B. Myneni, and J. Ross (Berlin Heidelberg: Springer-Verlag), 139–159. doi:10.1007/978-3-642-75389-310.1007/978-3-642-75389-3_5

Lewis, S. L., Edwards, D. P., and Galbraith, D. (2015). Increasing human dominance of tropical forests. *Science* 349, 827–832. doi:10.1126/science.aaa9932

Lewis, S. L., Lopez-Gonzalez, G., Sonké, B., Affum-Baffoe, K., Baker, T. R., Ojo, L. O., et al. (2009). Increasing carbon storage in intact African tropical forests. *Nature* 457, 1003–1006. doi:10.1038/nature07771

Livengood, T. A., Deming, L. D., A'Hearn, M. F., Charbonneau, D., Hewagama, T., Lisse, C. M., et al. (2011). Properties of an Earth-Like Planet Orbiting a Sun-Like Star: Earth Observed by the EPOXI Mission. *Astrobiology* 11, 907–930. doi:10.1089/ast.2011.0614

Marshak, A., Herman, J., Adam, S., Karin, B., Carn, S., Cede, A., et al. (2018). Earth Observations from DSCOVR EPIC Instrument. *BAMS* 99, 1829–1850. doi:10.1175/BAMS-D-17-0223.1

Marshak, A., Krotkov, N., Gorkavyi, N., Marchenko, S., Vasilkov, A., Knyazikhin, Y., et al. (2020). "Whole Earth imaging from the Moon South Pole (EPIC-Moon)," in *Whitepaper* . https://www.lpi.usra.edu/announcements/artemis/whitepapers/2054.pdf.

Marshak, A., Várnai, T., and Kostinski, A. (2017). Terrestrial glint seen from deep space: oriented ice crystals detected from the Lagrangian point. *Geophys. Res. Lett.* 44, 5197–5202. doi:10.1002/2017GL073248

Morton, D. C., Nagol, J., Carabajal, C. C., Rosette, J., Rosette, J., Palace, M., et al. (2016). Morton et al. reply. *Nature* 531, E6. doi:10.1038/nature16458

Myneni, R. B., Marshak, A. L., and Knyazikhin, Y. V. (1991). Transport theory for a leaf canopy of finite-dimensional scattering centers. *J. Quantitative Spectrosc. Radiative Transfer* 46, 259–280. doi:10.1016/0022-4073(91)90091-4

Myneni, R. B., Yang, W., Nemani, R. R., Huete, A. R., Dickinson, R. E., Knyazikhin, Y., et al. (2007). Large seasonal swings in leaf area of Amazon rainforests. *Proc. Natl. Acad. Sci.* 104, 4820–4823. doi:10.1073/pnas.0611338104

National Academies of Sciences (2018). *Thriving on Our Changing Planet: A Decadal Strategy for Earth Observation from Space*. Washington, DC: The National Academies Press. doi:10.17226/24938

Pan, Y., Birdsey, R. A., Fang, J., Houghton, R., Kauppi, P. E., Kurz, W. A., et al. (2011). A Large and Persistent Carbon Sink in the World's Forests. *Science* 333, 988–993. doi:10.1126/science.1201609

Pavolonis, M. J., Sieglaff, J., and Cintineo, J. (2018). Automated Detection of Explosive Volcanic Eruptions Using Satellite-Derived Cloud Vertical Growth Rates. *Earth Space Sci.* 5, 903–928. doi:10.1029/2018EA000410

Pisek, J., Arndt, S. K., Erb, A., Pendall, E., Schaaf, C., Wardlaw, T. J., et al. (2021). Exploring the Potential of DSCOVR EPIC Data to Retrieve Clumping Index in Australian Terrestrial Ecosystem Research Network Observing Sites. *Front. Remote Sens.* 2, 652436. doi:10.3389/frsen.2021.652436

Qin, W., Gerstl, S. A. W., Deering, D. W., and Goel, N. S. (2002). Characterizing leaf geometry for grass and crop canopies from hotspot observations: A simulation study. *Remote Sensing Environ.* 80, 100–113. doi:10.1016/S0034-4257(01)00291-7

Qin, W., Goel, N. S., and Wang, B. (1996a). The hotspot effect in heterogeneous vegetation canopies and performances of various hotspot models. *Remote Sensing Rev.* 14, 283–332. doi:10.1080/02757259609532323

Qin, W. H., Goel, N. S., and Wang, B. Q. (1996b). Estimation of leaf size from hotspot observations. *Remote Sensing a Sust. Future* Vols I - Iv, 1645–1647. Igarss '96 - 1996 International Geoscience and Remote Sensing Symposium.

Richard, D. T., Glenar, D. A., Stubbs, T. J., Davis, S. S., and Colaprete, A. (2011). Light scattering by complex particles in the Moon's exosphere: Toward a taxonomy of models for the realistic simulation of the scattering behavior of lunar dust. *Planet. Space Sci.* 59, 1804–1814. doi:10.1016/j.pss.2011.01.003

Robinson, T. D., Meadows, V. S., and Crisp, D. (2010). Detecting Oceans on Extrasolar Planets Using the Glint Effect. *ApJ ,*721, L67–L71. doi:10.1088/2041-8205/721/1/L67

Ross, J. K., and Marshak, A. L. (1988). Calculation of canopy bidirectional reflectance using the Monte Carlo method. *Remote Sensing Environ.* 24, 213–225. doi:10.1016/0034-4257(88)90026-0

Ross, J., and Marshak, A. (1991). Influence of the Crop Architecture Parameters on Crop Brdf - a Monte-Carlo Simulation. *Phys. Measurements Signatures Remote Sensing* 1 and 2, 357–360.

Sagan, C., Thompson, W. R., Carlson, R., Gurnett, D., and Hord, C. (1993). A search for life on Earth from the Galileo spacecraft. *Nature* 365, 715–721. doi:10.1038/365715a0

Saleska, S. R., Wu, J., Guan, K., Araujo, A. C., Huete, A., Nobre, A. D., et al. (2016). Dry-season greening of Amazon forests. *Nature* 531, E4–E5. doi:10.1038/nature16457

Samanta, A., Knyazikhin, Y., Xu, L., Dickinson, R. E., Fu, R., Costa, M. H., et al. (2012). Seasonal changes in leaf area of Amazon forests from leaf flushing and abscission. *J. Geophys. Res.* 117,

G01015. doi:10.1029/2011JG001818

Schull, M. A., Knyazikhin, Y., Xu, L., Samanta, A., Carmona, P. L., Lepine, L., et al. (2011). Canopy spectral invariants, Part 2: Application to classification of forest types from hyperspectral data. *J. Quantitative Spectrosc. Radiative Transfer* 112, 736–750. doi:10.1016/j.jqsrt.2010.06.004

Song, W., Knyazikhin, Y., Wen, G., Marshak, A., Mõttus, M., Yan, K., et al. (2018). Implications of Whole-Disc DSCOVR EPIC Spectral Observations for Estimating Earth's Spectral Reflectivity Based on Low-Earth-Orbiting and Geostationary Observations. *Remote Sensing* 10, 1594. doi:10.3390/rs10101594

Speyerer, E. J., Povilaitis, R. Z., Robinson, M. S., Thomas, P. C., and Wagner, R. V. (2016). Quantifying crater production and regolith overturn on the Moon with temporal imaging. *Nature* 538, 215–218. doi:10.1038/nature19829

Torres, O., Bhartia, P. K., Taha, G., Jethva, H., Das, S., Colarco, P., et al. (2020). Stratospheric Injection of Massive Smoke Plume from Canadian Boreal Fires in 2017 as Seen by DSCOVR-EPIC, CALIOP, and OMPS-LP Observations. *J. Geophys. Res. Atmos.* 125, 2020jd032579. doi:10.1029/2020JD032579

Tsuda, T. T., Hozumi, Y., Kawaura, K., Hosokawa, K., Suzuki, H., and Nakamura, T. (2018). Initial report on polar mesospheric cloud observations by Himawari-8. *Atmos. Meas. Tech.* 11, 6163–6168. doi:10.5194/amt-11-6163-2018

Varnai, T., Kostinski, A. B., and Marshak, A. (2020). Deep space observations of sun glints from marine ice clouds. *IEEE Geosci. Remote Sensing Lett.* 17 (5), 735–739. doi:10.1109/LGRS.2019.2930866

Walker, J. (2021). *Earth and Moon Viewer*. https://www.fourmilab.ch/cgi-bin/Earth.

Williams, D. M., and Gaidos, E. (2008). Detecting the glint of starlight on the oceans of distant planets. *Icarus* 195, 927–937. doi:10.1016/j.icarus.2008.01.002

Yang, B., Knyazikhin, Y., Mõttus, M., Rautiainen, M., Stenberg, P., Yan, L., et al. (2017). Estimation of leaf area index and its sunlit portion from DSCOVR EPIC data: Theoretical basis. *Remote Sensing Environ.* 198, 69–84. doi:10.1016/j.rse.2017.05.033

Conflict of Interest: Authors NG, MD, and AV are employed by Science Systems and Applications, Inc.The remaining authors declare that the research was conducted in the absence of any commercial or financial relationships that could be construed as a potential conflict of interest.

ORIGINAL RESEARCH
published: 08 September 2021
doi: 10.3389/frsen.2021.734071

Evaluation of Version 3 Total and Tropospheric Ozone Columns From Earth Polychromatic Imaging Camera on Deep Space Climate Observatory for Studying Regional Scale Ozone Variations

Natalya A. Kramarova[1*], Jerald R. Ziemke[2], Liang-Kang Huang[3], Jay R. Herman[4], Krzysztof Wargan[3,1], Colin J. Seftor[3], Gordon J. Labow[3] and Luke D. Oman[1]

[1] *NASA Goddard Space Flight Center, Greenbelt, MD, United States*
[2] *Goddard Earth Sciences Technology and Research (GESTAR)/Morgan State University, Baltimore, MD, United States*
[3] *Science Systems and Applications, Inc. (SSAI), Lanham, MD, United States*
[4] *University of Maryland, Baltimore County, Baltimore, MD, United States*

Edited by:
Gregory Schuster, National Aeronautics and Space Administration (NASA), United States

Reviewed by:
Yong Han, Sun Yat-sen University, China
Vijay Natraj, National Aeronautics and Space Administration (NASA), United States
David Flittner, National Aeronautics and Space Administration (NASA), United States

**** Correspondence:*** *Natalya A. Kramarova, natalya.a.kramarova@nasa.gov*

Specialty section: *This article was submitted to Satellite Missions, a section of the journal Frontiers in Remote Sensing*

Received: *30 June 2021*
Accepted: *26 August 2021*
Published: *08 September 2021*

Citation: *Kramarova NA, Ziemke JR, Huang L-K, Herman JR, Wargan K, Seftor CJ, Labow GJ and Oman LD (2021) Evaluation of Version 3 Total and Tropospheric Ozone Columns From Earth Polychromatic Imaging Camera on Deep Space Climate Observatory for Studying Regional Scale Ozone Variations. Front. Remote Sens. 2:734071. doi: 10.3389/frsen.2021.734071*

Discrete wavelength radiance measurements from the Deep Space Climate Observatory (DSCOVR) Earth Polychromatic Imaging Camera (EPIC) allows derivation of global synoptic maps of total and tropospheric ozone columns every hour during Northern Hemisphere (NH) Summer or 2 hours during Northern Hemisphere winter. In this study, we present version 3 retrieval of Earth Polychromatic Imaging Camera ozone that covers the period from June 2015 to the present with improved geolocation, calibration, and algorithmic updates. The accuracy of total and tropospheric ozone measurements from EPIC have been evaluated using correlative satellite and ground-based total and tropospheric ozone measurements at time scales from daily averages to monthly means. The comparisons show good agreement with increased differences at high latitudes. The agreement improves if we only accept retrievals derived from the EPIC 317 nm triplet and limit solar zenith and satellite looking angles to 70°. With such filtering in place, the comparisons of EPIC total column ozone retrievals with correlative satellite and ground-based data show mean differences within ±5-7 Dobson Units (or 1.5–2.5%). The biases with other satellite instruments tend to be mostly negative in the Southern Hemisphere while there are no clear latitudinal patterns in ground-based comparisons. Evaluation of the EPIC ozone time series at different ground-based stations with the correlative ground-based and satellite instruments and ozonesondes demonstrated good consistency in capturing ozone variations at daily, weekly and monthly scales with a persistently high correlation ($r^2 > 0.9$) for total and tropospheric columns. We examined EPIC tropospheric ozone columns by comparing with ozonesondes at 12 stations and found that differences in tropospheric column ozone are within ±2.5 DU (or ~±10%) after removing a constant 3 DU offset at all stations between EPIC and sondes. The analysis of the time series of zonally averaged EPIC tropospheric ozone revealed a statistically significant drop of ~2–4 DU (~5–10%) over the entire NH in spring and summer of 2020. This drop in tropospheric ozone is partially related to the unprecedented Arctic

stratospheric ozone losses in winter-spring 2019/2020 and reductions in ozone precursor pollutants due to the COVID-19 pandemic.

Keywords: total ozone, tropospheric ozone, EPIC, UV, ozone time series

INTRODUCTION

The DSCOVR spacecraft carrying the EPIC instrument was successfully launched on February 11, 2015, to the Earth-Sun Lagrange-1 (L_1) point at a nominal distance of 1.5×10^6 km from the Earth. After initial on-orbit testing, EPIC started routine operations in mid-June 2015 (Marshak et al., 2018). The DSCOVR EPIC instrument measures radiances in 10 narrow spectral bands (from 317.5 to 779.5 nm) backscattered from the illuminated portion of the Earth's surface and atmosphere. Four UV bands, 317.5, 325, 340 and 388 nm, are used to derive total column ozone (TOZ) amounts (Herman et al., 2018). The high spatial resolution of EPIC UV data (18×18 km^2) permits derivation of detailed synoptic maps of ozone distribution with multiple samples (4–9) at a given geographical location each day supporting studies of small scale, regional ozone transport. The EPIC total and tropospheric ozone column products, sampled from sunrise to sunset, serve as a pathfinder and provider of intercalibration data for the constellation of existing and future geostationary missions. The purpose of GEO constellation is to monitor air quality over three different continents: North America (TEMPO), Europe (Sentinel 4) and Asia (GEMS) with a major focus on regional pollution transport (CEOS Report, 2011). The Korean GEMS was launched on February 18, 2020. The two other missions are planned for launch in the next few years. From the GEO vantage point these instruments will monitor daily variations in ozone, nitrogen dioxide, and other key constituents of air pollution (Stark et al., 2013; Zoogman et al., 2016; Kim et al., 2020). EPIC views the entire sunlit portion of the Earth as it rotates in DSCOVR's field of view (FOV) in orbit about the L_1 position, thereby connecting all three regions observed with the geostationary missions. Additionally, EPIC provides important measurements in the Southern Hemisphere (SH) and high latitudes not covered by the current and planned geostationary missions.

Herman et al. (2018) provided a detailed description of the EPIC UV measurements, calibration techniques and ozone retrieval algorithm. They reported that EPIC Version 2 total ozone agreed within ±3% with ground-

based and satellite measurements. Here we present a new Version 3 of EPIC total ozone and a new tropospheric ozone column product. The tropospheric ozone column is derived by subtracting an independently measured stratospheric column from the EPIC total ozone. Version 3 processing includes several key modifications: 1) an improved geolocation of EPIC scenes applied in Version 3 Level 1 product (Blank et al., 2021) to ensure accuracy of solar/view angles calculations for each EPIC pixel; 2) an inclusion of simultaneous cloud-height information from EPIC A-Band (Yang et al., 2019) to improve the scene pressure and the estimated ozone amount below the cloud; 3) an addition of corrections for ozone and temperature profile shapes in the retrieval algorithm; and 4) an addition of column weighting functions and algorithm/error flags for each observation to facilitate error analysis.

In this paper we evaluate the accuracy and precision of the EPIC version 3 total and tropospheric ozone products by comparing them with correlative satellite and ground-based measurements. *Data and Methods* describes EPIC version 3 ozone products and correlative ozone measurements used in this study to evaluate EPIC retrievals. *Data and Methods* also describes the methodologies we apply in this study to compare and analyze the measurements. The results of comparisons are presented in *Results*. Our conclusions are summarized in *Summary and Discussion*.

DATA AND METHODS

EPIC Total Ozone

EPIC permits measurements of ozone, aerosol amounts, and cloud reflectivity, using a Charge-Coupled Device (CCD) detector with 2048 by 2048 pixels to obtain Earth images with 10 spectral filters: four at ultraviolet channels (317.5, 325, 340 and 388 nm), four at visible channels (443, 551, 680 and 687.75 nm) and two near-IR channels (764 and 779.5 nm). The UV filters have bandpass with full widths at half maximum of 1.0, 1.0, 2.7 and 2.6 nm, respectively. Because of telemetry limitations, only the blue 443 nm channel is downlinked at full resolution, while for the other channels, four (2 × 2) individual pixels are averaged onboard the spacecraft to yield an effective 1024 × 1024 pixel image corresponding to an 18 × 18 km^2 resolution at the observed center of the Earth's sunlit disk. The effective spatial resolution decreases as the secant of the angle between EPIC's sub-earth point and the normal to the earth's surface (i.e., at an angle of 60°, the

ground pixel size is ~36 × 36 km^2). The result of using the Earth imaging multi-filter EPIC instrument from the L_1 point is that measurements are derived simultaneously from sunrise to sunset over all illuminated latitudes from 13 to 22 times per 24 h as the Earth rotates (see Supplementary Figure S3).

Measurements for each EPIC channel are taken consecutively at an interval of ~27 s between adjacent wavelengths. Elaborate preprocessing is required to determine the geolocation of each pixel in the earth image, and to collocate images from different spectral channels to a common latitude × longitude grid. This geolocation procedure had been substantially improved in the recent v3 of EPIC Level 1 product (Blank et al., 2021) leading to notable improvements in EPIC Level 2 products, including ozone. Particularly, it resulted in more accurate estimation of solar/view angles for each EPIC pixel thereby improving radiance simulations and reducing errors in ozone retrievals. EPIC version 3 Level 1 data have been also corrected for the dark-current signal, flat-field, and stray-light contamination (Cede et al., 2021). In-flight EPIC radiometric calibrations are done by comparing EPIC measured albedo for each wavelength channel with coincident, scene-matched measurements from Suomi National Polar Partnership (SNPP) Ozone Mapping and Profiler Suite (OMPS) Nadir Mapper (Herman et al., 2018). To account for small differences in spectral resolution between the two instruments, OMPS albedo spectra were either interpolated (317.5 and 325 nm channels) or convolved (340 and 388 nm) with each EPIC filter transmission function. The resulting uncertainties of the EPIC radiometric calibration depend on the quality and stability of the OMPS calibration. OMPS has a calibration accuracy of 2%, while its wavelength dependence in the calibration is estimated to be better than 1% (Seftor et al., 2014). The EPIC absolute calibrations are updated every year.

Since the ozone retrieval algorithm relies on sun-normalized radiances and EPIC does not take solar measurements, a high-resolution solar irradiance spectrum (Dobber et al., 2008) is used to calculate radiance/irradiance ratios (albedos). The TOMRAD radiative transfer model is used to simulate EPIC radiances using a spherical geometry correction for large solar zenith angles (SZAs) and satellite look angles (SLAs) (Caudill et al., 1997). These calculated radiances are also then divided by the same solar irradiances to compute albedos. Spectrally resolved ozone absorption cross sections are from Brion et al. (1998), Daumont et al. (1992), and Malicet et

al. (1995). The reference solar spectrum and the calculated spectral albedos are convolved with EPIC filter transmission functions. To speed up the retrieval algorithm, calculated albedos at EPIC wavelengths are compiled in a look-up table (LUT) as a function of ozone profiles, SZA/SLA and reflecting surface pressure height. The EPIC ozone retrieval algorithm, described in (Herman et al., 2018), uses a triplet of wavelengths to derive total ozone column. Two ozone absorption channels either 317.5 and 340 nm or 325 and 340 nm, depending on optical depth conditions, are combined with the 388 nm measurement to form a triplet. The EPIC 388 nm channel is used to derive scene reflectivity (Herman et al., 2018). The reflectivity is assumed to change linearly with wavelength to account for aerosol contamination.

The triplet algorithm with wavelength-dependent reflectivity R_λ permits adjusting both the total ozone amount and the reflectivity at the ozone absorption wavelengths to account for the presence of aerosols. In cases with elevated aerosol amounts, the spectral slope in reflectivity can be significant, leading to an increase in reported residuals at ozone absorption channels that are computed with the 388 nm surface reflectivity. It is difficult to validate total ozone measurements over aerosol contaminated areas because the ground-based sensors like Dobson, Brewer and to a lesser extent Pandora are sensitive to aerosol contamination. To check for effectiveness of the implemented aerosol correction, we analyze EPIC ozone maps by comparing ozone values sampled over aerosol contaminated areas with the surrounding aerosol-free airmasses. Our analysis indicated that the EPIC retrieved TOZ over contaminated regions (caused by large smoke plumes or desert dust storm events) are consistent with those in the surrounding area. Figure 1 shows an example of wildfires that occurred in the western United States in summer 2020. The aerosol index (AI) (Figure 1A) was elevated over the western coast of United States on August 8, 2020. The aerosol corrected EPIC retrieved TOZ maps over the affected area are very smooth without apparent aerosol-driven features. The TOZ value averaged over the aerosol contaminated area (24°N-35°N and 122°W-135°W) with the AI> 5 was 282.4 DU and agreed well with 280.13 DU, the average over the same area but for aerosol-free pixels with AI<0.75. The triplet algorithm with a simple linear model for surface reflectivity, implemented for EPIC, provides an effective aerosol correction mechanism for background aerosol and Sun glint (near the image center) as well.

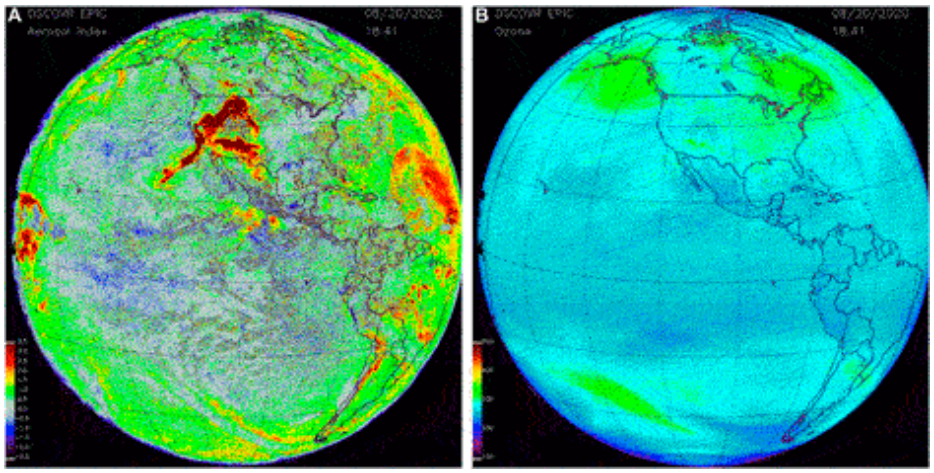

FIGURE 1 | EPIC synoptic maps of the aerosol index **(A)** and TOZ **(B)** on August 8, 2020, at 18:41 UTC. Elevated levels of aerosols (AI>5) are clearly seen over western United States from massive wildfires. The ozone algorithm's linear spectral dependence of reflectivity provides effective corrections for aerosol contamination. The corrected ozone fields are smooth without any apparent artificial structures imposed by wildfires. Ozone averaged over the aerosol contaminated area agrees well with the surrounding area.

The ozone version 3 retrieval algorithm accounts for ozone and temperature profile shape variations using seasonal zonally averaged climatology of ozone (McPeters and Labow, 2012) and temperature profiles. Calculated EPIC sun-normalized radiances stored in LUT are adjusted for differences between the seasonal climatological ozone (or temperature) profiles and the standard profiles.

Cloud height retrievals are obtained from EPIC oxygen A-band absorption measurements at 764 ± 0.2 nm and its reference wavelength 779.5 ± 0.3 nm (Yang et al., 2019). The EPIC simultaneous cloud-height product is now used in version 3 EPIC ozone algorithm for two purposes: 1) to adjust the scene surface pressure to properly simulate EPIC radiances; and 2) to estimate the unretrieved amount of ozone beneath clouds. The ozone climatology (McPeters and Labow, 2012) is used to substitute partial ozone columns below clouds, and the error in estimating cloud height for the high-altitude convective clouds can lead to errors in estimating total and tropospheric ozone columns in presence of such clouds. If the A-band cloud pressure height is not available (~2–3% of EPIC images that are flagged in the L2 product), the ozone retrieval algorithm uses cloud effective pressure height from the OMI-based Optical Centroid Pressure (OCP) climatology (Vasilkov et al., 2008), used for all EPIC images in previous EPIC ozone

versions. Figure 2 demonstrates how the simultaneous EPIC cloud height product helps reduce features in the synoptic TOZ maps produced by a large-scale convective cyclone. This is particularly important for tropospheric ozone studies that are sensitive to errors caused by the presence of clouds.

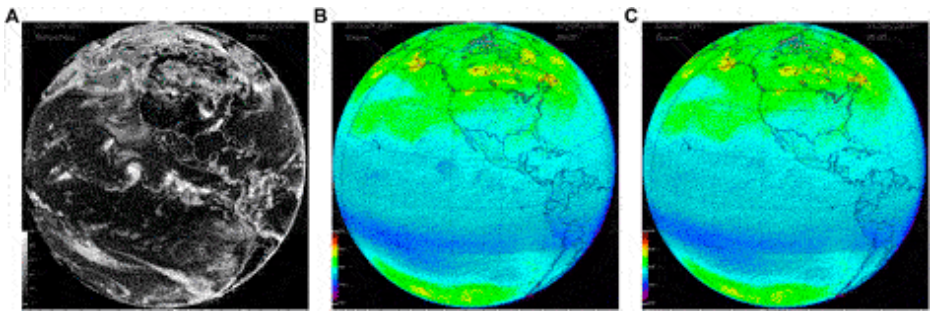

FIGURE 2 | EPIC synoptic maps of reflectivity derived from 380 nm channel **(A)** and EPIC retrieved TOZ processed using OPT climatology **(B)** and simultaneous A-Band cloud height **(C)**. The cyclonic activity in the tropical Pacific area west from Central America is clearly seen in the reflectivity map **(A)**. The TOZ map derived with climatological cloud heights **(B)** has artificial structures that are co-located with the cyclones. When the simultaneous cloud height product from EPIC is used in the ozone algorithm **(C)** it reduces artificial structures in the derived synoptic TOZ maps.

To evaluate consistency of EPIC TOZ, we compared retrievals derived from two different triplets. The EPIC algorithm switches between 317.5 and 325 nm channels depending on optical depth conditions. At low optical depth ($\tau < 1.5$), which corresponds to small and moderate SZA and SLA, the algorithm uses the 317.5 nm channel. When $\tau > 1.5$, the algorithm switches to the 325 nm triplet that more easily penetrates to the surface. Since the natural ozone variability in the tropics is relatively low, we should expect very little changes in retrieved TOZ as a function of SZA or SLA. Therefore, we can evaluate consistency of EPIC retrievals as shown in Figure 3 by looking at the tropical zonal mean values retrieved from two triplets. The plots in Figure 3 show that TOZ averages derived with the 317 nm triplet (black lines) have very small variations at low and moderate SZA/SLA but starts to deviate when SZA/SLA > ~70°. Larger errors in ozone retrievals at high SZA/SLA are related to the accuracy of radiance simulations using an approximation for atmospheric sphericity.

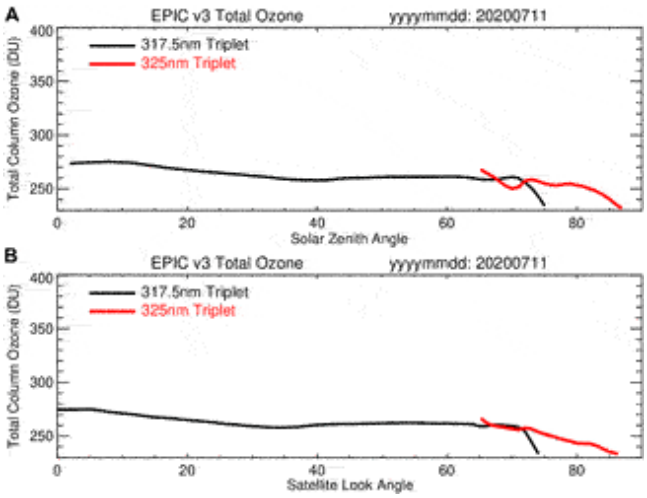

FIGURE 3 | EPIC version-3 total column observations (in DU) on July 11, 2020 averaged for an entire day over a wide equatorial zone (20°S-20°N) as a function of SZA **(A)** and SLA **(B)**. EPIC retrievals with 317.5 nm triplet are shown in black and 325 nm triplet in red. In this study, we use EPIC total ozone retrievals from 317.5 nm triplet only (algorithm flag equal 1, or 101, or 111) and limit SZA and SLA to less than 70°.

Figure 3 reveals inconsistency between EPIC 325 nm retrievals (red lines) and 317 nm retrievals (black lines) when they overlap. Since the 325 nm triplet has reduced ozone sensitivity compared to the 317 nm triplet, the retrieval errors in measured and simulated radiances will be amplified with the 325 nm triplet. These results are also supported by comparison with external measurements. Conditions with high optical depth typically correspond to early morning and late afternoon hours at the edges of the EPIC images, where EPIC has larger biases compared to other instruments (see Supplementary Figure S4). For scientific analysis, we recommend using EPIC total ozone retrievals from 317.5 nm triplet only (which corresponds to algorithm flag equal 1, or 101, or 111) and limiting the SZA and SLA to less than 70°. In this study EPIC data had been filtered using these criteria.

EPIC Tropospheric Ozone Algorithm

To derive tropospheric column ozone (TCO) from EPIC, an independent measure of the stratospheric ozone column is needed. The stratospheric column is then subtracted from EPIC TOZ to obtain tropospheric column ozone. Limb sounders like Aura MLS and OMPS LP have dense samplings and provide an accurate estimate of stratospheric ozone with high vertical resolution (e.g., Hubert et al., 2016; Kramarova et al., 2018; Wargan et al.,

2020). These sounders are flown on polar-orbiting satellites and make measurements at the same local solar time with ~14 orbits a day. Several techniques were tested to fill gaps between the orbits including the wind-trajectory method and data assimilation (Ziemke et al., 2014). Our analysis shows that the assimilated stratospheric ozone profiles provide the best overall measure of the stratospheric column ozone. We use the Modern-Era Retrospective analysis for Research and Applications, Version 2 (MERRA-2) ozone fields (Gelaro et al., 2017; Wargan et al., 2017) for this purpose. MERRA-2 assimilated stratosphere column ozone was found to agree within ±1–2 DU and standard deviations 2–4 DU with original MLS along-track measurements from the tropics to high latitudes. The MERRA-2 data assimilation system ingests Aura OMI v8.5 total ozone and MLS v4.2 stratospheric ozone profiles to produce global synoptic maps of ozone profiles from the surface to the top of the atmosphere; for our analyses we use MERRA-2 ozone profiles reported every 3 hours (0, 3, 6, … , 21 UTC) at a resolution of 0.625° longitude × 0.5° latitude (GMAO, 2015). MERRA-2 ozone profiles were integrated vertically from the top of the atmosphere down to tropopause pressure to derive maps of stratospheric column ozone. Tropopause pressure was determined from MERRA-2 re-analyses using standard PV-θ definition (2.5 PVU and 380 K). The resulting maps of stratospheric column ozone at 3-h intervals from MERRA-2 were then space-time collocated with EPIC footprints and subtracted from the EPIC total ozone, thus producing daily global maps of residual tropospheric column ozone sampled at the precise EPIC pixel times. These measurements of tropospheric ozone were further binned to 1^{o} latitude × 1^{o} longitude resolution. Figure 4 shows a schematic diagram that demonstrates the residual approach.

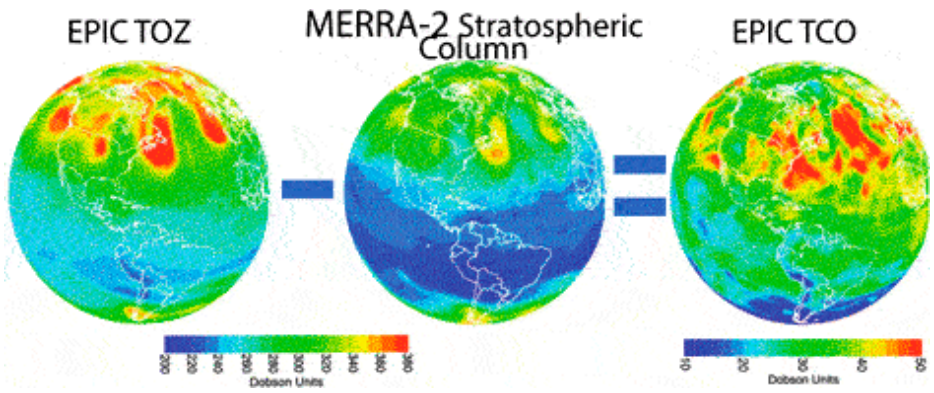

FIGURE 4 | Schematic illustration of the residuals approach for deriving tropospheric ozone columns. The left plot shows a synoptic TOZ map derived from EPIC on June 24, 2019. The center plot shows a map of stratospheric ozone column from MERRA-2 for the same time. The TCO is derived by subtracting MERRA-2 stratospheric column from TOZ.

UV measurements have reduced sensitivity to ozone changes in the boundary layer. To facilitate error analysis, Column Weighting Functions (CWF) have been included in EPIC version 3 processing (see in the Supplementary Material) to help users interpret EPIC total ozone retrievals and indicate the weight of measurements in each layer. The shape of CWF are determined by the sensitivity of measured albedos to changes in ozone in different atmospheric layers. CWF are typically close to 1 in all layers except for the boundary layer (Supplementary Figure S1) indicating that the measurements are very sensitive to ozone changes in those layers. CWF in the lowest boundary layer ranges between 0 and 0.7, with low values close to 0 observed over high terrain or high clouds when measurements in the boundary layer are not available. CWF represent the fraction of ozone variations in that layer that can be retrieved. The magnitude of CWF in the boundary layer depends on SZA/SLA, reflectivity, and scene pressure (terrain height).

For comparisons with independent measurements like sondes, we need to account for the limited sensitivity of UV satellite measurements to the variability of ozone in the low troposphere including the boundary layer (BL) below ~700 hPa. To do this, we used simulated tropospheric ozone derived from GEOS-Replay (Strode et al., 2020) constrained by the MERRA-2 meteorology through so-called replay method, whereby the analysis increments recalculated from MERRA-2 are used by the GEOS model in dynamical tendency calculations (Orbe et al., 2017). This correction

represents a seasonal-cycle adjustment, since ozone variability in the troposphere including BL is largely due to the seasonal-cycle. From the GEOS-Replay simulation we constructed a 12-years (2005–2016) average global seasonal climatology of tropospheric ozone columns in the BL based on 365 days of the year at $1^{o} \times 1^{o}$ horizontal gridding. To estimate adjustments to EPIC TCO, we first calculate the differences in BL ozone between this seasonal model-based climatology and the zonal-mean apriori values used in the EPIC retrieval algorithm (the ML climatology from McPeters and Labow, 2012). We then applied EPIC measured CWF to these BL ozone differences to estimate the ozone amount that EPIC measurements miss due to reduced sensitivity in the bottom layer (layer 0: 506 hPa -1,013 hPa). These corrections are then added to the EPIC tropospheric ozone columns to account for ozone variability in the BL (see in the Supplementary Material). Our analysis indicates that the global patterns for the corrections are very persistent between years dominated by strong seasonal variability.

Figure 5 shows the spatial distribution of the BL corrections for October 20, 2020, based on the GEOS-Replay model. There is a clear wave-1 structure in these corrections with a negative error of ~ 2–6 DU over the tropical Pacific Ocean. This is because the ML apriori monthly zonal means do not capture longitudinal ozone variability. Negative corrections also correspond to places with high terrain. Positive corrections such as those over Africa, the Arabian Peninsula, India, and east China are regions of seasonally recurring biomass burning and other pollution that cause an increase in the BL ozone.

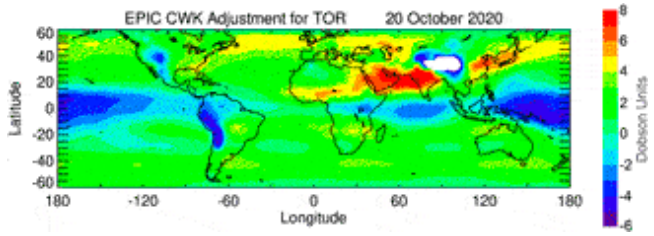

FIGURE 5 | Spatial map of the CWF adjustment for the EPIC TCO due to reduced EPIC sensitivity to BL ozone for 20 October 2021. This correction is derived by applying EPIC CWFs for the bottom layer (506 hPa-1000 hPa) to the differences between GEOS-Replay model and ML apriori ozone.

Tropospheric ozone derived from satellite instruments prior to EPIC has been limited to maps sampled at fixed local times. A great advantage of EPIC is that tropospheric maps can be made every 1–2 h from the sunlit portion of the Earth with samples across the range of local solar times. Such maps provide information at times not sampled by polar orbiting satellites, allowing us to better capture and study short-scale, regional variability of tropospheric ozone.

Correlative Satellite Measurements

To validate EPIC ozone measurements, we use data obtained from two satellite sensors that operate on board polar orbiting satellites, OMI (Ozone Monitoring Instrument) and OMPS (Ozone Mapping and Profiling Suite). OMPS was launched in October 2011 on the Suomi National Polar-orbiting Partnership (SNPP) satellite and includes both nadir- and limb-viewing modules. In this study we will use total ozone maps derived from OMPS Nadir Mapper (NM). The NM is a hyperspectral imaging push-broom sensor with a 110° cross-track field of view (FOV), 35 cross-track bins, and a 0.27° along track slit width corresponding to a 50 × 50 km^2 resolution. It measures solar backscattered ultraviolet radiation in a spectral range from 300 to 380 nm. The OMPS NM algorithm is based on the NASA version 8 total ozone algorithm (Bhartia and Wellemeyer, 2002) and uses a pair of wavelengths to derive total ozone. The ozone absorption cross-sections used in the OMPS NM algorithm are the same ones used for EPIC (Daumont et al., 1992; Malicet et al., 1995; Brion et al., 1998). The most recent version 2.1 of OMPS NM, which we used in this study, has been evaluated by (McPeters et al., 2019). They found that total column ozone data from the OMPS NM agree well with NOAA-19 SBUV/2 with a zonal average bias of −0.2% over the 60□ S to 60□ N latitude zone.

OMI, onboard the Aura satellite, started taking regular measurements in August 2004. OMI employs a hyperspectral imaging CCD in a push-broom mode to observe solar backscatter radiation in the 270–500 nm spectral range. The OMI sensor provides 60 cross-track bins with a FOV at nadir of about 13 km × 25 km. The wide scanning swath and 90-min polar orbit of OMI provides daily global maps of total ozone at 13:30 local solar equator crossing time. In this study, we use version 8.5 of OMI ozone data, processed with the version 8 algorithm (Bhartia and Wellemeyer, 2002). The most significant enhancement in OMI v8.5 is that the longer wavelengths

measured by OMI are used to infer cloud height on a scene-by-scene basis (Vasilkov et al., 2008). OMI data are processed using Bass and Paur (1984) ozone absorption cross-sections. In 2008 the OMI started to experience blockage of the center-right part of each swath caused by peeling of the protective film on the spacecraft. The affected cross-track positions are flagged and are not used in our analysis. Comparison of OMI total ozone retrievals with an ensemble of Brewer and Dobson instruments and satellite SBUV measurements shows 1–1.5% bias, and a small relative drift against SBUV of about 0.5% over 10 years (McPeters et al., 2015).

Correlative Ground-Based Measurements

We used a network of Brewer spectrophotometers at multiple locations to evaluate EPIC TOZ measurements. The Brewer instrument acquires measurements at five UV wavelengths (306.3, 310.1, 313.5, 316.8 and 320.0 nm) to retrieve total column ozone (Kerr et al., 1985). The Brewer spectrometers are routinely calibrated with a reference triad of Brewers located in Toronto (Fioletev et al., 2005). The daily Brewer total ozone values are reported to the World Ozone and Ultraviolet Data Center (WOUDC). Brewer spectrometers perform measurements throughout the day, but there are only a small number of stations that report hourly Brewer data with the rest reporting daily average ozone amounts. We used Brewer daily averages in this study.

Ozonesonde measurements launched on air balloons provide *in-situ* measurements of ozone vertical profiles in the troposphere and low stratosphere that provide valuable validation for EPIC TCO. In this study we use measurements from 12 stations with several stations updated into year 2020. There is about one measurement per week at many sonde locations. We use daily measurements from Southern Hemisphere ADditional OZonesondes (SHADOZ) (Thompson et al., 2017; Witte et al., 2017), World Ozone and Ultraviolet Data Center (WOUDC) and Network for the Detection of Atmospheric Composition Change (NDACC). In our analysis, each ozone profile was integrated vertically from ground up to the tropopause to derive TCO. Tropopause height was determined the same as for EPIC TCO using MERRA-2 analyses with standard PV-θ definition (2.5 PVU, 380 K).

The ground-based Pandonia Global Network (PGN) uses temperature stabilized Avantes spectrometers in each Pandora instrument that

simultaneously acquires direct-sun measurements in 300–525 nm range in oversampled steps of 0.5 nm every 40 s. Stray light from longer wavelengths is suppressed by using a short-wavelength bandpass filter. The Pandora ozone retrieval algorithm is based on an optimized spectral fitting within the ozone absorption range after correcting for aerosol amounts (Tzortziou et al., 2012; Herman et al., 2015; Herman et al., 2017). There are over 50 operating Pandora instruments within PGN and a number of additional Pandoras at various location through the world that are not yet incorporated into the official PGN.

RESULTS

Evaluation of EPIC TOZ

To evaluate the accuracy of EPIC calibrations, we compared EPIC version 3 TOZ retrievals with correlative satellite observations from OMPS NM and OMI. Figure 6 shows mean differences in Dobson Units (DU) between EPIC version 3 and OMPS and OMI as a function of latitude for different seasons (color lines). The mean differences were calculated over a period from the beginning of the EPIC mission in June 2015 up to the end of 2020. The EPIC data have been filtered as described above in *EPIC Total Ozone*. The data in Figure 6 were first averaged monthly and zonally prior to calculating these 6-years differences. The mean biases are mostly within ±5–7 DU (or 1.5–2.5%). The biases between EPIC and OMI and EPIC and OMPS are smaller and mostly positive in the tropical region (30°S-30°N). Outside the tropics, biases are larger and vary seasonally. In the SH biases are mostly negative with stronger biases during SH summer in January (Figure 6, black lines). The biases are somewhat smaller between EPIC and OMI particularly in the tropics and NH (Figure 6B), while differences with OMPS in the NH tend to be larger and negative in April and October (Figure 6A). During NH summer in July the biases between EPIC and OMPS rapidly change at higher latitudes turning from positive to negative. Differences between Figures 6A,B indicate the magnitude of differences between OMI and OMPS TOZ.

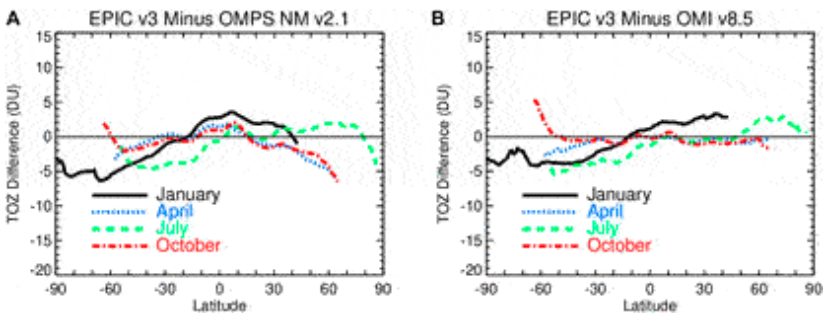

FIGURE 6 | Mean biases in TOZ between EPIC v3 and OMPS NM v2.1 **(A)** and EPIC v3 and OMI v8.5 **(B)** in DU. Biases are shown for 4 months (shown in different colors) and calculated over period from June 2015 to December 2020. Only EPIC retrievals with the algorithm flag equal to 1, or 101, or 111 and SZA and SLA <70° were used in these comparisons.

To evaluate the effect of the EPIC cloud correction implemented in version 3 by utilizing simultaneous cloud height retrievals from the EPIC oxygen A-band channel, we compared EPIC and OMI TOZ retrievals for different conditions: all coincident cases with reflectivity $0 < R < 1$, low-reflectivity cases $R < 0.15$, and cases with large reflectivity $R > 0.7$ (see Figure 7). The cloud height correction in the OMI algorithm uses the Optical Centroid Pressure (OCP) approach (Vasilkov et al., 2008) that utilizes OMI measurements in visible range between 460–490 nm. This algorithm is completely independent from the EPIC A-Band cloud heigh retrievals (Yang et al., 2019). There is a very good agreement between the two methods with differences less than 50 hPa over a broad range of cloud fraction values (see Supplementary Figure S2), which would result in an offset of less than 1 DU. The offset between two cloud height algorithms is larger at very low cloud fraction (<0.1), but it has almost no effect on retrieved ozone.

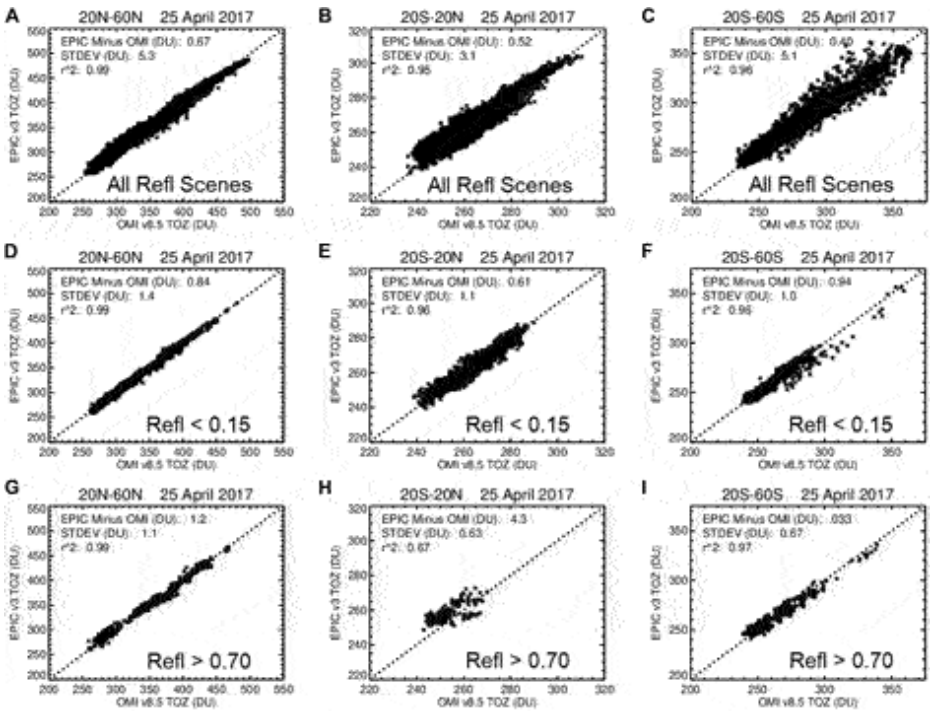

FIGURE 7 | Comparisons between coincident EPIC and OMI TOZ measurements on April 25, 2017 in Dobson Units for all conditions **(A–C)**, for cases with low scene reflectivity R < 0.15 with small cloud fraction and low-altitude clouds **(D–F)**, and for cases with reflectivity values above >0.7 **(G–I)** that effectively corresponds to conditions with high-altitude convective clouds. The comparisons are binned in 3 wide latitude zones: 20°N-60°N (left column), 20°S-20°N (center column) and 20°S-60°S (right column). The mean differences and standard deviations are shown on each panel.

Our analysis has revealed that the mean biases between EPIC and OMI TOZ remain the same for two subsets (R < 0.15 and 0 < R < 1, see Figures 7A–F). That means the cloud correction implemented in version 3 does not produce systematic errors in the EPIC TOZ retrievals. There is an increase in standard deviations of differences for the subset where all conditions (0 < R < 1) were included (Figures 7A–C). This is consistent with our expectations that the cloud correction would produce random noise in the retrieved ozone fields but not a systematic bias. When the scene reflectivity exceeds 0.7 it typically corresponds to conditions with large cloud fraction and high-altitude, convective clouds. The biases increase in the tropics between the two instruments for R > 0.7, but there is no change in mid-latitudes. A fraction of these increased biases in the tropics might be due to consistently larger cloud heights derived from the A-Band for high cloud fractions (see

Supplementary Figure S2). Additionally, differences in cloud coverage at the time of satellite measurements and satellites FOVs can contribute as well.

We also examined the relative degree of agreement between EPIC TOZ and ground-based measurements obtained from Brewer and Pandora instruments. The list of Brewer, Pandora and sonde stations used in this study is provided in Supplementary Table S1. Figure 8 shows time series of daily mean Brewer and EPIC TOZ measurements at six locations in 2018. These stations represent a wide range of latitudes with a long available record of daily Brewer measurements in 2015–2020. We did not include stations at high latitudes to avoid EPIC measurements at SZA and SLA that exceed 70°. These plots show sub-seasonal changes in TOZ as measured by EPIC and Brewers. The observed biases with Brewer measurements are within the range of differences found with satellite observations. There is a consistently high correlation between EPIC and Brewer measurements ($r^2 > 0.96$), indicating that EPIC can accurately capture day-to-day variations in TOZ.

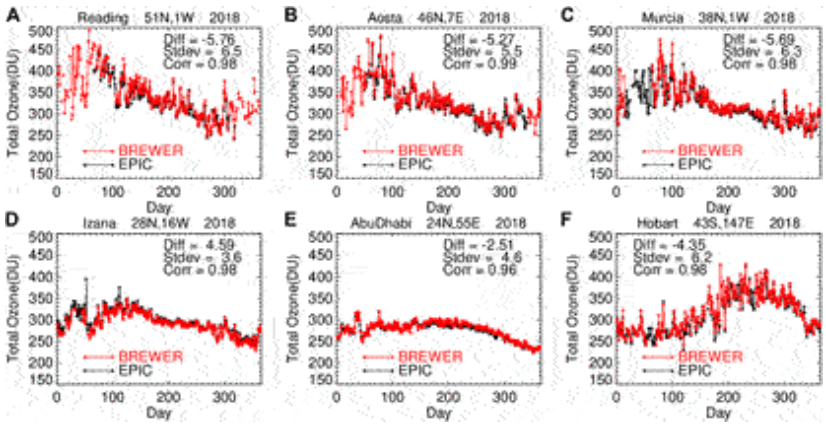

FIGURE 8 | Time series of daily-average Brewer TOZ measurements (red) and EPIC v3 daily overpasses (black) at 6 ground-based stations world-wide in 2018: **(A)** Reading, United Kingdom, **(B)** Aosta, Italy, **(C)** Murcia, Spain, **(D)** Izana, Spain, **(E)** Abu Dhabi, United Arab Emirates, and **(F)** Hobard, Australia. The mean differences, standard errors of the mean in DU and correlation coefficients are shown at each panel.

Figure 9 shows comparisons between EPIC and Pandora TOZ from 4 selected sites in the NH and SH where there is a long record of ground-based data from well-calibrated Pandora spectrometer instruments. We also compared with overpasses derived from OMI and OMPS NM. EPIC TOZ overpasses for each selected site include about 3–4 samples per day separated by 1–2 h, while OMI and OMPS overpasses have only 1 to 2

points per day, with most samples consisting of 1 point per day. When there are two points from consecutive polar orbits, they are separated by about 90 min. The ground-based Pandora data consists of ozone samples obtained every 40 s throughout each day for solar zenith angles SZA less than 70°. The time span of PGN Pandora data is much less than that for satellite data. Because of the different fields of view FOV (EPIC 20 × 20 km^2, OMI 13 × 24 km^2, OMPS 50 × 50 km^2 and Pandora about 50 × 50 m^2) and different sampling times (UT), the comparisons in Figure 9 are done for 3-months averages to verify calibration and retrieval algorithm rather than individual scene comparisons. The noise level in comparisons drop significantly depending on the averaging period (see Supplementary Figure S5). The 3-months averages (solid lines in Figure 9) match closely for all four instruments. The mean differences between EPIC and OMI and OMPS are smaller than 1% at all stations and consistent with zonally averaged results shown in Figure 6. Pandora TOZ measurements in the current version (PGN version 0P1) have significant differences with all three satellite instruments, but closely track the observed TOZ variation.

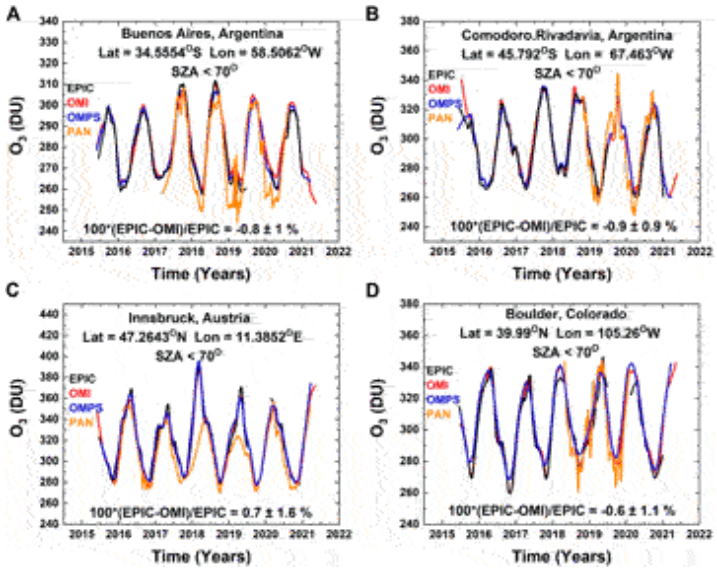

FIGURE 9 | A comparison of EPIC TOZ time series (black) with Pandora (red), OMI (blue) and OMPS (orange) at four ground-based stations: Buenos Aires, Argentina **(A)**, Comodoro, Argentina **(B)**, Innsbruck, Austria **(C)**, and Boulder, Colorado United States **(D)**. The lines are a Local-Linear Least-Squares (LOESS) fit to the data (Cleveland, 1979) equivalent to approximately a 3-months running average. The biases between EPIC and OMI (in %), indicated in each panel, are done for 3-months averages. EPIC data had been screened as described in *Earth Polychromatic Imaging Camera Total Ozone*.

To evaluate EPIC performance at short time scales, we have compared EPIC with ground-based Pandora and coincident OMI measurements at two ground-based locations over 1-year period (Figure 10). There is a lot of variability in TOZ during winter and spring at the mid-latitude station in Greenbelt, Maryland (Figure 10A), showing that EPIC agrees well with both Pandora and OMI. TOZ is lower in summer and autumn months as a part of the TOZ seasonal cycle. Pandora in Greenbelt seems to underestimate TOZ in summer months compared to both OMI and EPIC. Measurements at Fairbanks, Alaska show a significant seasonal change where TOZ is close to 400–450 DU in winter and then gradually dropping to ~250 DU in the late summer - early autumn (Figure 10B). EPIC captures these seasonal as well as smaller scale changes in TOZ compared to both Pandora and OMI. However, at high SZA (>70°) EPIC tends to underestimate TOZ compared to OMI. The two instruments also see ozone variability differently at high SZA conditions: OMI measurements are showing more small-scale variations (blue line in Figure 10B), while the EPIC curve (black line in Figure 10B) is smoother. This is partly because we considered all EPIC measurements at Fairbanks, including those from 325 nm triplet to cover winter months. These results suggest that retrievals from the 325 nm triplet, used at high SZA, are not just biased, but might also have less sensitivity to real changes in ozone. Further investigations are needed to understand the reason for reduced quality of 325 nm EPIC retrievals. Pandora measurements in Alaska also show low biases in summer months compared to EPIC and OMI.

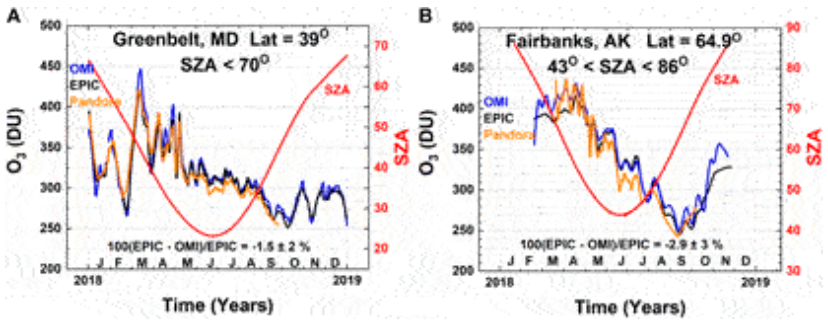

FIGURE 10 | Comparisons of EPIC TOZ (in DU) with ground-based Pandora and satellite OMI TOZ measurements in 2018 at two locations: **(A)** Greenbelt, MD, United States and **(B)** Fairbanks, Alaska, United States. Plots show time series of TOZ measurements derived by fitting the LOESS (equivalent to a 3-weeks moving average) to all available EPIC (black lines), Pandora (orange) and OMI (blue) measurements at both locations. The red curve shows the average SZA for all EPIC measurements with a scale shown on the right hand. At Greenbelt only EPIC measurements with SZA <70° were used, while at Fairbanks all available EPIC measurements were included.

Evaluation of EPIC Tropospheric Column Ozone

To evaluate EPIC TCO we use sonde observations at multiple stations (Figure 11). For the comparisons with sondes, we applied corrections for the boundary layer ozone as described in *Earth Polychromatic Imaging Camera Tropospheric Ozone Algorithm*. In Figure 11 we also applied −3 DU constant adjustment to EPIC TCO everywhere. This constant adjustment decreases biases between EPIC and sonde TCO at all stations. The 3 DU bias can be a result of ~0.3% error in 317.5 nm absolute radiance calibrations of EPIC, which is substantially below the ±1% quoted accuracy of EPIC and OMPS calibrations. Tropospheric ozone changes significantly with latitude and season. EPIC TCO accurately captures these variations from one station to another with the mean biases against independent sonde measurements of ±2.5 DU (or ~10%). It is important to note that there are numerous sources of errors in the residual method used to derive EPIC TCO including uncertainties in stratospheric ozone column, tropopause height, cloud height. In addition, ozone sondes provide local measurements over the station, while satellite EPIC TCO represent gridded averages. Therefore, larger noise levels (captured by standard deviations of differences) in these comparisons are expected.

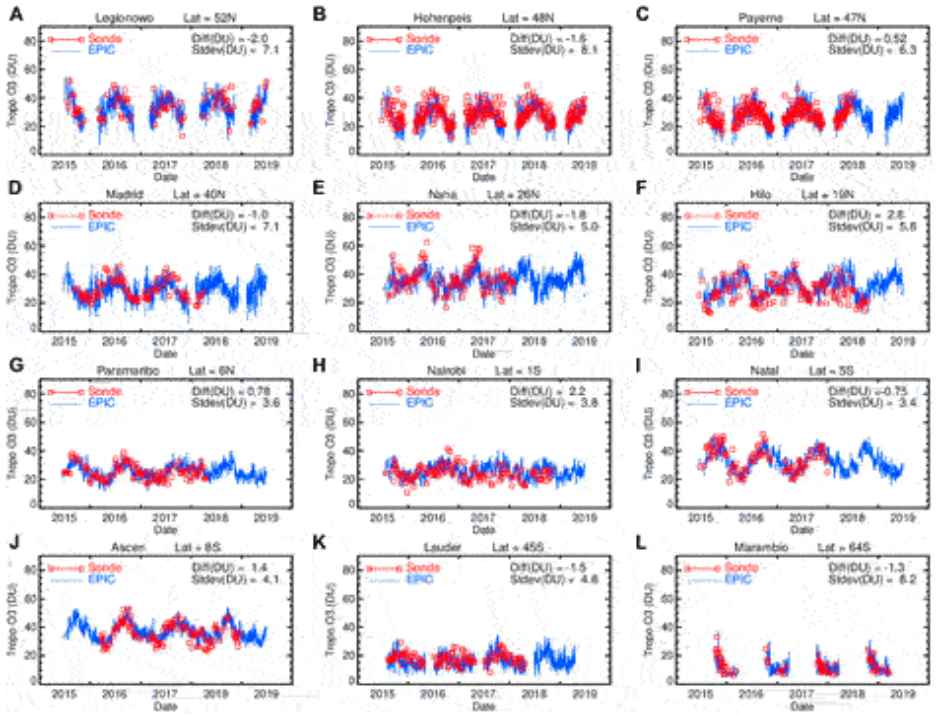

FIGURE 11 | Time series of EPIC (blue lines) and sonde (red squares) daily TCO in 2015–2019 at 12 ground-based locations: **(A)** Leginowo, Poland; **(B)** Hohenpeissenberg, Germany; **(C)** Payerne, Switzerland; **(D)** Madrid, Spain; **(E)** Naha, Japan; **(F)** Hilo, United States; **(G)** Paramaribo, Suriname; **(H)** Nairobi, Kenya; **(I)** Natal, Brazil; **(J)** Ascension Island; **(K)** Lauder, New Zeland; **(L)** Marambio, Antarctica. Mean differences and standard deviations in DU between EPIC and coincident sonde TCO measurements are quoted in each panel.

Figure 12 shows the monthly zonal mean EPIC TCO as a function of time and latitude. It shows that on average TCO values in the SH are smaller than those in the NH, in agreement with our understanding of tropospheric ozone chemistry. The seasonal cycle is not very strong in the SH, while it is very pronounced in the tropics and NH. In the tropics, the seasonal cycle in TCO peaks in September-November due largely to lightning and biomass burning, with a minimum seen in January-March (e.g., Sauvage et al., 2007). In the NH, the seasonal peak varies from spring months in the tropics/subtropics to summer months in the mid-latitudes due to variations in combined spring-summer stratosphere-troposphere exchange (STE) and pollution (Lelieveld and Dentener, 2000; de Laat et al., 2005; Ziemke et al., 2006; and references therein).

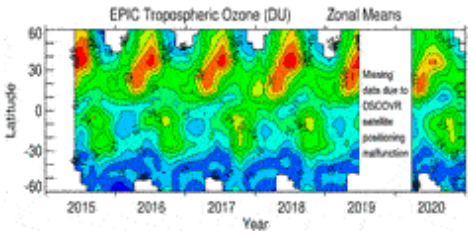

FIGURE 12 | EPIC monthly zonal mean TCO as a function of time and latitude. These TCO values were adjusted with CWF to account for reduced sensitivity to the boundary layer. Results are shown with 3 DU steps.

EPIC did not make observations between late June 2019 and February 2020 due to malfunctioning of the satellite positioning (now corrected). After measurements resumed, there were no significant calibration changes. However, a substantial drop of ~3–4 DU (~5–10%) in TCO over much of the NH in spring and summer of 2020 can be seen in Figure 12. A part of these TCO reductions in 2020 appears to be related to the unprecedented strong, cold, and long-lasting stratospheric polar vortex over the Arctic in winter and spring 2019–2020 (Lawrence et al., 2020; Manney et al., 2020) that led to substantial polar ozone losses (e.g., DeLand et al., 2020). Ground-based ozone observations (Steinbrecht et al., 2021) confirmed a reduction in both total and tropospheric ozone in spring and summer 2020 attributing ~25% of the reduction to the 2019/2020 Arctic ozone depletion. Another factor that potentially contributed to the observed reduction in EPIC TCO in the NH is related to the global COVID-19 pandemic. COVID-related measures in spring and summer 2020 resulted in the reduction of anthropogenic emissions including Volatile Organic Compounds (VOCs) and NO_X ($NO + NO_2$) which are precursors for tropospheric ozone production (e.g., Liu et al., 2020). Steinbrecht et al. (2021) found from ozonesonde analyses about 7% reduction in tropospheric ozone throughout the NH free troposphere in spring-summer 2020. The 2–4 DU (5–10%) reductions in zonal-mean EPIC TCO in the NH (Figure 12) are consistent with the 7% reductions described by Steinbrecht et al. (2021).

We also compared EPIC daily TCO with daily TCO derived from OMI and OMPS nadir-mapper satellite instruments. For OMI and OMPS (similar to EPIC), MERRA-2 stratospheric columns were space-time collocated with total ozone pixel measurements to derive TCO. Figures 13A–C show maps of TCO on July 7, 2020, as observed by these three satellite instruments. We

note that EPIC TCO measurements in Figure 13, as with all EPIC TCO measurements presented in this study, include the CWF correction for the boundary layer ozone discussed in *Earth Polychromatic Imaging Camera Tropospheric Ozone Algorithm*, while OMPS and OMI TCO have not been corrected. There is a good agreement in spatial patterns of TCO such as increased tropospheric ozone over the Midwest and eastern coast of the United States that extends over the Atlantic Ocean due to extra-tropical weather variability. There are missing data in OMI measurements caused by the sensor's row anomalies (i.e., seen as black bands in Figure 13B for OMI), but similarities in global patterns are seen. Figures 13D–I show one-to-one comparisons between EPIC TCO with OMI and OMPS TCO for three latitude zones (indicated). There is a good agreement in the NH and tropics with mean biases of less than ±2 DU, but there are strong negative biases of −4 to −5 DU in the SH with increased standard deviations. Similar negative biases were also observed in EPIC TOZ in the SH extra-tropics with respect to OMI and OMPS (see Figure 6) with the largest biases in July and January of about −5 DU.

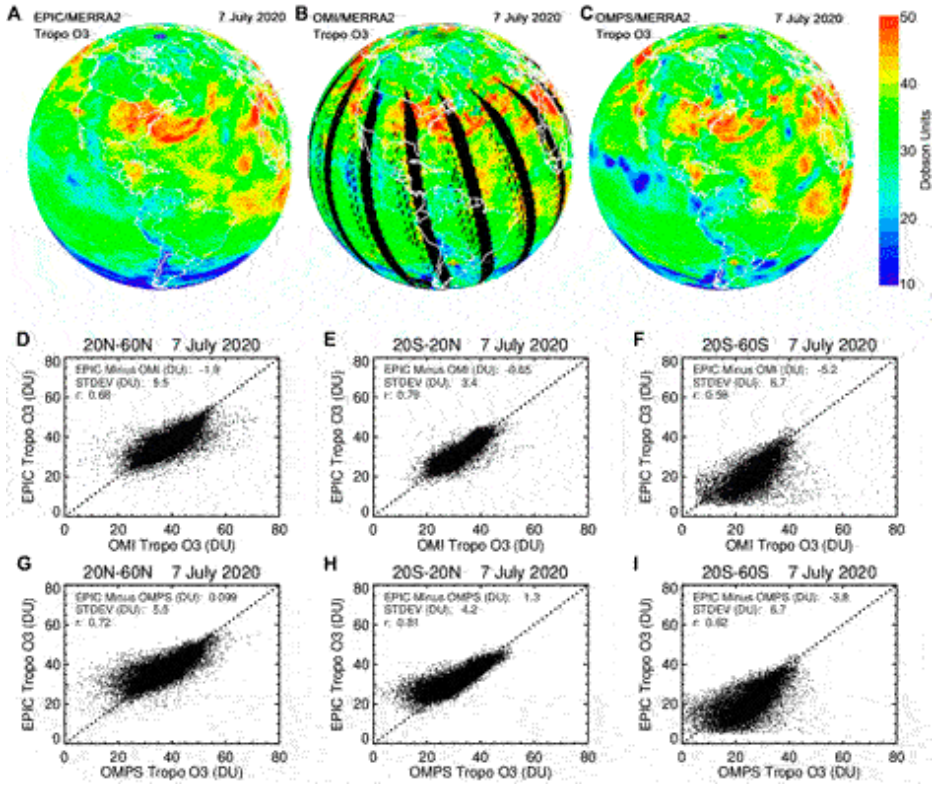

FIGURE 13 | The three upper color panels show daily maps of TCO (in DU) derived from EPIC **(A)**, OMI **(B)** and OMPS **(C)** on July 7, 2020. The lower panels **(D–I)** show scatter plots of EPIC TCO against coincident OMI (center row, **D–F**) and OMPS (lower row, **(G–I)**). The scatter plots are shown for three wide latitude zones: 20°N-60°N (left column, **D,G**), 20°S-20°N (center column, **E,H**) and 20°S-60°S (right column, **F,I**). The mean differences and corresponding standard deviations (both in DU) are shown in each panel along with correlation coefficients.

We compared coincident EPIC daily TCO with OMI and OMPS daily TCO over the entire EPIC operational period between June 2015 and December 2020 and calculated offsets and standard deviations as a function of month and latitude (Figure 14). We found that in the NH the biases are mostly positive and ranging between 1 and 3 DU. The biases with respect to OMPS become negative and increase at high northern latitudes. In the SH, EPIC TCO tends to have negative biases with OMI and OMPS, particularly in winter and summer months. A similar pattern can be seen in Figure 6 between EPIC and OMPS TOZ. The comparisons are less noisy in the tropics and during mid-latitude summer in the NH with standard deviations of 3–5 DU (10–15%). In wintertime in the NH the noise tends to increase almost by a factor of two up to 9 DU (or 40–50%), even though the seasonal

peak in TCO occurs during the summer. These indicate that the main uncertainties in the tropospheric ozone detection are related to increased errors in deriving TOZ at high SZA and reduced accuracy of stratospheric ozone columns in wintertime. Stratospheric ozone variability is increasingly larger in the winter hemisphere (e.g., Kramarova et al., 2018) as well as variations in tropopause heights, which would result in increased uncertainties in estimating stratospheric ozone columns from MERRA-2.

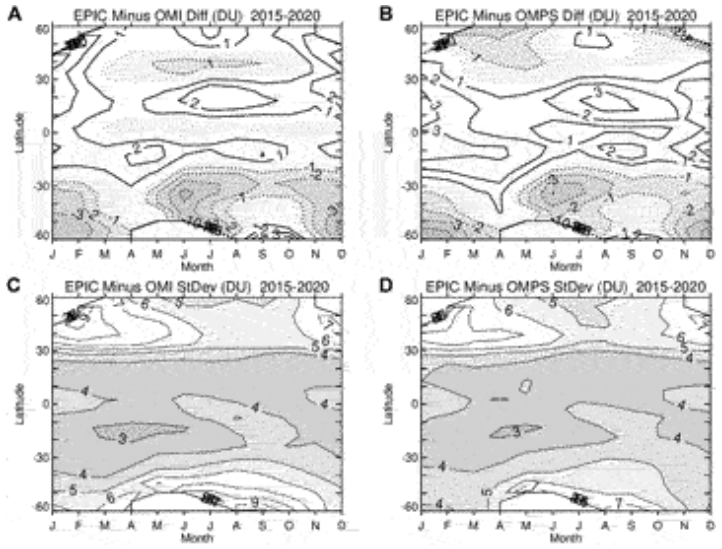

FIGURE 14 | Differences (in DU) between coincident EPIC TCO daily values and those from **(A)** OMI and **(B)** OMPS over the period between June 2015 and December 2020 shown as function of month and latitude. The positive differences are shown as solid lines in a-b, and negative as dashed lines and shaded. The corresponding 1-sigma standard deviations of the differences with OMI and OMPS are plotted as **(C–D)**, respectively.

SUMMARY AND DISCUSSION

In this study we evaluated EPIC ozone products processed with the version-3 ozone algorithm, which includes several modifications compared to previous version 2 (Herman et al., 2018). First, an improved geolocation of EPIC scenes is applied in Version 3 Level 1 product (Blank et al., 2021) that ensures the filters are viewing the same geographic scene and solar/view angles are accurately estimated for each EPIC pixel thereby reducing errors in ozone retrievals. Second, the inclusion of simultaneous cloud-height information from EPIC A-Band (Yang et al., 2019) improves the scene pressure and the estimated ozone amount below the cloud. We have demonstrated in this study that the cloud correction based on the

simultaneous EPIC A-Band retrievals reduces features in the EPIC total ozone fields imposed by cyclonic activity and does not produce systematic biases in ozone. The third change is the addition of corrections for ozone and temperature profile shapes in the retrieval algorithm. And finally, version 3 includes column weighting functions and algorithm/error flags for each observation to facilitate error analysis.

Comparisons of EPIC total ozone columns with satellite instruments (SNPP OMPS and Aura OMI) demonstrated good agreement with mean biases within ±5–7 DU (or 1.5–2.5%). Outside of the tropics, biases with other satellite instruments show seasonal variability. In the SH, EPIC shows mostly negative biases compared to both OMI and OMPS with stronger biases during SH summer in January. Comparisons of daily EPIC total ozone columns with ground-based Brewer instruments at 6 sites show good agreement between EPIC and Brewers in capturing day-to-day variations in total ozone with consistently high correlation ($r^2 > 0.9$). The mean differences between EPIC and Brewers are within the same range as with satellite observations, and there are no obvious latitudinal patterns.

We examined EPIC tropospheric ozone columns derived by subtracting MERRA-2 stratospheric ozone columns from EPIC total ozone measurements and adjusted for reduced EPIC sensitivity to the boundary layer ozone. We compared daily TCO with matching TCO derived from ozonesondes at 12 stations over the period 2015–2019. We found that after removing a constant 3 DU offset between EPIC and sondes globally (at all stations) the biases in tropospheric column ozone are within ±2.5 DU (or ~±10%). We found that EPIC TCO captures latitudinal and seasonal variations in tropospheric ozone. The 3 DU offset can be a result of ~0.3% error in 317.5 nm absolute radiance calibrations of EPIC (note, that it is substantially lower than the quoted accuracy, ±1%, of EPIC and OMPS calibrations). In addition, we compared coincident EPIC daily TCO with OMI and OMPS daily TCO over the entire EPIC operational period between June 2015 and December 2020 and found that biases in tropospheric column ozone have similar magnitude and patterns to those seen in total ozone comparisons.

Analysis of time series of zonal mean EPIC TCO indicated a substantial drop of ~2–4 DU (~5–10%) over much of the NH in spring and summer of 2020, which is consistent with the 7% reductions in tropospheric ozone from ground-based observations described by Steinbrecht et al. (2021). A part of

this reduction is related to unprecedented Arctic stratospheric ozone losses in winter-spring 2019/2020 and to reductions in ozone precursor pollutants due to the COVID-19 pandemic.

In this study, we mostly used EPIC data derived from the 317 nm triplet and limited SZA and SLA to less than 70°. Our analysis revealed consistent biases between EPIC retrievals derived from the two triplets (317 and the 325 nm) that cannot be explained by the natural ozone variability. We demonstrated that the inclusion of the 325 nm EPIC retrievals led to substantial increase in systematic biases. The EPIC ozone algorithm switches to 325 nm triplet for conditions with high optical depth, which typically correspond to high SZA and SLA. The exact reasons for increased errors in EPIC ozone retrievals derived from the 325 nm triplet are under investigation. Errors in radiance simulations with a pseudo-correction for atmospheric sphericity at high SZAs and SLAs, reduced sensitivity to ozone at 325 nm compared to 317 nm, and uncertainties in absolute calibrations of the two EPIC channels are the main factors to consider. The current exclusion of EPIC 325 nm retrievals limits applications of EPIC data for studying ozone variability in early morning and late afternoon hours or at polar latitudes in months with high SZAs.

DATA AVAILABILITY STATEMENT

Publicly available datasets were analyzed in this study. This data can be found here: EPIC Total ozone data are available at https://eosweb.larc.nasa.gov/project/DSCOVR/DSCOVR_EPIC_L2_TO3_03 EPIC overpass data for TOZ and TCO, used in this paper, are available at https://avdc.gsfc.nasa.gov/pub/DSCOVR/Kramarova_et_al_Data/. SNPP OMPS NM v2.1 and Aura OMI v8.5 total ozone data can be downloaded from https://ozoneaq.gsfc.nasa.gov/data/ozone/. OMPS and OMI overpass over ground-based stations are available at https://acd-ext.gsfc.nasa.gov/anonftp/toms/. Ground-based Brewer measurements can be found at WOUDC (https://woudc.org/), NDACC (http://www.ndsc.ncep.noaa.gov/). Pandora total ozone measurements are available at http://data.pandonia-global-network.org/. Sondes: SHADOZ (https://tropo.gsfc.nasa.gov/shadoz/), WOUDC (https://woudc.org/), NDACC (http://www.ndsc.ncep.noaa.gov/). MERRA-2 data can be found here: https://disc.gsfc.nasa.gov/datasets?project=MERRA-2.

AUTHOR CONTRIBUTIONS

NK is the leading author of the paper. She was responsible for writing the paper, analyzing results, drawing conclusions, and interacting with co-authors. JZ is responsible for tropospheric ozone algorithm. For this paper, JZ compared EPIC TOZ and TCO with measurements from OMI/OMPS, Brewers and ozonesondes. L-KH is responsible for maintaining and developing of the EPIC ozone retrieval algorithm. For this paper, L-KH evaluated effects of various algorithmic parameters (like cloud heights, aerosol correction, Level 1 adjustments) on changes in retrieved ozone. JH was responsible for comparisons between EPIC and Pandora measurements, as well as for evaluation of EPIC and OMI/OMPS total ozone overpasses at several ground-based stations. KW contributed to this paper by helping with MERRA-2 stratospheric ozone profiles needed for EPIC tropospheric ozone derivation. CS helped with the development of the EPIC ozone retrieval algorithm and with calibration of EPIC UV channels by providing calibrated OMPS measurements. GL helped with comparisons of EPIC TOZ with Brewer measurements. LO assisted with interpretation and application of the GEOS-Replay model data.

FUNDING

NK, JZ and L-KH were supported by NASA ROSES proposal “Improving total and tropospheric ozone column products from EPIC on DSCOVR for studying regional scale ozone transport” (18-DSCOVR18-0,011, DSCOVR Science Team). JH is supported DSCOVR/EPIC NASA project under UMBC task 00,011,511. L-KH, KW, CS and GL were supported by SSAI Support for Atmospheres, Modeling, and Data Assimilation (NNG17HP01C) contract with NASA GSFC. Luke Oman was supported by NASA Modeling, Analysis, and Prediction (MAP) program.

PUBLISHER’S NOTE

ACKNOWLEDGMENTS

Authors would like to thank P.K. Bhartia (NASA GSFC) and David Haffner (SSAI/NASA GSFC) for constructive discussion of the results presented in

this paper that helped to improve the manuscript. The GEOS-Replay simulation was supported by the NASA MAP program and the high-performance computing resources were provided by the NASA Center for Climate Simulation (NCCS). MERRA-2 is an official product of the Global Modeling and Assimilation Office at NASA GSFC, supported by NASA's Modeling, Analysis and Prediction (MAP) program. Authors would like to thank the editor GS and three reviewers (YH, VN, and DF) for their thoughtful comments and suggestions that improved the manuscript.

SUPPLEMENTARY MATERIAL

The Supplementary Material for this article can be found online at: https://www.frontiersin.org/articles/10.3389/frsen.2021.734071/full#supplementary-material

REFERENCES

Bass, A. M., and Paur, R. J. (1984). "The Ultraviolet Cross-Sections of Ozone. I. The Measurements," in *Proc. Quadrenniel Ozone Symp., Halkidiki, Greece, 3–7 September, 1984* ed . Editors C. Zerefos, A. Ghazi, and Dordecht. Reidel, 606–616.

Bhartia, P. K., and Wellemeyer, C. W. (2002). "OMI TOMS-V8 Total O3 Algorithm," in *Algorithm Theoretical Baseline Document: OMI Ozone Products* ed . Editor P. K. Bhartia, vol. II. ATBD-OMI-02, version 2.0, Aug. 2002.

Blank, K., Huang, L. K., Herman, J., and Marshak, A. (2021). EPIC Geolocation*Front. Remote Sens.* . (in preparation).

Brion, J., Chakir, A., Charbonnier, J., Daumont, D., Parisse, C., and Malicet, J. (1998). Absorption Spectra Measurements for the Ozone Molecule in the 350–830 Nm Region. *J. Atmos. Chem.* 30, 291–299. doi:10.1023/a:1006036924364

Caudill, T. R., Flittner, D. E., Herman, B. M., Torres, O., and McPeters, R. D. (1997). Evaluation of the Pseudo-spherical Approximation for Backscattered Ultraviolet Radiances and Ozone Retrieval. *J. Geophys. Res.* 102, 3881–3890. doi:10.1029/96jd03266

Cede, A., Huang, L.-K., McCauley, G., Herman, J., Blank, K., Kowalewski, M., et al. (2021). Raw EPIC Data Calibration. *Front. Remote Sens.* (in review). doi:10.3389/frsen.2021.702275

CEOS (2011). *Report of the Committee on Earth Observation Satellites (CEOS) Atmospheric Composition Constellation (ACC) "A Geostationary Satellite Constellation for Observing Global Air Quality: An International Path Forward"*. Available at: http://ceos.org/document_management/Virtual_Constellations/ACC/Documents/AC-VC_Geostationary-Cx-for-Global-AQ-final_Apr2011.pdf.

Cleveland, W. S. (1979). Robust Locally Weighted Regression and Smoothing Scatterplots. *J. Am. Stat. Assoc.* 74, 829–836. doi:10.1080/01621459.1979.10481038

Daumont, D., Brion, J., Charbonnier, J., and Malicet, J. (1992). Ozone UV Spectroscopy I: Absorption Cross-Sections at Room Temperature. *J. Atmos. Chem.* 15, 145–155. doi:10.1007/bf00053756

de Laat, A. T. J., Aben, I., and Roelofs, G. J. (2005). A Model Perspective on Total Tropospheric O3column Variability and Implications for Satellite Observations. *J. Geophys. Res.* 110, D13303. doi:10.1029/2004JD005264

DeLand, M. T., Bhartia, P. K., Kramarova, N., and Chen, Z. (2020). OMPS LP Observations of PSC Variability during the NH 2019–2020 Season. *Geophys. Res. Lett.* 47, e2020GL090216.

doi:10.1029/2020gl090216

Dobber, M., Voors, R., Dirksen, R., Kleipool, Q., and Levelt, P. (2008). The High-Resolution Solar Reference Spectrum between 250 and 550 Nm and its Application to Measurements with the Ozone Monitoring Instrument. *Sol. Phys.* 249, 281–291. doi:10.1007/s11207-008-9187-7

Fioletov, V. E., Kerr, J. B., McElroy, C. T., Wardle, D. I., Savastiouk, V., and Grajnar, T. S. (2005). The Brewer Reference Triad. *Geophys. Res. Lett.* 32, L20805. doi:10.1029/2005GL024244

Gelaro, R., McCarty, W., Suárez, M. J., Todling, R., Molod, A., Takacs, L., et al. (2017). The Modern-Era Retrospective Analysis for Research and Applications, Version 2 (MERRA-2). *J. Clim.* 30, 5419–5454. doi:10.1175/JCLI-D-16-0758.1

Global Modeling and Assimilation Office (GMAO) (2015b). *MERRA-2 inst3_3d_asm_Np: 3d,3-Hourly,Instantaneous,Pressure-Level,Assimilation,Assimilated Meteorological Fields V5.12.4, Greenbelt, MD, USA, Goddard Earth Sciences Data and Information Services Center (GES DISC)*. Accessed: [Data Access July 29, 2021]. doi:10.5067/QBZ6MG944HW0

Global Modeling and Assimilation Office (GMAO) (2015a). *MERRA-2 inst3_3d_asm_Nv: 3d,3-Hourly,Instantaneous,Model-Level,Assimilation,Assimilated Meteorological Fields V5.12.4*. Greenbelt, MD, USA: Goddard Earth Sciences Data and Information Services Center (GES DISC). Accessed: [Data Access Date]. doi:10.5067/WWQSXQ8IVFW8

Herman, J., Evans, R., Cede, A., Abuhassan, N., Petropavlovskikh, I., and McConville, G. (2015). Comparison of Ozone Retrievals from the Pandora Spectrometer System and Dobson Spectrophotometer in Boulder, Colorado. *Atmos. Meas. Tech.* 8, 3407–3418. doi:10.5194/amt-8-3407-2015

Herman, J., Evans, R., Cede, A., Abuhassan, N., Petropavlovskikh, I., McConville, G., et al. (2017). Ozone Comparison between Pandora #34, Dobson #061, OMI, and OMPS in Boulder, Colorado, for the Period December 2013-December 2016. *Atmos. Meas. Tech.* 10, 3539–3545. doi:10.5194/amt-10-3539-2017

Herman, J., Huang, L., McPeters, R., Ziemke, J., Cede, A., and Blank, K. (2018). Synoptic Ozone, Cloud Reflectivity, and Erythemal Irradiance from Sunrise to sunset for the Whole Earth as Viewed by the DSCOVR Spacecraft from the Earth-Sun Lagrange 1 Orbit. *Atmos. Meas. Tech.* 11, 177–194. doi:10.5194/amt-11-177-2018

Hubert, D., Lambert, J.-C., Verhoelst, T., Granville, J., Keppens, A., Baray, J.-L., et al. (2016). Ground-based Assessment of the Bias and Long-Term Stability of 14 Limb and Occultation Ozone Profile Data Records. *Atmos. Meas. Tech.* 9, 2497–2534. doi:10.5194/amt-9-2497-2016

Kerr, J. B., McElroy, C. T., Wardle, D. I., Olafson, R. A., and Evans, W. F. J. (1985). "The Automated Brewer Spectrophotometer," in *Atmospheric Ozone: Proceedings of the Quadrennial Ozone Symposium* ed . Editors C. S. Zerefos, and A. Ghazi (Hingham, Mass: Springer), 396–401. doi:10.1007/978-94-009-5313-0_80

Kim, J., Jeong, U., Ahn, M.-H., Kim, J. H., Park, R. J., Lee, H., et al. (2020). New Era of Air Quality Monitoring from Space: Geostationary Environment Monitoring Spectrometer (GEMS). *Bull. Am. Meteorol. Soc.* 101 (1), E1–E22. Retrieved Jun 15, 2021, from https://journals.ametsoc.org/view/journals/bams/101/1/bams-d-18-0013.1.xml. doi:10.1175/bams-d-18-0013.1

Kramarova, N. A., Bhartia, P. K., Jaross, G., Moy, L., Xu, P., Chen, Z., et al. (2018). Validation of Ozone Profile Retrievals Derived from the OMPS LP Version 2.5 Algorithm against Correlative Satellite Measurements. *Atmos. Meas. Tech.* 11, 2837–2861. doi:10.5194/amt-11-2837-2018

Lawrence, Z. D., Perlwitz, J., Butler, A. H., Manney, G. L., Newman, P. A., Lee, S. H., et al. (2020). The Remarkably Strong Arctic Stratospheric Polar Vortex of Winter 2020: Links to Record-Breaking Arctic Oscillation and Ozone Loss. *J. Geophys. Res. Atmos.* 125, e2020JD033271. doi:10.1029/2020JD033271

Lelieveld, J., and Dentener, F. J. (2000). What Controls Tropospheric Ozone?. *J. Geophys. Res.* 105, 3531–3551. doi:10.1029/1999JD901011

Liu, F., Page, A., Strode, S. A., Yoshida, Y., Choi, S., Zheng, B., et al. (2020). Abrupt Decline in Tropospheric Nitrogen Dioxide over China after the Outbreak of COVID-19. *Sci. Adv.* 6 (28), eabc2992. doi:10.1126/sciadv.abc2992

Malicet, J., Daumont, D., Charbonnier, J., Parisse, C., Chakir, A., and Brion, J. (1995). Ozone UV Spectroscopy. II. Absorption Cross-Sections and Temperature Dependence. *J. Atmos. Chem.* 21, 263–273. doi:10.1007/bf00696758

Manney, G. L., Livesey, N. J., Santee, M. L., Froidevaux, L., Lambert, A., Lawrence, Z. D., et al. (2020). Record-Low Arctic Stratospheric Ozone in 2020: MLS Observations of Chemical Processes and Comparisons with Previous Extreme Winters. *Geophys. Res. Lett.* 47, e2020GL089063. doi:10.1029/2020GL089063

Marshak, A., Herman, J., Adam, S., Karin, B., Carn, S., Cede, A., et al. (2018). Earth Observations from DSCOVR EPIC Instrument. *Bull. Amer. Meteorol. Soc.* 99 (9), 1829–1850. doi:10.1175/BAMS-D-17-0223.1

McPeters, R. D., Frith, S., and Labow, G. J. (2015). OMI Total Column Ozone: Extending the Long-Term Data Record. *Atmos. Meas. Tech.* 8, 4845–4850. doi:10.5194/amt-8-4845-2015

McPeters, R. D., and Labow, G. J. (2012). Climatology 2011: an MLS and Sonde Derived Ozone Climatology for Satellite Retrieval Algorithms. *J. Geophys. Res.* 117, a–n. doi:10.1029/2011JD017006

McPeters, R., Frith, S., Kramarova, N., Ziemke, J., and Labow, G. (2019). Trend Quality Ozone from NPP OMPS: the Version 2 Processing. *Atmos. Meas. Tech.* 12, 977–985. doi:10.5194/amt-12-977-2019

Orbe, C., Oman, L., Strahan, S., Waugh, D., Pawson, S., Takacs, L., et al. (2017). Large-Scale Atmospheric Transport in GEOS Replay Simulations. *J. Adv. Model. Earth Sy.* 9, 2545–2560. doi:10.1002/2017MS001053

Sauvage, B., Martin, R. V., van Donkelaar, A., and Ziemke, J. R. (2007). Quantification of the Factors Controlling Tropical Tropospheric Ozone and the South Atlantic Maximum. *J. Geophys. Res.* 112 (D11), D11309. doi:10.29/2006JD008008

Seftor, C. J., Jaross, G., Kowitt, M., Haken, M., Li, J., and Flynn, L. E. (2014). Postlaunch Performance of the Suomi National Polar-Orbiting Partnership Ozone Mapping and Profiler Suite (OMPS) Nadir Sensors. *J. Geophys. Res. Atmos.* 119 (7), 4413–4428. doi:10.1002/2013JD020472

Stark, H. R., Moller, H. L., Courreges-Lacoste, G. B., Koopman, R., Mezzasoma, S., and Veihelmann, B. (2013). The Sentinel-4 Mission and its Implementation. In *ESA Living Planet Symposium*. Edinburgh, UK: Vol. 722 of ESA Special Publication, 139.

Steinbrecht, W., Kubistin, D., Plass-Dülmer, C., Davies, J., Tarasick, D. W., von der Gathen, P., et al. (2021). COVID-19 Crisis Reduces Free Tropospheric Ozone across the Northern Hemisphere. *Geophys. Res. Lett.* 48, e2020GL091987. doi:10.1029/2020GL091987/

Strode, S. A., Wang, J. S., Manyin, M., Duncan, B., Hossaini, R., Keller, C. A., et al. (2020). Strong Sensitivity of the Isotopic Composition of Methane to the Plausible Range of Tropospheric Chlorine. *Atmos. Chem. Phys.* 20, 8405–8419. doi:10.5194/acp-20-8405-2020

Thompson, A. M., Witte, J. C., Sterling, C., Jordan, A., Johnson, B. J., Oltmans, S. J., et al. (2017). First Reprocessing of Southern Hemisphere Additional Ozonesondes (SHADOZ) Ozone Profiles (1998-2016): 2. Comparisons with Satellites and Ground-Based Instruments. *J. Geophys. Res. Atmos.* 122 (13), 025. doi:10.1002/2017JD027406

Tzortziou, M., Herman, J. R., Cede, A., and Abuhassan, N. (2012). High Precision, Absolute Total Column Ozone Measurements from the Pandora Spectrometer System: Comparisons with Data from a Brewer Double Monochromator and Aura OMI. *J. Geophys. Res.* 117 (D16), a–n. doi:10.1029/2012JD017814

Vasilkov, A., Joiner, J., Spurr, R., Bhartia, P. K., Levelt, P., and Stephens, G. (2008). Evaluation of the OMI Cloud Pressures Derived from Rotational Raman Scattering by Comparisons with Other

Satellite Data and Radiative Transfer Simulations. *J. Geophys. Res.* 113, D15S19. doi:10.1029/2007JD008689

Wargan, K., Kramarova, N., Weir, B., Pawson, S., and Davis, S. M. (2020). Toward a Reanalysis of Stratospheric Ozone for Trend Studies: Assimilation of the Aura Microwave Limb Sounder and Ozone Mapping and Profiler Suite Limb Profiler Data. *J. Geophys. Res. Atmospheres* 125, e2019JD031892. doi:10.1029/2019jd031892

Wargan, K., Labow, G., Frith, S., Pawson, S., Livesey, N., and Partyka, G. (2017). Evaluation of the Ozone Fields in NASA's MERRA-2 Reanalysis. *J. Clim.* 30 (8), 2961–2988. Retrieved Jun 29, 2021, from https://journals.ametsoc.org/view/journals/clim/30/8/jcli-d-16-0699.1.xml. doi:10.1175/jcli-d-16-0699.1

Witte, J. C., Thompson, A. M., Smit, H. G. J., Fujiwara, M., Posny, F., Coetzee, G. J. R., et al. (2017). First Reprocessing of Southern Hemisphere ADditional OZonesondes (SHADOZ) Profile Records (1998-2015): 1. Methodology and Evaluation. *J. Geophys. Res. Atmos.* 122, 6611–6636. doi:10.1002/2016JD026403

Yang, Y., Meyer, K., Wind, G., Zhou, Y., Marshak, A., Platnick, S., et al. (2019). Cloud Products from the Earth Polychromatic Imaging Camera (EPIC): Algorithms and Initial Evaluation. *Atmos. Meas. Tech.* 12, 2019–2031. doi:10.5194/amt-12-2019-2019

Ziemke, J. R., Chandra, S., Duncan, B. N., Froidevaux, L., Bhartia, P. K., Levelt, P. F., et al. (2006). Tropospheric Ozone Determined from Aura OMI and MLS: Evaluation of Measurements and Comparison with the Global Modeling Initiative's Chemical Transport Model. *J. Geophys. Res.* 111, D19303. doi:10.1029/2006JD007089

Ziemke, J. R., Olsen, M. A., Witte, J. C., Douglass, A. R., Strahan, S. E., Wargan, K., et al. (2014). Assessment and Applications of NASA Ozone Data Products Derived from Aura OMI/MLS Satellite Measurements in Context of the GMI Chemical Transport Model. *J. Geophys. Res. Atmos.* 119, 5671–5699. doi:10.1002/2013JD020914

Zoogman, P., Liu, X., Suleiman, R. M., Pennington, W. F., Flittner, D. E., Al-Saadi, J. A., et al. (2017). Tropospheric Emissions: Monitoring of Pollution (TEMPO). *J. Quantitative Spectrosc. Radiative Transfer* 186, 17–39. doi:10.1016/j.jqsrt.2016.05.008

Conflict of Interest: L-KH, KW, CS, and GL were employed by Science Systems and Applications, Inc. (SSAI).The remaining authors declare that the research was conducted in the absence of any commercial or financial relationships that could be construed as a potential conflict of interest.

ORIGINAL RESEARCH
published: 20 September 2021
doi: 10.3389/frsen.2021.748362

Atmospheric Correction of DSCOVR EPIC: Version 2 MAIAC Algorithm

A. Lyapustin[1*], Y. Wang[2], S. Go[2], M. Choi[2], S. Korkin[3], D. Huang[4], Y. Knyazikhin[5], K. Blank[1] and A. Marshak[1]

NASA Goddard Space Flight Center, Greenbelt, MD, United States
[2] *University of Maryland Baltimore County, Baltimore, MD, United States*
[3] *Universities Space Research Association, Columbia, MD, United States*
[4] *IEX Group, New York, NY, United States*
[5] *Earth and Environment Department, Boston University, Boston, MA, United States*

Edited by:
Feng Xu, University of Oklahoma, United States

Reviewed by:
Bing Lin, National Aeronautics and Space Administration, United States
Shaohua Zhao, Ministry of Ecology and Environment Center for Satellite Application on Ecology and Environment, China

**** Correspondence:** A. Lyapustin, Alexei.I.Lyapustin@nasa.gov*

***Specialty section:** This article was submitted to Satellite Missions, a section of the journal Frontiers in Remote Sensing*

***Received:** 27 July 2021*
***Accepted:** 02 September 2021*
***Published:** 20 September 2021*

***Citation:** Lyapustin A, Wang Y, Go S, Choi M, Korkin S, Huang D, Knyazikhin Y, Blank K and Marshak A (2021) Atmospheric Correction of DSCOVR EPIC: Version 2 MAIAC Algorithm. Front. Remote Sens. 2:748362. doi: 10.3389/frsen.2021.748362*

The Earth Polychromatic Imaging Camera (EPIC) onboard the Deep Space Climate Observatory (DSCOVR) provides multispectral images of the sunlit disk of Earth since 2015 from the L1 orbit, approximately 1.5 million km from Earth toward the Sun. The NASA's Multi-Angle Implementation of Atmospheric Correction (MAIAC) algorithm has been adapted for DSCOVR/EPIC data providing operational processing since 2018. Here, we describe the latest version 2 (v2) MAIAC EPIC algorithm over land that features improved aerosol retrieval with updated regional aerosol models and new atmospheric correction scheme based on the ancillary bidirectional reflectance distribution function (BRDF) model of the Earth from MAIAC MODIS. The global validation of MAIAC EPIC aerosol optical depth (AOD) with AERONET measurements shows a significant improvement over v1 and the mean bias error MBE = 0.046, RMSE = 0.159, and R = 0.77. Over 66.7% of EPIC AOD retrievals agree with the AERONET AOD to within ± (0.1 + 0.1AOD). We also analyze the role of surface anisotropy, particularly important for the backscattering view geometry of EPIC, on the result of atmospheric correction. The retrieved BRDF-based bidirectional reflectance factors (BRF) are found higher than the Lambertian reflectance by 8–15% at 443 nm and 1–2% at 780 nm for EPIC observations near the local noon. Due to higher uncertainties, the atmospheric correction at UV wavelengths of 340, 388 nm is currently performed using a Lambertian approximation.

Keywords: aerosol, surface reflectance, bidirectional reflectance distribution function, multi-angle implementation of atmospheric correction, atmospheric correction, EPIC

INTRODUCTION

The Earth Polychromatic Imaging Camera (EPIC) is a 10-channel Charge Coupled Device (CCD) onboard the Deep Space Climate Observatory (DSCOVR) satellite that orbits around the Sun–Earth Lagrange-1 (L1) point with a distance of about 1.5 million kilometers from the Earth (http://epic.gsfc.nasa.gov). Due to DSCOVR's unique Lissajous orbit, EPIC provides continuous observations of Earth's entire sunlit surface. EPIC has a relatively coarse spatial resolution but high temporal sampling rate as compared with polar-orbiting earth observing sensors. It produces up to 22 daily images in boreal summer and up to 13 images in boreal winter (Marshak, et al., 2018) giving 10–12 daytime observations over the same surface area in summer, and 6-7 images in winter. This provides diurnal

observations during times that are unavailable from the A-train sensors (e.g., early morning and late afternoon), for instance, for climatically important tropical regions of the world such as Amazonia where tropical convection generates more clouds in the afternoon. Another important feature of EPIC is its continuous observations in the backscattering range of angles near the "hotspot" (e.g., Gerstl, 1999). It allows unique measurements of the sunlit part of the leaf area index (SLAI) for vegetation. As the rate of photosynthesis is different for leaves under the direct and diffuse sunlight, knowledge of this parameter is important to modeling of the global bio-productivity (Yang et al., 2017).

EPIC acquires images in 10 narrowband channels, 317, 325, 340, 388, 443, 551, 680, 688, 764 and 779 nm, using 2048 × 2048 pixel CCD camera. The measurements are 2 × 2 pixels aggregated onboard except for the blue (443 nm) band. The standard calibration of the EPIC's raw imagery includes the dark, latency, temperature, stray-light and flat-field corrections (Cede et al., 2021). To track the post-launch changes and on-orbit trending of calibration, the EPIC's calibration is continuously updated using the underflight comparisons with other Earth observing instruments, e.g., Moderate Resolution Imaging Spectroradiometer (MODIS), Visible Infrared Imaging Radiometer Suite (VIIRS), Ozone Mapping and Profiler Suite (OMPS) on Suomi National Polar-orbiting Partnership (SNPP) satellite etc. (e.g., Geogdzhayev and Marshak, 2018; Herman et al., 2018; Doelling et al., 2019; Geogdzhayev et al., 2021).

To provide atmospheric correction of EPIC data over land, we adapted the Multi-Angle Implementation of Atmospheric Correction (MAIAC) algorithm originally developed for MODIS (Lyapustin et al., 2011a, Lyapustin et al., 2011b; Lyapustin et al., 2012; Lyapustin et al., 2018). The version 1 (v1) MAIAC EPIC Level 2 dataset was released in May 2018 and is available from the Atmospheric Science Data Center (ASDC) at NASA Langley Research Center (https://doi.org/10.5067/EPIC/DSCOVR/L2_MAIAC.001). This initial version used a global Sinusoidal projection with gridded products at 10 km resolution. It also used a simplified Lambertian model to perform atmospheric correction.

The goal of this paper is to present an updated v2 MAIAC EPIC algorithm which recently completed re-processing of the EPIC record of measurements since 2015 based on improved v3 geolocation (Blank et al.,

2021). The important v2 MAIAC updates include 1) a switch from global to regional (rotated) Sinusoidal projection which minimizes spatial distortions; 2) replacing approximate Lambertian atmospheric correction with more rigorous algorithm based on ancillary bidirectional reflectance distribution function (BRDF) database from MAIAC MODIS; 3) a new algorithm to simultaneously retrieve aerosol optical depth (AOD) and spectral absorption over land (Lyapustin et al., 2021a). The current paper focuses on cloud detection, aerosol retrieval and atmospheric correction over land, and provides the list of reported data products. Below, Gridding describes the v2 MAIAC gridding approach for EPIC. *Cloud Detection*, *Aerosol Retrieval Over Land*, *and Atmospheric Correction Over Land* provide technical details about cloud screening, aerosol retrievals and implemented atmospheric correction. The paper is concluded with a summary in *Concluding Remarks*.

GRIDDING

Gridding allows MAIAC to 1) track the same grid cell over time; and 2) store and dynamically update surface-related information for each grid cell for the cloud detection and aerosol retrievals. MAIAC stores spectral surface BRDF information (see *Retrieving Bidirectional Reflectance Distribution Function Model Parameters*); 3 × 3 standard deviation at 0.44 and 0.68 μm characterizing local surface heterogeneity; normalized difference vegetation index (NDVI); surface reflectance spectral ratio or spectral regression coefficient (SRC); and spectral water leaving reflectance over the ocean. This local information is updated with the rate of EPIC's cloud-free observations. Due to computer memory and computational power constraints, the global image is divided into eight 1000 × 1000 pixel tiles (Figure 1). Each tile is processed independently and in parallel with others to achieve optimal computational performance. The data are gridded to 10 km resolution which is close to the nadir resolution of the 443 nm channel and oversamples all other bands.

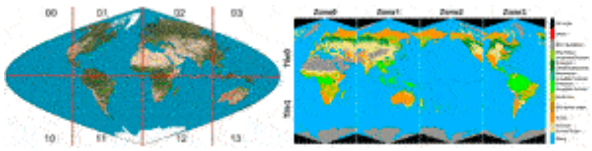

FIGURE 1 | (left) Global Sinusoidal projection in v1 MAIAC, and **(right)** Rotated Sinusoidal projection with global land cover types in v2 MAIAC EPIC algorithm. Also shown are the respective tiling systems.

The v1 MAIAC EPIC used a global Sinusoidal projection (Figure 1, left). This is an equal area projection which is an important property for the land analysis and applications. A serious limitation of this projection is the geographic distortions which grow away from the Greenwich meridian and equator. We introduced a rotated Sinusoidal projection (Figure 1, right) in v2 MAIAC EPIC. It is the same Sinusoidal projection rotated 90° four times to represent an entire landmass as well as the global ocean with significantly reduced distortions. There is a certain overlap between tiles, for instance Alaska can be found at the edge of tile 03 and near center of tile 02. The new projection keeps an equal area property, reduces geographic distortions, and can be easily re-projected to any standard projection without loss of information. It also keeps the same total number of pixels by filling in the significant empty space in the global Sinusoidal projection. For convenience, we offer data users a global mask of pixels with best representation (minimum distortions) to address the problem of overlap.

CLOUD DETECTION

MAIAC EPIC cloud mask algorithm consists of a group of tests that are designed to detect clouds with different spectral/spatial characteristics from the clear-sky conditions. As MAIAC does not require cloud type information, the cloud tests are applied sequentially, and the processing is terminated once cloud is detected.

Brightness Test

The brightness test aims to detect optically thick bright clouds that have a high albedo in the visible spectrum. A pixel is masked as cloud if the measured reflectance (R^m) exceeds the theoretical value at maximal AOD = 6 of the MAIAC look-up table (LUT) at a given view geometry (R_{max}) with a certain threshold:

$$R^m > R_{max} + \text{Thresh} \quad (1)$$

The threshold is 0.1 over bright Sahara region and 0.05 otherwise. The brightness test uses the EPIC blue channel (443 nm), where the surface is generally dark, and the reduction of TOA reflectance by absorbing aerosols (smoke/dust) and the difference in reflectance with non-absorbing clouds is maximal compared to longer wavelengths.

Spatial Variability Test

In general, clouds exhibit a larger spatial variance than aerosol and the ocean surface. The spatial variance test computed using 3 × 3 pixel window has been a standard technique for cloud detection over the ocean at moderate resolution ~1 km (e.g., Martins et al., 2002). Based on simulated EPIC observations from 1 km MODIS data, we selected the spatial variance threshold of 0.005 which achieves a reasonable balance between cloud filtering and fraction of clear pixels.

Over land surfaces, using a global threshold is problematic due to spatial variability of the land surface reflectance, in particular over bright deserts, in the urban regions and over agricultural areas. Working with gridded data, MAIAC keeps memory of the 3 × 3 standard deviation (σ) for each 10 km grid cell derived in cloud-free and low aerosol conditions. Similar to MAIAC MODIS, σ is computed for the red and blue bands and updated on cloud-free days from observations closest to nadir, when the observation footprint is minimal and spatial variance from surface is maximal. The implementation for EPIC follows test (C.4) in Lyapustin et al. (2018).

High Cloud Test

Detection of optically thin high clouds relies on EPIC measurements in the oxygen A-band. While this signal is low in cloud-free conditions due to absorption by molecular oxygen, presence of high clouds creates a relatively strong signal. Detection of high clouds employs a reflectance ratio measurement of oxygen A-band to the window channel (780 nm) divided by a theoretical reflectance ratio for surface elevation (Z) (Zhou et al., 2020):

$$\frac{R_{764}^{meas}/R_{780}^{meas}}{R_{764}^{theo}(Z)/R_{780}^{theo}(Z)} = \frac{\exp(-m\tau_{O2A})}{\exp(-m\tau_{O2A,Z})} \quad (2)$$

where τ_{O2A} and $\tau_{O2A,Z}$ are optical depth values due to O_2 absorption from the measured ratio and from the theoretical LUT, respectively, and $m = 1/\mu_0$

+ $1/\mu$ is an atmospheric airmass factor depending on cosines of solar (μ_0), and view (μ) zenith angles. A simple threshold-based approach is then used for high cloud detection: the pixel is considered cloudy if $\tau_{O2A,Z} - \tau_{O2A} > 0.056$.

Similarly to MAIAC MODIS, the above tests only serve for an initial cloud screening. The cloud mask is significantly enhanced following aerosol retrievals by limiting the small-scale spatial variability of AOD, and during the atmospheric correction through comparison of spectral reflectance with the predicted values based on the BRDF model.

AEROSOL RETRIEVAL OVER LAND

Aerosol Models

Following MAIAC MODIS Collection 6 algorithm, we are using eight prescribed regional aerosol models to represent variability of aerosol properties over global land. Geographic distribution and model parameters are provided in Lyapustin et al. (2018, Figure 4 and Table 1).

One known issue in MAIAC C6 was underestimation of AOD for the biomass burning aerosol at high AOD (e.g., Lyapustin et al., 2018; Schutgens et al., 2020; Sogacheva et al., 2020). As a remedy, in MODIS MAIAC C6.1 we adjusted the model parameters at AOD>0.6 based on the regional climatology analysis of the AERONET (Holben et al., 1998; Giles et al., 2019; Sinyuk et al., 2020) record. Similarly, to correct the known low bias of the mineral dust AOD over Western Sahara, we introduced a new corresponding region with the more absorbing dust model. These amendments are used in the v2 MAIAC EPIC and will be described in detail elsewhere.

Aerosol Retrieval Algorithm

MAIAC processing uses the ancillary NCEP ozone and column water vapor information. The over ocean processing also uses the NCEP wind speed.

Retrieval of SRC is a central component of MAIAC: it provides separation of the surface and atmospheric signals in the TOA measurements, and is required for aerosol retrievals. Because EPIC lacks the 2130 nm channel used in MAIAC MODIS, we define SRC as the ratio of the surface reflectance in Blue to Red ($SRC = \rho_{L,Blu}/\rho_{L,Red}$) bands. Reflectance $\rho_{L,\lambda}$ is a Lambertian reflectance resulting from the Rayleigh atmospheric

correction with low background aerosol. SRC is obtained as a minimum value over the 2-month period of time. Following Lyapustin et al. (2018), we are using two independent lines of update, shifted by 1 month. Thus, the SRC is dynamically updated at least every month or more frequently if a new minimum value is found. SRC is characterized in 4 bins in cosine of the solar zenith angle 1–0.9, 0.9–0.7, 0.7–0.45, and 0.45–0.2. The SRC for the morning and the afternoon observations is separate because of the change in geometry at a near-constant scattering angle, e.g., depending on the part of the orbit, the view zenith angle (VZA) may be higher than the solar zenith angle (SZA) in the morning but symmetrically lower in the afternoon and vice versa.

The AOD is obtained by matching the observed and theoretical TOA reflectance at 443 nm based on the look-up table. The surface reflectance ρ_B is evaluated from the atmospherically corrected $\rho_{L,Red}$ (AOD) at 680nm, $\rho_{L,Blu}$ = SRC*$\rho_{L,Red}$. This AOD is derived using the corresponding regional background aerosol models. When derived AOD is high (>0.6) and absorbing smoke or dust is detected, the v2 MAIAC runs a separate inversion of UV-vis observations providing AOD and spectral aerosol absorption (Lyapustin et al., 2021a, this issue).

At high altitudes (over 3.5 km, e.g. Tibetan plateau) where AOD is generally very low and MAIAC AOD retrievals do not have sufficient accuracy, we assume a fixed climatology AOD_{min} = 0.02 for the atmospheric correction.

AERONET AOD Validation

To assess accuracy of AOD retrieval, we conducted AERONET validation for 2015–2020 using level 2.0 AERONET version 3 data (Giles et al., 2019). The comparison uses EPIC AOD at 443 nm averaged over the 5 × 5 pixels window (50 km) with AERONET data selected within 30 min from the satellite observation. The EPIC data were filtered according to the Sun and view zenith angles less than ~63° and at least 50% coverage in the spatial window.

The validation results are presented in Figure 2. The site-level global statistics shows the correlation coefficient (R), root mean square error (RMSE) and the mean bias error (MBE, MAIAC–AERONET). MAIAC shows a good retrieval accuracy, with $R \geq 0.7$–0.8 and low RMSE and MBE,

over vegetated parts of the world including North and South America, north-central Eurasia and Oceania. AOD is generally overestimated over bright surfaces such as western United States and Australia. Such bias is typical for aerosol products based on a single-view satellite measurement, and it is exacerbated for EPIC due to unfavorable view geometry near the backscattering direction. The underestimation of AOD is obvious in regions of strong biomass burning, including central Africa, Indo-Gangetic plain and south Asia. Similar to the bias, the RMSE is generally low globally with the exception of the major dust and biomass burning aerosol source regions which also have a much higher annual average AOD. The correlation is generally high in regions with higher magnitude and variability of AOD. On the contrary, the low correlation is observed over regions with low aerosol loading and low natural variability, such as Australia or south of the South American continent.

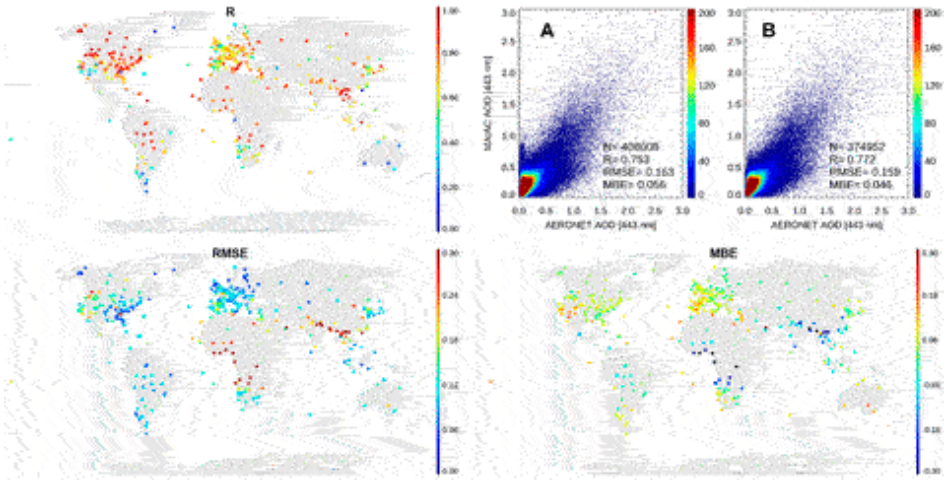

FIGURE 2 | Global AERONET validation of MAIAC EPIC AOD at 443 nm. The geographic distribution of the site-level results is displayed for the regression coefficient (R), root mean square error (RMSE) and the mean bias error (MBE). The two scatterplots show the summary validation using all AERONET sites (A) and its subset with 12 bright sites (see *Aeronet AOD Validation*) excluded.

The two scatterplots on the right summarize the global validation analysis. The left one 1) shows all AERONET sites. On the right scatterplot (b), we excluded 11 bright surface sites over the Western United States (*Bakersfield*; *Goldstone*; *KeyBiscayne*; *Neon_ONAQ*; *Railroad Valley*; *Sandila_NM_PSEL*; *TableMountain_CA*; *Tucson*; *UACJ_UNAM_ORS*; *White_Sands_HELSTF*; *Yuma*) and one site over Australia (*Birdsville*). These

sites are located in arid regions with low AOD and low AOD variability where MAIAC EPIC overestimates AOD and shows low *R*-values. Due to low cloudiness, these sites also contribute a disproportionate ~9% of the total matching points. Considering the right scatterplot as a baseline, MAIAC shows an overall correlation of 0.77 with RMSE ~ 0.159 and a mean bias of 0.046. Over 66.72% of MAIAC EPIC AOD agree with AERONET within the expected error (EE) of ±(0.1 + 0.1AOD). The v2 shows an improvement over v1 which had a global statistics of $R = 0.69$, RMSE = 0.17, MBE = 0.03 (unpublished).

ATMOSPHERIC CORRECTION OVER LAND

Following cloud detection and aerosol retrieval, the atmospheric correction (AC) algorithm derives spectral surface reflectance and updates the Ross-Thick Li-Sparse (RTLS, Lucht et al., 2000) BRDF model parameters,

$$\rho(\mu_0, \mu, \varphi) = k_L + k_V f_V(\mu_0, \mu, \varphi) + k_G f_G(\mu_0, \mu, \varphi) \qquad (3)$$

Here, volumetric (f_V) and geometric-optics (f_G) kernels are functions of the view geometry, and pixel-specific weights (k_L, k_V,k_G) describe different BRDF shapes. To account for the surface reflectance increase in the backscattering view geometry of EPIC, the volumetric kernel is multiplied by the hot-spot factor as suggested by Maignan et al. (2004) based on POLDER observations.

Atmospheric Correction: MAIAC Scaling Approach

The v1 MAIAC EPIC algorithm used a Lambertian model for the atmospheric correction, where the surface reflectance is derived from the following approximation to the TOA reflectance:

$$R^{TOA}(\mu_0, \mu, \varphi) \approx R^A(\mu_0, \mu, \varphi) + \rho T^d(\mu_0) T^u(\mu) / (1 - s\rho), \rho \equiv \rho(\mu_0, \mu, \varphi) \qquad (4)$$

Eq. 4 only requires the knowledge of atmospheric (path) reflectance (R^A), upward (T^u) and downward (T^d) atmospheric transmittance as functions of the cosines of Sun (μ_0) and view (μ) zenith angles and relative azimuth (φ), and spherical albedo of atmosphere (s). In the EPIC view angles near the hotspot where surface is brighter than in the other directions, the Lambertian approximation underestimates the surface reflectance (e.g., Wang et al.,

2010). An analysis of Lambertian biases was recently given by Lyapustin et al. (2021b) based on a comparison between the two MODIS surface reflectance products, the standard surface reflectance (SR) MOD09 based on Lambertian assumption, and the bidirectional reflectance factors (BRF) of algorithm MAIAC (MCD19A1).

The MAIAC atmospheric correction uses a rigorous expression for the TOA reflectance. Taking advantage of linearity of the RTLS function, it represents the TOA reflectance explicitly using weights of the RTLS model:

$$R^{TOA}(\mu_0,\mu,\varphi) = R^{A}(\mu_0,\mu,\varphi) + k_L F^{L}(\mu_0,\mu) + k_V F^{V}(\mu_0,\mu,\varphi) + k_G F^{G}(\mu_0,\mu,\varphi) + R^{nl}(\mu_0,\mu) \quad (5)$$

Here, *F*-functions are integrals of the atmospheric path radiance incident on surface and atmospheric Green's function (Lyapustin and Knyazikhin, 2001) with respective kernels of the RTLS model. R^{nl} is a weakly non-linear function of the surface reflectance, describing multiple light scattering between the surface and the atmosphere. The *F*-functions and R^{nl} are computed analytically using eight primary functions which are stored in the MAIAC LUT (e.g., Lyapustin et al., 2011a). For the purpose of atmospheric correction, let us re-write Equation 5 as follows:

$$R^{TOA}(\mu_0,\mu,\varphi) = R^{A}(\mu_0,\mu,\varphi) + cR^{Surf}(\mu_0,\mu,\varphi) \quad (6)$$

where R^{Surf} is a surface-reflected term combining the last four terms of Eq. 5, and $c \equiv c_\lambda$ is a spectrally dependent scaling factor. The R^{Surf} is computed using the BRDF model parameters stored in MAIAC memory for each grid cell (e.g., 1 km for MODIS and 10 km for EPIC). Then, the BRF is given by a scaled value:

$$r_\lambda = c_\lambda RTLS_\lambda(\mu_0,\mu,\varphi) \quad (7)$$

where $RTLS_\lambda$ is the BRDF model value for a given geometry. Because R^{Surf} is a nonlinear function of the surface reflectance, solving eqs. (6) and (7) takes 2 iterations (see Lyapustin et al., 2018, p. 5753).

Implementing rigorous atmospheric correction given by Eqs. (6) and (7). requires knowledge of the entire BRDF shape to correctly represent surface reflection of the direct Sun beam and of the diffuse (sky) light. In v2 MAIAC EPIC, we used the global Collection 6 MAIAC MODIS 1 km BRDF product MCD19A3 to develop an ancillary BRDF dataset for the EPIC 10-km grid

from the closest MODIS channels. The AC based on Eqs. (6) and (7). uses scaling approach and only requires knowledge of the relative BRDF shape rather than the absolute reflectance. For this reason, the wavelength difference between the EPIC and MODIS channels is not important as long as the land surface reflectance among the paired channels, and thus the BRDF shape, remain similar. The ancillary 10 km BRDF for EPIC was created for every month starting in 2015. Figure 3 illustrates the global RGB BRDF for nadir view and Sun at 45° for January and July of 2016.

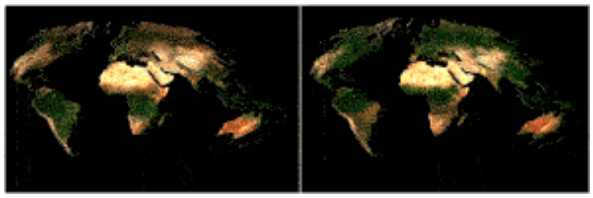

FIGURE 3 | The monthly average RGB surface BRDF for February **(left)** and July **(right)** of 2016 from MAIAC MODIS MCD19A3 product.

Figure 4 gives an example of atmospheric correction based on scaling (S) in the Blue and Red bands in columns 3 and 5, respectively. The result is shown as an excess of anisotropic over the Lambertian reflectance (BRF-ρ_L)/ρ_L (%). In agreement with theory, the difference is lowest when the Sun is near zenith, and it grows with the atmospheric airmass factor. It also increases with the total atmospheric optical thickness from NIR to Blue, for instance from ~3% at 780nm, ~10% at 680nm to 60–80% at 443 nm at high Sun/view zenith angles (μ_0,μ ~ 0.2). While this pattern agrees with theoretical expectations in general, the strong increase of BRF at high zenith angles, in particular at 443nm, does not seem realistic.

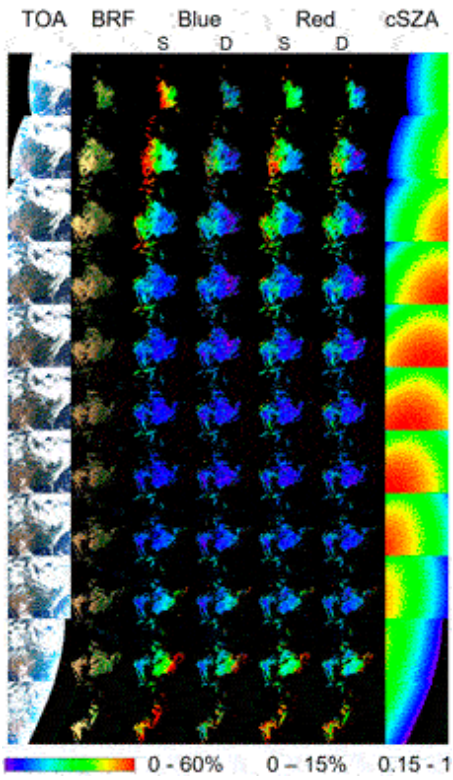

FIGURE 4 | Analysis of different schemes of atmospheric correction of EPIC over North America on June 13, 2020. The first and second columns show the EPIC's TOA and atmospherically corrected RGB BRF images. Columns 3–6 show the relative difference between anisotropic BRF and Lambert (ρ_L) reflectance (BRF-ρ_L/ρ_L)×100% in the Blue and Red bands, where BRF was computed using the scaling (S) and the "direct term" (D) methods. The last column displays the cosine of the solar zenith angle.

Atmospheric Correction: Separation of the Direct and Diffuse Reflectance

The scaling approach Eqs. (6) and (7) assumes that the BRDF model gives a good description of the surface reflectance at the angles of satellite observations. In this case, direct and diffuse surface-reflected signals at the TOA can be scaled using the same multiplier *c*. This approach works for MAIAC MODIS where the BRDF represents the view geometry sampled by MODIS. The ancillary MODIS BRDF was derived for the range of SZA observed near the local noon around 10:30 am (Terra) and 1:30 pm (Aqua) equatorial crossing time. Thus, it can be considered representative of the EPIC's view geometry within about ±2 h of the local noon. Outside of that range, at higher SZA both earlier in the morning and later in the afternoon, the MODIS BRDF can still be used to compute the reflection of the diffuse

sky irradiance assuming BRDF reciprocity, at least for the range of SZA agreeing with the VZA range of MODIS, ~0–62° accounting for the Earth's curvature. However, it cannot represent correctly the direct TOA reflectance $\rho(\mu_0,\mu,\varphi)\exp(-m\tau)$, where τ is an atmospheric optical depth, as MODIS does not make measurements at higher SZAs near the hotspot.

In this case, we can single out the direct reflectance in Eq. 6:

$$R^{TOA}(\mu_0,\mu,\varphi) = R^{A}(\mu_0,\mu,\varphi) + \rho(\mu_0,\mu,\varphi)e^{-m\tau} + g_\lambda R^{\mathrm{Dif}}(\mu_0,\mu,\varphi) \quad (8)$$

where the diffuse component of the surface-reflected signal at TOA is:

$$R^{\mathrm{Dif}}(\mu_0,\mu,\varphi) = R^{\mathrm{Surf}}(\mu_0,\mu,\varphi) - RTLS(\mu_0,\mu,\varphi)e^{-m\tau} \quad (9)$$

Above, ρ is the true surface BRF, and R^{Dif} and RTLS are computed with the ancillary MODIS BRDF. The g_λ is the spectral adjustment factor designed to account for the surface reflectance difference from the spectral shift between the paired EPIC - MODIS channels, e.g., for the Blue (443/465.5 nm), Green (555/553.5 nm), Red (680/644.9 nm) and NIR (779.5/855.6 nm) EPIC/MODIS center wavelengths, respectively. For each 10 km pixel, we compute the spectral adjustment factor g_λ using scaling atmospheric correction (Eqs. (6) and (7) near the local noon (within $\Delta\mu_0$ of ±0.1) where MODIS BRDF should be valid for both direct and diffuse terms, as we discussed above. In this case, g_λ is equivalent to the scaling factor c_λ. The g_λ is computed daily for each cloud-free 10 km grid cell at low AOD and is stored in MAIAC memory until updated with the next retrieval. Such approach allows us to evaluate the diffuse reflected term using the ancillary MAIAC MODIS BRDF, and compute BRF (ρ) from the direct reflected term in Eq. 8.

The described "direct term" (D) algorithm is more generic than the scaling approach. The resulting BRF_D (columns 4 and 6 of Figure 3 for the Blue and Red bands, respectively) can be compared to the scaling BRF_S in Figure 4. BRF_D shows a more constrained increase over the Lambertian reflectance up to SZA~70° which grows only to ~35% in the Blue band instead of ~60–80% for the scaling approach. Importantly, the anisotropic enhancement (of the Lambertian reflectance) remains nearly constant in the range of SZA~0–60°, though the uncertainty $\Delta\rho$ increases at high EPIC

SZA/VZA. The uncertainty is twofold: it is related to both the aerosol retrieval uncertainty ($\Delta\tau$) and to the uncertainty in the diffuse signal R^{Dif} introduced by the MODIS BRDF (ΔRTLS) which was defined for a relatively narrow range of SZA values of MODIS Terra and Aqua at a fixed overpass time, and the limited range of VZA≤62°. Moreover, while working well in the range of SZA/VZA~60°, the RTLS BRDF model has the problem of unconstrained growth of both geometric-optics and volumetric kernels at higher SZA/VZA, proportionally to a combination of terms $1/\mu_0$, $1/\mu$ (e.g., Gao et al., 2000). Finally, a significant uncertainty is related to the increase of the EPIC's footprint with VZA faster than 1/μ while the ancillary BRDF generated from 1 km MODIS still closely represents the 10 km grid box. For these reasons, the atmospheric correction problem (Eqs. (6) and (7) at high zenith angles becomes ill-posed and poorly constrained, with an exponential propagation of uncertainties:

$$\Delta\rho(\mu_0,\mu,\varphi) \sim -e^{m\tau}\left\{\Delta R^{A}(\Delta\tau) + g_1 R^{Dif}(\Delta\tau, \Delta RTLS)\right\} \quad (10)$$

Atmospheric Correction for EPIC

The above analysis showed limitations of both scaling and the "direct term" atmospheric correction methods, in particular at high SZA/VZA. The main limitations stem from the limited angular sampling of EPIC prohibiting deriving the self-consistent BRDF model in the full hemisphere of angles of incidence and reflection, and from the growing uncertainties of the ancillary MODIS BRDF model at high SZA/VZA in application to EPIC. Both Lambertian and scaling algorithms reproduce well the spatial pattern and the RGB color of the EPIC TOA images while, respectively, underestimating and overestimating the true BRF, especially at high zenith angles. The "direct term" algorithm shows rapidly growing uncertainties at high zenith angles. As it depends on the absolute ancillary BRDF model, this approach is also prone to spatial and spectral distortions in the resulting RGB BRF images. At the same time, this algorithm provides a realistic more constrained BRF increase over the Lambertian value, and a near-constant u = BRF/ρ_L ratio in the wide range of zenith angles up to ~50–60°. This ratio fully agrees with the BRF/ρ_L ratio of the scaling method evaluated for the observations near the local noon.

Given these findings, the MAIAC EPIC v2 AC approach in RGB and NIR bands is implemented as follows:

- Compute the Lambertian reflectance ($\rho_{L,\lambda}$) from Eq. 4;

- Compute BRF as $\rho(\mu_0,\mu,\varphi) = \rho_{L,\lambda}u_\lambda$;

- The anisotropic conversion factor u_λ is derived from "scaling" BRF_S, $u_\lambda = BRF_S/\rho_{L,\lambda}$, computed near the local noon where the scaling approach is valid. It is updated daily from the cloud-free observations near the local noon (within $\Delta\mu_0$ of ±0.1) and is stored in MAIAC′ memory for each 10 km grid cell.

The anisotropic conversion factor near the local noon gives the increase over the Lambertian reflectance from 1–2% at 780 nm to 8–15% at 443 nm. The uncertainty of the reported BRF is low for the EPIC observations near the local noon, and it is expected to significantly increase at zenith angles above ~60°. The selected empirical AC approach is fast and does not create spectral distortions, but it probably underestimates BRF at higher zenith angles. In near future, we plan to further explore both "scaling" and the "direct term" AC algorithms using BRDF model from the geostationary satellites which provide the full range of the solar zenith angle variations.

The MAIAC v2 algorithm reports both ρ_L and BRF reflectance values in the RGB and NIR channels. In the UV, where uncertainties are the largest, only the Lambertian reflectance is reported.

Figure 5 gives an example of atmospheric correction for the 1-month period of June 2–July 2, 2020, for a single 10 km bright surface grid cell in Arizona, United States. The derived surface reflectance displays a well-reproducible daily pattern in the visible–near infrared with surface reflectance increasing with SZA. The strongest growth is observed in the NIR in agreement with (Marshak, 2021). The pattern becomes less certain at UV wavelengths: the SR points tend to cluster within about ±0.01 of the mid-day value with occasional high and low outliers at both 388 and 340 nm wavelengths. On average, the AC produces a correct pattern with $\rho_{340}<\rho_{388}$ at μ,μ_0 above ≈0.6 (53°), and unstable result at higher SZA/VZA. This result is rather systematic and holds over both bright and dark vegetated surfaces. As the uncertainty in the UV SR rapidly grows with the airmass factor, the most accurate SR values at 340 and 388 nm are reported near the local noon.

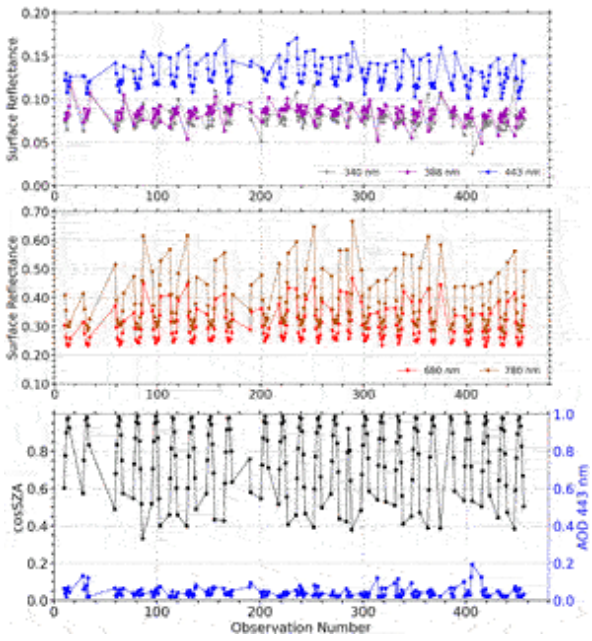

FIGURE 5 | The time series of surface reflectance in EPIC's UV-vis-NIR bands over the bright pixel in Arizona, United States, in June–early July of 2020. The bottom plot shows cosine of solar zenith angle and retrieved AOD at 443 nm. The *x*-axis counts consecutive EPIC observations from June 2 through July 2 of 2020.

Retrieving BRDF Model Parameters

Following computation of BRF, MAIAC proceeds with calculation of the RTLS parameters (K-coefficients) using the multi-angle dataset accumulated in the MAIAC Queue memory for each grid cell (up to 40 observations). This retrieval is performed for the four visible and near-IR bands only. After inversion, the new BRDF goes through several tests verifying "correctness" of its shape, and its consistency with the previous solution (Lyapustin et al., 2012). Figure 6 shows the daily BRF pattern (dots connected by solid lines) in the Blue-NIR EPIC bands for the pixel displayed in Figure 5 on two different days in June of 2020. The best-fit BRDF model is shown by the dashed lines. While the BRDF model error can reach several absolute percent of reflectance at high zenith angles, the typical *rmse* of the fit is low, within ~0.001–0.002.

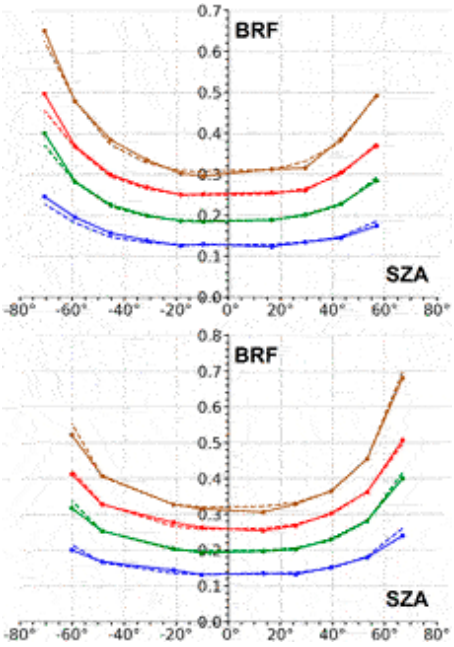

FIGURE 6 | An example of the retrieved BRF (dots connected by solid lines) and the best-fit BRDF model (dashed lines) for the bright surface pixel displayed in Figure 5. The BRF and BRDF are shown for 2 different days in June of 2020 in RGB bands (in respective color) and in the NIR (in brown). The SZA is positive in the morning, and negative in the afternoon.

It should be mentioned that the derived BRDF model describes only the range of the EPIC observations within 4–12° from the backscattering direction, and is not representative of the general BRDF shape. A failure of the DSCOVR gyroscopes in late June of 2019 led to EPIC being placed in a safehold mode till March of 2020. This period was required to find the engineering solution for the satellite navigation using startrackers and update the geolocation algorithm. After resuming operation, the DSCOVR orbit became less constrained and allows the range of angles ~2–12° from the exact backscattering since March 2020.

CONCLUDING REMARKS

This paper described the version 2 MAIAC land algorithm developed for processing of the DSCOVR EPIC data. The full MAIAC processing includes cloud detection, aerosol retrieval and atmospheric correction over both land and ocean.

Following MODIS, the standard MAIAC aerosol retrieval uses the regional background aerosol models to derive AOD. A global validation of AOD using AERONET for the period of 2015–2020 shows the overall good

performance with R = 0.77, RMSE = 0.159, and MBE = 0.046. The v2 shows an improvement over v1 MAIAC (R = 0.67, RMSE = 0.17) and compares favorably to MAIAC MODIS Collection 6 (R = 0.84, RMSE = 0.12, MBE = 0.01 (Lyapustin et al., 2018)) despite coarse spatial resolution and the backscattering view geometry. The positive bias of v2 MAIAC EPIC mostly comes from the retrievals over bright surfaces.

In cloud-free conditions, the retrieved AOD along with the ancillary NCEP ozone and water vapor information is used for the atmospheric correction of EPIC. MAIAC v2 reports AC results using both Lambert and anisotropic SR models. The Lambert model systematically underestimates SR in the EPIC's view geometry. The anisotropic atmospheric correction uses the ancillary monthly BRDF database based on MAIAC MODIS C6 RTLS BRDF. The uncertainties of anisotropic AC come from very different view geometries of MODIS and EPIC which overlap only for EPIC observations near the local noon. For this reason, the standard MAIAC scaling AC algorithm works only for the range of EPIC observations near the local noon. On the other hand, BRF retrieval from the direct surface-reflected term show a stable $(BRF-\rho_L)/\rho_L$ ratio in the wide range of EPIC's SZA. This led us to adapt a simple AC approach in the vis-NIR bands by upscaling the Lambertian SR, where the scale factor is computed from the EPIC observations near the local noon. At low to moderate AOD, the typical $(BRF-\rho_L)/\rho_L$ ratio near the local noon is ~1–2% in the NIR, and ~8–15% in the Blue EPIC bands.

Due to higher uncertainties, the AC in the UV uses the Lambertian model. It produces rather consistent results with uncertainty of about ±0.01 or less for Sun/view zenith angles less than ~53°, with most reliable retrievals near the local noon. At higher zenith angles, the UV SR may become unstable.

Over land, the MAIAC EPIC product suite includes the background model AOD at 443 and 550 nm, Lambert surface reflectance at 340, 388, 443, 551, 680 and 780 nm, and BRF and the BRDF model parameters for the RTLS model at 443, 551, 680 and 780 nm. It is important to note that the BRDF model is only relevant for the near hot-spot cone of the scattering angles observed by EPIC, although it covers the full range of variation in the Sun and view zenith angles. The reported spectral BRF is used as an input for Level 2 Vegetation Earth System Data Record (VESDR) (Yang et al., 2017; NASA/LARC/SD/ASDC-VESDR, 2021).

Over water, MAIAC data products include AOD, fine mode fraction (FMF) and Angstrom exponent, and "ocean color" (water-leaving reflectance) at 340, 388, 443, 551, 680 and 780 nm.

For detected absorbing smoke and dust aerosols, the v2 MAIAC retrieves AOD and spectral imaginary refractive index characterizing aerosol absorption from EPIC's UV-vis measurements. This capability was described in Lyapustin et al. (2021a). In this case, the v2 MAIAC reports AOD, single scattering albedo (SSA) at 443 nm, spectral absorption exponent (SAE) and imaginary refractive index at 680nm, and the goodness of fit for two effective heights of aerosol layer at 1 and 4 km.

The daily rate of global MAIAC retrievals ranges on average from 15 to 27%, reaching maximum during the boreal summer. This number is a proxy of the global cloud- and snow-free fraction of the Earth. The MAIAC product is distributed as compressed HDF5 files. The lossless compression gives approximately a 10-fold reduction of the file size, resulting in an average size of ~30 Mb.

The re-processing of version 3 EPIC L1B dataset for 2015–June 2021 with v2 MAIAC algorithm has been completed. The MAIAC EPIC products will soon be available for downloading from the Atmospheric Science Data Center (ASDC) at NASA Langley Research Center.

DATA AVAILABILITY STATEMENT

The datasets presented in this study can be found in online repositories. The names of the repository/repositories and accession numbers can be found below: NASA/LARC/SD/ASDC, 2018. DSCOVR EPIC L2 Multi-Angle Implementation of Atmospheric Correction (MAIAC) Atmospheric Correction data product. Available at: https://doi.org/10.5067/EPIC/DSCOVR/L2_MAIAC.001.

AUTHOR CONTRIBUTIONS

AL, DH, YW, and SK adapted MAIAC algorithm for EPIC; YW performed re-processing of EPIC data; SG and MC performed aerosol validation analysis; KB developed the geolocation algorithm; AL and DH wrote the initial draft of paper. All contributed to preparing the final version of the manuscript.

FUNDING

This work was funded by the NASA DSCOVR program (manager R. Eckman). We are grateful to the AERONET team for providing validation data and to the NASA Center for Climate Simulations used for the EPIC data processing.

PUBLISHER'S NOTE

REFERENCES

Blank, K., Huang, L.-K., Herman, J., and Marshak, A. (2021). EPIC Geolocation; Strategies to Reduce Uncertainty. *Front. Remote Sens* . (submitted May 26, 2021).

Cede, A., Huang, L. K., McCauley, G., Herman, J., Blank, K., Kowalewski, M., et al. (2021). Raw EPIC data calibration. *Front. Remote Sens.* 2. doi:10.3389/frsen.2021.702275

Doelling, D., Haney, C., Bhatt, R., Scarino, B., and Gopalan, A. (2019). The Inter-Calibration Of The Dscovr Epic Imager With Aqua-Modis And Npp-Viirs. *Remote Sensing* 11, 1609. doi:10.3390/rs11131609

Gao, F., Li, X., Strahler, A., and Schaaf, C. (2000). Evaluation of the Li Transit Kernel for BRDF Modeling. *Remote Sensing Rev.* 19 (1-4), 205–224. doi:10.1080/02757250009532419

Geogdzhayev, I. V., Marshak, A., and Alexandrov, M. (2021). Calibration Of The Dscovr Epic Visible And Nir Channels Using Multiple Leo Radiometers. *Front. Remote Sens.* 2, 671933. doi:10.3389/frsen.2021.671933

Geogdzhayev, I. V., and Marshak, A. (2018). Calibration Of The Dscovr Epic Visible And Nir Channels Using Modis Terra And Aqua Data And Epic Lunar Observations. *Atmos. Meas. Tech.* 11, 359–368. doi:10.5194/amt-11-359-2018

Gerstl, S. A. W. (1999). Building a Global Hotspot Ecology with Triana Data. *Remote Sens. Earth Science, Ocean, Sea Ice Appl.* 3868, 184–194. doi:10.1117/12.373094

Giles, D. M., Sinyuk, A., Sorokin, M. G., Schafer, J. S., Smirnov, A., Slutsker, I., et al. (2019). Advancements in the Aerosol Robotic Network (AERONET) Version 3 Database - Automated Near-Real-Time Quality Control Algorithm with Improved Cloud Screening for Sun Photometer Aerosol Optical Depth (AOD) Measurements. *Atmos. Meas. Tech.* 12, 169–209. doi:10.5194/amt-12-169-2019

Herman, J., Huang, L., McPeters, R., Ziemke, J., Cede, A., and Blank, K. (2018). Synoptic Ozone, Cloud Reflectivity, and Erythemal Irradiance from Sunrise to sunset for the Whole Earth as Viewed by the DSCOVR Spacecraft from the Earth-Sun Lagrange 1 Orbitflectivity, and Erythemal Irradiance from Sunrise to sunset for the Whole Earth as Viewed by the DSCOVR Spacecraft from the Earth–Sun Lagrange 1 Orbit. *Atmos. Meas. Tech.* 11, 177–194. doi:10.5194/amt11-177-201810.5194/amt-11-177-2018

Holben, B. N., Eck, T. F., Slutsker, I., Tanré, D., Buis, J. P., Setzer, A., et al. (1998). AERONET-A Federated Instrument Network and Data Archive for Aerosol Characterization. *Remote Sensing Environ.* 66, 1–16. doi:10.1016/s0034-4257(98)00031-5

Lucht, W., Schaaf, C. B., and Strahler, A. H. (2000). An Algorithm for the Retrieval of Albedo from Space Using Semiempirical BRDF Models. *IEEE Trans. Geosci. Remote Sensing* 38, 977–998.

doi:10.1109/36.841980

Lyapustin, A., Go, S., Korkin, S., Wang, Y., Torres, O., Jethva, H., et al. (2021a). Retrievals of Aerosol Optical Depth and Spectral Absorption from DSCOVR EPIC. *Front. Remote Sens.* 2, 645794. doi:10.3389/frsen.2021.645794

Lyapustin, A. I., Wang, Y., Laszlo, I., Hilker, T., G.Hall, F., Sellers, P. J., et al. (2012). Multi-angle Implementation of Atmospheric Correction for MODIS (MAIAC): 3. Atmospheric Correction. *Remote Sensing Environ.* 127, 385–393. doi:10.1016/j.rse.2012.09.002

Lyapustin, A., and Knyazikhin, Y. (2001). Green's Function Method for the Radiative Transfer Problem I Homogeneous Non-lambertian Surface. *Appl. Opt.* 40, 3495–3501. doi:10.1364/AO.40.003495

Lyapustin, A., Martonchik, J., Wang, Y., Laszlo, I., and Korkin, S. (2011a). Multiangle Implementation of Atmospheric Correction (MAIAC): 1. Radiative Transfer Basis and Look-Up Tables. *J. Geophys. Res.* 116, D03210. doi:10.1029/2010JD014985

Lyapustin, A., Wang, Y., Korkin, S., and Huang, D. (2018). MODIS Collection 6 MAIAC Algorithm. *Atmos. Meas. Tech.* 11, 5741–5765. doi:10.5194/amt-11-5741-2018

Lyapustin, A., Wang, Y., Laszlo, I., Kahn, R., Korkin, S., Remer, L., et al. (2011b). Multiangle Implementation of Atmospheric Correction (MAIAC): 2. Aerosol Algorithm. *J. Geophys. Res.* 116, D03211. doi:10.1029/2010JD014986

Lyapustin, A., Zhao, F., and Wang, Y. (2021b). A Comparison of Multi-Angle Implementation of Atmospheric Correction (MAIAC) and MOD09 Daily Surface Reflectance Products from MODIS. *Front. Remote Sens.* (in review).

Maignan, F., Bréon, F.-M., and Lacaze, R. (2004). Bidirectional Reflectance of Earth Targets: Evaluation of Analytical Models Using a Large Set of Spaceborne Measurements with Emphasis on the Hot Spot. *Remote Sensing Environ.* 90 (2), 210–220. doi:10.1016/j.rse.2003.12.006

Marshak, A. (2021). Alfonso Delgado-Bonal and Yuri Knyazikhin, Effect of Scattering Angle on Earth Reflectance. *Front. Remote Sens.* in review.

Marshak, A., Herman, J., Adam, S., Karin, B., Carn, S., Cede, A., et al. (2018). Earth Observations From Dscovr Epic Instrument. *Bull. Amer. Meteorol. Soc.* 99 (9), 1829–1850. doi:10.1175/BAMS-D-17-0223.1

Martins, J. V., Tanré, D., Remer, L., Kaufman, Y., Mattoo, S., and Levy, R. (2002). MODIS Cloud Screening for Remote Sensing of Aerosols over Oceans Using Spatial Variability. *Geophys. Res. Lett.* 29 (12), 1619. doi:10.1029/2001GL013252

NASA/LARC/SD/ASDC-VESDR (2021). Dscovr Epic Level 2 Vegetation Earth System Data Record (Vesdr), Version 2. In: *NASA Langley Atmospheric Science Data Center DAAC*, doi:10.5067/EPIC/DSCOVR/L2_VESDR.002

Schutgens, N., Sayer, A. M., Heckel, A., Hsu, C., Jethva, H., de Leeuw, G., et al. (2020). An AeroCom-AeroSat Study: Intercomparison of Satellite AOD Datasets for Aerosol Model Evaluation. *Atmos. Chem. Phys.* 20, 12431–12457. doi:10.5194/acp-20-12431-2020

Sinyuk, A., Holben, B. N., Eck, T. F., Giles, D. M., Slutsker, I., Korkin, S., et al. (2020). The AERONET Version 3 Aerosol Retrieval Algorithm, Associated Uncertainties and Comparisons to Version 2. *Atmos. Meas. Tech.* 13, 3375–3411. doi:10.5194/amt-13-3375-2020

Sogacheva, L., Popp, T., Sayer, A. M., Dubovik, O., Garay, M. J., Heckel, A., et al. (2020). Merging Regional and Global Aerosol Optical Depth Records from Major Available Satellite Products. *Atmos. Chem. Phys.* 20, 2031–2056. doi:10.5194/acp-20-2031-2020

Wang, Y., Lyapustin, A. I., Privette, J. L., Cook, R. B., SanthanaVannan, S. K., Vermote, E. F., et al. (2010). Assessment of Biases in MODIS Surface Reflectance Due to Lambertian Approximation. *Remote Sensing Environ.* 114, 2791–2801. doi:10.1016/j.rse.2010.06.013

Yang, B., Knyazikhin, Y., Mõttus, M., Rautiainen, M., Stenberg, P., Yan, L., et al. (2017). Estimation Of Leaf Area Index And Its Sunlit Portion From Dscovr Epic Data: Theoretical Basis. *Remote Sensing Environ.* 198, 69–84. doi:10.1016/j.rse.2017.05.033

Yang, Y., Meyer, K., Wind, G., Zhou, Y., Marshak, A., Platnick, S., et al. (2019). Cloud Products from the Earth Polychromatic Imaging Camera (EPIC): Algorithms and Initial Evaluation. *Atmos. Meas. Tech.* 12, 2019–2031. doi:10.5194/amt-12-2019-2019

Zhou, Y., Yang, Y., Gao, M., and Zhai, P.-W. (2020). Cloud Detection over Snow and Ice with Oxygen A- and B-Band Observations from the Earth Polychromatic Imaging Camera (EPIC). *Atmos. Meas. Tech.* 13, 1575–1591. doi:10.5194/amt-13-1575-2020

Conflict of Interest: At the time of this work, author DH was employed by the Science Systems and Applications Inc., Lanham, MD, United States (SSAI), and currently he is with the IEX Group, New York, NY.
The remaining authors declare that the research was conducted in the absence of any commercial or financial relationships that could be construed as a potential conflict of interest.

ORIGINAL RESEARCH
published: 20 September 2021
doi: 10.3389/frsen.2021.745938

Lagrange Point Missions: The Key to next Generation Integrated Earth Observations. DSCOVR Innovation

Francisco P. J. Valero[1*], Alexander Marshak[2] and Patrick Minnis[3]

[1] *Scripps Institution of Oceanography, University of California, San Diego, San Diego, CA, United States*
[2] *Goddard Space Flight Center, Greenbelt, MD, United States*
[3] *Science Systems and Applications, Inc., NASA Langley Research Center, Hampton, VA, United States*

Edited by:
Pavel Lytvynov, Generalized Retrieval of Atmosphere and Surface Properties (GRASP), France

Reviewed by:
Pengwang Zhai, University of Maryland, United States
Shaohua Zhao, Ministry of Ecology and Environment Center for Satellite Application on Ecology and Environment, China

**** Correspondence:*** *Francisco P. J. Valero, fvalero@ucsd.edu*

Specialty section: *This article was submitted to Satellite Missions, a section of the journal Frontiers in Remote Sensing*

Received: *22 July 2021*
Accepted: *01 September 2021*
Published: *20 September 2021*

Citation: *Valero FPJ, Marshak A and Minnis P (2021) Lagrange Point Missions: The Key to next Generation Integrated Earth Observations. DSCOVR Innovation. Front. Remote Sens. 2:745938. doi: 10.3389/frsen.2021.745938*

A new perspective for studying Earth processes has been soundly demonstrated by the Deep Space Climate Observatory (DSCOVR) mission. For the past 6 years, the first Earth-observing satellite orbiting at the Lagrange 1 (L1) point, the DSCOVR satellite has been viewing the planet in a fundamentally different way compared to all other satellites. It is providing unique simultaneous observations of nearly the entire sunlit face of the Earth at a relatively high temporal resolution. This capability enables detailed coverage of evolving atmospheric and surface systems over meso- and large-scale domains, both individually and as a whole, from sunrise to sunset, under continuously changing illumination and viewing conditions. DSCOVR's view also contains polar regions that are only partially seen from geostationary satellites (GEOs). To exploit this unique perspective, DSCOVR instruments provide multispectral imagery and measurements of the Earth's reflected and emitted radiances from 0.2 to 100 μm. Data from these sensors have been and continue to be utilized for a great variety of research involving retrievals of atmospheric composition, aerosols, clouds, ocean, and vegetation properties; estimates of surface radiation and the top-of-atmosphere radiation budget; and determining exoplanet signatures. DSCOVR's synoptic and high temporal resolution data encompass the areas observed during the day from low Earth orbiting satellites (LEOs) and GEOs along with occasional views of the Moon. Because the LEO and GEO measurements can be easily matched with simultaneous DSCOVR data, multiangle, multispectral datasets can be developed by integrating DSCOVR, LEO, and GEO data along with surface and airborne observations, when available. Such datasets can open the door for global application of algorithms heretofore limited to specific LEO satellites and development of new scientific tools for Earth sciences. The utility of the integrated datasets relies on accurate intercalibration of the observations, a process that can be facilitated by the DSCOVR views of the Moon, which serves as a stable reference. Because of their full-disc views, observatories at one or more Lagrange points can play a key role in next-generation integrated Earth observing systems.

Keywords: lagrange, surface, oceans, clouds, glint, aerosols, radiation, integrated

INTRODUCTION

Satellite remote sensing of the Earth has long relied on instruments aboard platforms in either low-Earth orbits (LEO, ~500–2000 km altitude) or geostationary orbits (GEO, at ~36,000 km). Although they can produce high-resolution views, LEOs can only scan a small portion of the surface at a given time, while a GEO can provide temporally continuous, though lower-resolution observations of a significant, though incomplete and unchanging portion of the Earth's disk. The entire disk of the planet can only be observed at the same time from a single platform at a great distance, such as the Lagrange points at ~1.5 million km, the Moon, or in transit to or from another heavenly body. The placement of satellites around the Lagrange L1 and L2 points was considered early in the satellite era by Farquhar (1960, 1968). The "Blue Marble" images of the Earth taken by the 1972 Apollo 17 spacecraft crew on their way to the Moon inspired then Vice President, Al Gore, in 1998 to propose to NASA a mission named *Triana* that would produce a continuous movie-like view of the Earth from L1 for dissemination via television and the internet as an inspiration and educational tool. Later that year, NASA issued a "request for proposals" to scientifically exploit the unique orbit of *Triana*. Thus, began the long and hard-fought battle for the *Triana* spacecraft, renamed the Deep Space Climate Observatory (DSCOVR) in 2003 (Valero, 2006), to reach the L1 position.

After traversing the customary stringent scientific peer-review process with nine other submissions, the winning proposal, authored by a team of scientists from several academic, government and private institutions led by the Scripps Institution of Oceanography, University of California, San Diego[1], would enhance the solar-viewing instruments on the *Triana* spacecraft with two new Earth-viewing instruments. Work to transform the concept into reality was immediately started by the science team and the NASA Goddard Space Flight Center which designed and built the spacecraft and managed the project. Soon thereafter, NASA requested a follow up review of the scientific value and justification of the mission, this time by the National Academy of Sciences/National Research Council (NAS/NRC). Although this request temporarily halted work on mission preparations, the ensuing review served to highlight the exceptional and innovative science and potential for future scientific advances that could be pioneered by this experimental mission.

In a December 1999 response to the NAS/NRC request, the *Triana* science team prepared and submitted a report describing the mission

scientific objectives (Valero et al., 1999). Following its review of the report and an oral review, the NAS/NRC released its conclusions on the scientific merits of the mission (National Research Council, 2000). A few notable conclusions in the NAS/NRC report are paraphrased below:

- "As an exploratory mission Triana has experimental and innovative aspects that carry more than usual risks but have the potential to make unique scientific contributions. The use of L1 for making Earth observations is itself experimental, since it will test the algorithms used to reduce remotely sensed data from a new combination of solar zenith angle and viewing backscattering angles". (Page 11 of the report)

- "Furthermore, the full-disk Earth observations provide a unique perspective from which to develop new databases and validate and augment existing and planned global databases. As an exploratory mission, Triana may well open up the use of deep space observation points such as L1 for Earth science. The task group believes that the potential impact is sufficiently valuable to Earth science that such a mission might have been viewed as an earlier NASA priority had adequate technology been available at reasonable cost." (Page two of the NAS report cover letter).

- "The task group therefore recommends that NASA seriously consider increasing the level of effort invested in development and testing of data reduction algorithms for the core Earth data products as soon as possible. In addition, it is concerned that there may be insufficient funding for scientific analysis of the data." (Page two of the NAS report cover letter).

In summary, *Triana* (DSCOVR) was found to be a strong and scientifically vital and feasible mission that will contribute unique data on Earth's climate systems. This positive final judgement of the NAS/NRC review of the mission scientific goals moved NASA to restart work on the *Triana* (DSCOVR) mission. In 2001, the instruments and spacecraft were built, but *Triana* was placed in "Stable Suspension" and finally cancelled due to shifting priorities within NASA.

Later, in November 2008, another agency, the National Oceanic and Atmospheric Administration (NOAA), discovered a solution to ensure continuing observation of critical space weather parameters. DSCOVR,

already built and equipped with solar monitoring instrumentation (a magnetometer, an electron electrostatic analyzer and a Faraday Cup), was chosen by NOAA as the replacement for its aging Advanced Composition Explorer (ACE) spacecraft (e.g., Clark, 2009). Launch preparations were re-initiated. In 2012, the U.S. Air Force allocated funds to procure a launch vehicle, the SpaceX Falcon nine rocket, and fund its operations. After more than 12 years in storage, suspensions, cancellations, reactivations and refurbishment and almost 17 years after the initial proposal, DSCOVR was finally launched on February 11, 2015.

To scientifically exploit the Earth-viewing instrument data, NASA issued a new request for proposals in 2013 to develop and utilize algorithms and processes to generate daytime products from data measured by those sensors. Proposals were selected in 2014 and funded later that year. Work on the algorithms began shortly thereafter and since 2016 a variety of Earth and atmosphere products have been generated for climate research. NOAA has also been providing important DSCOVR space weather data since July 27, 2016.

Because DSCOVR is the first Earth-observing satellite at the Sun-Earth Lagrange L1 point, it is an exploratory mission that tests and validates the scientific and observational concepts that motivated the original *Triana* mission. This paper serves as an introduction to the DSCOVR mission, its history, and its scientific findings. In particular, it discusses the unique features of the DSCOVR observations that demonstrate the potential of deep space observatories for advancing the Earth sciences. Also presented is the possibility of developing a globally Integrated Earth observation system by the synergistic association of data from space-based, airborne, and surface platforms, as enabled by DSCOVR.

Remote Sensing Instruments on DSCOVR

In addition to its space weather package, DSCOVR carries the Scripps' specified (built by Lockheed Martin) Earth Polychromatic Imaging Camera (EPIC) and the National Institute of Standards and Technology Advanced Radiometer (NISTAR). The EPIC consists of a telescope, a filter wheel, and a 2,048 × 2,048 pixel charged couple device (CCD) coated with hafnium. The Cassegrain telescope has a 0.62° field of view (FOV) that includes the full disc of the Earth, which subtends a solid angle of 0.5°, and some surrounding space. Light that comes into the telescope passes through some

field lenses then through one of the filters on the wheel and is focused on the CCD. Ten narrowband filters, hereafter referred to as channels (Table 1), reside on the wheel providing measurements in the ultraviolet (UV) range (first column in Table 1), and in the visible (VIS), and near-infrared (NIR) bands. Some of the VIS/IR channels correspond to their counterparts on the latest operational LEO and GEO imagers (column 2 in Table 1), while two others are in the oxygen A and B absorption bands (last column, Table 1). Including the instrument's point spread function yields a pixel resolution of 10 km at nadir. To reduce transmission time, the images for each channel, except at 443 nm, are reduced by averaging 2 × 2 arrays of pixels to yield a 1,024 × 1,024 pixel image. The resulting effective resolution is ~18 km at nadir. Due to a loss of transmission receivers around the globe during the hibernation of DSCOVR, the original planned hourly imagery has been reduced to between 13 and 22 images per day in boreal winter and summer, respectively. This sampling, however, is sufficient for most climate research (e.g., Holdaway et al., 2016a,b).

TABLE 1 | EPIC Channels: Central wavelength is λ, and full width, half maximum is FWHM.

λ (nm)	FWHM (nm)	λ (nm)	FWHM (nm)	λ (nm)	FWHM (nm)
317.5	1.0	443.0	2.6	687.75	0.84
325.0	1.0	551.0	3.0	764.0	1.02
340.0	2.7	680.0	1.6		
388.0	2.6	779.5	1.8		

Creating an image from the raw radiance measurements is not a straightforward process. In addition to applying at least six electronic and thermal corrections to obtain a raw calibration for each spectral image, the 10 images must be geolocated to common footprint in time and space. Each image requires a dwell time of 0.5–4.0 min for a given filter on the wheel. During that time, the Earth rotates and the spacecraft moves in its orbit. The spacecraft also undergoes a small amount of jitter and the atmospheric refraction alters the linear path of reflected light to the telescope. Marshak et al. (2018) describe the process used to correct for distortions in and discrepancies among the spectral images at a given time slot. Using an automated coastline detection approach, Molina-García et al. (2019) have

improved the geolocation of the EPIC images. The result is ten images that are projected onto a reference grid at the same common universal time (UTC).

EPIC's initial raw pixel data consist of 12-bit counts. Before being converted into physical units, the counts are corrected for various effects such as non-linearity in the response and stray light contamination (Cede et al., 2021). The corrected raw images are calibrated by regressing the raw EPIC counts against calibrated radiances from LEO imagers having similar channels. That process requires matching the EPIC and LEO imagers in time and space with the same viewing and illumination conditions. To calibrate the UV channels, Herman et al. (2018a) used reflectances measured by the Ozone Mapping and Profiler Suite (OMPS) on the Suomi National Polar-orbiting Partnership (S-NPP) satellite. The VIS/NIR channels outside of the oxygen absorbing bands have been calibrated using reflectances from the MODerate-resolution Imaging Spectroradiometer (MODIS) on the Terra and Aqua platforms and from the S-NPP Visible Infrared Imaging Suite (VIIRS) (Haney et al., 2016; Geogdzhayev and Marshak, 2018; Doelling et al., 2019a; Geogdzhayev et al., 2021). Since the lunar disc occasionally passes through the EPIC FOV (Figure 1) and the Moon has no atmosphere, the Moon is used to calibrate the EPIC oxygen absorption bands relative to their non-absorbing neighbors at 680.0 and 779.5 nm (Marshak and Ward, 2018; Geogdzhaev and Marshak, 2018).

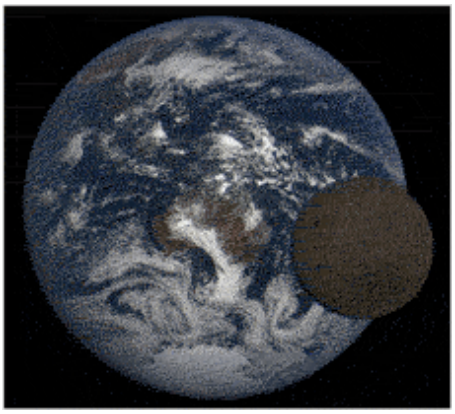

FIGURE 1 | Lunar transit of Earth observed in an EPIC RGB image, February 11, 2021. "Back" side of Moon is visible to the east of Australia.

The NISTAR comprises a set of three single-pixel active cavity radiometers that measure broadband irradiance from the entire Earth

hemisphere in three wavelength regions: shortwave (SW, 0.2–4.0 μm), NIR (0.7–4.0 μm), and total (0.2–100 μm). Measurements in those bands are taken every 4 minutes by placing the appropriate filter over each radiometer for 2 min followed by a shutter over the cavity for another 2 min to measure the offset. While originally designed to continuously monitor the sunlit side of the Earth, the small signal-to-noise ratios require averaging over a 4-h period to obtain a reliable flux. The raw filtered NISTAR irradiances are determined using prelaunch system-level optical calibration and the on-orbit offset measurements. To obtain a radiance from the Earth, the raw irradiances are first converted to radiances by dividing by the solid angle of the Earth disc. The resulting radiances are then unfiltered to obtain the "true" irradiance. Su et al. (2020) detail the processing of the NISTAR data and their conversion to usable scientific quantities.

Earth-Observing Characteristics of DSCOVR

As noted, the Lagrange points, L1 and L2, are unique locations for observing Earth from deep space. L1 and L2 are found along the Earth-Sun line: L1 between the Sun and the Earth and L2 beyond the Earth. Observational platforms at L1 and L2 would orbit the Sun in synch with Earth (the same orbital period as the Earth), thus, keeping their position "in line" with the Sun.

As a result, L1, L2 and the Earth orbit the Sun keeping on the same radial line as shown in Figure 2. From L1 the satellite has a continuous view of the entire sunlit face of the rotating Earth, including details of large-scale and mesoscale evolution of processes affecting the Earth's weather. L2 has a full view of the unilluminated opposing disc, so it can only use instruments that measure at non-solar wavelengths.

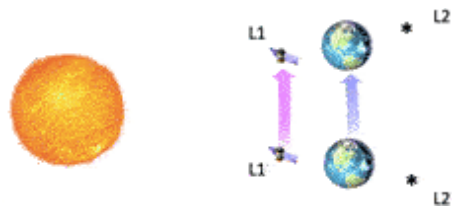

FIGURE 2 | L1 and L2 are positions on the Ecliptic plane where the net gravitational pull of the Earth and Sun equals the centripetal force required to orbit the Sun with the same orbital angular velocity as the Earth. Satellites at L1 and L2 keep the same Sun-Earth relative position and continuously view the full planet as the Earth rotates around its axis.

The equilibrium at the L1, L2 (and L3) points is unstable. If a spacecraft at L1, for example, drifted toward or away from Earth, it would fall toward the Sun or Earth. This is the reason why there is no accumulation of "space debris" or asteroids at these points. The contrary happens at the stable points, L4 and L5. To station a spacecraft at L1 or L2, it is necessary to place it in a non-repeating elliptical Lissajous orbit around the Lagrange point perpendicular to the Earth-Sun axis. Using this orbit can take DSCOVR off the axis by 4–12° (2–12° after March 2020) relative to Earth. In doing so, it keeps solar fluxes from interfering with transmissions, but alters the amount of sunlit Earth observable by the satellite as drawn in Figure 3. The relative azimuth angle ϕ_D, or off-axis angle due to the Lissajous orbit is shown Figure 3A. Also indicated is a set of scattering angles Θ illustrating the multidirectionality of the reflected sunlight. Figure 3B is a schematic of the sunlit and unlit fractions, A_v and A_d, respectively, seen by DSCOVR and the sunlit portion, A_h, that would be observed at L2. As ϕ_D approaches 180°, A_v tends toward unity. Thus, a small portion, 3–8%, of the sunlit disc is actually missed because of the Lissajous orbit.

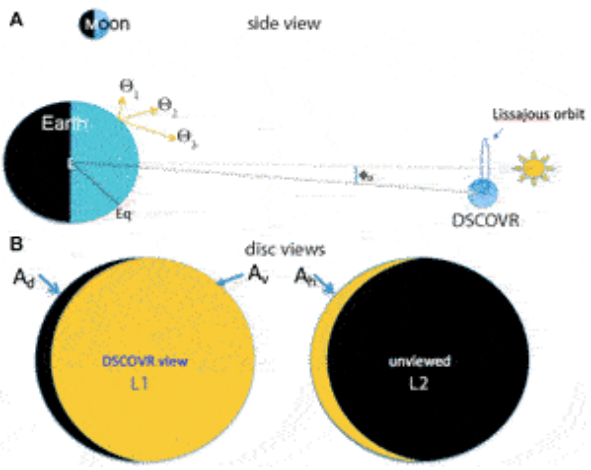

FIGURE 3 | Schematic of **(A)** Earth-Sun-DSCOVR geometry and **(B)** portion of sunlit Earth disc viewed by DSCOVR and the portion that would be viewed at L2 **(right)**. Golden area on **left** is the daytime area fraction, A_V, visible to DSCOVR and the black area, A_d, is the nighttime fraction seen by DSCOVR. The dark fraction is enhanced for purposes of illustration. The golden area on the **right** indicates the sunlit fraction, A_h, not seen by DSCOVR. Not to scale. (Adapted from Su et al., 2018).

Because of the tilt of the planet's axis of rotation, the northern or southern polar regions are observable from L1 during their respective summer solstices. The diagram in Figure 4 depicts the conditions applicable to the southern hemisphere around the summer solstice and the northern hemisphere during the winter solstice. The EPIC images in Figure 5 demonstrate this oscillating view. The northern polar region, including all of Greenland, is clearly seen on June 20, 2020 near the summer solstice in the Northern hemisphere (Figure 5A), while Figure 5B illustrates the DSCOVR view near the autumnal equinox on September 20, 2020. Most of Antarctica becomes viewable around the December solstice (Figure 5C). Because of the large viewing zenith angles (VZAs) and increased pixel size near the edge of the disc, the discernible detail is greatly reduced.

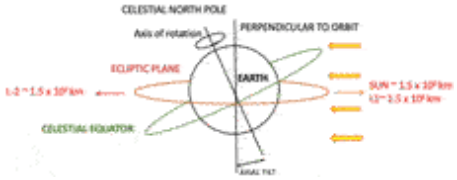

FIGURE 4 | In this diagram the Earth orbits the Sun in the ecliptic plane in the direction perpendicular to the drawing. It represents the southern hemisphere near the summer solstice and the northern hemisphere near the winter solstice.

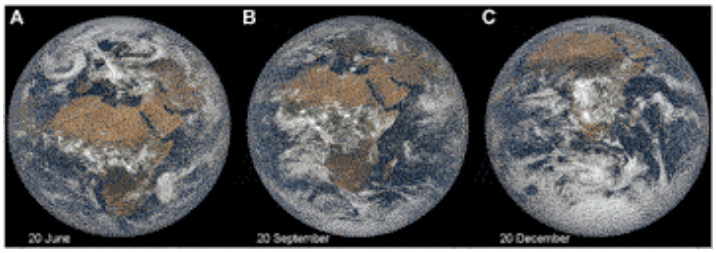

FIGURE 5 | EPIC RGB enhanced images (https://epic.gsfc.nasa.gov) during 2020 **(A)** Northern hemisphere summer solstice, **(B)** Autumnal equinox, and **(C)** Southern hemisphere summer solstice.

For the cases in Figures 5A,C a DSCOVR-like satellite at L2 would view the northern hemisphere polar region during the winter solstice and vice versa, respectively, giving full coverage of the globe. Thus, addition of a satellite at L2, performing measurements from local sunset to local sunrise (nighttime) would enable observations during the complete diurnal cycle,

day (L1) and night (infrared observations) (L2), which again, highlights the importance of adding a second platform at L2.

These nearly complete disc views contrast with the smaller areas observed by LEO and GEO satellites, as noted earlier. To obtain imagery or derived products that would provide 13–22 observations of the sunlit Earth as seen by DSCOVR requires stitching together of images from five GEOs and three or more LEOs. That process still necessitates inclusion of data taken up to 3 h from the nominal time (Khlopenkov et al., 2017). Combining all of those satellite images is a challenging task, requiring excellent intercalibration, significant angular adjustments, and edge blending to minimize artificial discontinuities. And that is only for some VIS/NIR imagery. No GEO UV or oxygen A and B band imagers are in operation, thus, only LEO satellites have been providing the information needed for retrieving ozone concentrations, surface UV irradiances, and various cloud and aerosol properties.

For example, the LEO Total Ozone Mapping Spectrometer (TOMS) samples the Earth in strips between 2000–3,000 km wide around local noon. The left image in Figure 6 depicts the ozone concentrations determined from TOMS UV data acquired over a period of ~45 min. All points are seen near local noon only (Sun synchronous satellite). The right panel shows the ozone concentrations determined from EPIC UV data on April 19, 2016 over a period of a few minutes (plus ~15 min data transmission time). As the Earth rotates, points are seen from sunrise to sunset at continuously changing solar illumination conditions. Construction of an ozone data set from TOMS or a similar instrument would require at least five appropriately equipped satellites in Sun-synchronous orbits with equally spaced equatorial crossing times.

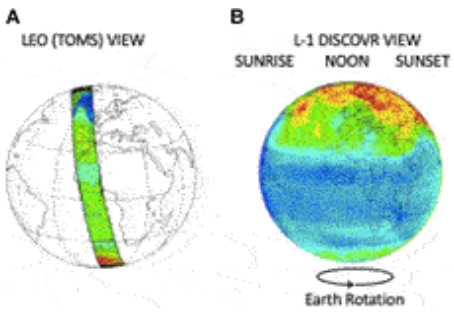

FIGURE 6 | (A) LEO (TOMS) vs. **(B)** DSCOVR views (Adapted from Herman et al. 2018a).

Some LEOs are in precessing orbits such that their equatorial crossing times increment forward or backward in time each day depending on the direction and inclination of the orbit. Those LEOs can cover the diurnal cycle for part of the Earth, but it usually takes a month or more to cover all local hours (e.g., Harrison et al., 1983). Obviously, GEOs cover the complete diurnal cycle each day but only for a fourth or fifth of the globe equatorward of 60° latitude or so. The edge of the GEO FOV along the subsatellite meridian is at ~72° latitude. Even so, data taken poleward of 60° are of minimal usability. Again, to cover all hours around the globe, data from four or five GEOs must be combined with all of the attendant issues noted above.

Each type of satellite has its unique viewing and illumination limitations. GEOs observe a given area at a constant VZA, but the solar zenith (SZA) and relative azimuth (RAA) angles change over the course of the day. Imagers on Sun-synchronous LEOs typically view an area over a wide range of RAA and VZA, but the range of SZA over a given area is constrained to those angles corresponding to ~±45 min around the equatorial crossing time. DSCOVR views a given location from a relatively constant RAA, i.e., ϕ_D in Figure 2, while both SZA and VZA vary in synch over the course of the day. The points on the surface that are in the ecliptic plane will be observed at VZAs and SZAs that range from 90° at sunrise to 0° at noon and back to 90° at local sunset. For points off the plane, the minimum VZA and SZA at local noon will increase latitudinally from the ecliptic. SZA and VZA will always be within a few degrees of each other. The result is that light reflected from any location on the planet is observed from DSCOVR at a scattering angle, $168° < \Theta < 178°$, close to direct backscatter at 180°. During many seasons, measurements are taken relatively infrequently at those scattering angles from LEO and GEO satellites [e.g., Minnis et al. (1998), Figure A1], so DSCOVR's nearly constant scattering angle everywhere on Earth is markedly different from those associated with other satellites. Yet, each scattering angle configuration has its advantages and problems, Marshak et al., 2021).

As pictured in Figure 2A, light is reflected anisotropically from the Earth-atmosphere system. The distribution of the radiant intensity varies over the hemisphere above a given location as a function of many factors such as surface type, terrain, and vegetation; cloud cover, height, phase, particle size and shape, and horizontal and vertical structure; aerosol type and optical depth; and absorbing gas concentrations among other parameters. To correct

for the anisotropy, remote sensing of the Earth from LEO and GEO satellites typically employs bidirectional reflectance distribution functions (BRDFs), also referred to as anisotropic directional models (ADMs). It is no different for DSCOVR, except that only a small portion of the BRDF is used at a given SZA because of the constrained angular range. Thus, it is important to know the BRDF very accurately for DSCOVR views because there are no measurements at other angles to balance out any biases that may be in the BRDF at a given scattering angle. GEO and LEO measurements are taken over a wide range of scattering angles and, hence, cover various portions of a given BRDF and, hence, averaging over several measurements can minimize any biases in the BRDF at any one set of viewing and illumination conditions.

SCIENTIFIC PRODUCTS AND ANALYSES

Surface and Atmospheric Properties

The proposed products from the EPIC observations include physical parameters related to land surface and ocean properties, atmospheric gases, and cloud and aerosol properties, while NISTAR data were to be used to study the top-of-atmosphere radiation budget. These parameters and others are being determined from DSCOVR data on an ongoing basis and used in a variety of scientific studies. Marshak et al. (2018) provide a review of the scientific results up to the time of that paper's acceptance. Many additional analyses of the DSCOVR measurements have been published since then, including those in this issue, and they are continuing.

Surface irradiance is derived over the sunlit part of the day from the EPIC reflectances. This includes broadband shortwave (Hao et al., 2019, 2020), photosynthetically active radiation at the ocean and land surfaces (Frouin et al., 2018; Hao et al., 2019, 2020; Zhang et al., 2020), and UV erythemal radiation that is harmful to life on the surface (Herman et al., 2018b, 2020). Spectral (Gao B.-C. et al., 2019) and broadband radiation leaving the surface is also derived from the EPIC data for the entire daylight period. Wen et al. (2020) exploited DSCOVR's L1 location to determine the impact of the 2017 total solar eclipse on the broadband shortwave surface radiation budget as the Sun's shadow traveled around the globe. The health and condition of vegetation is also monitored from DSCOVR by estimating the leaf area index (Yang et al., 2017), the enhanced vegetation index (Weber et al., 2020), and the clumping index (Pisek et al., 2021). The oxygen-B band

on EPIC allows the computation of a normalized difference vegetation index that represents an improvement over that computed using the typical visible and NIR channels on lower-orbit satellites (Marshak and Knyazikhin, 2017).

As noted earlier, the UV channels on EPIC are quite valuable for tracking ozone loading in the atmospheric column throughout the day (Herman et al., 2018a, 2020). Figure 7 provides an example of the column ozone and erythemal UV irradiance retrieved from EPIC at 18:40 UTC, June 21, 2016.

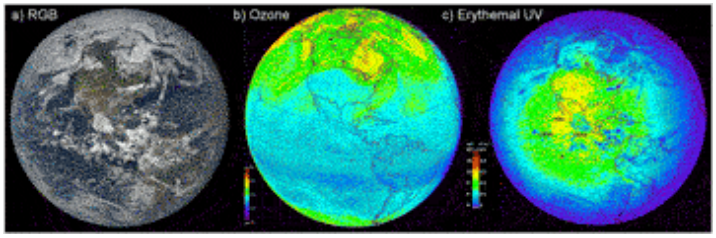

FIGURE 7 | Example of some UV-based products from EPIC, 18:40 UTC, June 21, 2016. **(A)** RGB image, **(B)** column ozone in Dobson units, and **(C)** Erythemal UV in Wm^{-2}. O3 levels are greatest in frontal areas and lowest in tropics. The erythemal UV decreases toward edge of disc because of increasing SZA. Relative maxima correspond to clearest areas. (Adapted from Herman et al., 2018b).

When combined with climatological information, the column ozone retrievals are converted to vertical profiles of ozone concentrations (Yang and Liu, 2019). Tracking of sulfur dioxide emitted into the atmosphere within volcanic ash plumes is also enabled by using the EPIC UV channels (Carn et al., 2016a, 2016, 2018). Torres et al. (2020) used the EPIC UV reflectances combined with a limb profiler and the lidar on the Cloud Aerosol Lidar and Infrared Pathfinder Satellite Observations (CALIPSO) satellite to detect and follow smoke plumes injected into the stratosphere by large forest fires in Canada. This tracking includes retrievals of the UV aerosol optical depths (AODv) and single scattering albedos (SSAv) of the smoke particles, which can reside a relatively long time in the atmosphere (e.g., Ahn et al., 2021). The UV aerosol index (UVAI), a standard EPIC product along with SO_2 and O_3 column loading and SSAv and AODv, has been employed with satellite-based lidar profiles of aerosol concentrations and modeling to quantify the impacts of pyrocumulonimbus injections of smoke aerosols into the upper troposphere and lower stratosphere (Christian et al., 2019).

Monitoring of aerosols is not confined to use of the UV channels. Aerosol optical depth is retrieved for each of the VIS/NIR channels for cloud-free regions. Additionally, the oxygen A and B bands are employed to retrieve smoke and dust aerosol layer heights with an RMSE ~0.5 km (Xu et al., 2017, 2019). Recently, Lyapustin et al. (2021) have combined the retrievals of UV and VIS/NIR aerosol optical depths (AOD) and single scattering albedos (SSA) using an innovative retrieval algorithm that utilizes sequences of EPIC images. The initial results are quite promising for improved estimates of those parameters at all wavelengths and development of the algorithms continues (e.g., Sasi et al., 2020).

Detection of clouds and retrievals of their properties using the EPIC channels for the original *Triana* mission were limited due to the absence of infrared window channels that are valuable for estimating cloud height and detecting thin cirrus and clouds in sunglint. During the refurbishment of DSCOVR after its long storage, two of the original channels were replaced with the oxygen A and B bands. That change mitigated the inability to determine cloud top height/pressure from EPIC. These channels along with other VIS/NIR channels have been used to determine cloud fraction (Yang et al., 2019; Delgado-Bonal et al., 2020), cloud phase and optical depth (Meyer et al., 2016) and cloud-top height/pressure (Yang et al., 2013, 2019; Davis et al., 2018a; Yin et al., 2020). An example of the cloud fraction retrieved from EPIC is compared with the higher resolution cloud retrieval composite from Khlopenkov et al. (2017) in Figure 8. EPIC retrievals have been supported with a body of radiative transfer studies that have determined how accurately certain parameters can be derived within the constraints of the EPIC characteristics (Davis et al., 2018b; Gao M. et al., 2019; Molina García et al., 2018a,b; Tian et al., 2020). Lacking any shortwave infrared channels (e.g., 1.6 μm), detection of clouds over snow and ice-covered surfaces has been difficult. Zhou et al. (2020, 2021) have greatly improved cloud detectability over those surfaces and in sunglint conditions over water surfaces using the oxygen A and B bands. Yang et al. (2019) describe the standard EPIC cloud products and their evaluation. As seen in the above citations, the cloud algorithms, like those for the other products, are evolving as more is learned about the information in the views from DSCOVR and in the EPIC channels.

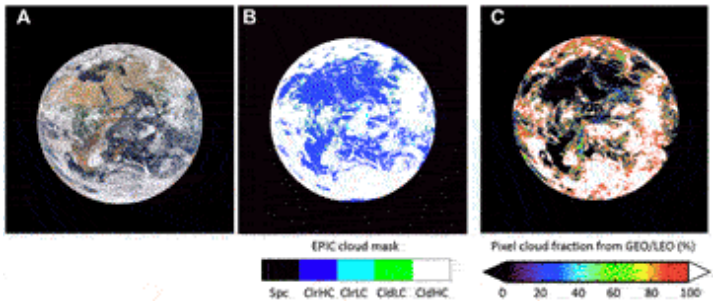

FIGURE 8 | Cloud fraction at 08:00 UTC, September 15, 2015. **(A)** EPIC RGB, **(B)** EPIC cloud mask, and **(C)** GEO/LEO cloud fraction for each EPIC pixel. GEO/LEO product is based mainly on a cloud mask using data with horizontal resolutions of 1–4 km. Good agreement is found in most areas. Monthly averages differ by only 1%. (Adapted from Yang et al. 2019).

As a result of DSCOVR's unique perspective, some of that information has been quite unexpected. Sun glints are flashes of bright specularly reflected light observed in the appropriate conditions over both water and land surfaces. Marshak et al. (2017) and Li et al. (2019) show that glints over land are caused by reflection from horizontally oriented ice platelets in cirrus clouds that are often quite thin. Detecting the glitter from those clouds at such a great distance was a surprise. In addition to sun glint observed from ocean surfaces and clouds (Varnai et al., 2020), Kostinski et al. (2021) detected extremely bright glints in EPIC reflectances from apparently small calm lakes at high altitudes in the Andes. Varnai et al. (2021) extracted the spectral properties of cloud glitter from various EPIC channels. Comparing glint observations with model simulations may provide new information on atmospheric dynamics.

Finally, in support of the Artemis mission, Gorkavyi et al. (2021) recently discussed what an EPIC-type instrument would see from the Moon's surface (see Figure 10). They showed that the lunar surface offers a unique opportunity to observe cloud glint reflection for different phase angles, to detect polar mesospheric and stratospheric clouds using whole-Earth limb imaging, and to estimate a full phase angle integrated albedo. In addition, observations from the Moon's surface will allow simultaneous imaging of the day and night parts during crescent phases of the Earth as well as the shadowed parts illuminated by lunar reflection of solar radiation.

Top-Of-Atmosphere Radiation

Measuring the daytime Earth radiation budget (ERB) using NISTAR was one of the prime objectives of the original *Triana* mission. There are many ways to measure the components of this essential climate parameter: the solar shortwave (SW) irradiance absorbed and longwave (LW) irradiance emitted into space by the Earth-atmosphere system. The former is inferred by measuring the solar radiation reflected by the planet and subtracting it from the incoming. The latter component can be measured using a radiometer with the appropriate spectral filter or by measuring the total irradiance and subtracting from it the reflected solar irradiance. In the absence of broadband radiometers, narrowband measurements have been employed to estimate the broadband fluxes with the aid of the appropriate conversion functions (e.g., Minnis and Harrison, 1984; Doelling et al., 2013).

The best estimates of the ERB to date have come from the Clouds and the Earth's Radiant Energy System (CERES; e.g., Loeb et al., 2018) and, yet, the initial CERES analyses (Loeb et al., 2009) found an improbably large imbalance in the budget (e.g., Charlson et al., 2005; Valero and Charlson, 2008). This large imbalance, ~6.5 Wm^{-2}, since reduced to 4.3 Wm^{-2} in the CERES Edition 4 product (Loeb et al., 2018), is the result of calibration, diurnal correction, and ADM uncertainties. To obtain a better balance, the fluxes are adjusted at one time to be consistent with the measured heat storage in the ocean-atmosphere system. Measuring the radiation budget from DSCOVR would provide an independent assessment of that adjustment.

To begin the process of determining the TOA radiation budget from NISTAR, it is necessary to establish BRDF values for the globe as viewed from DSCOVR (Minnis et al., 2001). Su et al. (2018) utilized the high-resolution cloud properties from the GEO/LEO cloud composite of Su et al. (2017) to select BRDF values for each EPIC pixel from the ADMs of Su et al. (2015a,b). The ADMs for the LW were selected in the same manner by Su et al. (2020). An example of the EPIC ADMs is shown in Figure 9 along with the EPIC RGB image and the composite cloud fraction for 12:17 UTC, May 15, 2017. The SW BRDFs were convolved with pixel broadband radiances estimated from the EPIC 443, 556, and 680-nm channels to compute the global reflected SW radiance and single valued SW BRDFs for the entire disk at each EPIC time. The SW result agreed with the CERES daily global albedos to within 2% with monthly RMS differences of 3.2–5.2 Wm^{-2}, values within the calibration and algorithm uncertainties. This

excellent agreement demonstrates the robustness of the BRDF values computed for each time slot. Su et al. (2020) found similar values by computing the global SW and LW ADMs by convolving the SW and LW ADM average radiances for each EPIC pixel in the same manner instead of using the EPIC-based radiances.

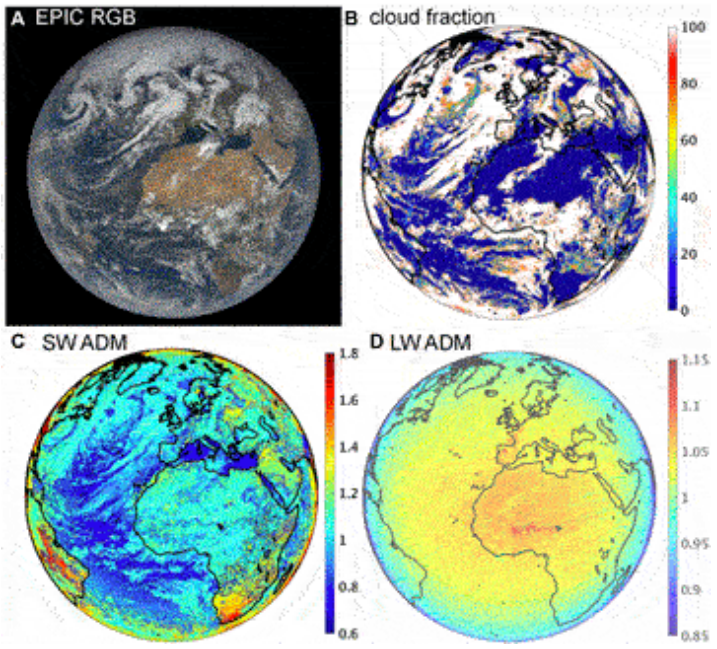

FIGURE 9 | Anisotropic directional models selected for each EPIC pixel at 12:17 UTC, May 15, 2017. **(A)** EPIC RGB image, **(B)** GEO/LEO cloud fraction for each EPIC pixel, **(C)** SW ADM, and **(D)** LW ADM. Ocean has less back scatter than land and other surfaces, except in sun glint. Global weighted average SW and LW ADMs for this scene are 1.275 and 1.041, respectively. (Adapted from Su et al., 2020).

The remaining step is to divide the NISTAR radiances by the BRDFs for each EPIC image. With that approach, Su et al. (2020) found that the NISTAR SW reflected flux is well correlated with CERES, but, on average, is 13.3 Wm^{-2} greater than CERES. The NISTAR LW flux exceeds that of CERES by 4.8 Wm^{-2}, but is poorly correlated. While much of the difference can be attributed to the uncertainties in the retrievals, explaining the SW flux bias requires more research. Part of the problem may be the lack of recalibrating the NISTAR after it was in long-term storage. Despite those differences, the NISTAR fluxes are still quite useful and have already been employed to evaluate climate model global albedo variability at time scales ranging from less than a few hours to several years (Feldman et al., 2021).

Ratios of fluxes from the NISTAR broadband NIR and full SW channels provide information that can also be used to constrain climate models and to serve as signatures of life on exoplanets (Carlson et al., 2019).

In addition to aiding the computation of the global BRDFs for NISTAR, the EPIC data have been employed in a variety of ways to study the spectral characteristics of the globe. Using four EPIC channels, Yang et al. (2018) found that the distributions of land and water surfaces on the sunlit Earth strongly affect the diurnal variation of global reflectance, while clouds dominate the seasonal cycles in average reflectance. Song et al. (2018) established that LEO and GEO imagers tend to overestimate the spectral reflectivity of the planet relative to that from EPIC. Herman et al. (2018b) were able to determine that the August 21, 2017 total eclipse reduced the sunlit Earth reflectance by ~10% in five nonabsorbing channels between 380 and 780 nm. The spectral variations in EPIC global reflectivity over the seasonal and diurnal cycles also provide information that can be used to determine the likelihood of biological activity on exoplanets (Jiang et al., 2018; Wen et al., 2019).

The Future: An Integrated Earth Observation System

From L1, the synoptic coverage and relatively high time resolution of the daytime radiances from the planet's surface and atmosphere, including the polar regions, represent a major enhancement of our ability to understand the processes and daily evolution of the Earth systems and climate/climate change. At each time slot, nearly the entire sunlit half of the globe is observed. Thus, any LEO or GEO imager observing the Earth at that time will also be in the EPIC field of view. Since the temporal resolution of GEO imagers is currently 15 min or better, there are large portions of the daytime disc where there will be nearly simultaneous matches of EPIC and GEO data and reasonable contemporaneity with LEO imager data over many other areas. The matching is not limited to VIS/IR imagers or satellites. Data from airborne and surface instruments, as well as active instruments such as lidars and microwave imagers on LEOs, are also within the EPIC footprints. Thus, the temporal resolution and broad coverage have great potential for a variety of synergistic and complementary studies that could yield improved and new products.

To facilitate those studies, Yi et al. (2001) proposed the development of a comprehensive dataset consisting of observations from LEOs and GEOs

attached to time and space-matched EPIC footprints. The composite developed by Khlopenkov et al. (2017) is the first step in realizing that possibility. While the comprehensive dataset proposed by Yi et al. (2001) has not yet been fully constructed, many of the papers cited earlier have begun the process of exploiting the matching potential of DSCOVR at L1. Among others, they include combined use of EPIC and lidar data from CALIPSO and the International Space Station (Christian et al., 2019), matched surface and EPIC data (e.g., Hao et al., 2019), and matched LEO/GEO and EPIC retrievals. Yet, there remain many possibilities for creatively and productively using combined datasets. For example, multiangle and multispectral retrievals of cloud (e.g., Chepfer et al., 2002; Pierce et al., 2010) and aerosol (e.g., Abdou et al., 2005) properties and perhaps surface characteristics (e.g., Chopping, 2008) could be accomplished with relative ease using such data. Moreover, they would provide complete diurnal and global coverage unavailable from LEO instruments specifically designed for such retrievals (e.g., Diner et al., 1998; Parol et al., 2004). Other multiangle studies employing GEO and EPIC data could be utilized to more thoroughly examine the reflectance fields at VZAs beyond the roughly 70° limit of LEO scanners.

Critical to using combined satellite datasets is accurate intercalibration of the individual instruments. As noted earlier, some of the EPIC channels were calibrated using data from similar channels on LEO/GEO satellites (e.g., Geogdzhayev and Marshak, 2018). Other channels were calibrated using the "back" side of the Moon viewed about 4 times each year in transit across the Earth disc. Lunar transits provide the opportunity to "calibrate" the Moon for each of those channels using EPIC data already normalized to a reference sensor such as VIIRS. That would provide a temporally stable reference for continued reliable calibration of the EPIC sensor array in the future. Because of its broad view and nearly hourly sampling, EPIC then could be used to monitor and adjust the calibration of similar channels on the host of current and upcoming LEO and GEO instruments as well as extraterrestrial probes (e.g., Doelling et al., 2019b). Having the comprehensive matched dataset would ease that process.

DSCOVR is the first satellite operating at a Lagrange point to serve as an Earth remote sensing platform. It was designed more than 2 decades ago and is operating at half of its initial capacity because of reduced Earth data receivers and transmission rates. Nevertheless, the DSCOVR project has

clearly been successful and has demonstrated great potential for studying the Earth, especially in conjunction with other surface, satellite, and airborne datasets. With its broad view of the Earth and calibration potential, DSCOVR could act as the anchor for an integrated Earth observing system (IEOS) using the suggested comprehensive combined observations could serve as the core dataset.

In the future, the IEOS should include both day and night observations of the whole planet using two satellites, one at L1 and another at L2. These are shown schematically in Figure 10 with some of the existing LEO (cyan) and GEO (magenta) satellites that would comprise the system along with surface and airborne sensors. The instruments on both satellites should use the latest technology to observe radiances in additional solar and infrared wavelengths and, perhaps, include polarization for some channels. While the solar channels may not be necessary for the L2 satellite, they could provide some basic scientific information by measuring the shorter wavelength radiation refracted around the Earth's edge and the crescent of reflected radiation by the small illuminated portion of the disc (see Figure 3). Infrared and broadband LW observations at L2 are technically challenging because the orbit allows some direct solar radiation to impact the spacecraft. The Earth signal would be swamped without appropriate shielding, precise thermal control, and minimization of the Lissajous orbit radius off the Earth-Sun axis. The latter is more feasible in the L2 position since there is minimal solar interference of signals transmitted from the spacecraft to Earth.

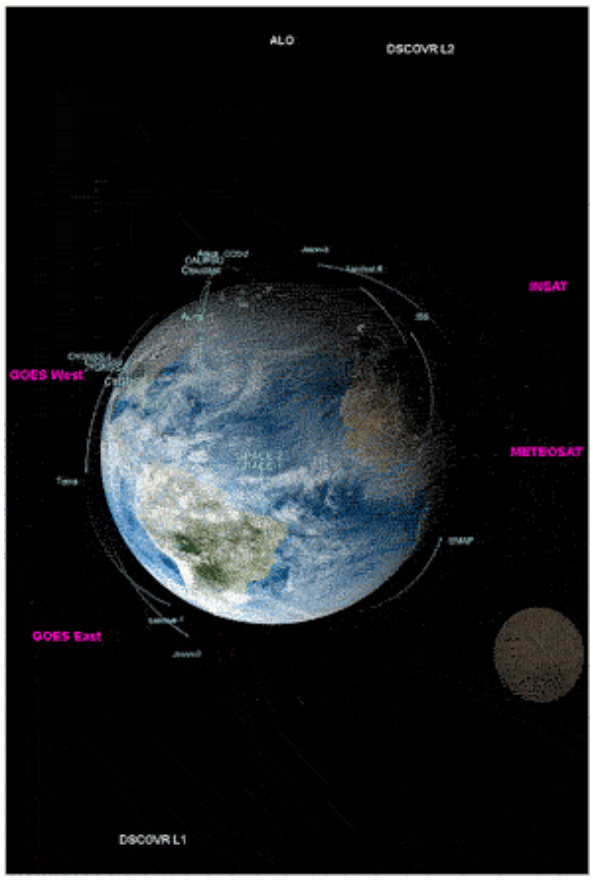

FIGURE 10 | Example diagram of a potential future integrated Earth observational system showing some LEO (cyan), GEO (magenta), and Lagrange point (white) satellites, and the Moon. (Surface and airborne platforms not shown.) (Adapted from NASA image, https://www.nasa.gov/image-feature/nasas-fleet-of-satellites-keep-an-eye-on-earth).

Temporal and spatial resolution of the Earth observations should also be greatly enhanced by employing a larger telescope on EPIC to reduce dwell time and by employing a denser CCD array, respectively. A larger telescope would also enable better IR spectral measurements at both L1 and L2. Taking advantage of such enhancements would require a faster onboard data processing and transmission system as well as additional ground receiving stations. Currently only one at Wallops, Virginia is used by DSCOVR.

Improved Lagrange-point radiation budget measurements are also possible. A revised version of NISTAR that includes a larger optical aperture, better thermal control and better calibration just prior to launch would provide a more stable and valuable complement to CERES. Inclusion of broadband channels on a revised EPIC would greatly reduce signal-to-noise ratios for radiation budget studies and provide a means for direct

intercalibration with CERES or any LEO system making similar measurements.

A satellite in an artificial Lagrange orbit (ALO) is also included at the top of Figure 10 to show a possible expansion beyond L2. An ALO is accomplished by employing the solar wind to maintain the orbit, which aligns the satellite above either of the poles, providing continuous GEO-like coverage of those regions at azimuth angles greatly different from those at L1 (Lazzarra et al., 2011).

CONCLUDING REMARKS

The instruments on DSCOVR are providing for the first time, synoptic, simultaneous mesoscale and large-scale spatial coverage of the Earth at high temporal-resolution from sunrise to sunset with periodic plain views of the sunlit polar regions, as well as the Moon, which serves as a spectro-radiometric calibration reference. The results of the DSCOVR-generated research to date are by themselves the validation of the scientific concepts that first motivated the original *Triana* mission. They demonstrate the scientific potential of observing the globe from deep space platforms. Data taken from satellites at Lagrange points can be easily combined with nearly all observations taken nearer the Earth to play a central role in building a globally integrated Earth observational system. At a minimum, Earth remote sensing from deep space should be incorporated into the NASA Earth Observing System and follow-on Lagrange point satellites should be designed and launched to fully exploit the unique potential of viewing the globe from deep space.

DATA AVAILABILITY STATEMENT

The datasets presented in this study can be found in online repositories. The names of the repository/repositories and accession number(s) can be found below: EPIC imagery are available at https://epic.gsfc.nasa.gov. Digital data and products can be accessed at the NASA Langley Atmospheric Science Data Center, https://earthdata.nasa.gov/eosdis/daacs/asdc.

AUTHOR CONTRIBUTIONS

FV developed the concept and wrote the first draft of the paper. AM and PM contributed to research for this paper and the development of several figures. All authors contributed to the writing of this paper.

PUBLISHER'S NOTE

All claims expressed in this article are solely those of the authors and do not necessarily represent those of their affiliated organizations, or those of the publisher, the editors and the reviewers. Any product that may be evaluated in this article, or claim that may be made by its manufacturer, is not guaranteed or endorsed by the publisher.

ACKNOWLEDGMENTS

Thanks to the late P. J. Crutzen. R. Charlson, C. Kennel and W. Wiscombe for many helpful discussions on DSCOVR. Thanks to W. Su for helpful discussions on the Earth radiation budget. Thanks to J. Herman for his contributions to the EPIC. Thanks to K. Blank for her help with EPIC images.

FOOTNOTES

[1]Original Science Team Membership: Valero, F.P.J., Doolittle, J.H., Hutchinson K.D., Gerstl, S.A.W., Lubin, D., Pope, S.K., Bush, B., Bucholtz, A., Ramanathan, V., Minnis, P., Pilewsky, P., Ride, S.K., Smith, G.L. and Wiscombe, W.J., Herman, J.R. joined the team immediately after NASA accepted the proposal.

REFERENCES

Abdou, W. A., Diner, D. J., Martonchik, J. V., Bruegge, C. J., Kahn, R. A., Gaitley, B. J., et al. (2005). Comparison of Coincident Multiangle Imaging Spectroradiometer and Moderate Resolution Imaging Spectroradiometer Aerosol Optical Depths Over Land and Ocean Scenes Containing Aerosol Robotic Network Sites. *J. Geophys. Res.* 110, D10S07. doi:10.1029/2004JD004693

Ahn, C., Torres, O., Jethva, H., Tiruchirapalli, R., and Huang, L. K. (2021). Evaluation of Aerosol Properties Observed by DSCOVR/EPIC Instrument From the Earth-Sun Lagrange 1 Orbit. *Geophys. Res. Atmos.* 126, e2020JD033651. doi:10.1029/2020JD033651

Carlson, B., Lacis, A., Colose, C., Marshak, A., Su, W., and Lorentz, S. (2019). Spectral Signature of the Biosphere: NISTAR Finds it in Our Solar System From the Lagrangian L-1 Point. *Geophys. Res. Lett.* 46, 10679–10686. doi:10.1029/2019GL083736

Carn, S. A., Clarisse, L., and Prata, A. J. (2016). Multi-Decadal Satellite Measurements of Global Volcanic Degassing. *J. Volcanology Geothermal Res.* 311, 99–134. doi:10.1016/j.jvolgeores.2016.01.002

Carn, S. A., Krotkov, N. A., Fisher, B. L., Li, C., and Prata, A. J. (2018). First Observations of Volcanic Eruption Clouds From the L1 Earth-Sun Lagrange Point by DSCOVR/EPIC. *Geophys. Res. Lett.* 45, 11456. doi:10.1029/2018GL079808

Carn, S. A. (2016). "On the Detection and Monitoring of Effusive Eruptions Using Satellite SO2 Measurements," in *Detecting, Modeling and Responding to Effusive Eruptions* ed . Editors A.J.L. Harris, T.F. de Groeve, and S.A. Carn (London: Geolog. Soc. London, Special Publications), 426, 277–292. doi:10.1144/SP426.28

Cede, A., Huang, L. K., Mccauley, G., Herman, J., Blank, K., Kowalewski, M., et al. (2021). Raw EPIC Data Calibration. *Front. Remote Sens.* 2, 671933. doi:10.3389/frsens.2021.671933

Charlson, R. J., Valero, F. P., and Seinfeld, J. H. (2005). Atmospheric Science. In Search of Balance. *Science* 308, 806–807. doi:10.1126/science.1108162

Chepfer, H., Minnis, P., Young, D., and Arduini, R. F. (2002). Estimation of Cirrus Cloud Effective Ice crystal Shapes Using Visible Reflectances From Dual-Satellite Measurements. *J.-Geophys.-Res.* 107 (D23), 21–1. doi:10.1029/2000JD000240

Chopping, M. J. (2008). "Terrestrial Applications of Multiangle Remote Sensing," in *Advances in Land Remote Sensing* ed . Editor S. Liang (Dordrecht: Springer), 95–144. doi:10.1007/978-1-4020-6450-0_5

Christian, K., Wang, J., Ge, C., Peterson, D., Hyer, E., Yorks, J., et al. (2019). Radiative Forcing and Stratospheric Warming of Pyrocumulonimbus Smoke Aerosols: First Modeling Results With Multisensor (EPIC, CALIPSO, and CATS) Views From Space. *Geophys. Res. Lett.* 46, 10061–10071. doi:10.1029/2019GL082360

Clark, S. (2009). Mothballed Satellite Sits in Warehouse, Waits for New Life. Space.Com. Available at: https://www.space.com/2286-mothballed-satellite-sits-warehouse-waits-life.html (Accessed March 2).

Davis, A. B., Ferlay, N., Libois, Q., Marshak, A., Yang, Y., and Min, Q. (2018a). Cloud Information Content in EPIC/DSCOVR's Oxygen A- and B-Band Channels: A Physics-Based Approach. *J. Quantitative Spectrosc. Radiative Transfer.* 220, 84–96. doi:10.1016/j.jqsrt.2018.09.006

Davis, A. B., Merlin, G., Cornet, C., Labonnote, L. C., Riédi, J., Ferlay, N., et al. (2018b). Cloud Information Content in EPIC/DSCOVR's Oxygen A- and B-Band Channels: An Optimal Estimation Approach. *J. Quantitative Spectrosc. Radiative Transfer.* 216, 6–16. doi:10.1016/j.jqsrt.2018.05.007

Delgado-Bonal, A., Marshak, A., Yang, Y., and Oreopoulos, L. (2020). Daytime Variability of Cloud Fraction From DSCOVR/EPIC Observations. *J. Geophys. Res. Atmos.* 125, e2019JD031488. doi:10.1029/2019JD031488

Diner, D. J., Beckert, J. C., Reilly, T. H., Bruegge, C. J., Conel, J. E., Kahn, R. A., et al. (1998). Multi-Angle Imaging SpectroRadiometer (MISR) Instrument Description and experiment Overview. *IEEE Trans. Geosci. Remote Sensing* 36, 1072–1087. doi:10.1109/36.700992

Doelling, D., Haney, C., Bhatt, R., Scarino, B., and Gopalan, A. (2019a). The Inter-Calibration of the DSCOVR EPIC Imager With Aqua-MODIS and NPP-VIIRS. *Remote Sensing* 11, 1609. doi:10.3390/rs11131609

Doelling, D., Khlopenkov, K., Haney, C., Bhatt, R., Bos, B., Scarino, B., et al. (2019b). Inter-Calibration of the OSIRIS-REx NavCams With Earth-Viewing Imagers. *Remote Sensing* 11, 2717. doi:10.3390/rs11222717

Doelling, D. R., Loeb, N. G., Keyes, D. F., Nordeen, M. L., Morstad, D., Nguyen, C., et al. (2013). Geostationary Enhanced Temporal Interpolation for CERES Flux Products. *J. Atmos. Oceanic Tech.* 30, 1072–1090. doi:10.1175/JTECH-D-12-00136.1

Farquhar, R. W. (1960). *Preliminary Considerations for Establishment of a Satellite in the Neighborhood of Centers of Libation*. Los Angeles, CA: M.S. Thesis, University of California.

Farquhar, R. W. (1968). *The Control and Use of Libation-point Satellites*. Palo Alto, CA: Ph.D. Dissertation, Stanford University, Department of Astronautics and Aeronautics.

Feldman, D. R., Su, W., and Minnis, P. (2021). Subdiurnal to Interannual Frequency Analysis of Observed and Modeled Reflected Shortwave Radiation from Earth. *Geophys. Res. Lett.* 48, e2020GL089221. doi:10.1029/2020GL089221

Frouin, R. J., Tan, J., Franz, B., Murakami, H., and Ramon, D. (2018). Estimating Photosynthetically Available Radiation at the Ocean Surface From EPIC/DSCOVR Data. *Remote Sens. Open Coastal Ocean Inland Waters.* , 10778. doi:10.1117/12.2501675

Gao, B.-C., Li, R.-R., and Yang, Y. (2019a). Remote Sensing of Daytime Water Leaving Reflectances of Oceans and Large Inland Lakes From EPIC Onboard the DSCOVR Spacecraft at Lagrange-1 Point. *Sensors* 19, 1243. doi:10.3390/s19051243

Gao, M., Zhai, P.-W., Yang, Y., and Hu, Y. (2019b). Cloud Remote Sensing With EPIC/DSCOVR Observations: a Sensitivity Study With Radiative Transfer Simulations. *J. Quantitative Spectrosc. Radiative Transfer.* 230, 56–60. doi:10.1016/j.jqsrt.2019.03.022

Geogdzhayev, I. V., Marshak, A., and Alexandrov, M. (2021). Calibration of the DSCOVR EPIC Visible and NIR Channels Using Multiple LEO Radiometers. *Front. Remote Sens.* 2, 671933. doi:10.3389/frsens.2021.671933

Geogdzhayev, I. V., and Marshak, A. (2018). Calibration of the DSCOVR EPIC Visible and NIR Channels Using MODIS and EPIC Lunar Observations. *Atmos. Meas. Tech.* 12, 2017–222. doi:10.5194/amt-2017-222

Gorkavyi, N., Carn, S., DeLand, M., Knyazikhin, Y., Krotkov, N., Marshak, A., et al. (2021). Earth Imaging From the Surface of the Moon With a DSCOVR/EPIC-Type Camera. *Front. Remote Sens.* 2, 724074. doi:10.3389/frsen.2021.724074

Haney, C., Doelling, D., Minnis, P., Bhatt, R., Scarino, B., and Gopalan, A. (2016). The Calibration of the DSCOVR EPIC Multiple Visible Channel Instrument Using MODIS and VIIRS as a Reference. *Earth Observing Syst. XXI.* 9972, 13. doi:10.1117/12.2238010

Hao, D., Asrar, G. R., Zeng, Y., Zhu, Q., Wen, J., Xiao, Q., et al. (2020). DSCOVR/EPIC-Derived Global Hourly and Daily Downward Shortwave and Photosynthetically Active Radiation Data at 0.1° × 0.1° Resolution. *Earth Syst. Sci. Data.* 12, 2209–2221. doi:10.5194/essd-12-2209-2020

Hao, D., Asrar, G. R., Zeng, Y., Zhu, Q., Wen, J., Xiao, Q., et al. (2019). Estimating Hourly Land Surface Downward Shortwave and Photosynthetically Active Radiation from DSCOVR/EPIC Observations. *Remote Sensing Environ.* 232, 111320. doi:10.1016/j.rse.2019.111320

Harrison, E. F., Minnis, P., and Gibson, G. G. (1983). Orbital and Cloud Cover Sampling Analyses for Multisatellite Earth Radiation Budget Experiments. *J. Spacecraft Rockets* 20, 491–495. doi:10.2514/3.25634

Herman, J., Cede, A., Huang, L., Ziemke, J., Torres, O., Krotkov, N., et al. (2020). Global Distribution and 14-Year Changes in Erythemal Irradiance, UV Atmospheric Transmission, and Total Column Ozone For2005-2018 Estimated From OMI and EPIC Observations. *Atmos. Chem. Phys.* 20, 8351–8380. doi:10.5194/acp-20-8351-2020

Herman, J., Wen, G., Marshak, A., Blank, K., Huang, L., Cede, A., et al. (2018a). Reduction in 317-780 Nm Radiance Reflected From the Sunlit Earth During the Eclipse of 21 August 2017. *Atmos. Meas. Tech.* 11, 4373–4388. doi:10.5194/amt-11-4373-2018

Herman, J., Huang, L., McPeters, R., Ziemke, J., Cede, A., and Blank, K. (2018b). Synoptic Ozone, Cloud Reflectivity, and Erythemal Irradiance From Sunrise to Sunset for the Whole Earth as Viewed by the DSCOVR Spacecraft From the Earth-Sun Lagrange 1 Orbit. *Atmos. Meas. Tech.* 11, 177–194. doi:10.5194/amt-11-177-2018

Holdaway, D., and Yang, Y. (2016a). Study of the Effect of Temporal Sampling Frequency on DSCOVR Observations Using the GEOS-5 Nature Run Results (Part II): Cloud Coverage. *Remote Sensing* 8 (5), 431. doi:10.3390/rs8050431

Holdaway, D., and Yang, Y. (2016b). Study of the Effect of Temporal Sampling Frequency on DSCOVR Observations Using the GEOS-5 Nature Run Results (Part I): Earth's Radiation Budget. *Remote Sensing* 8 (2), 98. doi:10.3390/rs8020098

Jiang, J. H., Zhai, A. J., Herman, J., Zhai, C., Hu, R., Su, H., et al. (2018). Using Deep Space Climate Observatory Measurements to Study the Earth as an Exoplanet. *Astronomical J.* 156, 26. doi:10.3847/1538-3881/aac6e2

Khlopenkov, K. V., Duda, D. P., Minnis, P., Su, W., Bedka, K. M., and Thieman, M. (2017). Development of Multi-Sensor Global Cloud and Radiance Composites for Earth Radiation Budget Monitoring from DSCOVR. *Proc. SPIE Conf. Remote Sens. Clouds Atmos.* XXII, 11–14. doi:10.1117/12.2278645

Kostinski, A., Marshak, A., and Várnai, T. (2021). Deep Space Observations of Terrestrial Glitter. *Earth Space Sci.* 8, e2020EA001521. doi:10.1029/2020EA001521

Lazzara, M. A., Coletti, A., and Diedrich, B. L. (2011). The Possibilities of Polar Meteorology, Environmental Remote Sensing, Communications and Space Weather Applications From Artificial Lagrange Orbit. *Adv. Space Res.* 48, 1880–1889. doi:10.1016/j.asr.2011.04.026

Li, J.-Z., Fan, S., Kopparla, P., Liu, C., Jiang, J. H., Natraj, V., et al. (2019). Study of Terrestrial Glints Based on DSCOVR Observations. *Earth Space Sci.* 6, 166–173. doi:10.1029/2018EA000509

Loeb, N. G., Doelling, D. R., Wang, H., Su, W., Nguyen, C., Corbett, J. G., et al. (2018). Clouds and the Earth's Radiant Energy System (CERES) Energy Balanced and Filled (EBAF) Top-Of-Atmosphere (TOA) Edition-4.0 Data Product. *J. Clim.* 31, 895–918. doi:10.1175/JCLI-D-17-0208.1

Loeb, N. G., Su, W., Doelling, D. R., Wong, T., Minnis, P., Thomas, S., et al. (2018). Earth's Top-of-Atmosphere Radiation Budget. *Comprehensive Remote Sensing* 5 (3), 67–84. (Oxford, UK: Elsevier) doi:10.1016/B978-0-12-409548.9.10367-7

Loeb, N. G., Wielicki, B. A., Doelling, D. R., Smith, G. L., Keyes, D. F., Kato, S., et al. (2009). Toward Optimal Closure of the Earth's Top-Of-Atmosphere Radiation Budget. *J. Clim.* 22, 748–766. doi:10.1175/2008JCLI2637.1

Lyapustin, A., Go, S., Korkin, S., Wang, Y., Torres, O., Jethva, H., et al. (2021). Retrievals of Aerosol Optical Depth and Spectral Absorption From DSCOVR EPIC. *Front. Remote Sens.* 2, 645794. doi:10.3389/frsen.2021.645794

Marshak, A., Delgado-Bonal, A., and Knyazikhin, Y. (2021). Effect of Scattering Angle on Earth Reflectance. *Front. Remote Sens.* 2, 719610. doi:10.3389/frsen.2021.719610

Marshak, A., Herman, J., Adam, S., Karin, B., Carn, S., Cede, A., et al. (2018). Earth Observations From DSCOVR EPIC Instrument. *Bull. Amer. Meteorol. Soc.* 99, 1829–1850. doi:10.1175/BAMS-D-17-0223.1

Marshak, A., and Knyazikhin, Y. (2017). The Spectral Invariant Approximation Within Canopy Radiative Transfer to Support the Use of the EPIC/DSCOVR Oxygen B-Band for Monitoring Vegetation. *J. Quantitative Spectrosc. Radiative Transfer.* 191, 7–12. doi:10.1016/j.jqsrt.2017.01.015

Marshak, A., Várnai, T., and Kostinski, A. (2017). Terrestrial Glint Seen From Deep Space: Oriented Ice Crystals Detected from the Lagrangian point. *Geophys. Res. Lett.* 44, 5197–5202. doi:10.1002/2017GL073248

Marshak, A., and Ward, A. (2018). Summary of DSCOVR EPIC and NISTAR Science Team Meeting. *The Earth Observer.* 30 (6), 16–22.

Meyer, K., Yang, Y., and Platnick, S. (2016). Uncertainties in Cloud Phase and Optical Thickness Retrievals From the Earth Polychromatic Imaging Camera (EPIC). *Atmos. Meas. Tech.* 9, 1785–1797. doi:10.5194/amt-9-1785-2016

Minnis, P., Garber, D. P., YoungArduini, D. F. R. F., Arduini, R. F., and Takano, Y. (1998). Parameterizations of Reflectance and Effective Emittance for Satellite Remote Sensing of Cloud Properties. *J. Atmos. Sci.* 55, 3313–3339. doi:10.1175/1520-0469(1998)055<3313:poraee>2.0.co;2

Minnis, P., and Harrison, E. F. (1984). Diurnal Variability of Regional Cloud and Clear-Sky Radiative Parameters Derived From GOES Data. Part III: November 1978 Radiative Parameters. *J. Clim. Appl. Meteorol.* 23, 1032–1051. doi:10.1175/1520-0450(1984)023<1032:dvorca>2.0.co;2

Minnis, P., Huang, J., Doelling, D. R., and Valero, F. P. (2001). Simulation and Correction of Triana-Viewed Earth Radiation Budget With ERBE Data. *Proc. SPIE 4540, Sensors, Systems, Next-generation Satellites V.* 12-17, 391–401. doi:10.1117/12.450681

Molina García, V., Sasi, S., Efremenko, D. S., Doicu, A., and Loyola, D. (2018a). Radiative Transfer Models for Retrieval of Cloud Parameters From EPIC/DSCOVR Measurements. *J. Quantitative Spectrosc. Radiative Transfer.* 213, 228–240. doi:10.1016/j.jqsrt.2018.03.014

Molina García, V., Sasi, S., Efremenko, D. S., Doicu, A., and Loyola, D. (2018b). Linearized Radiative Transfer Models for Retrieval of Cloud Parameters From EPIC/DSCOVR Measurements. *J. Quantitative Spectrosc. Radiative Transfer.* 213, 241–251. doi:10.1016/j.jqsrt.2018.03.008

Molina García, V., Sasi, S., Efremenko, D. S., and Loyola, D. (2019). Improvement of EPIC/DSCOVR Image Registration by Means of Automatic Coastline Detection. *Remote Sensing* 11 (15), 1747. doi:10.3390/rs11151747

National Research Council (2000). *Review of Scientific Aspects of the NASA Triana Mission: Letter Report*. Washington, DC: The National Academies Press. doi:10.17226/9789

Parol, F., Buriez, J. C., Vanbauce, C., Riedi, J., C.-Labonnote, L., Doutriaux-Boucher, M., et al. (2004). Review of Capabilities of Multi-Angle and Polarization Cloud Measurements from POLDER. *Adv. Space Res.* 33, 1080–1088. doi:10.1016/s0273-1177(03)00734-8

Pierce, J. R., Kahn, R. A., Davis, M. R., and Comstock, J. M. (2010). Detecting Thin Cirrus in Multiangle Imaging Spectroradiometer Aerosol Retrievals. *J. Geophys. Res.* 115, D08201. doi:10.1029/2009JD013019

Pisek, J., Arndt, S. K., Erb, A., Pendall, E., Schaaf, C., Wardlaw, T. J., et al. (2021). Exploring the Potential of DSCOVR EPIC Data to Retrieve Clumping Index in Australian Terrestrial Ecosystem Research Network Observing Sites. *Front. Remote Sens.* 2, 652436. doi:10.3389/frsen.2021.652436

Sasi, S., Natraj, V., Molina García, V., Efremenko, D. S., Loyola, D., and Doicu, A. (2020). Model Selection in Atmospheric Remote Sensing With an Application to Aerosol Retrieval From DSCOVR/EPIC, Part 1: Theory. *Remote Sensing* 12, 3724. doi:10.3390/rs12223724

Song, W., Knyazikhin, Y., Wen, G., Marshak, A., Mõttus, M., Yan, K., et al. (2018). Implications of Whole-Disc DSCOVR EPIC Spectral Observations for Estimating Earth's Spectral Reflectivity Based on Low-Earth-Orbiting and Geostationary Observations. *Remote Sensing* 10, 1594. doi:10.3390/rs10101594

Su, W., Corbett, J., Eitzen, Z., and Liang, L. (2015a). Next-generation Angular Distribution Models for Top-Of-Atmosphere Radiative Flux Calculation From CERES Instruments: Methodology. *Atmos. Meas. Tech.* 8, 611–632. doi:10.5194/amt-8-611-2015

Su, W., Corbett, J., Eitzen, Z., and Liang, L. (2015b). Next-generation Angular Distribution Models for Top-Of-Atmosphere Radiative Flux Calculation From CERES Instruments: Validation. *Atmos. Meas. Tech.* 8, 3297–3313. doi:10.5194/amt-8-3297-2015

Su, W., Liang, L., Doelling, D. R., Minnis, P., Duda, D. P., Khlopenkov, K., et al. (2018). Determining the Shortwave Radiative Flux from Earth Polychromatic Imaging Camera. *J. Geophys. Res. Atmos.* 123, 479–511. doi:10.1029/2018JD029390

Su, W., Minnis, P., Liang, L., Duda, D. P., Khlopenkov, K., Thieman, M. M., et al. (2020). Determining the Daytime Earth Radiative Flux From National Institute of Standards and Technology Advanced Radiometer (NISTAR) Measurements. *Atmos. Meas. Tech.* 13, 429–443. doi:10.5194/amt-13-429-2020

Tian, Q., Liu, Q., Guang, J., Yang, L., Zhang, H., Fan, C., et al. (2020). The Estimation of Surface Albedo From DSCOVR EPIC. *Remote Sensing* 12, 1897. doi:10.3390/rs12111897

Torres, O., Bhartia, P. K., Taha, G., Jethva, H., Das, S., Colarco, P., et al. (2020). Stratospheric Injection of Massive Smoke Plume From Canadian Boreal Fires in 2017 as Seen by DSCOVR-EPIC, CALIOP, and OMPS-LP Observations. *J. Geophys. Res. Atmos.* 125. doi:10.1029/2020JD032579

Valero, F. P. (2006). Keeping the DSCOVR Mission Alive. *Science.* 311 (5762), 775. doi:10.1126/science.311.5762.775c

Valero, F. P. J., and Charlson, R. J. (2008). Albedo-Watching Satellite Needed to Monitor Change. *Nature* 451 (718), 887. doi:10.1038/451887c

Valero, F. P. J., Herman, J., Minnis, P., Collins, W. D., Sadourny, R., Wiscombe, W., et al. (1999). Triana- a Deep Space Earth and Solar Observatory, NASA Background Report. Available at.

Varnai, T., Kostinski, A. B., and Marshak, A. (2020). Deep Space Observations of Sun Glints From Marine Ice Clouds. *IEEE Geosci. Remote Sensing Lett.* 17 (5), 735–739. doi:10.1109/LGRS.2019.2930866

Varnai, T., Marshak, A., and Kostinski, A. B. (2021). Deep Space Observations of Cloud Glints: Spectral and Seasonal Dependence. *IEEE Geosci. Remote Sensing Lett.* 17, 1–5. doi:10.1109/LGRS.2020.3040144

Weber, M., Hao, D., Asrar, G. R., Zhou, Y., Li, X., and Chen, M. (2020). Exploring the Use of DSCOVR/EPIC Satellite Observations to Monitor Vegetation Phenology. *Remote Sensing* 12, 2384. doi:10.3390/rs12152384

Wen, G., Marshak, A., Song, W., Knyazikhin, Y., Mõttus, M., and Wu, D. (2019). A Relationship Between Blue and Near-IR Global Spectral Reflectance and the Response of Global Average Reflectance to Change in Cloud Cover Observed from EPIC. *Earth Space Sci.* 6, 1416–1429. doi:10.1029/2019EA000664

Wen, G., Marshak, A., Tsay, S.-C., Herman, J., Jeong, U., Abuhassan, N., et al. (2020). Changes in Surface Broadband Shortwave Radiation Budget During the 2017 Eclipse. *J. Atmos. Chem. Phys.* , 2019–961. doi:10.5194/acp-2019-961

Xu, X., Wang, J., Wang, Y., Zeng, J., Torres, O., Reid, J. S., et al. (2019). Detecting Layer Height of Smoke Aerosols Over Vegetated Land and Water Surfaces via Oxygen Absorption Bands: Hourly Results From EPIC/DSCOVR in Deep Space. *Atmos. Meas. Tech.* 12, 3269–3288. doi:10.5194/amt-12-3269-2019

Xu, X., Wang, J., Wang, Y., Zeng, J., Torres, O., Yang, Y., et al. (2017). Passive Remote Sensing of Altitude and Optical Depth of Dust Plumes Using the Oxygen A and B Bands: First Results From EPIC/DSCOVR at Lagrange-1 Point. *Geophys. Res. Lett.* 44, 7544–7554. doi:10.1002/2017GL073939

Yang, B., Knyazikhin, Y., Mõttus, M., Rautiainen, M., Stenberg, P., Yan, L., et al. (2017). Estimation of Leaf Area Index and its Sunlit Portion From DSCOVR EPIC Data: Theoretical Basis. *Remote Sensing Environ.* 198, 69–84. doi:10.1016/j.rse.2017.05.033

Yang, K., and Liu, X. (2019). Ozone Profile Climatology for Remote Sensing Retrieval Algorithms. *Atmos. Meas. Tech.* 12, 4745–4778. doi:10.5194/amt-12-4745-2019

Yang, W., Marshak, A., Várnai, T., and Knyazikhin, Y. (2018). EPIC Spectral Observations of Variability in Earth's Global Reflectance. *Remote Sensing* 10 (2), 254. doi:10.3390/rs10020254

Yang, Y., Marshak, A., Mao, J., Lyapustin, A., and Herman, J. (2013). A Method of Retrieving Cloud Top Height and Cloud Geometrical Thickness With Oxygen A and B Bands for the Deep Space Climate Observatory (DSCOVR) Mission: Radiative Transfer Simulations. *J. Quantitative Spectrosc. Radiative Transfer.* 122, 141–149. doi:10.1016/j.jqsrt.2012.09.017

Yang, Y., Meyer, K., Wind, G., Zhou, Y., Marshak, A., Platnick, S., et al. (2019). Cloud Products From the Earth Polychromatic Imaging Camera (EPIC): Algorithms and Initial Evaluation. *Atmos. Meas. Tech.* 12, 2019–2031. doi:10.5194/amt-12-2019-2019

Yi, H. Y., Minnis, P., Nguyen, L., and Doelling, D. R. (2001). "A Proposed Multiangle Satellite Dataset Using GEO, LEO, and Triana," in *Proc. AMS 11th Conf. Satellite Meteorology and Oceanography* (Madison, WI, 570–573. Oct. 15-18. Available at: https://ams.confex.com/ams/pdfpapers/24404.pdf.

Yin, B., Min, Q., Morgan, E., Yang, Y., Marshak, A., and Davis, A. (2020). Cloud Top Pressure Retrieval With DSCOVR-EPIC Oxygen A and B Bands Observation. *Atmos. Meas. Tech.* 13, 1–18. doi:10.5194/amt-13-1-2020

Zhang, Z., Zhang, Y., Zhang, Y., Gobron, N., Frankenberg, C., Wang, S., et al. (2020). The Potential of Satellite FPAR Product for GPP Estimation: An Indirect Evaluation Using Solar-Induced Chlorophyll Fluorescence. *Remote Sensing Environ.* 240, 111686. doi:10.1016/j.rse.2020.111686

Zhou, Y., Yang, Y., Gao, M., and Zhai, P.-W. (2020). Cloud Detection Over Snow and Ice With Oxygen A- and B-Band Observations From the Earth Polychromatic Imaging Camera (EPIC). *Atmos. Meas. Tech.* 13, 1575–1591. doi:10.5194/amt-13-1575-2020

Zhou, Y., Yang, Y., Zhai, P.-W., and Gao, M. (2021). Cloud Detection Over Sunglint Regions With Observations From the Earth Polychromatic Imaging Camera. *Front. Remote Sens.* 2, 690010.

doi:10.3389/frsen.2021.690010

Conflict of Interest: Author PM is employed by the company Science Systems and Applications., Inc. under a non-personal services contract with NASA Langley Research Center.The remaining authors declare that the research was conducted in the absence of any commercial or financial relationships that could be construed as a potential conflict of interest.

ORIGINAL RESEARCH
published: 11 October 2021
doi: 10.3389/frsen.2021.747859

Global Daytime Mean Shortwave Flux Consistency Under Varying EPIC Viewing Geometries

Wenying Su[1*], Lusheng Liang[2], David P. Duda[2], Konstantin Khlopenkov[2] and Mandana M. Thieman[2]

[1] *Science Directorate, NASA Langley Research Center, Hampton, VA, United States*
[2] *Science Systems and Applications Inc., Hampton, VA, United States*

Edited by:
Alexei Lyapustin, Goddard Space Flight Center, National Aeronautics and Space Administration, United States

Reviewed by:
Catherine M. Naud, Columbia University, United States
Zhenzhu Wang, Aiofm (CAS), China

**** Correspondence:** Wenying Su, Wenying.Su-1@nasa.gov*

***Specialty section:** This article was submitted to Satellite Missions, a section of the journal Frontiers in Remote Sensing*

***Received:** 26 July 2021*
***Accepted:** 22 September 2021*
***Published:** 11 October 2021*

***Citation:** Su W, Liang L, Duda DP, Khlopenkov K and Thieman MM (2021) Global Daytime Mean Shortwave Flux Consistency Under Varying EPIC Viewing Geometries. Front. Remote Sens. 2:747859. doi: 10.3389/frsen.2021.747859*

One of the most crucial tasks of measuring top-of-atmosphere (TOA) radiative flux is to understand the relationships between radiances and fluxes,

particularly for the reflected shortwave (SW) fluxes. The radiance-to-flux conversion is accomplished by constructing angular distribution models (ADMs). This conversion depends on solar-viewing geometries as well as the scene types within the field of view. To date, the most comprehensive observation-based ADMs are developed using the Clouds and the Earth's Radiant Energy System (CERES) observations. These ADMs are used to derive TOA SW fluxes from CERES and other Earth radiation budget instruments which observe the Earth mostly from side-scattering angles. The Earth Polychromatic Imaging Camera (EPIC) onboard Deep Space Climate Observatory observes the Earth at the Lagrange-1 point in the near-backscattering directions and offers a testbed for the CERES ADMs. As the EPIC relative azimuth angles change from 168° to 178°, the global daytime mean SW radiances can increase by as much as 10% though no notable cloud changes are observed. The global daytime mean SW fluxes derived after considering the radiance anisotropies at relative azimuth angles of 168° and 178° show much smaller differences (<1%), indicating increases in EPIC SW radiances are due mostly to changes in viewing geometries. Furthermore, annual global daytime mean SW fluxes from EPIC agree with the CERES equivalents to within 0.5 Wm^{-2} with root-mean-square errors less than 3.0 Wm^{-2}. Consistency between SW fluxes from EPIC and CERES inverted from very different viewing geometries indicates that the CERES ADMs accurately quantify the radiance anisotropy and can be used for flux inversion from different viewing perspectives.

Keywords: radiance, flux, angular distribution models, radiance-to-flux inversion, Earth radiation budget

1 INTRODUCTION

The Deep Space Climate Observatory (DSCOVR) was launched on Feb. 11, 2015 and is the first Earth-observing satellite at the Lagrange-1 (L1) point, about 1.6 million kilometers from Earth. DSCOVR is in an elliptical Lissajous orbit around the L1 point and is not positioned exactly on the Earth-Sun line; therefore, only about 92–97% of the sunlit Earth is visible to DSCOVR (Su et al., 2018). Onboard DSCOVR, the National Institute of Standards and Technology Advanced Radiometer (NISTAR) provides continuous full disc global broadband irradiance measurements over most of the sunlit side of the Earth at near-backscattering relative azimuth angles (Figure 1). DSCOVR also carries the Earth Polychromatic Imaging Camera

(EPIC) which provides 2048 by 2048 pixel imagery 10 to 22 times per day in 10 spectral bands from 317 to 780 nm. DSCOVR's elliptical Lissajous orbit is a quasi-periodic orbit and its distance and viewing geometries change from day to day. Figure 2 shows the relative azimuth angles between DSCOVR and the solar plane from 2017 to 2020. From January 2017 to June 2019, the relative azimuth angles show small month-to-month variations and the maximum value does not exceed 175°. However, the relative azimuth angles of 2020 show large month-to-month changes (about twice the amplitude of previous years), with the maximum relative azimuth angle exceeding 178° in December.

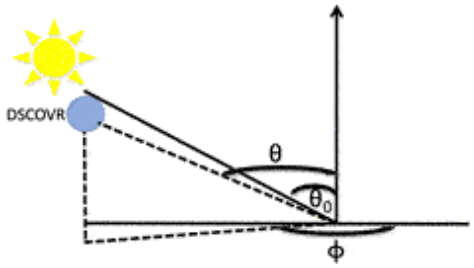

FIGURE 1 | DSCOVR viewing geometry, θ_0 is the solar zenith angle, θ is the DSCOVR viewing zenith angle, and ϕ is the relative azimuth angle between DSCOVR and the solar plane.

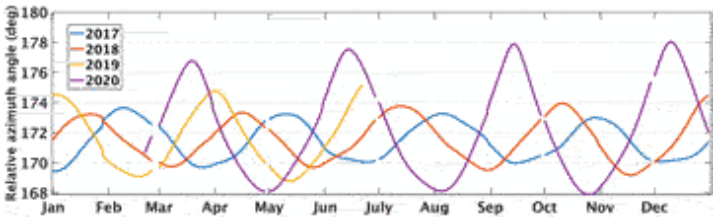

FIGURE 2 | Year-to-year variation of the relative azimuth angle for DSCOVR.

Su et al. (2018) developed a methodology to derive global daytime shortwave (SW) flux from EPIC spectral measurements. While EPIC does not measure the entire sunlit side of Earth, we refer to EPIC measurements as "global' daytime for simplicity. Their approach includes three steps: 1) derive broadband SW radiances from the EPIC narrowband measurements using pre-determined narrowband-to-broadband regression relationships and calculate the global daytime mean radiances ($\overline{I_{sw}}$); 2) derive global daytime mean anisotropy factors ($\overline{R_{sw}}$) using angular distribution models (ADMs, Su

et al., 2015a) developed by the Clouds and the Earth's Radiant Energy System (CERES) project, and using cloud properties in the EPIC cloud composite product (Khlopenkov et al., 2017) for scene identification; 3) derive global daytime mean SW flux: $\overline{F_{sw}} = \pi \overline{I_{sw}} / \overline{R_{sw}}$. These EPIC-based $\overline{F_{sw}}$ agree with the CERES fluxes within the EPIC view to within ±2%, well within the calibration and algorithm uncertainties of each instrument. This is the first time that CERES ADMs have been applied to the near-backscattering direction to derive flux and the good agreement indicates that CERES ADMs accurately account for the Earth's anisotropy in the near-backscattering direction.

Changes in the EPIC relative azimuth angles in 2020 offer another opportunity to examine whether CERES ADMs can capture the changes in radiance anisotropy as the relative azimuth angles moved from 170° to 178°. Anisotropies at these near-backscattering angles are rarely used to invert fluxes for CERES cross track observations. Theoretically, radiative fluxes inverted from different viewing geometries at a given solar zenith angle should be identical. Thus, good agreement between global daytime mean fluxes from EPIC and CERES that are derived using observations from near-backscattering directions and side-scattering directions can be used as an indication of the validity of the ADMs, similar to the consistency tests that have been done to validate the CERES ADMs (Su et al., 2015b). This paper will examine how $\overline{I_{sw}}$ and $\overline{R_{sw}}$ vary with relative azimuth angles and compare $\overline{F_{sw}}$ from EPIC derived at different backscattering directions with CERES counterparts to investigate if CERES ADMs capture the radiance anisotropy changes at different backscattering angles. Section 2 briefly describes the method used to derive EPIC-based broadband SW radiance and compares the radiances from EPIC under different relative azimuth angles. To convert radiances to fluxes, we rely on CERES ADMs which are functions of scene types defined using many variables (i.e., surface type, cloud fraction, cloud optical depth, cloud phase, etc). Section 3 describes the EPIC cloud composite product developed from cloud retrievals using imagers on low-Earth orbit and geostationary satellites. The EPIC cloud composite is used to provide scene identification for anisotropy characterization. Section 4 provides an overview of the CERES ADMs. EPIC-based SW fluxes and comparisons with CERES product are provided in section 5 and conclusions are in section 6.

2 DERIVING GLOBAL DAYTIME MEAN BROADBAND SHORTWAVE RADIANCES FROM EPIC MEASUREMENTS

EPIC channels of 443 nm, 551 nm, and 680 nm are used to derive the broadband SW radiances following the methodology developed by Su et al. (2018). The narrowband-to-broadband regression coefficients are derived using collocated Moderate Resolution Imaging Spectrometer (MODIS) narrowband reflectances (469, 550, and 645 nm) and CERES broadband reflectances within the CERES Single Scanner Footprint TOA/Surface Fluxes and Clouds (SSF) Edition 4 A product separately for ocean and non-ocean surfaces for all-sky conditions.

These narrowband-to-broadband regressions are then applied to the EPIC measurements to derive the "EPIC broadband" SW reflectance for each EPIC pixel. The pixel-level broadband SW reflectances are converted to radiances first, and the global daytime mean SW radiance at each EPIC image time is calculated following the simple average proposed by Yang et al. (2018).

Figure 3 shows the global daytime mean SW radiances ($\overline{I_{sw}}$) at the EPIC image times for May and December of 2017 and 2020. Relative azimuth angles are also included in Figure 3. The magnitude of $\overline{I_{sw}}$ depends on many factors: fractions of land, ocean, snow, and ice within the EPIC image, amount of clouds and cloud properties (optical depth, thermodynamical phase, and particle size, to a lesser extent), and also the viewing geometries. For a specific observation time (same date and time of different year), EPIC views the same portion of the Earth disc. Thus, changes in clouds and viewing geometries are the dominant factors affecting the magnitude of $\overline{I_{sw}}$. For May, $\overline{I_{sw}}$ of 2017 are greater than those of 2020 during the first half of the month when the relative azimuth angles differ the most between 2017 and 2020. Thereafter, the relative azimuth angles converge and the differences start to decrease. For December, $\overline{I_{sw}}$ of 2020 are consistently greater than those of 2017 except for the last few days of the month, and the largest difference exceeds 10 W $m^{-2}sr^{-1}$ (>10%). Next we demonstrate why it is unlikely any changes in clouds and/or aerosols can cause radiance changes of this magnitude, changes in viewing geometries are therefore a more plausible reason. Note the relative azimuth angels are between 176° and 178° during early December 2020, while they are close to 170° for the same period of 2017. The radiances from many Earth scenes can be very different when viewed at these different azimuth angles (Gatebe and King, 2016).

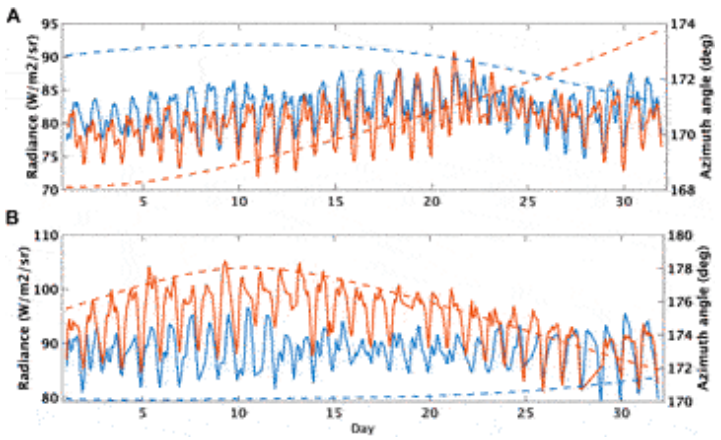

FIGURE 3 | Comparison of global daytime mean EPIC shortwave radiances **(left axis, solid lines)** and relative azimuth angels **(right axis, dashed lines)** between 2017 and 2020 for **(A)** May and **(B)** December. Blue lines are for 2017 and red lines are for 2020.

3 GLOBAL CLOUD PROPERTY COMPOSITE FOR EPIC

The Earth's surface and atmosphere are anisotropic reflectors resulting in a relatively complex variation of radiance leaving the Earth as a function of the viewing and illumination angles. Thus, converting radiances from EPIC to fluxes requires the use of ADMs to account for the reflectance anisotropies. We use the most comprehensive ADMs developed by the CERES team (Su et al., 2015a) and these ADMs are functions of scene types defined using many variables (i.e., surface type, cloud amount, cloud phase, cloud optical depth, etc). The EPIC cloud composite was developed to provide scene identifications for each EPIC pixel to determine the anisotropy factors (Khlopenkov et al., 2017; Su et al., 2018, 2020). The composite data include cloud property retrievals from multiple imagers on low Earth orbit (LEO) satellites (including MODIS, VIIRS, and AVHRR) and geostationary (GEO) satellites (including GOES-13, -15, -16, and -17, METEOSAT-8, -9, -10, and -11, MTSAT-2, and Himawari-8). All cloud properties were determined using a common set of algorithms, the Satellite ClOud and Radiation Property retrieval System (SatCORPS, Minnis et al., 2008a, 2016), based on the CERES cloud detection and retrieval system (Minnis et al., 2008b, 2011; 2010; Trepte et al., 2019). Cloud properties from these LEO/GEO imagers are optimally merged together to provide a seamless global composite product at 5-km resolution by using an aggregated rating that considers five parameters (nominal satellite resolution, pixel time relative to the EPIC observation time, viewing zenith angle, distance from day/night terminator,

and Sun glint factor to minimize the usage of data taken in the glint region) and selects the best observation at the time nearest to the EPIC measurements. The global composite data are then remapped into the EPIC field of view by convolving the high-resolution cloud properties with the EPIC point spread function (PSF) defined with a half-pixel accuracy to produce the EPIC composite. PSF-weighted averages of radiances and cloud properties are computed separately for each cloud phase, because the LEO/GEO cloud products are retrieved separately for liquid and ice clouds (Minnis et al., 2008a). Ancillary data (i.e. surface type, snow and ice map, skin temperature, precipitable water, etc.) needed for anisotropic factor selections are also included in the EPIC composite. These composite images are produced for each observation time of the EPIC instrument (typically 300 to 600 composites per month).

Figure 4 shows retrieved liquid and ice cloud properties for January 4, 2017 at 11:15 UTC. The EPIC RGB image taken at this time is shown in Figure 5. At this image time, 56% of the daytime portion of the Earth is covered by clouds and about 2/3 of the clouds are of liquid phase. The optical depths of liquid clouds are mostly less than 6, but there are some very thick clouds with optical depth exceeding 22 in the Southern Ocean. The effective cloud heights of these liquid clouds are between ~ 1 and 6 km and the effective radii are less than 25 μm. The optical depths of ice clouds are of similar magnitude as liquid clouds. As expected, the ice clouds are higher and with larger radii than liquid clouds.

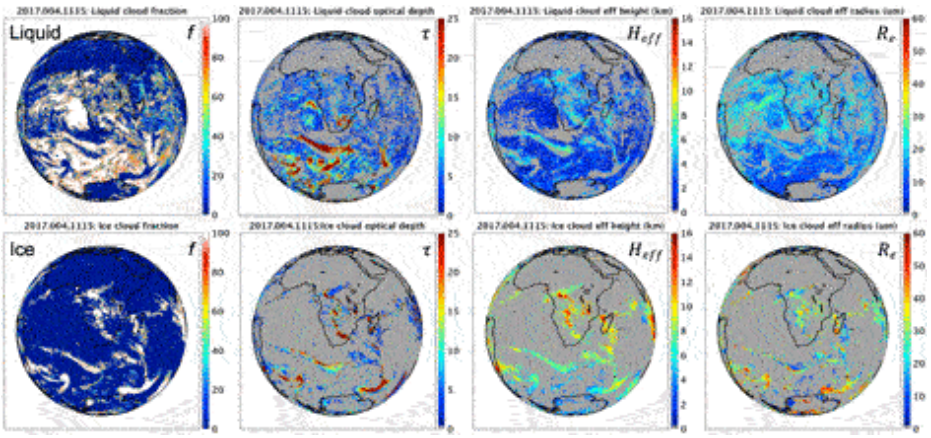

FIGURE 4 | Cloud properties retrieved from the LEO/GEO EPIC composite for January 4, 2017 at 11:15 UTC. Figures from left to right show cloud fraction (%), cloud optical depth, cloud effective height (km), and cloud effective droplet radius (*μm*) for liquid phase clouds **(top row)** and ice phase clouds **(bottom row)**.

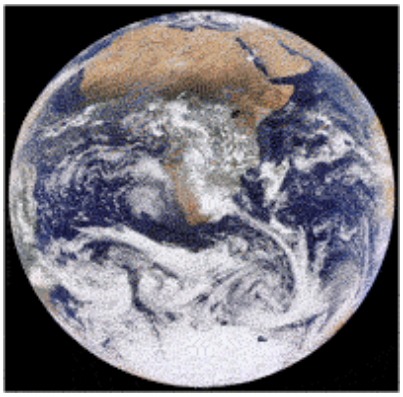

FIGURE 5 | The RGB image from EPIC observation taken at 11:15 UTC on January 4, 2017.

Cloud fractions for the EPIC pixels can be averaged to provide the global daytime mean cloud fraction ($\overline{f_d}$) at each EPIC image time. Figure 6 shows $\overline{f_d}$ at each EPIC image time for May and December using data from 2017 to 2020. Strong diurnal cycle is evident for $\overline{f_d}$, this is because the sunlit side of the Earth is centered over the Pacific Ocean where clouds are prevalent during earlier UTC hours and centered over Africa where there are few clouds over Sahara desert around 12 UTC. Cloud fractions within the EPIC views are a few percent higher in December than in May. This is because the very cloudy Southern Ocean and Antarctic are not within the EPIC view in May. The overall $\overline{f_d}$ are fairly consistent from year to year, though there are

some small variations in $\overline{f_d}$ due to transient weather systems. Thus, cloud change is not the cause for the large variations of $\overline{I_{sw}}$ shown in Figure 3.

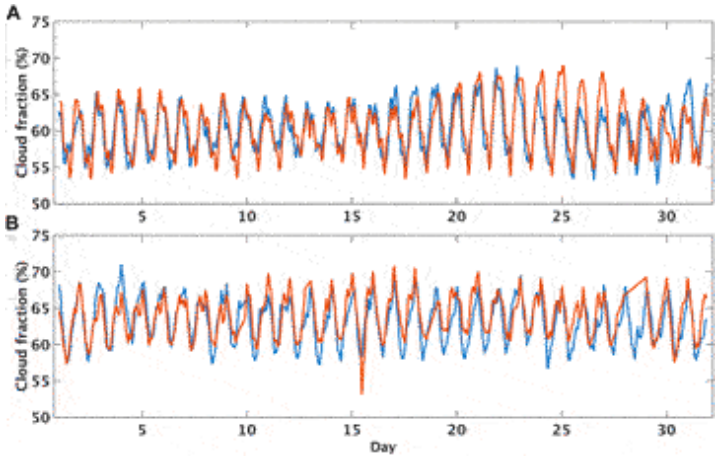

FIGURE 6 | Comparison of global daytime mean cloud fraction derived from EPIC composite between 2017 and 2020 for **(A)** May and **(B)** December. Blue lines are for 2017 and red lines are for 2020.

4 ANGULAR DISTRIBUTION MODELS

Angular distribution models (ADMs) describe the relationship between radiance (I) and flux (F):

$$F(\theta_0, \chi) = \frac{\pi I(\theta_0, \theta, \phi, \chi)}{R(\theta_0, \theta, \phi, \chi)}, \qquad (1)$$

where θ_0 is the solar zenith angle, θ is the satellite viewing zenith angle, ϕ is the relative azimuth angle between the instrument and the solar plane, and R is the anisotropic factor that relates radiance to flux. For isotropic surfaces, the radiance does not depend on viewing geometry (θ, ϕ) and R is reduced to one for all viewing geometry. However, all surfaces on Earth exhibit anisotropic characteristics that can vary drastically from one scene to another which make determining the radiative flux from radiance measurement very challenging. Thus, quantifying the relationships between radiance and flux over different scene types is a critical part of determining fluxes from satellite radiance measurements.

Currently the most comprehensive ADMs available are the ones developed by the CERES team (Loeb et al., 2005; Su et al., 2015a). Realizing the importance of quantifying the anisotropies over different scene

types and the deficiencies of the 12 scene-type ADMs developed for ERBE (Suttles et al., 1988), the CERES instruments are designed to fly together with an imager (MODIS for Terra and Aqua) and are also equipped with a special rotating azimuth plan (RAP) scan mode (Wielicki et al., 1996). When an instrument is placed in RAP mode, the instrument scans in elevation as it rotates in azimuth, thus acquiring radiance measurements from a wide range of viewing combinations. There are two CERES instruments on Terra and Aqua. At the beginning of their missions, one of the CERES instruments was always placed in RAP mode to maximize the angular coverage, while the other instrument was in cross track mode to maximize the spatial coverage. Figure 7 shows the logarithm sample number distributions using Aqua flight model 3 (in RAP mode) and Aqua flight model 4 (in cross track mode) observations of April 2004 when solar zenith angles are between 40° and 50°. When CERES instrument is placed in RAP mode, the observations are almost evenly distributed across all (θ, ϕ) bins, except when $\theta > 80^\circ$. However, when CERES instrument is in cross track mode, the observations are concentrated in limited side-scattering angular bins. The sample distributions of RAP and cross-track mode are very similar for other solar zenith angle ranges. Figure 7 illustrates the critical role that RAP scan mode plays in collecting data for developing $R(\theta_0, \theta, \phi)$. It also indicates that only a small angular fraction of $R(\theta_0, \theta, \phi)$ is used in the CERES radiance-to-flux conversion.

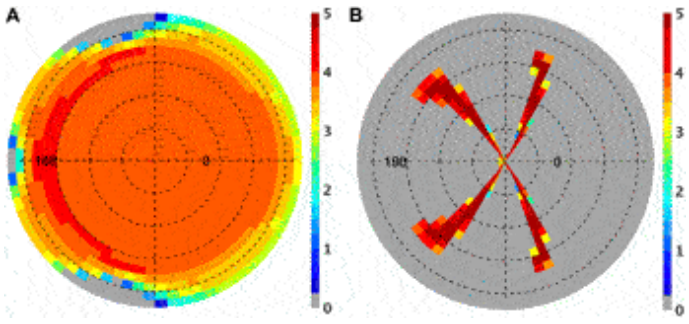

FIGURE 7 | Logarithm of sample numbers in each 5° viewing zenith angle and 5° relative azimuth angle bin of all observations within 40° and 50° solar zenith angles for the Aqua CERES instrument in RAP mode **(A)** and in cross track mode **(B)** using data of april 2004. Grey color indicates no observations.

As mentioned early, DSCOVR at the L1 point observes the Earth in near-backscattering directions and offers a testbed for the CERES ADMs in these

unique directions. Su et al. (2018) used the CERES ADMs and the scene identification provided by the EPIC cloud composite product to derive the global daytime mean anisotropy factors to convert the global daytime mean radiances to fluxes. They derived the EPIC SW fluxes for 2017. These fluxes agree with those derived from CERES synoptic products to within ±2% and demonstrate that the CERES ADMs accurately account for the Earth's anisotropy in the near-backscatter direction.

Note the relative azimuth angles range between about 170° and 174° during 2017, whereas the relative azimuth angles can be as large as 178° during 2020 (see Figure 2). As the EPIC observation moves closer to the due backscattering directions, the radiance anisotropy increases for liquid cloud due to glory feature and for clear vegetated surface due to hot spot feature (Gatebe and King, 2016). CERES ADMs capture these changes when viewing geometries move from near-backscattering directions to backscattering directions. Figure 8 shows how anisotropic factors change as the relative azimuth angle moves from 170° (near backscatter) to 179° (backscatter) for clear cropland (a) and water clouds over ocean (b). For clear cropland, the CERES ADMs are constructed using the Ross-Li model (Roujean et al., 1992; Li and Strahler, 1992) that accounts for the hot spot effect (Maignan et al., 2004) on regional and calendar month basis. The clear cropland anisotropic factor increases by up to 30% around $\theta = 40^{\circ}$ (the hot spot) when the relative azimuth angle moves from 170° to 179°. For liquid clouds, the CERES ADMs are constructed as a function of $ln\ (f\tau)$ using measured radiances with an angular resolution of 2° (Su et al., 2015a). Figure 8B shows the anisotropic factors for $ln\ (f\tau) = 8$, they increases by up to 9% around the glory ($\theta = 60^{\circ}$) when the relative azimuth angle moves from 170° to 179°.

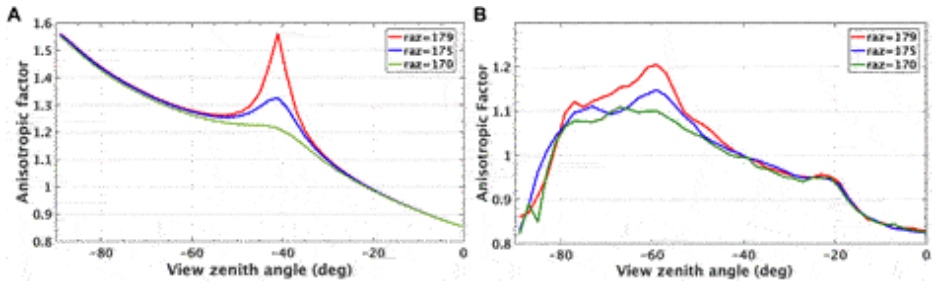

FIGURE 8 | Anisotropic factors at near-backscattering directions for relative azimuth angle of 179° (red), 175° (blue), and 170° (green) for **(A)** clear cropland in December with solar zenith angle of 40° and **(B)** for liquid clouds ($ln\ (f\tau)$=8) over ocean with solar zenith angle of 60°.

Figure 9 shows the anisotropic factors at the EPIC pixel level for December 5 for 2017 and 2020 at UTC hours around 06:00 and 11:00. As shown in Figure 3B, the relative azimuth angle for December 5, 2017 is around 170° and is around 177° for December 5, 2020. Shifting to larger relative azimuth angles in 2020 results in larger anisotropic factors, most notably over land regions due to the hot spot effects. For the two EPIC image times, $\overline{R_{sw}}$ are 1.343 and 1.375 for 2020 compared to 1.241 and 1.254 for 2017, representing 8–10% increase in radiance anisotropy.

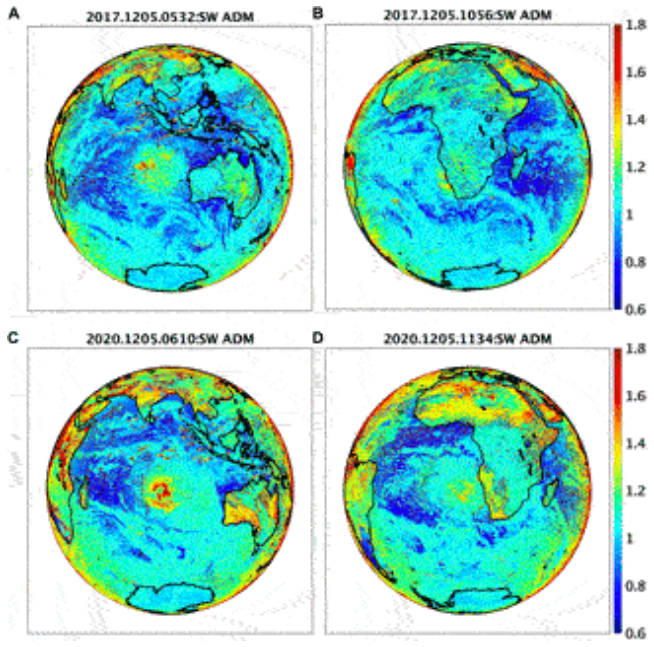

FIGURE 9 | Anisotropic factors at the EPIC pixel level for December 5, 2017 (top row) at image time of 05:32 UTC **(A)**, and 10:56 UTC **(B)**, and for December 5, 2020 (bottom row) at image time of 06:10 UTC **(C)**, and 11:34 UTC **(D)**.

5 EPIC SW FLUX

Using $\overline{I_{sw}}$ and $\overline{R_{sw}}$ described above, we can calculate $\overline{F_{sw}}$ for each EPIC image time. Figure 10 compares $\overline{F_{sw}}$ between 2017 and 2020 for May and December. Despite the large differences in $\overline{I_{sw}}$ between these 2 years, especially for December (see Figure 3), $\overline{F_{sw}}$ are similar. For May 2017, $\overline{F_{sw}}$ is 198.6 Wm^{-2}; and for May 2020, $\overline{F_{sw}}$ is 196.5 Wm^{-2}. For December 2017, $\overline{F_{sw}}$ is 223.4 Wm^{-2}; and for December 2020, $\overline{F_{sw}}$ is 220.1 Wm^{-2}.

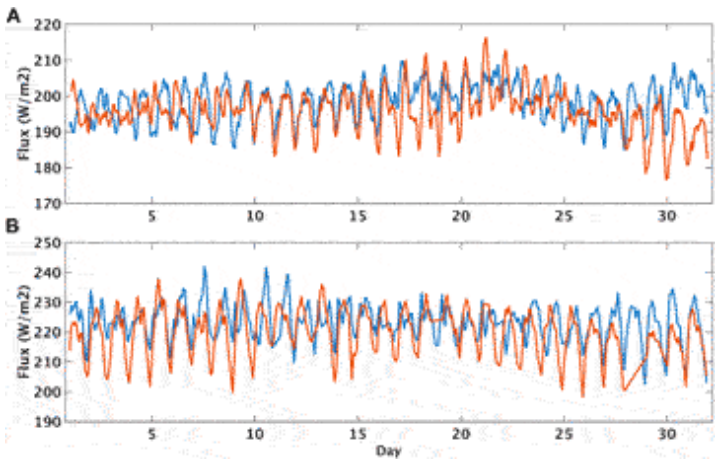

FIGURE 10 | Comparison of global daytime mean EPIC shortwave fluxes between 2017 and 2020 for **(A)** May and **(B)** December. Blue lines are for 2017 and red lines are for 2020.

As there are no direct TOA flux measurements, global daytime mean SW fluxes from EPIC are compared against CERES Edition 4 Synoptic radiative fluxes and cloud product (SYN1deg, Doelling et al., 2013). SYN1deg data product provides hourly cloud properties and fluxes for each 1° latitude by 1° longitude. Hourly fluxes within SYN1deg are from CERES observations at the CERES overpass times and for the hours between CERES observations they are inferred from hourly GEO imager measurements. The GEO visible and infrared measurements are used to derive broadband radiances using observation-based narrowband-to-broadband regression relationships and radiance-to-flux conversion algorithms. These GEO derived fluxes are used to fill in the hour boxes between CERES observations between 60°S and 60°N. For regions in the high latitudes, CERES instruments on the polar-orbiting Terra and Aqua satellites provide sufficient temporal coverage. Several procedures are implemented to ensure the consistency between the MODIS-derived and GEO-derived cloud properties, and between the CERES fluxes and the GEO-based fluxes. These include calibrating GEO visible radiances against the well-calibrated MODIS 0.65 μm radiances by ray-matching MODIS and GEO coincident radiances; applying similar cloud retrieval algorithms to derive cloud properties from MODIS and GEO observations; and normalizing GEO-based broadband fluxes to CERES fluxes using coincident measurements (Doelling et al., 2013).

The hourly gridded SYN1deg fluxes are integrated by considering only the grid boxes that are visible to the EPIC to produce the global mean

daytime fluxes that are comparable to those from the EPIC measurements following the method developed by Su et al. (2018). Figure 11 compares the global daytime mean hourly fluxes from EPIC and SYN1deg for May 2017 (a) and May 2020 (b). The biases and root-mean-square (RMS) errors are comparable for the EPIC SW fluxes for both May 2017 and May 2020, despite changes in EPIC viewing angles. For May 2017, the relative azimuth angle at the beginning of the month is 173° and decreases to about 171° near the end of the month. For May 2020, the relative azimuth angle starts around 168° and increases to close to 174° near the end of the month (see Figure 3A). Figure 12 compares the global daytime mean hourly fluxes from EPIC and SYN1deg for December 2017 (a) and December 2020 (b). Similar to the comparison results for May, both Decembers compare favorably with the global daytime fluxes from SYN1deg with the mean biases less than 0.6 W m^{-2} and RMS error less than 3 W m^{-2}, despite that December 2020 has the largest relative azimuth angles (~ 178°) seen during the entire DSCOVR observational period. Additionally, the relative azimuth angles are quite different for December 2017 and December 2020. For December 2017, the relative azimuth angle stayed close to 170° until December 22 and then started to increase slightly. For December 2020, the relative azimuth angle started around 175° and reached the maximum around December 10 before decreasing to about 172° by the end of the month. The good agreement shown in Figures 11, 12 demonstrate that the CERES ADMs used for radiance-to-flux conversion capture the radiance anisotropy changes for EPIC observations taken at different relative azimuth angles from 168° to 178°.

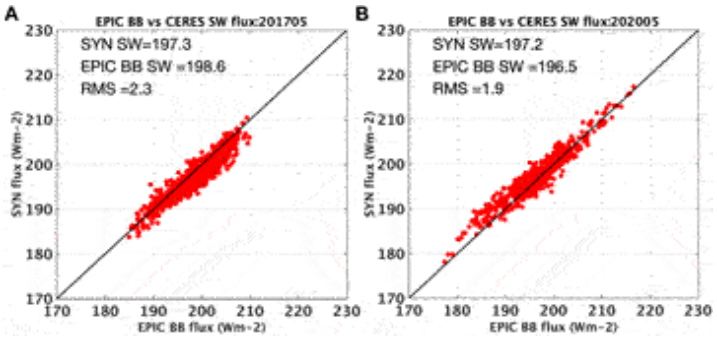

FIGURE 11 | Comparison of global daytime mean shortwave flux between EPIC and CERES SYN for May 2017 **(A)** and May 2020 **(B)**.

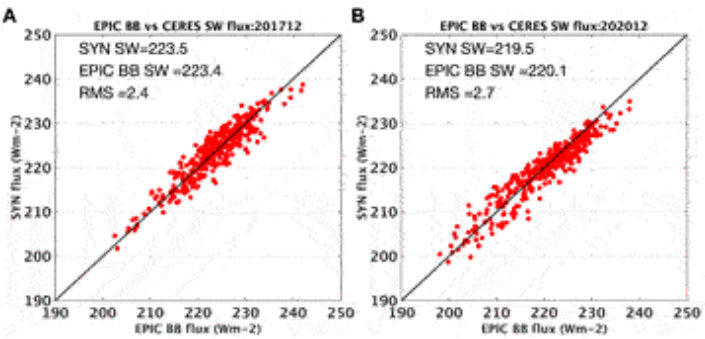

FIGURE 12 | Comparison of global daytime mean shortwave flux between EPIC and CERES SYN for December 2017 **(A)** and December 2020 **(B)**.

Figure 13 compares SW fluxes from CERES SYN1deg product with those from EPIC at all coincident hours of 2017–2020. Excellent agreements are found between these two datasets with the mean biases of 0.5 Wm^{-2} and RMS errors less than 3 Wm^{-2}, despite large changes in viewing geometries (Figure 2). The SW flux agreement between these two data sets is within the uncertainties from CERES calibration, EPIC calibration, narrowband-to-broadband regression, and the angular distribution models. This comparison indicates that the method developed to calculate the global anisotropic factors from the CERES empirical ADMs using the EPIC cloud composites for scene identifications is robust and that the CERES angular distribution models accurately account for the Earth's anisotropy in the near-backscattering to due-backscattering directions.

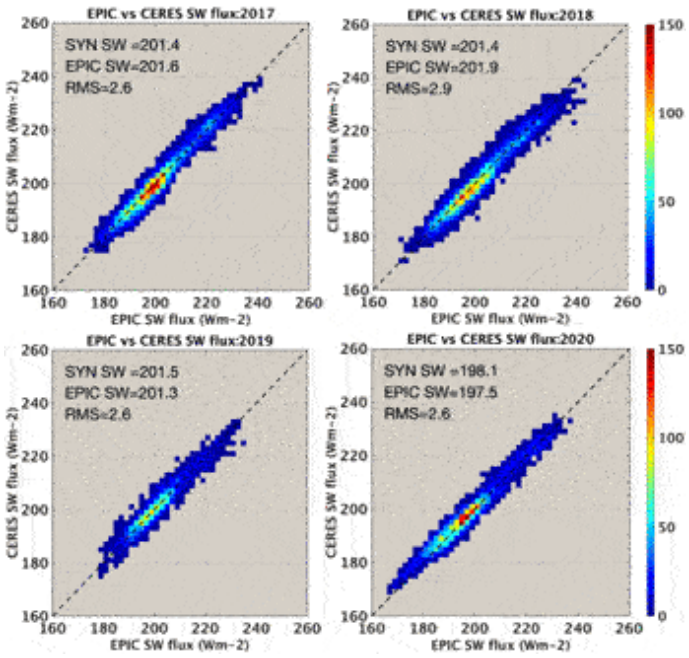

FIGURE 13 | Comparison of coincident hourly SW fluxes from EPIC and CERES SYN1deg for 2017–2020.

CONCLUSION

DSCOVR is the first Earth-observing satellite at the Lagrange-1 (L1) point with two Earth observing instruments aim to provide continuous observations of the sunlit side of the Earth. DSCOVR is in an elliptical Lissajous orbit around the L1 point where the EPIC and NISTAR view the Earth from a small range of relative azimuth angle from 168° to 178°. This viewing geometry is unique to EPIC as instruments (i.e., MODIS and CERES) on Terra and Aqua view the Earth mostly from side-scattering angles. Thus applying the CERES ADMs to EPIC observations offers an opportunity to test the performance of radiance-to-flux conversion in the near back-scattering angles.

Previous study by Su et al. (2018) demonstrates that the CERES ADMs accurately account for the Earth's anisotropy using 2017 EPIC observations when the relative azimuth angle is between 170° and 174°. However, the relative azimuth angle in 2020 shows large month-to-month variations, changing from 168° to 178°. The SW radiances change rapidly within these angular ranges and can increase significantly for many scene types, most notably for liquid clouds and vegetated surface. EPIC observations indeed show that the global daytime mean SW radiances can increase by as much as

10% as the relative azimuth angle increases from 170° to 178°. The increase in SW radiance is the result of EPIC viewing angle shifts closer to due-backscattering direction, and it is not because the Earth is more reflective (which could happen with significant increases of aerosols and clouds). When the anisotropies of the radiance fields are considered the resulting fluxes are very similar and do not show systematic differences.

The EPIC SW fluxes derived at different relative azimuth angles are compared against the CERES SYN1deg hourly SW fluxes. The biases of monthly mean fluxes (EPIC-SYN1deg) are less than 1.3 Wm^{-2} and RMS errors are less than 2.7 Wm^{-2} between EPIC and SYN1deg SW fluxes. These biases and RMS errors are independent of the EPIC viewing geometries, even for the largest relative azimuth angle differences observed between December 2017 and December 2020. The comparison is extended to include all coincident hours for data collected from 2017 to 2020. The annual global daytime mean SW fluxes from these two datasets agree to within 0.5 Wm^{-2} and the RMS errors are less than 3.0 Wm^{-2}. This study demonstrates that the CERES ADMs capture the anisotropy changes for relative azimuth angles between 168° and 178°. Furthermore, CERES instruments view the Earth mostly from side-scattering angles and the good agreement between global daytime mean fluxes from EPIC and CERES SYN1deg shows that fluxes inverted from different viewing angles are consistent with each other. Flux consistency is an indication that the CERES ADMs provide accurate characterization of the anisotropy for different Earth scenes and can be used for flux inversion from different viewing perspectives.

DATA AVAILABILITY STATEMENT

The original contributions presented in the study are included in the article/Supplementary Material, further inquiries can be directed to the corresponding author.

AUTHOR CONTRIBUTIONS

WS designed the study, analyzed the data, and wrote the first draft of the paper. LL analyzed the data. DD, KK, and MT produced the EPIC cloud composite data. All authors reviewed the paper.

FUNDING

This work was supported by NASA DSCOVR program.

PUBLISHER'S NOTE

All claims expressed in this article are solely those of the authors and do not necessarily represent those of their affiliated organizations, or those of the publisher, the editors and the reviewers. Any product that may be evaluated in this article, or claim that may be made by its manufacturer, is not guaranteed or endorsed by the publisher.

ACKNOWLEDGMENTS

The authors thank Alexander Marshak, Steven Lorentz, YinanYu, and Alan Smith for helpful discussions on DSCOVR viewing angles.

REFERENCES

Doelling, D. R., Loeb, N. G., Keyes, D. F., Nordeen, M. L., Morstad, D., Nguyen, C., et al. (2013). Geostationary Enhanced Temporal Interpolation for CERES Flux Products. *J. Atmos. Oceanic Technol.* 30, 1072–1090. doi:10.1175/jtech-d-12-00136.1

Gatebe, C. K., and King, M. D. (2016). Airborne Spectral BRDF of Various Surface Types (Ocean, Vegetation, Snow, Desert, Wetlands, Cloud Decks, Smoke Layers) for Remote Sensing Applications. *Remote Sensing Environ.* 179, 131–148. doi:10.1016/j.rse.2016.03.029

Li, X., and Strahler, A. H. (1992). Geometric-Optical Bidirectional Reflectance Modeling of the Discrete Crown Vegetation Canopy: Effect of crown Shape and Mutual Shadowing. *IEEE Trans. Geosci. Remote Sensing* 30, 276–292. doi:10.1109/36.134078

Loeb, N. G., Kato, S., Loukachine, K., and Manalo-Smith, N. (2005). Angular Distribution Models for Top-Of-Atmosphere Radiative Flux Estimation from the Clouds and the Earth's Radiant Energy System Instrument on the Terra Satellite. Part I: Methodology. *J. Atmos. Oceanic Technol.* 22, 338–351. doi:10.1175/jtech1712.1

Maignan, F., Bréon, F.-M., and Lacaze, R. (2004). Bidirectional Reflectance of Earth Targets: Evaluation of Analytical Models Using a Large Set of Spaceborne Measurements with Emphasis on the Hot Spot. *Remote Sensing Environ.* 90, 210–220. doi:10.1016/j.rse.2003.12.006

Minnis, P., Bedka, K., Trepte, Q. Z., Yost, C. R., Bedka, S. T., Scarino, B., et al. (2016). "A Consistent Long-Term Cloud and Clear-Sky Radiation Property Dataset from the Advanced Very High Resolution Radiometer (AVHRR)," in *Climate Algorithm Theoretical Basis Document (C-ATBD)* (Asheville, NC: CDRP-ATBD-0826 Rev 1–NASA,NOAA CDR Program). doi:10.7289/V5HT2M8T

Minnis, P., Nguyen, L., Palikonda, R., Heck, P. W., Spangenberg, D. A., Doelling, D. R., Ayers, J. K., Smith, Jr., W. L., Khaiyer, M. M., Trepte, Q. Z., Avey, L. A., Chang, F.-L., Yost, C. R., Chee, T. L., and Szedung, S.-M. (2008a). "Near-Real Time Cloud Retrievals from Operational and Research Meteorological Satellites," in *Proc. SPIE 7108, Remote Sens. Clouds Atmos. XIII*, *(Cardiff, Wales, UK*, *October 13, 2008)* (Wales, UK: Cardiff). doi:10.1117/12.800344

Minnis, P., Sun-Mack, S., Trepte, Q. Z., Chang, F.-L., Heck, P. W., Chen, Y., et al. (2010). "CERES Edition 3 Cloud Retrievals," in *13th Conference on Atmospheric Radiation (Oregon, Portland: Am. Meteorol. Soc.)*, *(Portland, Oregon*, *June-July 28-02, 2010)*.

Minnis, P., Sun-Mack, S., Young, D. F., Heck, P. W., Garber, D. P., Chen, Y., et al. (2011). CERES Edition-2 Cloud Property Retrievals Using TRMM VIRS and Terra and Aqua MODIS Data-Part I: Algorithms. *IEEE Trans. Geosci. Remote Sensing* 49, 4374–4400. doi:10.1109/TGRS.2011.2144601

Minnis, P., Trepte, Q. Z., Sun-Mack, S., Chen, Y., Doelling, D. R., Young, D. F., et al. (2008b). Cloud Detection in Nonpolar Regions for CERES Using TRMM VIRS and TERRA and AQUA MODIS Data. *IEEE Trans. Geosci. Remote Sensing* 46, 3857–3884. doi:10.1109/tgrs.2008.2001351

Roujean, J.-L., Leroy, M., and Deschamps, P.-Y. (1992). A Bidirectional Reflectance Model of the Earth's Surface for the Correction of Remote Sensing Data. *J. Geophys. Res.* 97, 20,455–20,468. doi:10.1029/92jd01411

Su, W., Corbett, J., Eitzen, Z., and Liang, L. (2015a). Next-Generation Angular Distribution Models for Top-Of-Atmosphere Radiative Flux Calculation from CERES Instruments: Methodology. *Atmos. Meas. Tech.* 8, 611–632. doi:10.5194/amt-8-611-2015

Su, W., Corbett, J., Eitzen, Z., and Liang, L. (2015b). Next-Generation Angular Distribution Models for Top-Of-Atmosphere Radiative Flux Calculation from CERES Instruments: Validation. *Atmos. Meas. Tech.* 8, 3297–3313. doi:10.5194/amt-8-3297-2015

Su, W., Khlopenkov, K. V., Duda, D. P., Minnis, P., Bedka, K. M., and Thieman, M. (20172017). "Development of Multi-Sensor Global Cloud and Radiance Composites for Earth Radiation Budget Monitoring from DSCOVR," in *Remote Sensing of Clouds and the Atmosphere XXII* ed . Editors A. Comeron, E. I. Kassianov, K. Schafer, R. H. Picard, and K. Weber (Warsaw, Poland: Proc. SPIE 10424), 10424K. doi:10.1117/12.2278645

Su, W., Liang, L., Doelling, D. R., Minnis, P., Duda, D. P., Khlopenkov, K., et al. (2018). Determining the Shortwave Radiative Flux from Earth Polychromatic Imaging Camera. *J. Geophys. Res. Atmos.* 123. doi:10.1029/2018JD029390

Su, W., Minnis, P., Liang, L., Duda, D. P., Khlopenkov, K., Thieman, M. M., et al. (2020). Determining the Daytime Earth Radiative Flux from National Institute of Standards and Technology Advanced Radiometer (NISTAR) Measurements. *Atmos. Meas. Tech.* 13, 429–443. doi:10.5194/amt-13-429-2020

Suttles, J. T., Green, R. N., Minnis, P., Smith, G. L., Staylor, W. F., Wielicki, B. A., et al. (1988). Angular Radiation Models for Earth-Atmosphere System, Vol. I, Shortwave Radiation. Tech. rep., NASA RP-1184.

Trepte, Q. Z., Bedka, K. M., Chee, T. L., Minnis, P., Sun-Mack, S., Yost, C. R., et al. (2019). Global Cloud Detection for CERES Edition 4 Using Terra and Aqua MODIS Data. *IEEE Trans. Geosci. Remote Sensing* 57, 9410–9449. doi:10.1109/TGRS.2019.2926620

Wielicki, B. A., Barkstrom, B. R., Harrison, E. F., Lee, R. B., Louis Smith, G., and Cooper, J. E. (1996). Clouds and the Earth's Radiant Energy System (CERES): An Earth Observing System Experiment. *Bull. Amer. Meteorol. Soc.* 77, 853–868. doi:10.1175/1520-0477(1996)077<0853:catere>2.0.co;2

Yang, W., Marshak, A., Várnai, T., and Knyazikhin, Y. (2018). EPIC Spectral Observations of Variability in Earth's Global Reflectance. *Remote Sens (Basel)* 10, 254. doi:10.3390/rs1002025410.3390/rs10020254

Conflict of Interest: Authors LL, DD, KK, and MT were employed by the Science Systems and Applications Inc.The remaining author declares that the research was conducted in the absence of any commercial or financial relationships that could be construed as a potential conflict of interest.

ORIGINAL RESEARCH
published: 25 October 2021
doi: 10.3389/frsen.2021.766628

Hourly Mapping of the Layer Height of Thick Smoke Plumes Over the Western U.S. in 2020 Severe Fire Season

Zhendong Lu[1], Jun Wang[1,2*], Xiaoguang Xu[3], Xi Chen[2], Shobha Kondragunta[4], Omar Torres[5], Eric M. Wilcox[6] and Jing Zeng[2]

[1] *Interdisciplinary Graduate Program in Informatics, The University of Iowa, Iowa City, IA, United States*
[2] *Department of Chemical and Biochemical Engineering, Center for Global and Regional Environmental Research, Iowa Technology Institute, The University of Iowa, Iowa City, IA, United States*
[3] *Joint Center for Earth Systems Technology and Department of Physics, University of Maryland Baltimore County, Baltimore, MD, United States*
[4] *NOAA/NESDIS, College Park, MD, United States*
[5] *NASA Goddard Space Flight Center, Greenbelt, MD, United States*
[6] *Division of Atmospheric Sciences, Desert Research Institute, Reno, NV, United States*

Edited by:
Gregory Schuster, Langley Research Center, National Aeronautics and Space Administration (NASA), United States

Reviewed by:
Jason Tackett, Langley Research Center, National Aeronautics and Space Administration (NASA), United States
Jinji Ma, Anhui Normal University, China

**** Correspondence:*** *Jun Wang, jun-wang-1@uiowa.edu*

Specialty section: *This article was submitted to Satellite Missions, a section of the journal Frontiers in Remote Sensing*

Received: *29 August 2021*
Accepted: *30 September 2021*
Published: *25 October 2021*

Citation: *Lu Z, Wang J, Xu X, Chen X, Kondragunta S, Torres O, Wilcox E and Zeng J (2021) Hourly Mapping of the Layer Height of Thick Smoke Plumes Over the Western U.S. in 2020 Severe Fire Season. Front. Remote Sens. 2:766628. doi: 10.3389/frsen.2021.766628*

A series of huge smoke plume events from the largest wildfire season recorded in California's modern history has occurred in 2020. Here, a research algorithm was modified to retrieve the aerosol optical centroid height (AOCH) and aerosol optical depth (AOD) from Earth Polychromatic Imaging Camera (EPIC) measurements. The research focus is to gain insights of the algorithm's feasibility in heavy smoke conditions to study the diurnal variation of AOCH; this is only made possible via EPIC due to its unique position at Lagrange-1 point and its equipment of O_2 B-band at which the vegetated surface reflectance is low. Vicarious calibration is applied to the EPIC 443, 680 and 688 nm channels based on the Tropospheric Monitoring Instrument (TROPOMI) observation. This new calibration leads to a better agreement of AOCH values between EPIC retrievals and the counterparts derived from the Cloud-Aerosol Lidar with Orthogonal Polarization (CALIOP) aerosol extinction vertical profile. The hourly variation of AOCH up to 0.45 km on September 7 is shown to have important implications for estimating hourly change of surface $PM_{2.5}$, although more quantitative studies are needed in the future.

Keywords: DSCOVR EPIC, thick smoke layer, AOCH, California fires, surface $PM_{2.5}$, hourly variation, aerosol retrieval algorithms

INTRODUCTION

The vertical distribution of smoke aerosols from wildfires has several important effects on the weather, climate and air quality. First, via absorbing and scattering of radiation, the altitude of smoke plumes can influence how aerosols alter the thermodynamic structure of atmosphere in the vertical dimension, thus affecting the formation and lifecycle of clouds (Wilcox, 2012). Second, the smoke aerosols can be entrained into the clouds and serve as condensation nuclei for cloud formation, thereby affecting the microphysics and radiative effect of clouds. This process highly depends on the vertical distance between aerosol layer and clouds (Rajapakshe et al.,

2017). Third, the relative vertical position of aerosols and clouds determines the sign and magnitudes of the aerosol radiative effects (Wang and Christopher, 2006a; Zarzycki and Bond, 2010; Ge et al., 2014). Lastly, the characterization of smoke vertical distribution is also very important for the retrieval of aerosol optical depth and single scattering albedo using near-UV observations (Torres et al., 1998; Ahn et al., 2021), as well as the remote sensing of surface air quality (Wang and Christopher, 2003). On the one hand, for a given total column aerosol loading, the lower the smoke layer is, the more severe the surface particulate matter pollution would be (Val Martin et al., 2013; Seo et al., 2015; Griffin et al., 2020). On the other hand, the aerosol layer height (ALH) regulates the transport of aerosol particles, with high altitudes favoring the long-range transport, thereby affecting the air quality and human health over the downwind region (Wang et al., 2006b; Val Martin et al., 2013; Tian et al., 2017).

Unfortunately, the operational datasets of ALH from observational sources are very limited. Although spaceborne lidars, such as Cloud-Aerosol Lidar with Orthogonal Polarization (CALIOP), can provide accurate aerosol vertical extinction profile, their footprint diameters are narrow (90 m for CALIOP) at the ground, and consequently, the lidar data is very sparse over time and space. Passive satellite remote sensing has a much wider swath but contains less information of aerosol vertical distribution (Xu et al., 2018). In addition, the diurnal variation of the ALH is not well understood, because most passive sensors with the capability of retrieving ALH are placed at the sun-synchronous orbits. The deficiency of aerosol vertical distribution information leads to large uncertainty and inter-model variability in the simulation of aerosol vertical profile by current climate models (Koffi et al., 2012; Kipling et al., 2016; Koffi et al., 2016), which brings large uncertainty in climate change prediction and air quality forecasting.

Here we present a first attempt to map hourly variation of smoke vertical distribution from space during the 2020 severe fire season. This study builds upon the past work that presented an algorithm to retrieve hourly aerosol optical centroid height (AOCH) from the oxygen absorption A- and B-bands of the Earth Polychromatic Imaging Camera (EPIC) for the smoke plumes over Hudson Bay–Great Lakes area (Xu et al., 2017; Xu et al., 2019). The EPIC is onboard the Deep Space Climate Observatory (DSCOVR) satellite that is parked at Lagrange-1 point (Marshak et al., 2018). This study, however, differs from the past work in several aspects. First, we update the

EPIC calibration via the vicarious calibration study that uses the accurate radiance measurements by the Tropospheric Monitoring Instrument (TROPOMI) observation in the oxygen absorption bands. This is needed because EPIC does not have the onboard calibration, and the official after-launch calibration of EPIC measurements at visible and near infrared (NIR) channels (Geogdzhayev and Marshak, 2018) has not been updated since 2017 (https://epic.gsfc.nasa.gov). In addition, the uncertainty of EPIC calibration is probably larger than we expected before (See section *Data, EPIC L1B*). Second, we seek to retrieve AOCH for the smoke plumes that are optically much thicker than the cases that were studied in the past work. Few studies have studied the altitudes of the smoke plumes associated with the fires in August-December of 2020, the largest wildfire season in California's modern history (Morris and Dennis, 2021). The two most severe smoke pollution events occurred on September 7–9 and September 14–16, respectively, and they are therefore selected for this study. Finally, not only the change of smoke layer height from both source and downwind regions but also the implications of this work to estimate surface $PM_{2.5}$ pollution are demonstrated. Of particular interest is the diurnal variation of AOCH that can be uniquely observed by EPIC, as well as its implication for surface air quality.

DATA

EPIC L1B

The EPIC imager is aboard the DSCOVR platform, which was launched in February 2015 to the Lagrange-1 point that gives EPIC a unique viewing perspective to provide the measurements of the sunlit Earth disk every 1–2 h. The EPIC level 1B data used in this study are obtained from NASA Aura Validation Data Center (https://avdc.gsfc.nasa.gov/pub/DSCOVR/Level1b_v03/). The EPIC instrument uses a 30-cm aperture Cassegrain telescope to measure the backscattered solar radiance at 10 narrow bands including oxygen A and B bands with a spatial resolution of 10 km at nadir and 20 km at a viewing zenith angle of 60°. The raw data from EPIC are post-launch calibrated using the well-calibrated measurement from Ozone Mapping and Profiler Suite (OMPS) for four UV (ultraviolet) channels, MODIS Aqua and Terra level 1B top-of-atmosphere (TOA) reflectance for four visible and NIR channels, and EPIC lunar observations for two oxygen absorption bands (Geogdzhayev and

Marshak, 2018; Marshak et al., 2018). However, the official calibration coefficients for the EPIC measurements at visible and NIR channels have not been updated since 2017 (https://epic.gsfc.nasa.gov).

Besides from Geogdzhayev and Marshak (2018), several other studies carried out the calibration for EPIC visible and NIR channels using MODIS, Visible Infrared Imaging Radiometer (VIIRS) or Multi-angle Imaging Spectroradiometer (MISR) data as references (Haney et al., 2016; Doelling et al., 2019; Geogdzhayev et al., 2021). The inter-comparison of calibration coefficients from different studies indicates that the accuracy of EPIC inter-calibration depends on the referenced satellite sensor, the platform upon which the sensor resides and the calibration methodology. For example, the uncertainties of MODIS (Aqua and Terra) and VIIRS/S-NPP (Suomi National Polar-Orbiting Partnership) onboard calibration for reflective solar bands (RSB) are both ~2% (Choi et al., 2016; Xiong et al., 2017), but a 6% positive bias exists for the VIIRS/S-NPP M5 band (672 nm) with respect to MODIS/Aqua B1 channel (646 nm) after accounting for the different spectral response functions of the two instruments (Sayer et al., 2017). However, Doelling et al. (2019) reported that the relative difference in EPIC calibration at 680 nm between using VIIRS/S-NPP M5 band and MODIS/Aqua B1 band is only 3%, indicating an uncertainty of at least 1.5% in their calibration process itself, which is higher than the calibration discrepancy of 0.3% at 680 nm between ATO-RM (all-sky tropical ocean ray-matching) and DCC-RM (deep convective cloud ray-matching) algorithms adopted by their study. Additionally, the calibration difference in the specific referenced sensor onboard different platforms also contributes to the uncertainty of EPIC calibration. The calibration differences between MODIS Aqua and Terra for RSB are within 1.5% (Xiong et al., 2020), but MODIS/Aqua-based EPIC calibration coefficients at 780 nm is 2% lower than that derived from MODIS/Terra (Geogdzhayev et al., 2021). The calibration coefficients for VIIRS/S-NPP at RSB are lower than that of VIIRS/NOAA-20 by 3–7% (Xiong et al., 2020). The MODIS-based EPIC calibration by Doelling et al. (2019) agrees with Geogdzhayev and Marshak (2018) within 1.6% and Geogdzhayev et al. (2021) within 2.6%. Overall, the uncertainty of EPIC calibration using MODIS or VIIRS data as references can be up to 8.5% as we analyzed above, with 7% attributable to the satellite data used as reference (Sayer et al., 2017; Xiong et al., 2020) and at least 1.5% attributable to the calibration process itself.

There are also disagreements regarding the degradation of EPIC instruments among different studies. For instance, Geogdzhayev and Marshak, (2018) reported that there is little degradation of EPIC instruments for four visible and NIR channels based on an 18-month EPIC calibration using MODIS (Aqua and Terra) data. In contrast, Doelling et al. (2019) concluded that the trend of EPIC gain is within 0.15% per year based on a 4-year calibration using VIIRS/S-NPP data. However, Geogdzhayev et al. (2021) found the trend of EPIC calibration coefficient at 443 nm is statistically significant ($p = 0.006$) with a value of 0.27% per year based on a 5-year EPIC calibration derived from multiple Low Earth Orbit (LEO) instruments. These disagreements again underscore the need to adjust EPIC calibrations for aerosol retrievals. Considering the degradation trend at 443 nm of 0.27% per year (Geogdzhayev et al., 2021) from June 2015 to September 2020, the total uncertainty of EPIC 443 nm in September 2020 could be up to 10%. Indeed, it is not uncommon that the algorithms for aerosol retrievals need further calibration adjustment to the satellite L1B data, such as the empirical corrections to the MISR data (Limbacher and Kahn, 2015; Garay et al., 2020) and MODIS data (Sayer et al., 2015).

EPIC L2 UVAI

The EPIC level 2 UV aerosol product (version 3) obtained from the NASA Langley Research Center Atmospheric Science Data Center (https://doi.org/10.5067/EPIC/DSCOVR/L2_AER_03) are also used in this study. The EPIC UV aerosol retrieval algorithm (Ahn et al., 2021) uses a set of aerosol models, which are identical to those assumed in OMI (Ozone Monitoring Instrument) algorithm (Herman et al., 1997; Torres et al., 2007; Jethva and Torres, 2011; Torres et al., 2013), to represent the carbonaceous aerosols from wildfires and biomass burning, dust and sulfate-based aerosols. The EPIC UV Aerosol Index (UVAI) is derived from 340 to 388 nm radiances for all sky conditions (Torres et al., 2018; Ahn et al., 2021). It is indicative of the presence of absorbing aerosols (smoke, dust, or both particles) at free troposphere and above. The UVAI is sensitive to ALH, aerosol optical depth (AOD) and single scattering albedo (SSA) (Hsu et al., 1999). Jeong and Hsu (2008) retrieved SSA by using UVAI derived from OMI data, MODIS AOD and ALH from CALIOP, then they derived ALH by constraining UVAI, AOD and SSA. Lee et al. (2020) followed the same idea but replace MODIS AOD and OMI UVAI with VIIRS AOD and UVAI from OMPS-NM (Ozone Mapping and Profiler Suite Nadir Mapper). Xu et al.

(2019) found the relationship between EPIC UVAI and EPIC ALH varies with different AOD values. In summary, there is no monotonic relationship between UVAI and ALH, because of the dependence of UVAI on the aerosol loading and absorption properties; for the same UVAI value, it can be a result of various combinations of AOD, SSA, and ALH.

CALIOP L2 Aerosol Profile

CALIOP is an elastic backscatter lidar measuring the attenuated backscattered signal at both 532 and 1,064 nm. It is aboard the Cloud-Aerosol Lidar and Infrared Pathfinder Satellite Observation (CALIPSO) spacecraft in a sun-synchronous orbit with an equatorial crossing time of around 13:30 local time and a repeat cycle of 16 days (Winker et al., 2009). Vertical profiles of aerosol extinction coefficient at 532 nm are obtained from CALIOP level 2 Aerosol Profile product (https://doi.org/10.5067/CALIOP/CALIPSO/CAL_LID_L2_05kmAPro-Standard-V4-21), which has a vertical resolution of 60 m and a horizontal resolution of 5 km. The aerosol extinction profile from CALIOP level 2 product is used to validate the EPIC AOCH retrievals.

TROPOMI L1B

The calibrated hyperspectral measurements at visible and near infrared bands from TROPOMI level 1B product (UVIS bands: https://doi.org/10.5067/SENTINEL5P/S5P_L1B_RA_BD3_HiR.1; NIR bands: https://doi.org/10.5067/SENTINEL5P/S5P_L1B_RA_BD6_HiR.1) are convolved to conduct the soft-calibration for EPIC level 1B data. TROPOMI is aboard the Sentinel-5 Precursor (S5P) satellite, which was launched to a sun-synchronous polar orbit on October 13, 2017. With a local overpassing time of around 13:30, TROPOMI can cover the near-global domain in a single day (Veefkind et al., 2012). TROPOMI contains 4 spectrometers covering the ultraviolet (UV), visible (UVIS), NIR and shortwave infrared (SWIR). The spectral resolutions for UV, UVIS, NIR and SWIR bands are 0.45–0.5, 0.45–0.65, 0.34–0.35 and 0.225–0.227 nm, respectively. The footprint size is 5.5×7 km^2 for SWIR bands, 5.5×3.5 km^2 for UVIS, NIR and UV band 2 (300–332 nm) and 5.5×28 km^2 for UV band 1 (267–300 nm).

TROPOMI has the onboard calibration capacity. Its regular calibration is conducted on the eclipse side of the orbit with the internal light sources of

TROPOMI to correct the degradation and gain drifts of UV, UVIS and NIR detectors over time. The uncertainty of pre-launch calibration for absolute radiance and irradiance at UVIS and NIR bands is in the range of 0.8–1.3% (Kleipool et al., 2018), and the gain drifts with respect to pre-launch calibration can always be corrected to below 0.1%. The solar angular dependence of the irradiance radiometry is calibrated after launch with higher accuracy and angular sampling than pre-launch calibration. The inconsistency of the absolute irradiance calibration in the overlapped spectral range between UV and UVIS bands are corrected during the in-flight calibration. See more details in Ludewig et al. (2020). The reflectance data from TROPOMI is estimated to have an uncertainty of 1% (Kleipool et al., 2018; Ludewig et al., 2020).

TROPOMI L2 Aerosol Layer Height

The smoke AOCH values retrieved from EPIC are also compared with the ALH from S5P_L2__AER_LH version 1 product (https://doi.org/10.5270/S5P-j7aj4gr) provided by TROPOMI. The TROPOMI ALH retrieval uses the optimal estimation method for spectral fitting with various aerosol layer pressures and aerosol optical thicknesses in the oxygen A-band. By training a neural network model, the hyperspectral TROPOMI TOA radiance can be simulated with high speed to reduce the computation cost in the ALH algorithm (de Graaf et al., 2019; Nanda et al., 2019). The TROPOMI ALH retrieval algorithm assumes a uniform distribution of aerosols in a single layer with a constant thickness of 50 hPa, and it adopts a single aerosol model with single scattering albedo equal to 0.95 and the Henyey-Greenstein phase function for which the asymmetry factor is 0.7 (de Graaf et al., 2019). The TROPOMI ALH is shown to have a mean negative bias of more than 2 km over land, as compared with CALIOP data, primarily due to the high surface reflectance in O_2 A-band that is not favorable for aerosol retrievals (Griffin et al., 2020; Nanda et al., 2020).

EPA Surface $PM_{2.5}$

Hourly measurements of surface $PM_{2.5}$ concentrations are collected from United States Environmental Protection Agency (EPA) Air Quality System (https://www.epa.gov/aqs). The $PM_{2.5}$ dry mass concentrations are measured by Beta Attenuation Monitor (Schweizer et al., 2016), Tapered Element Oscillating Microbalance (Sofowote et al., 2014) techniques, and other

methods (Wang et al., 2006b). The data closest to the EPIC overpass time are used to investigate the relationship of smoke layer height and surface $PM_{2.5}$ pollution.

MODIS/Aqua L2 AOD and AERONET AOD

Aqua is a sun-synchronous satellite passing over the equator in the local afternoon, with a payload imaging sensor MODIS onboard. MCD19A2 AOD product (https://doi.org/10.5067/MODIS/MCD19A2.006) at 1 km resolution based on MODIS MAIAC algorithm is used in this study to compare the AOD retrieved from EPIC. The validation of global MAIAC AOD retrievals during 2000–2016 shows 66% of total retrievals agree with AERONET within $\pm 0.05 \pm 0.1$ (Lyapustin et al., 2018), where is AOD measured by AErosol RObotic NETwork or AERONET. The AERONET AOD is derived based on Beer-Lambert-Bouguer law from the direct sun measurements by ground-based sun photometers at multiple wavelengths. The AERONET instruments are calibrated routinely at least twice per year, and the absolute uncertainty of AOD from a newly calibrated field instrument is no larger than 0.01 at the wavelength longer than 440 nm under cloud-free condition (Holben et al., 1998).

METHODS

Vicarious Calibration of EPIC With TROPOMI Data

Hyperspectral measurements at UVIS and NIR bands from TROPOMI are convolved to EPIC narrow bands at 443, 551, 680, 688, 764 and 780 nm using the spectral response function of the EPIC instrument (Chen et al., 2021). To evaluate and update the EPIC level 1B calibration, we picked four boxes with each box containing 10 × 10 EPIC pixels over a convective cloud in eastern United States on September 15, 2020 and compared the EPIC TOA reflectance with convolved and well-calibrated TROPOMI TOA (top-of-atmosphere) reflectance (Figure 1). The near-Lambertian reflectance of convective cloud weakens the geometric dependence of TOA reflectance and thus minimizes the discrepancy between EPIC and TROPOMI observations (Doelling et al., 2013). High-resolution TROPOMI observations are re-gridded to EPIC grid size. The atmospheric window channel 443 nm is used for the EPIC AOD retrieval and the ratio of O_2 B absorption band to the continuum band (688/680) plays an important role in EPIC AOCH retrieval.

Therefore, we scale the original EPIC L1B data based on the ratios of TROPOMI TOA reflectance to EPIC counterparts at 443, 680 and 688 nm. 764 and 780 nm are not scaled since the ratio of 764/780 nm from EPIC is very close to that of TROPOMI data (Figure 1). No other channels are used in our algorithm.

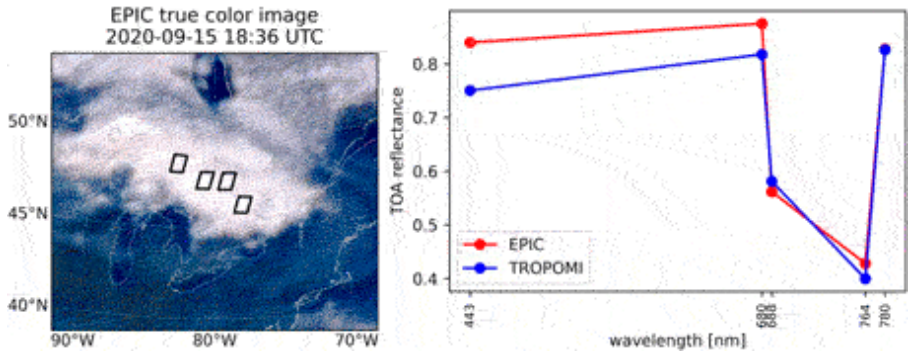

FIGURE 1 | Comparison of TOA reflectance from EPIC and TROPOMI. Four boxes **(thick black polylines)** with each box containing 10 × 10 pixels over a convective cloud in Eastern America on September 15, 2020, are selected for the comparison **(left)**. Mean TOA reflectance of 400 pixels from EPIC and TROPOMI at 443, 680, 764 and 780 nm are compared **(right)**. TROPOMI TOA reflectance values are convolved to EPIC narrow bands using the spectral response function of EPIC. Evaluation of the AOD and AOCH retrievals.

There are several advantages in using TROPOMI data to derive the EPIC calibration coefficients compared to using MODIS and VIIRS data. First, as a young mission launched in October 2017, TROPOMI has a lower calibration uncertainty (~1%) for the reflectance at the TOA (Kleipool et al., 2018; Ludewig et al., 2020) than MODIS and VIIRS (~2%) (Choi et al., 2016; Xiong et al., 2017); this superiority is due to TROPOMI's onboard calibration facility including the daily measurements of spectral radiances directly from the Sun. Second, the convolution of hyperspectral measurements of TROPOMI to EPIC narrow bands using EPIC spectral response functions avoids the complex correction accounting for the different position and bandwidth between EPIC and MODIS (or VIIRS) channels. MODIS (or VIIRS) channels have bandwidth of 10 nm or larger, while EPIC bands have bandwidth of ~2 nm or less. Finally, any systematic bias in TROPOMI spectrometers could be cancelled out since the TROPOMI measurements used in the vicarious calibration are reflectance-based, because all optical elements for the Earth-view mode are included in the

optical path for solar irradiance measurement in TROPOMI instrument (Ludewig et al., 2020).

EPIC Retrieval

The smoke AOCH algorithm was originally developed and described in detail by Xu et al. (2017) and Xu et al. (2019). It assumes a quasi-Gaussian aerosol vertical profile characterized by total column AOD and the extinction peak height with a half-width parameter of 1 km following Xu et al. (2017). The height at which the aerosol extinction peaks retrieved by our algorithm is the optical centroid height, so that it is called AOCH (aerosol optical centroid height). The ALH is a broader terminology referring to the aerosol vertical position information retrieved from passive satellite remote sensing techniques, such as aerosol stereo height from MISR (Nelson et al., 2013), aerosol injection height from MODIS MAIAC thermal technique (Lyapustin et al., 2020) and aerosol mid-layer height from TROPOMI (Nanda et al., 2019). After cloud screening using reflectance at 443, 551 and 780 nm, AOD is retrieved from using EPIC atmospheric window channel 443 nm, and the AOCH is derived subsequently based on the ratios of oxygen A and B bands to their respective neighboring continuum bands (764/780 and 688/680). Following Xu et al. (2019), the surface reflectance for water surface comes from GOME-2 Lambert-equivalent reflectivity (LER) product (Tilstra et al., 2017). A 10-year climatology of Lambertian surface reflectance from MODIS BRDF/Albedo product (MCD43) (Schaaf et al., 2002) is applied for the land surface. Cloud mask is conducted through the spatial homogeneity tests at 443 and 551 nm, as well as the brightness tests with the prescribed threshold of TOA reflectance at 443 and 680 nm for land and 443, 680, and 780 over water. The water pixels with a sun glint angle smaller than 30° are removed (Levy et al., 2013). The retrieval algorithm is based on the lookup table constructed by running the radiative transfer model UNL-VRTM (Unified and Linearized Vector Radiative Transfer Model) (Spurr, 2008; Spurr et al., 2012; Wang et al., 2014). Those pixels with EPIC UVAI less than 1 are removed since we only focus on the heavy smoke plume here.

Validation of EPIC AOD and AOCH

AOD retrieved from EPIC is compared against the AOD from the MODIS/Aqua level 2 MYD04_3K product qualitatively. The collocated aerosol extinction profiles at 532 nm from CALIOP level 2 product are used

to calculate an extinction weighted aerosol height $AOCH_{\mathrm{CALIOP}}$ for the validation of EPIC AOCH.

$$AOCH_{\mathrm{CALIOP}} = \frac{\sum_{i=1}^{n} \beta_{\mathrm{ext},i} Z_i}{\sum_{i=1}^{n} \beta_{\mathrm{ext},i}} \quad (1)$$

where $\beta_{\mathrm{ext,i}}$ is 532 nm aerosol extinction coefficient at vertical level i with an altitude of Z_{i}. The EPIC AOCH from EPIC retrieval is also compared with TROPOMI level 2 aerosol layer height product. The EPIC retrievals from the measurements closest to the overpass time of Aqua, CALIPSO and TROPOMI for each day are used in the validation. It is worth noting that CALIOP may lack sufficient sensitivity to detect the aerosol amount at the vertical resolution of 60 m and therefore the level 2 data product would report those layers as no-aerosols (Winker et al., 2013). However, since aerosols are omnipresent in the atmosphere, the accumulation of these below-the-detection-limit 60-m layer of aerosols can lead to a biased CALIOP AOCH. Here, to account for this effect, we, as in our past study (Xu et al., 2019), assume a exponentially decayed background aerosol profile with a columnar AOD of 0.07 for those clear-air layers from CALIOP level 2 data.

RESULTS

Further Assessment of EPIC L1B Calibration

The EPIC TOA reflectance values at 443 and 680 nm are much lower than the TROPOMI counterparts, while they are relatively close to each other at 688, 764 and 780 nm. The ratios of mean TOA reflectance of TROPOMI to EPIC are used as scaling factors as vicarious calibration of EPIC measurements at 443, 680 and 688 nm, which are 0.894, 0.934 and 1.03, respectively. It is not surprising that we need the corrections of −10.6% and −6.6% at 443 and 680 nm to align EPIC reflectance values to TROPOMI ones, since the EPIC calibration uncertainty is 10% at 443 nm and 8.5% at other visible and NIR bands (See section DATA/EPIC L1B), and an uncertainty of 1.2–1.3% exists in TROPOMI UVIS channels (Kleipool et al., 2018). While we also had similar findings for other cases (figure not shown), more studies are needed in the future to reduce the EPIC calibration uncertainty. The channels of 764 and 780 nm are not scaled since the discrepancy of the 764/780 ratio between EPIC and TROPOMI is small, and

it is the ratio of oxygen absorption band to continuum band (688/680 and 764/780) matters in the AOCH retrieval. Besides, the AOCH over land is primarily retrieved from the ratio of O_2 B band and its continuum, because the O_2 B band has a much lower land surface reflectance than O_2 A band.

Figure 2 shows the comparison of EPIC AOD with and without the vicarious calibration (VC) to the MODIS MAIAC AOD. The EPIC AOD retrieved after the VC is lower than that before the VC (i.e., using the calibration coefficient published in Geogdzhayev and Marshak, 2018), which is expected because EPIC TOA reflectance at 443 nm used for AOD retrieval decreases after VC. Generally, EPIC AOD retrieval captures the smoke plumes shown in the EPIC true color image and shares a similar spatial pattern with MODIS MAIAC AOD. However, the EPIC AOD values after the VC are lower than MAIAC AOD values. Note that the AOD retrievals from EPIC and MODIS MAIAC algorithm are at different wavelengths. It is not surprising the EPIC AOD at longer wavelength (680 nm) is lower than MAIAC AOD at shorter wavelength (550 nm). Previous studies reported the Angstrom exponent (AE) at 550–680 nm for aging smoke particles is at the range of 1.4–2.2 (Reid et al., 1999; Sicard et al., 2019). The ratio of AOD at 680 nm to that at 550 nm is around 0.63–0.74 for this range of AE, which is consistent with the comparison between EPIC 680 nm AOD and MODIS MAIAC 550 nm AOD. Besides, EPIC AOD retrieval has a larger spatial coverage than MAIAC AOD over the areas with extremely heavy smoke plumes. On September 9 and 14, MAIAC algorithm has little valid retrievals over the downwind region of the west coast of United States and South of the Great Lakes, respectively, which can be identified as heavy smoke layers from the EPIC true color images (Figure 1) and EPIC UVAI data (Figure 2). This is understandable because the operational algorithm can often mis-classify heavy aerosol layers as cloud layers and so, no retrievals of AOD are made in these cases (Shi et al., 2019). In addition, we also compared our EPIC AOD retrieval to the AERONET level 1.5 AOD product. We find the root mean square error (RMSE) decreases from 0.68 to 0.37 and the correlation coefficient (R) value increase by 0.25 after the VC. This suggests a better EPIC AOD retrieval with the VC (figure not shown). We will continue to assess the VC once the best quality level 2.0 AOD data is available.

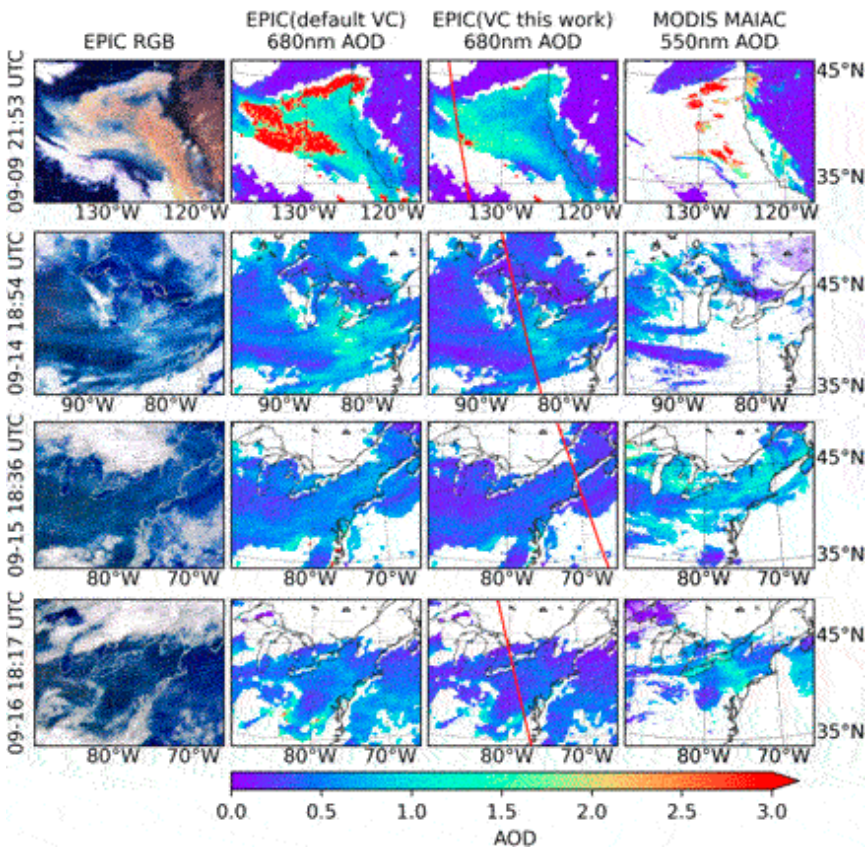

FIGURE 2 | Comparison of EPIC AOD and MODIS MAIAC AOD for September 9 and 14–16. The first column is EPIC true color image composed of 443, 551 and 680 nm measurements. The second and third columns are EPIC 680 nm AOD retrievals without and with vicarious calibration. The red lines in the third columns are the CALIOP sub-orbital tracks on each day. The last column is MODIS MAIAC AOD at 550 nm.

The EPIC AOCH retrievals before and after the VC are compared with TROPOMI operational ALH product from KNMI (Royal Netherlands Meteorological Institute) (Figure 3). The EPIC AOCH values increase by 3–4 km after the VC, mainly due to the VC-induced increase of 688/680 ratio. TROPOMI operational ALH values is lower than EPIC AOCH values with the VC by 2–3 km. However, TROPOMI operational ALH product has large uncertainty especially over land. Nanda et al. (2020) reported that TROPOMI ALH product has a negative bias and can be lower than CALIOP ALH by 2.41 km over land and 1.03 km over ocean on average.

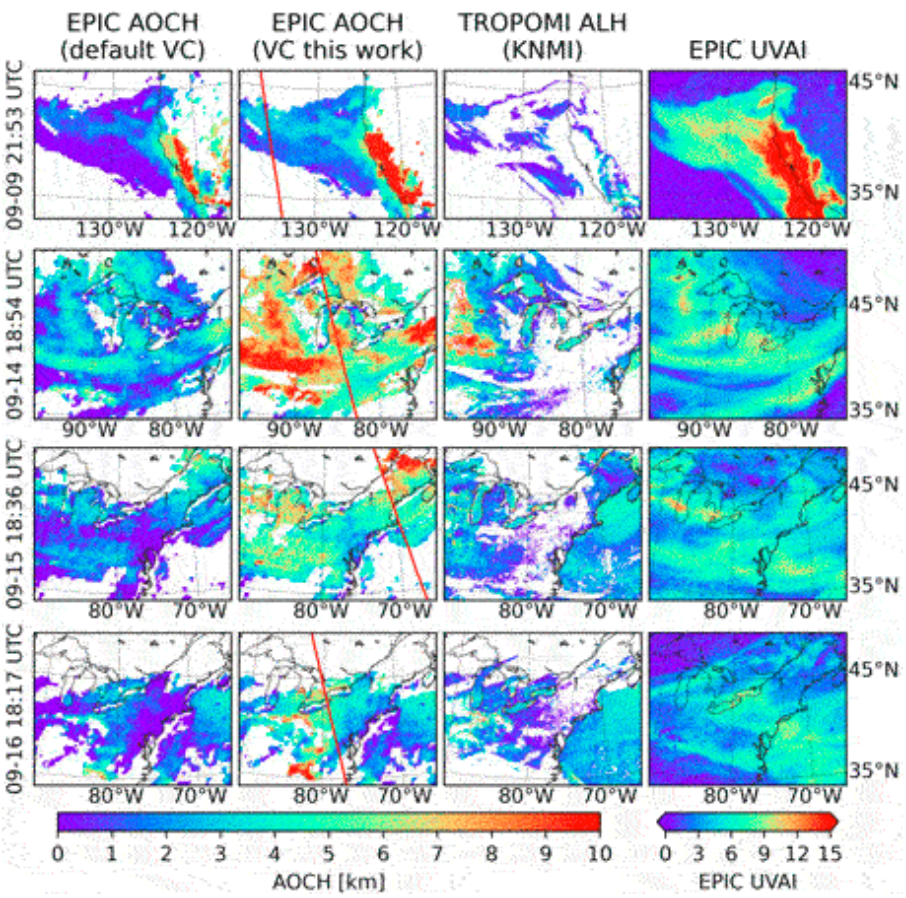

FIGURE 3 | Comparison of EPIC AOCH and TROPOMI operational ALH product for September 9 and 14–16. The first and second columns are EPIC AOCH retrievals without and with vicarious calibration. The red lines in the second columns are the CALIOP sub-orbital tracks on each day. The third column is the TROPOMI operational ALH product from KNMI. The last column is the EPIC UVAI.

To further evaluate the EPIC AOCH retrieval with the VC, the extinction-weighted heights calculated from the CALIOP aerosol extinction profile are used (Figures 4, 5). The CALIOP tracks are marked by the red lines in Figure 3. As shown by Figure 4, the EPIC AOCH after the VC matches the CALIOP AOCH well, while the EPIC AOCH retrieval without the VC is lower than the CALIOP AOCH by 1–3 km. Figure 5 indicates that not only the RMSE reduces from 2.76 to 0.91 km after the VC, but the correlation coefficient (R) also improves from 0.736 to 0.885. The discrepancy between CALIOP AOCH and EPIC counterparts with the VC is generally less than 1 km, which is lower than the uncertainty of more than 2 km over land for TROPOMI operational ALH product (Nanda et al., 2020; Chen et al., 2021).

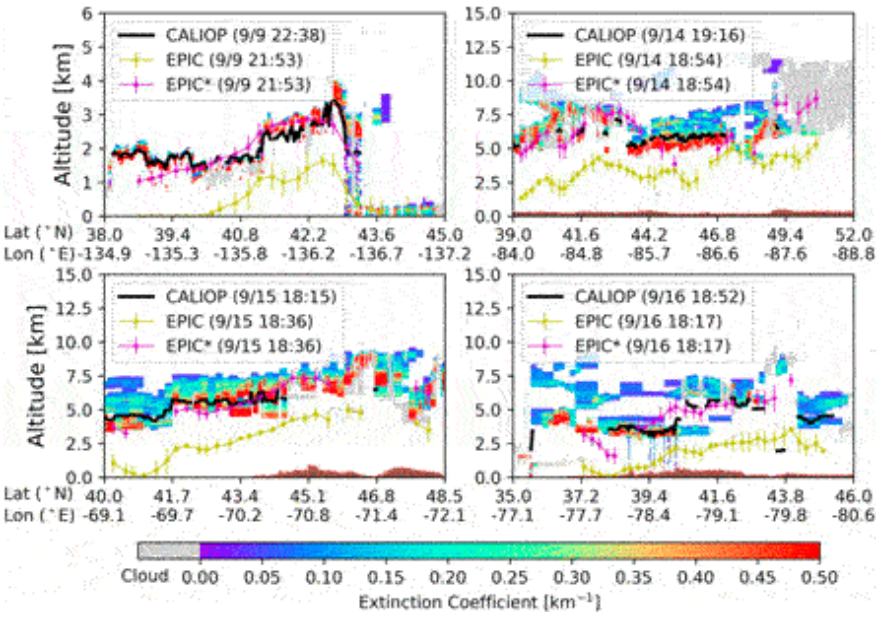

FIGURE 4 | Comparison of EPIC AOCH and CALIOP aerosol extinction profile as well as CALIOP AOCH for September 9 and 14–16. The CALIOP tracks are marked by red lines in Figure 3. The CALIOP AOCH values are represented by black lines, and EPIC AOCH retrievals with the vicarious calibration (EPIC*) and without the vicarious calibration (EPIC) are marked by pink and yellow lines respectively.

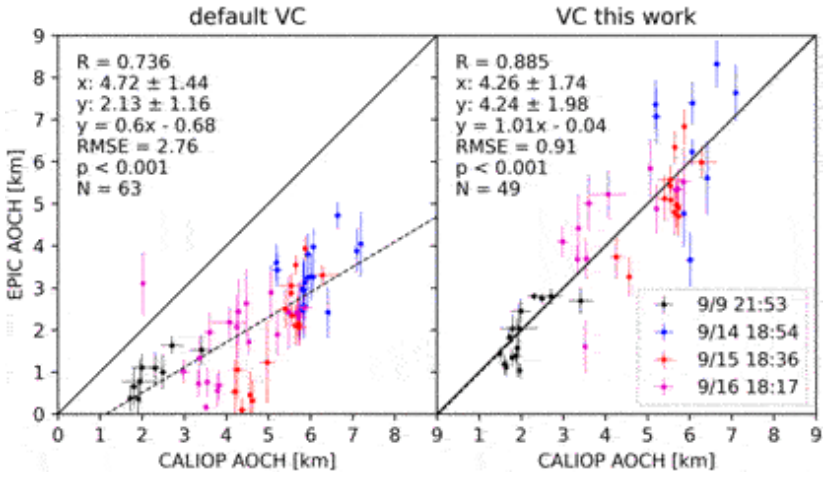

FIGURE 5 | Scatter plot of EPIC AOCH retrieval and CALIOP AOCH for September 9 and 14–16. The left panel shows the EPIC retrieval without the vicarious calibration, and the right panel shows that with the vicarious calibration.

Hourly Change of AOCH and Its Potential Application to Surface $PM_{2.5}$ Estimate

The diurnal variation of smoke layer height over land from local morning to local noon time (17:06–20:42 UTC) on September 7 is investigated to reveal the implications of aerosol layer height on the surface $PM_{2.5}$ pollution (Figure 6). We did not extend the analysis to the afternoon because the fire activity and probably the smoke optical depth reach the peak in the late afternoon (Giglio et al., 2006). It would be more helpful to investigate the time period when the smoke optical depth changes little, but show a large hourly variation, since our focus here is to illustrate the implications of hourly variation of smoke height on the surface $PM_{2.5}$. The heavy smoke layer extended from California to the Colorado, which can be clearly seen from the EPIC true color image and UVAI maps. The surface $PM_{2.5}$ concentrations measured at EPA sites in California, southern Nevada and Utah exceed the National Ambient Air Quality Standard (NAAQS) for 24-h $PM_{2.5}$ pollution (35 μg m^{-3}). The mean AOCH values of the smoke plume decreased from 6.0 to 4.3 km within 216 min. The hourly variations have significant impacts on the surface $PM_{2.5}$ pollution. In the areas indicated by the black ellipse in Figure 6, the $PM_{2.5}$ concentrations increase during this time period as the smoke layer was descending. Meanwhile, the AOD does not show much temporal variation.

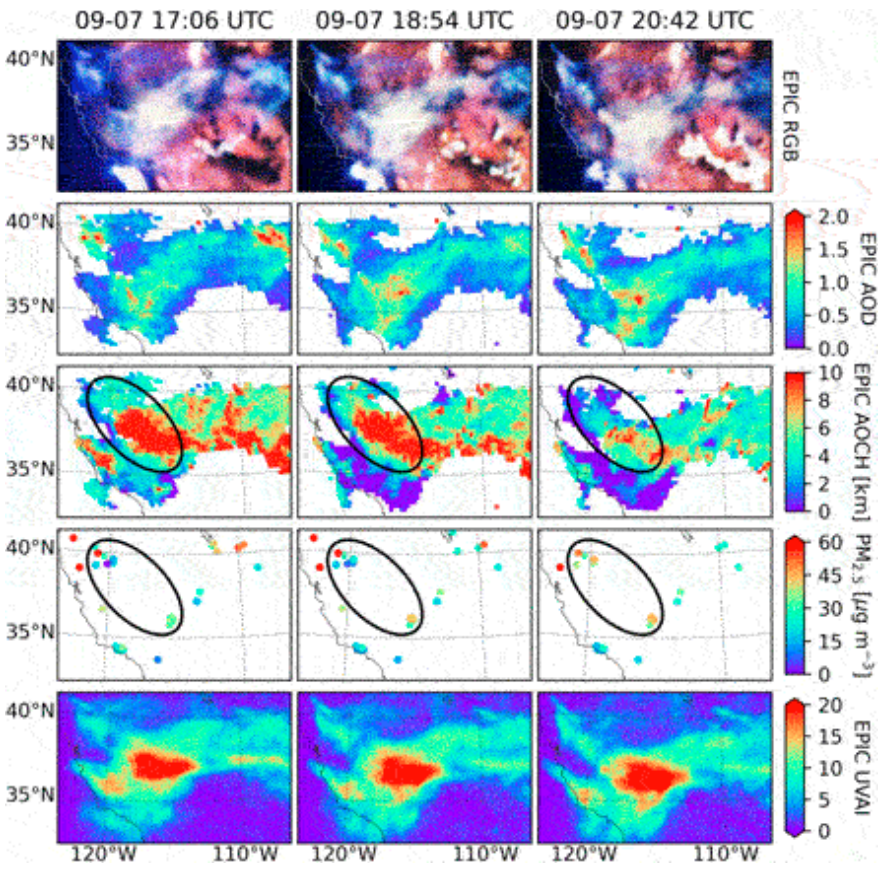

FIGURE 6 | Diurnal variation of EPIC AOCH and its implication on surface $PM_{2.5}$ concentration from 17:06 to 20:42 UTC on September 7, 2020. The first row is EPIC true color image, and the second row is the EPIC AOD. The third row is the EPIC AOCH retrievals, and the fourth row is the EPA surface $PM_{2.5}$ mass concentrations at 17:00, 19:00 and 21:00 UTC respectively. The last row is EPIC UVAI.

For comparison, we also studied the hourly change of smoke height and surface $PM_{2.5}$ over Eastern United States from 15:00 to 16:48 UTC on September 15 (Figure 7). Since the long-range transport diffuses the smoke plumes, the smoke layer in Eastern United States exhibits a smaller AOD than that over western United States on September 7. The majority of $PM_{2.5}$ measurements in Eastern United States on September 15 are lower than 20 μg m^{-3}. The $PM_{2.5}$ concentrations are higher in the southwest of the research domain indicated by the pink circle in Figure 7 than that in the northeast indicated by the black circle, with the AOD values even lower in the southwest than northeast. Again, this is due to the lower smoke height in the southwestern region, which also indicates the smoke plumes already

affected the surface $PM_{2.5}$ concentrations at least in the southwestern region. However, since both the AOD and AOCH do not show much hourly variation in the whole Eastern United States domain, the surface $PM_{2.5}$ concentrations remain at similar level during these 2 hours.

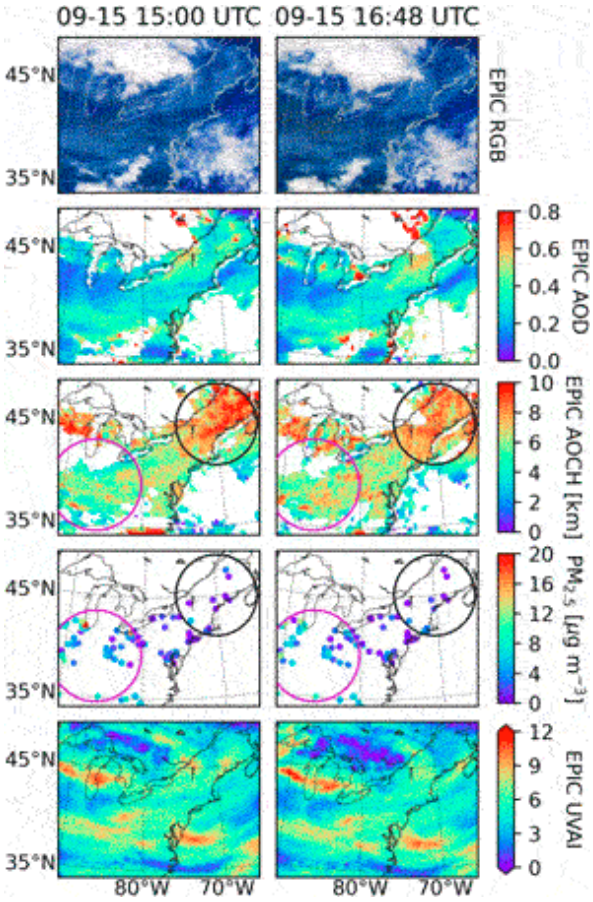

FIGURE 7 | Same as Figure 6, but for 15:00–16:48 UTC on September 15, 2020.

SUMMARY

This study applied vicarious calibration to EPIC measurements based on the TROPOMI level 1B data to retrieve the smoke aerosol optical centroid heights for the 2020 California fire events on September 7, 9 and 14–16, because the EPIC instrument does not have on-board calibration and its after-launch calibration is out of date. The cases of September 9 and 14–16 are used for validation of the EPIC retrievals after the new calibration. Subsequently, the implication of hourly variation of the smoke heights on the surface $PM_{2.5}$ pollution on September 7 and 15 is investigated.

The vicarious calibration leads to important improvement of the EPIC AOCH retrieval. Without the new calibration, the EPIC AOCH is lower than the CALIOP AOCH by 1–3 km, while after the vicarious calibration, the EPIC AOCH retrieval matches with the CALIOP AOCH very well. The RMSE of the AOCH retrievals reduces from 2.76 to 0.91 km, and the correlation coefficient increases from 0.736 to 0.885 after the vicarious calibration. The TROPOMI operational ALH product is lower than the new EPIC AOCH retrieval by 2–3 km, which is consistent with Nanda et al. (2020).

The case studies on September 7 and 15 indicate that the spatial and diurnal variations of smoke plume height have significant implications on the surface $PM_{2.5}$ pollution. The hourly change of smoke height and the response of surface $PM_{2.5}$ thereafter are of particular interest as it can be uniquely investigated via EPIC observations. The descending of the smoke height in ~3.5 h on September 7 leads to the increase of surface $PM_{2.5}$ concentrations. By contrast, the smoke height did not change much during 15:00–16:48 UTC on September 15 over Eastern United States, and there is little hourly variation in $PM_{2.5}$ concentrations during this time period.

This study is the among the first to demonstrate the feasibility to retrieve simultaneous *hourly* AOD and AOCH for thick smoke plumes in the United States from a passive-sensing instrument without on-board calibration, such as EPIC; hourly AODs from geostationary satellites have been available but without AOCH information. As the big fires occurred in many parts of the world in the last several years and are likely to continue as a result of global warming, the impacts of these fires on air quality have to be mitigated with the better monitoring and predictions of smoke transport, specially the placement of smoke layer in the vertical with respect to the planetary boundary layer where human live. While more studies are needed, the work here shows the critical value of passive sensors such as EPIC to derive hourly AOCH and mapping the vertical movement of smoke layer with large spatial coverage, all of which can potentially needed to the improvement of surface air quality monitoring and prediction.

The major limitation of our current algorithm includes two perspectives: 1) the surface reflectance is assumed to be Lambertian, and we will consider BRDF in the future; 2) sometimes the retrieval results have some shattered cloud contamination, and we plan to apply the spectral slope test as in Chen

et al. (2021) and post processing to further remove the cloud noise. In addition, we are going to improve the algorithm in the following perspectives: 1) calculate the UVAI online and set some threshold to determine whether to do the retrieval for each pixel; 2) develop some techniques to separate the smoke and dust aerosol and apply proper aerosol model in the retrieval; 3) retrieve hourly AOCH and AOD from EPIC operationally.

DATA AVAILABILITY STATEMENT

The original contributions presented in the study are included in the article/Supplementary Material, further inquiries can be directed to the corresponding author.

AUTHOR CONTRIBUTIONS

ZL performed the retrievals and data analysis. ZL and JW wrote the paper. JW designed the research. XX developed the retrieval algorithm. XC generated the lookup table and convolved the TROPOMI L1B data. SK, OT, and EW contributed to writing. JZ contributed to the research design. ZL and JW also refined the algorithm.

FUNDING

This work is supported by the NASA DSCOVR program (grant #: 80NSSC19K1283), NASA's Applied Science program, HAQST science team (grant #: 80NSSC21K0428), NASA's FIREX-AQ program (grant #: 80NSSC18K0791), NASA's Terra/Aqua/SNPP program (grant #: 80NSSC18K0846), and NOAA GEO-XO program (NA21OAR4310249).

PUBLISHER'S NOTE

REFERENCES

Ahn, C., Torres, O., Jethva, H., Tiruchirapalli, R., and Huang, L. K. (2021). Evaluation of Aerosol Properties Observed by DSCOVR/EPIC Instrument from the Earth-Sun Lagrange 1 Orbit. *Geophys. Res. Atmos.* 126 (12), e2020JD033651. doi:10.1029/2020JD033651

Chen, X., Wang, J., Xu, X., Zhou, M., Zhang, H., Castro Garcia, L., et al. (2021). First Retrieval of Absorbing Aerosol Height over Dark Target Using TROPOMI Oxygen B Band: Algorithm Development and Application for Surface Particulate Matter Estimates. *Remote Sensing Environ.* 265, 112674. doi:10.1016/j.rse.2021.112674

Choi, T., Shao, X., Cao, C., and Weng, F. (2016). Radiometric Stability Monitoring of the Suomi NPP Visible Infrared Imaging Radiometer Suite (VIIRS) Reflective Solar Bands Using the Moon. *Remote Sensing* 8 (1), 15. Retrieved from https://www.mdpi.com/2072-4292/8/1/15.

de Graaf, M., de Haan, J. F., and Sanders, A. F. J. (2019). TROPOMI ATBD of the Aerosol Layer Height. Retrieved from http://www.tropomi.eu/sites/default/files/files/publicSentinel-5P-TROPOMI-ATBD-Aerosol-Height.pdf.

Doelling, D., Haney, C., Bhatt, R., Scarino, B., and Gopalan, A. (2019). The Inter-calibration of the DSCOVR EPIC Imager with Aqua-MODIS and NPP-VIIRS. *Remote Sensing* 11 (13), 1609. Retrieved from. doi:10.3390/rs11131609https://www.mdpi.com/2072-4292/11/13/1609.

Doelling, D. R., Morstad, D., Scarino, B. R., Bhatt, R., and Gopalan, A. (2013). The Characterization of Deep Convective Clouds as an Invariant Calibration Target and as a Visible Calibration Technique. *IEEE Trans. Geosci. Remote Sensing* 51 (3), 1147–1159. doi:10.1109/tgrs.2012.2225066

Garay, M. J., Witek, M. L., Kahn, R. A., Seidel, F. C., Limbacher, J. A., Bull, M. A., et al. (2020). Introducing the 4.4 Km Spatial Resolution Multi-Angle Imaging SpectroRadiometer (MISR) Aerosol Product. *Atmos. Meas. Tech.* 13 (2), 593–628. doi:10.5194/amt-13-593-2020

Ge, C., Wang, J., and Reid, J. S. (2014). Mesoscale Modeling of Smoke Transport over the Southeast Asian Maritime Continent: Coupling of Smoke Direct Radiative Effect below and above the Low-Level Clouds. *Atmos. Chem. Phys.* 14 (1), 159–174. doi:10.5194/acp-14-159-2014

Geogdzhayev, I. V., Marshak, A., and Alexandrov, M. (2021). Calibration of the DSCOVR EPIC Visible and NIR Channels Using Multiple LEO Radiometers. *Front. Remote Sens.* 2 (12). doi:10.3389/frsen.2021.671933

Geogdzhayev, I. V., and Marshak, A. (2018). Calibration of the DSCOVR EPIC Visible and NIR Channels Using MODIS Terra and Aqua Data and EPIC Lunar Observations. *Atmos. Meas. Tech.* 11 (1), 359–368. doi:10.5194/amt-11-359-2018

Giglio, L., Csiszar, I., and Justice, C. O. (2006). Global Distribution and Seasonality of Active Fires as Observed with the Terra and Aqua Moderate Resolution Imaging Spectroradiometer (MODIS) Sensors. *J. Geophys. Res.* 111 (G2), a–n. doi:10.1029/2005JG000142

Griffin, D., Sioris, C., Chen, J., Dickson, N., Kovachik, A., de Graaf, M., et al. (2020). The 2018 Fire Season in North America as Seen by TROPOMI: Aerosol Layer Height Intercomparisons and Evaluation of Model-Derived Plume Heights. *Atmos. Meas. Tech.* 13 (3), 1427–1445. doi:10.5194/amt-13-1427-2020

Haney, C., Doelling, D., Minnis, P., Bhatt, R., Scarino, B., and Gopalan, A. (2016). “The Calibration of the DSCOVR EPIC Multiple Visible Channel Instrument Using MODIS and VIIRS as a Reference,”. *Earth Observing Systems Xxi* ed . Editors J. J. Butler, X. Xiong, and X. Gu, 9972. doi:10.1117/12.2238010

Herman, J. R., Bhartia, P. K., Torres, O., Hsu, C., Seftor, C., and Celarier, E. (1997). Global Distribution of UV-Absorbing Aerosols from Nimbus 7/TOMS Data. *J. Geophys. Res.* 102 (D14), 16911–16922. doi:10.1029/96jd03680

Holben, B. N., Eck, T. F., Slutsker, I., Tanré, D., Buis, J. P., Setzer, A., et al. (1998). AERONET-A Federated Instrument Network and Data Archive for Aerosol Characterization. *Remote Sensing Environ.* 66 (1), 1–16. doi:10.1016/s0034-4257(98)00031-5

Hsu, N. C., Herman, J. R., Torres, O., Holben, B. N., Tanre, D., Eck, T. F., et al. (1999). Comparisons of the TOMS Aerosol index with Sun-Photometer Aerosol Optical Thickness: Results and Applications. *J. Geophys. Res.* 104 (D6), 6269–6279. doi:10.1029/1998JD200086

Jeong, M.-J., and Hsu, N. C. (2008). Retrievals of Aerosol Single-Scattering Albedo and Effective Aerosol Layer Height for Biomass-Burning Smoke: Synergy Derived from "A-Train" Sensors. *Geophys. Res. Lett.* 35 (24). doi:10.1029/2008GL036279

Jethva, H., and Torres, O. (2011). Satellite-based Evidence of Wavelength-dependent Aerosol Absorption in Biomass Burning Smoke Inferred from Ozone Monitoring Instrument. *Atmos. Chem. Phys.* 11 (20), 10541–10551. doi:10.5194/acp-11-10541-2011

Kipling, Z., Stier, P., Johnson, C. E., Mann, G. W., Bellouin, N., Bauer, S. E., et al. (2016). What Controls the Vertical Distribution of Aerosol? Relationships between Process Sensitivity in HadGEM3-UKCA and Inter-model Variation from AeroCom Phase II. *Atmos. Chem. Phys.* 16 (4), 2221–2241. doi:10.5194/acp-16-2221-2016

Kleipool, Q., Ludewig, A., Babić, L., Bartstra, R., Braak, R., Dierssen, W., et al. (2018). Pre-launch Calibration Results of the TROPOMI Payload On-Board the Sentinel-5 Precursor Satellite. *Atmos. Meas. Tech.* 11 (12), 6439–6479. doi:10.5194/amt-11-6439-2018

Koffi, B., Schulz, M., Bréon, F.-M., Dentener, F., Steensen, B. M., Griesfeller, J., et al. (2016). Evaluation of the Aerosol Vertical Distribution in Global Aerosol Models through Comparison against CALIOP Measurements: AeroCom Phase II Results. *J. Geophys. Res. Atmos.* 121 (12), 7254–7283. doi:10.1002/2015JD024639

Koffi, B., Schulz, M., Bréon, F.-M., Griesfeller, J., Winker, D., Balkanski, Y., et al. (2012). Application of the CALIOP Layer Product to Evaluate the Vertical Distribution of Aerosols Estimated by Global Models: AeroCom Phase I Results. *J. Geophys. Res.* 117 (D10), a–n. doi:10.1029/2011jd016858

Lee, J., Hsu, N. C., Sayer, A. M., Seftor, C. J., and Kim, W. V. (2021). Aerosol Layer Height with Enhanced Spectral Coverage Achieved by Synergy between VIIRS and OMPS-NM Measurements. *IEEE Geosci. Remote Sensing Lett.* 18, 949–953. doi:10.1109/lgrs.2020.2992099

Levy, R. C., Mattoo, S., Munchak, L. A., Remer, L. A., Sayer, A. M., Patadia, F., et al. (2013). The Collection 6 MODIS Aerosol Products over Land and Ocean. *Atmos. Meas. Tech.* 6 (11), 2989–3034. doi:10.5194/amt-6-2989-2013

Limbacher, J. A., and Kahn, R. A. (2015). MISR Empirical Stray Light Corrections in High-Contrast Scenes. *Atmos. Meas. Tech.* 8 (7), 2927–2943. doi:10.5194/amt-8-2927-2015

Ludewig, A., Kleipool, Q., Bartstra, R., Landzaat, R., Leloux, J., Loots, E., et al. (2020). In-flight Calibration Results of the TROPOMI Payload on Board the Sentinel-5 Precursor Satellite. *Atmos. Meas. Tech.* 13 (7), 3561–3580. doi:10.5194/amt-13-3561-2020

Lyapustin, A., Wang, Y., Korkin, S., and Huang, D. (2018). MODIS Collection 6 MAIAC Algorithm. *Atmos. Meas. Tech.* 11 (10), 5741–5765. doi:10.5194/amt-11-5741-2018

Lyapustin, A., Wang, Y., Korkin, S., Kahn, R., and Winker, D. (2020). MAIAC Thermal Technique for Smoke Injection Height from MODIS. *IEEE Geosci. Remote Sensing Lett.* 17 (5), 730–734. doi:10.1109/lgrs.2019.2936332

Marshak, A., Herman, J., Adam, S., Karin, B., Carn, S., Cede, A., et al. (2018). Earth Observations from DSCOVR EPIC Instrument. *Bull. Am. Meteorol. Soc.* 99 (9), 1829–1850. doi:10.1175/bams-d-17-0223.1

Morris, G., and Dennis, C. (2021). Fire Siege. Retrieved from https://www.fire.ca.gov/media/hsviuuv3/cal-fire-2020-fire-siege.pdf.

Nanda, S., de Graaf, M., Veefkind, J. P., Sneep, M., ter Linden, M., Sun, J., et al. (2020). A First Comparison of TROPOMI Aerosol Layer Height (ALH) to CALIOP Data. *Atmos. Meas. Tech.* 13 (6), 3043–3059. doi:10.5194/amt-13-3043-2020

Nanda, S., de Graaf, M., Veefkind, J. P., ter Linden, M., Sneep, M., de Haan, J., et al. (2019). A Neural Network Radiative Transfer Model Approach Applied to the Tropospheric Monitoring Instrument Aerosol Height Algorithm. *Atmos. Meas. Tech.* 12 (12), 6619–6634. doi:10.5194/amt-12-6619-2019

Nelson, D., Garay, M., Kahn, R., and Dunst, B. (2013). Stereoscopic Height and Wind Retrievals for Aerosol Plumes with the MISR INteractive eXplorer (MINX). *Remote Sensing* 5 (9), 4593–4628.

Retrieved from. doi:10.3390/rs5094593https://www.mdpi.com/2072-4292/5/9/4593.

Rajapakshe, C., Zhang, Z., Yorks, J. E., Yu, H., Tan, Q., Meyer, K., et al. (2017). Seasonally Transported Aerosol Layers over Southeast Atlantic Are Closer to Underlying Clouds Than Previously Reported. *Geophys. Res. Lett.* 44 (11), 5818–5825. doi:10.1002/2017gl073559

Reid, J. S., Eck, T. F., Christopher, S. A., Hobbs, P. V., and Holben, B. (1999). Use of the Ångstrom Exponent to Estimate the Variability of Optical and Physical Properties of Aging Smoke Particles in Brazil. *J. Geophys. Res.* 104 (D22), 27473–27489. doi:10.1029/1999jd900833

Sayer, A. M., Hsu, N. C., Bettenhausen, C., Holz, R. E., Lee, J., Quinn, G., et al. (2017). Cross-calibration of S-NPP VIIRS Moderate-Resolution Reflective Solar Bands against MODIS Aqua over Dark Water Scenes. *Atmos. Meas. Tech.* 10 (4), 1425–1444. doi:10.5194/amt-10-1425-2017

Sayer, A. M., Hsu, N. C., Bettenhausen, C., Jeong, M. J., and Meister, G. (2015). Effect of MODIS Terra Radiometric Calibration Improvements on Collection 6 Deep Blue Aerosol Products: Validation and Terra/Aqua Consistency. *J. Geophys. Res. Atmos.* 120 (23). doi:10.1002/2015jd023878

Schaaf, C. B., Gao, F., Strahler, A. H., Lucht, W., Li, X., Tsang, T., et al. (2002). First Operational BRDF, Albedo Nadir Reflectance Products from MODIS. *Remote Sensing Environ.* 83 (1), 135–148. doi:10.1016/S0034-4257(02)00091-3

Schweizer, D., Cisneros, R., and Shaw, G. (2016). A Comparative Analysis of Temporary and Permanent Beta Attenuation Monitors: The Importance of Understanding Data and Equipment Limitations when Creating PM 2.5 Air Quality Health Advisories. *Atmos. Pollut. Res.* 7 (5), 865–875. doi:10.1016/j.apr.2016.02.003

Seo, S., Kim, J., Lee, H., Jeong, U., Kim, W., Holben, B. N., et al. (2015). Estimation of PM10 Concentrations over Seoul Using Multiple Empirical Models with AERONET and MODIS Data Collected during the DRAGON-Asia Campaign. *Atmos. Chem. Phys.* 15 (1), 319–334. doi:10.5194/acp-15-319-2015

Shi, Y. R., Levy, R. C., Eck, T. F., Fisher, B., Mattoo, S., Remer, L. A., et al. (2019). Characterizing the 2015 Indonesia Fire Event Using Modified MODIS Aerosol Retrievals. *Atmos. Chem. Phys.* 19 (1), 259–274. doi:10.5194/acp-19-259-2019

Sicard, M., Granados-Muñoz, M. J., Alados-Arboledas, L., Barragán, R., Bedoya-Velásquez, A. E., Benavent-Oltra, J. A., et al. (2019). Ground/space, Passive/active Remote Sensing Observations Coupled with Particle Dispersion Modelling to Understand the Inter-continental Transport of Wildfire Smoke Plumes. *Remote Sensing Environ.* 232, 111294. doi:10.1016/j.rse.2019.111294

Sofowote, U., Su, Y., Bitzos, M. M., and Munoz, A. (2014). Improving the Correlations of Ambient Tapered Element Oscillating Microbalance PM2.5 Data and SHARP 5030 Federal Equivalent Method in Ontario: A Multiple Linear Regression Analysis. *J. Air Waste Manag. Assoc.* 64 (1), 104–114. doi:10.1080/10962247.2013.833145

Spurr, R. (2008). LIDORT and VLIDORT: Linearized Pseudo-spherical Scalar and Vector Discrete Ordinate Radiative Transfer Models for Use in Remote Sensing Retrieval Problems.

Spurr, R., Wang, J., Zeng, J., and Mishchenko, M. I. (2012). Linearized T-Matrix and Mie Scattering Computations. *J. Quantitative Spectrosc. Radiative Transfer* 113 (6), 425–439. doi:10.1016/j.jqsrt.2011.11.014

Tian, P., Cao, X., Zhang, L., Sun, N., Sun, L., Logan, T., et al. (2017). Aerosol Vertical Distribution and Optical Properties over China from Long-Term Satellite and Ground-Based Remote Sensing. *Atmos. Chem. Phys.* 17 (4), 2509–2523. doi:10.5194/acp-17-2509-2017

Tilstra, L. G., Tuinder, O. N. E., Wang, P., and Stammes, P. (2017). Surface Reflectivity Climatologies from UV to NIR Determined from Earth Observations by GOME-2 and SCIAMACHY. *J. Geophys. Res. Atmos.* 122 (7), 4084–4111. doi:10.1002/2016JD025940

Torres, O., Ahn, C., and Chen, Z. (2013). Improvements to the OMI Near-UV Aerosol Algorithm Using A-Train CALIOP and AIRS Observations. *Atmos. Meas. Tech.* 6 (11), 3257–3270. doi:10.5194/amt-6-3257-2013

Torres, O., Bhartia, P. K., Herman, J. R., Ahmad, Z., and Gleason, J. (1998). Derivation of Aerosol Properties from Satellite Measurements of Backscattered Ultraviolet Radiation: Theoretical Basis. *J. Geophys. Res.* 103 (D14), 17099–17110. doi:10.1029/98jd00900

Torres, O., Bhartia, P. K., Jethva, H., and Ahn, C. (2018). Impact of the Ozone Monitoring Instrument Row Anomaly on the Long-Term Record of Aerosol Products. *Atmos. Meas. Tech.* 11 (5), 2701–2715. doi:10.5194/amt-11-2701-2018

Torres, O., Tanskanen, A., Veihelmann, B., Ahn, C., Braak, R., Bhartia, P. K., et al. (2007). Aerosols and Surface UV Products from Ozone Monitoring Instrument Observations: An Overview. *J. Geophys. Res.* 112 (D24). doi:10.1029/2007JD008809

Val Martin, M., Heald, C. L., Ford, B., Prenni, A. J., and Wiedinmyer, C. (2013). A Decadal Satellite Analysis of the Origins and Impacts of Smoke in Colorado. *Atmos. Chem. Phys.* 13 (15), 7429–7439. doi:10.5194/acp-13-7429-2013

Veefkind, J. P., Aben, I., McMullan, K., Förster, H., de Vries, J., Otter, G., et al. (2012). TROPOMI on the ESA Sentinel-5 Precursor: A GMES mission for Global Observations of the Atmospheric Composition for Climate, Air Quality and Ozone Layer Applications. *Remote Sensing Environ.* 120, 70–83. doi:10.1016/j.rse.2011.09.027

Wang, J., and Christopher, S. A. (2003). Intercomparison between Satellite-Derived Aerosol Optical Thickness and PM2.5mass: Implications for Air Quality Studies. *Geophys. Res. Lett.* 30 (21). doi:10.1029/2003gl018174

Wang, J., and Christopher, S. A. (2006a). Mesoscale Modeling of Central American Smoke Transport to the United States: 2. Smoke Radiative Impact on Regional Surface Energy Budget and Boundary Layer Evolution. *J. Geophys. Res.* 111 (D14). doi:10.1029/2005jd006720

Wang, J., Christopher, S. A., Nair, U. S., Reid, J. S., Prins, E. M., Szykman, J., et al. (2006b). Mesoscale Modeling of Central American Smoke Transport to the United States: 1. "Top-Down" Assessment of Emission Strength and Diurnal Variation Impacts. *J. Geophys. Res.* 111 (D5). doi:10.1029/2005jd006416

Wang, J., Xu, X., Ding, S., Zeng, J., Spurr, R., Liu, X., et al. (2014). A Numerical Testbed for Remote Sensing of Aerosols, and its Demonstration for Evaluating Retrieval Synergy from a Geostationary Satellite Constellation of GEO-CAPE and GOES-R. *J. Quantitative Spectrosc. Radiative Transfer* 146, 510–528. doi:10.1016/j.jqsrt.2014.03.020

Wilcox, E. M. (2012). Direct and Semi-direct Radiative Forcing of Smoke Aerosols over Clouds. *Atmos. Chem. Phys.* 12 (1), 139–149. doi:10.5194/acp-12-139-2012

Winker, D. M., Tackett, J. L., Getzewich, B. J., Liu, Z., Vaughan, M. A., and Rogers, R. R. (2013). The Global 3-D Distribution of Tropospheric Aerosols as Characterized by CALIOP. *Atmos. Chem. Phys.* 13 (6), 3345–3361. doi:10.5194/acp-13-3345-2013

Winker, D. M., Vaughan, M. A., Omar, A., Hu, Y., Powell, K. A., Liu, Z., et al. (2009). Overview of the CALIPSO Mission and CALIOP Data Processing Algorithms. *J. Atmos. Oceanic Tech.* 26 (11), 2310–2323. doi:10.1175/2009jtecha1281.1

Xiong, X., Angal, A., Chang, T., Chiang, K., Lei, N., Li, Y., et al. (2020). MODIS and VIIRS Calibration and Characterization in Support of Producing Long-Term High-Quality Data Products. *Remote Sensing* 12 (19), 3167. Retrieved from. doi:10.3390/rs12193167https://www.mdpi.com/2072-4292/12/19/3167.

Xiong, X. X., Angal, A., Barnes, W., Chen, H. D., Chiang, V., Geng, X., et al. (2017). "Updates of MODIS On-Orbit Calibration Uncertainty Assessments," in *Earth Observing Systems Xxii* ed . Editors J. J. Butler, X. Xiong, and X. Gu. Vol. 10402.

Xu, X., Wang, J., Wang, Y., and Kokhanovsky, A. (2018). *Passive Remote Sensing of Aerosol Height. Remote Sensing of Aerosols, Clouds, and Precipitation*. Elsevier, 1–22. doi:10.1016/b978-0-12-810437-8.00001-3

Xu, X., Wang, J., Wang, Y., Zeng, J., Torres, O., Reid, J. S., et al. (2019). Detecting Layer Height of Smoke Aerosols over Vegetated Land and Water Surfaces via Oxygen Absorption Bands: Hourly

Results from EPIC/DSCOVR in Deep Space. *Atmos. Meas. Tech.* 12 (6), 3269–3288. doi:10.5194/amt-12-3269-2019

Xu, X., Wang, J., Wang, Y., Zeng, J., Torres, O., Yang, Y., et al. (2017). Passive Remote Sensing of Altitude and Optical Depth of Dust Plumes Using the Oxygen A and B Bands: First Results from EPIC/DSCOVR at Lagrange-1 point. *Geophys. Res. Lett.* 44 (14), 7544–7554. doi:10.1002/2017gl073939

Zarzycki, C. M., and Bond, T. C. (2010). How Much Can the Vertical Distribution of Black Carbon Affect its Global Direct Radiative Forcing?*Geophys. Res. Lett.* 37, a–n. doi:10.1029/2010gl044555

Conflict of Interest: The authors declare that the research was conducted in the absence of any commercial or financial relationships that could be construed as a potential conflict of interest.

ORIGINAL RESEARCH
published: 28 October 2021
doi: 10.3389/frsen.2021.766805

Vegetation Angular Signatures of Equatorial Forests From DSCOVR EPIC and Terra MISR Observations

Xiangnan Ni[1,2], Yuri Knyazikhin[1*], Yuanheng Sun[1,3], Xiaojun She[1,4], Wei Guo[2,5], Oleg Panferov[6] and Ranga B. Myneni[1]

[1] *Department of Earth and Environment, Boston University, Boston, MA, United States*
[2] *Department of Earth and Environmental Sciences, Xi'an Jiaotong University, Xi'an, China*
[3] *School of Earth and Space Sciences, Peking University, Beijing, China*
[4] *School of Geographic Sciences, Southwest University, Chongqing, China*
[5] *Department of Geography, University of California Los Angeles, Los Angeles, CA, United States*
[6] *Department of Life Sciences and Engineering, University of Applied Sciences, Bingen, Germany*

Edited by:
Gregory Schuster, National Aeronautics and Space Administration (NASA), United States

Reviewed by:
Igor Geogdzhayev, Columbia University, United States
Alexei Lyapustin, National Aeronautics and Space Administration, United States

**** Correspondence:*** *Yuri Knyazikhin, jknjazi@bu.edu*

Specialty section: *This article was submitted to Satellite Missions, a section of the journal Frontiers in Remote Sensing*

Received: *30 August 2021*
Accepted: *04 October 2021*
Published: *28 October 2021*

Citation: *Ni X, Knyazikhin Y, Sun Y, She X, Guo W, Panferov O and Myneni RB (2021) Vegetation Angular Signatures of Equatorial Forests From DSCOVR EPIC and Terra MISR Observations. Front. Remote Sens. 2:766805. doi: 10.3389/frsen.2021.766805*

In vegetation canopies cross-shading between finite dimensional leaves leads to a peak in reflectance in the retro-illumination direction. This effect is called the hot spot in optical remote sensing. The hotspot region in reflectance of vegetated surfaces represents the most information-rich directions in the angular distribution of canopy reflected radiation. This paper presents a new approach for generating hot spot signatures of equatorial forests from synergistic analyses of multiangle observations from the Multiangle Imaging SpectroRadiometer (MISR) on Terra platform and near backscattering reflectance data from the Earth Polychromatic Imaging Camera (EPIC) onboard NOAA's Deep Space Climate Observatory (DSCOVR). A canopy radiation model parameterized in terms of canopy spectral invariants underlies the theoretical basis for joining Terra MISR and DSCOVR EPIC data. The proposed model can accurately reproduce both MISR angular signatures acquired at 10:30 local solar time and diurnal courses of EPIC reflectance (NRMSE < 9%, R^2 > 0.8). Analyses of time series of the hot spot signature suggest its ability to unambiguously detect seasonal changes of equatorial forests.

Keywords: DSCOVR EPIC, terra MISR, vegetation hotspot signature, directional area scattering factor (DASF), seasonality, tropical forests

INTRODUCTION

The global forest ecosystem absorbs about 25% of the total anthropogenic CO_2 emission from atmosphere via carbon accumulation to forest biomass (Reichstein et al., 2013). Forests store 75% of terrestrial carbon, and account for 40% of the carbon exchange with atmosphere each year (Schlesinger and Bernhardt, 2012). Within the forest ecosystem, tropical forests contain about 40–50% of the terrestrial carbon stock (Lewis et al., 2009) and are potentially responsible for about 70% of terrestrial carbon sink (Pan et al., 2011). Monitoring and quantifying changes in tropical forests therefore play a critical role in understanding the global carbon cycle and future climate change.

Monitoring of dense vegetation such as equatorial rainforests represents the most complicated case in optical remote sensing because reflection of

solar radiation saturates and becomes weakly sensitive to vegetation changes. At the same time, the satellite data are strongly influenced by changing sun-sensor geometry. This makes it difficult to discriminate between vegetation changes and sun-sensor geometry effects. For instance, studies on Amazon forest seasonality based on analyses of data from single-viewing sensors disagree on whether there is more greenness in the dry season than in the wet season: the observed increase in vegetation indices were explained by an increase in leaf area, an artifact of sun-sensor-geometry and changes in leaf age through the leaf flush (Huete et al., 2006; Brando et al., 2010; Samanta et al., 2012; Morton et al., 2014; Saleska et al., 2016). The impact of droughts on Amazon forests has also been debated (Saleska et al., 2007; Samanta et al., 2010; Samanta et al., 2011; Xu et al., 2011). Conflicting conclusions among these studies arose from different interpretations of surface reflectance data acquired under saturation conditions (Bi et al., 2015). Developing methodologies that allow us to unambiguously interpret reflectance of dense forests is worthy of special attention.

Broadly used approaches for interpretation of satellite data from single-viewing sensors consider the viewing and solar zenith angle dependence of reflected radiation to be a problematic source of noise or error, requiring a correction or normalization to a "standard" sun-sensor geometry (Lyapustin et al., 2018). Transformation of such data to a fixed standard sun-sensor geometry therefore invokes statistical assumptions that may not apply to specific scenes. The lack of information about angular variation of forest reflected radiation introduces model uncertainties that in turn may have significant impact on interpretation of satellite data (Gorkavyi et al., 2021).

Unlike single-angle methodologies, multiangle approaches exploit angular variation of surface reflected radiation as unique and rich sources of diagnostic information and enable the rigorous use of the radiative transfer theory. In vegetation canopies cross-shading between finite dimensional leaves leads to a peak in reflectance in the retro-illumination direction. This effect is called the hot spot in optical remote sensing (Gerstl and Simmer, 1986; Ross and Marshak, 1988; Kuusk, 1991; Myneni, 1991). The hotspot region in reflectance of vegetated surfaces represents the most information-rich directions in the angular distribution of canopy reflected radiation. The hot spot phenomenon correlates with canopy architectural parameters such as foliage size and shape, crown geometry and within-crown foliage arrangement, foliage grouping, leaf area index and its sunlit fraction (Ross

and Marshak, 1991; Qin et al., 1996; Goel et al., 1997; Qin et al., 2002; Yang et al., 2017; Pisek et al., 2021). Angular signatures that include the hot spot region are critical for monitoring phenological changes in equatorial forests (Bi et al., 2015). Availability of hot spot signatures of equatorial forests would make monitoring their changes more reliable.

The Multiangle Imaging SpectroRadiometer (MISR) on Terra platform provides simultaneous multiangle observations of surface reflectance since December 1999. Its observing strategy allows for a good angular variation of surface reflectance in equatorial zone. However spatially and temporally varying phase angle[1] could be far from zero, making frequent observations of canopy reflectance in the hot spot region impossible. The NASA's Earth Polychromatic Imaging Camera (EPIC) onboard NOAA's Deep Space Climate Observatory (DSCOVR) was launched on February 11, 2015 to the Sun-Earth Lagrangian L1 point where it began to collect radiance data of the entire sunlit Earth every 65–110 min in June 2015. It provides imageries in near backscattering directions (Marshak et al., 2018).

The DSCOVR EPIC observations therefore provide unique information required to extend angular sampling of the MISR sensor to the hot spot region. The objectives of this paper are to 1) develop a new methodology that synergistically incorporates features of Terra MISR and DSCOVR EPIC observation geometries and results in hot spot signatures of equatorial forests; 2) generate angular signatures of equatorial rainforests for the period of concurrent Terra MISR and DSCOVR EPIC data and asses their quality; 3) demonstrate their value for monitoring seasonal changes of the equatorial forests.

THEORETICAL BASIS

Reflectance of Dense Vegetation

The Bidirectional Reflectance Factor (BRF) is defined as the ratio of the surface-reflected radiance to radiance reflected from an ideal Lambertian surface into the same beam geometry and illuminated by the same mono-directional beam (Martonchik et al., 2000; Schaepman-Strub et al., 2006). It describes the magnitude and angular distribution of surface reflected radiation in the absence of atmosphere and varies with the directions to the Sun, $\Omega_0 \sim (\theta_0, \varphi_0)$, and to the sensor, $\Omega \sim (\theta, \varphi)$. In this paper, the directions are expressed in terms of zenith, θ_0 and θ, and azimuthal, φ_0 and φ, angles. We will use symbols μ_0 and μ for $\cos\theta_0$ and $\cos\theta$, respectively.

For sufficiently dense vegetation such as equatorial forests, the BRF can be accurately approximated as (Knyazikhin et al., 2013)

$$BRF_\lambda(\Omega_0, \Omega) = \frac{\rho(\Omega_0, \Omega) i_0}{1 - p} \times \frac{\omega_\lambda (1 - p)}{1 - p\omega_\lambda} = DASF(\Omega_0, \Omega) \times W_\lambda . \quad (1)$$

The first factors on the right-hand side of Eq. 1 is the Directional Area Scattering Factor (DASF), which describes the canopy BRF if the foliage does not absorb radiation. The spectrally invariant DASF is a function of canopy geometrical properties, such as the tree crown shape and size, spatial distribution of trees on the ground, and within-crown foliage arrangement (Knyazikhin et al., 2013). The second factor, W_λ, is the Canopy Scattering Coefficient (CSC), i.e., the fraction of intercepted radiation that has been reflected from, or diffusively transmitted through, the vegetation (Smolander and Stenberg 2005; Lewis and Disney 2007). The spectrally varying CSC is weakly sensitive to variation in the sun-sensor geometry. It conveys information about leaf optical properties (Knyazikhin et al., 2013; Latorre-Carmona et al., 2014; Adams et al., 2018).

Our forest BRF is parameterized in terms of spectrally invariant parameters (Knyazikhin et al., 2011; Stenberg et al., 2016). Here i_0 is the canopy interceptance defined as the portion of photons from the incident solar beam that collide with foliage elements for the first time. The symbol ρ designates the directional escape probability, i.e., the probability by which a photon scattered by a foliage element will exit the vegetation in the direction Ω through gaps. Spherical integration of $\pi^{-1}\rho|\cos\theta|$ results in $1 - p$, where p is the recollision probability, defined as the probability that a photon scattered by a foliage element in the canopy will interact within the canopy again. The spherical integration significantly weakens the sensitivity of p to sun-sensor geometry. Finally, ω_λ is the wavelength dependent leaf albedo, i.e., the fraction of radiation incident on a leaf surface that is reflected or transmitted.

The directional escape probability controls the shape of the BRF. Indeed, photons scattered by sunlit leaves will escape the vegetation in the retro-illumination direction with unit probability since their paths are free of foliage elements. Photon paths in off-backscattering directions are more likely obstructed by leaves and the likelihood of photons escaping the canopy is consequently reduced. We follow methodology developed in (Yang et al., 2017) to simulate the hot spot effect. Kuusk's model of the hot spot

incorporated into the extinction coefficient of the radiative transfer equation is used to estimate the escape probability (Supplementary Appendix SA).

Our primary objective is to derive DASF from Terra MISR and DSCOVR EPIC observations. For vegetation canopies with a dark background, or sufficiently dense vegetation where the impact of canopy background is negligible, the DASF can be directly retrieved from the BRF spectrum in the weakly absorbing spectral interval, without involving canopy reflectance models, prior knowledge, or ancillary information regarding leaf scattering properties. We follow methodology developed in (Marshak and Knyazikhin 2017; Song et al., 2018) to approximate this variable using BRFs at NIR and green spectral bands: DASF is the ratio $R/(1-s)$ where R and s are intercept and slope of the line passing two points $\left(\frac{BRF_\lambda}{\omega_\lambda},\ BRF_\lambda\right)$, λ =green, NIR. Thus,

$$DASF(\Omega_0,\Omega)=\frac{BRF_{\text{green}}BRF_{\text{NIR}}}{BRF_{\text{green}}-\beta\left(BRF_{\text{NIR}}-BRF_{\text{green}}\right)}. \quad (2)$$

Here $\beta=(1-\omega_{\text{NIR}})\omega_{\text{green}}/(\omega_{\text{NIR}}-\omega_{\text{green}})$ where ω_{NIR} and ω_{green} represent leaf albedo of the brightest leaf at NIR and green spectral bands integrated over bandwidths. Its values are $\omega_{555}=0.461$, $\omega_{865}=0.978$ ($\beta=0.0196$) for MISR and $\omega_{551}=0.490$ $\omega_{779}=0.966$ ($\beta=0.035$) for EPIC. These values were obtained from Lewis and Disney's approximation (Lewis and Disney, 2007) of the PROSPECT model (Féret et al., 2008) with the following parameters: chlorophyll content of 16 μg cm^{-2}; equivalent water thickness of 0.005 cm^{-1}, and dry matter content of 0.002 g cm^{-1}.

Approximation of DASF

The probability of photons escaping the vegetation canopy depends on scattering order. The directional escape probability in Eq. 1 is an average over scattering orders (Supplementary Appendix SB). We approximate $\rho(\Omega_0,\Omega)$ by probabilities calculated for single scattered photons (Supplementary Appendix SC). We use the inclination index of foliage area to parameterize the leaf normal distribution (Ross 1981). This index characterizes the deviation of leaf orientation from the spherical distribution. It allows us to approximate the geometry factor, G, that appears in (Supplementary Appendix SA7 as $G=0.5\alpha$, where the weight α varies between 0 and 2. The leaf normals, Ω_L, are simulated by spherical

distribution corrected for the deviation, i.e., $g(\Omega_L) = \alpha$. The corresponding scattering anisotropy (Supplementary Appendix SA2) becomes:

$$j(\Omega) = \frac{\frac{1}{3\pi}(\sin\vartheta - \gamma\cos\vartheta) + \frac{\tau_L}{3}\cos\vartheta}{0.5\pi}, \qquad (3)$$

where $\vartheta = \pi - \mathrm{acos}\Omega\Omega_0$ is the scattering angle (the angle between incident and scattered radiation) and τ_L represents the leaf transmittance, which was set to 0.5 in our calculations. Under these assumptions DASF in the upward directions rearranges to the form (Supplementary Appendix SC)

$$DASF \approx \frac{\rho_1 i_0}{1 - p^{(1)}} = \frac{1}{1 - p^{(1)}} \frac{j(\Omega)}{\mu_0 \mu} \frac{1 - t^{\psi L}}{\psi}. \qquad (4)$$

Here $p^{(1)}$ is the single scattering approximation of the recollision probability (Supplementary Appendix SC); $t = \exp(-0.5) = 0.61$; $\psi = \mu_0^{-1} + \mu^{-1}(1 - \varkappa_{HS})$; the factor $\varkappa_{HS}$ is defined by Supplementary Appendix SA4, and L is an effective extinction coefficient. Thus, our model depends on two parameters. They are the hot spot parameter *h* that appears in $\varkappa_{HS}$ and the effective extinction coefficient *L*. The former determines the shape of DASF, while the latter controls its magnitude.

MATERIALS AND METHODS

Study Area

Our study is focused on equatorial evergreen broadleaf forests that include Amazonian central rainforests (0°–10°S and 70°–60°W), Congo rainforests in Central Africa (5°S–5°N and 20°–30°E) and Southeast Asian rainforests (19.80°–26.57°N and 92.5°–105°E). Figure 1 shows locations of our study area. The seasonal transition between wet and dry seasons is a distinct feature of tropical rainforests, which leads to intra-annual patterns of leaf flushing and abscission.

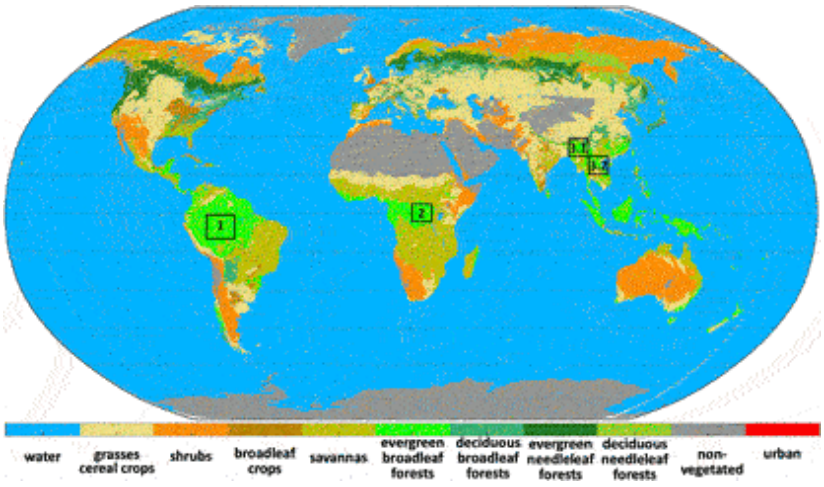

FIGURE 1 | DSCOVR EPIC 10 km land cover map (WWW-VESDR 2021) on Robinson projection with Center meridian at 20°E. Our study area includes Amazonian central rainforest (Region 1: 0°–10°S and 70°–60°W), Congo rainforests (Region 2: 5°S–5°N and 20°–30°E) and Southeast Asian rainforest (Region 3.1: 23.50°–26.57°N and 92.5°–98.62°E; Region 3.2: 19.80°–21.54°N and 97.93°–105°E). Our study areas are depicted as squares, which are part of evergreen broadleaf forests.

About 95% of our Amazonian central rainforest is covered with terra firme rainforests (Nepstad et al., 1994). The average annual rainfall during the 2000–2019 period is about 2,600 mm. The seasonal cycle consists of a short dry season, June to October, and a long wet season thereafter.

The equatorial rainforests of Central Africa are the second largest and least disturbed of the biodiversly-rich and highly productive rainforests on Earth (Cook et al., 2020). Our study area includes central and part of western and northeast Congolian lowland forests. The Congo basin exhibits bimodal precipitation pattern and has two wet and two dry seasons per year (Yang et al., 2015). The wet seasons occur in March-April-May and September-October-November, while dry season months are December-January-February and June-July-August. The average annual rainfall over the past 2 decades is about 1761 mm.

Our third region consists of two sub-regions depicted as Region 3.1 (23.50–26.57°N and 92.5–98.62°E) and 3.2 (19.80–21.54°N and 97.93–105°E). The first one is a subtropical moist broadleaf forest ecoregion in Mizoram–Manipur–Kachin rain forests. It occupies the lower hillsides of the mountainous border region joining India, Bangladesh, and Burma (Myanmar). The average annual rainfall over the past 20 years is about 1,545 mm. The dry season is from October to April, and wet season is May

to September. Region 3.2 represents a subtropical moist broadleaf forest ecoregion in Northern Indochina. The wet seasons occur in May to September while dry season months are October to April.

Data Used

Various variables from several independent satellite sensors over our study area were used in this research. These include land cover maps and leaf area index (LAI) from the MODerate resolution Imaging Spectroradiometer (MODIS), precipitation from Tropical Rainfall Measuring Mission (TRMM), surface bidirectional reflectance factor (BRF) from Multi-angle Imaging SpectroRadiometer (MISR) on the Terra platform and BRF from Earth Polychromatic Imaging Camera (EPIC) on Deep Space Climate Observatory (DSCOVR).

MODIS land cover dataset. Collection 6 Terra and Aqua MODIS land cover product from 2001 to 2019 at yearly temporal frequency and 0.05° spatial resolution (Friedl and Sulla-Menashe 2015) was used to identify our study area. This product provides several classification schemes. The map of LAI classification scheme was adopted in this research. Figure 2 illustrates LAI classification scheme used by DSCOVR EPIC operational algorithm for the generation of Vegetation Earth System Data Record (WWW-VESDR 2021).

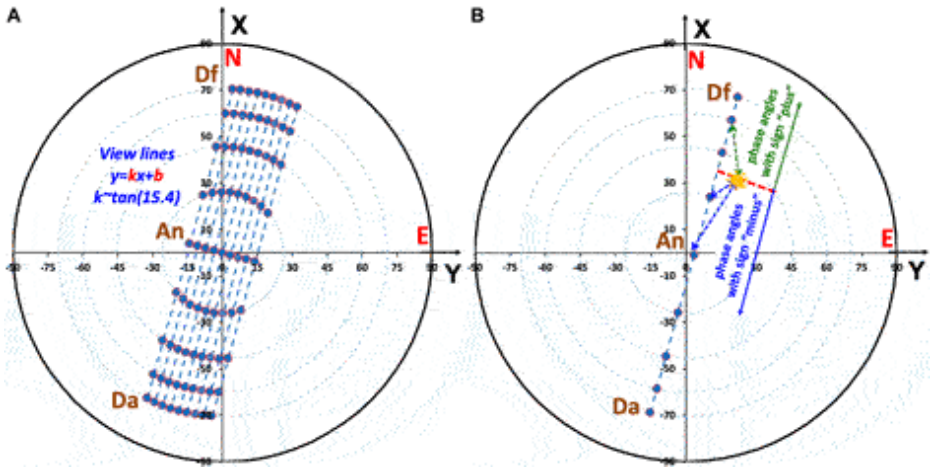

FIGURE 2 | MISR observing geometry. Here the *X* and Y axes point toward the North and East, respectively. **(A)** Directions from ground pixel to MISR cameras form view lines on the polar plane, each characterizing by slope, *k*, and intercept, *b*. **(B)** Sun-sensor geometry is parametrized in terms the solar zenith angle (SZA), intercept *b* and phase angle (PA), the latter is the angle between the directions to the Sun and sensor. We assign the sign "plus" to the phase angle if the MISR view direction approaches the direction to the sun from North (i.e., above the dotted red line perpendicular to the MISR view line), and "minus" otherwise.

MODIS LAI datasets. Collection 6 Terra and Aqua MODIS LAI products (Myneni et al., 2015a; Myneni et al., 2015b) for the period February 2000 to December 2019 were used in this study. The LAI dataset provides 8-days composite LAI at 500-m spatial resolution. The C6 MODIS LAI product was evaluated against ground-based measurements of LAI and through inter-comparisons with other satellite LAI products (Yan et al., 2016; Yan et al., 2016).

TRMM precipitation dataset. Monthly precipitation data from the TRMM (3B43 version 7) at 0.25° spatial resolution for the period January 2000 to December 2019 (WWW-TRMM 2011) was used in this study. This dataset provides the best-estimate precipitation rate and root-mean-square precipitation-error estimates by combining four independent precipitation fields (Huffman et al., 2007).

DSCOVR EPIC MAIAC dataset. Level 2 DSCOVR EPIC Multi-Angle Implementation of Atmospheric Correction (MAIAC, version 1) surface BRF and aerosol optical depth (AOD) at 551 nm from 2016 to 2019 were also used. The EPIC instrument has provided imageries in near backscattering directions with the phase angle between 4° and 12° at ten ultra-violet to near infrared (NIR) narrow spectral bands until June 27, 2019,

when the spacecraft was placed in an extended safe hold due to degradation of the inertial navigation unit (gyros). DSCOVR returned to full operations on March 2, 2020 after the navigation problem had been resolved. After March 2020 the range of phase has substantially increased towards backscattering reaching 2° (Lyapustin et al., 2021; Marshak et al., 2021).

The MAIAC BRF are available at four spectral bands; they are 433 (band width 3.0) nm, 551 (3.0) nm, 680 (2.0) nm and 780 (2.0) nm. Data are projected on a 10-km SIN grid and available at 65–110 min temporal frequency (WWW-MAIAC 2018). EPIC sees Amazonian rainforests between 11 UTC and 18 UTC, Congo forests between 5 UTC and 14 UTC and Southeast Asian rainforests between 1 and 7 UTC.

MISR datasets. The MISR sensor views each 1.1 km ground pixel symmetrically about the nadir in the forward and aftward directions along the spacecraft's flight track. Image data are acquired with nominal view zenith angles relative to the surface reference ellipsoid of 0.0^0 (camera An), 26.1^0 (Af and Aa), 46.5^0 (Bf and Ba), 60.0^0 (Cf and Ca) and 70.5^0 (Df and Da) in four spectral bands centered at 446 (band width 41.9 nm), 558 (28.6) nm, 672 (21.9) nm, and 866 (39.7) nm. MISR obtains global coverage between ±82° latitudes in 9 days (Diner et al., 1998; Diner et al., 1999). Level 2 version 3 MISR land surface (WWW-MISR_SURFACE 1999) and aerosol (WWW-MISR_AEROSOL 1999) products for the period of January 2016 to December 2019 over our study area were used. The surface reflectance parameter BRF in 9 view angles and four MISR spectral bands is at 1.1 km spatial resolution. The aerosol optical depth is available at 4.4 km spatial resolution. Both parameters are projected on Space Oblique Mercator (SOM) projection, in which the reference meridian nominally follows the spacecraft ground track.

Directions from ground pixel to MISR cameras form view lines on the polar plane, which are characterized by slope, $k = \tan \upsilon_K$, and intercept, b (Figure 2A). The slope is aligned with ground track and is roughly constant with $\upsilon_K \approx 15.5°$. The intercept is associated with location of pixel within the MISR 360 km swath. We parameterize MISR BRF in terms of the solar zenith angle, phase angle and intercept. The phase angle, γ, is calculated as

$$\gamma = \mathrm{acos}\Omega\Omega_0 = \mathrm{acos}\left(\cos\theta\cos\theta_0 + \sin\theta\sin\theta_0\cos\left(\varphi - \varphi_0\right)\right), \quad (5)$$

where $\Omega_0 \sim (\theta_0, \varphi_0)$ and $\Omega \sim (\theta, \varphi)$ are directions from ground pixel to the Sun and sensor, respectively. We assign the sign "plus" to the phase angle if the MISR view direction approaches to the direction to the Sun from North, i.e., $\sin\theta\cos(\upsilon_K - \varphi) > \sin\theta_0\cos(\upsilon_K - \varphi_0)$, and "minus" otherwise (Figure 2B).

Data Processing

The MODIS LAI and TRMM precipitation data over forested pixels were selected using flags indicating highest retrieval quality. The 8-days 500 m LAI products over our study area (Figure 1) were spatially aggregated to 0.01° and 0.1° resolutions which were then used in our analyses.

The MISR and DSCOVR EPIC surface BRF over our study area were first refined by removing pixels with aerosol optical depth over 0.3. MISR and EPIC datasets were further re-projected to 0.01° and 0.1° Climate Modeling Grids (CMG), respectively. For each pixel, MISR and EPIC DASFs were calculated using Eq. 2, which then were used to generate monthly DASFs. If there were several observations of a pixel within a given month, a median DASF value was assigned to such pixel.

Area-averaged DASF as a function of mean SZA and phase angle, γ, is defined as

$$DASF(SZA, \gamma) = \frac{\sum_{xy\in A} DASF_{xy}\left(SZA_{xy}, VZA_{xy}\right)\cos SZA_{xy}}{\sum_{xy\in A}\cos SZA_{xy}}, \tag{6}$$

where the summation is over pixels (x, y) in the selected area A at which the phase angle takes a given value γ.

Hot Spot Parameter and Effective Extinction Coefficient

Equation 4 is used to simulate DASF. It depends on the hot spot parameter, h, and effective extinction coefficient, L. The former is a function of SZA and determines the angular shape of DASF, while the latter controls its magnitude and depends on LAI. The following two-step fitting technique was implemented to derive equations for h and L using monthly MISR DASF.

Step 1: *Matching angular shapes of observed and modeled DASF.* For a given month, we used SZA_{xy} and monthly average MODIS LAI as a first approximation to the effective extinction coefficient (i.e., $L_{xy} \approx LAI_{xy}$) to simulate $DASF_{xy}$ at each pixel (x, y) in MISR view angles as a function of h.

Next, we used Eq. 6 to calculate area-averaged simulated-DASF as a function of hot spot parameter, *h*. Finally, we selected *h* that minimized $(R^2 - 1)^2 + (s - 1)^2$, where R^2 and *s* are the coefficient of determination and slope of the relationship between area averaged values of observed and simulated DASFs. The selected hot spot parameter provides the best agreement between angular shapes of modeled and observed DASF.

Step 2: *Matching magnitudes of observed and modeled DASF.* For a given month, we used SZA and *h* (*SZA*) to simulate $DASF_{xy}$ at MISR view angles as a function of *L*. Eq. 6 was used to calculate area averaged simulated-DASF as a function of effective extinction coefficient, *L*, i.e., $\overline{DASF}_{mod}(\gamma, L)$. We selected *L* that minimizes Normalized Root Mean Square Error (NRMSE) between simulated, $\overline{DASF}_{mod}$, and observed, $\overline{DASF}_{MISR}$, area-averaged DASFs, i.e.,

$$NRMSE(L) = \frac{\sqrt{\frac{1}{N}\sum_{\gamma}\left[\overline{DASF}_{mod}(\gamma, L) - \overline{DASF}_{MISR}(\gamma)\right]^2}}{\frac{1}{N}\sum_{\gamma}\overline{DASF}_{MISR}(\gamma, L)} \rightarrow min. \quad (7)$$

This value of *L* matches magnitudes of observed and modelled DASFs.

Monthly MISR DASF data for the 2017 to 2019 period over our study area (Figure 1) were used to execute our two-step fitting procedure. The SZA exhibits small variation within our regions during a month and therefore can be accurately represented by its monthly mean. A time series of the solutions to the Step-1 procedure therefore gives a set of the hot spot parameters corresponding to different SZA. Seasonal variations of LAI in equatorial forests allowed us to accumulate solutions to the Step-2 procedure corresponding to different values of MODIS LAI. We used those sets to derive dependences of the hot spot parameter and effective extinction coefficient on SZA and LAI, respectively.

Figure 3 shows an example of our two-step fitting technique for Congo forests (region 2) in September-2018. As illustrated in Figure 4, Eq. 4 approximates observed DASF to within NRMSE = 8% and R^2 = 0.85. The largest difference between observed and simulated DASFs occurred at phase angles above 90^0. Such points are separated by an ellipse in Figure 4. For PA > 90^0, MISR BRFs were mainly acquired by off-nadir F and D cameras, which have higher uncertainties compared to near nadir observations.

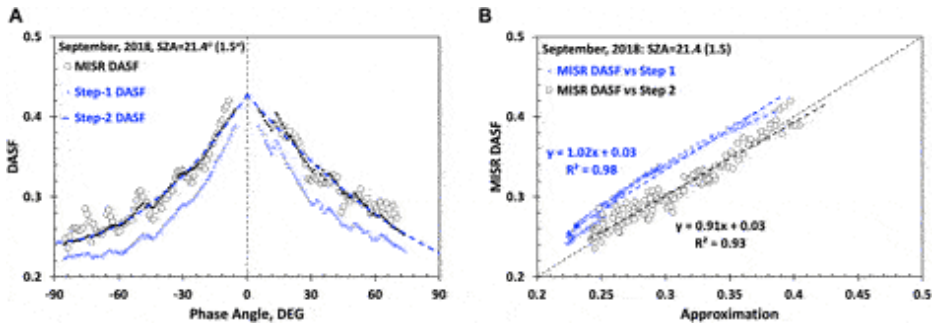

FIGURE 3 | (A) MISR DASF of region 2 (Congo forests) in September-2018 (hollow circles). Its step-1 and step-2 approximations are shown as crosses and dots, respectively. The dashed line is a polynomial fit to the Step-2 approximation. **(B)** MISR DASF versus step-1 (crosses) and step-2 (circles) approximations. NRMSEs between MISR DASF and its Step 1 and Step 2 approximations are 12 and 4%, respectively. Mean SZA (std) = 21.2^0 (1.5^0), h = 0.8, LAI = 5.6, L = 7.15.

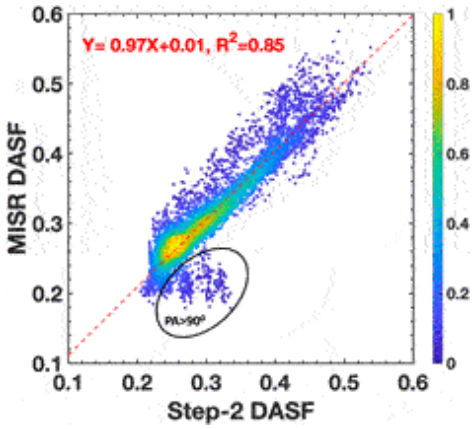

FIGURE 4 | MISR DASF *vs*. its Step-2 approximation accumulated over our study area during the 2017 to 2019 period. NRMSE = 8%; R^2 = 0.85. The ellipse separates values of DASF at Phase Angles (PA) above 90^0.

The sets of solutions to the Steps 1 and 2 procedures allowed us to regress the hot spot parameter, h, and effective extinction coefficient, L, *versus* SZA and MODIS LAI, respectively, as (Figure 5)

$$h(SZA) = 5.96 - 5.90\cos SZA \approx 11.92\sin^2\frac{SZA}{2}, \qquad (8)$$

$$L = 2.93 \cdot LAI_{MODIS} - 8.53 \qquad (9)$$

There was no correlation between L and SZA, as expected.

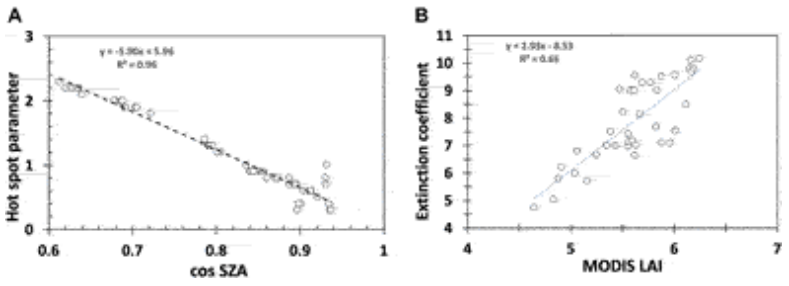

FIGURE 5 | (A). Hot spot parameter *h* vs. cos (SZA). **(B)** The effective extinction coefficient vs MODIS LAI derived from monthly MISR DASF for the period between 2017 and 2019.

Thus, our model for DASF of equatorial forests is generated by Eq. 4 with the hot spot parameter h and effective extinction coefficient L given by Eqs 8, 9. It has two input parameters; they are Sun position in the sky, $\Omega_0 \sim (\theta_0, \varphi_0)$, and MODIS LAI.

RESULTS

Assessment of DASF

Observed versus modeled DASF. We used monthly MISR DASF for the period between 2017 and 2019 to derive equations for the hot spot parameter and effective extinction coefficient. The proximity between observed and modeled DASFs were characterized by NRMSE = 8%, $R^2 = 0.85$ (Figure 4). We analyzed modelled and observed monthly DASF for Year 2016 to see if the performance metrics is similar to that of the training data set. Figure 6 illustrates monthly MISR DASF and its simulated counterpart for Amazonian forests in April 2016. The largest differences between them are at high phase angles. Figure 7 shows MISR DASF plotted versus modeled DASF accumulated over our study area during Year 2016. The comparison suggests a good performance of Eq. 4 to simulate MISR DASF over equatorial forests.

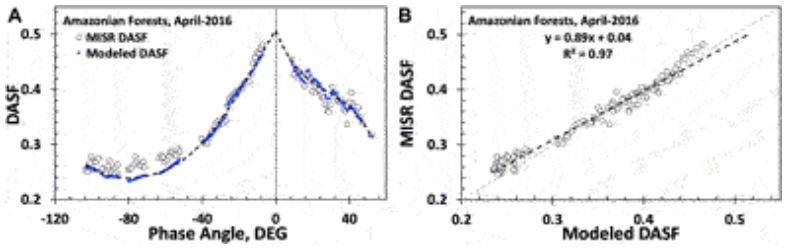

FIGURE 6 | (A) MISR DASF of Amazonian forests in April-2016 (hollow circles) and its approximation by Eq. 4 (dots). The dashed line is a polynomial fit to the modeled DASF. **(B)** MISR DASF vs. modeled DASF. NRMSE = 4%.

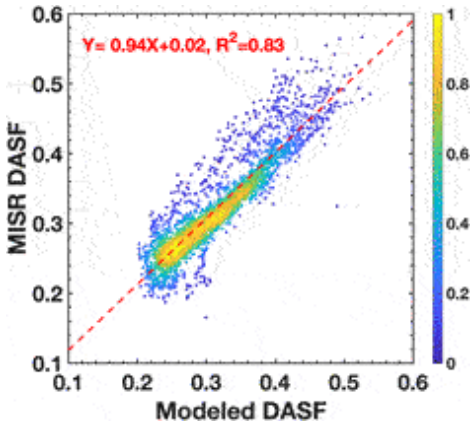

FIGURE 7 | MISR DASF *vs.* its approximation by Eq. 4 accumulated over our study area during Year 2016. NRMSE = 9.2%; R^2 = 0.83.

Diurnal variations of observed and modeled DASFs. The next step in the assessment of our approach is to see if the model can reproduce diurnal variation of monthly EPIC DASF. Figure 8 shows examples of diurnal variations in observed and modeled DASFs for 3 regions in our study area. As one can see the largest deviation between model and observation occurs when SZA exceeds 60^0. The uncertainty of the MAIAC BRF product is low for the EPIC observations near the local noon. It however may significantly increase at high zenith angles resulting in an underestimation of surface BRF (Lyapustin et al., 2021). And this is what we see in Figure 8.

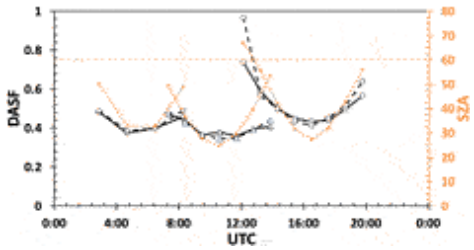

FIGURE 8 | Diurnal courses of monthly EPIC DASF (solid line), modeled DASF (dashed line) and SZA (dotted line) for region 3.2 in Southeast Asian (diamonds), Congo (triangles) and Amazonian (circles) forests on 2017-02-24, 2018-06-14 and 2018-07-24, respectively. A SZA level of 60^0 is shown as a horizontal dashed line. NRMSE values for Southeast Asian, Congo and Amazonian forests are 3.9, 3.6 and 16.3%, respectively. RMSE for Amazonian forests is 3.1% if SZA < 60^0.

Scatter plot of diurnal courses of modeled and EPIC DASFs accumulated over Amazonian, Congo forests and region 3.2 in southeast Asia during the 2017 to 2019 period is shown in Figure 9. Note that data from December to November over Congo forests are not present in this plot. For these regions, our model approximates diurnal courses of the observed DASFs to within NRMSE = 7% with $R^2 = 0.82$.

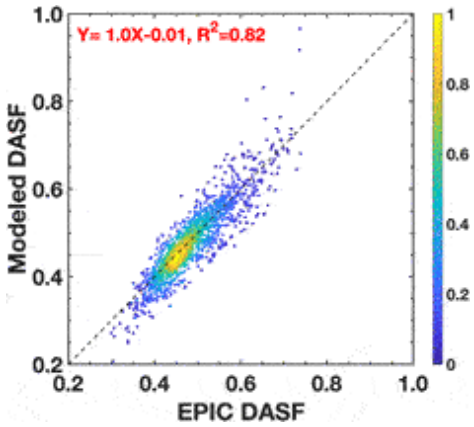

FIGURE 9 | Correlation between diurnal courses of modeled and EPIC DASFs accumulated over Amazonian, Congo forests and region 3.2 in southeast Asia during the 2017 to 2019 period. Data from December to February over Congo forests are excluded. NRMSE = 7%. The relationship between these data is characterized by a regression line with a slope of 1 and negligible intercept; $R^2 = 0.82$.

On average, modeled DASF over Congo during December through February overestimates observed DASF by about 20%. About 70% of data on the scatter plane are located within a 15% circle centered at mean values

of EPIC and modeled DASFs and therefore differ from respective mean values by less than 15%.

For the region 3.1 in Southeast Asian rainforest, modeled DASF overestimates observations by about 5%. The data are also concentrated on the scatter plane: about 75% of data on the model-vs.-observation scatter plane are concentrated within a 15% circle centered at mean values of observed and modeled DASFs. The R^2 is consequently low ($Y = 0.8X+0.08$, $R^2 = 0.32$).

In summary, Eq. 4 can accurately reproduce DASF in terms of proximity to both angular variations observed by MISR and diurnal courses measured by DSCOVR EPIC sensor. It therefore provides a strong basis for synergy of DSCOVR EPIC and Terra MISR sensors to monitor changes in equatorial forests. Our next step is to see if the model can detect changes.

Monitoring Equatorial Forests

The forest structural organization determines the magnitude and angular variation of DASF (Schull et al., 2011; Knyazikhin et al., 2013). Its angular signatures therefore provide unique and rich sources of diagnostic information about forests. Here we analyze DASF over our study area to see if it can detect seasonal changes of the equatorial forests.

The seasonal transition between wet and dry seasons is a distinct feature of equatorial rainforests, which leads to intra-annual patterns of leaf flushing and abscission (Samanta et al., 2012; Bi et al., 2015). Since our study is focused on structurally intact and undisturbed regions of the equatorial forests (i.e., no changes in forest geometry), variation in leaf area is a key factor causing variation in DASF.

We start with analyses of variation in the DASF acquired over Amazonian central rainforest. *In situ* studies and satellite data indicated higher leaf area during the dry season relative to the wet season (Huete et al., 2006; Hutyra et al., 2007; Myneni et al., 2007; Hilker et al., 2014; Jones et al., 2014). The growth-limiting impact of water deficit on rainforest during the dry season is alleviated through deep roots and hydraulic redistribution (Oliveira et al., 2005; Pierret et al., 2016), resulting in a sunlight mediated seasonality in leaf area (Bi et al., 2015). Figure 10 illustrates these findings, that is, green leaf area increases during the dry season (June to October), has high values during the early part of the wet season (November to October) and decreases thereafter (March to May).

FIGURE 10 | Annual courses of monthly-average precipitation and LAI over the Amazonian central rainforest. Monthly data were accumulated over the time period February 2000 to December 2019.

Let us compare observed DASFs from the late dry season (October) and middle part of the wet season (March). Eq. 4 predicts that an increase in the effective extinction coefficient, with SZA unchanged, increases the magnitude of DASF at all phase angles, i.e., results in an upward shift in the angular signature of the DASF, as illustrated in Figure 3. The SZAs in the select region of Amazonian forests in March (SZA = 25.5, std = 1.2) and October (SZA = 20.5, std = 1.1) are very close. At low SZA such a small difference minimally impacts the shape of angular signatures. As one can see in Figure 11, both MISR and EPIC show a distinct decrease in DASF in all phase angles between October and March with no discernible change in the overall shape of the angular signatures. Such a simple change in magnitude can only result from a change in LAI since other structural variables, such as tree crown shape and size do not vary seasonally in this forest.

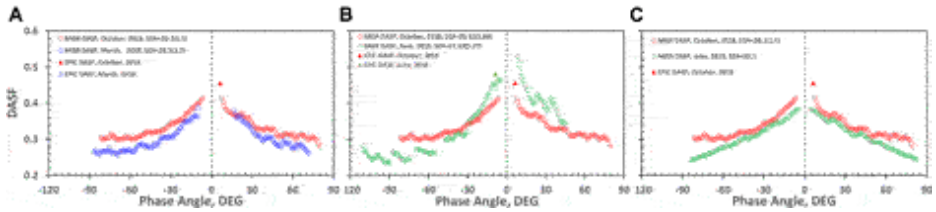

FIGURE 11 | Changes in MISR (circles) and EPIC (triangle) DASFs of Amazonian central rainforests from October to March **(A)**, from June to October **(B)** and transformation of EPIC DASF in June to sun-sensor geometry in March **(C)**. Numbers in parentheses in legends show std of solar zenith angle. Relative difference between MISR and EPIC DASFs is below 8%. Values of NRMSE between MISR DASF and its modeled counterpart do not exceed 9%.

Let us now consider DASF in the early (June) and late (October) dry seasons. LAI has changed from about 5.5 to 6.4. MISR and EPIC measurements are made at significantly higher SZA in June (SZA = 37.6, std = 2.3) compared to October (SZA = 20.6, std = 1.1). The magnitude and shape of angular signatures are impacted when both canopy properties and SZA vary as middle panel in Figure 11 illustrates. This makes the comparison of the signatures difficult. We can transform the June's signature to the sun-sensor geometry in October using Eq. 4. As right panel of Figure 11 demonstrates the transformed DASF is a downward shift of the October's DASF, indicating a lower LAI in June. DASFs of the remining regions in our study area exhibit similar behavior (not shown here).

Our next example demonstrates time series of DSCOVR EPIC DASF acquired over the Congolese forests. The Congo basin exhibits bimodal precipitation pattern and has two wet and two dry seasons per year (Yang et al., 2015). The wet seasons occur in March -April-May and September-October-November, while dry season months are December to February and June to August. Unlike Amazonian forests, monthly average LAI follow the patterns of precipitation (Figure 12). It exhibits notable bimodal seasonal variations.

FIGURE 12 | Annual courses of monthly-average precipitation and LAI over the Congolese forests. Monthly data were accumulated over the period February 2000 to December 2019.

The above analyses have demonstrated that an increase in LAI, with SZA unchanged, results in an upward shift in the angular signature of the DASF (Figure 3). The EPIC DASF at fixed solar zenith and phase angles therefore should covary with LAI. The Earth-observing geometry of the EPIC sensor is characterized by phase angle between 2^0 and 12^0. A question then arises whether or not such small variation in phase angle can be ignored. Therefore, we examine two algorithms to generate EPIC time series. The first one

selects EPIC observations at SZA = 25^0, 30^0 and 45^0 irrespective of values of the phase angle. If there are no reflectance data under these illumination conditions during a month, we transform DASF to a desired SZA. In the second case, we select observation at fixed sun-sensor geometries. Figure 13 shows LAI and DASF at fixed SZA = 30^0 and varying phase angle. At low SZA, the EPIC time series correlates well with the bimodal seasonal variation of LAI, as expected. This also suggests that Eq. 4 is an effective tool to fill missing data at a given fixed SZA.

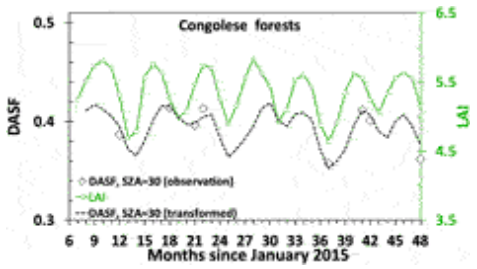

FIGURE 13 | Time series of LAI (circles), observed (diamonds) and transformed (dashed line) EPIC DASF at SZA = 30^0 for the period from 2015 to 2018.

An increase in SZA however can eliminate the bimodal feature of DASF. This is illustrated in Figure 14 showing annual courses of EPIC DASF generated by the two algorithms introduced above. As one can see in left panel of this figure, the EPIC time series at SZA = 45^0 becomes flat between May and October. Two factors are responsible for this effect. First, the decrease of phase angle to its local minimum in July enhances DASF and therefore tends to suppress decrease in DASF due to the dry season decrease in LAI. At low SZA LAI has a stronger impact on DASF than phase angle. The impact of phase angle however increases with SZA and can become a dominant factor causing variation in DASF. In our example, this occurs at a SZA of 45^0 and higher. As right panel of Figure 14 illustrates, DASF at fixed SZA and phase angle retains its bimodal property. Thus, both SZA and phase angle should be taken into account when analyzing DSCOVR EPIC data. Eq. 4 therefore becomes of particular importance for analyses of EPIC observations over vegetated land. A strong effect of phase angle on EPIC reflectance was recently documented in (Marshak et al., 2021). Our analyses reinforce this effect.

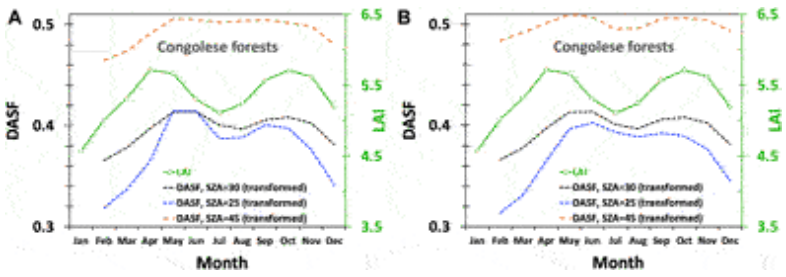

FIGURE 14 | Annual courses of LAI and transformed EPIC DASF at SZA = 25^0, 30^0 and 45^0 with **(A)** varying and **(B)** fixed phase angles. Monthly data were accumulated over the period 2015 to December 2018.

SUMMARY AND CONCLUSIONS

We used Directional Area Scattering Function (DASF) to characterize angular signatures of equatorial forests. It describes the canopy BRF if the foliage does not absorb radiation and is a purely structural variable. For vegetation canopies with a dark background, or sufficiently dense vegetation where the impact of canopy background is negligible, the DASF can be accurately approximated from the BRF in the weakly absorbing spectral intervals without involving canopy reflectance models, prior knowledge, or ancillary information regarding leaf scattering properties (Knyazikhin et al., 2013). Equation 2 is used to obtain approximations of DASF from the Terra MISR and DSCOVR EPIC data. The DASF becomes independent on spectral band composition of a sensor acquiring surface reflectance data, which is an important prerequisite for achieving consistency and complementarity between DSCOVR EPIC and Terra MISR observations.

We adapted a model for the canopy hot spot implemented in the operational algorithm for generation of Earth System Data Record (VESDR) from DSCOVR EPIC observations (Yang et al., 2017; WWW-VESDR 2021). In this approach, the sunlit leaves are treated as a stochastic reflecting boundary, which depends on distribution of leaves in the canopy space and the Sun position in the sky. Photons reflected by the boundary can either enter the vegetation canopy or exit it. The shaded leaves represent the interior points. Their interactions with photons are described by a stochastic radiative transfer equation. The directional escape probability that appears in Eq. 1 is a weighted sum of photons reflected by the boundary and canopy interior points. Kuusk's model of the hot spot incorporated into the extinction coefficient (Supplementary Appendix SA) is used to evaluate the escape

probability as a function of scattering order, which is then used to calculate the average escape probability (Supplementary Appendix SB). Contributions of multiple scattered photons are accounted by the recollision probability.

Here we simplified this model. First, a one-dimensional radiative transfer equation is used to simulate canopy radiative regime (Supplementary Appendix SA6). Second, the average escape probability is approximated by a probability calculated for first order scattered photons (Supplementary Appendix SC). Under these assumptions, DASF is approximated by a simple equation that depends on two parameters. They are the hot spot parameter that appears in the canopy hot spot coefficient and the effective extinction coefficient. The former determines the shape of DASF, while the latter controls its magnitude. These two parameters should be specified to generate angular signatures of equatorial forests.

In spite of substantial theoretical advancement in modeling the radiative transfer in vegetation canopies, quantitative data on the hot spot are still few and far between. Here we specified the hot spot parameter by fitting shapes of observed and modeled DASF using MODIS LAI as an initial approximation to the effective extinction coefficient. The hot spot parameter was found to be almost proportional to $1 - \cos SZA$ (R^2 = 0.96) with a coefficient of proportionality around 6 (left panel in Figure 5). The trigonometric term can be interpreted as a correction of the canopy hot spot coefficient (Supplementary Appendix SA4) for errors due to its approximation by a constant value (Supplementary Appendix SA) whereas the coefficient of proportionality as a mean linear dimension of foliage elements (Knyazikhin and Marshak 1991; Nilson 1991) specific to equatorial forests. This equation for the hotspot parameter was used in all our calculations.

The effective extinction coefficient determines the magnitude of the DASF. Theoretically this variable can be obtained by replacing the 3D extinction coefficient with an effective value that provides a best agreement between horizontally averaged canopy reflectances and solutions of 1D radiative transfer equations. Basically, it depends on LAI, leaf normal distributions and clumping indices. In our approach, the effective extinction coefficient was obtained by matching magnitudes of MISR and shape-adjusted modeled DASFs. This coefficient was found to be linearly related to the MODIS LAI (R^2 = 0.65, right panel in Figure 5). We used this relationship in all our calculations.

Note the MODIS LAI was used as a first approximation to the effective extinction coefficient, which then was iterated to its optimal value. Alternatively, one can use relationships between LAI and various vegetation induces (e.g., NDVI) to make rough estimates of LAI first and then iterate them to the extinction coefficient. This procedure may result in relationships between the extinction coefficient and vegetation indices, which can make the model dependent on the hot spot parameter and vegetation indices.

Our model for angular signatures of equatorial forests can accurately reproduce both MISR angular signatures acquired at 10:30 local solar time and diurnal course of EPIC reflectance (NRMSE<9%, R^2 > 0.8) and therefore assures consistency and complementarity between DSCOVR EPIC and Terra MISR observations. This provides a powerful tool to argue for changes in vegetation structure as it was demonstrated in our analyses of seasonal variations of angular signatures acquired over equatorial forests.

DATA AVAILABILITY STATEMENT

Publicly available datasets were analyzed in this study. This data can be found here: DSCOVR EPIC and Terra MISR data were obtained from the NASA Langley Research Center Atmospheric Science Data Center (ASDC) (https://epic.gsfc.nasa.gov). The MODIS products were acquired from the Land Processes (LP) Distributed Active Archive Center (DAAC) (https://lpdaac.usgs.gov). TRMM 3B43 data are publicly available from the NASA Goddard Earth Sciences (GES) Data and Information Services Center (DISC) (https://disc.gsfc.nasa.gov).

AUTHOR CONTRIBUTIONS

YK and RM conceived the project. YK and XN conducted analyses of DSCOVR EPIC and Terra MISR and MODIS data. YK led the writing of manuscript.

FUNDING

This study was supported by the NASA DSCOVR project under grants 80NSSC19K0762 (YK) and 80NSSC19K0760 (RM). XN was supported by the Chinese Scholarship Council (201906280404).

PUBLISHER'S NOTE

All claims expressed in this article are solely those of the authors and do not necessarily represent those of their affiliated organizations, or those of the publisher, the editors and the reviewers. Any product that may be evaluated in this article, or claim that may be made by its manufacturer, is not guaranteed or endorsed by the publisher.

ACKNOWLEDGMENTS

DSCOVR EPIC and Terra MISR data were obtained from the NASA Langley Research Center Atmospheric Science Data Center (ASDC) (https://epic.gsfc.nasa.gov). The MODIS products were acquired from the Land Processes (LP) Distributed Active Archive Center (DAAC) (https://lpdaac.usgs.gov). TRMM 3B43 data are publicly available from the NASA Goddard Earth Sciences (GES) Data and Information Services Center (DISC) (https://disc.gsfc.nasa.gov.

SUPPLEMENTARY MATERIAL

The Supplementary Material for this article can be found online at: https://www.frontiersin.org/articles/10.3389/frsen.2021.766805/full#supplementary-material

FOOTNOTES

[1]The phase angle is the angle between the directions to the Sun and sensor

REFERENCES

Adams, J., Lewis, P., and Disney, M. (2018). Decoupling Canopy Structure and Leaf Biochemistry: Testing the Utility of Directional Area Scattering Factor (DASF). *Remote Sensing* 10 (12), 1911. doi:10.3390/rs10121911

Bi, J., Knyazikhin, Y., Choi, S., Park, T., Barichivich, J., Ciais, P., et al. (2015). Sunlight mediated seasonality in canopy structure and photosynthetic activity of Amazonian rainforests. *Environ. Res. Lett.* 10 (6), 064014. doi:10.1088/1748-9326/10/6/064014

Brando, P. M., Goetz, S. J., BacciniBeck, A., Nepstad, D. C., Beck, P. S. A., and Christman, M. C. (2010). Seasonal and interannual variability of climate and vegetation indices across the Amazon. *Proc. Natl. Acad. Sci.* 107 (33), 14685–14690. doi:10.1073/pnas.0908741107

Cook, K. H., Liu, Y., and Vizy, E. K. (2020). Congo Basin drying associated with poleward shifts of the African thermal lows. *Clim. Dyn.* 54 (1), 863–883. doi:10.1007/s00382-019-05033-3

Diner, D. J., Asner, G. P., Davies, R., Knyazikhin, Y., Muller, J. P., Nolin, A. W., et al. (1999). New directions in earth observing: Scientific applications of multiangle remote sensing. *Bull. Am. Meteorol. Soc.* 80 (11), 2209–2228. doi:10.1175/1520-0477(1999)080<2209:NDIEOS>2.0.CO;2

Diner, D. J., Beckert, J. C., Reilly, T. H., Bruegge, C. J., Conel, J. E., Kahn, R. A., et al. (1998). Multi-angle Imaging SpectroRadiometer (MISR) instrument description and experiment overview. *IEEE Trans. Geosci. Remote Sensing* 36 (4), 1072–1087. doi:10.1109/36.700992

Féret, J.-B., François, C., Asner, G. P., Gitelson, A. A., Martin, R. E., Bidel, L. P. R., et al. 2008. "PROSPECT-4 and 5: Advances in the leaf optical properties model separating photosynthetic pigments." *Remote Sensing Environ.* 112 (6):3030–3043. doi:10.1016/J.Rse.2008.02.012

Friedl, M., and Sulla-Menashe, D. (2015). "MCD12C1 MODIS/Terra+Aqua Land Cover Type Yearly L3 Global 0.05Deg CMG V006 [Data set]," in *NASA EOSDIS Land Processes DAAC* . Sioux Falls, South Dakota: USGS Earth Resources Observation and Science (EROS) Center. doi:10.5067/MODIS/MCD12C1.006

Gerstl, S. A. W., and Simmer, C. (1986). Radiation physics and modelling for off-nadir satellite-sensing of non-Lambertian surfaces. *Remote Sensing Environ.* 20 (1), 1–29. doi:10.1016/0034-4257(86)90011-8

Goel, N. S., Qin, W., and Wang, B.. 1997 "On the estimation of leaf size and crown geometry for tree canopies from hotspot observations." *J. Geophys. Res.* 102 (D24):29543–29554. doi:10.1029/97jd01110

Gorkavyi, N., Carn, S., DeLand, M., Knyazikhin, Y., Krotkov, N., Marshak, A., et al. (2021). Earth Imaging From the Surface of the Moon with a DSCOVR/EPIC-Type Camera. *Front. Remote Sens.* 2, 24. doi:10.3389/frsen.2021.724074

Hilker, T., Lyapustin, A. I., Tucker, C. J., Hall, F. G, Ranga, B., Myneni, R. B., et al. (2014). Vegetation dynamics and rainfall sensitivity of the Amazon. *Proc. Natl. Acad. Sci. USA* 111 (45), 16041–16046. doi:10.1073/pnas.1404870111

Huang, D., Knyazikhin, Y., Dickinson, R. E., Rautiainen, M., Stenberg, P., Disney, M., et al. (2007). Canopy spectral invariants for remote sensing and model applications. *Remote Sensing Environ.* 106 (1), 106–122. doi:10.1016/j.rse.2006.08.001

Huang, D., Knyazikhin, Y., Wang, W., Deering, D., Stenberg, P., Shabanov, N., et al. (2008). Stochastic transport theory for investigating the three-dimensional canopy structure from space measurements. *Remote Sensing Environ.* 112 (1), 35–50. doi:10.1016/j.rse.2006.05.026

Huete, A. R., Didan, K., Shimabukuro, Y. E., Ratana, P., Saleska, S. R., Hutyra, L. R., et al. (2006). Amazon rainforests green-up with sunlight in dry season. *Geophys. Res. Lett.* 33, 6. doi:10.1029/2005GL025583

Huffman, G. J., Bolvin, D. T., Nelkin, E. J., Wolff, D. B., Adler, R. F., Gu, G., et al. (2007). The TRMM Multisatellite Precipitation Analysis (TMPA): Quasi-Global, Multiyear, Combined-Sensor Precipitation Estimates at Fine Scales. *J. Hydrometeorology* 8 (1), 38–55. doi:10.1175/JHM560.1

Hutyra, L. R., Munger, J. W., Saleska, S. R., Gottlieb, E., Daube, B. C., Dunn, A. L, et al. (2007). Seasonal controls on the exchange of carbon and water in an Amazonian rain forest. *J. Geophys. Res.* 112 (G3), a–n. doi:10.1029/2006JG000365

Jones, M. O., Kimball, J. S., and Nemani, R. R. (2014). Asynchronous Amazon forest canopy phenology indicates adaptation to both water and light availability. *Environ. Res. Lett.* 9 (12), 124021. doi:10.1088/1748-9326/9/12/124021

Knyazikhin, Y., and Marshak, A. (1991). "Fundamental Equations of Radiative Transfer in Leaf Canopies, and Iterative Methods for Their Solution," in *Photon-vegetation Interactions: applications in plant physiology and optical remote sensing* ed . Editors R. B. Myneni, and J. Ross (Berlin Heidelberg: Springer-Verlag), 9–43. doi:10.1007/978-3-642-75389-3_2

Knyazikhin, Y., Schull, M. A., Stenberg, P., Mottus, M., Rautiainen, M., Yang, Y., et al. (2013). Hyperspectral remote sensing of foliar nitrogen content. *Proc. Natl. Acad. Sci.* 110 (3), E185–E192. doi:10.1073/pnas.1210196109

Knyazikhin, Y., Schull, M. A., Xu, L., Myneni, R. B., and Samanta, A. (2011). Canopy spectral invariants. Part 1: A new concept in remote sensing of vegetation. *J. Quantitative Spectrosc. Radiative Transfer* 112 (4), 727–735. doi:10.1016/j.jqsrt.2010.06.014

Kuusk, A. (1991). "The Hot Spot Effect in Plant Canopy Reflectance," in *Photon-vegetation Interactions: applications in plant physiology and optical remote sensing* ed . Editors R. B. Myneni,

and J. Ross (Berlin Heidelberg: Springer Berlin Heidelberg), 139–159. doi:10.1007/978-3-642-75389-3_5

Latorre-Carmona, P., Knyazikhin, Y., Alonso, L., Moreno, J. F., Pla, F., and Yang Yan, Y. (2014). On Hyperspectral Remote Sensing of Leaf Biophysical Constituents: Decoupling Vegetation Structure and Leaf Optics Using CHRIS-PROBA Data Over Crops in Barrax. *IEEE Geosci. Remote Sensing Lett.* 11 (99), 1579–1583. doi:10.1109/LGRS.2014.2305168

Lewis, P., and Disney, M.. 2007 "Spectral invariants and scattering across multiple scales from within-leaf to canopy." *Remote Sensing Environ.* 109 (2):196–206. doi:10.1016/J.Rse.2006.12.015

Lewis, S. L., Lopez-Gonzalez, G., Sonké, B., Affum-Baffoe, K., Baker, T. R., Ojo, L. O., et al. (2009). Increasing carbon storage in intact African tropical forests. *Nature* 457 (7232), 1003–1006. doi:10.1038/nature07771

Lyapustin, A., Wang, Y., Go, S., Choi, M., Korkin, S., Huang, D., et al. (2021). Atmospheric Correction of DSCOVR EPIC: Version 2 MAIAC Algorithm. *Front. Remote Sens.* 2, 31. doi:10.3389/frsen.2021.748362

Lyapustin, A., Wang, Y., Korkin, S., and Huang, D. (2018). MODIS Collection 6 MAIAC algorithm. *Atmos. Meas. Tech.* 11 (10), 5741–5765. doi:10.5194/amt-11-5741-2018

Marshak, A., Delgado-Bonal, A., and Knyazikhin, Y. (2021). Effect of Scattering Angle on Earth Reflectance. *Front. Remote Sens.* 2, 22. doi:10.3389/frsen.2021.719610

Marshak, A., Herman, J., Adam, S., Karin, B., Carn, S., Cede, A., et al. (2018). Earth Observations from DSCOVR EPIC Instrument. *Bull. Am. Meteorol. Soc.* 99 (9), 1829–1850. doi:10.1175/bams-d-17-0223.1

Marshak, A., and Knyazikhin, Y. (2017). The spectral invariant approximation within canopy radiative transfer to support the use of the EPIC/DSCOVR oxygen B-band for monitoring vegetation. *J. Quantitative Spectrosc. Radiative Transfer* 191, 7–12. doi:10.1016/j.jqsrt.2017.01.015

Martonchik, J. V., Bruegge, C. J., and Strahler., A. H. (2000). A review of reflectance nomenclature used in remote sensing. *Remote Sensing Rev.* 19 (1-4), 9–20. doi:10.1080/02757250009532407

Morton, D. C., Nagol, J., Carabajal, C. C., Rosette, J., Palace, M., Cook, B. D., et al. (2014). Amazon forests maintain consistent canopy structure and greenness during the dry season. *Nature* 506 (7487), 221–224. doi:10.1038/nature13006

Myneni, Ranga. B. (1991). Modeling radiative transfer and photosynthesis in three-dimensional vegetation canopies. *Agric. For. Meteorology* 55 (3), 323–344. doi:10.1016/0168-1923(91)90069-3

Myneni, R. B., Knyazikhin, Y., and Park., T. (2015a). “MOD15A2H MODIS/Terra Leaf Area Index/FPAR 8-Day L4 Global 500m SIN Grid V006 [Data set],” in *NASA EOSDIS Land Processes DAAC* . Sioux Falls, South Dakota: USGS Earth Resources Observation and Science (EROS) Center. doi:10.5067/MODIS/MOD15A2H.006

Myneni, R. B., Knyazikhin, Y., and Park, T. (2015b). “MYD15A2H MODIS/Aqua Leaf Area Index/FPAR 8-Day L4 Global 500m SIN Grid V006 [Data set],” in *NASA EOSDIS Land Processes DAAC* . Sioux Falls, South Dakota: USGS Earth Resources Observation and Science (EROS) Center. doi:10.5067/MODIS/MYD15A2H.006

Myneni, R. B., Yang, W., Nemani, R. R., NemaniDickinson, A. R., Dickinson, R. E., Knyazikhin, Y., et al. (2007). Large seasonal swings in leaf area of Amazon rainforests. *Proc. Natl. Acad. Sci.* 104 (12), 4820–4823. doi:10.1073/pnas.0611338104

Nepstad, D. C., de Carvalho, C. R., Davidson, E. A., Jipp, P. H., Lefebvre, P. A., Negreiros, G. H., et al. (1994). The role of deep roots in the hydrological and carbon cycles of Amazonian forests and pastures. *Nature* 372 (6507), 666–669. doi:10.1038/372666a0

Nilson, T. (1991). “Approximate Analytical Methods for Calculating the Reflection Functions of Leaf Canopies in Remote Sensing Applications,” in *Photon-Vegetation Interactions: Applications in Optical Remote Sensing and Plant Ecology* ed . Editors R. B. Myneni, and J. Ross (Berlin, Heidelberg: Springer Berlin Heidelberg), 161–190. doi:10.1007/978-3-642-75389-3_6

Oliveira, R. S., Dawson, T. E., and Burgess, D. C. (2005). Hydraulic redistribution in three Amazonian trees. *Oecologia* 145 (3), 354–363. doi:10.1007/s00442-005-0108-2

Pan, Y., Birdsey, R. A., Fang, J., Houghton, R., Kauppi, P. E., Kurz, W. A., et al. (2011). A Large and Persistent Carbon Sink in the World's Forests. *Science* 333 (6045), 988–993. doi:10.1126/science.1201609

Pierret, A., Maeght, J.-L., Clément, C., Montoroi, J.-P., Hartmann, C., and Gonkhamdee, S. (2016). Understanding deep roots and their functions in ecosystems: an advocacy for more unconventional research. *Ann. Bot.* 118 (4), 621–635. doi:10.1093/aob/mcw130

Pisek, J., Arndt, S. K., Erb, A., Pendall, E., Schaaf, C., Wardlaw, T. J., et al. (2021). Exploring the Potential of DSCOVR EPIC Data to Retrieve Clumping Index in Australian Terrestrial Ecosystem Research Network Observing Sites. *Front. Remote Sens.* 2, 6. doi:10.3389/frsen.2021.652436

Qin, W., Gerstl, S. A. W., Deering, D. W., and Goel, N. S. (2002). Characterizing leaf geometry for grass and crop canopies from hotspot observations: A simulation study. *Remote Sensing Environ.* 80 (1), 100–113. doi:10.1016/S0034-4257(01)00291-7

Qin, W., Goel, N. S., and Wang., B. (1996). The hotspot effect in heterogeneous vegetation canopies and performances of various hotspot models. *Remote Sensing Rev.* 14 (4), 283–332. doi:10.1080/02757259609532323

Reichstein, M., Bahn, M., Ciais, P., Frank, D., Mahecha, M. D., Seneviratne, S. I., et al. (2013). Climate extremes and the carbon cycle. *Nature* 500 (7462), 287–295. doi:10.1038/nature12350

Ross, J. K., and Marshak, A. L.. 1988 "Calculation of canopy bidirectional reflectance using the Monte Carlo method." *Remote Sensing Environ.* 24 (2):213–225. doi:10.1016/0034-4257(88)90026-0

Ross, J., and Marshak, A. (1991). Influence of the Crop Architecture Parameters on Crop Brdf - a Monte-Carlo Simulation. *Phys. Measurements Signatures Remote Sensing* 1 (2319), 357–360.

Ross, Juhan. (1981). *The radiation Regime and Architecture of Plant Stands*. The Hague: Dr. W. Junk.

Saleska, S. R., Didan, K., Huete, A. R., and da Rocha, H. R. (2007). Amazon Forests Green-Up during 2005 Drought. *Science* 318 (5850), 612. doi:10.1126/science.1146663

Saleska, S. R., Wu, J., Guan, K., Araujo, A. C., Huete, A., Nobre, A. D., et al. (2016). Dry-season greening of Amazon forests. *Nature* 531 (7594), E4–E5. doi:10.1038/nature16457

Samanta, A., Costa, M. H., Nunes, S. A., Xu, L., and Myneni, R. B. (2011). Comment on "Drought-Induced Reduction in Global Terrestrial Net Primary Production from 2000 through 2009". *Science* 333 (6046), 1093. doi:10.1126/science.1199048

Samanta, A., Ganguly, S., Hashimoto, H., Devadiga, S., Vermote, E., Knyazikhin, Y., et al. (2010). Amazon forests did not green-up during the 2005 drought. *Geophys. Res. Lett.* 37 (5), a–n. doi:10.1029/2009GL042154

Samanta, A., Knyazikhin, Y., Xu, L., Dickinson, R. E., Fu, R., Costa, M. H., et al. (2012). Seasonal changes in leaf area of Amazon forests from leaf flushing and abscission. *J. Geophys. Res.* 117. doi:10.1029/2011jg001818

Schaepman-Strub, G., Schaepman, M. E., Painter, T. H., Dangel, S., and Martonchik, J. V.. 2006 "Reflectance quantities in optical remote sensing-definitions and case studies." *Remote Sensing Environ.* 103 (1):27–42. doi:10.1016/J.Rse.2006.03.002

Schlesinger, W. H., and Bernhardt, E. S. (2012). *Biogeochemistry: An Analysis of Global Change*. 3 ed. Cambridge: Academic Press.

Schull, M. A., Knyazikhin, Y., Xu, L., Samanta, A., Carmona, P. L., Lepine, L., et al. (2011). Canopy spectral invariants, Part 2: Application to classification of forest types from hyperspectral data. *J. Quantitative Spectrosc. Radiative Transfer* 112 (4), 736–750. doi:10.1016/j.jqsrt.2010.06.004

Smolander, S., and Stenberg, P. (2005). Simple parameterizations of the radiation budget of uniform broadleaved and coniferous canopies. *Remote Sensing Environ.* 94 (3), 355–363. doi:10.1016/J.Rse.2004.10.010

Song, W., Knyazikhin, Y., Wen, G., Marshak, A., Mõttus, M., Yan, K., et al. (2018). Implications of Whole-Disc DSCOVR EPIC Spectral Observations for Estimating Earth's Spectral Reflectivity Based on Low-Earth-Orbiting and Geostationary Observations. *Remote Sensing* 10 (10), 1594. doi:10.3390/rs10101594

Stenberg, P., Mõttus, M., and Rautiainen, M. (2016). Photon recollision probability in modelling the radiation regime of canopies - A review. *Remote Sensing Environ.* 183, 98–108. doi:10.1016/j.rse.2016.05.013

Vladimirov, V. S. (1963). *Mathematical problems in the one-velocity theory of particle transport*, Vol. AECL-1661. Clark River, Ontario: Atomic Energy of Canada Limited.

WWW-MAIAC (2018). "DSCOVR EPIC L2 Multi-Angle Implementation of Atmospheric Correction (MAIAC), Version 01," in *NASA Langley Atmospheric Science Data Center DAAC* . doi:10.5067/EPIC/DSCOVR/L2_MAIAC.001

WWW-MISR_AEROSOL (1999). "MISR Level 2 Aerosol parameters V003," in *NASA Langley Atmospheric Science Data Center DAAC* . https://asdc.larc.nasa.gov/project/MISR/MIL2ASAE_3.

WWW-MISR_SURFACE (1999). "MISR Level 2 Surface parameters V003," in *NASA Langley Atmospheric Science Data Center DAAC* . doi:10.5067/TERRA/MISR/MIL2ASLS_L2.003-23

WWW-TRMM (2011). "Tropical Rainfall Measuring Mission (TRMM) (2011), TRMM (TMPA/3B43) Rainfall Estimate L3 1 month 0.25 degree x 0.25 degree V7," in *Goddard Earth Sciences Data and Information Services Center (GES DISC)* . 10.5067/TRMM/TMPA/MONTH/7.

WWW-VESDR (2021). "DSCOVR EPIC Level 2 Vegetation Earth System Data Record (VESDR), Version 2," in *NASA Langley Atmospheric Science Data Center DAAC* . doi:10.5067/EPIC/DSCOVR/L2_VESDR.002

Xu, L., Samanta, A., Costa, M. H., Ganguly, S., Nemani, R. R., and Myneni, R. B. (2011). Widespread decline in greenness of Amazonian vegetation due to the 2010 drought. *Geophys. Res. Lett.* 38 (7), a–n. doi:10.1029/2011GL046824

Yan, K., Park, T., Yan, G., Chen, C., Yang, B., Liu, Z., et al. (2016). Evaluation of MODIS LAI/FPAR Product Collection 6. Part 1: Consistency and Improvements. *Remote Sensing* 8 (5), 359. doi:10.3390/rs8050359

Yan, K., Park, T., Yan, G., Liu, Z., Yang, B., Chen, C., et al. (2016). Evaluation of MODIS LAI/FPAR Product Collection 6. Part 2: Validation and Intercomparison. *Remote Sensing* 8 (6), 460. doi:10.3390/rs8060460

Yang, B., Knyazikhin, Y., Mõttus, M., Rautiainen, M., Stenberg, P., Yan, L., et al. (2017). Estimation of leaf area index and its sunlit portion from DSCOVR EPIC data: Theoretical basis. *Remote Sensing Environ.* 198, 69–84. doi:10.1016/j.rse.2017.05.033

Yang, W., Seager, R., Cane, M. A., and Lyon, B. (2015). The Annual Cycle of East African Precipitation. *J. Clim.* 28 (6), 2385–2404. doi:10.1175/JCLI-D-14-00484.1

Conflict of Interest: The authors declare that the research was conducted in the absence of any commercial or financial relationships that could be construed as a potential conflict of interest.The reviewer AL declared a past co-authorship with one of the author YK to the handling editor.

ORIGINAL RESEARCH
published: 12 November 2021
doi: 10.3389/frsen.2021.715296

Earth Polychromatic Imaging Camera Geolocation; Strategies to Reduce Uncertainty

Karin Blank[1*], Liang-Kang Huang[1,2], Jay Herman[1,3] and Alexander Marshak[1]

[1] *Goddard Space Flight Center, Greenbelt, MD, United States*
[2] *Science Systems and Applications, Inc., Lanham, MD, United States*
[3] *University of Maryland Baltimore County, Baltimore, MD, United States*

Edited by:
Yingying Ma, Wuhan University, China

Reviewed by:
Lan Gao, University of Oklahoma, United States
Igor Geogdzhayev, Columbia University, United States

**** Correspondence:** Karin Blank, karin.b.blank@nasa.gov*

***Specialty section:** This article was submitted to Satellite Missions, a section of the journal Frontiers in Remote Sensing*

***Received:** 26 May 2021*
***Accepted:** 11 October 2021*
***Published:** 12 November 2021*

***Citation:** Blank K, Huang L-K, Herman J and Marshak A (2021) Earth Polychromatic Imaging Camera Geolocation; Strategies to Reduce Uncertainty. Front. Remote Sens. 2:715296. doi: 10.3389/frsen.2021.715296*

Earth Polychromatic Imaging Camera occupies a unique point of view for an Earth imager by being located approximately 1.5 million km from the planet at Earth-Sun Lagrange point, L1. This creates a number of unique challenges in geolocation, some of which are distance and mission specific. To solve these problems, algorithmic adaptations need to be made for calculations used for standard geolocation solutions, as well as artificial intelligence-based corrections for star tracker attitude and optical issues. This paper discusses methods for resolving these issues and bringing the geolocation solution to within requirements.

Keywords: geolocation, geolocation accuracy, geolocation algorithm, deep space climate observatory (DSCOVR), earth polychromatic imaging camera (EPIC)

INTRODUCTION

Instrument

The Earth Polychromatic Imaging Camera (EPIC) is an instrument on the Deep Space Climate Observatory (DSCOVR), which orbits the L1 Earth-Sun Lagrange point. As an Earth viewing instrument, it has a unique view of the planet, taking 13–21 images daily at local noon. The instrument is a 30 cm Cassegrain telescope with 2048x2048 charge-coupled device (CCD), using two filter wheels, and containing a set of 10 bands at wavelengths between 317 and 780 nm (Figure 1) (DSCOVR:EPIC, 2016).

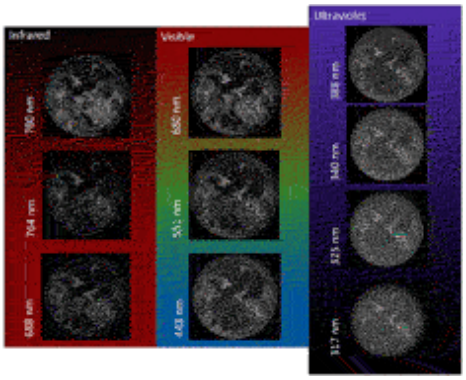

FIGURE 1 | Images of the Earth taken in different wavelength by EPIC. The leftmost panel are infrared bands; middle are visible; right are ultraviolet. The range permits EPIC to engage in land, cloud, and atmospheric studies as well as produce color images.

A typical imaging session consists of 10 images taken once of each band. In creating the science products, the images are calibrated into units of counts/second and then geolocation is calculated (Marshak et al., 2018).

Geolocation

Geolocation for EPIC images is unique because it not only has to operate across the entire illuminated Earth's surface, but also has to do so from a 1.5 million kilometers away. The algorithm creates ancillary science products per pixel, of the latitude and longitude; Sun azimuth and zenith angles; viewing azimuth and zenith angles; and viewing angle deltas due to Earth atmosphere refraction. For the level 1a (L1a) product, these values are calculated per pixel and mapped into the original image's orientation. In the level 1b (L1b), the images and the relative products are remapped, so that north is pointed up and the pixels across the bands are aligned with each other. Bands within the visual range are combined to produce natural color images (Figure 2) of the rotation Earth (https://epic.gsfc.nasa.gov).

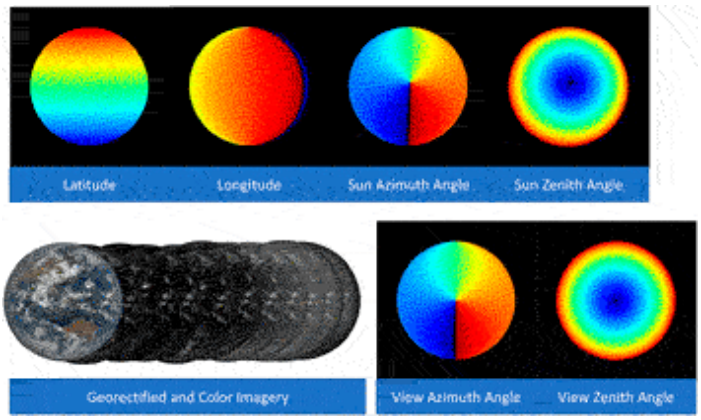

FIGURE 2 | Examples of EPIC geolocation products.

It takes about 7 minutes for EPIC to take a set of ten exposures in an imaging session. While the instrument is performing this action, there are several articles of motion occurring. First, the spacecraft is moving, traveling its 6-months Lissajous orbit, rotating on its axis, and making externally driven linear motions to adjust its pointing so that Earth is centered in the view (Figure 3). Second, the subject of the imaging, typically Earth, is rotating on its axis 15° per hour, resulting in approximately a 4-pixel rotational offset between the first and final image in the set.

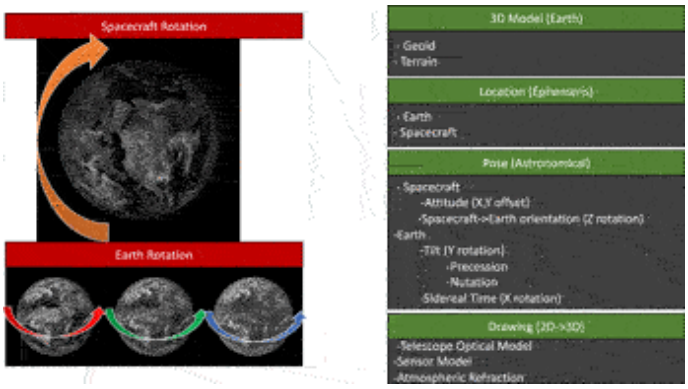

FIGURE 3 | Different corrections made by the EPIC geolocation software and the inputs needed for the different parts of the program.

In order to geolocate these images, it is necessary to develop a three-dimensional model of each pixel location. A useful model of the Earth's body is generated based on the SRTM30 dataset (Shuttle Radar Topography Mission) and rotated into EPIC's view using spacecraft attitude and ephemeris information, as well as astronomical calculations of the seasonal Earth's position. This is then lined up with the actual EPIC images and permits the calculation of the latitude, longitude, and relevant Sun and viewing angles. The results of this product are then written into the L1a dataset. In order to generate the L1b, using the 3D coordinates, the pixels for all 10 bands are "spun" into the same orientation, redrawn in 2D, and written into a shared latitude and longitude grid.

More details, as well as a mathematical description of the algorithm can be found in the "EPIC Geolocation and Color Imagery" document (Blank, 2019) found in the references.

PROBLEMS

Although the geolocation seems straightforward, there are several challenges that prevent an uncomplicated implementation of this algorithm. The first is that the accuracy of the star tracker is below what is needed to understand the orientation of the instrument and Earths' body; the second is linked to problems with the optical distortion model of the EPIC telescope; the third is a potential issue with time stamp accuracy.

Star Tracker and Guidance

The star tracker, a Ball Aerospace CT633, contains an imager that looks at stars in the dark sky and matches the resulting star images against its star catalog (Ball, 2021). Using this information, it is able to obtain the attitude of the spacecraft relative to the Earth's ecliptic plane. From there, with the ephemeris of the Earth and Sun, it is possible to determine how the spacecraft is oriented regarding Earth. If this information was within requirements, it would be possible to calculate directly the per pixel values for the geolocation.

Unfortunately, it is not perfect, an issue that was known when the spacecraft was initially developed as "Triana" in 1999. At that time, engineers had developed a software solution to help mitigate this issue, using images from EPIC to help reorient the spacecraft regarding Earth. But in 2010, when the spacecraft was recommissioned and renamed DSCOVR, its focus transitioned from an Earth science to a space weather mission. EPIC went from the primary instrument to secondary and the EPIC Earth-orienting software was removed. As a result, without the additional correction, the nominally 0.5° Earth images can be anywhere within the field of view.

The accuracy of the star tracker attitude is not adequate for geolocation of the EPIC images. It can be as much as ±0.05° on the x, y offset and ±1° in rotation.

Time

Because the net error in the geolocation was across multiple dimensions, it was difficult to identify exactly the source of all the errors. One potential issue was that the time stamp in the images was not sufficiently accurate. The EPIC images are sensitive to time within a 30 s resolution, but it takes approximately 90 s to go through the process of taking an image. This process includes moving the filter wheel, taking the exposure, processing the image and storing it into memory. The timestamp must also be copied from multiple systems, from the spacecraft to the instrument computer; it adds up to the potential for the appended timestamp to not match the actual exposure time. This would translate to an X axis rotation error in rotating the Earth into the EPIC view. This source of error was investigated and resolved as part of this work.

Optical Distortion

After an initial implementation of the EPIC Geolocation, it became evident there were problems with the optical distortion model of the telescope. This model accounts for both radial and tangential distortion common to lenses. An example of it is to photograph a rectangular grid and view the results. A wide-angle lens with have barrel distortion; a telephoto lens, such as EPIC, will have a pincushion distortion (Figure 4).

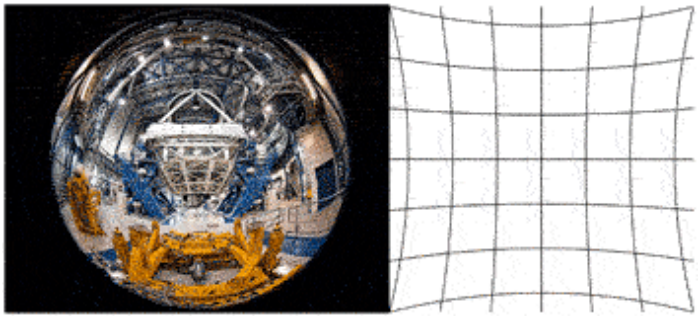

FIGURE 4 | Left: Image taken with wide angle lens demonstrating barrel distortion. Credit ESO/José Francisco Salgado. Right: Grid demonstrating pincushion distortion. Credit: Wikipedia/WolfWings.

The formula used for repairing optical distortion is as follows:

Calculate the delta between the physical CCD center and the optical center:

$$\Delta x = x - x_c$$

$$\Delta y = y - y_c$$

Radial distance:

$$r = \sqrt{\Delta x^2 + \Delta y^2}$$

The pixel offset, according to the optical model, is then:

$$x' = \Delta x + \left(K_1 r^2 + K_2 r^4 + K_3 r^6\right) + P_1\left(r^2 + 2\Delta x^2\right) + 2P_2(\Delta x \Delta y)\left(1 + P_3 r^2 + P_4 r^4\right)$$

$$y' = \Delta y + \left(K_1 r^2 + K_2 r^4 + K_3 r^6\right) + 2P_1(\Delta x \Delta y) + P_2\left(r^2 + 2\Delta y^2\right) \times \left(1 + P_3 r^2 + P_4 r^4\right)$$

The parts $(K_1r^2 + K_2r^4 + K_3r^6)$ and $(1 + P_3r^2 + P_4r^4)$ above are infinite expansions in the original formula; here shown are only the terms needed to correct for EPIC where the K's and the P's are the parameters that are derived from the optical model.

When comparing results and performing offset analysis, it appeared that there was an error bias that started from the middle of the CCD to the bottom right corner.

Typical Solutions for Geolocation Error

A typical solution to solving geolocation errors is to find control points and warp the images to fit. This was done with success in corrections to early versions of the geolocated product such as used for the algorithm. Here, the data was control point matched and regridded into a new projection. Although this solution worked well for the MAIAC algorithm, it would not make a universal solution for all EPIC science algorithms. Because DSCOVR is constantly in motion as each band is being taken, each image has a unique geolocation solution and therefore a unique set of errors. Some science products, such as ozone, are very sensitive to the band's colocation. Using warping risks introducing artifacts into these datasets.

Another solution was to use control points and develop a solution to the rotational and x, y linear offsets in the image. Although this could resolve these errors to some degree, it cannot fix problems at far viewing angles of the Earth images or the optical distortion error. This is due to a loss of contrast at higher viewing angles because of atmospheric scattering, as well as a decrease of spatial resolution in the data cause by the Earth's curvature. Although at 2048 × 2048 the nadir image resolution (point spread function) is 18km, by 70° viewing angle it has degraded to approximately 18km/cost (70°) per pixel, which is 53 km resolution.

Summary of Functions to Be Solved

To resolve the problems with geolocation requires finding a solution for the 16 inputs to the algorithm that are below requirements. These include:

x offset–Earth's x location from the center of the image.

y offset–Earth's y location from the center of the image.

Z Earth/DSCOVR rotational offset.

X Earth time rotational offset

plus 13 coefficients in the optical distortion model, including linear offset, radial distortion, and tangential distortion.

The x, y, and rotational offset corrections need will need to be calculated for every image; the optical distortion model only needs to be resolved once. The computational complexity of resolving such a problem with brute force is O (n), where n is the range of error from the computed result. Multi-Angle Implementation of Atmospheric Correction (MAIAC) algorithm (Huang, 2019).

METHODS

To reduce the massive problem required the implementation of an EPIC simulator and an artificial intelligence (AI) program. The EPIC simulator is used to generate images of the Earth in different configurations. The AI is used to select potential matches between the simulated images and the actual EPIC picture and determine which solutions are worthwhile to explore.

Earth Polychromatic Imaging Camera Simulator

The EPIC simulator consists of an astronomical calculator, an Earth model, an instrument model, and MODIS (Moderate Resolution Imaging Spectroradiometer) data (Figure 5). It is very similar, and shares much of the code used for EPIC geolocation but is used instead to generate MODIS images simulated to look like EPIC images. The simulator works with any geolocated dataset and has been also tested with VIIRS, GOES-16, and Himawari-8 (see Acronyms for definitions). It can also take EPIC images from another band or time period and convert it into another point of view.

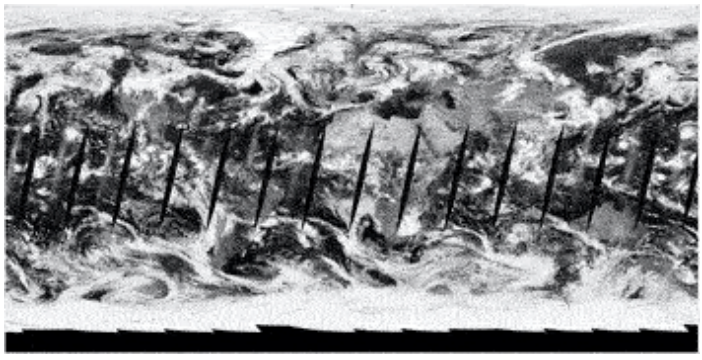

FIGURE 5 | MODIS full day image in equirectangular projection. From https://worldview.earthdata.nasa.gov/.

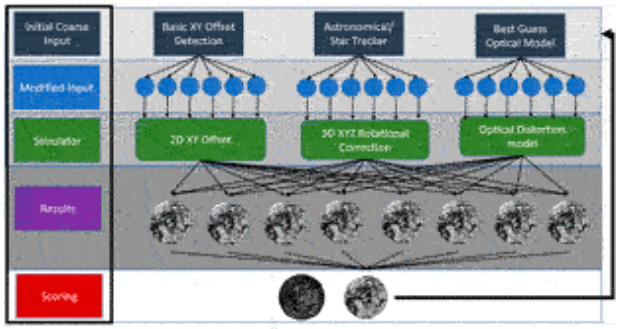

FIGURE 6 | Diagram demonstrating back propagation correction for the EPIC Geolocation.

The astronomical calculator takes the date and time, and calculates the apparent sidereal time, obliquity, precession, nutation, and annual aberration. This determines the "pose" of the Earth at the time the image is taken.

To determine the pose in relation to the camera view angle, the Sun and Spacecraft ephemeris, along with the spacecraft attitude quaternions, are used to calculate the viewing angles.

Using a terrain model of the Earth, the geoid, a 3D model of the Earth is generated in Cartesian coordinates. Then, with the astronomical pose and camera viewing angles, the 3D model is "spun" into the pose it would be in as viewed from the spacecraft. The set of Cartesian coordinates is then clipped so that only those seen by the spacecraft are in the model, and the ones on the far side (not imaged) of the Earth are removed.

Using the telescope optical model, the Cartesian coordinates are mapped into the 2D coordinates of the detector array. MODIS RGB data obtained from WorldView Web Mapping Service (https://worldview.earthdata.nasa.gov/) is then redrawn with the 2D coordinates. The result is a MODIS image that has been reprojected into the EPIC point of view.

Using this simulator, it is possible to generate images to test the instrument's various configurations. Anything that is input into the geolocation algorithm can be modified to determine how it would affect the resulting image. This can be used to resolve the errors in attitude and optical distortion.

Back Propagation

After the simulator, the next step is to automate the correction process. This is done in a way similar to back propagation (BP) in neural networks.

In this situation, each input to the geolocation is treated as a node; the link between them is the calculation. Each coefficient is initially fed the naïve solution for the input.

The program then generates a coarse spread of potential values. The range of these values is based on the known error range of the inputs. Using this coarse spread, possible configurations of attitude and optical model are fed to the simulator generating dozens of low-resolution Earths. These Earth images are then scored against the actual EPIC image; the coefficients that generated the best match are then propagated back into the algorithm.

The algorithm repeats, but this time with the updated coefficients in the nodes. Another spread is generated, this time at a finer resolution than before. Dozens of Earths are simulated in different configurations, this time at a medium resolution. The simulated earths are then scored, using the Pearson correlation calculation, against the actual EPIC image and the winner is then used to update the coefficients.

The algorithm is run repeatedly, each time at a finer resolution, until it has resolved all the coefficients to meet the geolocation requirements of results within 0.5 pixels. Essentially, what happens is the AI is teaching itself how to draw Earth images so they look like EPIC images; as a result, we learn the necessary coefficients for the geolocation.

When the AI is done, the naïve geolocation algorithm is then run with the updated coefficients and generates the subsequent level 1 products.

Use in Solving Star Tracker

The star tracker attitude solution is necessary for three inputs into the model; the horizontal (y) and vertical (x) offsets of the centroid in the image, and the rotation required to make Earth's north face the top of the image. The star tracker x and y offsets have never been used in the naïve algorithm, as the error was too great: instead, a centroiding algorithm was used to find the edge of the Earth and center based on that. This algorithm, however, could not always center the Earth within half-a-pixel requirements. This was due partially because the atmosphere makes the edges unsharp. The other reason is because DSCOVR's orbit is slightly off the Earth-Sun line, so the Sun terminator line is contained in all the images. This means that on one side of the Earth, the edge is always darker and less distinct, and that the location of the terminator is orbit dependent and moves accordingly.

Because of the lack of sharpness of the land in the images due to the atmosphere, and because some images, such as the UV bands, lack distinct surface features, it is necessary to use as much intelligence from the images as possible. By using the EPIC-simulating MODIS images, cloud features, as well as interior land features, can be used to assist the correction.

As there are 10 bands in EPIC, the best band available is used with the simulator; every other band uses EPIC data. The preferred band to use is 780 nm as it has the maximum contrast. If that is not available, then it will choose, in order of preference, 680, 551, 443, 388, 340, 325, 317, 764, and 688 nm. The order is based on the relative correlation scores of these bands to the MODIS image.

The initial back propagation generates a three-value coarse spread for each of the coefficients. For the x and y offsets, this starts at eight pixels, the worst possible error, and for the rotation it starts at 1°. Nine Earths are simulated, scored, and the best result is then put back into the propagation algorithm. This is repeated with each round doubling the precision in resolution until the algorithm reaches the equivalent of 0.25-pixel accuracy.

Use in Solving Time

The method for the time coefficient was the same as that for the star tracker and was calculated alongside those coefficients in earlier tests. It was found that there was no significant error in the image time stamp, and adjustment for this coefficient was subsequently removed.

Use in Solving Optical Distortion

In order to solve the coefficients for optical distortion, the back-propagation (BP) algorithm needs to be used to solve the rotation error to the best of its ability, followed by then applying the BP algorithm to the optical distortion formula. Because we lack ideal images for solving optical distortion, it is necessary to perform the BP correction for optical distortion hundreds of times and collate the results. An ideal image would be a gridded surface that covers the entire field of view–unfortunately that doesn't exist from the point of view of L1. An alternative would be using a star field image. However, EPIC is not suited for imaging stars, as the filters limit the amount of light such that the exposure would be longer than the spacecraft can stay still. We did attempt to image the stars without the filters, however we found that

without the refractive index supplied by the filters, the star images were out of focus.

Using images of the Earth has its own challenges. The optical distortion benefits most from information near the edges of the CCD. However, EPIC images have low data content at the edges, due to the Earth tending to be centered. Furthermore, because of atmospheric haze and distance distortion, the sharpness of the land mass decreases as the viewing angle increases, which means that there is less useful information as you get closer to the edge of the sphere. This is less of a problem with the infrared 780 nm band than the other bands; therefore, we limit the use to this band alone.

Due to these issues, the back propagation does not perform optimally; therefore, it is necessary to run it multiple times on different images and aggregate the results. To reduce the amount of computation required, a program was written to scan through the available EPIC images and pick only best suited for this application. In this situation, we take advantage of the noisy pointing from the star tracker and select images where the Earth is situated closer to the edges of the CCD. To avoid any seasonal or orbital biases, the images were further down selected to be dispersed somewhat evenly, timewise, over the course of 2 years.

The BP algorithm was then run with the attitude and optical distortion correction across approximately 350 images. Outliers selected based on the optical center coordinates were removed. The datasets were then broken into a 2016 and 2017 set, the results then collated by averaging the coefficient values. The 2016 and 2017 coefficient sets were found to be almost identical, which was a good indication that the process could produce consistent results. They were then collected together into a final model. Since the run of this model in 2018, there has been no evidence of drift in the geolocation solution, which indicates the distortion is stable. Because of this, and the fact that this calculation is resource intensive in both computation and in user time, it has not been rerun since then.

EXAMPLE RUN

In the following example run to resolve the star tracker error, the software was run for seven iterations with gradually finer resolutions. The graphs in Figures 7, 8 show the delta between each run and the final solution. In the star tracker this is for the x and y centroid offsets and the rotation to north

angle. As can be seen, after the initial coarse calculation, the results rapidly converge and approach the solution (Figures 7, 8).

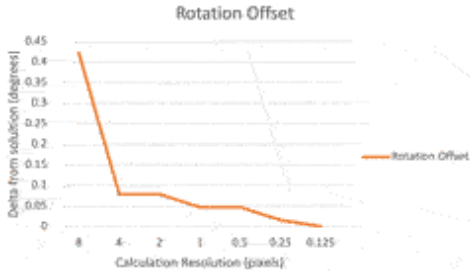

FIGURE 7 | Chart demonstrates the software converging on the solution of the x and y centroid offsets as the resolution of each pass increases.

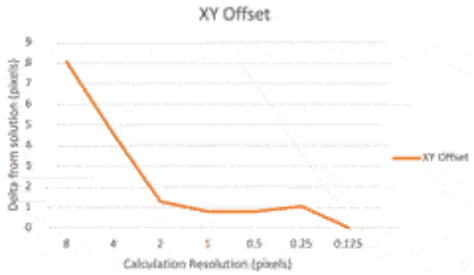

FIGURE 8 | Chart demonstrates the software converging on the solution of the rotational correction as each pass increases in resolution.

Below (Figure 9) is an example of the final simulated image using MODIS data and the calculated solution, versus the original EPIC image.

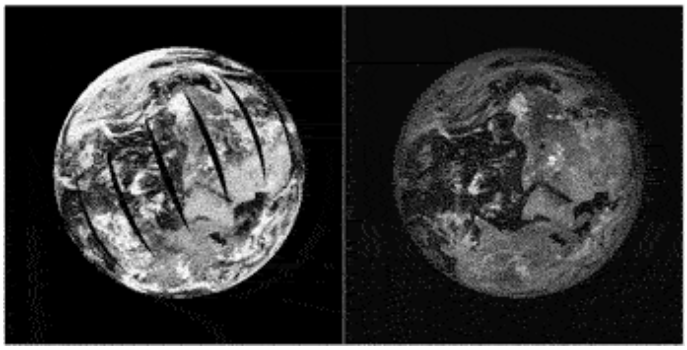

FIGURE 9 | Left: MODIS data simulated as EPIC portraying the final solution of the algorithm. Right: Actual EPIC image the algorithm was performed against.

RESULTS

Optical Distortion Solution

The results of the optical distortion solution revealed a severe tangential distortion. Tangential distortion is caused by a skewing of the optical system. The likely result of this is a lift of several millimeters of the CCD at the lower right corner. It is difficult to ascertain when exactly this happened but based on reviews of work orders performed on the reassembly of the instrument, as well as due to some other issues witnessed with the CCD not seen during ground testing, the probability is that it happened during launch.

The improved optical distortion model resolves this issue.

On the left (Figure 10) is the theoretical ideal optical distortion model, which is likely what was intended by the optical designers. This contains only the radial distortion part of the model. On the right is the actual model with both the tangential and radial distortion.

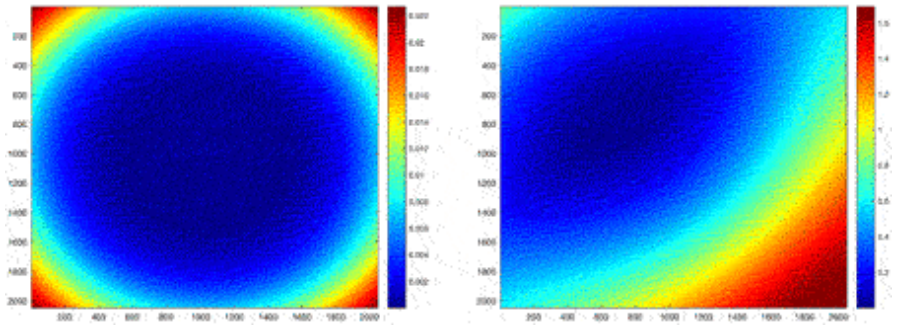

FIGURE 10 | Left: Optical distortion solution, radial component only. Right: Optical distortion solution, radial and tangential components. The color indicates magnitude of offset due to distortion in pixels.

Star Tracker + Optical Distortion Solution

The back-propagation algorithm resolved the star tracker issue. Prior to this solution, results could be off, in the worst case, by as much as eight pixels. Results are now within 1-pixel accuracy within 70° viewing angle. It may be better than that but results higher than 70° are difficult to judge; the pixel resolution decreases to 53 km per pixel and the reduction in contrast because of atmospheric scattering makes land less visible.

Below (Figure 11) is an example of the final results including both the star tracker and optical distortion solution. On the left is the original solution

with the naïve algorithm, on the right, the improved solution.

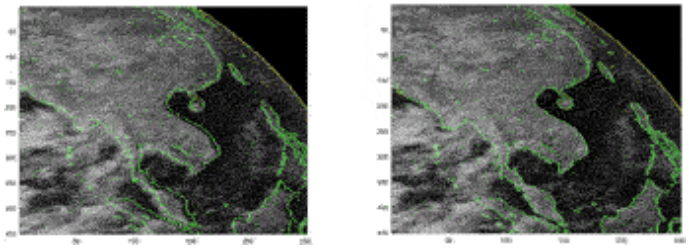

FIGURE 11 | Left: Original, naïve geolocation solution. Right: Improved geolocation solution with back propagation.

CONCLUSION

The AI enhanced BP method resolved the accuracy with the EPIC geolocation due to precision issues with the star tracker attitude and optical distortion model. It can potentially be used on other instruments and missions to resolve accuracy issues due to error in the inputs, as well as resolve calibration issues. It provides an alternative to traditional warping and transformation methods and provides a solution free from distortion.

It can also potentially be used for identifying ambiguous or complex errors, as well as certifying that an input meets requirements.

DATA AVAILABILITY STATEMENT

Publicly available datasets were analyzed in this study. This data can be found here: https://search.earthdata.nasa.gov/.

AUTHOR CONTRIBUTIONS

KB designed the solutions discussed, wrote the software and the majority of the paper. L-KH, JH, AM were involved in validation of technique and identifying issues that needed to be resolved. All authors contributed to manuscript revision, read, and approved the submitted version.

FUNDING

Resources supporting this work were provided by the NASA High-End Computing (HEC) Program through the NASA Center for Climate Simulation (NCCS) at Goddard Space Flight Center.

PUBLISHER'S NOTE

All claims expressed in this article are solely those of the authors and do not necessarily represent those of their affiliated organizations, or those of the publisher, the editors and the reviewers. Any product that may be evaluated in this article, or claim that may be made by its manufacturer, is not guaranteed or endorsed by the publisher.

ABBREVIATIONS

AI, artificial intelligence; BP, back propagation; CCD, charge-couple device; DSCOVR, deep space climate observatory; EPIC, earth polychromatic imaging camera; GOES-16, geostationary operational environmental satellite 16; L1, earth-sun lagrange 1; L1a, Level 1a; L1b, Level 1b; MAIAC, multi-angle implementation of atmospheric correction; MODIS, moderate resolution imaging spectroradiometer; SRTM, shuttle radar topography mission; VIIRS, visible infrared imaging radiometer suite.

REFERENCES

Ball (2021). CT-633 Stellar Attitude Sensor. Available at: ftp://apollo.ssl.berkeley.edu/pub/Pointing_Studies/Hardware/Ball%20CT%20633.pdf (Accessed on April 16, 2021).

Blank, K. (2019). EPIC Geolocation and Color Imagery Algorithm Revision 6. NASA/ASDC. Available at: https://asdc.larc.nasa.gov/documents/dscovr/DSCOVR_EPIC_Geolocation_V03.pdf.

DSCOVR:EPIC (2016). What Is EPIC. Available at: https://epic.gsfc.nasa.gov/about/epic (Accessed on April 16, 2021).

ESO (2021). Up Close and Personal with the Very Large Telescope. Available at: https://www.eso.org/public/images/potw1049a/(Accessed on April 15, 2021).

Huang, D., and Lyapustin, A. (2019). *The MAIAC Algorithm for DSCOVR EPIC and Initial Analysis of Data Products*.

Marshak, A., Herman, J., Szabo, A., Blank, K., Cede, A., Carn, S., et al. (2018). Earth Observations from DSCOVR/EPIC Instrument. *Bull. Am. Meteorol. Soc.* 99, 1829–1850. doi:10.1175/BAMS-D-17-0223.1

Wikipedia (2021a). Distortion (Optics). Available at: https://en.wikipedia.org/wiki/Distortion_(optics) (Accessed on April 16, 2021).

Wikipedia (2021b). File: Pincushion distortion.Svg. Available at: https://en.wikipedia.org/wiki/File:Pincushion_distortion.svg (Accessed on April 16, 2021).

Yang, K., Fleig, A. J., Wolfe, R. E., and Nishihama, M. (2000). "MODIS Band-To-Band Registration," in *Geoscience and Remote Sensing Symposium, 2000. Proceedings. IGARSS 2000.*

Conflict of Interest: L-KH was employed by Science Systems and Applications, Inc.

The remaining authors declare that the research was conducted in the absence of any commercial or financial relationships that could be construed as a potential conflict of interest.

ORIGINAL RESEARCH
published: 18 November 2021
doi: 10.3389/frsen.2021.777806

Operational Detection of Sun Glints in DSCOVR EPIC Images

Tamás Várnai[1,2*], Alexander Marshak[2] and Alexander Kostinski[3]

[1] *Joint Center for Earth Systems Technology, University of Maryland Baltimore County, Baltimore, MD, United States*
[2] *NASA Goddard Space Flight Center, Greenbelt, MD, United States*
[3] *Department of Physics, Michigan Technological University, Houghton, MI, United States*

Edited by:
Yongxiang Hu, Langley Research Center, National Aeronautics and Space Administration (NASA), United States

Reviewed by:
Jun Wang, The University of Iowa, United States
Bastiaan Van Diedenhoven, Netherlands Institute for Space Research (NWO), Netherlands

**** Correspondence:** Tamás Várnai, tamas.varnai@nasa.gov*

***Specialty section:** This article was submitted to Satellite Missions, a section of the journal Frontiers in Remote Sensing*

***Received:** 15 September 2021*
***Accepted:** 29 October 2021*
***Published:** 18 November 2021*

***Citation:** Várnai T, Marshak A and Kostinski A (2021) Operational Detection of Sun Glints in DSCOVR EPIC Images. Front. Remote Sens. 2:777806. doi: 10.3389/frsen.2021.777806*

Satellite images often feature sun glints caused by the specular reflection of sunlight from water surfaces or from horizontally oriented ice crystals occurring in clouds. Such glints can prevent accurate retrievals of

atmospheric and surface properties using existing algorithms, but the glints can also be used to infer more about the glint-causing objects—for example about the microphysical properties and radiative effects of ice clouds. This paper introduces the recently released operational glint product of the Earth Polychromatic Camera (EPIC) onboard the Deep Space Climate Observatory (DSCOVR) spacecraft. Most importantly, the paper describes the algorithm used for generating the key component of the new product: a glint mask indicating the presence of sun glint caused by the specular reflection of sunlight from ice clouds and smooth water surfaces. After describing the glint detection algorithm and glint product, the paper shows some examples of the detected glints and discusses some basic statistics of the glint population in a yearlong dataset of EPIC images. These statistics provide insights into the performance of glint detection and point toward possibilities for using the glint product to gain scientific insights about ice clouds and water surfaces.

Keywords: EPIC, sun glint, ice cloud, horizontally oriented particles, operational product, DSCOVR

INTRODUCTION

Sun glints often affect Earth observations taken from a wide range of spacecrafts, for example from the polar-orbiting Terra and Aqua satellites, the Geostationary Operational Environmental Satellite (GOES) series, or Deep Space Climate Observatory (DSCOVR). The glints are caused by the specular reflection of sunlight through single scattering from highly reflective objects. Such objects include the ocean or other water surfaces and ice crystals that float in clouds at a horizontal orientation and reflect sunlight as a mirror consisting of a myriad of tiny pieces (e.g., Lynch et al., 1994; Lynch and Livingston, 2001; Konnen, 2017). Ice crystals of certain shapes—especially hexagonal plates—float in clouds at a systematic horizontal orientation due to stabilizing aerodynamic forces. This orientation is stable, because, as Katz (1998) put it: "…*if the plate tilts, the wake of the leading edge partly shields the trailing edge from the flow, reducing the drag on it; the resulting torque restores the horizontal orientation*…".

In many cases, Sun glints prevent the accurate retrievals of atmospheric and surface properties using existing algorithms (e.g., Wang and Bailey, 2001; Remer et al., 2005), but the glints can also be used to learn more about the glint-causing objects (e.g., Bréon and Henriot, 2006; Lin et al., 2016) or

even about atmospheric aerosols (Kaufman et al., 1997; Ottaviani et al., 2013; Knoebelspiesse et al., 2021).

Over the past 2 decades, several studies examined ice clouds using glint observations taken from low-Earth orbit satellites. Some studies characterized clouds using polarized measurements of Sun glint taken by the POLDER (Polarization and Directionality of the Earth's Reflectances) instrument (Chepfer et al., 1999; Bréon and Dubrulle, 2004; Noel and Chepfer, 2004), while others used glint (that is, specular reflection) affecting Cloud-Aerosol Lidar with Orthogonal Polarization (CALIOP) lidar returns (e.g., Noel and Chepfer, 2010; Kikuchi et al., 2021). These studies provided numerous insights about the horizontally oriented ice crystals causing the glints, but some critical questions remain unresolved—for example, as Zhou et al., 2013 noted, it is still unclear how common these crystals are.

This paper discusses the detection of glints in images taken by the Earth Polychromatic Camera (EPIC) onboard DSCOVR spacecraft (Marshak et al., 2018). DSCOVR orbits the Sun at the L1 Lagrangian point located about 1.5 million km away from Earth, which allows EPIC to constantly view almost the entire sunlit side of Earth. EPIC captures about 22 multispectral images per day between late April and early September, and about 13 images per day during the rest of the year.

EPIC offers excellent opportunities to study glint-causing ice clouds. EPIC data is especially well-suited for identifying and analyzing glint signals from clouds because, unlike most other satellite instruments, EPIC uses a filter wheel to take images at multiple wavelengths. This helps because using a filter wheel means that EPIC takes the images at each wavelength at slightly different times. For example, red (680 nm) images are taken about 4 min after blue (443 nm) images. During these few minutes, the Earth's rotation changes the normal direction of the observed scenes by about a degree (moving the scenes by more than 100 km), which can affect whether EPIC observations at a specific wavelength will capture or miss any narrowly focused specular reflection from ice clouds or smooth water surfaces. Therefore, sharp brightness differences between EPIC images taken a few minutes apart can identify Sun glints.

In recent years, several studies used EPIC images to study glints from ice clouds (Marshak et al., 2017; Li et al., 2019; Várnai et al., 2020a; Várnai et al., 2020b; Kostinski et al., 2021). These studies showed that Sun glint from ice clouds appears quite frequently in EPIC images (e.g., Marshak et al.

(2017) and found that one in three images with land in the center contains a glint from an ice cloud), explored issues such as spectral and seasonal variations in glint reflectances, and even used glints for testing the accuracy of geolocation of EPIC images (Kostinski et al., 2021).

This paper describes an algorithm developed for the automatic detection of Sun glint from clouds and smooth water surfaces that occur in EPIC images. This algorithm is used in generating the recently released EPIC operational glint data product (https://epic.gsfc.nasa.gov/science/products/glint) that provides glint identification for the entire EPIC data series. After describing the glint detection algorithm and the operational glint product in Section Glint Detection Algorithm and in the Appendix, respectively, Section Initial Examination of Glint Product provides initial analysis of the new glint product using both individual examples and through a brief statistical analysis of the detected glints. Finally, Section Summary offers a brief summary.

GLINT DETECTION ALGORITHM

Basic Approach

The operational glint detection algorithm is based on the approach first introduced in Marshak et al. (2017). The algorithm works by comparing two EPIC observations of the same scene taken at slightly different geometry: one image that captures any tightly focused specular reflection from horizontal objects in the scene, and another image that narrowly misses any such reflection, as the scene has a slightly different sun-view geometry in this second image. In glint studies, the sun-view geometry is often characterized through the glint angle (δ), which is defined as the angle between the actual satellite view direction and the direction that would look straight into the specular reflection from a perfectly horizontal surface. The algorithm reports a glint if the reflectance (R) is much higher for the observation that can capture the glint because of its smaller glint angle.

Earlier studies showed that the specular reflection from ice clouds extends to glint angles of about 2° (e.g., Várnai et al., 2020a; Kostinski et al., 2021) due factors such as: 1) the roughly 0.5° angular diameter of the solar disc, 2) wobbling that can tilt horizontally oriented crystals by up to 1° in ice clouds due to local turbulence effects (e.g., Katz, 1998; Bréon and Dubrulle, 2004), 3) diffraction that occurs when sunlight encounters very small ice

crystals (e.g., Crawford, 1968), 4) small ripples or capillary waves in mostly smooth water surfaces. We note that if wind and currents make water rough, the wide range of wave slopes will spread specular reflection into a wide range of view directions, which makes glints appear larger but fainter in satellite images (Várnai et al., 2020a). The current operational product, however, aims at detecting glints from clouds and smooth water surfaces (for example from calm small lakes (a few km in diameter), as in Kostinski et al., 2021); extending the product to also detect diffuse glints from rough water surfaces (for example using the model developed in Cox and Munk (1954)) is left to the future.

As mentioned in the introduction, EPIC can provide observations of a scene at several glint angles because it takes multispectral observations using a filter wheel—which means that it captures images at different wavelengths at slightly different times. For example, the 388 nm ultraviolet (UV) images are taken about 5 min after blue images. During these 5 min, the Earth's rotation changes the normal direction of the observed scenes by 1.25°. Considering the law of reflection, a 1.25° change in the orientation of the reflector will change the direction of specularly reflected light by 2.5°. Thus, if δ was 0° for a pixel in the blue image, δ will be 2.5° in the UV image. This means that if the pixel contains a large number of horizontally oriented ice crystals that cause a strong glint through specular reflection, EPIC data can reveal this by showing that

$$R_{\text{blue}} \gg R_{\text{UV}} \qquad (1)$$

We note, however, that EPIC can detect even faint glints for which Eq. 1 is not satisfied. Faint glints don't satisfy Eq. 1 because, in the absence of glint, $R_{\text{blue}} < R_{\text{UV}}$ due to the stronger Rayleigh scattering at shorter wavelengths—and so faint glints may lift R_{blue} only to be comparable or slightly larger than R_{UV}. As described below, the EPIC glint detection can identify such faint glints by using thresholds that specify what R_{blue} values imply glint for a given R_{UV}.

As a preparation for the in-depth description of the glint detection algorithm, let us mention three considerations:

- We will describe the detection process only for blue glints, as the operational processing uses the exact same method for green (551 nm) and red glints (except that we use in Eq. 1

R_{green} or R_{red} instead of R_{blue} as the “glint wavelength”, and we can use R_{blue} instead of R_{UV} as the “non-glint wavelength”).

• Since the basis for glint detection lies in specular reflection causing higher reflectances for smaller glint angles, the process for detecting blue glints does not consider any pixels where the glint angle is larger in the blue image than in the UV image.

• The algorithm needs to avoid false glint detections when clouds that are just outside a pixel in the UV image appear inside the pixel in the blue image because of wind drift, cloud growth, or differences in the exact location of pixel boundaries in the blue and UV images. Thus, the algorithm follows Marshak et al. (2017) and uses not the R_{UV} of the pixel itself, but the maximum reflectance within a 3 × 3 pixel area centered on the pixel.

Ultimately, the algorithm flags a pixel as blue glint if $R_{blue} > T\ (R_{UV})$, where $T\ (R_{UV})$ is a threshold function value determined by taking into account spectral variations in scene reflectivity. Since spectral variations can be markedly different over different surfaces, the operational algorithm uses separate T threshold functions for three basic surface types: water, desert, and non-desert land. The surface type at the location of each EPIC pixel is determined from the 0.05° latitude-longitude resolution global map of surface cover provided in the MCD12C1 product of the Moderate Resolution Imaging Spectroradiometer (MODIS) instrument (DOI: 10.5067/MODIS/MCD12C1.006). The exact method for determining the $T\ (R_{UV})$ threshold function values for the entire range of possible R_{UV} values is described in the next section.

Threshold Selection

Admittedly, the selection of glint detection thresholds is somewhat arbitrary and involves a trade-off between accuracy and sensitivity. As usual, if we prioritize accuracy and use very strict thresholds, we will miss detecting some not-so-clear-cut cases affected by relatively faint glints. On the other hand, if we prioritize sensitivity, we will capture not only actual glints but will likely have many false detections as well. The EPIC glint product uses T glint detection thresholds that result in a False Alarm Rate (FAR) of 10%. This means that in 10% of pixels flagged as glint, R_{blue} exceeds $T\ (R_{UV})$

not because of glint, but because of other factors such as strong spectral variations in surface albedo—for example if a red dust plume drifts over the blue ocean.

We determine the glint detection thresholds using a pragmatic statistical approach. This approach avoids the need for physical modeling, which would be greatly complicated by variations in surface spectral properties and in the areal extent, altitude, phase, and optical thickness of clouds (which may also vary within the roughly 8 by 8 km-size EPIC pixels). We note, however, that the absence of physical modeling does not mean the lack of physical basis or constraints: The physics of specular reflection is essential to the method as it is based on glints being limited to locations with suitable sun-view geometries and relies on the constraint that glint from clouds have a narrow angular spread (typically less than 2°).

In determining what T thresholds will result in a *FAR* of 10%, we will rely on the statistical probabilities (P) that, for a random pixel, R_{blue} exceeds T (R_{UV}) due to any (glint or non-glint) reason (P_{any}) or due to non-glint factors (P_{ng}), respectively. Specifically, we state that non-glint factors do not vary much at small glint angles ($P_{ng}(\delta < 2°) \approx P_{ng}(2° < \delta < 5°)$), and that cloud glints rarely extend to glint angle $\delta > 2°$ ($P_{any}(2° < \delta < 5°) \approx P_{ng}(2° < \delta < 5°)$). Based on these considerations, we can express the total *FAR* of the glint detection algorithm (applied to pixels with $\delta < 2°$) as

$$FAR(\delta < 2^{\circ}) = \frac{P_{ng}(\delta < 2^{\circ})}{P_{any}(\delta < 2^{\circ})} \approx \frac{P_{ng}(2^{\circ} < \delta < 5^{\circ})}{P_{any}(\delta < 2^{\circ})} \approx \frac{P_{any}(2^{\circ} < \delta < 5^{\circ})}{P_{any}(\delta < 2^{\circ})} \tag{2}$$

We use Eq. 2 in determining the T (R_{UV}) thresholds for each possible R_{UV} value through a three-step statistical analysis of all EPIC images taken during 2018. First, for each possible R_{UV} value, we calculate the probability distribution functions $PDF(R_{\mathrm{blue}} \mid R_{\mathrm{UV}}, \delta < 2°)$ and $PDF(R_{\mathrm{blue}} \mid R_{\mathrm{UV}}, 2° < \delta < 5°)$. Second, for each possible R_{UV}, we calculate P_{any} for a wide range of candidate T values as

$$P_{\mathrm{any}}(T|R_{UV}, \delta < 2^{\circ}) = \int_{R^{*}}^{\infty} PDF(R_{blue}|\, R_{UV}, \delta < 2^{\circ}) dR_{blue} \tag{3a}$$

and

$$P_{any}(T|R_{UV}, 2^\circ < \delta < 5^\circ) = \int_{R^*}^{\infty} PDF(R_{blue}|R_{UV}, 2^\circ < \delta < 5^\circ) dR_{blue} \quad (3b)$$

Third, for each R_{UV}, we select the T value that, in Eqs 3a, 3b, yields such P_{any} values that, in Eq. 2, will give a FAR close to 0.1 (Figure 1).

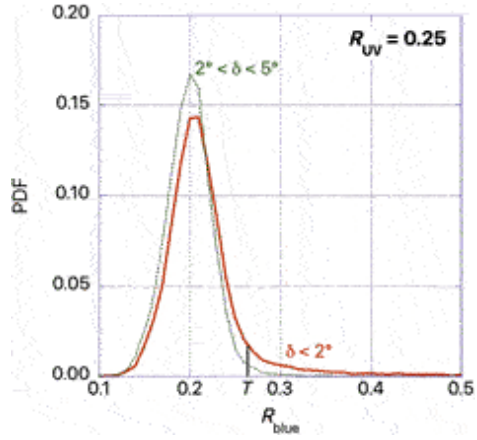

FIGURE 1 | Illustration of threshold selection for the detection of blue glints over non-desert land at pixels where the 388 nm UV reflectance is 0.25. The green solid and red dashed curves show the PDFs based on all EPIC images taken in 2018 for two different ranges of the glint angle (δ). Cloud glints often enhance reflectances < 2°, thus creating the long tail of the red curve. The black vertical bar indicates the T threshold value that was selected because it leads to a 10% false alarm ratio: The area to the right of this line [representing an integral in Eq. (2)] is 10 times smaller under the green (no glint) curve than under the red (glint-affected) curve.

Finally, for robust glint detections, we need to consider that the $T(R_{UV})$ threshold functions determined through the procedure described above can feature random jumps or drops due to sampling noise caused by the finite size of our dataset (containing all EPIC images taken in 2018). To avoid such unphysical jumps and drops, the raw T values are adjusted through a series of three smoothing operations:

- Resetting to zero the PDF values for RUV bins containing three or fewer pixels,
- Fitting a fourth or eighth order polynomial to the raw $T(R_{UV})$ functions (eighth order is used when this reduces the root mean square error of the fit by at least 10%),

- Using linear extrapolation of T (R_{UV}) to obtain thresholds outside the range of R_{UV} values observed in 2018.

The final T thresholds obtained at the end of this smoothing process are illustrated in Figure 2. The figure shows that the T threshold values are capped at the saturation level of the EPIC blue detector ($R_{blue} \approx 1.3$), as it would be pointless to set a threshold higher than any reflectance reported by EPIC. At lower reflectances, T increases with R_{UV}; the discernible changes in the slope of this increase are likely caused by transitions from clear sky to partly and then fully cloudy situations as R_{UV} increases.

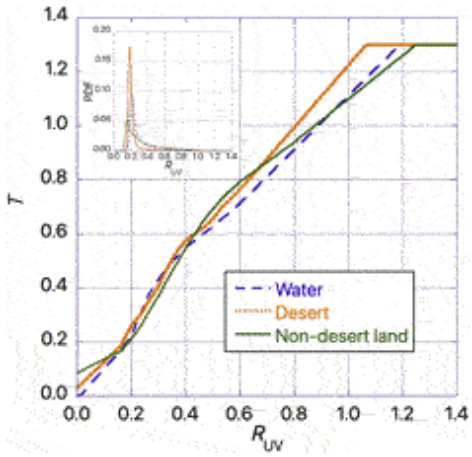

FIGURE 2 | Threshold values used in the detection of blue glints. Pixels are flagged as glint if their blue reflectance exceeds the T threshold value for the pixel's 388 nm reflectance R_{UV}. The inset shows the PDFs of R_{UV} for the three surface types, indicating that the most frequently used threshold values occur at moderate R_{UV} values.

Glint Detection Algorithm

Using the basic approach described in Section Basic Approach and the thresholds discussed in Section Threshold Selection, the operational algorithm detects blue glints through the following process:

- Eliminate EPIC images if data for any of the bands used by the algorithm is missing.
- Cycle through each pixel in the image and eliminate pixels if $\delta > 2°$ or if $\delta_{blue} > \delta_{UV}$. This occurs if the distance from the specular point (where $\delta = 0°$) exceeds about 100 km.

- Identify the surface type of the pixel based on its coordinates and a global map of surface types (obtained from the MODIS MCD12C1 surface cover product).
- Based on the surface type and R_{UV} (the maximum 388 nm reflectance in the 3 × 3 pixel area around the pixel), select the T glint detection threshold value to be used.
- Flag the pixel as glint if $R_{blue} > T$, or as non-glint if $R_{blue} \leq T$.

INITIAL EXAMINATION OF GLINT PRODUCT

This section discusses an initial examination of the glint product. In the absence of independent datasets that could make the traditional validation of the new EPIC glint product possible, this section provides insights about the performance and characteristics of the new product first by showing a few examples of the operational glint mask, and then by presenting an initial statistical analysis of glint detection results.

Glint Examples

Figure 3 shows glint detection results for four EPIC images, three containing glints from ice clouds and one from the smooth ocean surface. Additional examples can be found at the EPIC website at https://epic.gsfc.nasa.gov/science/products/glint.

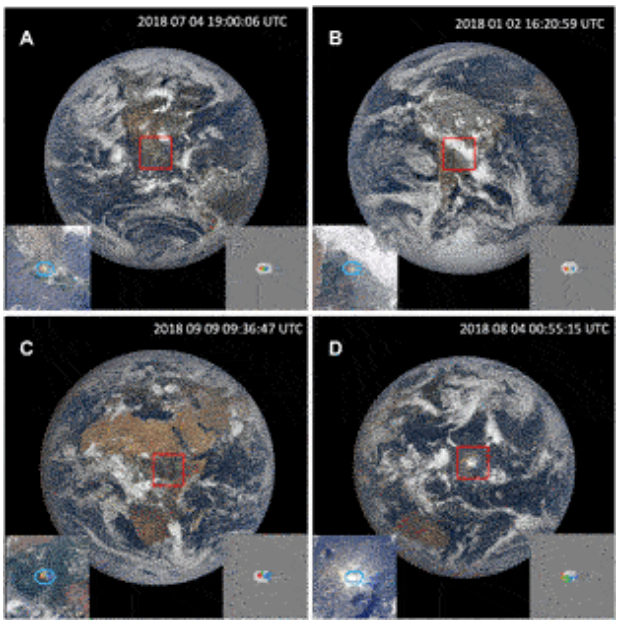

FIGURE 3 | Sample sun glints caused by specular reflection from ice crystals in clouds **(A–C)** and from smooth ocean surface **(D)**. The insets show the glint-affected areas in detail **(left inset),** as well as the EPIC glint mask **(right inset).** Different colors in this rendering of the glint mask indicate which wavelength(s) in the EPIC observations are affected by glint, with yellow and turquoise indicating the overlap of red and green, or blue and green glints, respectively. Light grey means "no glint", while dark gray indicates that no glint detection is attempted as the glint angle exceeds 2°.

Figure 3A shows the glint displayed in Figure 1 of Várnai et al. (2020b). The figure illustrates that in case of extensive ice clouds, EPIC images can feature a colorful pattern in which the eastern and western edges of the glint appear blue and red, respectively, while the middle appears green. Green and especially red glints appear to the west of blue glints because EPIC takes the red (green) images 4 (3) minutes after taking the blue image—and during this time, the rotation of Earth brings a more westward location into the position where EPIC can observe specular reflection from horizontal objects. The typical distance between blue and red glints is about 100 km.

Figure 3B illustrates that glints affecting different EPIC bands can overlap, for example the overlap of red and green glints creates a yellow glint.

Figure 3C shows that in rare occasions, cloud glints can extend all the way up to 2° glint angle. This may indicate intense turbulence that increases the wobbling of horizontally oriented ice crystals.

Figure 3D shows a bright glint from the smooth ocean surface. For two reasons, we believe that while clouds may contribute to the glint at a few pixels, the vast majority of this glint originates from the water surface and not from clouds. First, the glint extends to a much larger area (and larger glint angles) than any cloud glints EPIC observed over land. The presence of glint at even large glint angles indicates that while the reflecting object may be smooth for a water surface, it is not nearly as uniformly flat as the horizontal ice crystals are in clouds. Second, for almost all glint pixels, the oxygen A-band ratios ($R_{764\ \mathrm{nm}}/R_{780\ \mathrm{nm}}$) are below the 0.45 threshold that has been proposed to distinguish surface and cloud glints (Várnai et al., 2020b). We point out that the glint mask readily detects this bright glint, but it does not detect the relatively faint diffuse glints from rough ocean surfaces, which appear relatively dark grey in the image. We note that such diffuse glints from rough ocean surfaces have been detected in images of several satellite instruments such as MODIS or the Multi-angle Imaging SpectroRadiometer (MISR) (e.g., Feng et al., 2017; Knobelspiesse et al., 2021).

Finally, a comparison of glint latitudes in Figure 3 illustrates that, as discussed in Marshak et al. (2017), the latitude of glint observations shifts with the seasons, with glints being detected in the Northern Hemisphere in July (Panel A), in the Southern Hemisphere in January (Panel B), and around the equator in September and April (Panels C and D).

Glint Statistics

Following the individual examples discussed above, this section presents some basic statistics about the glints detected by the operational algorithm in all EPIC images taken during 2017. The goal of this initial statistical analysis lies not in providing physical insights on atmospheric or surface properties, but in getting an initial glimpse of glint product behaviors. (We note that statistics for 2018 were very similar to those for 2017, but the examination of interannual variability is left to a future study of the entire EPIC data series.)

Figure 4 shows what fraction of pixels were flagged as glint for various surface types and glint colors, as a function of glint angle. The figure reveals several notable features discussed below.

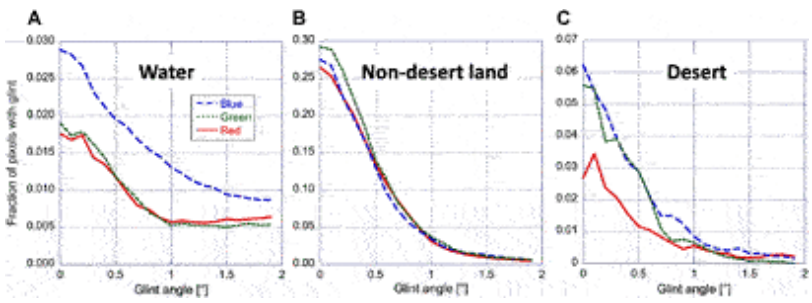

FIGURE 4 | Fraction of all pixels for which the glint mask indicates the presence of glint, plotted separately for each surface type and EPIC band as a function of glint angle (the angle between the actual EPIC view direction and the direction of looking straight into the specular reflection from a perfectly horizontal surface). As discussed in the text, the differences in glint detection frequency over various surface types come from a combination of differences in ice cloud populations and in glint detection sensitivity.

The dominant feature of all panels in Figure 4 is a sharp increase in the fraction of pixels with glint at small glint angles. This is consistent with glint reflectances being largest at small glint angles (e.g., Várnai et al., 2020a; Várnai et al., 2020b; Kostinski et al., 2021) and can be attributed to specular reflection from horizontally oriented ice crystals in clouds and from very smooth water surfaces (such as small, calm lakes, as in Kostinski et al., 2021).

Figure 4A reveals that glints are detected more frequently in the blue EPIC band than in the green and red bands. (The figure considers all glints regardless of whether they come from the surface or clouds.) Green and red glints may be detected less frequently because, similarly to green (or red) glints, glintless white clouds also increase the ratios of green to blue reflectances or red to blue reflectances—which makes it harder to identify glints with a high confidence. The panel also shows that glint detections do not drop to zero at larger glint angles, probably due to somewhat wavy water surfaces that spread specular reflection into a wider range of glint angles.

A comparison of the peak values in Panels a, b, and c reveals that, even for blue glints, glint detection is much less frequent over ocean than land. Considering that about a third of land pixels is classified desert in our dataset, the land-ocean difference is roughly 7-fold, which is roughly twice as large as the factor of 3.5 between glint-caused reflectance enhancements over land and ocean in Figure 2A of Várnai et al. (2020b). This may show that it is harder to identify individual glints over ocean than over land and calls for future improvements in the detection of ice cloud glints over ocean.

The combination of Panels b and c shows that for very small glint angles, glints are detected at about 22% of all observations taken over land. Considering that at the latitudes of EPIC glint observations, the average ice cloud cover above land varies between 20 and 50% during the course of a year (Várnai et al., 2020b, based on King et al., 2013), finding glints in 22% of pixels suggests that glint detection over land is highly effective and that horizontally oriented crystals are quite prevalent in ice clouds. It is important to keep in mind, though, that glint may be observed even if horizontal ice crystals occur only in a portion of a typically 8 by 8 km size EPIC pixel. This implies that horizontal ice crystals likely occur over less than 22% of the actual land area. Moreover, we note that while the sharp drop-off in glint probability with glint angle suggests a dominance of such almost perfectly horizontal surfaces that seem more likely in clouds than in lakes or rivers, future studies will be needed to estimate the relative frequencies of cloud and surface glints.

The comparison of Panels b and c reveals that glints are detected less frequently over desert than non-desert land, due to the lower frequency of ice clouds (and lakes). Finally, we point out that over desert, red glints are detected less frequently than green or blue glints. This seems to indicate that changes in mineral composition of the typically brownish desert can create red patches even without glint, which makes it more difficult to identify red glints with high confidence.

By displaying the number and typical size of glints, Table 1 shows that over all surface types, glints are more frequently detected for the EPIC blue band than for the green or red bands—but also that blue glints are systematically smaller than green or red ones. Overall, the total glint area is similar for all bands over non-desert land, whereas over water and desert, blue glints cover the largest areas despite their smaller sizes.

TABLE 1 | Number and size of glints detected by the EPIC glint product. The numbers in parentheses indicate, what the fraction of all glints detected over a certain surface type are detected at each color.

	Water			Non-desert land			Desert		
	Blue	**Green**	**Red**	**Blue**	**Green**	**Red**	**Blue**	**Green**	**Red**
Number of glints	955 (59%)	341 (21%)	330 (20%)	651 (39%)	540 (32%)	491 (29%)	112 (51%)	59 (27%)	47 (22%
Mean size (pixel)	23	35	38	27	35	35	15	21	20
Median size (pixel)	5	12	13	12	22	20	7	12	10
Total glint area (pixel)	21,595	11,875	12,555	17,405	18,778	17,218	1,735	1,219	917

Over water, blue glints may cover the largest areas due to the higher effectiveness of blue glint detection mentioned above. Similarly, the higher detection effectiveness discussed at Figure 3C may explain why, over desert, blue glints cover larger areas than red glints. The difference between the total area of blue and green glints over desert comes from small blue glints detected at relatively large (>1°) glint angles (Figure 3C), but future studies will be needed to explain these glints.

Finally, we note that for all surface types and EPIC bands, the median of the glint size is much smaller than the mean. This implies that glint size distributions have long tails toward large sizes, indicating a significant occurrence of very large glints. Such large glints may occur in cases of extensive ice cloud cover or large calm water surfaces (as in Figures 3C,D) but, detector saturation artifacts may also play a role (as in the lower right panel of Figure 1 in Marshak et al., 2017). As discussed in the next section, the origin of large—and small—glints can be best explored using additional information not present in the current, initial version of the EPIC operational glint product.

SUMMARY

This paper described the recently released operational glint product of the Earth Polychromatic Camera (EPIC) onboard the Deep Space Climate Observatory (DSCOVR) spacecraft. First, the paper outlined the basic approach used for obtaining the key parameter provided in the product: a glint mask that identifies glints caused by the specular reflection of sunlight from ice clouds and smooth water surfaces. This mask can help in identifying cases when various EPIC products may be less accurate due to the effects of glints and can also help in learning more about the glint-causing clouds or water bodies.

Building on earlier studies (Marshak et al., 2017; Várnai et al., 2020a), glints are detected by comparing two EPIC images having slightly different sun-view geometries: One capturing the glint and the other missing the glint's narrowly focused intense specular reflection. Pixels are flagged as glint if their reflectances in the two images differ substantially. After outlining the general approach, the paper described the glint detection algorithm in detail—including, the method used for obtaining glint detection thresholds that keep the likelihood of erroneous ("false") detections below 10%.

After describing the glint detection process, the paper illustrated various features of the detected glints and provided basic statistics of the glint population observed in a yearlong dataset of EPIC images. These examples and statistics characterized glint populations and yielded insights into the performance of glint detection, and help guiding both future product development and scientific usage. For example, the results indicated a substantial underdetection of cloud glints over ocean, as glints from the water surface (that are often too wide to be detected by our method) made it harder to identify cloud glints with a high confidence. We expect to study this underdetection and improve the detection of glint pixels in the future.

While the current paper considered only the glint product by itself, the main scientific benefits will likely come from combining the glint product with other information. For example, the glint product could be combined with EPIC data on oxygen absorption, with visible EPIC reflectances, or with cloud products from other satellites. EPIC observations in the oxygen A and B absorption bands could help in determining whether glints are caused by water surfaces or ice clouds (Marshak et al., 2017; Várnai et al., 2020a). The initial analysis of oxygen absorption band data for the detected glints indicate behaviors that are very similar to those in earlier studies. For example, oxygen A-band histograms over ocean suggest that just under two-thirds (≈64%) of blue glints come from the ocean surface, very close to the 60% indicated by Figure 2A of Várnai et al. (2020a). Over land, the histogram of blue glint oxygen A-band ratios ($R_{764\ \mathrm{nm}}/R_{780\ \mathrm{nm}}$) peaked at 0.36—close to 0.37 peak in Figure 3A of Marshak et al. (2017) that suggested typical cloud altitudes around 5–8 km. Further analysis [considering the EPIC cloud product (Yang et al., 2019) as well] is expected to yield more details about the altitude and temperature of clouds producing glints. (We note that studying blue glints appears most promising, as the location of these glints are least likely to be affected by cloud glints at the wavelengths used by the EPIC cloud product.) In addition, EPIC visible reflectances could help estimate reflectance enhancements caused by glints (Várnai et al., 2020a; Várnai et al., 2020b) and from this, the fraction of horizontally oriented ice crystals in ice clouds. Other collocated datasets—for example global reanalyses or cloud products from satellites that view the glint area from directions not affected by glint—could help identify conditions favoring the formation of horizontally oriented ice crystals and provide new information on the microphysical and radiative properties of ice clouds.

DATA AVAILABILITY STATEMENT

This paper discusses and analyzes publicly available datasets that can be obtained at https://asdc.larc.nasa.gov/project/DSCOVR/DSCOVR_EPIC_L2_GLINT_01.

AUTHOR CONTRIBUTIONS

TV developed the presented glint detection algorithm and performed the data analysis. AM helped in the algorithm development and participated in data analysis. AK participated in the data analysis. All authors contributed to the writing and editing of the manuscript.

FUNDING

This work was supported in part by the NASA DSCOVR Project and in part by the National Science Foundation (NSF) under Grant AGS-1639868.

PUBLISHER'S NOTE

ACKNOWLEDGMENTS

We thank Marshall Sutton and the Atmospheric Science Data Center at the NASA Langley Research Center for incorporating the glint detection code into the operational processing of DSCOVR data.

REFERENCES

Bréon, F.-M., and Dubrulle, B. (2004). Horizontally Oriented Plates in Clouds. *J. Atmos. Sci.* 61, 2888–2898. doi:10.1175/jas-3309.1

Bréon, F. M., and Henriot, N. (2006). Spaceborne Observations of Ocean Glint Reflectance and Modeling of Wave Slope Distributions. *J. Geophys. Res.* 111, C06005. doi:10.1029/2005JC003343

Chepfer, H., Brogniez, G., Goloub, P., Bréon, F. M., and Flamant, P. H. (1999). Observations of Horizontally Oriented Ice Crystals in Cirrus Clouds with POLDER-1/ADEOS-1. *J. Quantitative Spectrosc. Radiative Transfer* 63, 521–543. doi:10.1016/S0022-4073(99)00036-9

Cox, C., and Munk, W. (1954). Measurement of the Roughness of the Sea Surface from Photographs of the Sun's Glitter. *J. Opt. Soc. Am.* 44, 838–850. doi:10.1364/JOSA.44.000838

Crawford, F. (1968). *Waves, Berkeley Physics Course, 3*. Berkeley, CA, USA: McGraw-Hill.

Feng, L., Hu, C., Barnes, B. B., Mannino, A., Heidinger, A. K., Strabala, K., et al. (2017). Cloud and Sun-glint Statistics Derived from GOES and MODIS Observations over the Intra-Americas Sea for GEO-CAPE mission Planning. *J. Geophys. Res. Atmos.* 122, 1725–1745. doi:10.1002/2016JD025372

Katz, J. I. (1998). Subsuns and Low Reynolds Number Flow. *J. Atmos. Sci.* 55, 3358–3362. doi:10.1175/1520-0469(1998)055<3358:salrnf>2.0.co;2

Kaufman, Y. J., Tanré, D., Gordon, H. R., Nakajima, T., Lenoble, J., Frouin, R., et al. (1997). Passive Remote Sensing of Tropospheric Aerosol and Atmospheric Correction for the Aerosol Effect. *J. Geophys. Res.* 102, 16815–16830. doi:10.1029/97JD01496

Kikuchi, M., Okamoto, H., and Sato, K. (2021). A Climatological View of Horizontal Ice Plates in Clouds: Findings from Nadir and Off-Nadir CALIPSO Observations. *Geophys. Res. Atmos.* 126, e2020JD033562. doi:10.1029/2020JD033562

Knobelspiesse, K., Ibrahim, A., Franz, B., Bailey, S., Levy, R., Ahmad, Z., et al. (2021). Analysis of Simultaneous Aerosol and Ocean Glint Retrieval Using Multi-Angle Observations. *Atmos. Meas. Tech.* 14, 3233–3252. doi:10.5194/amt-14-3233-2021

Können, G. P. (2017). Rainbows, Halos, Coronas and Glories: Beautiful Sources of Information. *Bull. Amer. Meteorol. Soc.* 98, 485–494. doi:10.1175/BAMS-D-16-0014.1

Kostinski, A., Marshak, A., and Várnai, T. (2021). Deep Space Observations of Terrestrial Glitter. *Earth Space Sci.* 8, e2020EA001521. doi:10.1029/2020EA001521

Li, J.-Z., Fan, S., Kopparla, P., Liu, C., Jiang, J. H., Natraj, V., et al. (2019). Study of Terrestrial Glints Based on DSCOVR Observations. *Earth Space Sci.* 6, 166–173. doi:10.1029/2018EA000509

Lin, Z., Li, W., Gatebe, C., Poudyal, R., and Stamnes, K. (2016). Radiative Transfer Simulations of the Two-Dimensional Ocean Glint Reflectance and Determination of the Sea Surface Roughness. *Appl. Opt.* 55, 1206–1215. doi:10.1364/ao.55.001206

Lynch, D. K., Gedzelman, S. D., and Fraser, A. B. (1994). Subsuns, Bottlinger's Rings, and Elliptical Halos. *Appl. Opt.* 33, 4580–4589. doi:10.1364/AO.33.004580

Lynch, D. K., and Livingston, W. (2001). *Color and Light in Nature*. Cambridge, U.K.: Cambridge Univ. Press.

Marshak, A., Herman, J., Adam, S., Karin, B., Carn, S., Cede, A., et al. (2018). Earth Observations from DSCOVR EPIC Instrument. *Bull. Amer. Meteorol. Soc.* 99, 1829–1850. doi:10.1175/BAMS-D-17-0223.1

Marshak, A., Várnai, T., and Kostinski, A. (2017). Terrestrial Glint Seen from Deep Space: Oriented Ice Crystals Detected from the Lagrangian point. *Geophys. Res. Lett.* 44, 5197–5202. doi:10.1002/2017GL073248

Noel, V., and Chepfer, H. (2010). A Global View of Horizontally Oriented Crystals in Ice Clouds from Cloud-Aerosol Lidar and Infrared Pathfinder Satellite Observation (CALIPSO). *J. Geophys. Res.* 115, D00H23. doi:10.1029/2009JD012365

Noel, V., and Chepfer, H. (20042004). Study of Ice crystal Orientation in Cirrus Clouds Based on Satellite Polarized Radiance Measurements. *J. Atmos. Sci.* 61, 2073–2081. doi:10.1175/1520-0469(2004)061<2073:soicoi>2.0.co;2

Ottaviani, M., Knobelspiesse, K., Cairns, B., and Mishchenko, M. (2013). Information Content of Aerosol Retrievals in the Sunglint Region. *Geophys. Res. Lett.* 40, 631–634. doi:10.1002/grl.50148

Remer, L. A., Kaufman, Y. J., Tanré, D., Mattoo, S., Chu, D. A., Martins, J. V., et al. (2005). The MODIS Aerosol Algorithm, Products, and Validation. *J. Atmos. Sci.* 62, 947–973. doi:10.1175/JAS3385.1

Várnai, T., Kostinski, A. B., and Marshak, A. (2020a). Deep Space Observations of Sun Glints from marine Ice Clouds. *IEEE Geosci. Remote Sensing Lett.* 17, 735–739. doi:10.1109/LGRS.2019.2930866

Várnai, T., Marshak, A., and Kostinski, A. B. (2020b). Deep Space Observations of Cloud Glints: Spectral and Seasonal Dependence. *IEEE Geosci. Remote Sensing Lett.* , 1–5. doi:10.1109/LGRS.2020.3040144

Wang, M., and Bailey, S. W. (2001). Correction of Sun Glint Contamination on the SeaWiFS Ocean and Atmosphere Products. *Appl. Opt.* 40, 4790–4798. doi:10.1364/ao.40.004790

Yang, Y., Meyer, K., Wind, G., Zhou, Y., Marshak, A., Platnick, S., et al. (2019). Cloud Products from the Earth Polychromatic Imaging Camera (EPIC): Algorithms and Initial Evaluation. *Atmos. Meas. Tech.* 12, 2019–2031. doi:10.5194/amt-12-2019-2019

Zhou, C., Ping Yang, P., Dessler, A. E., and Faming Liang, F. (2013). Statistical Properties of Horizontally Oriented Plates in Optically Thick Clouds from Satellite Observations. *IEEE Geosci. Remote Sensing Lett.* 10, 986–990. doi:10.1109/LGRS.2012.2227451

APPENDIX DESCRIPTION OF GLINT PRODUCT FILES

The operational EPIC glint product generated by the method described above is publicly available at the NASA Atmospheric Science Data Center (ASDC) at https://eosweb.larc.nasa.gov. There is a separate glint product file for each individual EPIC image, with each file containing three parameters for each pixel: Surface type, glint angle, and glint mask.

- The surface type flag shows whether the area of a pixel is covered mainly by water (value = 0), desert (value = 2), or non-desert land (value = 1)
- The glint angle tells how favorable the EPIC view direction is for glint detection and can help in using glints for inferring scene properties.
- The glint mask indicates whether or not glint has been detected (1 = glint, 0 = no glint).

We mention that while the surface type flag is provided in a 2-D array that (matching the EPIC image size) contains 2048 rows and 2048 columns, the glint angle and glint mask values are provided in 3-D arrays containing 2048 rows, 2048 columns, and three layers (one layer for each of the blue, green, and red spectral bands). In order to reduce the data volume by enabling a more effective file compression, the values of all parameters are set to −1 for pixels where glint detection is not attempted as the glint angle exceeds 2°.

Conflict of Interest: The authors declare that the research was conducted in the absence of any commercial or financial relationships that could be construed as a potential conflict of interest.

ORIGINAL RESEARCH
published: 24 January 2022
doi: 10.3389/frsen.2021.765913

Radiometric Stability Assessment of the DSCOVR EPIC Visible Bands Using MODIS, VIIRS, and Invariant Targets as Independent References

Conor Haney[1*], David R. Doelling[2], Wenying Su[2], Rajendra Bhatt[2], Arun Gopalan[1] and Benjamin Scarino[1]

[1] *Science Systems and Applications, Inc., Hampton, VA, United States*
[2] *NASA Langley Research Center, Hampton, VA, United States*

Edited by:
Alexander Marshak, National Aeronautics and Space Administration, United States

Reviewed by:
Gerhard Meister, National Aeronautics and Space Administration (NASA), United States
Igor Geogdzhayev, Columbia University, United States

**** Correspondence:** Conor Haney, conor.o.haney@nasa.gov*

***Specialty section:** This article was submitted to Satellite Missions, a section of the journal Frontiers in Remote Sensing*

***Received:** 27 August 2021*
***Accepted:** 11 November 2021*
***Published:** 24 January 2022*

***Citation:** Haney C, Doelling DR, Su W, Bhatt R, Gopalan A and Scarino B (2022) Radiometric Stability Assessment of the DSCOVR EPIC Visible Bands Using MODIS, VIIRS, and Invariant Targets as Independent References. Front. Remote Sens. 2:765913. doi: 10.3389/frsen.2021.765913*

The DSCOVR mission was designed to take advantage of the first Lagrangian position (L1) to continuously observe the Earth sunlit disk. To facilitate EPIC V03 data product validation and fusion, the EPIC V03 navigation and calibration stability is assessed. The Aqua-MODIS, NPP-VIIRS, and N20-VIIRS based radiometric scaling factors are also provided. The V03 navigation error was 15.5 km, a 50% improvement over V02 and within what can be achieved by an objective image alignment algorithm. Both the navigation accuracy and precision were improved in V03 and were found to be comparable across all EPIC visible channels. The all-sky tropical ocean and deep convective cloud ray-matched MODIS- and VIIRS-referenced EPIC inter-calibration gains are within 0.4% of one-another, and are also within 0.4% of a previous study's NPP-VIIRS-referenced gains. The inter-calibration study reveals that EPIC bands 5 and 6 degraded mostly within the first year of operation and becoming stable thereafter, whereas bands 7 and 10 were stable during the 6-years record. The capability of the V03 navigation allowed EPIC stability to be monitored using DCC and Libya-4 invariant targets. The EPIC V03 calibration was mostly stable within 0.3% over the 6-years record, as determined from inter-calibration and invariant target monitoring methods. Remarkably, both the DCC- and Libya-4-based methods were able to confirm the stability of the E-8 and E-9 oxygen absorptions—a stability comparable to that of the E-7 and E-10 reference bands. No significant change in the navigation accuracy or calibration stability was observed after the DSCOVR 2019 safe mode incident. The impressive stability of the DSCOVR EPIC L1B V03 channel radiances can greatly benefit the Earth remote sensing community by providing diurnally complete daytime radiative flux and environmental retrievals for future sensors located at L1.

Keywords: DSCOVR/EPIC, MODIS, VIIRS, calibration, DCC, Libya-4

INTRODUCTION

The Deep Space Climate Observatory (DSCOVR), launched on February 11, 2015, orbits the first Lagrange point (L1)—about 1.5 million km from the Earth in roughly the direction of the Sun. This orbit location allows the DSCOVR satellite instruments to have unique views of both the Sun and the Earth. The Earth Polychromatic Imaging Camera (EPIC) is an Earth-facing instrument on DSCOVR that has a constant view of the sunlit side of the Earth, almost entirely in the backscattering direction (Marshak et al., 2018).

The EPIC sensor images the Earth between 10 and 22 times during a 24-h interval using a CCD array. A filter wheel allows the EPIC sensor to observe the Earth at 10 different narrow spectral channels ranging from the UV to the NIR. These channels lead to formulation of various Level-2 products that enable investigation of aerosols, ozone, clouds, vegetation, volcanic SO_2, and glint (Marshak et al., 2018). The diurnal sampling capability of EPIC allows for more robust daily averaged retrievals compared to the capabilities of single daytime sun-synchronous, low Earth orbit (LEO) instruments such as the MODerate Resolution Imaging Spectroradiometer (MODIS) and Visible Infrared Imaging Radiometer Suite (VIIRS). This advantage is especially important for maritime stratus regions where morning clouds often dissipate by the afternoon, or for afternoon convective monitoring over land where morning clear skies transition to thunderstorms in the late afternoon. Furthermore, the EPIC diurnally derived broadband shortwave fluxes are consistent with the geostationary imager based broadband SW fluxes derived for the CERES SYN1deg product (Su et al., 2018).

The EPIC retrievals are validated against coincident MODIS and VIIRS (M/V) retrievals. To compare the EPIC with M/V retrievals, the EPIC channel radiances must be radiometrically scaled against the M/V L1B calibration reference. The M/V L1B calibrated radiances are referenced to their onboard solar diffusers and are not radiometrically scaled with one another. For some visible bands, the NPP-VIIRS and N20-VIIRS calibrated radiances can differ by 3% (Uprety and Cao, 2020; Moyer et al., 2021; Mu et al., 2021; Wu et al., 2020). The future CLARREO Pathfinder instrument will provide an absolute calibration reference in space with which the EPIC sensor calibration can be anchored to (Wielicki et al., 2013; Shea et al., 2020). Until an absolute calibration reference in space is realized, EPIC visible channel calibration coefficients for Aqua-MODIS, NPP-VIIRS, and N20-VIIRS are needed for data fusion and are provided for in this study.

In this study, we aim to complete the EPIC V03 navigation assessment initiated by Doelling et al., 2019, which aligned the EPIC coincident images with the well-navigated M/V images. The assessment utilized 2 days of EPIC R06 data, the precursor to EPIC V03, and found that the navigation was an improvement over V02. This refinement in navigation resulted from the improved geolocation and CCD array flatfielding accuracy in V03 (Kostinski et al., 2021). This furthered study also provides a calibration stability assessment of the EPIC sensor, which does not contain any onboard

calibration systems. Two independent inter-calibration approaches are utilized that rely on coincident ray-matched radiance pairs. The first method remaps the coincident EPIC and M/V pixel-level radiances over all-sky tropical ocean (ATO-RM) and inter-calibrates the angular matched radiance pairs. The second method utilizes only ray-matched deep convective cloud (DCC-RM) targets to inter-calibrate M/V with EPIC. Agreement between the two independent inter-calibration methodologies and the recently published Geogdzhayev et al. (2021) EPIC calibration coefficients should not only ensure robust EPIC calibration coefficients, but also lend confidence to the capability of the calibration methods. Particular attention is given to determine if there were any EPIC calibration discontinuities experienced during the DSCOVR spacecraft safe mode incident between June 2019 and February 2020.

With the anticipated EPIC V03 navigation improvement, we attempt to apply a Pseudo Invariant Calibration Site (PICS) or Earth invariant target approach to monitor the stability of EPIC visible bands. PICS are widely used amongst satellite calibration teams for monitoring the onboard calibration systems, because the method simply relies on a stable Earth target rather than on concurrent sensors, thereby avoiding sensor-embedded calibration drifts. The DCC and Libya-4 invariant target (IT) methodologies were chosen to assess the stability of the EPIC visible channels. Sun-synchronous sensor based invariant target methodologies were modified for consideration of the random local time sampling of the EPIC images over the invariant target. The DCC-IT and Libya-4 stability results are verified with the ATO-RM and DCC-RM stability assessment.

Methodology section describes the EPIC, MODIS, and VIIRS datasets, the navigation accuracy assessment strategy, the ATO-RM and DCC-RM methodologies, and the DCC-IT and Libya-4 invariant target approaches. The EPIC calibration coefficient formulas that describe the EPIC sensor degradation are also discussed in *Methodology* section. *Results* section provides the EPIC V03 navigation assessment. The Aqua-MODIS, NPP-VIIRS, and N20-VIIRS referenced EPIC calibration coefficients and comparison with the Geogdzhayev et al. (2021) coefficients are likewise found in *Results* section. The Libya-4 and DCC invariant target results and overall EPIC stability assessment finishes *Results* section. *Conclusions* section contains the summary.

METHODOLOGY

Data

The EPIC L1B data were obtained from the NASA Langley Atmospheric Science Data Center Distributed Active Archive Center (ASDC DAAC). Both EPIC V03 (July 2015–February 2020) and V02 (July 2015–July 2019) are used in this study. EPIC V02 data is only available up until the safe mode incident, whereas the V03 data was processed from the beginning of the record and continues after the safe mode event. The EPIC imager employs a filter wheel to observe the Earth in 10 reflective solar band channels using the same CCD array. The first four bands are UV channels and are not evaluated in this study. The remaining visible bands are utilized and are listed in Table 1. The EPIC imager requires ~7 min to step through all 10 channels. The CCD array nominal pixel resolution is ~8-km. To facilitate data transmission, the pixel resolution is degraded by a factor of 2, except for band 5. The EPIC image is geo-rectified onto a common latitude and longitude 2048 by 2048 (8-km nominal resolution) grid for all 10 bands. The view and solar angles are based on the measurement time. For convenience, the EPIC observed photon (12-bit) counts sec^{-1} are simply referred to as *counts* in this manuscript.

TABLE 1 | EPIC, MODIS, and VIIRS band nomenclature used for this study (ID), and wavelength center and width (FWHM) in nm obtained from https://avdc.gsfc.nasa.gov/pub/DSCOVR/EPIC_NISTAR_Documents/DSCOVR-EPIC-Description.pdf, https://modis.gsfc.nasa.gov/sci_team/meetings/199310/presentations/x153_refl_bands.pdf, and https://ladsweb.modaps.eosdis.nasa.gov/missions-and-measurements/viirs/. The bands are listed by increasing wavelength.

EPIC			Aqua-MODIS			NPP/N20-VIIRS		
Band ID	Center (nm)	Width (nm)	Band ID	Center (nm)	Width (nm)	Band ID	Center (nm)	Width (nm)
E-5	443	3	M_{Aq}-3	469	20	M3	490	20
E-6	551	3	M_{Aq}-4	555	20	M4	555	20
E-7	680	2	M_{Aq}-1	645	50	I1	640	75
	—	—	—	—	—	M5	673	21
E-8	687.75	0.8	—	—	—	—	—	—
E-9	764	1	—	—	—	—	—	—
E-10	779.5	2	—	—	—	—	—	—
	—	—	M_{AQ}-2	858.5	35	M7	865	39

The L1B MODIS data used in this study are from Aqua-MODIS Collection 6.1 (C6.1), which have a nominal resolution of 1 km. For VIIRS L1B, the Suomi-NPP and N20 NASA Land Science Investigator-led Processing System (LandSIPS) data are used. The NPP-VIIRS data are from

Collection 1, and the N20-VIIRS data are from Collection 2. The M bands are observed at a 750-m nominal resolution, whereas the I band resolution is 375 m. The I band pixel reflectances are first aggregated into the M band resolution. The M/V pixels are subsampled at 2 and 1.5 km, respectively, for this study. The M/V bands utilized in this study are listed in Table 1 along with their respective EPIC band pairings. Note that the EPIC band 10 (0.780 μm) is paired with both the M/V 0.65-μm and 0.86-μm channels because most M/V based retrievals rely on the 0.86-μm band rather than their equivalent VIIRS M6 (0.746 μm) or MODIS B15 (0.748 μm) counterparts. MODIS band 2 (0.865 μm) is not utilized in this study, because both the ATO-RM and DCC-RM methods are adversely impacted by the MODIS band 2 saturated measurements over very bright targets.

Table 1 defines the sensor band nomenclature used in this study. EPIC bands are defined by a prefix of E, for example, E-5 for EPIC band 5. The Aqua MODIS bands are designated by a prefix of M_{Aq} followed by the MODIS band number, for example, M_{Aq}-1 is Aqua MODIS band 1. The NPP-VIIRS and N20-VIIRS bands are denoted by V_{NPP} and V_{N20}, respectively, and followed by their respective I or M band numbers, such as V_{NPP}-I1 or V_{N20}-I1. Table 1 shows the band center wavelengths and their respective band widths. Note the very narrow EPIC bands compared with their respective M/V bands. The VIIRS M5 band is also narrower than the corresponding I1 band.

EPIC Navigation

Unlike near-Earth sensors, aligning the EPIC CCD array onto the Earth and computing the pixel coordinates from the sensor pointing vector is very challenging given the DSCOVR distance from Earth. Even after focused study to rectify, residual navigation errors still remain in V03 and need to be evaluated. An automated EPIC image geolocation correction algorithm was developed to mitigate spatial discrepancies when inter-calibrating coincident EPIC and M/V images (Haney et al., 2016 and Doelling et al., 2019). The image geolocation correction algorithm also evaluates the EPIC navigation accuracy. The navigation accuracy is limited by the 0.25° latitude by longitude spatial resolution used to shift the underlying EPIC image. Because the EPIC and M/V inter-calibration events occur mostly at the center, i.e., near the sub-satellite point, of the EPIC image, the navigation accuracy results are only valid near the EPIC sub-satellite domain.

A detailed description of the geolocation correction algorithm is found in Haney et al. (2016) and is briefly summarized here. For a given EPIC image, coincident (within 15-min) M/V granules within ±30° in latitude from the equator are identified. The 5-min MODIS or 6-min VIIRS granule pixel-level reflectances are gridded into a 0.25° latitude by longitude grid. The associated EPIC image pixel counts are similarly gridded. For each M/V granule, the EPIC grid is shifted by ±5 grid cells in both the East-West and North-South direction. For each of the 121 EPIC grid shifts, the M/V reflectance and EPIC grid cell count pairs are linearly regressed and the square of the Pearson correlation coefficient (R^2) is noted. The grid shift with the largest R^2 value is considered the optimal navigation correction. The process is repeated with the remaining coincident M/V granules in the EPIC domain. The navigation correction algorithm is best suited for images with contrasting features such as coastlines and cloud boundaries.

ATO-RM

The all-sky tropical ocean ray-matching inter-calibration methodology follows closely that described in Doelling et al. (2019). The advantage of ATO-RM methodology is that it compares the full Earth-viewed visible radiance dynamic range between sensors. The 15-min coincident aligned EPIC counts with M/V gridded reflectances (from *EPIC Navigation*) are first aggregated into a 0.5° grid (note that gridding in this manner may reduce the visible dynamic range). A relative to the mean grid cell standard deviation threshold of 70% is applied based on the imager pixel reflectances to mitigate the impact of 1) heterogeneous scenes, 2) cloud spatial shifts due to the time matching differences, and 3) any residual EPIC navigation errors. Grid cells located over ocean glint and land are avoided. The EPIC and M/V view zenith angle (VZA), relative azimuthal angles (RAZ), and scattering angles are matched within 15°. A graduated angle matching (GAM) approach is applied, which further restricts the angle matching over dark scenes that exhibit anisotropic behavior, while maintaining the initial angle matching for the more Lambertian bright scenes (Doelling et al., 2016). The first quartile of the visible dynamic range requires the VZA and RAZ to be matched within 5°, while the second quartile requires them to be within 10°. The 15° angle matching is retained for the 3rd and 4th quartiles. The M/V reflectances are adjusted to the EPIC SZA by the ratio of the EPIC and M/V cosine SZA (μ_0) as shown in Eq. 1 for MODIS.

$$Ref_{MODIS} \times \left(\frac{\mu_{0EPIC}}{\mu_{0MODIS}} \right) \times d^{-2} \times SBAF_{EPIC/MODIS} = gain \times Count_{EPIC} \quad (1)$$

An ATO, reflectance-based 2nd order spectral band adjustment factor (SBAF) based on the Scanning Imaging Absorption Spectrometer for Atmospheric Chartography (SCIAMACHY) hyper-spectral radiances is applied to the M/V channel reflectances to mitigate the impact of the spectral band differences (Bovesmann et al., 1999; Scarino et al., 2016). The ATO-RM EPIC channel counts and LEO imager reflectance pairs are then linearly regressed monthly. Any EPIC count and imager reflectance pairs that are outside of 4 × the linear regression standard error are removed as a way of avoiding any residual mis-navigated pairs. Figure 1A shows the ATO-RM E-7 and V_{NPP}-I1 reflectance pair scatter plot for May 2020. The linear regression through the space offset or EPIC count of zero (referred to as the force fit) is used to compute the monthly gain. The corresponding linear regression offset is -352, which is very close to the assumed space count of zero in relation to the large dynamic range of EPIC counts (Figure 1A). The tightly aligned dark reflectance pairs and the increased scatter about the bright pairs in Figure 1A are a result of the GAM methodology.

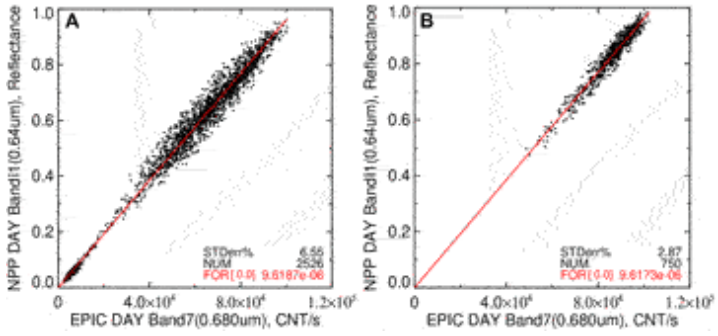

FIGURE 1 | The **(A)** ATO-RM and **(B)** DCC-RM E-7 count and V_{NPP}-I1 reflectance pair scatter plots for May 2020 with associated linear regression (solid red line). The number of pairs (*NUM*), standard error (*STDerr%*), and linear regression slope through an offset of 0 (*FOR*) in count^{-1} or gain (Eq. 1) is given in the lower right.

Imager Calibration Drift Mitigation

Because ATO ray-matching utilizes contemporaneous observations between the EPIC and LEO imagers, it is essential that all LEO imager drifts are removed prior to performing the stability assessment of the EPIC channels.

We performed independent assessments of the MODIS and VIIRS L1B calibration stability using the DCC and Saharan Desert invariant targets (Doelling et al., 2013; Bhatt et al., 2014). During 2015–2021, both MODIS instruments' visible bands calibration in C6.1 L1B radiances were found stable, except for some embedded residual scan-angle dependencies remaining near the end of the MODIS cross-track scans (Bhatt et al., 2019). Similarly, noticeable temporal calibration drifts were observed in some of the reflective solar bands L1B radiances for the two VIIRS instruments. The NPP-VIIRS C1 data shows a positive trend of ~0.6% in the I1 band from 2012 through 2018. During April 2018, a LUT update was implemented to make the record post-April 2018 more stable and consistent with that of 2012. As such, there is a ~0.6% discontinuity between the pre- and post-April 2018 NPP-VIIRS data in C1. The newly released C2 of NPP-VIIRS data from NASA LandSIPS has a consistent calibration LUT implemented across the full record and is believed to have these drifts corrected in the L1B radiances. Figure 2A shows the V_{NPP}-I1-based E-7 monthly gains plotted over the EPIC record. As expected, the gain (open circles) appears to decrease over time due to the VIIRS LUT update during April 2018. The I1 band radiances from N20-VIIRS C2 data were also found to have a minor downward temporal trend of ~0.6% over the 3-year period. As such, the V_{N20}-I1-based E-7 monthly gains also show a downward trend (Figure 2B). The presence of these drifts in the VIIRS L1B products was confirmed with the VIIRS Characterization and Support Team at Goddard Space Flight Center. The time-dependent magnitudes of these temporal drifts were characterized based the DCC invariant target analysis. Correction factors were derived from the DCC-based drift analysis and were applied to stabilize the ATO-RM VIIRS radiances prior to computing the EPIC monthly gains from the ATO-RM data. The filled circles in Figure 2 shows both the V_{NPP}-I1 and V_{N20}-I1 based E-7 monthly gains after applying the drift correction —revealing a near stable record.

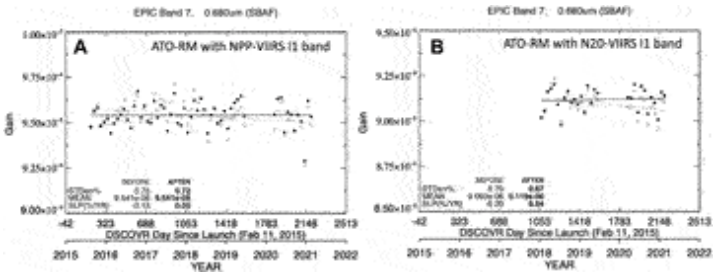

FIGURE 2 | (A) The ATO-RM E-7/V_{NPP}-I1 monthly gains and associated linear trend line before (open circles and dotted line) and after (filled circles and solid line) V_{NPP}-I1 drift-corrected reflectances. The EPIC gain is in count^{-1}. The before and after standard error (*STDerr%*), mean, and linear trend [*SLP* (*%/yr*)] are located in the lower left corner. **(B)** Same as **(A)** but for N20-VIIRS based monthly gains for E-7.

DCC-RM

The deep convective cloud ray-matching (DCC-RM) methodology relies on very bright TOA tropical targets that are nearly spectrally flat (for wavelengths <1 μm) and nearly isotropic for SZA and VZA conditions less than 40°. The DCC-RM inter-calibration has increased signal to noise, reduced SBAF uncertainty, and allows for greater angle matching tolerance compared with those of the ATO-RM approach. The EPIC DCC-RM is outlined in Doelling et al. (2019) and is summarized here. The *EPIC Navigation* section coincident angle matched EPIC and M/V-aligned 0.25° gridded radiances are identified as DCC targets if their corresponding M_{Aq}-31 or $V_{NPP/N20}$-M15 11 μm BT measurements are less than 220 K. A visible and IR spatial homogeneity threshold of 5% and 2.5 K based on the relative standard deviation of the M/V pixel values within the 0.25° grid cell is applied. Unlike the ATO-RM, the DCC-RM includes ocean and land grid cells. The approximate DCC linear regression SBAF (Scarino et al., 2016) is applied to the M/V drift-corrected (*Imager Calibration Drift Mitigation*) and EPIC SZA-adjusted channel reflectances (Eq. 1). The EPIC count and LEO channel reflectance pairs are linearly regressed monthly through the space count of zero and a 4 × standard error outlier filter is applied. Figure 1B shows the DCC-RM E-7 count and V_{NPP}-I1 reflectance pair scatter plot for May 2020, which can be compared with the corresponding ATO-RM plot in Figure 1A. Both methods provide a nearly identical force fit result (within 0.1%). As expected, there are fewer DCC-RM reflectance pairs compared

with ATO-RM given that only 0.3% of the tropics contain DCC (Hong et al., 2005).

DCC Invariant Target Methodology

The DCC-IT methodology was formulated in the ground-breaking work of Hu et al. (2004). The EPIC DCC-IT calibration method is based on the Doelling et al. (2011) and Doelling et al. (2013) DCC-IT methodology, which relies on the fact that when the large ensemble of DCC-identified pixel TOA reflectances are analyzed collectively, they behave as an invariant target. The DCC-IT methodology has been well established in the calibration community and is used to monitor the onboard calibration of M/V (Doelling et al., 2013; Bhatt et al., 2014; Mu et al., 2017; Angal et al., 2018; Wang and Cao 2015; Wang and Cao 2020). The methodology has been further developed and utilized for this study for daily monitoring, which requires increased DCC sampling than needed by monthly monitoring methods (Doelling et al., 2021). The EPIC DCC-IT methodology relies on the DCC-RM spatially matched, but not necessarily angle matched, EPIC with M/V coincident images, including necessary 11 μm BT information (see *DCC-RM* section). Typically, for high pixel resolution (~1 km) imagers, a BT threshold of 205 K is used to identify DCC pixels. Furthermore, a homogeneity filter of 1 K (IR) and 3% (visible) based on the 8 surrounding M/V pixels is effective in filterering out the less bright anvil pixels (Doelling et al., 2013). Due to the low pixel resolution, any 0.25° grid cell with a M/V BT less than 220 K is utilized. Applying homogeneity filters would severely limit the sample size required by the large ensemble methodology. As such, no homogeneity thresholds are applied. The SZA and VZA thresholds are expanded to 60°. Because the matched EPIC images are tied to the 13:30 local sampling time of Aqua, NPP, and N20 sun-synchronous satellites, the diurnal-dependent DCC lifecycle over land is not aliased into the DCC reflectance. The individual DCC-identified grid cell counts are corrected for both overhead Sun conditions by dividing by the cosine of the SZA and by the Earth-Sun distance as follows.

$$DCC_{count} = \frac{Count_{EPIC} \times d^2}{\mu_{0EPIC}} \qquad (2)$$

The monthly frequency probability density function (PDF) of E-7 DCC_{counts} are shown in Figure 3A. Each month contains between 20 k and

100 k DCC_{count}. The monthly PDF shapes are fairly consistent over the record. Typically for high pixel resolution sensors, the monthly PDF mode DCC_{count} is tracked over time. However, for EPIC, the PDF peak is not well defined and the monthly PDF mode DCC_{count} is very noisy. The application of the Hu et al. (2004) DCC bidirectional reflectance distribution function (BRDF) model did not enhance the PDF peak. A future empirical EPIC DCC BRDF model based on the first 3-years of EPIC DCC_{count} may reduce the PDF mode noise and enhance the peak. Since the PDF mean is more stable than the mode, the PDF mean DCC_{count} is used to monitor the sensor stability. Figure 3B shows the monthly DCC_{count} over the EPIC record. The DCC_{count} response shows a distinct seasonal cycle. The DCC_{count} is deseasonalized using the ratio-to-moving average method as described in Bhatt and Wu (2017). The deseasonalization process is a multi-step procedure where a monthly seasonal index (SI) is first computed from the average relative ratio between an individual month DCC response and a 12-months centered running mean. The monthly DCC responses are then divided by the month-specific SI value to yield a deseasonalized DCC timeseries. The ratio-to-moving average method requires at least two complete years of data to compute monthly SI, and leaves intact any drift in the time series. The deseasonalized DCC_{count} values are also shown in Figure 3B. The deseasonalized E-7 record linear trend standard error was reduced by 20% from 1.54 to 1.23%. Deseasonalization also reduced the linear trend from -0.04%/yr to -0.01%/yr because the monthly gain variation at the beginning and end of the record may have impacted the trend.

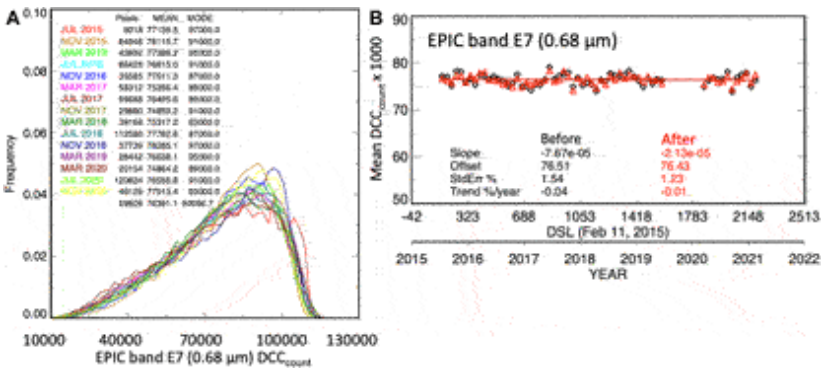

FIGURE 3 | (A) The July, November, and March over the EPIC record monthly probability density functions (PDF) of the E-7 DCC_{count} (Eq. 2). The number of monthly DCC identified grid cells (*Pixels*), mean DCC_{count} (*MEAN*), and PDF mode DCC_{count} (*MODE*) statistics are located in the upper left corner. The monthly PDF lines are color coordinated with the month and year column of the statistics. **(B)** The DCC E-7 monthly mean DCC_{count} and associated linear trend line before (black open circles and line) and after (red open triangles and line) deseasonalization. The linear regression slope (DCC_{count}/day), offset, mean DCC_{count}, standard error (*STDerr%*), and linear trend are located at the bottom of the plot.

Libya-4 Invariant Target Methodology

The Libya-4 desert site, center location at 28.55°N and 23.4°E, is a CEOS recommended Cal/Val site and is one of the most used PICS for calibration and stability monitoring (Cosnefroy et al., 1996; Teillet and Chander, 2010; Chander et al., 2013). Staylor and Suttles (1990) computed AVHRR calibration degradation using the Libyan desert based on a BRDF model developed by the Nimbus-7 ERB measurements. In other desert-based PICS studies, Teillet et al. (1990) used White Sands, NM to inter-calibrate the AVHRR and Landsat-TM sensors using a historical BRDF. Kaufman and Holben (1993) used an Egyptian desert PICS and Kogan et al. (1996) used several Saharan desert PICS to determine the AVHRR degradation. Cosnefroy et al. (1996) characterized multiple Saharan and Arabian deserts as potential PICS by their clear-sky frequency, temporal stability, and surface brightness, while Moulin et al. (1996) utilized four Saharan invariant desert targets to monitor and calibrate the geostationary Meteosat-2 sensor visible channel. Often the Libya-4 desert site was used to produce official AVHRR calibration coefficients (Rao et al., 1994; Rao and Chen, 1996; Rao et al., 1999). Furthermore, the sun-synchronous M/V sensor onboard calibration have been validated using Libya-4 (Doelling et al., 2015, Bhatt et al., 2014b. Uprety and Cao, 2015, Wu et al., 2016, Xiong et al., 2010b). Lastly, the

Libya-4 site is one of multiple PICS used to determine the MODIS response versus scan-angle (RVS) real-time corrections (Sun et al., 2014; Mu et al., 2018).

The Libya-4 region of interest (ROI) is 0.6° in latitude and longitude region centered at 28.55°N and 23.4°E. For a given EPIC image, the Libya-4 ROI center and 8 surrounding pixels counts are averaged and the relative standard deviation is computed. The EPIC sensor views the Libya-4 desert on daily basis. Unlike the set geostationary sensor imaging schedules, the EPIC images are not scanned at fixed GMT times. The EPIC PICS methodology cannot rely on an annually repeating daily angular observations to remove BRDF effects (Bhatt et al., 2014). Although the Libya-4 desert is sampled by EPIC several times a day, only the EPIC images observed between 10 and 12 GMT, which are closest to local noon (10:45 GMT) are utilized. Local noon images avoid the large SZA and VZA conditions observed near the terminator. Because occasional clouds can impact the Libya-4 TOA reflectance, only clear-sky conditions are utilized. A relative standard deviation homogeneity (sigma) threshold is used to delineate clear-sky and cloudy conditions. Figure 4A shows that most daily sigma values are less than 250 counts, which is the chosen threshold for identifying clear-sky conditions.

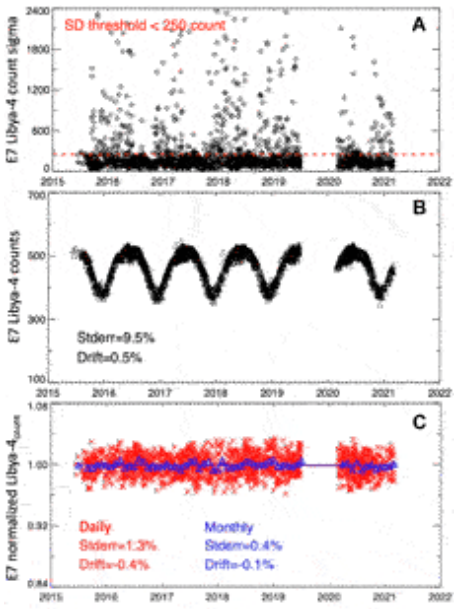

FIGURE 4 | (A) The EPIC E-7 (0.68 μm) daily standard deviation of the count of the Libya-4 ROI (0.6° in latitude and longitude region centered at 30°N and 30°E). The red dashed line represents a count value of 250. Counts below the red dashed line indicate clear-sky conditions. **(B)** The E-7 Libya-4 clear-sky daily counts. The linear regression standard error and trend (%/year) statistics are located in the lower left corner (trend line not shown). **(C)** The E-7 Libya-4_{count} daily (red x and red solid line) and monthly mean (blue open triangles and blue solid line) associated trend lines. The trend line standard error (*Stderr*) in % and drift in %/yr are given at the bottom of the plot.

Figure 4B shows a large seasonal cycle of the clear-sky daily E-7 Libya-4 counts over the EPIC record owed to the SZA seasonal variation. Because the DSCOVR orbit about L1 is not synchronized with the Earth's declination angle, the Libya-4 daily RAZ does not repeat annually (Marshak et al., 2018), and therefore a BRDF model is required to mitigate angular reflectance effects. The EPIC Libya-4 counts are first converted to scaled reflectance by adjusting for the Earth-Sun distance corrections and normalizing by the cosine of the SZA, as described in Eq. 2 for DCC pixels. A semi-empirical BRDF model is then constructed using the first 3-years of the EPIC scaled reflectance data over Libya-4, based on a linear combination of two kernel functions (Roujean et al., 1992). Due to the large range of angular conditions observed over the year, multiple BRDF models across the observed angular domain are constructed as follows: 6° VZA and SZA bins between 0° and 60°, and a single RAZ bin is defined between 165° and 180°. The multiple BRDF models are an improvement over a single BRDF model

covering the angular domain. The multiple BRDF models also account for seasonal variation of the atmosphere above the desert surface because the SZA is a function of time of year, where overhead Sun conditions are realized in summer and the oblique Sun in winter. Although the Sahara Desert has low humidity, the hot air temperature allows for greater atmospheric precipitable water (PW), which is exponentially dependent with temperature. Additionally, the multiple BRDF approach was successful in modeling anvil cloud top BRDF reflectance across the full range of SZA angles (Scarino et al., 2020).

The daily clear-sky Libya-4 observed scaled reflectances are divided by the predicted reflectances from the multiple BRDF models to derive normalized Libya-4 counts (Libya-4_{count}), which are shown in Figure 4C. The seasonal cycle is successfully removed after applying the multiple BRDF models. The daily linear trend standard error of daily E-7 normalized Libya-4_{count} is 1.3%. By averaging the daily Libya-4_{count} into monthly values, the linear trend drift and standard error are measured as 0.1 and 0.4% over the 6-years EPIC record. The remarkable Libya-4_{count} stability suggests that EPIC navigation accuracy is sufficient, the Libya-4 invariant target methodology is robust, and that Libya-4 reflectance is invariant over time.

EPIC Calibration Coefficients

Previous studies have used linear trends to describe the EPIC visible channel on-orbit degradation (Doelling et al., 2019; Geogdzhayev et al., 2021). The EPIC visible *gain* is tracked from the day since launch (*dsl*) of February 11, 2015 as follows:

$$gain = offset + slope \times dsl \qquad (3)$$

where the *offset* and *slope* are the linear regression coefficients. Figure 5A shows the E-5 (0.46 μm) gain linear trends, where the solid lines represent ATO-RM and the dashed lines represent DCC-RM, and the black, green, and red monthly gains are calibrated against Aqua, NPP, and N20, respectively. Note the consistency of the ATO-RM and DCC-RM linear trends given the independent ATO-RM and DCC-RM monthly gain variability. The N20 ATO-RM and DCC-RM E-5 linear gain trends seem more stable when compared with their Aqua and NPP counterparts. Herman et al. (2018) (their Figure 2) indicated that most of the EPIC degradation occurred during the

first year of operation for all UV channels. The shorter wavelength EPIC UV channels showed more degradation than the longer wavelength UV channels. To determine if the E-5 early record degradation was greater than the later record, the 2015–2017 and the 2018–2021 linear trends were computed and are shown in Figure 5B. The 2018 breakpoint (Figure 5B vertical blue line) coincides with the beginning of the N20 record. The 2015–2017 Aqua and NPP based ATO-RM linear trend E-5 gains were 0.48%/yr and 0.45%/yr, respectively, whereas the 2018–2021 linear trend gains were 0.04%/yr and 0.10%/yr, respectively, which represents a reduction of ~75%, becoming more in line with the N20 linear trend gain of -0.02%/yr. In this study, the early record temporal trends are evaluated for statistical significance at 95% confidence level using the approach described by Weatherhead et al., 1998. According to Eq. 3 from Weatherhead et al. (1998), the minimum detectable trend for a given timeseries is governed by the length of the record, noise about the trend, and the autocorrelation of the monthly gains. Detection of smaller-magnitude trends requires a lower standard error and longer record length. For E-5, the Aqua and NPP ATO-RM linear trend standard error is less than the DCC-RM standard error (Figure 5A), indicating that the ATO-RM trends are able to confidently detect smaller-magnitude trends over the same record length. The Aqua and NPP ATO-RM linear trends are 0.14%/yr and 0.18%/yr, respectively, and have exceeded the corresponding minimum detectable trend values of 0.11%/yr and 0.10%/yr, respectively, based on the Weatherhead statistics. The observed trends exceed the minimum detectable trend thresholds, thereby, proving their statistical significance. Similarly, prior to 2018 (Figure 5B), the Aqua and NPP ATO-RM linear trends were found to be significant, whereas the post-2018 trends were found to be insignificant. This indicates that the E-5 degradation found in the overall trend was realized prior to 2018. For E-6, the Aqua and NPP 2015–2017 ATO-RM linear trends were 0.61 and 0.48% (not shown), however, the post-2018 Aqua, NPP, and N20 ATO-RM linear trends were 0.03%/yr, 0.17%/yr, and 0.09%/yr, respectively, proving E-6 also degraded mostly in the early record. To sum up, the overall and pre-2018 record for E-5 and E-6 had statistically significant linear trends, whereas the significance test failed for post-2018 record, suggesting that the degradation occurred during the early record.

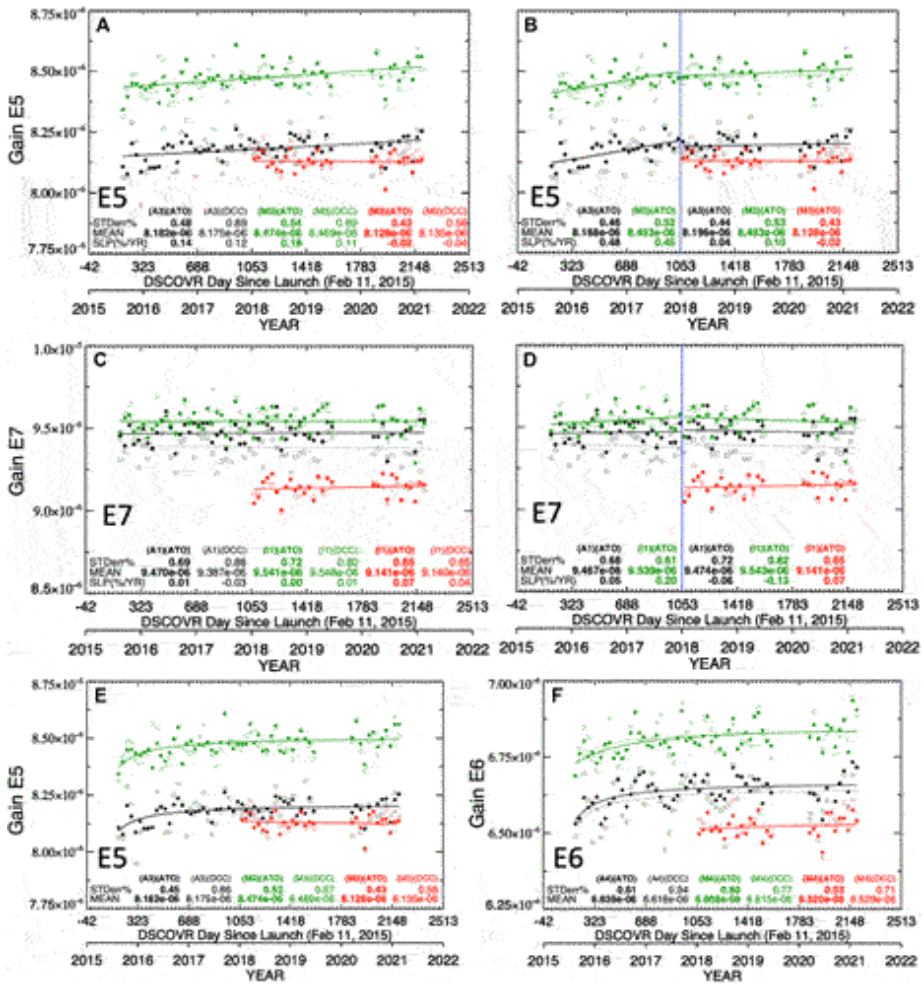

FIGURE 5 | (A) The time series of E-5 with M_{Aq}-3 (black), V_{NPP}-M3 (green) and V_{N20}-M3 (red) ATO-RM (solid circles and solid line) and DCC-RM (open circles and dotted line) monthly reflectance gains (ref/count) and linear trends. Also shown are the standard error (*STDerr%*), mean gain (ref/count), and slope *SLP*(*%/YR*). **(B)** Same as **(A)** except for E-5 time series before 2018 and after 2018 as delineated by the vertical blue line. Both ATO-RM and DCC-RM monthly gains and linear trends are plotted but only the ATO-RM statistics are listed. **(C)** Same as **(A)** except for E-7, **(D)** same as **(B)** except for E-7. **(E)** same as **(A)** except an asymptotic trend is used. **(F)** same as **(E)** except for E-6.

Relying on two independent pre- and post-breakpoint linear regression trends to define the E-5 temporal gain in Figure 5B is problematic, since there will be a discontinuity between the two trends at the breakpoint. A continuous piecewise linear regression solves the problem of the discontinuity at the breakpoint. However, the Figure 5B 2018 breakpoint position is arbitrary. The breakpoint was shifted between 2016 and 2019 to evaluate the pre- and post-breakpoint trend significance. Shifting the

breakpoint backwards from 2019 leads to the pre-breakpoint trend becoming insignificant once the breakpoint reaches mid-2017, as shortening the length of the record reduces the confidence in the trend. The E-5 gain record is too noisy to set an accurate single or multiple breakpoints to describe an E-5 gain that becomes more stable over time. An asymptotic or an exponential dampening function may better describe the E-5 (Figure 5E) and E-6 (Figure 5F) gains as they become increasingly more stable over time. The asymptotic fit is more sensitive to the first few monthly gains in the record than a linear trend. Given that the E-5 gains are noisy, the asymptotic fit may exaggerate the gain during the first few months.

The same analysis is carried out for the E-7 band. The E-7 gain based on V_{NPP}-I1 ATO-RM (Figure 2), DCC_{count} (Figure 3B), and Libya-4_{count} (Figure 4C) has been shown to be stable. Figure 5C confirms that the NPP ATO-RM and DCC-RM linear trend gains are stable and that Aqua and N20 show similar stable linear trend gains, where all trends are within ±0.07%/yr. Figure 5D shows that the Aqua ATO-RM before and after 2018 linear trend gains were within ±0.06%/yr. However, the NPP ATO-RM monthly gain is trending slightly upward before 2018 trends and trending downward after 2018. Perhaps the NPP calibration drift correction (*Imager Calibration Drift Mitigation*) did not completely mitigate the LUT update impact. Unlike E-5 and E-6, the E-7 (Figures 5C,D) gain is nearly stable over the record and shows no signs of greater degradation during the earlier record. The overall, pre- and post-2018 E-7 ATO-RM linear trends were found to be insignificant, suggesting that the E-7 gain is stable over the record. Similarly, The E-10 Aqua and NPP 2015–2017 ATO-RM linear trends were 0.02%/yr and 0.16%/yr (not shown), and were comparable to the post-2018 Aqua, NPP, and N20 ATO-RM linear trends of 0.01%/yr, -0.09%/yr, and 0.08% %/yr, respectively, demonstrating good stability throughout the EPIC record and their associated trends were found to be insignificant.

In order to account for the greater E-5 and E-6 degradation in the early record, an asymptotic trend is applied to the monthly gains

$$gain = g_0 + g_1 \times \exp\left(\frac{g_2}{dsl}\right) \qquad (4)$$

where g_0, g_1, and g_2 are the asymptotic trend coefficients and *exp* is the natural exponent. The asymptotic trends are applied to the E-5 and E-6 gains in Figures 5E,F, respectively. As expected, the asymptotic fit also shows

most of the EPIC degradation at the beginning of the record and a near stable trend after 2018. Although the asymptotic trends did not significantly reduce the trend standard error (Figure 5E) compared with linear trends (Figure 5A), the asymptotic trends seem to capture the degradation more accurately. The E-6/M_{Aq}-4 (Figure 5F) asymptotic trend shows a greater degradation during the first year of EPIC than the E-5 channel and is probably due to the greater monthly E-6 gain noise and not associated with the E-6 degradation. Although the asymptotic fit does not perfectly describe the E-5 and E-6 degradation over the record, it is more accurate in characterizing the sensor radiometric trend compared to applying a linear fit. This study utilizes the asymptotic fit from Eq. 4 to derive the E-5 and E-6 gain and employs the linear fit from Eq. 3 to obtain the E-7, E-8, E-9, and E-10 gain. Similar exponential optical degradation for shorter visible wavelengths was also observed in other visible imagers (Fougnie et al., 2007; Eplee et al., 2012; Xiong et al., 2010a; Xiong et al., 2019).

RESULTS

V03 Navigation Assessment

Figure 6 shows the navigation error frequency for E-7/V_{NPP}-I1 for V02 and V03. The navigation error is the number of EPIC 0.25° grid cell shifts required to optimally align with the underlying VIIRS granule (see *EPIC Navigation* section). Figure 6A shows that the navigation error for V02 was centered within two 0.25° grid cells to the northeast, whereas Figure 6B shows that the V03 navigation error were mostly positioned at the center indicating that no navigation correction was required. The V02 navigation correction encompassed a much broader part of the northeast quadrant than that for V03, which covers a narrow section slightly northwest. Comparing the V02 and V03 navigation error frequency plots suggests that V03 has improved both navigation accuracy and precision over V02. Table 2 reveals that the EPIC V03 NPP E-7/V_{NPP}-I1 navigation accuracy was -11.1 ± 16.2 km and 11.0 ± 15.1 km in the longitude and latitude directions, respectively, which is smaller than the 0.25° grid resolution or the 25-km navigation accuracy that can be achieving by shifting the EPIC gridded image. The EPIC channel images taken during a 7-min period are geo-rectified so that the individual EPIC channel images are aligned. We should expect the EPIC navigation error to be similar for all EPIC and M/V band

pairings. Table 2 verifies that the EPIC band navigation accuracy is in good agreement whether aligned with Aqua, NPP, or N20 as well as with the various EPIC band pairs. To assess the EPIC V02 and V03 navigation accuracy, all of the band pair Table 2 column data are simply averaged. The EPIC V02 navigation errors were 32.2 ± 31.5 km and 17.3 ± 19.4 km in longitude and latitude, respectively, whereas the EPIC V03 were -10.9 ± 12.1 km and 11.0 ± 14.7 km. The Doelling et al., 2019 V02 error assessments were 27.4 ± 35.9 km and 15.9 ± 19.9 km, respectively, within close agreement with this study. After applying the Pythagorean theorem, the V02 and V03 navigation errors were 36.5 and 15.5 km, respectively, more than a 50% reduction. After the DSCOVR safe mode anomaly ended in early 2020, EPIC no longer employs gyroscope or reaction wheel inputs, which were replaced by a star tracking technique for pointing knowledge (Geogdzhayev et al., 2021). The EPIC V03 E-7/V_{NPP}-I1 2018–2019 navigation errors were -10.2 ± 15.3 km and 11.2 ± 14.7 km in longitude and latitude, respectively, whereas the 2020–2021 errors were -10.3 ± 14.0 km and 10.6 ± 14.4 km. The pre- and post-EPIC safe mode anomaly navigation error difference is insignificant, indicating that the EPIC navigation performance is similar whether based on the star-tracking or the gyroscope.

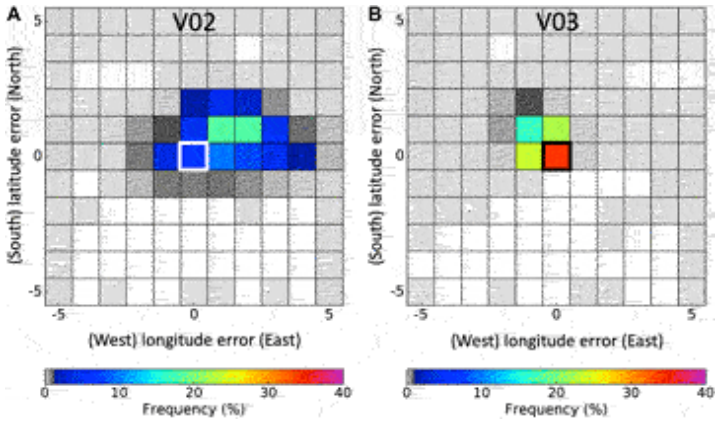

FIGURE 6 | The E-7/V_{NPP}-I1 (0.65 μm) **(A)** V02 and **(B)** V03 navigation error frequency plots in 0.25° latitude and longitude grid increments. The center white or black box represents no spatial shift or perfect navigation. Note the improved V03 navigation accuracy and precision based on 26,351 E-7/V_{NPP}-I1 total image shifts.

TABLE 2 | The V02 and V03 mean and standard deviation (σ) navigation error in the East-West and North-South direction in km with respect to Aqua-MODIS, NPP-VIIRS, and N20-VIIRS analogous band pairs with EPIC. See Table 1 for band pair nomenclature. Statistics in the table are calculated under the assumption that a 0.25° navigation shift translates to a distance of 25 km.

LEO	Band Pairing	EPIC V02				EPIC V03			
		East-West Error (km)		North-South Error (km)		East-West Error (km)		North-South Error (km)	
		Mean	σ	Mean	σ	Mean	σ	Mean	σ
Aqua	E-5/M_{Aq}-3	33.4	30.1	19.6	18.7	−11.4	15.2	11.4	14.0
	E-6/M_{Aq}-4	31.0	30.7	18.6	18.8	−10.9	15.0	11.5	13.7
	E-7/M_{Aq}-1	30.8	30.9	18.6	19.0	−10.5	14.7	11.4	13.6
	E-10/M_{Aq}-1	30.6	31.2	18.5	19.3	−10.6	14.8	11.2	13.8
NPP	E-5/V_{NPP}-M3	31.6	34.1	17.0	20.1	−11.9	16.6	11.2	15.6
	E-6/V_{NPP}-M4	31.2	33.8	16.6	20.0	−11.5	16.4	11.0	15.3
	E-7/V_{NPP}-I1	31.1	33.8	16.7	20.0	−11.1	16.2	11.0	15.1
	E-7/V_{NPP}-M5	30.9	34.0	16.5	20.0	−11.2	16.2	10.9	15.0
	E-10/V_{NPP}-I1	30.7	33.9	16.7	20.2	−11.1	16.3	10.8	15.5
	E-10/V_{NPP}-M5	30.7	33.9	16.6	20.2	−11.2	16.3	10.8	15.4
	E-10/V_{NPP}-M7	30.7	33.7	16.6	19.8	−11.2	15.8	10.8	14.8
N20	E-5/V_{N20}-M3	35.2	29.6	17.4	19.2	−11.0	14.9	11.1	15.1
	E-6/V_{N20}-M4	33.7	29.2	16.9	19.0	−10.7	14.8	10.9	14.8
	E-7/V_{N20}-I1	33.6	29.5	17.1	19.0	−10.2	14.8	10.9	14.6
	E-7/V_{N20}-M5	33.6	29.5	17.1	19.0	−10.3	14.8	10.9	14.6
	E-10/V_{N20}-I1	33.3	29.4	17.1	19.2	−10.4	14.6	10.7	14.7
	E-10/V_{N20}-M5	33.3	29.4	17.1	19.2	−10.4	−14.6	10.7	14.6
	E-10/V_{N20}-M7	33.4	29.4	16.9	19.1	−10.5	−14.5	10.7	14.4

Both V02 and V03 navigation error frequency plots show cases where the EPIC image shifting is well outside of the typical navigation errors observed, which are indicated by the light gray shading in Figure 6. These M/V granules were mostly positioned outside of the EPIC 0.25° gridded domain (±30° in latitude) allowing only a small snippet of the granule available for shifting. Due to the small snippet domain, the May 2020 EPIC count and NPP reflectance pair scatter plot (Figure 1A) only contained one pair that was located outside of the ±1 latitude/longitude shift in Figure 5B. We are confident that these large spurious image shifts are not impacting the overall ATO-RM and DCC-RM monthly gains. Perhaps a snippet size threshold could be used for future EPIC navigation assessments.

EPIC DCC-RM and ATO-RM Calibration Gains

Figure 5 qualitatively shows that the DCC-RM and ATO-RM trend lines are mostly consistent, except for E-7/M_{Aq}-1 (compare the Figure 5C and Figure 5D solid and dashed black lines). Table 3 quantitatively lists the DCC-RM and ATO-RM mean gain difference over the 6-years EPIC record. The mean gain difference is mostly less than 0.4% for all band pairs, except for E-7/M_{Aq}-1 and E-10/M_{Aq}-1, and are similar to the Doelling et al. (2019) (see

their Table 2) mean gain differences, which were also less than 0.4%. Note that the consistent ATO-RM and DCC-RM gain differences validate the robustness of the unique band pair and scene type SBAFs required in Eq. 1, given the very narrow 3 nm EPIC spectral bands (Table 1).

TABLE 3 | EPIC V03 channel ATO-RM and DCC-RM mean gain and trend standard error over the EPIC (2015–2021) record with respect to the Aqua, NPP, and N20 band pairings. Note that the Aqua-MODIS, NPP-VIIRS, and N20-VIIRS channels are independently calibrated against their respective solar diffusers and the resulting gains are not expected to match between imagers. The ATO-RM and DCC-RM gain difference is also given. Note that the two independent ray-matching methods provide very similar gain differences.

LEO	Band Pair	ATO-RM Mean Gain	ATO-RM STDerr %	DCC-RM Mean Gain	DCC-RM STDerr%	Mean Diff % (DCC-ATO)
Aqua	E-5/M_{Aq}-3	8.1817e-6	0.45	8.1754e-6	0.86	−0.08
	E-6/M_{Aq}-4	6.6363e-6	0.61	6.6183e-6	0.94	−0.27
	E-7/M_{Aq}-1	9.4704e-6	0.69	9.3871e-6	0.88	−0.88
	E-10/M_{Aq}-1	1.4374e-5	0.99	1.4210e-5	1.08	−1.14
NPP	E-5/V_{NPP}-M3	8.4735e-6	0.52	8.4694e-6	0.67	−0.05
	E-6/V_{NPP}-M4	6.8081e-6	0.60	6.8148e-6	0.77	+0.10
	E-7/V_{NPP}-I1	9.5408e-6	0.72	9.5477e-6	0.80	+0.07
	E-7/V_{NPP}-M5	9.6727e-6	0.71	9.6593e-6	0.79	−0.14
	E-10/V_{NPP}-I1	1.4471e-5	1.02	1.4524e-5	0.98	+0.37
	E-10/V_{NPP}-M5	1.4673e-5	0.95	1.4707e-5	0.96	+0.23
	E-10/V_{NPP}-M7	1.4991e-5	0.86	1.4950e-5	0.99	−0.27
N20	E-5/V_{N20}-M3	8.1282e-6	0.43	8.1347e-6	0.56	+0.08
	E-6/V_{N20}-M4	6.5202e-6	0.53	6.5291e-6	0.71	+0.14
	E-7/V_{N20}-I1	9.1414e-6	0.65	9.1396e-6	0.65	−0.02
	E-7/V_{N20}-M5	9.2411e-6	0.65	9.2346e-6	0.66	-0.07
	E-10/V_{N20}-I1	1.3864e-5	1.05	1.3898e-5	1.04	+0.25
	E-10/V_{N20}-M5	1.4013e-5	1.03	1.4043e-5	1.04	+0.21
	E-10/V_{N20}-M7	1.4423e-5	1.04	1.4382e-5	1.05	−0.28

The E-7/M_{Aq}-1 and E-10/M_{Aq}-1 show a mean gain difference of −0.9% and −1.1%, respectively. As reported in Bhatt et al. (2019), the MODIS L1B C6.1 M_{Aq}-1 reflectances have residual RVS angle dependence of 1.5% for the left-side or backscatter-side of the scan. The residual RVS increases with greater VZA, which would explain the ATO-RM and DCC-RM gain difference, since the DCC-RM limits the VZA to 40°, whereas the ATO-RM does not limit the VZA (Doelling et al., 2019). Note the residual RVS is not mitigated in the *Imager Calibration Drift Mitigation* section, since the DCC-IT calibration drift correction only corrects the nadir response.

Although, the two independent inter-calibration methods provide consistent EPIC band pair calibration coefficients, they do not provide similar Aqua-MODIS, NPP-VIIRS, or N20-VIIRS referenced EPIC calibration coefficients, given that their L1B reflectances are calibrated against their respective onboard solar diffusers. Table 3 provides the EPIC 6-

years record mean gains referenced to the M/V imager L1B reflectance. For example, the E-7/V_{NPP}-I1 mean gain is 4.4% greater than the corresponding E-7/V_{N20}-I1 gain, similar to the NPP and N20 VIIRS imager calibration differences found by other studies (Uprety et al., 2020; Moyer et al., 2021; Mu et al., 2021; Wu et al., 2020).

EPIC DCC-RM Gain Comparison with Previous Study

The DCC-RM V03 gains are compared against the EPIC coefficients provided by Geogdzhayev et al. (2021). The Geogdzhayev et al. (2021) approach (referred to DCC-G in this study) identifies all EPIC pixels with a corresponding M/V imager reflectance greater than 0.6 and a relative standard deviation less than 10%. The EPIC pixel count and imager reflectance ratios are binned according to their relative standard deviation values and a linear regression is used to infer the ratio with a relative standard deviation of zero. The independent DCC-RM and DCC-G gains are compared in Table 4 for the EPIC record ending before the June 2019 safe mode incident. The EPIC and NPP band pair DCC-RM and DCC-G gains agreed within 0.4%, similar to the ATO-RM and DCC-RM gain differences.

TABLE 4 | The EPIC V03 channel DCC-RM and the Geogdzhayev et al., 2021 mean gain for the record ending in June 2019 before the safe mode incident. The DCC-RM method drift-corrected the Aqua and NPP channel reflectances, while Geogdzhayev et al., 2021 combined the Terra and Aqua MODIS reflectances to compute the MODIS based gains. Note that Geogdzhayev et al., 2021 used E-10/M_{Aq}-2 while this study uses E-10/M_{Aq}-1.

LEO	Band Pair	Geogdzhayev et al., 2021 Gain	DCC-RM Mean Gain	Diff %
Aqua	E-5/M_{Aq}-3	8.330e-6	8.2368e-06	−1.12
	E-6/M_{Aq}-4	6.617e-6	6.6361e-06	+0.29
	E-7/M_{Aq}-1	9.238e-6	9.3713e-06	+1.44
	E-10/M_{Aq}-1	1.4538e-5	1.4191e-05	−2.39
NPP	E-5/V_{NPP}-M3	8.528e-6	8.4989e-06	−0.34
	E-6/V_{NPP}-M4	6.842e-6	6.8405e-06	−0.02
	E-7/V_{NPP}-M5	9.658e-6	9.6855e-06	+0.28
	E-10/V_{NPP}-M7	1.4887e-5	1.4942e-05	+0.37

The Aqua based DCC-RM and DCC-G EPIC band pair gains differed from +1.4% to −2.4%. Geogdzhayev et al. (2021) combined Terra and Aqua-MODIS reflectances and report that Terra-MODIS is brighter by 0.6%, −0.1%, -0.2%, and 2.0% for M_{Aq}-3, M_{Aq}-4, M_{Aq}-1, and M_{Aq}-2 bands, respectively. Doelling et al. (2015) (their Table 3) reports that Terra-MODIS L1B C6 (2002–2015) is +0.9%. -0.1%, -1.3%, and +0.6% brighter than the

above Aqua-MODIS bands, respectively. The Geogdzhayev et al. (2021) and Doelling et al. (2015) Terra and Aqua-MODIS band gain differences explains much of the Table 4 EPIC/Aqua band pair differences. The EPIC E-5, E-6, and E-7 L1B V03 absolute calibration is more consistent with the Terra-MODIS L1B C6 calibration than the Aqua-MODIS L1B C6 calibration. Some of the DCC-G E-10/M_{Aq}-2 and DCC-RM E-10/M_{Aq}-1 difference may be due to the M_{Aq}-1 and M_{Aq}-2 absolute calibration difference and that the M_{Aq}-2 band reflectance saturates over bright clouds.

Invariant Target Validation

The EPIC DCC and Libya-4 invariant target reflectance are validated by comparing with the corresponding Aqua and NPP ATO-RM and DCC-RM monthly gains. The normalized EPIC invariant target monthly DCC_{count} and Libya-4_{count} as well as the ATO-RM and DCC-RM gains (after normalizing over the 6-years record) are plotted in Figure 7 with their respective temporal trends. By normalizing the Aqua and NPP ATO-RM and DCC-RM gains, the M/V absolute calibration difference is removed. The inverse of the DCC_{count} and Libya-4_{count}, which is proportional to the gain, is plotted to facilitate comparison amongst these methods. Qualitatively, The DCC_{count} and Libya-4_{count} trends are mostly consistent with their corresponding Aqua and NPP ATO-RM and DCC-RM trends. In spite of the sparce DCC_{count} sampling, the DCC_{count} has shown to be remarkably stable. The Libya-4_{count} stability confirms that the EPIC V03 navigation accuracy is sufficient to monitor the EPIC degradation utilizing PICS.

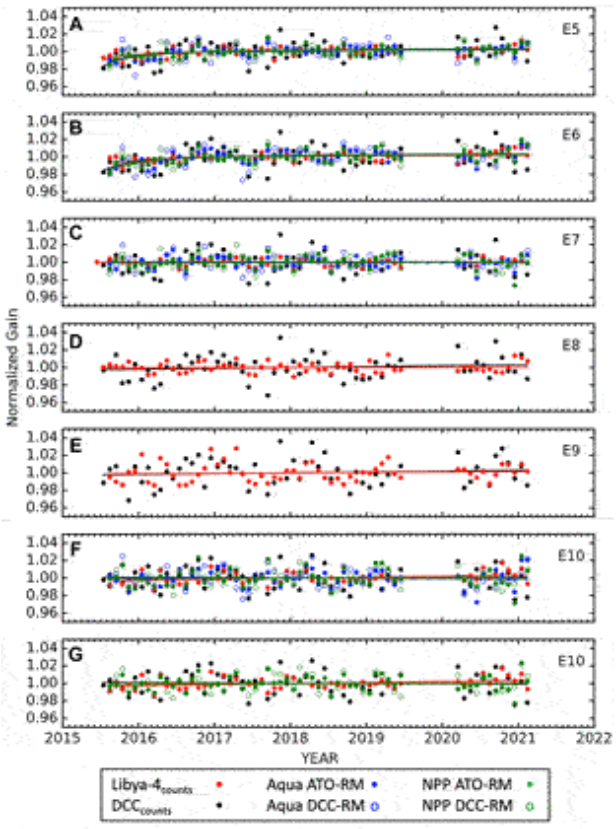

FIGURE 7 | Time series of the EPIC band normalized response showing the inverse of the DCC_{counts} (black) and Libya-4_{counts} (red), as well as the Aqua-MODIS (blue), and NPP-VIIRS (green) monthly gains. Filled circles and solid lines for Aqua-MODIS and NPP-VIIRS represent ATO-RM, and open circles with dashed lines represent the DCC-RM counterparts. **(A)** through **(E)** show the corresponding E-5, E-6, E-7, E-8, and E-9 time series, respectively. **(F)** shows DCC_{counts}, Libya-4_{counts}, ATO-RM, and DCC-RM with M_{Aq}-1 and V_{NPP}-I1, **(G)** same as **(F)** except V_{NPP}-M7 instead of M_{Aq}-1 and V_{NPP}-I1.

Notably, both DCC_{count} and Libya-4_{count} are able to monitor the stability of the E-8 and E-9 bands, which is not possible with the M/V ATO-RM or DCC-RM methods because they do not have oxygen A and B band channels. The E-8 and E-9 stability is on par with their E-7 and E-10 reference channels. Given that the E-8 and E-9 gains are stable, perhaps the oxygen absorption bands can be used to locate DCC cells located at the tropopause without the aid of a concurrent IR sensor in future studies (Fougnie and Bach, 2009). Note, currently the EPIC calibration team utilizes the moon as an invariant target to monitor the degradation of the EPIC visible channels (Geogdzhayev and Marshak, 2018). The E-7 gain is

transferred to the E-8 channel, by assuming the lunar reflectance is the same for both E-7 and E-8 bands, since the moon has no atmosphere.

EPIC Stability Assessment

The Figure 7 EPIC channel stability using Aqua and NPP ATO-RM and DCC-RM gains as well as the DCC_{counts} and Libya-4_{counts} are quantified in Table 5. The trend uncertainty for ATO-RM and DCC-RM methods are mostly within 1% over the EPIC record. The Libya-4_{count} has a slightly lower uncertainty than the ray-matching methods, while the DCC_{count} has a greater uncertainty than the ray-matching methods. All methods have mostly smaller trend uncertainties for the EPIC shorter wavelengths than for the longer wavelengths.

TABLE 5 | The monthly gain linear regression standard error (*STDerr%*) and *slope* (% over the 6-years record) for all invariant targets and band pairs. The E-5 and E-6 band linear regression statistics are performed twice (2015–2017 and 2018–2021, separated by a "/").

Dataset	Band or Band Pair	STDerr%	SLP%
DCC-IT	E-5	1.40/0.95	3.0/0.5
	E-6	1.50/1.08	3.5/0.3
	E-7	1.23	0.1
	E-8	1.30	0.6
	E-9	1.50	0.5
	E-10	1.30	-0.2
Libya-4	E-5	0.76/0.53	2.0/0.9
	E-6	0.64/0.68	2.0/1.1
	E-7	0.37	0.0
	E-8	0.59	0.1
	E-9	1.04	0.3
	E-10	0.61	0.7
Aqua—ATO-RM	E-5/M_{Aq}-3	0.78/0.43	2.7/0.2
	E-6/M_{Aq}-4	1.04/0.61	3.4/0.2
	E-7/M_{Aq}-1	0.69	0.1
	E-10/M_{Aq}-1	0.99	0.1
Aqua—DCC-RM	E-5/M_{Aq}-3	1.24/0.69	2.8/0.0
	E-6/M_{Aq}-4	1.37/0.69	3.1/0.0
	E-7/M_{Aq}-1	0.88	−0.2
	E-10/M_{Aq}-1	1.07	−0.3
NPP—ATO-RM	E-5/V_{NPP}-M3	0.78/0.54	2.6/0.6
	E-6/V_{NPP}-M4	0.86/0.70	2.7/0.9
	E-7/V_{NPP}-I1	0.73	0.0
	E-7/V_{NPP}-M5	0.71	0.1
	E-10/V_{NPP}-I1	1.02	0.1
	E-10/V_{NPP}-M5	0.94	0.2
	E-10/V_{NPP}-M7	0.86	0.1
NPP—DCC-RM	E-5/V_{NPP}-M3	0.91/0.63	2.3/0.3
	E-6/V_{NPP}-M4	1.07/0.80	2.8/0.9
	E-7/V_{NPP}-I1	0.80	0.0
	E-7/V_{NPP}-M5	0.79	0.2
	E-10/V_{NPP}-I1	0.98	0.1
	E-10/V_{NPP}-M5	0.96	0.2
	E-10/V_{NPP}-M7	0.98	0.0

All stability methods show EPIC channel degradation is mostly less than 0.3% over the EPIC record, excluding the early record of E-5 and E-6. The

asymptotic fit has probably over-estimated the early E-5 and E-6 early record degradation due to the magnitude of the monthly gain noise. The greatest single EPIC band method degradation discrepancy was for the E-5 and E-6 bands for both the pre-2018 and post-2018 records. Generally greater degradation was observed for smaller wavelengths than for larger wavelengths. The E-7 band was the most stable of the visible EPIC bands, where all methods showed within a 0.2% degradation over the record. The near stable E-7 record has the potential of monitoring concurrent satellite sensor stability, similar to lunar and Earth invariant targets. The E-10 stability is within 0.4% for most methods over the record, except for Libya-4. Note that the invariant target-based stability may be aliased with the natural variability of the reflectance over target. The same holds true for methods relying on well-calibrated sensors such as M/V, where unaccounted calibration drifts may be embedded in the record.

To determine if the 8-month EPIC safe mode anomaly caused a discontinuity in the monthly gains, a *t*-test of the 2018–2019 and 2020–2021 mean gains was performed to determine if the two gains differed significantly. All ATO-RM, DCC-RM and DCC_{count} gains had *t*-test statistics less than 1. The Libya-4_{counts} *t*-test statistics had a value less than 2.0, which denotes the 95% confidence level and suggests that no calibration discontinuity was observed after the safe-mode incident.

CONCLUSION

The DSCOVR mission was designed to take advantage of the L1 position to continuously observe the Earth sunlit disk. The frequent daily EPIC observations are optimized for diurnal and backscatter condition studies. The EPIC sensor retrievals are processed into various aerosol, ozone, cloud, vegetation, volcanic SO^2, and glint Level-2 products. These products are now being validated and integrated for their diurnal utility with corresponding MODIS and VIIRS (M/V) products. The EPIC sensor does not have any onboard calibration systems, resulting in an uncalibrated EPIC L1B V03 dataset. To facilitate the EPIC data validation and fusion, an assessment of the navigation accuracy and calibration stability is performed along with providing the M/V sensor and band specific radiometric scaling factors.

The EPIC navigation accuracy was assessed by aligning the individual EPIC channel images onto their corresponding M/V granule images. The navigation error was similar across the EPIC visible channels, validating the

EPIC geo-rectification algorithm. Both the EPIC V03 navigation accuracy and precision was improved over V02. The V02 and V03 navigation errors were 36.5 and 15.5 km, respectively, a 50% reduction and within what can be achieved by the image alignment algorithm. After the EPIC 2019 safe mode incident, EPIC navigation relied on star-tracking rather than gyroscope and no significant difference in navigation accuracy was observed.

The EPIC visible channel calibration gains, which have been radiometrically scaled to their analogous Aqua-MODIS, NPP-VIIRS, and N20-VIIRS channels is provided in Table 3. Both ATO-RM and DCC-RM independent inter-calibration method channel pair gains were mostly within 0.4%. The EPIC channel DCC-RM gains were within 0.4% compared with the Geogdzhayev et al., 2021 NPP-VIIRS referenced gains. The EPIC based NPP and N20-VIIRS calibration gain differences were similar to other inter-calibration studies.

The EPIC sensor calibration stability was assessed by the ATO-RM and DCC-RM inter-calibration method gains that relied on the stable Aqua-MODIS and NPP-VIIRS channel reflectances, which were corrected for any residual calibration drifts using DCC targets. By comparing the individual EPIC channel with analogous referenced Aqua-MODIS and NPP-VIIRS gains with their corresponding later record N20-VIIRS gains, the E-5 and E-6 calibration degraded mostly during the first year of operation and became stable thereafter. This was also observed for the EPIC UV channels (Herman et al., 2018). The E-7 and E-10 bands were found to be stable across the full EPIC record. Asymptotic temporal trends were used to describe the E-5 and E-6 degradation, while linear trends defined the remaining EPIC visible bands.

The improved EPIC V03 navigation allowed the EPIC stability to be monitored using DCC and Libya-4 invariant targets. The invariant target stability results were found consistent to those from the ray-matching methods. Most methods indicated that the EPIC V03 L1B radiances were within 0.3% over the 6-years EPIC record, excluding the early record of E-5 and E-6 with an associated uncertainty of ~1%. Remarkably, both the DCC and Libya-4 were able to determine the stability of the E-8 and E-9 oxygen absorption bands, which were similar to their E-7 and E-10 reference bands. Lastly, no significant EPIC calibration discontinuity was observed across the 2019 safe mode incident.

The impressive stability of the DSCOVR EPIC L1B V03 channel radiances achieved without onboard calibration systems can greatly benefit the Earth remote sensing community. EPIC's distance from the Earth minimizes the effects of harmful reflected solar radiation on the optics compared to low Earth orbit sensors. Having a future constellation of overlapping L1 satellite sensors can provide a stable record of environmental retrievals and has the potential of monitoring the stability of near-Earth orbit sensors. As sensor detector, optics, pointing, and data transmission technology improves over time, the L1 position will have the ability to monitor regional diurnal variations through the lens of a single sensor and will be an important addition to sun-synchronous satellite retrieved observations to monitor the Earth's climate.

DATA AVAILABILITY STATEMENT

The datasets presented in this study can be found in online repositories. The names of the repository/repositories and accession number(s) can be found below: DSCOVR EPIC L1B data: https://asdc.larc.nasa.gov/project/DSCOVR/DSCOVR_EPIC_L1B_3 Aqua-MODIS L1B data: https://ladsweb.modaps.eosdis.nasa.gov/archive/allData/61/MYD021KM/ VIIRS L1B data: https://ladsweb.modaps.eosdis.nasa.gov/archive/.

AUTHOR CONTRIBUTIONS

CH processed and plotted all of the EPIC navigation, ATO-RM, and DCC-RM calibration results and prepared the initial draft of the manuscript. DD formulated and directed the methodology, validation, and results analysis, as well as revised the manuscript. WS reviewed and provided feedback on the manuscript. RB processed and plotted all of the EPIC DCC and Libya-4 invariant target calibration results. BS and AG determined the SBAF coefficients. All authors contributed to the methodology, validation, results analysis and reviewed the manuscript.

FUNDING

This study was supported by NASA ROSES proposal NNH14ZDA001N-DSCOVR A.22 DSCOVR Earth Science Algorithms. The DSCOVR EPIC data were obtained from the NASA Langley Research Center Atmospheric Science Data Center. The MODIS and VIIRS granules were obtained from the CERES project.

PUBLISHER'S NOTE

ACKNOWLEDGMENTS

The authors would like to thank the reviewers of the manuscript. The authors are appreciative of the helpful discussions with the NASA EPIC and MODIS calibration teams as well as the NOAA VIIRS calibration teams.

REFERENCES

Angal, A., Xiong, X., Mu, Q., Doelling, D. R., Bhatt, R., and Wu, A. (2018). Results from the Deep Convective Clouds-Based Response versus Scan-Angle Characterization for the MODIS Reflective Solar Bands. *IEEE Trans. Geosci. Remote Sensing* 56 (2), 1115–1128. doi:10.1109/TGRS.2017.2759660

Bhatt, R., Doelling, D. R., Angal, A., Xiong, X., Haney, C., Scarino, B. R., et al. (2020). Response versus Scan-Angle Assessment of MODIS Reflective Solar Bands in Collection 6.1 Calibration. *IEEE Trans. Geosci. Remote Sensing* 58 (4), 2276–2289. doi:10.1109/TGRS.2019.2946963

Bhatt, R., Doelling, D. R., Angal, A., Xiong, X., Scarino, B., Gopalan, A., et al. (2017). Characterizing Response versus Scan-Angle for MODIS Reflective Solar Bands Using Deep Convective Clouds. *J. Appl. Remote Sens.* 11, 016014. doi:10.1117/1.JRS.11.016014

Bhatt, R., Doelling, D. R., Morstad, D., Scarino, B. R., and Gopalan, A. (2014). Desert-Based Absolute Calibration of Successive Geostationary Visible Sensors Using a Daily Exoatmospheric Radiance Model. *IEEE Trans. Geosci. Remote Sensing* 52 (6), 3670–3682. doi:10.1109/TGRS.2013.2274594

Bhatt, R., Doelling, D., Wu, A., Xiong, X., Scarino, B., Haney, C., et al. (2014b). Initial Stability Assessment of S-NPP VIIRS Reflective Solar Band Calibration Using Invariant Desert and Deep Convective Cloud Targets. *Remote Sensing* 6, 2809–2826. doi:10.3390/rs6042809

Bovesmann, H., Burrows, J. P., Buchwitz, M., Frerick, J., Noël, S., Rozanov, V. V., et al. (1999). SCIAMACHY: Mission Objectives and Measurement Modes. *J. Atmos. Sci.* 56, 127–150.

Chander, G., Hewison, T. J., Fox, N., Wu, X., Xiong, X., and Blackwell, W. J. (2013). Overview of Intercalibration of Satellite Instruments. *IEEE Trans. Geosci. Remote Sensing* 51 (3), 1056–1080. doi:10.1109/TGRS.2012.2228654

Cosnefroy, H., Leroy, M., and Briottet, X. (1996). Selection and Characterization of Saharan and Arabian Desert Sites for the Calibration of Optical Satellite Sensors. *Remote Sensing Environ.* 58 (1), 101–114. doi:10.1016/0034-4257(95)00211-1

Doelling, D., Haney, C., Bhatt, R., Scarino, B., and Gopalan, A. (2019). The Inter-calibration of the DSCOVR EPIC Imager with Aqua-MODIS and NPP-VIIRS. *Remote Sensing* 11, 1609. doi:10.3390/rs11131609

Doelling, D., Haney, C., Bhatt, R., Scarino, B., and Gopalan, A. (2021). Daily Monitoring Algorithms to Detect Geostationary Imager Visible Radiance Anomalies. *Submitted Can. J. Remote Sensing* .

Doelling, D. R., Haney, C. O., Scarino, B. R., Gopalan, A., and Bhatt, R. (2016). Improvements to the Geostationary Visible Imager ray-matching Calibration Algorithm for CERES Edition 4. *J. Atmos.*

Ocean. Technol. 33, 2679–2698. doi:10.1175/jtech-d-16-0113.1

Doelling, D. R., Morstad, D., Scarino, B. R., Bhatt, R., and Gopalan, A. (2013). The Characterization of Deep Convective Clouds as an Invariant Calibration Target and as a Visible Calibration Technique. *IEEE Trans. Geosci. Remote Sensing* 51, 1147–1159. doi:10.1109/tgrs.2012.2225066

Doelling, D. R., Wu, A., Xiong, X., Scarino, B. R., Bhatt, R., Haney, C. O., et al. (2015). The Radiometric Stability and Scaling of Collection 6 Terra- and Aqua-MODIS VIS, NIR, and SWIR Spectral Bands. *IEEE Trans. Geosci. Remote Sensing* 53 (8), 4520–4535. doi:10.1109/TGRS.2015.2400928

Eplee, R. E., Meister, G., Patt, F. S., Barnes, R. A., Bailey, S. W., Franz, B. A., et al. (2012). On-orbit Calibration of SeaWiFS. *Appl. Opt.* 51, 8702–8730. doi:10.1364/ao.51.008702

Fougnie, B., and Bach, R. (2009). Monitoring of Radiometric Sensitivity Changes of Space Sensors Using Deep Convective Clouds: Operational Application to PARASOL. *IEEE Trans. Geosci. Remote Sensing* 47 (3), 851–861. doi:10.1109/TGRS.2008.2005634

Fougnie, B., Bracco, G., Lafrance, B., Ruffel, C., Hagolle, O., and Tinel, C. (2007). PARASOL In-Flight Calibration and Performance. *Appl. Opt.* 46, 5435–5451.

Geogdzhayev, I. V., Marshak, A., and Alexandrov, M. (2021). Calibration of the DSCOVR EPIC Visible and NIR Channels Using Multiple LEO Radiometers. *Front. Remote Sens.* 2, 6719333. doi:10.3389/frsen.2021.671933

Geogdzhayev, I. V., and Marshak, A. (2018). Calibration of the DSCOVR EPIC Visible and NIR Channels Using MODIS Terra and Aqua Data and EPIC Lunar Observations. *Atmos. Meas. Tech.* 11, 359–368. doi:10.5194/amt-11-359-2018

Haney, C., Doelling, D., Minnis, P., Bhatt, R., Scarino, B., and Gopalan, A. (2016). "The Calibration of the DSCOVR EPIC Multiple Visible Channel Instrument Using MODIS and VIIRS as a Reference," in *Proc. SPIE 9972, Earth Observing Systems XXI*, *(San Diego, CA, United States*, *28 August - 1 September 2016)* (SPIE), 99720P. doi:10.1117/12.2238010

Herman, J., Huang, L., McPeters, R., Ziemke, J., Cede, A., and Blank, K. (2018). Synoptic Ozone, Cloud Reflectivity, and Erythemal Irradiance from Sunrise to sunset for the Whole Earth as Viewed by the DSCOVR Spacecraft from the Earth-Sun Lagrange 1 Orbit. *Atmos. Meas. Tech.* 11, 177–194. doi:10.5194/amt-11-177-2018

Hong, G., Heygster, G., Miao, J., and Kunzi, K. (2005). Detection of Tropical Deep Convective Clouds from AMSU-B Water Vapor Channels Measurements. *J. Geophys. Res.* 110, D05205. doi:10.1029/2004JD004949

Hu, Y., Wielicki, B. A., Ping Yang, P., Stackhouse, P. W., Lin, B., and Young, D. F. (2004). Application of Deep Convective Cloud Albedo Observation to Satellite-Based Study of the Terrestrial Atmosphere: Monitoring the Stability of Spaceborne Measurements and Assessing Absorption Anomaly. *IEEE Trans. Geosci. Remote Sensing* 42, 2594–2599. doi:10.1109/tgrs.2004.834765

Kaufman, Y. J., and Holben, B. N. (1993). Calibration of the AVHRR Visible and Near-IR Bands by Atmospheric Scattering, Ocean Glint and Desert Reflection. *Int. J. Remote Sensing* 14 (1), 21–52. doi:10.1080/01431169308904320

Kogan, F. N., Sullivan, J. T., and Bu, P. (1996). Testing post-launch Calibration for the AVHRR Sensor on World Desert Targets during 1985–1993. *Adv. Space Res.* 17 (1), 47–50. doi:10.1016/0273-1177(95)00444-J

Kostinski, A., Marshak, A., and Várnai, T. (2021). Deep Space Observations of Terrestrial Glitter. *Earth Space Sci.* 8, e2020EA001521. doi:10.1029/2020EA001521

Marshak, A., Herman, J., Adam, S., Karin, B., Carn, S., Cede, A., et al. (2018). Earth Observations from DSCOVR EPIC Instrument. *Bull. Am. Meterol. Soc.* 99, 1829–1850. doi:10.1175/BAMS-D-17-0223.1

Moulin, C., Lambert, C. E. J. Poitou., Poitou, J., and Dulac, F. (1996). Long Term (1983-1994) Calibration of the Meteosat Solar (VIS) Channel Using Desert and Ocean Targets. *Int. J. Remote Sensing* 17 (6), 1183–1200. doi:10.1080/01431169608949076

Moyer, D. I., Uprety, S., Wang, W., Cao, C., and Guch, I. (2021). “S-NPP/NOAA-20 VIIRS Reflective Solar Bands On-Orbit Calibration Bias Investigation,” in *Proc. SPIE 20219, Earth Observing Systems*, *(San Diego, CA, United States*, *1-5 AUGUST 2021)* (SPIE), 1182912. doi:10.1117/12.2595175

Mu, Q., Angal, A., Wu, A., and Xiong, X. (2021). “Performance Assessment of the NOAA-20 VIIRS RSB Using Deep Convective Clouds,” in *Proc. SPIE 20219, Earth Observing Systems XXVI*, *(San Diego, CA, United States*, *1-5 AUGUST 2021)* (SPIE), 1182918. doi:10.1117/12.2593514

Mu, Q., Chang, T., Wu, A., and Xiong, X. (2018). “Evaluating the Long-Term Stability and Response versus Scan Angle Effect in the SNPP VIIRS SDR Reflectance Product Using a Deep Convective Cloud Technique,” in *Proc. SPIE 10644, Algorithms and Technologies for Multispectral, Hyperspectral, and Ultraspectral Imagery XXIV*, *(Orlando, FL, United States*, *15-19 April 2018)* (SPIE), 106440O. doi:10.1117/12.2304395

Mu, Q., Wu, A., Xiong, X., Doelling, D., Angal, A., Chang, T., et al. (2017). Optimization of a Deep Convective Cloud Technique in Evaluating the Long-Term Radiometric Stability of MODIS Reflective Solar Bands. *Remote Sensing* 9, 535. doi:10.3390/rs9060535

Rao, C. R. N., and Chen, J. (1996). Post-launch Calibration of the Visible and Near-Infrared Channels of the Advanced Very High Resolution Radiometer on the NOAA-14 Spacecraft. *Int. J. Remote Sensing* 17, 2743–2747. doi:10.1080/01431169608949104

Rao, C. R. N., Weinreb, M. P., and Chen, J. (1994). Recalibration of the Advanced Very High Resolution Radiometer for Climate Change Research. *Adv. Space Res.* 14 (1), 117–120. doi:10.1016/0273-1177(94)90359-X

Rao, C. R. N., Chen, J., Sullivan, J. T., and Zhang, N. (1999). Post-launch Calibration of Meteorological Satellite Sensors. *Adv. Space Res.* 23 (8), 1357–1365. doi:10.1016/S0273-1177(99)00284-7

Roujean, J. L., Leroy, M. J., and Deschamps, P. Y. (1992). A Bidirectional Reflectance Model of the Earth’s Surface for the Correction of Remote Sensing Data. *J. Geophys. Res.* 97 (D18), 20455–20468. doi:10.1029/92jd01411

Scarino, B. R., Bedka, K., Bhatt, R., Khlopenkov, K., Doelling, D. R., and Smith Jr, W. L. (2020). A Kernel-Driven BRDF Model to Inform Satellite-Derived Visible Anvil Cloud Detection. *Atmos. Meas. Tech.* 13, 5491–5511. doi:10.5194/amt-13-5491-2020

Scarino, B. R., Doelling, D. R., Minnis, P., Gopalan, A., Chee, T., Bhatt, R., et al. (2016). A Web-Based Tool for Calculating Spectral Band Difference Adjustment Factors Derived from SCIAMACHY Hyperspectral Data. *IEEE Trans. Geosci. Remote Sensing* 54, 2529–2542. doi:10.1109/TGRS.2015.2502904

Shea, Y., Fleming, G., Kopp, G., Lukashin, C., Pilewskie, P., Smith, P., et al. (2020). “Clarreo Pathfinder: Mission Overview and Current Status,” in *IGARSS 2020 - 2020 IEEE International Geoscience and Remote Sensing Symposium*, *(Waikoloa, HI, USA*, *26 Sept.-2 Oct. 2020)* (IEEE), 3286–3289. doi:10.1109/IGARSS39084.2020.9323176

Staylor, W. F., and Suttles, J. T. (1990). Reflection and Emission Models for Deserts Derived from Nimbus-7 ERB Scanner Measurements. *J. Clim. Appl. Meteorol.* 25 (2), 196–202. doi:10.1175/1520-0450(1986)025<0196:raemfd>2.0.co;2

Su, W., Liang, L., Doelling, D. R., Minnis, P., Duda, D. P., Khlopenkov, K. V., et al. (2018). Determining the Shortwave Radiative Flux from Earth Polychromatic Imaging Camera. *J. Geo. Res. Atmos.* 123, 11479–11491. doi:10.1029/2018jd029390

Sun, J., Xiong, X., Angal, A., Chen, H., Wu, A., and Geng, X. (2014). Time-Dependent Response versus Scan Angle for MODIS Reflective Solar Bands. *IEEE Trans. Geosci. Remote Sensing* 52 (6), 3159–3174. doi:10.1109/tgrs.2013.2271448

Teillet, P. M., and Chander, G. (2010). Terrestrial Reference Standard Sites for Postlaunch Sensor Calibration. *Can. J. Remote Sensing* 36 (5), 437–450. doi:10.5589/m10-079

Teillet, P. M., Slater, P. N., Ding, Y., Santer, R. P., Jackson, R. D., and Moran, M. S. (1990). Three Methods for the Absolute Calibration of the NOAA AVHRR Sensors In-Flight. *Remote Sensing Environ.* 31, 105–120. doi:10.1016/0034-4257(90)90060-Y

Uprety, S., Cao, C., and Shao, X. (2020). Radiometric Consistency between GOES-16 ABI and VIIRS on Suomi NPP and NOAA-20. *J. Appl. Rem. Sens.* 14 (3), 1. doi:10.1117/1.JRS.14.032407

Uprety, S., and Cao, C. (2015). Suomi NPP VIIRS Reflective Solar Band On-Orbit Radiometric Stability and Accuracy Assessment Using Desert and Antarctica Dome C Sites. *Remote Sensing Environ.* 166, 106–115. doi:10.1016/j.rse.2015.05.021

Wang, W., and Cao, C. (2015). DCC Radiometric Sensitivity to Spatial Resolution, Cluster Size, and LWIR Calibration Bias Based on VIIRS Observations. *J. Atmos. Oceanic Tech.* 32 (1), 48–60. doi:10.1175/JTECH-D-14-00024.1

Wang, W., and Cao, C. (2020). Evaluation of NOAA-20 VIIRS Reflective Solar Bands Early On-Orbit Performance Using Daily Deep Convective Clouds Recent Improvements. *IEEE J. Sel. Top. Appl. Earth Observations Remote Sensing* 13, 3975–3985. doi:10.1109/JSTARS.2020.3007863

Weatherhead, E. C., Reinsel, G. C., Tiao, G. C., Meng, X.-L., Choi, D., Cheang, W.-K., et al. (1998). Factors Affecting the Detection of Trends: Statistical Considerations and Applications to Environmental Data. *J. Geophys. Res.* 103 (D14), 17149–17161. doi:10.1029/98JD00995

Wielicki, B. A., Young, D. F., Mlynczak, M. G., Thome, K. J., Leroy, S., Corliss, J., et al. (2013). Achieving Climate Change Absolute Accuracy in Orbit. *Bull. Am. Meteorol. Soc.* 94 (10), 1519–1539. doi:10.1175/bams-d-12-00149.1

Wu, A., Mu, Q., Angal, A., and Xiong, X. (2020). "Assessment of MODIS and VIIRS Calibration Consistency for Reflective Solar Bands Calibration Using Vicarious Approaches," in *Proc. SPIE 11530, Sensors, Systems, and Next-Generation Satellites XXIV*, *(United Kingdom*, *21-25 September 2020)* (SPIE), 1153018. doi:10.1117/12.2573022

Wu, A., Xiong, X., Cao, C., and Chiang, K.-F. (2016). Assessment of SNPP VIIRS VIS/NIR Radiometric Calibration Stability Using Aqua MODIS and Invariant Surface Targets. *IEEE Trans. Geosci. Remote Sensing* 54 (5), 2918–2924. doi:10.1109/TGRS.2015.2508379

Xiong, X., Angal, A., Twedt, K. A., Chen, H., Link, D., Geng, X., et al. (2019). MODIS Reflective Solar Bands On-Orbit Calibration and Performance. *IEEE Trans. Geosci. Remote Sensing* 57 (9), 6355–6371. doi:10.1109/TGRS.2019.2905792

Xiong, X., Sun, J., Xie, X., Barnes, W. L., and Salomonson, V. V. (2010a). On-Orbit Calibration and Performance of Aqua MODIS Reflective Solar Bands. *IEEE Trans. Geosci. Remote Sensing* 48, 535–546. doi:10.1109/TGRS.2009.2024307

Xiong, X., Wu, A., Wenny, B., Choi, J., and Angal, A. (2010b). Progress and Lessons from MODIS Calibration Intercomparison Using Ground Test Sites. *Can. J. Remote Sensing* 36 (5), 540–552. doi:10.5589/m10-082

Conflict of Interest: CH, AG and BS was employed by Science Systems and Applications, Inc.

The remaining authors declare that the research was conducted in the absence of any commercial or financial relationships that could be construed as a potential conflict of interest.

ORIGINAL RESEARCH
published: 15 February 2022
doi: 10.3389/frsen.2022.780243

Cloud Height Daytime Variability From DSCOVR/EPIC and GOES-R/ABI Observations

A. Delgado-Bonal[1,2*], A. Marshak[1], Y. Yang[1] and L. Oreopoulos[1]

[1] Earth Sciences Division, NASA Goddard Space Flight Center, Greenbelt, MD, United States
[2] Universities Space Research Association, Columbia, MD, United States

Edited by:
Feng Xu, University of Oklahoma, United States

Reviewed by:
Zhao-Cheng Zeng, University of California, Los Angeles, United States
Jianping Guo, Chinese Academy of Meteorological Sciences, China

**** Correspondence:** A. Delgado-Bonal, alfonso.delgadobonal@nasa.gov, orcid.org/0000-0001-6488-9281*

***Specialty section:** This article was submitted to Satellite Missions, a section of the journal Frontiers in Remote Sensing*

***Received:** 20 September 2021*
***Accepted:** 20 January 2022*
***Published:** 15 February 2022*

***Citation:** Delgado-Bonal A, Marshak A, Yang Y and Oreopoulos L (2022) Cloud Height Daytime Variability From DSCOVR/EPIC and GOES-R/ABI Observations. Front. Remote Sens. 3:780243. doi: 10.3389/frsen.2022.780243*

One of the largest uncertainties in climate sensitivity predictions is the influence of clouds. While some aspects of cloud formation and evolution are well understood, others such as the diurnal variability of their heights remains largely unexplored at global scales. Aiming to fill that fundamental

gap in cloud knowledge, this paper studies the daytime evolution of cloud top height using the EPIC instrument aboard the DSCOVR satellite, complemented by coincident cloud height retrievals by GOES-R's ABI instrument. Both datasets indicate that cloud height exhibits a minimum around midday for low clouds with amplitudes between 250 and 600 m depending on the season. The two datasets also agree that high clouds exhibit a contrasting behavior with steady increase of cloud height from morning to evening. We investigate dependences on the type of underlying surface, finding that the amplitude of the diurnal cycles is weaker over ocean than over land for both EPIC and ABI retrievals. We also find a positive correlation between cloud fraction and height over ocean which turns negative over land for low clouds, while for high clouds the correlation is largely positive.

Keywords: cloud height, global variability, DSCOVR, Earth Polychromatic Imaging Camera (EPIC), diurnal cloud cycles

INTRODUCTION

The diurnal variability of cloud fraction and its associated radiative influence is linked to the evolution of the boundary layer depth, determined by the balance between entrainment, subsidence, advection, and turbulent fluxes (Antonia et al., 1977; Wood and Bretherton 2004; Guo et al., 2011; Painemal et al., 2013; Mazzitelli et al., 2014). Solar heating drives air to rise, which then cools adiabatically until it reaches saturation with respect to liquid or ice, and forms droplets or ice particles. Over land, as the sun heats the surface, cloud cover starts increasing early in the morning as the boundary layer deepens, reaching a maximum around noon and early afternoon and continuing with a decrease of cloud cover later in the afternoon. Over ocean, cloud cover evolution follows a diametrically opposite cycle: peak cloud fraction during nighttime, followed by decrease during the morning, a minimum around noon, and a steady increase during the afternoon (Delgado-Bonal et al., 2020a; Delgado-Bonal et al., 2021).

Besides cloud fraction, cloud height is the other main cloud property greatly affecting the Earth's greenhouse effect, and its response to increasing surface temperature represents a strong but not well-understood feedback process in the climate system (Zelinka and Hartmann (2010); Davies and Molloy 2012). Knowledge of cloud top and cloud base help to reduce the estimation of uncertainties of cloud forcing (Xu et al., 2021). Long-term

trends in global cloud heights have not been quantified yet, partially due to large interannual fluctuations associated with major regional events such as ENSO that mask low frequency variability.

Although the signal of cloud height changes on a global scale may not be clear, changes in the regional level are detectable because the amplitude of at those scales can be much larger than the changes in the globally-averaged value. Analyses with the Multiangle Imaging SpectroRadiometer (MISR) instrument on the Terra satellite found unexplained differences between the Northern and Southern Hemisphere from March 2000 to February 2015, the former decreasing the cloud top height averaged value at −16 ± 5 m/decade and the latter increasing it at 14 ± 4 m/decade (Davies and Molloy 2012; Evan and Norris 2012; Davies et al., 2017).

At smaller temporal and spatial scales, fluctuations of cloud height are even more dramatic. Interannual global variations of cloud top heights reveal significant signals, with anomalies up to 80 m due to La Niña [2007–2008 and 2011] and El Niño [2009, 2013] events. Metrics of ENSO and Hadley-Walker circulations strength also correlate significantly with the interannual regional changes in cloud height (Davies et al., 2017).

Cloud height variability has been observed with a variety of sensors applying different principles to retrieve cloud top height (Marchand 2013; Lelli et al., 2014). Zhao et al. (2020) used MODIS data from 2000 to 2018 to conclude that cloud top height in East Asia has increased at an average rate of 0.020 km per year, exhibiting different seasonal rates and a positive correlation with sea surface temperature, indicating that cloud top height may be modulated by changes close to the surface (Zhao et al., 2020). Using reflected solar ultraviolet-visible (UV-VIS) measurements taken from 1996 to 2003 by the global ozone monitoring experiment (GOME) instrument, Loyola et al. (2010) obtained a decreasing cloud top height trend of −4.8 m per year within the ±60° of latitude belt.

The drastic changes of cloud height inter-annual variations at different scales give an idea of the importance of analyzing regional features. Small land areas such as in the Zhao et al. (2020) study over East Asia find different sign and order of magnitude for cloud height changes compared to the entire Northern Hemisphere (Davies et al., 2017). Additionally, the magnitudes of the changes differ between land and ocean and are ultimately driven by the climatology of each region.

Higher frequency cloud height changes such as diurnal variations are difficult to analyze globally given the orbital characteristics of sun-synchronous satellites. For example, while the MISR instrument aboard the Terra satellite could be used to study interannual variations (Davies and Molloy 2012), its fixed equator crossing time at approximately 10:30 am local time does not allow it to quantify diurnal variations in cloud height. The importance of monitoring cloud diurnal variabilities cannot be overstated since they are intimately related to the planet's energy balance and climate change. Even with other cloud properties remaining unchanged, changes in the diurnal variability of cloud fraction of various cloud types could have an important impact on the net radiation at surface (Cairns 1995). As an example, early deforestation in the Amazon basin led to a change of low and high cloud fractions, resulting in a change of local cloud diurnal contribution to the time-mean shortwave surface flux of 20 Wm^{-2}, equivalent to a change of 0.05 in surface albedo (Cutrim et al., 1995).

As the boundary layer depth changes every day, a repeating cycle of cloud cover and cloud height manifests itself. Variability in the height of low clouds has been reported for different regions, mainly stratocumulus regions in the southeastern Pacific (Minnis and Harrison 1984; Minnis et al., 1992; Zuidema et al., 2009) where modulations of the boundary layer are attributed to the blocking effects of the Andes which increases subsidence and induces convergence and upward motions in the lower troposphere (Painemal et al., 2013; Zuidema et al., 2009). *In situ* observations in this region have also documented the diurnal pattern of cloud height (de Szoeke et al., 2012) and although limited in their sampling frequency, suggest that cloud top heights exhibit diurnal variations in this region that are larger than in the northeast Pacific (Minnis et al., 1992; Garreaud et al., 2001; Bretherton et al., 2010), highlighting once again the importance of regional features and topography on the diurnal cycles of cloud top height.

Diurnal changes in cloud height have also been studied with numerical models (Garreaud et al., 2001). Unfortunately, it is well-known that these models have poor skill in simulating realistically the diurnal evolution of cloud properties, which materializes as underestimation of amplitudes and misplacement of the local times of maximum and minimum cloud top height occurrence (Abel et al., 2010; Yin and Porporato 2017).

Quantifying global diurnal variations in cloud height requires resolving simultaneously and with high accuracy both temporal and spatial gradients.

On the spatial side, techniques with high vertical resolution such as radio occultation fail to provide spatial information (von Engeln et al., 2005), while active instruments despite offering excellent vertical resolution suffer from limited horizontal coverage, as in the case of Cloud–Aerosol Lidar and Infrared Pathfinder Satellite Observations (CALIPSO). On the temporal side, sampling limitations that come with sun-synchronous orbits (Zuidema et al., 2009; Xie et al., 2012) affect instruments such as the Moderate Resolution Imaging Spectroradiometer (MODIS) and MISR.

Extensive spatial coverage is crucial for understanding the regional nuances in cloud diurnal cycles. Geostationary satellite systems such as GOES-R (currently including GOES-16 and GOES-17) combine extensive spatial coverage with a high-frequency sampling of 10 min. These satellites rely on visible and infrared measurements to track cloud coverage and vertical motions. The infrared bands of the Advanced Baseline Imager (ABI) are used to simultaneously retrieve Cloud Top Height, Cloud Top Temperature, and Cloud Top Pressure for each cloudy pixel (Schmit et al., 2017). Earlier satellites of the GOES family have been used to quantify the diurnal cycles of marine clouds in the southeastern Pacific (Minnis et al., 1992; Painemal et al., 2013).

However, to obtain a truly global and detailed view of planetary cloudiness beyond what is provided by a single geostationary satellite, it is necessary to either aggregate data from multiple geostationary and sun-synchronous satellites as is done by the International Satellite Cloud Climatology Project (ISCCP) (Rossow and Schiffer, 1991) or to use the recently available measurements of the Earth Polychromatic Imaging Camera (EPIC) aboard the Deep Space Climate Observatory (DSCOVR) spacecraft (Marshak et al., 2018). EPIC observes the planet from approximately 1.5 million km, always facing the sunlit side of the planet. Unlike the GOES-R satellites which relies on thermal infrared bands, EPIC derives the cloud height from observations of the O2 A-band (779.5 and 764 nm), and B-band (680 and 688 nm) pairs (Yang et al., 2019).

In this study, we use retrievals from both EPIC and ABI aboard GOES-R to quantify the diurnal evolution of cloud top height for their overlapping coverage area. Previous analyses of cloud fraction from EPIC and ISCCP showed that the diurnal evolution of high and low cloud fractions is different (Cairns 1995; Delgado-Bonal et al., 2021), However, the accompanying cycles of cloud top heights have hitherto not been examined. Here, we apply

a separation between high and low clouds to resolve more meaningfully the diurnal cycle of height for different kinds of clouds.

Data and Methods Section presents a brief overview of the ABI and EPIC cloud effective height algorithms, and details the methodology used to study diurnal variations of cloud height. Absolute values of cloud height depend critically on the technique and wavelengths used in the derivation and cannot generally be directly compared. However, we maintain that it is acceptable to compare relative changes in cloud top height between different measurement techniques and between measurements and models (Davies et al., 2017). Quantifying the amplitude and shape of diurnal cloud height cycles derived from two sensors using different retrieval principles can serve as a two-way cross-validation of the respective retrievals. *Results* Section describes in some detail the cloud height cycles of low and high clouds from EPIC and ABI, both from global and regional perspective. EPIC and ABI are alike from the perspective of being able to track regional cloudiness throughout the daytime, albeit at a smaller spatial scale for ABI. To provide a statistically reliable picture of the cloud height diurnal cycles, we aggregate observations at hourly local times. Once the diurnal evolution of cloud coverage and height has been fully described in terms of cloud fraction and height, we evaluate the correlation between the two variables throughout their daily global evolution. This paper employs the EPIC statistically derived diurnal maps at fixed local times to investigate the correlation of cloud fraction and cloud top height in order to characterize regional behavior.

DATA AND METHODS

The NOAA product from the GOES-R series of satellites provides an official binary clear-sky mask, classifying each pixel as clear or cloudy. The cloud mask algorithm uses 9 out of the 16 ABI spectral bands to detect clouds based on spectral, spatial and temporal signatures (Heidinger, 2012). The thresholds for this binary classification were derived from analysis of space-borne lidar and current geostationary imager data. The primary validation sources are data from Spinning Enhanced Visible and InfraRed Imager (SEVIRI) and the Cloud-Aerosol LIdar with Orthogonal Polarization (CALIOP) aboard the Cloud-Aerosol Lidar and Infrared Pathfinder Satellite Observations (CALIPSO) satellite. The latter has an inherent high sensitivity to cloud presence over all surface types and under all illumination conditions (Schmit et al., 2017).

GOES-R ABI infrared observations aiming to measure the height of clouds are impacted by their wavelength-dependent emissivity, and by emissions from the surface and atmosphere. Also, clouds often exhibit complex vertical structures that violate the assumptions of the single layer plane parallel models. To provide reliable cloud top retrievals, the ABI Cloud Height Algorithm (ACHA) uses the 13.3 μm CO_2 channels coupled with multiple longwave IR windows (10.4, 11 and 12 μm) within an optimal estimation framework where an analytical radiative transfer model has central role. Cloud-top pressure and cloud-top height are derived from the cloud-top temperature product and the atmospheric temperature profile provided by Numerical Weather Prediction data. GOES-R retrievals combine therefore the sensitivity to cloud height offered by the CO_2 channel with the sensitivity to ice cloud microphysics offered by the window channels, so no microphysical assumptions need to be invoked (Heidinger and Straka 2013).

EPIC's 2,048 × 2,048 pixel CCD array provides reflectances at ten channels spanning from the ultraviolet (318, 325, 340, and 388 nm) to the visible (443, 551, 680, and 688 nm) and near infrared (764 and 780 nm). The cloud product algorithm uses a surface-type based threshold method for cloud masking, applied on the reflectances at the 388, 680, 780 nm and O2 A- and B-band channels. The results are comparable with those provided by geostationary (GEO) and low Earth orbit (LEO) satellites, with differences of only 1.5% in the global cloud fraction of collocated datasets (Yang et al., 2019). The EPIC cloud mask algorithm provides confidence level flags for its cloud detection outcomes; less than 3% of the total number of pixels are flagged as low confidence cloudy.

Unlike ABI, the EPIC cloud top height is derived from observations of O_2 A-band (779.5 and 764 nm) and B-band (680 and 688 nm) pairs. Due to photon penetration into the cloud, for a given optical thickness and particle properties, the radiance measured by EPIC's A- and B-bands is not only a function of cloud top height, but also a function of the cloud extinction coefficient profile (Yang et al., 2013). Therefore, EPIC's retrievals correspond to an "effective" cloud top height, a measure of the mean height from which light is scattered ("centroid"), an important parameter that has been widely used in trace gas retrievals and climate studies (Stammes et al., 2008; Wang et al., 2011; Joiner et al., 2012). Since ABI-derived cloud top heights from IR methods are also not true geometrical top heights, and therefore also considered "effective," but in a different sense, we will simply

refer to “cloud top height” in many of the discussions that follow, with the understanding that the retrieval principles for the two cases are very different and responsible for the discrepancies in cloud top height values.

The EPIC A-band and B-band cloud effective pressure retrievals are based on the Mixed Lambertian-Equivalent Reflectivity concept, extensively studied and applied in operational settings (Koelemeijer et al., 2001; Wang et al., 2008; Joiner et al., 2012; Yang et al., 2013). In this model, it is assumed that the pixel contains two Lambertian reflectors, the surface and the cloud. The cloud is assumed to be opaque, i.e., no photon penetration occurs (even if that is not true in reality). Cloud effective pressure and cloud effective fraction are simultaneously retrieved and converted to cloud height using the co-located atmosphere profile provided by GEOS-5 FP-IT (Lucchesi, 2015). EPIC cloud effective height can be obtained either from the A- or B-band, providing slightly different values due to the difference in photon penetration depths, which contains information on cloud vertical structure. In this paper, we use the less noisy A-band value (Yang et al., 2019).

Both EPIC and GOES-R products are labeled in UTC time. Exploiting their vast coverage areas, each dataset can be split into different local time zones depending on the longitude and UTC acquisition time. Figure 1 shows an EPIC RGB image whose clouds have been enhanced for the purpose of illustration. The center of the image always corresponds to local noon, while the left and right edges to sunrise and sunset respectively. Since EPIC acquires up to 13 (in Boreal winter) and up to 22 (in Boreal summer) images per day, the local time of observation for various regions varies by day, providing thus an average diurnal cycle of cloudiness when accumulated over time. Geostationary satellites with their high frequency data acquisition are also capable of observing cloud evolution throughout the day, but their coverage is limited to a fixed portion of the Earth. In order to create comparable datasets for EPIC and GOES-R, we partition the observation field into 1×1 grid cells. We follow a nearest neighbor algorithm to find the matching grid cell for each pixel by minimizing the Euclidean distance between the longitude and latitude coordinates of each pixel and the center of each grid cell. We then calculate average values of cloud height for each grid cell.

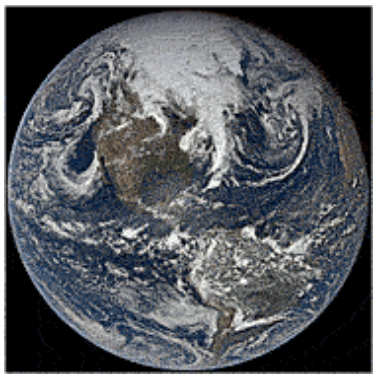

FIGURE 1 | EPIC RGB image corresponding to 2020-05-01 17:54:31 UTC. The image has been enhanced to show the cloud coverage in detail.

By making use of the ability to track the daily evolution of cloud properties, we split the data into local hourly bins, creating 24 local time maps for each satellite's imagery. For EPIC, we repeat this process with 4 years of data from June 2015 to June 2019 (approximately 16,500 full disk images) while for ABI we use all the available retrievals for 2020 (approximately 52,500 images). The DSCOVR satellite was placed in a safe mode in June 2019 for almost 9 months, prompting us to use the 4 years of consistent data prior to that date. For the purposes of our statistics, we assume an ergodic seasonal behavior which allows us to average each season of data for the 4 years to obtain a single mean map for each season. For ABI, we use the latest complete full year available and average by season. Given the large amount of data captured by ABI, 1 year of data is sufficient to provide stable statistics. We then average the cloud height of all the local time maps across the number of observations for each grid cell and across all years for a particular season, obtaining thus seasonally-averaged maps of cloud height at all local times.

This methodology has proven useful in determining diurnal cycles with EPIC data and quantifying the diurnal variability of cloud fraction for low and high clouds consistently with previous research (Delgado-Bonal et al., 2021). Due to EPIC's location at the L1 point, the best pixel resolution is achieved at nadir (~ 8 km); off nadir the pixels become elliptical with the long axis larger by a factor of about 1/cos(SZA) and the short axis unaffected. Furthermore, as the Earth's axis is tilted 23.5° relative to its orbital plane around the Sun, high northern latitudes in boreal winter and high southern latitudes in boreal summer are excluded from EPIC's field of

view. Moreover, some regions suffer discontinuity behaviors in contiguous zones along meridians during December-January-February due to lower availability of data at specific local times, but broad patterns can be easily inferred by observing adjacent zones.

We quickly realized that the diurnal behavior of high and low clouds is distinct and thus study it separately. We consider all ABI clouds below 3,000 m as low clouds, and all clouds above 6,000 m as high clouds. Changing these cutoffs by ±1,000 m does not impact our results substantially. For EPIC, we assign the low and high cloud classes based on the most likely thermodynamic cloud phase (liquid or ice) provided in the Level 2 datasets (Yang et al., 2019) with all liquid clouds classified as low and all ice clouds classified as high. EPIC's cloud thermodynamic phase determination is based on cloud effective temperature, which is inferred from the cloud effective pressure derived from the EPIC O_2 A-band observations (Meyer et al., 2016; Yang et al., 2019). Cloudy pixels are classified as ice if the effective temperature is lower than 240K, and as liquid if it exceeds 260K, while the rest of cloudy pixels are classified as unknown to avoid potentially erroneous classifications. This methodology has been tested against MODIS (Meyer et al., 2016), yielding agreement in the thermodynamic phase of approximately 77% of the pixels, categorizing 21% of them as unknown, and misclassifying only about 2% with respect to MODIS. By using the most likely thermodynamic phase, we avoid possible distortions of the daytime cycles due to misclassified pixels.

RESULTS

Integrated Area Results

While diurnal variations in cloud top height have been previously reported for regions of various sizes, ranging from specific locations of field experiments to larger domains spanning like Eastern Asia or the contiguous United States, there has never been a truly global analysis. In this section, EPIC is employed for this task. At the same time, we also examine the degree to which EPIC's views of cloud top height diurnal patterns are consistent with those from ABI over land (GOES-16) and over ocean (GOES-17). Similar to the low/high discrimination, land-ocean separation is important for capturing the distinct nature of continental and marine clouds, expected to have different amplitudes and phases in their diurnal cycles. A

prerequisite for such an analysis is matching the overlapping portions of domains viewed by EPIC and ABI.

To avoid potential sunrise and sunset artifacts at the edge of EPIC images, we only consider pixels with local times between early morning (8:00) and late afternoon (16:00), while for ABI we extend to nighttime. Figure 2 shows the diurnal cycle results for the integrated area of GOES-16 over land, along with the same area for EPIC, and the full global average of EPIC. Each column represents one season, with the top panels corresponding to high clouds and the bottom panel to low clouds.

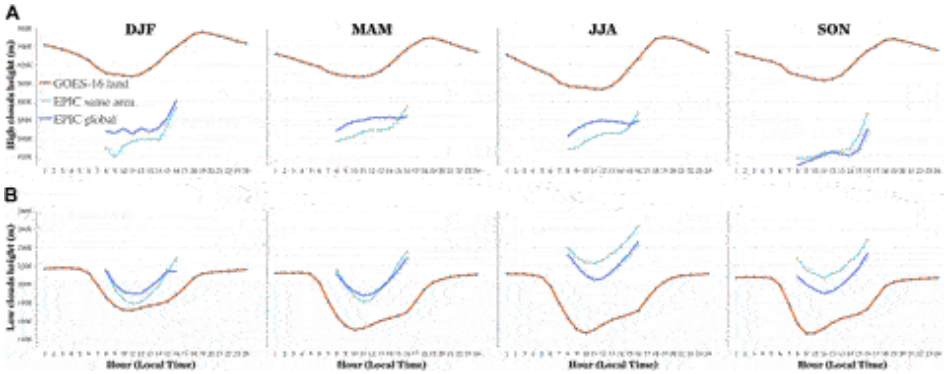

FIGURE 2 | Diurnal cycles of cloud height for GOES-16 (red line) and EPIC over land. EPIC results are shown for the whole globe (dark blue) and for the same areas as GOES-16 (light blue). Each column is a different season for high **(A)** and low **(B)** clouds.

ABI cloud top height diurnal cycles for low clouds over land reveal a minimum around 10 am Local Time (LT), whose amplitude varies from approximately 250 m in boreal winter to a maximum of 600 m in boreal summer. The same area analyzed with EPIC yields a minimum around 11 am LT and an amplitude of approximately 450 m. The cycles for the whole globe obtained with EPIC have similar shape as that for the GOES-16 domain although slightly displaced in the vertical axis.

Along with the mean values, we determine the standard deviation of the mean for each 1-by-1 degree cell. Then, we average the standard deviation for the whole globe to provide an hourly global standard deviation associated with every hourly point showed in Figures 2, 3. For low clouds over land, we obtain a standard deviation of approximately 550 m for ABI, and of 500 m for EPIC. This value of standard deviation indicates that the effective cloud top heights even within the same cloud group (low/high) exhibit significant variability for a particular time of the day. For example, in our analysis,

clouds at 7,000 m and at 14,000 m are considered high clouds and are aggregated together in our statistical analyses. To obtain the sampling error of the mean, we divide the standard deviation by the square root of the size of sample and multiply the result with the Z score of a 95% confidence interval (Z = 1.96). By doing so, we obtain a sampling error of less than 10 m for both EPIC and ABI. This suggests that our sample is sufficiently large to calculate mean values accurately.

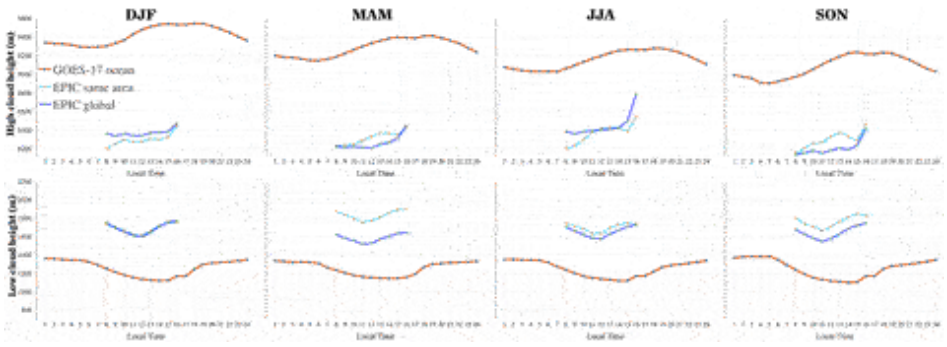

FIGURE 3 | As Figure 2, but for GOES-17 over ocean.

As stated above, direct comparison of the absolute values of cloud top heights derived from instruments with different capabilities and algorithmic philosophies is not advisable. Furthermore, differences arise since low clouds for GOES-R have been defined as those with tops below 3,000 m whereas EPIC uses a definition directly linked to retrieved thermodynamic phase. We therefore focus only on comparing the shapes of the diurnal cycle curves. Despite the different definitions, the existence of a characteristic diurnal cycle of cloud height even at these very large scales is undeniable in both cases, echoing behavior previously seen only in regional studies (Zuidema et al., 2009; An et al., 2017; Painemal et al., 2013; Zhao et al., 2020).

The cycles of high clouds over land show a distinctive sinusoidal wave shape. For GOES-16, cloud top height has a minimum before noon followed by a steady increase that peaks around 19 h. Throughout the day, the standard deviation for high clouds is approximately 600 m. For the same area, EPIC generally shows the same monotonic increase during the day, with a maximum at the time of the last retrieval we retain, at 4 pm LT, with a standard deviation around 500 m. In this case, global results deviate from the regional picture: although an increase in cloud top effective height during daytime is seen, it is not as clear as that for the GOES-17 disc.

Figure 3 shows the corresponding results for GOES-17 and EPIC, this time over ocean. The marine environment has a discriminating effect on the amplitude of the cycles, which is manifested in both low and high clouds. GOES-17 results for low clouds indicate that the magnitude of the diurnal cycle is approximately 200 m, which matches the EPIC results for the same region and for the whole globe, as well as previous findings in the southern Pacific (Painemal et al., 2013). The cycles for high clouds are also characterized by smaller amplitudes, with their minima shifted to early morning for GOES-17 but maintaining the same progressive increase during daytime for both satellites. The standard deviation for both EPIC and GOES-R is approximately 500 m for clouds over ocean.

Diurnal Cycle Maps

Figure 4 shows two distinct moments of the diurnal low cloud height cycles in boreal spring for GOES-16 (top) and GOES-17 (bottom). The left column presents the average cloud top height between 11:00 am and noon LT, while the right column shows the same disc at midnight. The figures illustrate the transition over land from lower clouds around noon (blue hues) to higher clouds at midnight (red hues). A smaller total change from noon to midnight is seen over ocean. The land grid cells of the two GOES-16 colormaps of Figure 4, when averaged, provide two of the points for the timeseries of Figure 2. Similarly, two of the points of Figure 3 come from the average of ocean only grid cells for the GOES-17 images in Figure 4.

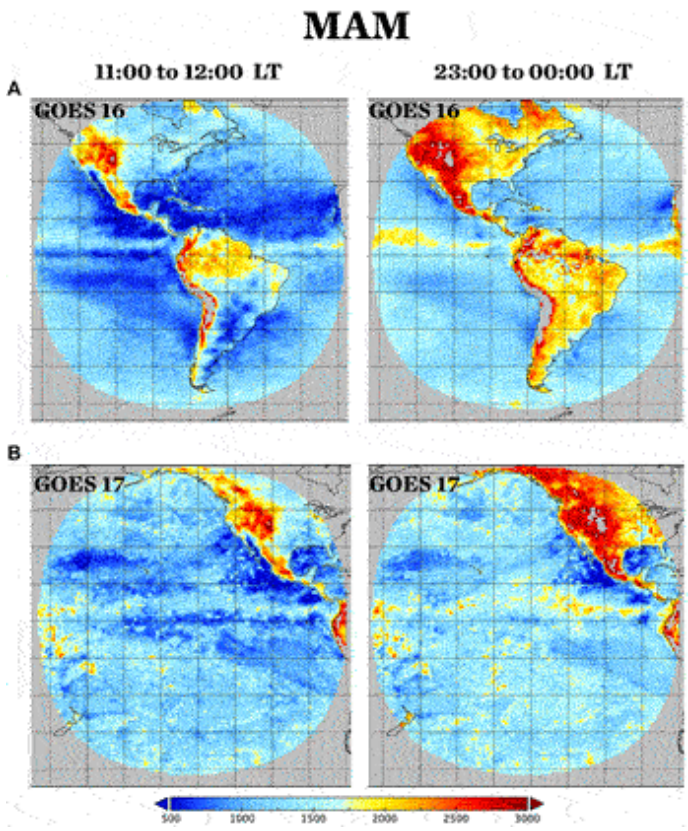

FIGURE 4 | GOES-16 **(A)** and GOES-17 **(B)** diurnal cycle of low clouds height in meters. Left column shows the cloud top height at noon local time and the right column shows the values at midnight. Cloud top height is higher during nighttime for both satellites.

The diurnal cycles for low clouds seen by EPIC have the same broad characteristics. Since EPIC observations are limited to daytime, Figure 5 shows the global view of cloud top height at early morning, noon and evening. The morning-to-noon transition is characterized by a shift from red to blue shades, only to be followed by an increase of cloud top height in the afternoon, recovering the distinctive red tints over most of the continental areas. While these cycles are generally similar across the globe, regional differences can be spotted by careful examination of Figure 5. For example, by looking at the diurnal cycles over the United States and Brazil, one observes that Brazil shows the expected increase in the afternoon while half of the United States area remains with lower cloud heights. Besides being regionally dependent, the diurnal cycles evolve throughout the year.

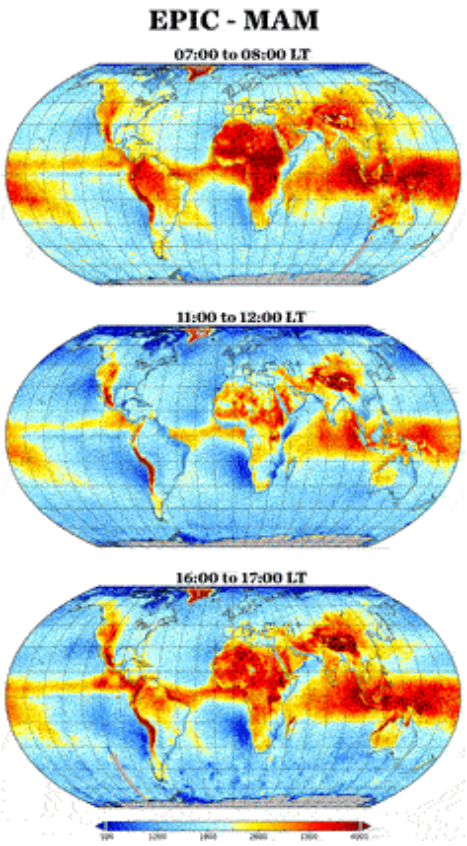

FIGURE 5 | EPIC cloud height for liquid clouds in meters at three selected times for Boreal spring.

Cloud Fraction/Cloud Height Correlation

Previous analyses studying the potential link between cloud fraction and cloud height have been limited to the correlation in time derived from daily data. For example, Gryspeerdt et al. (2014) investigated the strength of the relationships between cloud fraction and cloud top pressure (which translates to cloud top height) using data from MODIS Terra, defining the correlation as the slope of a linear regression between the two quantities. The study found a strong interrelationship between the two variables, likely due to deep convective systems having both high cloud fraction and cloud height. However, given Terra's fixed equator crossing time at 10:30 am, these findings do not inform us about intraday correlations.

Once the diurnal cycles of cloud fraction (Delgado-Bonal et al., 2021) and cloud height have been characterized using EPIC, their co-evolution during the day can be examined. In general, cloud fraction over land peaks around noon, which contrasts with the minimum cloud fraction over ocean

found at that time. Due to this contrasting diurnal evolution of cloud fraction between land and ocean, An et al., 2017 found a negative correlation between cloud base height and cloud fraction over the contiguous United States, while Painemal et al., 2013 found a positive correlation between cloud top height and cloud fraction for two locations over the southern Pacific. However, the sign of these correlations is not necessarily representative of ocean and land behavior overall, as evidenced by the variety of diurnal behaviors seen regionally. Figure 6 shows two examples of oceanic regions, only 5° in latitude apart, with opposing correlations between cloud fraction and cloud effective height.

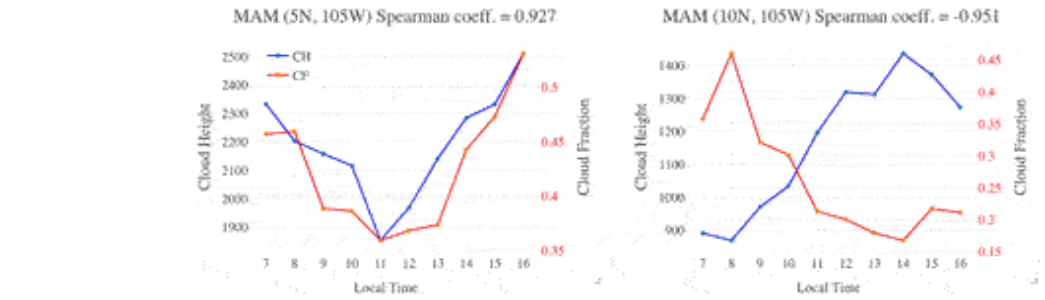

FIGURE 6 | Example of diurnal evolution of cloud fraction and cloud effective height in meters using EPIC for two locations in the Pacific Ocean during Boreal spring. Even though the locations are physically close, they have opposite correlation coefficient sign.

To quantify correlation, we use Spearman's ρ as a nonparametric measure of rank correlation (Myers and Well 2003, pp. 508) with a range between +1 (positive correlation) and −1 (negative correlation). This statistical quantity is not limited to linear correlations and assesses how well the relationship between two variables can be described using a monotonic function. A positive value of the coefficient indicates that as the value of one variable increases, so does the value of the other variable, and vice-versa. Figure 6 left shows an example of a positive correlation between cloud top height and cloud fraction seen by EPIC with a Spearman's coefficient of +0.927 while the right side of the figure has a negative coefficient of −0.951.

Exploiting EPICs spatial and temporal advantages, Figure 7 shows the correlation between cloud top height and cloud fraction for low clouds, separately for the four seasons. Over ocean, Boreal summer emerges as the season of strongest correlation, and with positive correlations dominating because as cloud fractions decrease during daytime over ocean, reaching a minimum around noon, cloud top heights also decrease, a state of affairs also

reported by Painemal et al., 2013. However, it must be noted that this is not a general finding since other oceanic locations such as the west coast of central America are characterized by a negative correlation during boreal summer that turns positive during boreal winter. The variety of behaviors highlights the importance of EPIC in characterizing diurnal cycles.

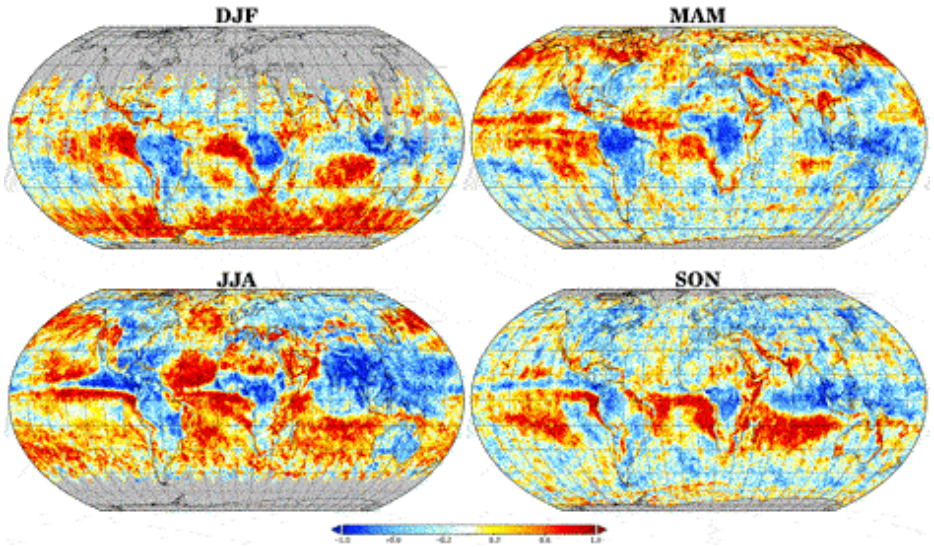

FIGURE 7 | Spearman correlation coefficient between cloud fraction and cloud effective height for low clouds using EPIC. Blue colors indicate a negative correlation while red colors a positive one.

Figure 8 shows EPIC's counterpart correlation map for high clouds. In this case, a positive correlation between high cloud fraction and cloud height is observed for most of the globe. High cloud fraction evolves diurnally regardless of the surface type, with higher cloud fraction values in the afternoon than in the morning and noon (see discussion and appendixes in Delgado-Bonal et al., 2021). The diurnal cloud height cycles obtained in this paper (see Figures 2, 3) follow a similar behavior during the day, with cloud height increasing from morning to evening, hence resulting in mostly positive regional correlations.

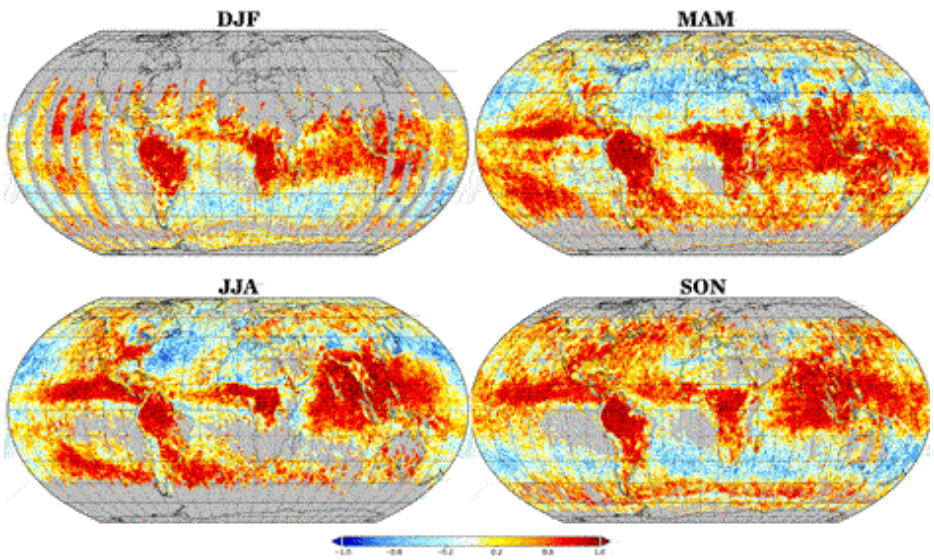

FIGURE 8 | As Figure 7 but for high clouds.

CONCLUSIONS AND DISCUSSION

Radiation fluxes depend strongly and nonlinearly on the diurnal variations of cloud properties (Bergman and Salby 1997; Delgado-Bonal et al., 2020b), with the amount of radiation reflected to space depending on how cloud fraction changes during daytime correlate with the cycle of solar insolation. On the thermal infrared side, cloud height is also a major controlling factor of the planet's energy balance since low and high clouds have different impacts on the greenhouse effect. Understanding cloud height variability is thus essential for the characterization of the planet's climate. While previous research has focused on interannual variability or regional studies because of lack of appropriate observations, this paper employs appropriate data from EPIC and GOES-R to study diurnal cloud top height cycles over large areas.

EPIC and ABI use different principles and parts of the spectrum to retrieve cloud top height, so the physical meaning of what cloud height they retrieve and how it relates to the true geometrical cloud top height is different. We use this to our advantage to show that, regardless of methodology, the diurnal cycles of cloud height for both low and high clouds cannot only be clearly inferred, but also compared in terms of their relative shapes which have a prominent signal for even global averages. Sensible changes in thresholds or definitions used to distinguish between low and high clouds do not impact the conclusions in any meaningful way.

To provide a holistic view of daytime cloud height cycles for the entire planet EPIC retrievals are more appropriate. The results from this instrument are generally in agreement with those from the ABI instrument aboard geostationary satellites, and prior research which was more geographically limited. EPIC theoretical analyses show that its cloud height retrievals are influenced by the solar zenith angle (SZA); because of the observation geometry from the L1 point is essentially the same as the viewing zenith angle, a convex shape with a minimum during midday was expected (Yang et al., 2013). The extent of the impact of such a systematic dependence is unknown. In order to minimize possible interference of a geometrical artifact in the results, we elected to report the diurnal cycles only from 8 am to 4 pm LT. EPIC results for the integrated areas presented in Figures 2, 3 did indeed reveal the expected convex behavior for low clouds. At the same time, our results show that: 1) we can achieve consistency with previous findings; 2) the convex behavior is not found for high clouds; 3) the amplitudes of those convex cycles are different between land and ocean; and 4) the diurnal cycles from ABI are similar even though these retrievals are not affected by the same geometrical effects.

Finally, we explore the daytime correlation between cloud fraction and cloud height Since the thermodynamic and dynamical structure of the location may affect that relationship, we develop global correlation maps using Spearman's coefficient. We show that, for low clouds, the correlation is seasonally and regionally dependent, being generally positive over ocean and negative over land as a consequence of the opposite diurnal behavior of cloud fraction for the two underlying surfaces. On the other hand, high clouds are positively correlated for the most part of the globe since the amounts of high clouds evolve independently of the surface type.

In summary, we showed that:

- For low clouds, cloud height exhibits a minimum around midday with amplitudes between 250 and 600 m. On the contrary, high clouds exhibit a steady increase from morning to evening of approximately 500 m.
- The amplitude of the diurnal cycles is smaller over ocean than over land.
- The correlation between cloud fraction and height for low clouds is mostly positive over ocean and negative over land. For high

clouds, the correlation is largely positive.

DATA AVAILABILITY STATEMENT

The data sets used in this investigation are available at the NASA's Atmospheric Science Data Center (ASDC), located in the Science Directorate located at NASA'S Langley Research Center in Hampton, Virginia. The collection is called "DSCOVR EPIC CLOUD Product Version 03" and is accessible at: https://earthdata.nasa.gov/eosdis/daacs/asdc. EPIC images are accessible at: https://epic.gsfc.nasa.gov.

AUTHOR CONTRIBUTIONS

AD-B and AM. analyzed the data. YY developed the EPIC L2 cloud datasets. AD-B, AM, YY, and LO discussed the results and wrote the paper.

FUNDING

AD-B research was supported by the DSCOVR Science Management project. AM acknowledges support from NASA's DSCOVR Science Management project. YY would like to acknowledge funding support from the NASA DSCOVR Science Team Program. LO gratefully acknowledges support from NASA's MEaSUREs program.

PUBLISHER'S NOTE

REFERENCES

Abel, S. J., Walters, D. N., and Allen, G. (2010). Evaluation of Stratocumulus Cloud Prediction in the Met Office Forecast Model during VOCALS-REx. *Atmos. Chem. Phys.* 10, 10541–10559. doi:10.5194/acp-10-10541-2010

An, N., Wang, K., Zhou, C., and Pinker, R. T. (2017). Observed Variability of Cloud Frequency and Cloud-Base Height within 3600 M above the Surface over the Contiguous United States. *J. Clim.* 30 (10), 3725–3742. doi:10.1175/JCLI-D-16-0559.1

Antonia, R. A., Danh, H. Q., and Prabhu, A. (1977). Response of a Turbulent Boundary Layer to a Step Change in Surface Heat Flux. *J. Fluid Mech.* 80 (1), 153–177. doi:10.1017/S002211207700158X

Bergman, J. W., and Salby, M. L. (1997). The Role of Cloud Diurnal Variations in the Time-Mean Energy Budget. *J. Clim.* 10, 1114–1124. doi:10.1175/1520-0442(1997)010<1114:trocdv>2.0.co;2

Bretherton, C. S., Wood, R., George, R. C., Leon, D., Allen, G., and Zheng, X. (2010). Southeast Pacific Stratocumulus Clouds, Precipitation and Boundary Layer Structure Sampled along 20° S during VOCALS-REx. *Atmos. Chem. Phys.* 10, 10639–10654. doi:10.5194/acp-10-10639-2010

Cairns, B. (1995). Diurnal Variations of Cloud from ISCCP Data. *Atmos. Res.* 37, 1–3. doi:10.1016/0169-8095(94)00074-N

Cutrim, E., Martin, D. W., and Rabin, R. (1995). Enhancement of Cumulus Clouds over Deforested Lands in Amazonia. *Bull. Amer. Meteorol. Soc.* 76, 1801–1805. doi:10.1175/1520-0477(1995)076<1801:eoccod>2.0.co;2

Davies, R., Jovanovic, V. M., and Moroney, C. M. (2017). Cloud Heights Measured by MISR from 2000 to 2015. *J. Geophys. Res. Atmos.* 122, 3975–3986. doi:10.1002/2017JD026456

Davies, R., and Molloy, M. (2012). Global Cloud Height Fluctuations Measured by MISR on Terra from 2000 to 2010. *Geophys. Res. Lett.* 39, a–n. doi:10.1029/2011GL050506

de Szoeke, S. P., Yuter, S., Mechem, D., Fairall, C. W., Burleyson, C. D., and Zuidema, P. (2012). Observations of Stratocumulus Clouds and Their Effect on the Eastern Pacific Surface Heat Budget along 20°S. *J. Clim.* 25 (24), 8542–8567. doi:10.1175/JCLI-D-11-00618.1

Delgado-Bonal, A., Marshak, A., Yang, Y., and Holdaway, D. (2020b). Analyzing Changes in the Complexity of Climate in the Last Four Decades Using MERRA-2 Radiation Data. *Sci. Rep.* 10, 922. doi:10.1038/s41598-020-57917-8

Delgado-Bonal, A., Marshak, A., Yang, Y., and Oreopoulos, L. (2020a). Daytime Variability of Cloud Fraction from DSCOVR/EPIC Observations. *J. Geophys. Res. Atmos.* 125, e2019JD031488. doi:10.1029/2019JD031488

Delgado-Bonal, A., Marshak, A., Yang, Y., and Oreopoulos, L. (2021). Global Daytime Variability of Clouds from DSCOVR/EPIC Observations. *Geophys. Res. Lett.* 48, e2020GL091511. doi:10.1029/2020GL091511

Evan, A. T., and Norris, J. R. (2012). On Global Changes in Effective Cloud Height. *Geophys. Res. Lett.* 39, a–n. doi:10.1029/2012GL053171

Garreaud, R. D., Rutllant, J., Quintana, J., Carrasco, J., and Minnis, P. (2001). CIMAR-5: A Snapshot of the Lower Troposphere over the Subtropical Southeast Pacific. *Bull. Amer. Meteorol. Soc.* 82 (10), 2193–2208. doi:10.1175/1520-0477-82.10.2193

Gryspeerdt, E., Stier, P., and Grandey, B. S. (2014). Cloud Fraction Mediates the Aerosol Optical Depth-Cloud Top Height Relationship. *Geophys. Res. Lett.* 41, 3622–3627. doi:10.1002/2014GL059524

Guo, J., Zhang, J., Yang, K., Liao, H., Zhang, S., Huang, K., et al. (2011). Investigation of Near-Global Daytime Boundary Layer Height Using High-Resolution Radiosondes: First Results and Comparison with ERA5, MERRA-2, JRA-55, and NCEP-2 Reanalyses. *Atmos. Chem. Phys.* 21, 17079–17097. doi:10.5194/acp-21-17079-2021

Heidinger, A. (2012). *ABI Cloud Height Algorithm Theoretical Basis Document*. NOAA/NESDIS/STAR. Version 3.0 July.

Heidinger, A., and Straka, W. C. (2013). *ABI Cloud Mask Algorithm Theoretical Basis Document*. NOAA/NESDIS/STAR, SSEC/CIMSS. Version 3.0 June 11.

Joiner, J., Vasilkov, A. P., Gupta, P., Bhartia, P. K., Veefkind, P., Sneep, M., et al. (2012). Fast Simulators for Satellite Cloud Optical Centroid Pressure Retrievals; Evaluation of OMI Cloud Retrievals. *Atmos. Meas. Tech.* 5 (3), 529–545. doi:10.5194/amt-5-529-2012

Koelemeijer, R. B. A., Stammes, P., Hovenier, J. W., and de Haan, J. F. (2001). A Fast Method for Retrieval of Cloud Parameters Using Oxygen A Band Measurements from the Global Ozone Monitoring Experiment. *J. Geophys. Res.* 106, 3475–3490. doi:10.1029/2000JD900657

Lelli, L., Kokhanovsky, A. A., Rozanov, V. V., Vountas, M., and Burrows, J. P. (2014). Linear Trends in Cloud Top Height from Passive Observations in the Oxygen A-Band. *Atmos. Chem. Phys.* 14, 5679–5692. doi:10.5194/acp-14-5679-2014

Loyola R., D. G., Thomas, W., Spurr, R., and Mayer, B. (2010). Global Patterns in Daytime Cloud Properties Derived from GOME Backscatter UV-VIS Measurements. *Int. J. Remote Sensing* 31 (16), 4295–4318. doi:10.1080/01431160903246741

Lucchesi, R. (2015). *File Specification for GEOS-5 FP-IT*. GMAO Office Note No. 2 (Version1.3), 60. Available from http://gmao.gsfc.nasa.gov/pubs/office_notes.

Marchand, R. (2013). Trends in ISCCP, MISR, and MODIS Cloud-Top-Height and Optical-Depth Histograms. *J. Geophys. Res. Atmos.* 118, 1941–1949. doi:10.1002/jgrd.50207

Marshak, A., Herman, J., Adam, S., Karin, B., Carn, S., Cede, A., et al. (2018). Earth Observations from DSCOVR EPIC Instrument. *Bull. Amer. Meteorol. Soc.* 99, 1829–1850. doi:10.1175/BAMS-D-17-0223.1

Mazzitelli, I. M., Cassol, M., Miglietta, M. M., Rizza, U., Sempreviva, A. M., and Lanotte, A. S. (2014). The Role of Subsidence in a Weakly Unstable marine Boundary Layer: a Case Study. *Nonlin. Process. Geophys.* 21, 489–501. doi:10.5194/npg-21-489-2014

Meyer, K., Yang, Y., and Platnick, S. (2016). Uncertainties in Cloud Phase and Optical Thickness Retrievals from the Earth Polychromatic Imaging Camera (EPIC). *Atmos. Meas. Tech.* 9, 1785–1797. doi:10.5194/amt-9-1785-2016

Minnis, P., and Harrison, E. F. (1984). Diurnal Variability of Regional Cloud and Clear-Sky Radiative Parameters Derived from GOES Data. Part II: November 1978 Cloud Distributions. *J. Clim. Appl. Meteorol.* 23 (7), 1012–1031. doi:10.1175/1520-0450(1984)023<1012:dvorca>2.0.co;2

Minnis, P., Heck, P. W., Young, D. F., Fairall, C. W., and Snider, J. B. (1992). Stratocumulus Cloud Properties Derived from Simultaneous Satellite and Island-Based Instrumentation during FIRE. *J. Appl. Meteorol.* 31, 317–339. doi:10.1175/1520-0450(1992)031<0317:scpdfs>2.0.co;2

Myers, J. L., and Well, A. D. (2003). *Research Design and Statistical Analysis*. 2nd ed. New York: Lawrence Erlbaum Associates Publishers.

Painemal, D., Minnis, P., and O'Neill, L. (2013). The Diurnal Cycle of Cloud-Top Height and Cloud Cover over the Southeastern Pacific as Observed by GOES-10. *J. Atmos. Sci.* 70 (8), 2393–2408. doi:10.1175/JAS-D-12-0325.1

Rossow, W. B., and Schiffer, R. A. (1991). ISCCP Cloud Data Products. *Bull. Amer. Meteorol. Soc.* 72, 2–20. doi:10.1175/1520-0477(1991)072<0002:icdp>2.0.co;2

Schmit, T. J., Griffith, P., Gunshor, M. M., Daniels, J. M., Goodman, S. J., and Lebair, W. J. (2017). A Closer Look at the ABI on the GOES-R Series. *Bull. Am. Meteorol. Soc.* 98, 681–698. doi:10.1175/BAMS-D-15-00230.1

Stammes, P., Sneep, M., de Haan, J. F., Veefkind, J. P., Wang, P., and Levelt, P. F. (2008). Effective Cloud Fractions from the Ozone Monitoring Instrument: Theoretical Framework and Validation. *J. Geophys. Res.* 113, D16S38. doi:10.1029/2007JD008820

von Engeln, A., Teixeira, J., Wickert, J., and Buehler, S. A. (2005). Using CHAMP Radio Occultation Data to Determine the Top Altitude of the Planetary Boundary Layer. *Geophys. Res. Lett.* 32, L06815. doi:10.1029/2004GL022168

Wang, P., Stammes, P., van der A, R., Pinardi, G., and van Roozendael, M. (2008). FRESCO+: an Improved O2 A-Band Cloud Retrieval Algorithm for Tropospheric Trace Gas Retrievals. *Atmos. Chem. Phys.* 8, 6565–6576. doi:10.5194/acp-8-6565-2008

Wang, P., Stammes, P., and Mueller, R. (2011). Surface Solar Irradiance from SCIAMACHY Measurements: Algorithm and Validation. *Atmos. Meas. Tech.* 4, 875–891. doi:10.5194/amt-4-875-2011

Wood, R., and Bretherton, C. S. (2004). Boundary Layer Depth, Entrainment, and Decoupling in the Cloud-Capped Subtropical and Tropical Marine Boundary Layer. *J. Clim.* 17 (18), 3576–3588. doi:10.1175/1520-0442(2004)017<3576:bldead>2.0.co;2

Xie, F., Wu, D. L., Ao, C. O., Mannucci, A. J., and Kursinski, E. R. (2012). Advances and Limitations of Atmospheric Boundary Layer Observations with GPS Occultation over Southeast Pacific Ocean. *Atmos. Chem. Phys.* 12, 903–918. doi:10.5194/acp-12-903-2012

Xu, H., Guo, J., Li, J., Liu, L., Chen, T., Guo, X., et al. (2021). The Significant Role of Radiosonde-Measured Cloud-Base Height in the Estimation of Cloud Radiative Forcing. *Adv. Atmos. Sci.* 38, 1552–1565. doi:10.1007/s00376-021-0431-5

Yang, Y., Marshak, A., Mao, J., Lyapustin, A., and Herman, J. (2013). A Method of Retrieving Cloud Top Height and Cloud Geometrical Thickness with Oxygen A and B Bands for the Deep Space Climate Observatory (DSCOVR) Mission: Radiative Transfer Simulations. *J. Quantitative Spectrosc. Radiative Transfer* 122, 141–149. doi:10.1016/j.jqsrt.2012.09.017

Yang, Y., Meyer, K., Wind, G., Zhou, Y., Marshak, A., Platnick, S., et al. (2019). Cloud Products from the Earth Polychromatic Imaging Camera (EPIC): Algorithms and Initial Evaluation. *Atmos. Meas. Tech.* 12, 2019–2031. doi:10.5194/amt-12-2019-2019

Yin, J., and Porporato, A. (2017). Diurnal Cloud Cycle Biases in Climate Models. *Nat. Commun.* 8, 2269. doi:10.1038/s41467-017-02369-4

Zelinka, M. D., and Hartmann, D. L. (2010). Why Is Longwave Cloud Feedback Positive? *J. Geophys. Res.* 115, D16117. doi:10.1029/2010JD013817

Zhao, M., Zhang, H., Wang, H.-B., Zhou, X.-X., Zhu, L., An, Q., et al. (2020). The Change of Cloud Top Height over East Asia during 2000-2018. *Adv. Clim. Change Res.* 11 (2), 110–117. doi:10.1016/j.accre.2020.05.004

Zuidema, P., Painemal, D., de Szoeke, S., and Fairall, C. (2009). Stratocumulus Cloud-Top Height Estimates and Their Climatic Implications. *J. Clim.* 22 (17), 4652–4666. doi:10.1175/2009JCLI2708.1

Conflict of Interest: The authors declare that the research was conducted in the absence of any commercial or financial relationships that could be construed as a potential conflict of interest.

ORIGINAL RESEARCH
published: 09 March 2022
doi: 10.3389/frsen.2022.766917

Unique NISTAR-Based Climate GCM Diagnostics of the Earth's Planetary Albedo and Spectral Absorption Through Longitudinal Data Slicing

Andrew A. Lacis[1*], Barbara E. Carlson[1], Gary L. Russell[1], Alexander Marshak[2] and Wenying Su[3]

[1] *NASA Goddard Institute for Space Studies, New York, NY, United States*
[2] *NASA Goddard Space Flight Center, Greenbelt, MD, United States*
[3] *NASA Langley Research Center, Hampton, VA, United States*

Edited by:
Feng Xu, University of Oklahoma, United States

Reviewed by:
Jake J. Gristey, University of Colorado Boulder, United States
Zhao-Cheng Zeng, University of California, Los Angeles, United States

**** Correspondence:** Andrew A. Lacis, aalacis@gmail.com*

***Specialty section:** This article was submitted to Satellite Missions, a section of the journal Frontiers in Remote Sensing*

***Received:** 30 August 2021*
***Accepted:** 17 February 2022*
***Published:** 09 March 2022*

***Citation:** Lacis AA, Carlson BE, Russell GL, Marshak A and Su W (2022) Unique NISTAR-Based Climate GCM Diagnostics of the Earth's Planetary Albedo and Spectral Absorption Through Longitudinal Data Slicing. Front. Remote Sens. 3:766917. doi: 10.3389/frsen.2022.766917*

Deep Space Climate Observatory (DSCOVR) measurements of Earth's reflected solar and emitted thermal radiation permit a unique model/data comparison perspective that is not readily available from other satellite data. The key factor is the unique Lissajous orbital viewing geometry from the Lagrangian L1 point, which enables a continuous view of Earth's sunlit hemisphere. The National Institute of Standards and Technology Advanced Radiometer (NISTAR) is the DSCOVR Mission energy budget instrument, which views the reflected and emitted radiation of the Earth's sunlit hemisphere by means of single pixel active cavity full-spectrum (Band-A, 0.2–100 μm) and filtered solar wavelength (Band-B, 0.2–4.0 μm; and Band-C, 0.7–4.0 μm) radiometer measurements. An additional solar wavelength photodiode channel (0.3–1.1 μm) provides a calibration reference. The objective of this study is the assessment of climate GCM performance via direct model/data comparisons. Such comparisons are difficult due to quasi-chaotic natural variability present in real-world observational data and in climate GCM simulations. This is where the unique DSCOVR viewing geometry makes possible the longitudinal data slicing methodology for more direct model/data comparison. The key point of the longitudinal slicing approach is that data integration over the entire sunlit hemisphere eliminates the quasi-chaotic meteorological weather-scale noise, while preserving intra-seasonal and planetary-scale variability. The rotation of the Earth that retrieves this climate-style, large-scale longitudinal and seasonal variability. The hemispheric averaging is accomplished automatically in NISTAR measurements with its single-pixel view of the Earth. For climate GCMs, this requires implementing the Sunlit Hemisphere Sampling (SHS) scheme to operate on the GCM run-time output data, utilizing the DSCOVR Satellite Ephemeris data to assure precise viewing geometry between NISTAR measurements and GCM output data, while averaging out the meteorological weather noise. However, GCM generated data are radiative fluxes, while NISTAR (and EPIC) measurements are near-backscattered radiances. Conversing NISTSR measurements into radiative fluxes cannot be accomplished using NISTAR data alone, even with detailed support from conventional satellite data. But the identical viewing geometry of Earth's sunlit hemisphere, and synergistic analyses of EPIC data make it feasible for this conversion of NISTAR near-backscatter radiances into radiative fluxes.

Keywords: deep space climate observatory, self-consistent space/time data sampling, longitudinal slicing, pinwheel format, composite data,

sunlit hemisphere observations, climate diagnostic data

INTRODUCTION

Figure 1 is a schematic representation of the NISTAR and EPIC measurements from the Lagrangian L1 point 1.4 to 1.6 × 10^6 km from the Earth in the direction of the Sun, where the disk-image of the Earth is roughly the size of the Moon as viewed from Earth. To be specific, the DSCOVR Satellite is not precisely located at the Lagrangian L1 point. The DSCOVR Satellite is actually orbiting around the Lagrangian L1 point in a Lissajous orbit (Koon et al., 2000) as shown in Figure 2. The Lissajous orbit is forever evolving in shape with a roughly 6-month period. The solar illumination of the earth is determined by the Solar Ephemeris whereby (in the GCM simulations) the grid-box local solar zenith angle changes are updated on an hourly basis, as is the seasonal change in solar irradiance due to the Earth's orbital motion around the Sun. But, for viewing Earth from the Lissajous orbit, the DSCOVR Satellite viewing geometry must conform to the specification given by the DSCOVR Satellite Ephemeris.

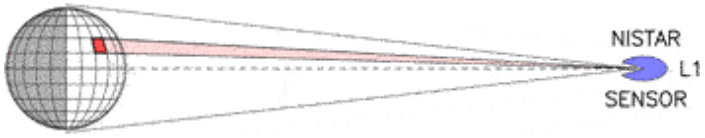

FIGURE 1 | Schematic diagram of NISTAR view of the Earth's sunlit hemisphere from the Lissajous orbit around the solar Lagrangian L1 point. NISTAR views the entire sunlit hemisphere as a single pixel in 4 broadband channels, while companion instrument EPIC records spatially resolved images.

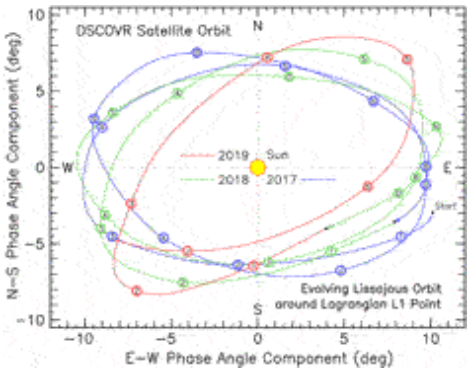

FIGURE 2 | The phase angle (also Sun-Earth-Satellite angle, or 180°—scattering angle) defines the angular separation between the DSCOVR Satellite and the Sun, as viewed from the Earth. The color-coded sky-map traces its evolving Lissajous orbital path around the Lagrange L1 point starting from 1 January 2017 (blue) to 27 June 2019 (red). The directions N S, and W E, represent the Satellite displacement relative to the Sun. Circles depict the mid-month orbital positions with the numbers 1 to 6 representing months January to June of the first orbit of the year, and the letters J to D standing for July to December of the second orbit of the year.

The changes in DSCOVR viewing geometry directly affect the amount of reflected SW radiation that NISTAR and EPIC receive (Marshak et al., 2021), and require explicit use of the DSCOVR Satellite Ephemeris in the GCM SHS modeling to account for the changing GCM grid-box projected area, as seen from the DSCOVR Satellite perspective. With this explicit SHS modeling in place, the GCM SHS sampled output data are collected with the same Sun-Satellite viewing geometry of Earth as is the case for NISTAR and EPIC observational data. The principal unresolved difference that remains is that the GCM data are radiative fluxes, whereas the NISTAR and EPIC data are near-backscatter radiances.

The Lissajous orbit also has a radial component that affects the radial Earth-Satellite distance (Marshak et al., 2018), which instills an inverse square distance dependence in the Earth reflected and emitted radiances. Since NISTAR views the Earth as a single pixel, the NISTAR measurements need to be normalized to a fixed standard distance. For EPIC, the size of the Earth's image on the detector automatically changes in response to the distance change.

NISTAR: CAVITY RADIOMETER DATA

NISTAR, the DSCOVR Mission's global energy budget instrument, is a cavity radiometer with four broadband channels designed to measure the

reflected and emitted radiation eminating from the Earth's sunlit hemisphere. As described in Figure 3, Band-A is an open filter position, measuring the Total Outgoing radiation (TOR) over the solar and thermal spectral regions (0.2–100 μm). Given that NISTAR observations of the Earth are from the vicinity of the Lagrangian L1 point, and are near zero phase angle, the expected reflected solar SW flux from the sunlit hemisphere would be near 200 Wm^{-2}, and the outgoing longwave (OLR) near 240 Wm^{-2}. However, the NISTAR data are near-backscattered radiances that are sensitive to phase angle variability (Marshak et al., 2021). The NISTAR near-backscattered radiance-to-flux conversion is still an ongoing endeavor. Because of the complexity, it may be that a uniform scaling factor might not be adequate for the radiance to flux conversion. Accordingly, the NISTAR data are still being expressed in their relative radiance units, as indicated in the figure labels.

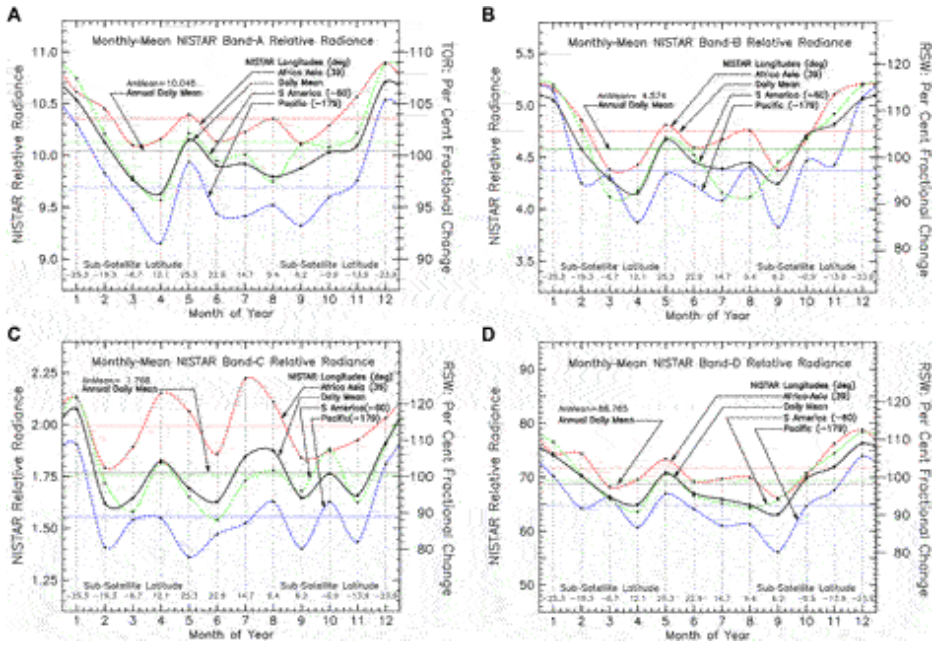

FIGURE 3 | Four-hour averaged NISTAR measurements for year 2017 of the longitudinally sliced seasonal variability of the Band-A (0.2–100 μm) Total Outgoing Radiation TOR **(A)**, Band-B (0.2–4 μm) Reflected Solar Radiation RSR **(B)**, Band-C (0.7–4 μm) Near-Infrared Reflected Solar Radiation NIR **(C)**, and Band-D Silicon Diode (0.3–1.1 μm) Visible Reflected Solar Radiation VIS **(D)**. The heavy black lines depict (longitudinal) full day averages. The colored lines represent the longitudinal slicing as the Earth rotates, whereby the specified geographical area with the high-noon Sun is also identified by its central meridian. The seasonal change in the Lissajous orbital sub-satellite latitude is tabulated at figure bottom.

There is seasonal asymmetry clearly evident in the NISTAR data directly attributable to the (Figure 2) Lissajous orbital phase angle change that shifts the DSCOVR Satellite viewing geometry of the Earth. In January, the DSCOVR sub-satellite latitude is at its southern extreme (−25.3^{o}). With its Lissajous orbital motion oriented in the same direction as the change in solar declination, by mid-May NISTAR is viewing the Earth from its northern extreme (+25.3^{o}). It then takes until December to return to its southern extreme.

The seasonal variability of longitudinally sliced NISTAR data is shown in Figure 3. Monthly-mean averages are accumulated for different geographic regions, based on their sub-solar longitude as the Earth rotates. The respective color-coded lines correspond to the central meridian of a major landmass area (Africa-Asia, 39° E longitude), a mostly ocean view of the sunlit hemisphere (Pacific Ocean, 179° W longitude), and an intermediate land-ocean region (S America 60° W longitude). The NISTAR data are also tabulated in accord with the Greenwich Mean Time (GMT), where each hour of GMT corresponds to a 15^{o} shift in longitude. Notably, the continental Africa-Asia region has the highest reflectivity, while the Pacific region has the lowest reflectivity, with S America in between. NISTAR Band-A also includes a thermal component, for which the highest day-time surface temperature would occur over the Africa-Asia region, and the lowest over the Pacific.

NISTAR Band-C measures the NIR (0.7–4 μm) portion of the reflected solar radiation, compared to (0.2–4 μm) for Band-B. This selects the spectral region that is most sensitive to the elevated spectral reflectivity of vegetation, located longward of the 0.7 μm chlorophyl red edge. Compared to the Band-B RSR measurement, the NISTAR Band-C measurement shows strong enhancement over the Africa-Asia region, thus qualifying as the “vegetation” channel.

Band-D (0.3–1.1 μm) is a silicon diode measurement, intended more as a calibration reference. It is similar to the Band-B spectral response, but with a reduced NIR contribution. The heavy black line depicts measurements averaged over a full rotation of the Earth, and thus all longitudes. It serves as reference for the longitudinal variability that is displayed by the longitudinal data slicing.

Figure 4 further illustrates how the low signal-to-noise problem complicates the analysis of NISTAR active cavity measurements. In the

NISTAR active cavity approach, the electrical current that acts to maintain a fixed cavity temperature needs to be averaged over a substantial time interval to diminish the background noise. In Figure 3, the NISTAR Level 1B data are near-hourly averages spanning roughly 15° in longitude, thus averaging out a substantial amount of longitudinal variability. Meanwhile, in Figure 4, the selected meridional data samples are from shorter time-averaged NISTAR Level 1B data products, corresponding to longitudinal swaths of approximately 4° in width. Figure 4 seasonal plots show far greater noisiness than Figure 3, particularly for Band-C, for which the April-May and July-August peaks become truncated, clearly demonstrating the need for data averaging to reduce the data noise. However, given that direct averaging of Figure 4 data does not fully reproduce Figure 3 results, points to potential data artifacts, or to more complex calibration issues.

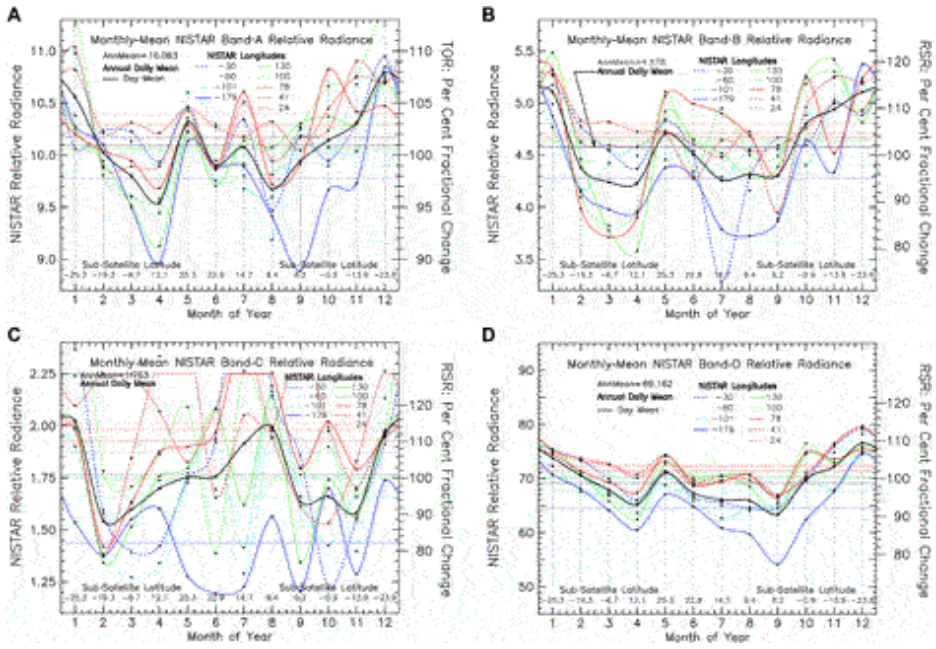

FIGURE 4 | NISTAR measurements for year 2017 of the longitudinally sliced seasonal variability of the Band-A (0.2–100 μm) Total Outgoing Radiation TOR **(A)**, Band-B (0.2–4 μm) Reflected Solar Radiation RSR **(B)**, Band-C (0.7–4 μm) Near-Infrared Reflected Solar Radiation NIR **(C)**, and Band-D Silicon Diode (0.3–1.1 μm) Visible Reflected Solar Radiation VIS **(D)**. The underlying NISTAR measurements here are basically the same as in Figure 3 heavy black lines depict the daily (longitudinal) average. The NISTAR Relative Radiance units are the archived data units.

There are several different sources for the increased noisiness of the data. While a few of the plotted points might appear to be artifacts, there is a

physical basis behind the enhanced variability. Part of the problem is in the sampling. For example, the monthly-means for March are interpolated points, since no data are archived for that month. Also, there are some months with only a few days of archived data, which would bias the seasonal context of the points from their monthly-mean position, due to the large shifts in orbital position that the DSCOVR spacecraft can undergo in just 1 month (see Figure 2). But the change in the sunlit fraction projected area of the image disk is small, varying only by ~0.25%, from 0.995.

On the other hand, the radiative effects of the rapidly changing phase angle have a more significant effect. It is within the near-backscatter range of phase angles (especially for scattering angles greater than 175^{o}) that the reflected radiation particularly sensitive to small changes in the scattering angle. For spherical (liquid water) cloud droplets, the magnitude of backscattered radiation depends not only on cloud optical depth, but also on the cloud particle size, including the size distribution variance (e.g., Hansen and Travis, 1974). Also, depending on the precise viewing geometry, oriented ice crystals can exhibit substantial increased in brightness (Marshak et al., 2017). Thus, there is little doubt that much of the variability seen in the NISTAR data arises from a changing distribution in the cloud and land/ocean surface contributions, each with a different set of phase angle dependent backscattering properties. It is unlikely the climate GCM radiative fluxes will be expressible in terms of the near-backscattered radiances any time soon. Meanwhile, efforts are continuing to refine the sunlit hemisphere-mean radiance-to-flux conversion factors based on EPIC image analyses.

The design feature of the DSCOVR measurements is that taking the difference between Band-A and Band-B would isolate the LW component of the outgoing thermal radiation (OLR), which might also have a backscatter phase angle dependence, but to a much lesser degree than the SW measurements. The main calibration issue that affects the OLR determination is the need to determine the absolute transmission characteristics of the Band-B transmission filter. This needs to be determined indirectly because of no internal calibration source in the instrument. Then the remaining SW (beyond Band-B) needs to be characterized and subtracted to isolate the OLR signal.

Figure 5 depicts the unique spectral ratios that are available from NISTAR data. One obvious advantage of spectral ratios is that to first order, most of the NISTAR calibration, backscattered radiance, and viewing

geometry issues cancel out. But more importantly, the NISTAR NIR/SW spectral ratio, that straddles the chlorophyl 0.7 μm red edge, is a key climate-specific measurement that is not readily available from the current satellite data. The choice of this spectral pivot point identifies vegetated regions on the basis of their higher NIR spectral albedo. Thus, as the Earth rotates, longitudinal slicing identifies and ranks the geographical regions by their NIR reflectivity. This is a novel diagnostic of GCM radiative modeling performance, and also serves as a biosphere identifier in exoplanet studies (Carlson et al., 2019).

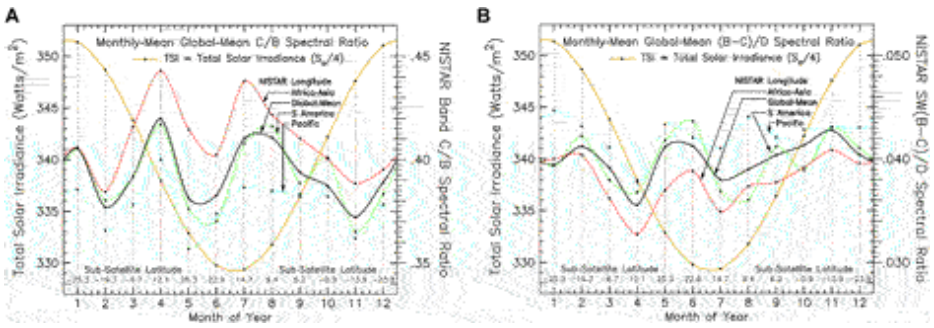

FIGURE 5 | Seasonal variability of longitudinally sliced NISTAR Band-C (0.7–4 μm)/Band-B (0.2–4 μm) NIR/SW spectral ratio for year 2017 **(A)**, and the inverse VIS/VIS + spectral ratio of Bands-(B-C) (0.2–0.7 μm)/Band-D (0.3–1.1 μm) **(B)**. The colored curves represent longitudinally sliced hemispheric views of geographical regions identified by their noon-time meridians. The heavy black lines represent full-day averages. The heavy yellow curves depict the seasonal variation of the Total Solar Irradiance (TSI) as referenced by the *Y*-axis scale at left.

Figure 5 shows the maximum spectral ratio (red line) to be over Africa-Asia in April and July. As expected, the minimum spectral ratio is over the Pacific (blue), but the large April-to-May seasonal variability is not expected, and could indicate that NIR water vapor absorption or GCM cloud distribution inaccuracies could also be a factor. At Figure 5B, the inverse (B–C)/D ratio emphasizes visible cloudy areas. Also shown is the seasonal TSI, depicted by the heavy yellow curve (and *Y*-axis at left), showing no apparent correlation with the seasonal variability of the NISTAR data.

A somewhat better view of the seasonal variability is obtained in the pinwheel format shown in Figure 6, where the NISTAR data are plotted as a function of the DSCOVR sub-satellite latitude. This is possible since the DSCOVR satellite effectively makes two full orbits per year. This also illustrates more clearly the effect of the Lissajous orbit on the seasonal

variability of the NISTAR data stream. As shown in Figure 6A, the DSCOVR sub-satellite latitude is at its southern extreme (−25.3°) in January. Because the Lissajous orbital motion is oriented in the same direction as the solar declination change, by mid-May NISTAR is viewing the Earth from its northern extreme (+25.3°). It then takes until December to return to its southern extreme. The solid red line illustrates the rapid January-to-May northward trek for the Africa-Asia meridian, while the much slower May-to-December southward return trek is denoted by the red dash line. Notable on the southward return trek is the pronounced June-to-September chlorophyl-fueled hump that can be associated with the northern hemisphere growing season (with its peak in July). At Figure 6B are the corresponding results from the GISS ModelE2 NIR/SW spectral ratio output data. On the positive side, the relative order of the longitudinal slicing agrees with the NISTAR data. But, the amplitude and seasonal variability of the GCM surface albedo climatology is far too small.

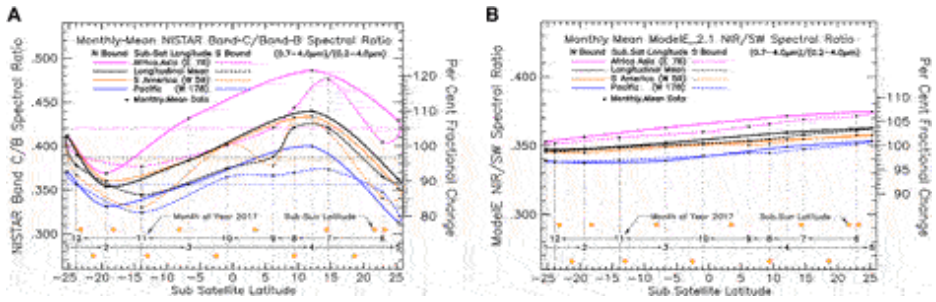

FIGURE 6 | Seasonal variability of longitudinally sliced NISTAR Band-C (0.7–4 μm)/Band-B (0.2–4 μm) NIR/SW spectral ratio for year 2017 **(A)**, expressed in pinwheel format, and plotted as a function of the DSCOVR sub-satellite latitude. Noted at figure bottom are the mid-month positions of the DSCOVR spacecraft in terms of its sub-satellite location (numbers identify the month of year 2017), and the corresponding sub-solar latitude (declination) denoted by the yellow circles. At **(B)** are the corresponding NIR/SW spectral ratio results from the GISS ModelE2 reflected SW diagnostics output data sampled in accord with the DSCOVR Satellite Ephemeris viewing geometry and aggregated over the sunlit hemisphere.

Figure 7A illustrates the basic features of the seasonal variability of the Earth's global energy balance. The annual-mean global average Total Solar Irradiance (TSI) is 340.2 Wm^{-2} (Kopp and Lean, 2011). The heavy yellow curve depicts the seasonal TSI radiative forcing change due to the Earth's orbital motion, which in ModelE2 is defined by the Solar Ephemeris. The red dash curve is the ModelE2 Total Outgoing Radiation (TOR = RSR + OLR) run for thousands of years to global energy balance equilibrium under pre-

industrial conditions. The red curve is the ModelE2 TOR for current climate conditions, which displays the current global-mean energy imbalance of 1.14 Wm^{-2}, showing also that there is seasonal variability present in the global energy imbalance. Compared to the TSI radiative forcing, the TOR amplitude is much reduced, but with a bimodality in phase. The observational data from CERES (Loeb et al., 2018) and ISCCP (Zhang et al., 2004) depicted by the green and blue dash curves, respectively, exhibit similar variability, but with a phase shift by about a month compared to the ModelE2 data. The differences may be small in the absolute sense, but they are significant. The climate system response to applied TSI forcing is not simply a radiative issue, but also involves land/ocean energy transports, sequestration and transport of absorbed solar energy, and its later release to the atmosphere.

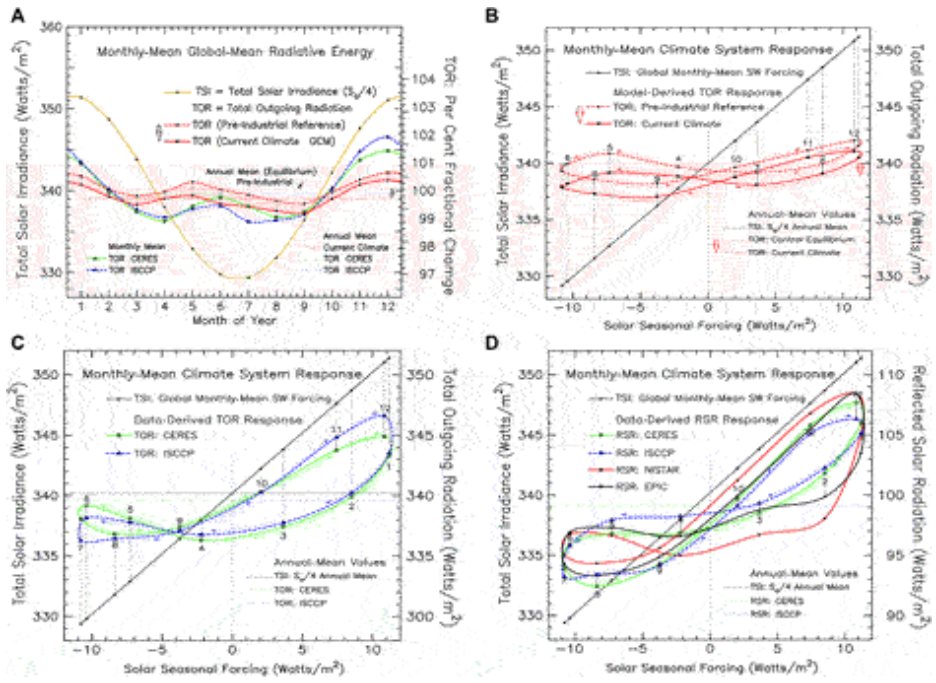

FIGURE 7 | Seasonal energy balance of the Earth between the incoming Total Solar Irradiance (TSI) and the Total Outgoing Radiation (TOR) computed by the GISS ModelE2 for current climate (solid red line) and pre-industrial (red dash line) conditions with comparison to CERES and ISCCP data **(A)**. The heavy yellow line depicts the seasonal change in TSI radiative forcing. The CERES and ISCCP TOR determinations are depicted by the green and blue dash lines, respectively. **(B)** displays the GCM seasonal TOR variability in pinwheel format (relative to the Solar Seasonal Forcing). **(C)** displays the CERES and ISCCP seasonal TOR variability, shown in **(A)**, in the same pinwheel format. **(D)** compares the reflected solar radiation RSR in pinwheel format between CERES and ISCCP results and NISTAR Band-B (solid red) and EPIC (black) derived SW flux results. The numbered black dots connected by the vertical dotted lines refer to the monthly-mean mid-points of TSI and the corresponding reflected SW flux.

Upper right displays the ModelE2 results in the more compact pinwheel format that provides a more compact perspective on the seasonal variability of the global energy variables. Since the TSI changes are precisely known in time and magnitude, TSI radiative forcing can serve as the *X*-axis. All climate variables are in fact functions of solar radiative forcing, with the time of year defining the *Y*-axis of the variable. Thus, on the left side Y-scale, TSI traces out the black slanted line with the black dots marking the monthly mean TSI values of the year, with July at the negative extreme and January at the positive extreme. Likewise, on the right-side *Y*-axis, the ModelE2 TOR monthly means are plotted in accord with the time-of-year that is also implicit with the *X*-axis solar forcing. If the heat capacity of the climate

variable was close to zero, the pinwheel path of that variable would be a slanted line like that of the TSI forcing that retraces itself. If, on the other hand, the heat capacity was infinitely large, the pinwheel path would then be a horizontal line equal to its global annual-mean value. As it is, the ModelE2 TOR traces out near-horizontal bow-tie shaped figures with basically equal lobes that are rotating clockwise in the northern hemisphere winter lobe and in the counter-clockwise direction in the summer lobes. The seasonal change in global energy imbalance appears to be more pronounced in the NH summer lobes.

Figure 7C shows the CERES and ISCCP TOR data in pinwheel format. Except for a few points in April, July, and November, December, there is close agreement between CERES and ISCCP. As in the case of ModelE2, the direction of pinwheel rotation is clockwise in the NH winter lobe and counter-clockwise in the summer lobe. However, the winter lobe is much larger than the summer lobe for CERES and ISCCP. While the CERES/ISCCP NH summer lobe is mostly horizontal, the winter lobe exhibits a strongly inclined slope. The pinwheel shape, slope, directionality, and hysteresis are the product of virtually all of the GCM physical processes. It may well be that the CERES and ISCCP TOR results are suggesting the ModelE2 coupled atmosphere-ocean treatment may be seasonally too rigid, and that there should be some seasonal shift in model dynamics that can simulate a somewhat smaller heat capacity during the NH winter months relative to the summer. To sort out the different possibilities, future GCM runs are needed to identify and quantify the factors that affect the shape and slope of the pinwheel response to the seasonal change in solar radiative forcing.

The Figure 7D shows the reflected SW in pinwheel format for the CERES and ISCCP results and NISTAR Band-B (solid red) and EPIC (black) derived SW flux results. There is qualitative agreement between the CERES/ISCCP pinwheels and the NISTAR/EPIC pinwheels as to overall shape, slope orientation, and direction of rotation. But the agreement is much tighter between CERES and ISCCP then with EPIC and NISTAR. The EPIC results are a first step in the conversion of backscattered spectral radiances into their radiative flux equivalents (Su et al., 2018; Su et al., 2020). For this, the EPIC spectral radiances were converted to broadband fluxes using MODIS/CERES-based regression relationships, and then, by means of the CERES angular distribution models, into the EPIC reflected SW fluxes,

which were then integrated over the sunlit hemisphere to produce the monthly-mean data points for the EPIC pinwheel. The EPIC global-mean CERES-based cloud anisotropy factors were also used to convert NISTAR data into radiative flux units for the NISTAR pinwheel (Su et al., 2018).

Compared to TOR pinwheels in Lower left, the RSR pinwheels exhibit somewhat steeper orientation and more equality in lobe size. Otherwise, the direction rotation remains clockwise in NH winter lobes and counter-clockwise in the summer lobes. Higher frequency oscillation that are evident in the EPIC and NISTAR pinwheels, but not in the CERES/ISCCP pinwheels, are likely residuals originating from phase angle backscatter and Earth-Satellite distance changes due to the Lissajous orbital motion.

As illustrated in Figure 8 the pinwheel format representations enable a concise comparison of global energy budget components, and they underscore the need for precise radiance-to-flux conversion for a more productive model/data intercomparison. Top row of Figure 8 displays NISTAR Band-A, Band-B, and Bands-(A-B) monthly-mean, full-day average Level 1B radiance data in pinwheel format representing the TOR, RSR, and OLR global energy budget components (but with twice the solar SW included in TOR, and incomplete subtraction of the total SW in the OLR component). The heavy green pinwheels represent the Level 1B NISTAR data as archived without having the Earth-Satellite distance dependence due to the Lissajous orbital motion removed. Since NISTAR views the Earth as a single pixel, the changing Lissajous orbital distance imparts an inverse square variance on the NISTAR measurement. While the changing Earth-Satellite distance effect on the size of the sunlit fraction of the projected disk image is tiny (0.25%), and thus of little concern, the distance square effect on the NISTAR measurement can be as large as ± 13.8%, given that the Lissajous orbital distance of the DSCOVR Satellite from Earth ranges from a minimum near 1.4×10^6 km to a maximum near 1.6×10^6 km.

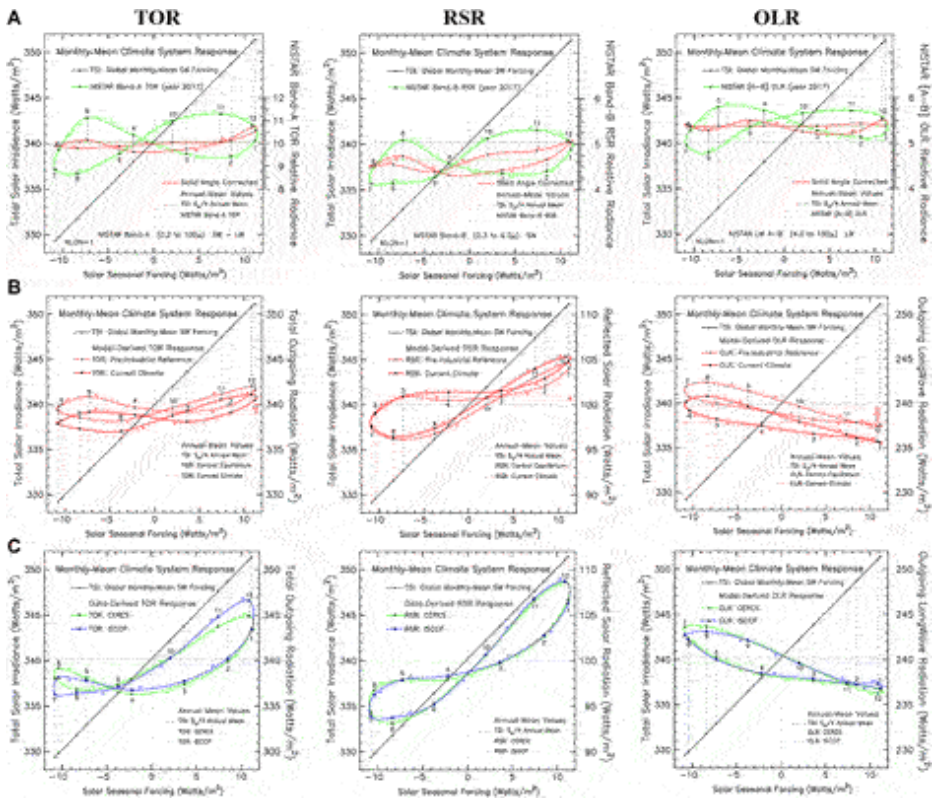

FIGURE 8 | (A) Seasonal NISTAR data for Total Outgoing Radiation (TOR), Reflected Solar Radiation (RSR), and Outgoing Longwave Radiation (OLR) in pinwheel format. The heavy green pinwheels are full-day (longitudinal) average Level 1B monthly-mean data. The red-dash curves represent the green pinwheel data but include inverse square Earth-Satellite distance correction. **(B)** Seasonal variability of global monthly-mean ModelE2 TOR, RSR, OLR pinwheels for pre-industrial (red dash) and current climate (solid red) conditions. **(C)** Seasonal variability of global monthly-mean CERES (green) and ISCCP (blue dash) pinwheels for TOR, RSR, and OLR.

The changing Earth-Satellite distance effect on the NISTAR pinwheel shape is significant, as shown by the red dash distance normalization. Radiance-to-flux conversion is also a much-needed transformation for model/data comparison. Due to its complexity, simple scaling is not sufficient. Another significant factor involved in the pinwheel comparison is the fact that the NISTAR pinwheel is for a projected image of the sunlit hemisphere, where latitudinal viewing perspective from the Lissajous orbital position comes into play, while the CERES, ISCCP, and GCM pinwheels represent global-mean averages in satellite retrieval data product format. Based on these considerations, the NISTAR RSR pinwheel in Figure 8 is transformed into the Figure 7D RSR pinwheel that is more like the EPIC and CERES/ISCCP RSR pinwheels. Thus, except for the spectral ratio results

(for which the distance change, backscatter radiance, and viewing geometry issues cancel out), the full analysis of NISTAR measurements is still a work in progress, despite its promising prospects.

The Figure 8B displays the ModelE2 TOR, RSR, and OLR pinwheels, showing in more detail the seasonal change in the global energy budget between the pre-industrial and current climate conditions. Overall, there has been a decrease by 1.14 Wm^{-2} in global-mean energy balance, as indicated by the TOR pinwheel. Interestingly, this has been accompanied by a modest increase in RSR by 0.55 Wm^{-2}, and a dominating decrease in OLR by 1.69 Wm^{-2}. Moreover, the RSR increase has occurred during the months of September to April, with hardly any change taking place in the reflected SW during the summer months of May to August. For RSR, the pinwheel direction of rotation is the same as for TOR, clockwise in the NH winter lobe and counter-clockwise in the summer, with the summer lobe being substantially larger than the winter lobe. For the OLR pinwheel, there is little change in shape between pre-industrial and current climate, just an overall decrease in OLR by 1.69 Wm^{-2} due to accumulating greenhouse gas radiative forcing. But, the OLR pinwheel shape, orientation, and rotation are quite different from the RSR pinwheel. Instead of two lobes, it is basically a single large summer lobe, with the winter lobe shrunken down to near-nothing. The slope of the OLR pinwheel orientation is negative, and the direction of rotation is clockwise, opposite that of the RSR pinwheel.

For comparison, Figure 8C displays the CERES (green) and ISCCP (blue dash) pinwheels for TOR, RSR, and OLR. The CERES and ISCCP pinwheels are in good agreement with each other. The RSR lobes are near-equal in size and are closely oriented in slope with the TSI slanted line. Their direction of rotation is the same as that of the TOR pinwheels, clockwise in the NH winter lobe and counter-clockwise in the summer lobe. The CERES and ISCCP OLR pinwheels are very similar to the ModelE2 OLR pinwheels, in shape, size, orientation, and direction of rotation. Perhaps that should not be surprising since climate GCMs are typically tuned to reproduce the historic trend in global surface temperature, with less attention focused on the accuracy of the reflected SW radiation. If the ModelE2 global surface temperatures are in agreement with observations, then it is likely that the OLR is also in agreement.

However, there is a small but persistent difference between the CERES and ISCCP OLR pinwheels in July and also in December. In July, the

CERES OLR is about 1 Wm^{-2} higher than ISCCP, and in December, the CERES OLR is about 1 Wm^{-2} lower than ISCCP. This difference is most likely due to a difference in cloud altitude, and less likely to cloud fraction, since the CERES and ISCCP RSR pinwheels show no significant differences. Thus, CERES appears to detect clouds at a lower altitude than ISCCP in July, but at a higher altitude in December. Or, it is also possible that CERES detects more ice clouds (with lower emissivity) in the July time frame, and fewer ice clouds than ISCCP during December.

The RSR slope difference between CERES/ISCCP and ModelE2 is harder to explain. It can't simply be due to clouds, since clouds also affect the OLR. It would need to be limited to seasonal cloud albedo or cloud optical depth differences, to which the OLR is less sensitive. Ultimately, it is the GCM energy transports and energy sequestration that must be involved in defining the pinwheel. The NISTAR and EPIC data are essential for resolving the pinwheel differences between the CERES/ISCCP and ModelE2 pinwheels. At this point in time, NISTAR data calibration and signal-to-noise issues limit their effectiveness. EPIC data analysis has made more rapid progress and serve as a bridge to NISTAR data improvement.

DISCUSSION

NISTAR and EPIC measurements provide a unique perspective of the Earth's sunlit hemisphere from their Lissajous orbit vantage point, which makes possible a new format model/data comparison. Because the climate system is highly variable both in space and in time with differences in viewing geometry, spatial resolution, and diurnal cycle sampling time between observations and climate model output, this can produce biases and distortion. In addition, both climate GCMs and the real world operate in quasi-chaotic fashion, which produces a "natural" uncorrelated variability that is an unavoidable source of uncertainty in model/data comparisons.

This "weather noise" problem is mitigated by integrating the input data over the entire sunlit hemisphere, which NISTAR does naturally with its single-pixel observations, and EPIC with its full-disk image analysis. This approach provides broad-brush climate-type information that summarizes the climate system's response to the seasonally changing solar radiative forcing. These sunlit-disk data points are further averaged over time as monthly-means. With weather noise averaged out, the rotation of the Earth preserves the longitudinal variability of the land/ocean distribution, and retains

planetary-scale fluctuations such as the MJO and ENSO/La Niña variability. Longitudinal slicing is then used to display the data.

On the climate GCM end, identical space-time sampling can be implemented to integrate the GCM run-time output data over the sunlit hemisphere to reproduce the viewing geometry identical to that of the DSCOVR Satellite NISTAR and EPIC measurements. That is accomplished with the Sunlit Hemisphere Sampling (SHS) simulator that has been installed in the GISS ModelE2 to generate climate-style output data with the same self-consistent space-time sampling as the NISTAR data. The key difference that still remains is that the GCM data are in radiative flux format, while NISTAR data are near-backscatter radiances.

The anisotropy problem is largely alleviated in the case of the NISTAR Band-C/Band-B spectral ratio analysis, which is a more robust measurement in that the viewing geometry, calibration, and backscattered radiance issues are, for the most part, cancel out. This spectral ratio measurement is of fundamental importance since there are no similar measurements available from conventional satellite data. The NISTAR spectral ratio measurements have demonstrated their value as a novel radiative modeling diagnostic tool to assess climate GCM performance, showing for example, that the GISS ModelE2 does not have sufficient seasonal or longitudinal spectral variability in reflected SW flux, although ModelE2 does reproduce the relative longitudinal ordering that is seen in the NISTAR data (Carlson et al., 2019).

However, because of spectral dependence of the backscatter radiance-to-flux anisotropy, there might be only partial anisotropy cancelation in the Band-C/Band-B spectral ratio. The anisotropy parameter is likely to be larger for Band-B than it is for Band-C (Marshak et al., 2021), in which case the NISTAR spectral ratio variability would be reduced, thus mitigating the spectral ratio disagreement between NISTAR and ModelE2 in Figure 6. Such reduction in the NISTAR spectral ratio amplitude would improve the comparison with the GCM results. The coming CERES/Libera mission should help to resolve all of these spectral ratio issues.

For added perspective, the NISTAR data comparison in Figure 6 uses the pinwheel format for the spectral ratio comparison. Here, the DSCOVR sub-satellite latitude serves as the *X*-axis, helping to highlight the relative importance of the Lissajous orbital motion on the seasonal asymmetry that is apparent in the time-series plots. The DSCOVR Satellite is at its southern-most extreme in January of 2017. Its orbital motion, when in phase with the

change in solar declination, carries it to its northern-most extreme in only 4 months by May. The return trip which is out of phase with the solar declination change, takes about 8 months to get back to the southern-most extreme by January of the following year. This asymmetric change in the Lissajous orbital viewing perspective accounts for much of the seasonal asymmetry that is evident in the time-series plot in Figure 5.

The "bow-tie" shaped pinwheel perspective t in Figures 7, 8, uses the (–11 Wm^{-2} to +11 Wm^{-2}) change in the solar seasonal radiative forcing as the reference *X*-axis, which is appropriate for the NISTAR global energy balance visualization. In this format, the left *Y*-axis and the slanted line refer to the incident solar irradiance, for which the maximum TSI is at the upper right corner in January, and minimum TSI at lower left in July. The right-hand *Y*-axis represents the reflected SW flux, with the implicit time dependence inferred from the seasonal solar radiative forcing, which defines the placement of the monthly-mean data points.

If the heat capacity of the climate system was negligible, and the reflected SW flux was directly proportional to TSI, the shape of the reflected SW pinwheel response would be a slanted line that tracks the change in TSI. For a very large heat capacity, the pinwheel shape would simply be a horizontal line. As it is, the Earth's climate system has both a large heat capacity and the added complexity that a large amount of heat energy is being sequestered by the southern oceans during the NH winter months, transported northward, and then added to the outgoing LW radiation during the NH summer months, with corresponding changes in the global cloud cover. As shown by the CERES/ISCCP reflected solar radiation (RSR) pinwheels in Figure 8, maximum RSR occurs in December.

The decrease in RSR is more rapid than the decrease in the TSI, with increasing energy going into ocean for sequestration. This imparts a clockwise rotation to the NH winter lobe of the pinwheel. The enhanced decrease in RSR (and planetary albedo) continues through March, slowing down substantially from March to June, as TSI undergoes its most rapid decrease. As a result, this shifts the pinwheel into its NH summer lobe where the direction of rotation is counter-clockwise since the rate of change during this time period is more rapid for TSI than it is for RSR. There is an accelerated RSR decrease from June to August as TSI reaches its minimum in July, and begins increasing again. This completes the pinwheel NH summer lobe turn-around, setting it up for a more in-step return back to its

December maximum. The CERES/ISCCP RSR seasonal change in the reflected SW radiation is in close agreement with the EPIC results while the results at individual meridians exhibit a high degree of seasonal variability.

Except for its much smaller NH winter lobe, the ModelE2 RSR pinwheel in Figure 8 is basically similar to the CERES/ISCCP RSR pinwheel. The NISTAR RSR pinwheel has little resemblance, implying significant seasonal variability for the RSR backscattered radiance to flux conversion. But, the overall slope of the NISTAR RSR pinwheel is actually in better agreement with the slope of the ModelE2 RSR pinwheel, than it is with the slopes of the CERES and ISCCP RSR pinwheels. The NISTAR OLR pinwheel shows little similarity to the ModelE2/CERES/ISCCP OLR pinwheels. It is probable that in this case that the problem may be the incomplete subtraction of solar radiation in the NISTAR Band-A minus the Band-B differencing. Interestingly, the orientation of the OLR pinwheel, which is practically orthogonal to the RSR pinwheel orientation, underscores the phase difference between the energy sequestration and that of the solar SW radiative forcing.

While NISTAR was designed to produce hemisphere-averaged energy budget data of the Earth without numerical aggregation, the problem is that the NISTAR data are near-backscattered radiances that are aggregated from a broad range of contributors which have different backscattering properties, with an ever-changing viewing geometry that makes quantitative comparison to climate GCM data problematic. It would appear that essentially real-time anisotropy correction is needed to convert the near-backscattered NISTAR radiances into radiative fluxes with sufficient accuracy for global energy balance analysis and comparisons (Su et al., 2015; 2021).

The importance of accounting for near-backscattered radiation of NISTAR and EPIC measurements is discussed in by Marshak et al. (2021). Their Figure 7 shows large differences and strong dependence on the scattering angle of reflected radiation by ice and water clouds in the near-backscatter direction with the region between 175° to 180° scattering angle being most prominent. Ice cloud and water cloud particles have scattering functions that are different in this near-backscatter angle range. Moreover, flat-plate ice cloud particles often appear in oriented configuration to cause glint (Marshak et al., 2017). Furthermore, there are finite sized scatterers in vegetation canopies that can cast shadows. In such vegetation canopies, shadowing is minimized under backscatter conditions, and thus produce enhanced brightening for decreasing phase angle (Marshak et al., 2021).

Mishchenko et al. (2002) describe exact vector theory results for coherent backscattering for discrete random media, showing sharply-peaked backscattering brightness enhancement by over 50% for spherical particulates at 0° phase angle, compared to phase angles just larger than 10°.

The principal climate system constituents, ocean, land, snow, ice, vegetation, as well as aerosols, water and ice clouds, possess significantly different backscattering properties. As a result, the sunlit-hemisphere anisotropy parameter that would describe the hemisphere-mean anisotropy of NISTAR data will vary as the mix of climate constituents changes due to the rotation of the Earth, and also in response to the Lissajous orbital change in phase angle. Basically, there is no simple methodology to define the NISTAR sunlit-hemisphere anisotropy parameter to convert backscattered NISTAR radiances into radiative flux equivalents with sufficient accuracy for quantitative global energy balance comparisons to climate GCM simulations, which are invariably in the form of radiative fluxes.

To help address this situation, a study was initiated by Su et al. (2018; 2020) to convert EPIC spectral radiances into reflected SW fluxes to calibrate the NISTAR Band-B backscatter radiances. For this, the EPIC spectral radiances were converted to broadband SW radiances using MODIS/CERES-based regression relationships, and then transformed to radiative fluxes using the CERES angular distribution models. These transformations were performed at the pixel level. Integration over the entire sunlit hemisphere converted each EPIC image into a single climate-style data point of reflected SW flux. In way, 5388 EPIC images for year 2017 were processed to generate a table of 12 × 24 monthly-mean planetary albedo points.

These sunlit hemisphere averages were normalized relative to the CERES global annual-mean value for reflected SW radiative flux of 99.1 Wm^{-2} (Loeb et al., 2018), and divided by the Total Solar Irradiance 340.2 Wm^{-2} (Kopp and Lean, 2011), The tabulated EPIC planetary albedo points serve as the input data for the longitudinal slicing methodology to map and analyze the seasonal and longitudinal variability of the Earth's global energy balance in terms of its planetary albedo, as described in our companion paper (Carlson et al., 2022). They are also the first order reference for NISTAR Band-B anisotropy calibration for converting the near-backscatter radiances to radiative fluxes. The process of NISTAR radiometry channel calibration is a complex iterative endeavor that involves characterization of the Band-B

and Band-C cutoff filter transmission properties, which must be accomplished while simultaneously battling poor signal-to-noise as the radiometer channel calibration is being established. Also, as the Earth rotates, the anisotropy parameter derived from EPIC data keeps changing as the land/ocean/cloud distribution changes and as the EPIC viewing geometry changes.

In view of the above, it has become clear that the accuracy of the NISTAR Band-B radiative flux is totally dependent on the successful outcome of the EPIC data conversion to radiative flux. If the principal objective of NISTAR measurements was only to serve an observational reference for the seasonal variability of the Earth's global energy balance geared to climate GCM comparisons, then the NISTAR measurements could well be viewed as largely superfluous. But, as already noted, it is the spectral discrimination such as the Band-C/Band-B spectral ratio, which to a large extent is not directly dependent on precise radiance-to-flux conversion, that makes the NISTAR measurements unique. With more precise calibration, there are other spectral interval combinations available such as Vis Band (Band-B—Band-C, 0.2–0.7 μm), the Near-IR Band (Band-D—Vis Band, 0.7–1.1 μm), and the Mid-IR Band (Band-B—Band-D, 1.1–4 μm). The Vis Band samples the least absorbing part of the solar spectrum, while the Near-IR and Mid-IR Bands sample spectral regions with different amounts of absorption by water vapor and reflection by surface vegetation. Nevertheless, the usefulness of these NISTAR spectral intervals for differentiating the radiative effects of clouds, water vapor, and surface vegetation are strongly dependent on the stability of the NISTAR radiometric calibration and the effectiveness of the data noise suppression for the present Level 1B version of the NISTAR data compilation that has been the topic of this study to assess and analyze.

Overall, it is the longitudinal slicing aspect of the NISTAR and EPIC data that makes DSCOVR Mission measurements so unique in their role as key climate modeling diagnostic tools. In our prior NISTAR line plot data comparisons, radiative flux comparability was the key objective. Thus, accurate radiance-to-flux conversion was required. Also available are Hovmöller format comparisons, specifically optimized for geographical pattern visualization that are a natural fit to longitudinal slicing, and are shown in Figure 9 for NISTAR Band-B (Left), and photodiode Band-D (Right).

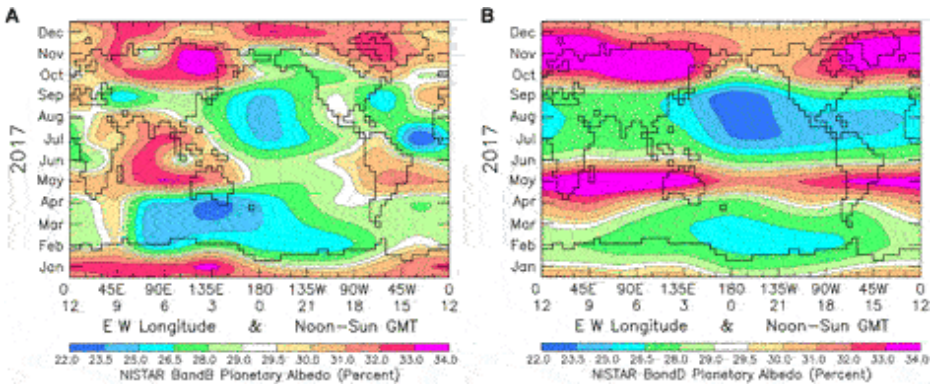

FIGURE 9 | (A) NISTAR solar shortwave (SW) near-backscatter relative radiances for year 2017 from Figure 4B for Band-B (0.2–4 μm), and **(B)** for photodiode Band-D (0.3–1.1 μm) from Figure 4D, displayed as planetary albedo in Hovmöller format. In both cases, the NISTAR relative radiances are uniformly normalized to the CERES global annual-mean of 99.1 Wm–2 (Loeb et al. (2018), to yield a global annual-mean of 29.1 percent for the planetary albedo. In the Hovmöller format, the Y-scale has the time running upward starting from January at the bottom, through December at the top. The X-scale has the longitude running from 0° E longitude at the left and 0° W longitude at the right. The X-scale also references the GMT of the noon-time Sun, starting at GMT = 0 at the Date Line at the center, increasing westward toward the left, as the Earth rotates. A 5 ° × 4 ° GCM world map is included for geographic reference.

Since terrestrial weather patterns typically tend to evolve in the East-West direction, rather than North-South, Hovmöller (1949) found it more informative to average meteorological data over the North-South dimension, before plotting the latitude-averaged data as a function of longitude, with time increasing upward along the *Y*-axis. For convenience the X-scale is centered over the Central Pacific Ocean Date Line, and also includes the Greenwich Mean Time (GMT) of the high-noon Sun at that longitude. By nature of their single-pixel measurement, NISTAR data are automatically in Hovmöller format. Each point on the Hovmöller map represents a sunlit-hemisphere average (with both latitudinal and longitudinal meteorological activity averaged out). The rotation of the Earth retrieves the planetary-scale variability, hence longitudinal slicing by the Earth's rotation. To facilitate geographic location of different longitudes, a coarse-grid GCM 5° × 4° world map is included.

Figure 9A shows NISTAR Band-B backscattered relative radiance data from Figure 4A arbitrarily normalized to a planetary albedo (with global annual-mean equal to the CERES value of 29.1%, Loeb et al., 2018), interpolated to cover the full range of longitude and GMT, and replotted in

Hovmöller format. This arbitrary action implies the assumption of a globally uniform annual-mean anisotropy parameter for transforming the NISTAR backscattered radiances of uncertain calibration into radiative fluxes that match the CERES global annual-mean flux of 99.1 Wm^{-2}. The objective is to assess and demonstrate how the "vanilla" version of the NISTAR Band-B data compares relative to the more idealized version derived from the analysis of EPIC data described in our companion paper (Carlson et al., 2021), which is also a part of the DSCOVR EPIC/NISTAR: 5-years of Observing Earth from the first Lagrangian Point.

Figure 10A is the EPIC version of what the ideal NISTAR Band-B planetary albedo data for year 2017 should look like in their Hovmöller format (from Carlson et al., 2021, their Figure 3). What stands out in the Hovmöller format is the evolving pattern of variability, in particular, the 2017 February-March La Niña feature with the 30° peak-to-peak longitudinal waves, that is not readily apparent in the NISTAR/EPIC line plots. The world map places this La Niña feature as occurring in the mid-Pacific, with the longitudinal waves extending some 90° eastward.

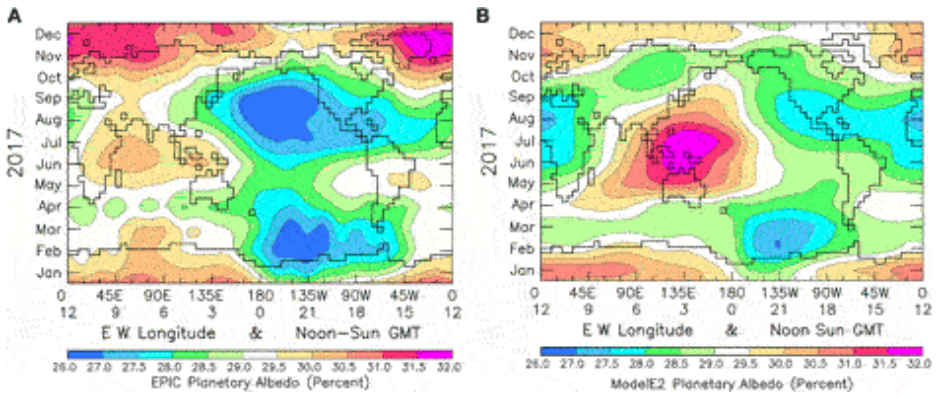

FIGURE 10 | Hovmöller-style contour plot of the EPIC **(A)** and the GISS ModelE2 **(B)** planetary albedo for the year 2017. In both cases, the EPIC and GCM SW flux is normalized to the CERES global annual-mean of 99.1 Wm–2 (Loeb et al. (2018), to yield a global annual-mean of 29.1 percent for the planetary albedo. The Y-scale has time running upward starting with January at the bottom through December at the top. The X-scale is longitude running from 0° E longitude at the left to 0° W longitude at the right. GMT references the location of high-noon Sun. The world map is included for longitudinal reference. The data for the EPIC **(A)** and GISS ModelE2 **(B)** year 2017 planetary albedo are reproduced here from Carlson et al. (2021) modeling results.

In terms of the overall pattern of variability, NISTAR Band-B planetary albedo in Figure 9 shows strong resemblance to the EPIC results in Figure

10, re-affirming the thinking that the NISTAR data have the intrinsic stand-alone capability to detect changes in climate system variability, such as La Niña activity, even without resolving the anisotropy issue. Though the sparse longitudinal sampling of the NISTAR Band-B data (in Figures 4, 9) precludes conclusive confirmation, there is reason to expect that with higher longitudinal sampling, the Band-B data would have detected the longitudinal wave activity that is seen in Figure 10A EPIC data. The main reason why the February-March La Niña feature does not appear in the Figure 9 NISTAR Band-B data is because the NISTAR March data are missing in all of the NISTAR data channels. Hence, the plotted results for March are all spline interpolation values. Another take-away on this topic is that data averaging for noise suppression needs to be carefully managed in order to preserve the longitudinal information. It is anticipated that the now available Version 3 of the NISTAR Level 1B of archived data with improved calibration and noise reduction will permit improved model/data cmparisons.

Other conclusions that can be drawn from the comparison of Figures 9, 10, given that the range of variability for the NISTAR Band-B planetary albedo is substantially larger than for the EPIC planetary albedo, is that the radiance-to-flux conversion exhibits space-time variability. Also, the space-time variability of the relative brightness ratios is such that the anisotropy parameter does not maintain the same time dependence with longitude, or the same longitudinal dependence with time. This implies that a significant fraction of the anisotropy dependence must come from changong ice and water cloud distributions, which have different backscattering properties, and thus require real-time EPIC image analyses (e.g., Su et al., 2018; 2020) in order to convert NISTAR Band-B radiances into radiative fluxes.

The Figure 9 comparison of NISTAR Band-B (Left) with the photodiode Band-D results (Right) identifies the large decreases in reflected radiance that are evident in Band-B data in Figure 4, and appear as bull's-eye features in Figure 9A during March-April, June, July, September and November, but are absent in the photodiode Band-D Hovmöller map in Figure 9B. Band-D has less absorption, but with better signal-to-noise than Band-B. But the Figure 9 Band-B/Band-D comparison also shows what may be a calibration inconsistency. As denoted in the NISTAR line-plot Figure 3 through 6, the DSCOVR sub-Satellite latitude is 25.3° S in January, 25.3° N in June, and 23.9° S in December. Why is the Band-D reflectance so much smaller in

January when the DSCOVR Satellite is even more strongly over Antarctica in January than in December?

For Band-B, the relative reflectance level over the E longitude region is approximately the same for January, June and December, contrary to the Band-D results. By comparison the EPIC planetary albedos in Figure 10A, are by far the highest in November-December, but with peak reflectivity occurring over the 0° to 45° W longitude Atlantic Ocean region, while the NISTAR Band-B October-November peak is over the 135° E longitude East-Asia region. Most likely, this regional difference in reflectance must be due to the regional differences in near-backscatter ice and water cloud distributions, but Australia land-surface albedos may also be involved.

However, the more far-reaching take-away from the Figure 9 Band-B/Band-D comparison are the spectral differences between Band-B and Band-D that become most evident during the summer months June through September over the continental longitudes. Band-B includes the Mid-IR (1.1–4 μm) spectral region that is not being measured by the photodiode Band-D, which, over vegetated areas, would add significantly more to the reflected radiation, than over the ocean areas.

Clearly, the other spectral intervals that are possible with the NISTAR spectral bands, such as the Band-B—Band-C, Vis Band (0.2–0.7 μm), the Band-D—Band-B + Band-C, Near-IR Band (0.7–1.1 μm), and Band-B—Band-D, Mid-IR Band (1.1–4 μm). These synthesized NISTAR spectral bands are designed to provide improved spectral discrimination that would be more effective in differentiating between the different climate system constituents. The Vis Band, with minimum atmospheric absorption, would be the primary cloud assessment band. The Near-IR Band would have sensitivity to cloud, vegetation albedo, and moderate water vapor absorption, while the Mid-IR Band would be more sensitive to vegetated surface albedo and to strong water vapor absorption. However, because of calibration inconsistencies and the obvious artifacts in the NISTAR Figure 4 Band-B and Band-C data, Hovmöller plots for these spectral bands are not yet ready for prime time. In addition, it is also more than likely that the anisotropy parameters needed to transform the synthesized spectral radiances into radiative fluxes would also differ greatly between the different spectral bands.

Figure 10B displays the Hovmöller contour map for the planetary albedo for the GISS ModelE2 climate GCM for the year 2017. As discussed in

Carlson et al. (2021), the EPIC *vs*. ModelE2 was used to deduce that the GISS ModelE2 overestimated clouds over ocean areas and underestimated clouds over the continental land areas, in addition to identifying the year 2017 La Niña feature in the EPIC planetary albedo data. In comparing the normalized NISTAR Band-B planetary albedo in Figure 9A with the GCM results in Figure 10, it is clear that NISTAR Band-B results, even with the arbitrary anisotropy normalization, are a far closer fit to the EPIC planetary albedo, than the ModelE2 results. Also, from this comparison, it is clear from Figure 9A that the maximum summer-month planetary albedo (hence, cloud reflectivity) occurs over the Asia continental longitudes, while the significantly higher GCM planetary albedo occurs over the East-Asia/West-Pacific Ocean region. These are conclusions that could have been reached independently just from direct comparison to NISTAR Band-B data, without requiring the benefit from EPIC data insight.

Furthermore, the claim was made that NISTAR measurements should also be capable of detecting La Niña activity by means of Hovmöller contour maps of longitudinally sliced monthly-mean NISTAR Band-B radiances. Because of overly sparse longitudinal sampling, this conjecture could not be fully demonstrated with the present data. Actually, it is the spectral discrimination of NISTAR data that is their strong point. This was demonstrated earlier in the study by Carlson et al. (2019) regarding the capabilities of the NISTAR Band-C/Band-B spectral ratio for constraining climate GCM treatment of the spectral absorption of solar radiation, and identifying a biosphere signature through the spectral partitioning at the 0.7 μm vegetation red edge. The additional Vis, Near-IR, and Mid-IR synthetic spectral bands (also still to be demonstrated) further expand on the unique NISTAR data capability of spectral discrimination between key constituents of the climate system, that remains unmatched by EPIC data, or by any other current satellite measurements.

On the other hand, the EPIC data are unique in providing the sunlit-hemisphere integrated longitudinally sliced radiative fluxes along with the corresponding cloud radiative properties that enable a more complete understanding of the seasonal and longitudinal variability of Earth's planetary albedo including identification of the 2017 La Niña feature in the 2017/2018 EPIC planetary albedo data and providing of observational constraints for climate GCM cloud treatment constraints (Carlson et al., 2021). Moreover, there are additional unique enhancements of the EPIC data

analyses that can be implemented to further enhance model/data comparisons of climate GCM modeling results. In particular, this involves data integration over the sunlit hemisphere, so as to retain latitudinal information, and to include other climate system variables in the EPIC Composite database that has enabled cloud properties to be added to the list of La Niña feature subject to longitudinal slicing. This is a capability that can be readily implemented in the climate GCM output data sampling, but cannot be reproduced within the NISTAR data processing.

In view of the foregoing, the DSCOVER Mission instruments EPIC and NISTAR, each in its own way, and as a complimentary synergistic matching pair, working together they provide a unique advance in quantitative model/data intercomparison. The key for this advancement is the longitudinal slicing capability made possible by the viewing geometry of the Earth's sunlit hemisphere from the Lagrangian L1 point, and by the rotation of the Earth. The DSCOVR Satellite viewing geometry, which can be precisely reproduced in the climate GCM output data sampling, provides for identical space-time sampling of the observational, as well as of the GCM generated output data. Integrating the observational data over the sunlit hemisphere in the EPIC images, as well as in the single-pixel NISTAR measurement, averages out the weather noise, resulting in climate-style data points that retain planetary-scale information about the climate system. The same principles apply to the corresponding integration of the climate GCM output data over the sunlit hemisphere in accord with the Lissajous orbit viewing geometry from the Lagrangian L1 point. As an additional point, the near-hourly EPIC images of Earth's sunlit hemisphere correspond closely to the GCM output data sampling for a 1-h radiation time step.

The nature of the longitudinally sliced variability is planetary scale and subtle, as evident from the year 2017 La Niña feature, which is accompanied by characteristic longitudinal oscillations exhibiting a 30° (~3,000 km) peak-to-peak variability. Comparing individual EPIC images from February 2017 with similar images from February 2018, shows no discernable differences in cloud distribution or other cloud properties. Yet the feature persists.

Some Future Considerations

The principal objective of this study was to assess the capabilities of the first version of the NISTAR Level 1B data. Difficulties with the initial data quality led to some of the NISTAR objectives to be performed through EPIC

data analysis. This dual approach has led to an improved understanding of the NISTAR data limitations and capabilities. Given that both NISTAR and EPIC measurements are near-backscatter radiances, radiance-to-flux conversion is key for model/data comparisons, since the climate GCM output data are all radiative flux based. For NISTAR, there is no real option for a data-based radiance-to-flux conversion. But for EPIC data, using MODIS-based regression relationships and CERES angle models, Su et al. (2018) developed the EPIC radiance-to-flux conversion procedure, which has made possible our NISTAR/EPIC/ModelE2 intercomparisons.

Now that the Version 3 NISTAR Level 1B data have become available, there is every expectation that the improved calibration and signal-to-noise management will make good in demonstrating that Band-B data with improved longitudinal resolution should be able to duplicate the EPIC La Niña activity detection without the need for radiance-to-flux conversion. Similarly, Hovmöller plots of the synthetic Vis, Near-IR, and Mid-IR NISTAR spectral bands even without radiance-to-flux conversion should enable improved discrimination between different climate system constituents. Thus, the (0.2–0.7 μm) Vis Band should respond more directly to cloud variability, and the (0.7–1.1 μm) Near-IR Band would have more sensitivity to cloud, vegetation albedo, and moderate water vapor absorption, while the (1.1–4 μm) Mid-IR Band would be more sensitive to vegetated surface albedo and strong water vapor absorption.

There is of course a need for having available the anisotropy parameters for the for the synthetic Vis, Near-IR, and Mid-IR NISTAR spectral bands, if for no other reason than to see if there is a significant difference in the Hovmöller plot patterns for the NISTAR near-backscatter radiances compared to radiative fluxes. The EPIC-based analysis is unlikely to provide this information since the EPIC-based radiative fluxes are derived for the full SW spectrum. What would be helpful here, would be to develop a climatology of anisotropy parameters for the synthesized spectral bands that would provide an approximate value for the spectral anisotropy parameters. Anything more would be an enormous computational burden.

For the NISTAR-derived (Band-A—Band-B) LW thermal flux determination, there is no other substitute for the EPIC-derived radiance-to-flux conversion factors. Here, the EPIC results for reflected solar SW flux are absolutely essential for accurate determination of the NISTAR LW radiative flux. This involves a potentially scene-dependent spectral

calibration of Band-B filter transmission, and accurate knowledge of the near-backscattered anisotropy to enable the accurate subtraction of the NISTAR Band-B near-backscattered radiance from Band-A radiance to obtain the NISTAR LW back-scattered thermal emission, which then needs to be converted to a LW radiative flux.

Since the NISTAR no-filter (0.2–100 μm) Band-A makes full spectrum measurements, there is sometimes expressed expectation that global energy balance (or imbalance) determination might be possible. That lofty goal is well beyond the reach of any NISTAR, or EPIC measurement. That is because there is no definitive way to confirm the calibration of the spectral transmissivity of the Band-B filter, and even when the Band-B filter transmission has been accounted for, the LW emissivity in the viewing direction is dependent on the atmospheric temperature profile and the vertical cloud distribution.

It is also possible that an iterative inverse approach could be successfully utilized to resolve the NISTAR LW radiative flux determination. Figure 8 shows that the CERES, ISCCP, and GCM OLR pinwheel renditions of the LW radiative fluxes are in basic agreement. The approach would then be to see what it takes to convert the NISTAR Band-A—Band-B near-backscattered radiances into pinwheel format so as to reproduce the seasonal pinwheel variability.

Nevertheless, the seasonal variability of global reflected SW radiation and global emitted LW radiation provides compelling observational constraints and a diagnostic assessment of climate GCM performance. Thus, it is important to have an observational basis for all aspects of the SW and LW components of the global energy balance and their seasonal variability. To this end, satellite measurements have shown that, on an annual basis, reflected solar SW radiation is nearly identical from both hemispheres despite large differences in land-ocean distribution (Vonder Haar and Suomi, 1971). The large differences in surface albedo, imply significant compensation to achieve hemispheric symmetry in reflected solar SW radiation. This has been further analyzed and quantified (e.g., Voigt et al., 2013, 2014; Stephens et al., 2015). This is just one example where the modeling and understanding of the NISTAR global SW and LW measurements requires going beyond what is currently available. NISTAR measurements with their single-pixel capability are clearly limited to recording only a global-mean LW and SW response. However, the

asymmetric hemispheric components that form the global NISTAR response could be fully resolved in the EPIC and GCM sunlit hemisphere integrated results.

Application to Exoplanet Observations

By their very nature, the NISTAR single-pixel measurements of the sunlit hemisphere from a shifting Lissajous orbital position do have more than a passing similarity to current ongoing exoplanet observations, except that for exoplanet observations, the typical viewing geometry covers a far more extreme range of phase angle than the small change in phase angle for NISTAR measurements. We commented on this aspect in our earlier (Carlson et al., 2019) paper. The basic NISTAR data stream is a continuous time-series acquisition of single-pixel measurements of the Earth, made for several different spectral intervals, as the Earth continues to rotate. That is the same basic format that applies to exoplanet observing. The biggest difference is that for the Earth, we know precisely the rotation period, length of year, tilt of rotation axis, the land/ocean geography, clouds, atmospheric structure and composition, etc. For exoplanets, all of these quantities are unknowns that need to be determined.

In earlier studies, Jiang et al. (2018) used spatially resolved EPIC images of Earth as proxies to simulate exoplanet observations by constructing a NISTAR-like time-series from the EPIC data. A similar analysis regarding the information content in EPIC data was also performed by Yang et al. (2018), and more recently by Boyd et al. (2022). In these examples, EPIC images of the Earth sunlit hemisphere are used as the starting point where all the input data are known, and where the changing viewing geometry is also known. From this, a single-pixel time-series is generated, that can then be inverted to retrieve the basic input information such as the Earth's rotation period, as well as changing land/ocean and cloud distributions. In a similar study, Gu et al. (2021) constructed single point spectral light curves from a year of EPIC images to serve as exoplanet proxy data, and then applied a Principal Component analysis for their spectral image reconstruction.

In our experience with NISTAR and with the sunlit hemisphere averaged EPIC data, where the information content resides in the longitudinal ordering of the data time-series, we found that the optimum in display to be the Hovmöller format contour map. The success of this approach relies on the longitudinal precision in tabulating the time-series observational data relative

to the Earth's rotation period. Here, the precision of the data resides in the time of data acquisition and that relationship to the Earth's period of rotation. The amplitude of each data point's intensity is displayed less precisely via the more limited resolution of the Hovmöller color bar. The Hovmöller approach was able to extract and display the year 2017 La Niña feature and the associated planetary-scale longitudinal oscillations that were not otherwise discernable in the time-series line plots.

Also important in probing the Earth's biosphere, and similarly for exoplanet studies, is selecting spectral intervals that will emphasize the space-time variability that is associated with some physical spectral characteristic. As an example, the choice of the 0.7 μm vegetation red edge pivot point for the NISTAR Band-C enable the NISTAR Band-C/Band-B spectral ratio to be sensitive in identifying vegetated surface albedos. Clearly, this is partial to the terrestrial climate system. But then, that is probably part of the objective to facilitate the identification of Earth-like exoplanets in preference to all others.

CONCLUSIONS

This paper describes a unique model/data comparison approach. Longitudinal slicing consists of averaging observational and model generated data over the entire sunlit hemisphere, and by using the rotation of the Earth to extract the longitude dependent information. This is made possible by the unique NISTAR viewing geometry from the DSCOVR Satellite location in its Lissajous orbit around the Lagrangian L1 point. From there, NISTAR makes single-pixel measurements of reflected solar and emitted thermal radiation from the entire sunlit hemisphere of the Earth.

The principal advantage of the longitudinal slicing methodology is that the sampling of climate GCM output data with the same viewing geometry as the DSCOVR Mission NISTAR and EPIC measurements establishes a precise and self-consistent space-time sampling between observational data and climate model generated output data. In the process, this averaging of data over the entire sunlit hemisphere averages out the quasi-chaotic meteorological weather noise, but preserves the large-scale seasonal and planetary-scale variability.

The unique aspect of the NISTAR measurements is in providing observational constraints and diagnostic support for climate GCM performance evaluation in the form of seasonal and longitudinal broadband

spectral comparisons that are not available from other satellite data sources. The NISTAR Band-C/Band-B spectral ratio in particular, has established that the treatment of absorbed solar SW radiation in the GISS ModelE2 exhibits inadequate spectral contrast between SW radiation that is absorbed shortward of 0.7 μm, and the radiation that is absorbed longward of 0.7 μm. This deficiency in spectral absorption points to inadequate specification of the vegetated surface albedo and/or the radiative modeling of the absorption of SW radiation under cloudy sky conditions.

The NISTAR full-disk single-pixel measurements of the sunlit hemisphere of Earth are also a realistic example and test case for the analysis of exoplanet observations. The NISTAR data stream is a time-series of reflected solar radiation which can be inverted and analyzed to infer basic aspects of the terrestrial climate system such as planet's rotation rate, seasonal change, polar icecaps, and climate system variability.

DATA AVAILABILITY STATEMENT

Publicly available datasets were analyzed in this study. The NISTAR Level 1B data and the EPIC data used here are available from the Langley DAAC as well as OPeNDAP. DSCOVR data used for this study can be downloaded from: https://eosweb.larc.nasa.gov/project/dscovr/dscovr_nistar_1lb_2.

AUTHOR CONTRIBUTIONS

BC and Al developed the concept for the longitudinal slicing of hemisphere-mean data and NISTAR spectral ratio as a biosphere signature. AL and GR developed the Sunlit Hemisphere Sampling (SHS) code. GR coded and ran the ModelE2 SHS simulations. WS converted the EPIC spectral radiances into radiative fluxes and produced the hemisphere-mean tables of EPIC SW fluxes and the composite cloud properties. AM assisted with NISTAR data and DSCOVR Ephemeris data, providing insight on topical emphasis and relevance to DSCOVR Mission objectives. Al, BC, GR, WS, and AM wrote and edited the text. AL made most of the figures.

FUNDING

Funding for this investigation has been provided by the NASA DSCOVR Project through WBS grant 437949.02.07.01.13.

PUBLISHER'S NOTE

All claims expressed in this article are solely those of the authors and do not necessarily represent those of their affiliated organizations, or those of the publisher, the editors and the reviewers. Any product that may be evaluated in this article, or claim that may be made by its manufacturer, is not guaranteed or endorsed by the publisher.

ACKNOWLEDGMENTS

We thank the NASA Earth Science Research Division managed by Jack Kaye, and the DSCOVR Program managed by Richard Eckman for support.

REFERENCES

Boyd, P. T., Wilson, E. L., Smale, A. P., Supsinskas, P., Livengood, T. A., and Hewagama, T. (2022). EarthShine: Observing Our World as an Exoplanet from the Surface of the Moon. *J. Astron. Telesc. Instrum. Syst. (Jatis)* 8, 014003. doi:10.1117/1.JATIS.8.1.014003

Carlson, B. E., Lacis, A. A., Russell, G., Marshak, A., and Su, W. (2021). *Unique Observational Constraints on the Seasonal and Longitudinal Variability of the Earth's Planetary Albedo and Cloud Distribution Inferred from EPIC Measurements*. Frontiers in Remote Sensing.

Carlson, B., Lacis, A., Colose, C., Marshak, A., Su, W., and Lorentz, S. (2019). Spectral Signature of the Biosphere: NISTAR Finds it in Our Solar System from the Lagrangian L-1 point. *Geophys. Res. Lett.* 46, 10679–10686. doi:10.1029/2019GL083736

Gu, L., Fan, S., Li, J., Bartlett, S. J., Natraj, V., Jiang, J. H., et al. (2021). Earth as a Proxy Exoplanet: Deconstructing and Reconstructing Spectrophotometric Light Curves. *Astronomical J.* 161 (3), 122. doi:10.3847/1538-3881/abd54a

Hansen, J., and Travis, L. (1974). Light Scattering in Planetary Atmospheres. *Space Sci. Rev.* 16, 527–610. doi:10.1007/BF00168069

Hovmöller, E. (1949). The Trough-And-ridge Diagram. *Tellus* 1 (2), 62–66. doi:10.3402/tellusa.v1i2.8498

Jiang, J. H., Zhai, A. J., Herman, J., Zhai, C., Hu, R., Su, H., et al. (2018). Using Deep Space Climate Observatory Measurements to Study the Earth as an Exoplanet. *Astronomical J.* 156 (1), 26. doi:10.3847/1538-3881/aac6e2

Koon, W. S., Lo, M. W., Marsden, J. E., and Ross, S. D. (2000). "Dynamical Systems, the Three-Body Problem and Space Mission Design," in *Proceedings of the International Conference on Differential Equations Berlin 1999*. Editors B. Fiedler, K. Groger, and J. Sprekels (IEEE). doi:10.1142/446910.1142/9789812792617_0222

Kopp, G., and Lean, J. (2011). A New, Lower Value of Total Solar Irradiance: Evidence and Climate Significance. *Geophys. Res. Lett.* 38, L01706. doi:10.1029/2010gl045777

Loeb, N. G., Doelling, D. R., Wang, H., Su, W., Nguyen, C., Corbett, J. G., et al. (2018). Clouds and the Earth's Radiant Energy System (CERES) Energy Balanced and Filled (EBAF) Top-Of-Atmosphere (TOA Data Product. *J. Clim.* 31, 895–918. doi:10.1175/JCI-D-17-0208.110.1175/jcli-d-17-0208.1

Marshak, A., Delgado-Bonal, A., and Knyazikhin, Y. (2021). Efect of Scattering Angle on Earth's Reflectance. *Front. Remote Sensing.* 2, 719610. doi:10.3389/frsen.2021.719610

Marshak, A., Herman, J., Szabo, A., Blank, K., Simon, C., Cede, A., et al. (2018). Earth Observations from DSCOVR EPIC Instrument. *Bull. Am. Meteorol. Soc.* 99, 1829–1850. doi:10.1175/BAMS-D-17-0223.1

Marshak, A., Varnai, T., and Kostinski, A. (2017). Terrestrial Glint Seen from Deep Space: Oriented Ice Crystals Detected from the Lagrangian point. *Geophys. Res. Lett.* 44, 5197–5202. doi:10.1002/2017GL073248

Mishchenko, M., Tishkovets, V., and Litvinov, P. (2002). "Exact Results of the Vector Theory of Coherent Backscattering from Discrete Random media: an Overview," in *Optics of Cosmic Dust* ed . Editors G. Videen,1, and M. Kocifaj (Dordrecht: Kluwer Academic Publishers), 239–260. doi:10.1007/978-94-010-0628-6_15

Stephens, G. L., O'Brien, D., Webster, P. J., Pilewski, P., Kato, S., and Li, J. (2015). The Albedo of Earth. *Rev. Geophys.* 53, 141–163. doi:10.1002/2014RG000449

Su, W., Liang, L., Duda, D. P., Khlopenkov, K., and Thieman, M. M. (2021). Global Daytime Mean Shortwave Flux Consistency under Varying EPIC Viewing Geometries. *Front. Remote Sens* 2, 747859. doi:10.3389/frsen.2021.747859

Su, W., Corbett, J., Eitzen, Z., and Liang, L. (2015). Next-Generation Angular Distribution Models for Top-Of-Atmosphere Radiative Flux Calculation from CERES Instruments: Methodology. *Atmos. Meas. Tech.* 8, 611–632. doi:10.5194/amt-8-611-2015

Su, W., Liang, L., Doelling, D. R., Minnins, P., Duda, D. P., Khopenkov, K., et al. (2018). Determining the Shortwave Radiative Flux from Earth Polychromatic Imaging Camera. *J. Geophys. Res.* 123, 11479–11491. doi:10.1029/2018jd029390

Su, W., Minnis, P., Liang, L., Duda, D. P., Khlopenkov, K., Thieman, M., et al. (2020). Determining the Daytime Earth Radiative Flux from National Institute of Standards and Technology Advanced Radiometer (NISTAR) Measurements. *Atmos. Meas. Tech.* 13, 429–443. doi:10.5194/amt-13-429-2020

Voigt, A., Stevens, B., Bader, J., and Mauritsen, T. (2014). Compensation of Hemispheric Albedo Asymmetries by Shifts of the ITCZ and Tropical Clouds. *J. Clim.* 27, 1029–1045. doi:10.1175/JCLI-D-13-00205.1

Voigt, A., Stevens, B., Bader, J., and Mauritsen, T. (2013). The Observed Hemispheric Symmetry in Reflected Shortwave Irradiances. *J. Clim.* 26, 468–477. doi:10.1175/jcli-d-12-00132.1

Vonder Haar, T. H., and Suomi, V. E. (1971). Measurements of the Earth's Radiation Budget from Satellite during a Five-Year Period. Part I: Extended Time and Space Means. *J. Atmos. Sci.* 28, 305–314. doi:10.1175/1520-0469(1971)028<0305:moterb>2.0.co;2

Yang, W., Marshak, A., Varnai, T., and Kostincki, A. (2018). EPIC Spectral Observations of Variability in Earth's Global Reflectance. *Remote Sens.* 10, 254. doi:10.3390/rs10020254

Zhang, Y.-C., Rossow, W. B., Lacis, A. A., Oinas, V., and Mishchenko, M. I. (2004). Calculation of Radiative Fluxes from the Surface to Top of Atmosphere Based on ISCCP and Other Global Data Sets: Refinements of the Radiative Transfer Model and the Input Data. *J. Geophys. Res.* 109, D19105. doi:10.1029/2003JD004457

Conflict of Interest: The authors declare that the research was conducted in the absence of any commercial or financial relationships that could be construed as a potential conflict of interest.

ORIGINAL RESEARCH
published: 11 March 2022
doi: 10.3389/frsen.2022.790723

Temporal Variation of the Shortwave Spherical Albedo of the Earth

A. Penttilä[1*], K. Muinonen[1,2], O. Ihalainen[1,3], E. Uvarova[1], M. Vuori[1], G. Xu[1,4], J. Näränen[2], O. Wilkman[2], J. Peltoniemi[2], M. Gritsevich[2,5], H. Järvinen[6] and A. Marshak[7]

[1] *Department of Physics, University of Helsinki, Helsinki, Finland*
[2] *Finnish Geospatial Research Institute FGI, National Land Survey of Finland, Kirkkonummi, Finland*
[3] *VTT Technical Research Centre of Finland Ltd., Espoo, Finland*
[4] *Institute of Meteorology and Climate Research, Karlsruhe Institute of Technology, Karlsruhe, Germany*
[5] *Institute of Physics and Technology, Ural Federal University, Ekaterinburg, Russia*
[6] *Institute for Atmospheric and Earth System Research, University of Helsinki, Helsinki, Finland*
[7] *NASA Goddard Space Flight Center, Greenbelt, MD, United States*

Edited by:
Hartmut Boesch, University of Leicester, United Kingdom

Reviewed by:
Bing Lin, National Aeronautics and Space Administration (NASA), United States
Yves Julien, University of Valencia, Spain

**** Correspondence:** A. Penttilä, antti.i.penttila@helsinki.fi*

***Specialty section:** This article was submitted to Satellite Missions, a section of the journal Frontiers in Remote Sensing*

***Received:** 07 October 2021*
***Accepted:** 07 February 2022*
***Published:** 11 March 2022*

Citation: *Penttilä A, Muinonen K, Ihalainen O, Uvarova E, Vuori M, Xu G, Näränen J, Wilkman O, Peltoniemi J, Gritsevich M, Järvinen H and Marshak A (2022) Temporal Variation of the Shortwave Spherical Albedo of the Earth. Front. Remote Sens. 3:790723. doi: 10.3389/frsen.2022.790723*

The Earth's spherical albedo describes the ratio of light reflected from the Earth to that incident from the Sun, an important variable for the Earth's radiation balance. The spherical albedo has been previously estimated from satellites in low-Earth orbits, and from light reflected from the Moon. We developed a method to derive the Earth's spherical shortwave albedo using the images from the Earth Polychromatic Imaging Camera (EPIC) on board National Oceanic and Atmospheric Administration's (NOAA) Deep Space Climate Observatory (DSCOVR). The satellite is located in the Lagrange 1 point between the Earth and the Sun and observes the complete illuminated part of the Earth at once. The method allows us to provide continuously updated spherical albedo time series data starting from 2015. This time series shows a systematic seasonal variation with the mean annual albedo estimated as 0.295±0.008 and an exceptional albedo maximum in 2020, attributed to unusually abundant cloudiness over the Southern Oceans.

Keywords: albedo, EPIC camera, DSCOVR, shortwave radiation, radiation budget

INTRODUCTION

Solar radiation is the primary energy source of the Earth and largely determines Earth's climate. The proportion of the incoming solar radiation reflected back to space by the Earth is described by the spherical (i.e., Bond) albedo. It depends on the reflective properties of the Earth and thus it is affected by the proportion of the highly reflective areas relative to darker areas. For example, the melting of the Antarctic and Greenland ice sheets results in increased absorption and decreased albedo. The Earth's spherical albedo is an indicator of the radiation budget and thus driving the global weather and climate processes.

In the first half of the 20th century, estimates of the spherical albedo were based on an indirect method of observing the Earth-lit Moon (Stephens et al., 2015), and this method is still used (Goode et al., 2021). The earliest satellite measurement of the spherical albedo was made in 1959 by the Explorer 7 satellite and its value has remained approximately 0.3 ever since (Kandel and Viollier, 2010). Since 1997 the albedo is being overseen by the Clouds and

the Earth's Radiant Energy System (CERES), which includes five satellites and seven CERES radiometers (see Wielicki et al., 1996). As of 2017, only five radiometers are operational. The CERES albedo product is a combination of observations from several instruments seeing different parts of the Earth, and as it takes numerous hours for the CERES to scan the entire Earth while the cloud cover of the Earth evolves in a matter of minutes, the spherical albedo evaluation method by the CERES instruments can have noticeable uncertainties in the measured albedo value (Wielicki et al., 1996; Kandel and Viollier, 2010).

To measure the spherical albedo directly one needs to simultaneously detect radiation reflected by the Earth from all directions, which renders such measurements impractical. To circumvent this, we use the Earth Polychromatic Imaging Camera (EPIC) on board the Deep Space Climate Observatory (DSCOVR) spacecraft combined with angular distribution models (ADM) provided by the CERES based on many years of dedicated measurements. A related approach was presented in Su et al. (2018), Su et al. (2020) for the outgoing flux from Earth, instead of deriving the spherical albedo, using EPIC and NISTAR data.

The DSCOVR is a spacecraft orbiting in the Lagrange point 1 around 1.5 million kilometers from Earth, which allows the EPIC to always view practically the entire sunlit hemisphere of the Earth. The DSCOVR was launched in 2015, and the EPIC has been operational ever since apart from one 6-month maintenance break in 2019 (Marshak et al., 2018). Data from the EPIC instrument, with the CERES ADM models, allows us to propose an algorithm that automatically translates directional reflectance obtained from the EPIC images into estimated value of shortwave spherical albedo. We have launched a web service that collects the computed spherical albedo of the Earth from the whole operational period and updates the data daily with the latest observations[1]. This daily time series of the Earth's albedo spans over 7 years in time. This enables us to analyze the pattern of temporal variation in albedo over a year which demonstrates anomalies in albedo behavior. The accurate estimate of the shortwave spherical albedo is important in evaluating the energy balance of the earth's climate system.

The aim of this article is to derive a novel method for estimating the spherical shortwave albedo of the Earth using EPIC imagery and introduce the results. The objective is to improve the estimation of the global albedo value resulting in enhanced input for the radiation budget models of the

Earth. In this article, we introduce first the EPIC imagery and the methods that we use to derive the albedo in *Materials and Methods*. In *Results*, we show the results of the albedo estimation over the years 2015–2021. Finally in *Discussion* we discuss the implications of the results.

MATERIALS AND METHODS

Spherical Albedo From the EPIC Images

The EPIC images constitute a time series of the sunlit part of the Earth, including the atmosphere, starting from June 2015 and continuing at the present time. There are usually about 22 images per day during Northern Hemisphere summer, and 13 during winter. Each multispectral image has 10 wavelength channels between 317 and 780 nm. The channels have full-width-at-half-maximum (FWHM) values between 1 and 3 nm (Ohtake et al., 2010; Ohtake et al., 2013; Geogdzhayev and Marshak, 2018; Herman et al., 2018).

Each image pixel represents the radiance reflected by the corresponding area of Earth. This radiance is a function of the reflective properties of the area, and the solar and satellite angles. The DSCOVR satellite is located in the first Lagrange point between the Earth and the Sun, therefore the radiance is observed close to the backscattering geometry with satellite and solar angles being almost equal. To convert measured narrowband radiances at backscattering into integrated broadband albedo values at top-of-atmosphere (TOA; see *Narrowband-to-Broadband and Radiance-to-Radiosity Transformations* for more details), we apply the ADMs provided by the CERES project (Su et al., 2015a; Su et al., 2015b). The ADMs are provided for several surface types and cloud fractions, and we combine these into three types for our analysis: clear land, clear ocean, and cloud-covered areas. The reason for this is that the angular resolution of the tabulated ADMs available at the CERES project web pages[2] is only 10°, and we want to interpolate with a finer resolution in the backscattering direction and combining similar surface types gives us more robust estimation (see *Scattering Geometry and Interpolation of Angular Distribution Models*). Additionally, estimating temporary cloud fractions from EPIC images is challenging, a more robust method can be developed for simple clear versus cloud-covered area estimation. Land or ocean surface classification is available from the International Geosphere–Biosphere Programme, and temporal cloud coverage we estimate from the EPIC images using a logistic

regression model with input from EPIC channels at 325, 551, and 780 nm (see *Cloud Classification in EPIC Images*).

The TOA albedo values for each pixel over the Earth's sunlit disk are averaged for albedo of the Earth at each narrowband wavelength channel. Finally, the narrowband albedos are summed with weights from incident solar spectra at each channel, obtained from NOAA's climate data record of solar spectral irradiance (Coddington et al., 2015; see *Narrowband-to-Broadband and Radiance-to-Radiosity Transformations*). The solar spectrum is taken as constant in this study with only the distance between the Earth and the Sun influencing the total flux level.

The daily averaged time series has been filtered to remove outliers. For some EPIC images, not all the wavelength channels are present. If there is not a proper coverage of usable images over the day, some parts of Earth are not present, and this would introduce a bias to the mean albedo of that day. Therefore, these days are left out from our time series data. There is a period between mid-2019 and early 2020 when the EPIC camera was not operational.

We derive the mean yearly shortwave spherical albedo of the Earth by grouping the daily time series values by the day in the year, averaging per day, and finally averaging over days in a year.

Narrowband-to-Broadband and Radiance-to-Radiosity Transformations

The EPIC images contain 10 narrowband channels, namely at 317, 325, 340, 388, 443, 551, 680, 688, 764, and 780 nm. The FWHM values for the channels are between 1 and 3 nm. The channels are measuring the directional radiance. On the other hand, we are interested in the broadband value of the TOA integrated radiosity, i.e., reflected flux integrated over all directions, and the broadband albedo, i.e., the ratio of the reflected flux to the incident flux.

The ADMs provide the conversion from directional broadband radiance to TOA integrated radiosity. They are applied for example in Su et al. (2018), Su et al. (2020) for broadband radiance that is first derived with a narrowband-to-broadband conversion model from the EPIC images. In this work we first apply the ADMs and second the narrowband-to-broadband conversion, but we would like to point out that both of these conversations

can be described together with a single linear transform and that the order of narrowband-to-broadband and radiance-to-radiosity is interchangeable.

After the radiance-to-radiosity conversion with the ADMs we combine the narrowband channels into a broadband estimate. We use 8 of the 10 EPIC channels for this conversion. Channels at 688 and 764 nm are measuring the O_2 absorption and are left out of the conversion, since they do not describe the reflectance outside these narrow channels. The solar spectral irradiance (Coddington et al., 2015) is convoluted with the response curves of the eight EPIC channels to give weights for the narrowband contributions that are summed together for the broadband estimate.

As the EPIC channels range from 317 to 780 nm, strictly speaking this is the coverage of our broadband estimate. The portion of the solar input in this range is 52.7%. In ultraviolet (UV) below 317 nm there is only 0.5% of the total energy, so we can safely extend the validity of our broadband range into UV. The CERES ADMs, on the other hand, are derived for shortwave broadband range of 300–5000 nm. The use of ADMs to the broadband with wavelength range of 317–780 nm only can be a source of bias in our estimate. However, Su et al. (2018) reports successful usage of ADMs with only three EPIC channels (443, 551, and 680 nm) for narrowband-to-broadband transformation.

Cloud Classification in EPIC Images

The algorithm for cloud classification in the EPIC images was trained with a manually prepared data set of spectral radiances together with subjective cloudy/clear label decision. For image data, we collected images from the first week of every month in 2018. We converted the original HDF5 library data for one multi-channel image into PNG image stack of all the wavelength channels. We opened the image stacks in ImageJ[3], and manually selected areas of either clear or cloud-covered land and ocean surfaces. The spectral radiance values of pixels within these areas were recorded together with the label (1) clear land/(2) clear ocean/(3) cloud-covered area. Altogether, we produced 338 areas of clear land, 331 areas of clear ocean, and 481 areas of cloud-covered areas. Each area contains several tens of pixels, the mean values over the areas were employed in the analysis. The ice sheet covered areas, such as Antarctica, are indistinguishable from cloud-covered areas.

A logistic regression model was separately fitted into data with clear land and cloud-covered areas, and data with clear ocean and cloud-covered areas.

A logistic regression model has a linear function modeling the log-odds of the probability of an event. In our case, the event is that the surface is covered with clouds. The model can be written as

$$p = \frac{1}{1 + e^{-(\beta_0 + \beta_1 x_1 + \cdots + \beta_k x_k)}}$$

where p is the probability of cloud-cover, and $\beta_0 + \beta_1 x_1 + \cdots + \beta_k x_k$ is the linear function with unknown coefficients β_i and known radiances x_i from channels $1, \ldots, k$.

We executed forward-selection stepwise regression to optimize the model with the best value of the Bayesian Information Criterion (BIC) statistics of the model. We ended up with models with a constant coefficient β_0 and three coefficients for the EPIC wavelength channels at 325, 551, and 780 nm. For land vs. clouds model, all the four coefficients were tested significant with *p*-values less than 0.1%. For ocean vs. clouds model, all other but the coefficient for the channel 780 nm were significant with the same *p*-value limit. The values for the model coefficients are given in Table 1. The final classification is done with the probability limit of $1/2$: if $p \leq 1/2$ the pixel is classified as cloud-covered. The channel values in this stage are in the counts/second units and are not yet converted into directional radiance.

TABLE 1 | The fitted coefficient values for the logistic regression models for cloud-covered vs. clear surface.

	β_0	β_1 (325 nm)	β_2 (551 nm)	β_3 (780 nm)
Clear/cloud-covered land	312.58	−0.014156	−0.017217	0.019545
Clear/cloud-covered ocean	36.451	0.017356	−0.0039826	0.0022967

Scattering Geometry and Interpolation of Angular Distribution Models

We found it realistic to successfully classify pixels of clear or cloudy land or ocean areas from the EPIC images, but not different cloud types (water or ice) or levels of cloud cover that are present in CERES ADMs. ADMs are also divided into different wind speeds for ocean and into different vegetation types for land. To exploit these, wind speeds on ocean pixels would need to be connected from weather models into our analysis together with up-to-date land cover information. We feel that this would complicate the albedo estimation too much at this stage and could be a topic for future

development. We decided to emphasize more the interpolation of the scattering geometry inside the ADM models over having many ocean/land/cloud subtype ADMs.

The scattering geometry in the EPIC observations is such that the observation is always done close to backscattering. The phase angle between the Sun and the DSCOVR spacecraft, as seen from Earth, is below 12° except for few rare cases in years 2020–21. On average, phase angle has been 8.2°. After the break in the DSCOVR operations in 2019, the minimum phase angle has gradually started to decrease (see Figure 7). It was never below 4° before 2020, but now the minimum value is 1.8°.

While in terms of phase angle EPIC is observing close to backscattering, the local solar zenith angle on each Earth pixel varies between 0° and 90°. The ADM tables, on the other hand, have 10° bins for all the three angles (solar zenith, viewing zenith, azimuth). So, our backscattering geometry implies that we need ADM table values inside cells where the solar and viewing zenith angles are in the same bin and azimuth angle is in the bin 0–10°. Thus, the 3-dimensional (in angle) ADM tables will reduce for our purposes to 1-dimensional tables that can be parametrized with the solar zenith angle only.

We find the reduced 1-dimensional table binning of 10° too coarse as it would introduce inaccuracies when applied to pixels having the solar zenith angle anywhere between 0° and 90°. Therefore, we interpolate the reduced ADM tables over the 0° and 90° range using a cubic spline interpolation. We use these interpolated coefficients when converting the TOA radiances measured by EPIC into integrated TOA albedos. We find that the reduced 1-dimensional tables show relatively similar behavior for all clear ocean surfaces regardless of the wind speed, for all clear land surfaces, and for all cloud-covered areas regardless of the cloud type or coverage. Thus, our final set of ADM coefficients come from interpolated data on these three categories, averaged over their subtypes.

RESULTS

The time series of the daily spherical shortwave albedo of the Earth is shown in Figure 1. One can see the evident annual cycle and the typical variation in the albedo with $\pm 3\sigma$ value of ± 0.024 around the mean. The mean albedo of the Earth, from the currently available data up to 2 September 2021, is 0.295 ± 0.008. The value agrees well with the earlier estimates of 0.286–0.301 by

satellites in low-Earth orbits, see Kandel and Viollier (2010), and 0.297 from earthshine measurements done by observing the Moon, see Goode et al. (2001), Goode et al. (2021).

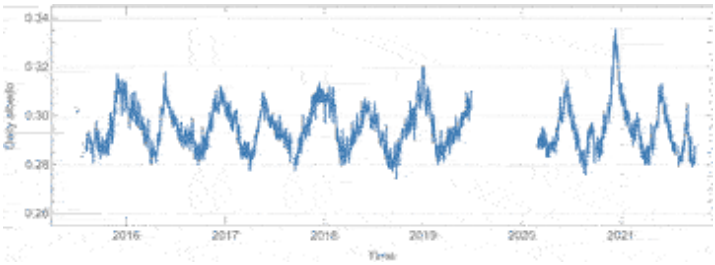

FIGURE 1 | Daily average of the Earth's albedo over the whole operational time of the EPIC camera.

The yearly annual cycle on albedo can be seen more clearly from Figure 2, where the years have been stacked together. In each year, there are two minima and two maxima. The minima are located close to the Northern and Southern equinoxes, and the maxima slightly before the Northern and Southern solstices. This indicates that the reflectivity of the Earth is at maximum, when either one of the pole areas are tilted more towards the Sun.

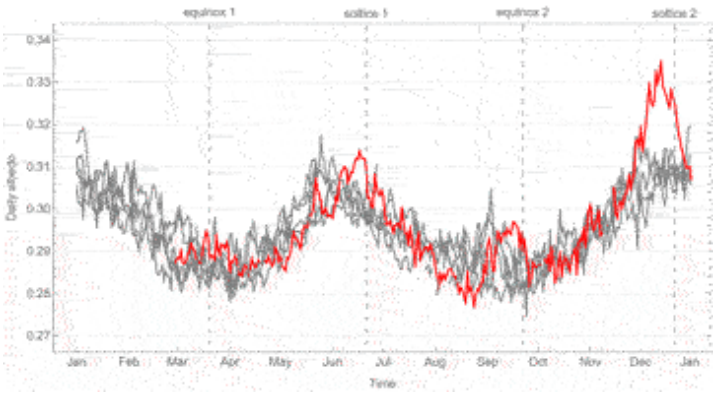

FIGURE 2 | Daily averages of the Earth's albedo with all years stacked together. Data from the year 2020 is highlighted with red color, years 2015–2019 and 2021 are shown in gray.

In Figure 3, we show the derived spherical albedo values on the map. The values are averaged over the months of the equinoxes (March and September) and solstices (June and December). These maps can give further insight of the input of different surface types and the annual variation in the albedo. The polar areas show large contributions during albedo maxima.

Interestingly, the Indonesia region in the equator shows high albedos throughout the year. The clouds over the ocean areas are high in albedo, but because of their transient nature, only the most constantly cloud-covered areas show up in the monthly averaged maps.

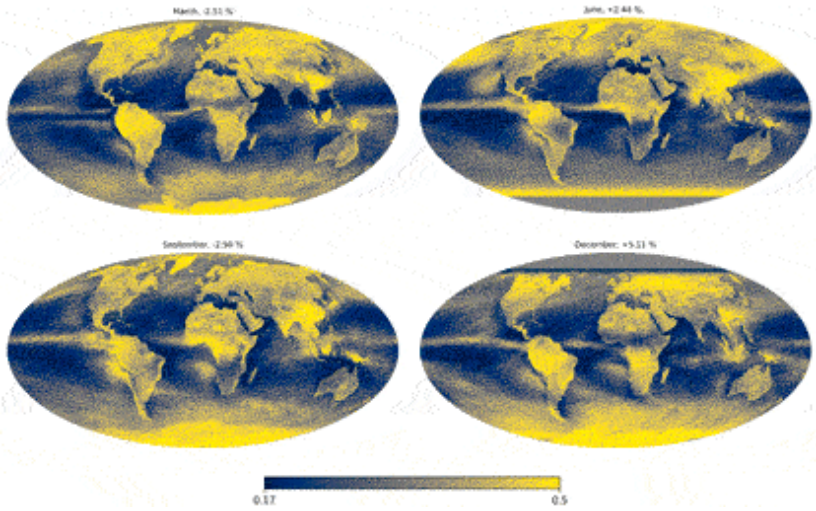

FIGURE 3 | The spherical albedo of the Earth. The monthly averages are presented for the months of equinoxes (March and September) and solstices (June and December). Darker and bluer values indicate lower albedo, brighter and more yellow values higher albedo.

The year 2020 is highlighted with red color in Figure 2 because of the anomaly in the second annual maximum. In the EPIC data, there are observations of four other Northern solstice maxima, but the one in 2020 is significantly higher. We can verify the anomaly in December 2020 statistically by studying the monthly averages for each year. The combined monthly averages are shown in Figure 4, plotted as variations from the overall average albedo in a box-and-whiskers chart. The one-way analysis-of-variance test of the differences in the mean monthly values over several years can find significant (p-value less than 0.1%) differences for all months. However, by far the smallest p-value, and therefore the largest difference, is for December, formally less than 10^{-29}.

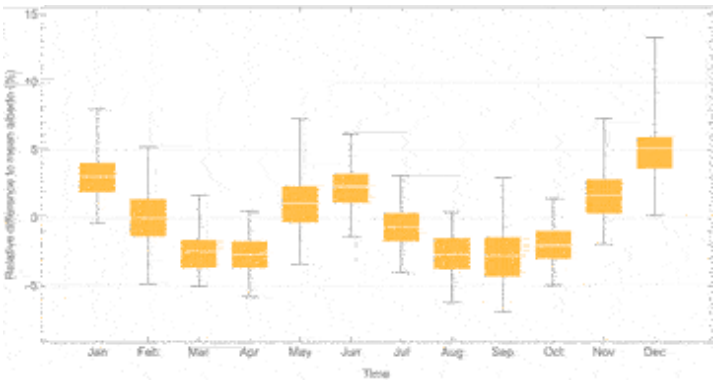

FIGURE 4 | Monthly variation in the daily averages of the Earth's spherical albedo. Values are relative differences from the overall mean albedo of 0.295. The horizontal white line shows the average over the month, the box indicates the range from the first quartile to the third quartile, and the lines the range from the minimum to the maximum.

When conducting *t*-tests for year pairs inside a month, we find that the only year which differs from all the other years when using the Bonferroni-corrected *p*-value limit of $0.001/m_i$, where m_i is the number of yearly data sets on month i, is the year 2020 and months August and December. Bonferroni correction is a method to counteract the bias when doing multiple statistical tests on the same phenomena. From these analyses, we conclude that the largest yearly variations in a month are in December, and that is mainly due to year 2020.

We can conclude on the results on temporal variation on Earth's spherical albedo by summarizing that there are two maxima and two minima. The main maximum occurs in December–January during the Southern Hemisphere summer and the Southern solstice, and the secondary maximum in June during the Northern Hemisphere summer and the Northern solstice. The minimum values are in March–April, and on September, around equinoxes. The coefficient of variation, that is the standard deviation divided by mean, of the daily average values over a year is 2.7%, and the range of minimum-to-maximum deviation of the daily averages from annual average is 0.031 (10.3 percentage points in scale relative to the mean annual albedo). In December 2020, the daily albedo values were up to 0.023 (7.2%, on December 13) larger than the average daily value over all the years.

DISCUSSION

Annual Albedo Variation

The annual variation of the Earth's spherical (Bond) albedo is described for the first time in detail. Previous investigations mainly describe the variations on the incident solar flux due to the Earth's elliptic orbit (see Figure 5 in Kandel and Viollier, 2010), as for us, this effect is considered and properly accounted for Su et al. (2018), Su et al. (2020) are using also EPIC images, but they do not reduce the albedo but produce outgoing fluxes. The accurate annual albedo behavior enables the detailed analysis of local geographic and atmospheric effects on the albedo during a year.

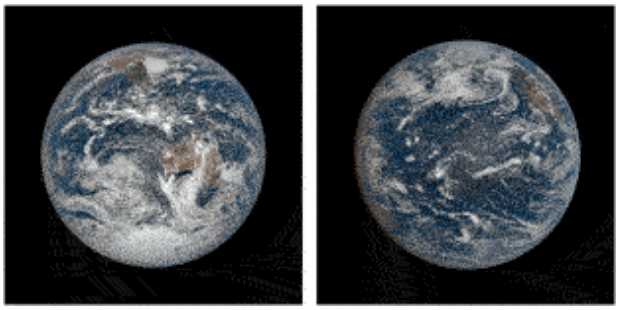

FIGURE 5 | EPIC natural color constructed images, taken at 2020-12-13 at 04:40 UCT (left), and 2020-08-04 at 22:25 UCT (right). The image on the left has one of the largest albedos in 2020 (0.350), and the image on the right has one of the lowest (0.253). Image credits: NASA EPIC team, https://epic.gsfc.nasa.gov/.

The Earth contains regions of low albedo (e.g., cloud-free ocean areas, vegetated land areas) and high albedo (e.g., clouds, ice and snow surfaces). Diurnal and annual variations in the albedo time series (Figure 1) result from a modulation of these two aspects, depending on the apparent longitude (diurnal variations) and latitude (annual variations). Especially, the cloud-covered ocean areas increase the albedo. The daily cloud-covered ocean fraction, estimated from the EPIC images, has the correlation coefficient value of 86% with the daily albedo value (see Figure 7).

In annual albedo variations, the main albedo maximum occurs in December, around Southern solstice, when the Antarctic ice sheet, sea ice, and snow cover are visible entirely. At this time, cloud formations of the mid-latitude cyclones over the Southern Ocean are well pronounced. Albedo is further enhanced by the shallow convective cloud cover over the subtropical oceans and the relatively small areas of cloud-free ocean areas visible, on average, at this time of the year.

The secondary albedo maximum occurs in June, around Northern solstice, when the Greenland ice sheet and sea ice in the Arctic Ocean are well exposed. Cloud formations of the mid-latitude cyclones of the North Atlantic and Pacific storm tracks are active, although reduced from their winter maxima. Deep convective clouds of the inter-tropical convergence zone are on the Northern Hemisphere at this time of the year. Again, relatively little cloud-free ocean areas are visible.

The main albedo minimum precedes the main maximum in August–September when neither of the Polar regions is visible. At this time of year, there are relatively few shallow convective clouds over the subtropical Northern Atlantic and Pacific, as well as over the Mediterranean. North Atlantic and Pacific storm track activities are near to their minima. Also, vegetation is at its maximum extent in the Sahel region. Monsoon is in active phase over the Indian peninsula and South-East Asia, thus enhancing the albedo. The secondary minimum precedes the secondary maximum in March–April.

The solar energy input at the Earth's average distance from the Sun is 1361 W/m^2 for the sunlit disk of the Earth over all wavelengths (Coddington et al., 2015). The EPIC filters range from 317 to 780 nm in wavelength and the portion of the solar input between these wavelengths is 52.7%. We can make a rough estimate that the albedo derived here is valid for somewhat longer wavelengths, say to 60% of the reflection or absorption of the total solar input. With this estimate, the input energy that is absorbed into the area of sunlit Earth's disk and atmosphere is about 4.9 W/m^2 more during the albedo minimum in September than on average. During the albedo maximum in December, about 8.7 W/m^2 less energy is absorbed.

Exceptional Albedo Maximum in December 2020

An exceptional albedo occurred on 13 December 2020 and persisted for about a week before and after the peak value. This anomaly coincides with the main annual maximum in December. Our main explanation is a short-lived and exceptional maximum in the amount of shallow convective clouds over the subtropical Indian Ocean and the Pacific east of Australia, see Figure 5. The development of exceptionally wide shallow cloud cover coincides and is favoured by a constellation of several mature mid-latitude cyclones, feeding moist air from the subtropics towards the Antarctic. At the time of the maximum albedo, all relevant large-scale atmosphere-ocean

indicators were in close-to-neutral stages[4]: the Madden-Julian oscillation (MJO) phase centre was in the Oceanic continent, but the amplitude was weak; the Indian Ocean Dipole (IOD) was neutral; El Niño–Southern Oscillation (ENSO) was in a weak La Niña phase (El Niño 3.4 index) and returning to neutral.

In December 2020, the EPIC-derived daily albedo was elevated to 0.334 from its typical December value of 0.312 in 2015–2019. Assuming these to represent well the planetary reflectivity, the emission temperature of the Earth would decrease by 2.1 K through a 7.8 $\mathrm{W/m^2}$ reduction in the absorbed solar radiation. For comparison, the global mean sensible heat flux from the Earth surface to the atmosphere amounts to about 20 $\mathrm{W/m^2}$ and the absorbed solar radiation in the atmosphere to about 80 $\mathrm{W/m^2}$ (Hartmann, 2015). It is therefore fair to treat the short-term albedo peak in December 2020 as quite remarkable.

Effect of Phase Angle on Albedo

The phase angle of EPIC observations varies between 2° and 12°. After the DSCOVR operations break in 2019, the phase angle variation has increased, and the minimum phase angle has decreased from previous 4°–1.8° (Marshak et al., 2021). These decreasing phase angles introduce a possible source of bias in our albedo estimation. The resolution in the binned data of the ADM models that we use is 10° in all three angles, indicating that we do not have exact information on how possible backscattering effects (self-shadowing, coherent backscattering) are behaving on small phase angles inside this bin.

Currently, we can only estimate the possible bias resulting from small phase angles. We can do this by computing the deviations of daily albedo values from the average-year albedo values, and by modeling how they are changing as a function of the observation phase angle. From Figure 6 we can see that there is an obvious correlation between these, the linear correlation coefficient being −0.59. Decreasing phase angles are introducing a positive bias, on average, into the albedo values. A second-degree linear fit has the *p*-values of all the model coefficients significant below 0.1% level, and a slightly better value (0.37) of adjusted R^2 measure of the model than with the first-degree model (0.36). According to this model, there can be up to 0.01 positive average bias coming from the phase angle effect if the phase angle approaches 2°.

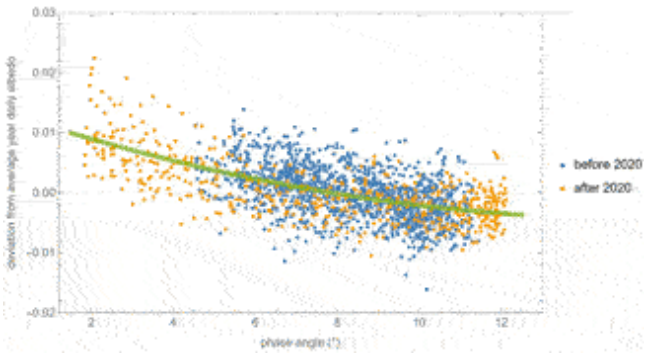

FIGURE 6 | Differences between daily albedo values and corresponding values from an average year, as a function of the phase angle of the observation. The solid line shows the second-degree linear fit to the data. The data before and after the DSCOVR operations break in 2019–2020 is shown with different colors, but the model is fitted to both sets together.

This same bias can also be roughly estimated from the small upturns in daily albedo values in November 2020 and March 2021, see Figures 1, 7. These upturns are simultaneous with local phase angle minima of about 2°. Graphical estimation of possible excess in albedo values in these upturns also suggests a value of 0.01 at most.

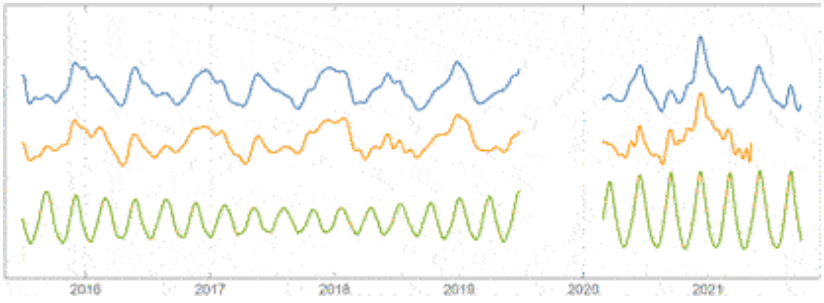

FIGURE 7 | The daily average albedo values (blue lines), the daily average fraction of clouds over oceans (orange lines), and the scattering angle (complement of the Sun-Earth-vehicle angle) of the EPIC observations (green lines). The curves have different vertical scales and have been shifted in vertical direction and rescaled for improved visualization.

The exceptional albedo values in December 2020 were at most 0.023 larger than the average December value. This exceptional value was received at the time of local phase angle minima of the DSCOVR spacecraft, 2.1°. We conclude that the effect of the phase angle can explain, at maximum, about half of the difference, and that December 2020 is exceptional in our albedo time series even when taking the possible phase angle effect into account.

CONCLUSION

We introduce here a novel method for following the spherical shortwave albedo of Earth. The albedo values are updated daily and in almost real time with only a few days delay. The data processing pipeline is fully automated and the estimated albedo values are publicly available. The average yearly albedo estimated with our method, 0.295±0.008, agrees well with the previous works on the albedo. With the albedo time series presented here from 2015 up to date we can study the seasonal variations in albedo, and we find an annual trend with two maxima and two minima, approximately associated with the solstice and the equinox dates. We can also find one anomalous feature with the unusually large yearly maximum in December 2020.

The variations in the albedo can support studies of the radiation budget of Earth and its temporal variation. As the method can also map the albedo values geographically one can relate better the varying local weather and climate conditions with the variations in the albedo.

This method of deriving the spherical shortwave albedo from the EPIC imagery is presented here for the first time. There are several aspects in this method with prospects for further studies and improvements. The cloud classification could probably be improved by taking the local solar zenith angle into account in the model. The CERES ADMs have editions with more detailed angular binning (Edition 4, Su et al., 2015a; Su et al., 2015b). They are not publicly available as they are much larger in size and coupled with the CERES software libraries, however, with adequate resources they could be employed. The increased variation in the phase angle of the EPIC observations after 2020 might call for modeling the effect of the phase angle in the albedo estimation. Finally, a detailed comparison of our albedo estimate to other estimates of albedo or outgoing flux would be very interesting.

DATA AVAILABILITY STATEMENT

The raw image data supporting the conclusion of this article is available at the NASA EarthData site at https://asdc.larc.nasa.gov/data/DSCOVR/EPIC/. The produced albedo data is available at https://albedo.physics.helsinki.fi/.

AUTHOR CONTRIBUTIONS

The method and algorithm were designed by AP, KM OI, EU, MV, GX, and OW. The algorithm was coded by AP, OI, EU, MV, and OW. The web service was designed by AP, KM, EU, MV, and coded by AP and MV. The data in this article was prepared by AP, as well as the statistical analysis on the data. The article was written by AP, KM, EU, MG, and HJ. All authors provided input and comments to the article.

FUNDING

Funding is received from Academy of Finland projects 298137, 325805, and 333034.

PUBLISHER'S NOTE

ACKNOWLEDGMENTS

We acknowledge that computational resources are provided by CSC—IT Center for Science Ltd., Finland.

FOOTNOTES

[1]http://albedo.physics.helsinki.fi.

[2]https://ceres.larc.nasa.gov/data/angular-distribution-models/.

[3]https://imagej.github.io.

[4]Bureau of Meteorology, climate monitoring, http://www.bom.gov.au/climate/. Accessed 31 January 2022.

REFERENCES

Coddington, O., Lean, J. L., Lindholm, D., Pilewskie, P., and Snow, M.NOAA CDR Program (2015). *NOAA Climate Data Record (CDR) of Solar Spectral Irradiance (SSI), NRLSSI Version 2*. NOAA National Centers for Environmental Information. accessed 2020-10-21. doi:10.7289/V51J97P6

Geogdzhayev, I. V., and Marshak, A. (2018). Calibration of the DSCOVR EPIC Visible and NIR Channels Using MODIS Terra and Aqua Data and EPIC Lunar Observations. *Atmos. Meas. Tech.* 11, 359–368. doi:10.5194/amt-11-359-2018

Goode, P. R., Pallé, E., Shoumko, A., Shoumko, S., Montañes-Rodriguez, P., and Koonin, S. E. (2021). Earth's Albedo 1998-2017 as Measured from Earthshine. *Geophys. Res. Lett.* 48, e2021GL094888. doi:10.1029/2021GL094888

Goode, P. R., Qiu, J., Yurchyshyn, V., Hickey, J., Chu, M.-C., Kolbe, E., et al. (2001). Earthshine Observations of the Earth's Reflectance. *Geophys. Res. Lett.* 28 (9), 1671–1674. doi:10.1029/2000GL012580

Hartmann, D. (2015). *Global Physical Climatology*. 2nd Edition. Elsevier Science, 498. ISBN: 9780123285317.

Herman, J. R., Huang, L., McPeters, R. D., Ziemke, J., Cede, A., and Blank, K. (2018). Synoptic Ozone, Cloud Reflectivity, and Erythemal Irradiance from Sunrise to sunset for the Whole Earth as Viewed by DSCOVR Spacecraft from the Earth-Sun Lagrange-1. *Atmos. Meas. Tech.* 11, 1–18. doi:10.5194/amt-11-177-2018

Kandel, R., and Viollier, M. (2010). Observation of the Earth's Radiation Budget from Space. *Comptes Rendus Geosci.* 342 (4), 286–300. doi:10.1016/j.crte.2010.01.005

Marshak, A., Delgado-Bonal, A., and Knyazikhin, Y. (2021). Effect of Scattering Angle on Earth Reflectance. *Front. Remote Sens.* 2. doi:10.3389/frsen.2021.719610

Marshak, A., Herman, J., Adam, S., Karin, B., Carn, S., Cede, A., et al. (2018). Earth Observations from DSCOVR EPIC Instrument. *Bull. Am. Meteorol. Soc.* 99 (9), 1829–1850. doi:10.1175/BAMS-D-17-0223.1

Ohtake, M., Matsunaga, T., Yokota, Y., Yamamoto, S., Ogawa, Y., Morota, T., et al. (2010). Deriving the Absolute Reflectance of Lunar Surface Using SELENE (Kaguya) Multiband Imager Data. *Space Sci. Rev.* 154, 57–77. doi:10.1007/s11214-010-9689-0

Ohtake, M., Pieters, C. M., Isaacson, P., Besse, S., Yokota, Y., Matsunaga, T., et al. (2013). One Moon, many Measurements 3: Spectral Reflectance. *Icarus* 226, 364–374. doi:10.1016/j.icarus.2013.05.010

Stephens, G. L., O'Brien, D., Webster, P. J., Pilewski, P., Kato, S., and Li, J.-l. (2015). The Albedo of Earth. *Rev. Geophys.* 53 (1), 141–163. doi:10.1002/2014RG000449

Su, W., Corbett, J., Eitzen, Z., and Liang, L. (2015a). Next-generation Angular Distribution Models for Top-Of-Atmosphere Radiative Flux Calculation from CERES Instruments: Methodology. *Atmos. Meas. Tech.* 8, 611–632. doi:10.5194/amt-8-611-2015

Su, W., Corbett, J., Eitzen, Z., and Liang, L. (2015b). Next-generation Angular Distribution Models for Top-Of-Atmosphere Radiative Flux Calculation from CERES Instruments: Validation. *Atmos. Meas. Tech.* 8, 3297–3313. doi:10.5194/amt-8-3297-2015

Su, W., Liang, L., Doelling, D. R., Minnis, P., Duda, D. P., Khlopenkov, K., et al. (2018). Determining the Shortwave Radiative Flux from Earth Polychromatic Imaging Camera. *J. Geophys. Res. Atmos.* 123 (20), 479–511. doi:10.1029/2018JD029390

Su, W., Minnis, P., Liang, L., Duda, D. P., Khlopenkov, K., Thieman, M. M., et al. (2020). Determining the Daytime Earth Radiative Flux from National Institute of Standards and Technology Advanced Radiometer (NISTAR) Measurements. *Atmos. Meas. Tech.* 13 (2), 429–443. doi:10.5194/amt-13-429-2020

Wielicki, B. A., Barkstrom, B. R., Harrison, E. F., Lee, R. B., Louis Smith, G., and Cooper, J. E. (1996). Clouds and the Earth's Radiant Energy System (CERES): An Earth Observing System Experiment. *Bull. Amer. Meteorol. Soc.* 77 (5), 853–868. doi:10.1175/1520-0477(1996)077<0853:catere>2.0.co;2

Conflict of Interest: Author OI was employed by the company VTT Technical Research Centre of Finland Ltd.

The remaining authors declare that the research was conducted in the absence of any commercial or financial relationships that could be construed as a potential conflict of interest.

PERSPECTIVE
published: 11 March 2022
doi: 10.3389/frsen.2022.796273

EPIC/DSCOVR as a Pathfinder in Cloud Remote Sensing Using Differential Oxygen Absorption Spectroscopy

Anthony B. Davis[1*], Yuekui Yang[2] and Alexander Marshak[2]

[1] *NASA Jet Propulsion Laboratory, California Institute of Technology, Pasadena, CA, United States*
[2] *NASA Goddard Space Flight Center, Greenbelt, MD, United States*

Edited by:
Yongxiang Hu, National Aeronautics and Space Administration (NASA), United States

Reviewed by:
Chao Liu, Nanjing University of Information Science and Technology, China

**** Correspondence:*** *Anthony B. Davis, Anthony.B.Davis@jpl.nasa.gov*

Specialty section: *This article was submitted to Satellite Missions, a section of the journal Frontiers in Remote Sensing*

Received: *16 October 2021*
Accepted: *19 January 2022*
Published: *11 March 2022*

Citation: *Davis AB, Yang Y and Marshak A (2022) EPIC/DSCOVR as a Pathfinder in Cloud Remote Sensing Using Differential Oxygen Absorption Spectroscopy. Front. Remote Sens. 3:796273. doi: 10.3389/frsen.2022.796273*

We argue that the Earth Polychromatic Imaging Camera (EPIC) on the Deep Space Climate ObserVatoRy (DSCOVR) platform has blazed new pathways in observational technology, starting with its ~ 1.5 × 106 km stand-off

distance, but also in remote sensing science. We focus here on EPIC's two oxygen absorption channels that 1) are unique in their spectral sampling and 2) have stimulated deep innovation in cloud remote sensing using Differential Oxygen Absorption Spectroscopy (DO_2AS). Although first formulated 6 decades ago, DO_2AS-based cloud probing from overhead assets is still an emerging observational technique. It is indeed somewhat paradoxical that one should use absorption by a gas to assay scattering by particles. After surveying the history of space-based DO_2AS, and looking into its future, we see that EPIC/DSCOVR marks an inflection point in this important development. EPIC's unique DO_2AS capability motivated a notable sequence of papers revisited here. This research indeed spawned a rare occurrence of information content analysis coming from radically different—yet complementary—perspectives. First, we adopted the increasingly popular machinery of optimal estimation (OE) that is grounded in Bayesian statistics and uses a somehow linearized radiative transfer (RT) model. Nonetheless, OE feels like a black-box algorithm that outputs a number of "degrees of freedom" (a.k.a. independent pieces of information about clouds under observation). However, the very same conclusions are reached using fully transparent physics-based modeling for the RT, with a few approximations that enable closed-form analytical formulation. Lastly, we preview a novel DO_2AS technique for regaining shortwave sensitivity to cloud optical thickness past the threshold where cloud reflectivity flattens off.

Keywords: DSCOVR, EPIC, oxygen A-band, oxygen B-band, clouds, pathlength distribution, pathlength moments

1 INTRODUCTION AND OUTLINE

Since the beginning of operational satellite meteorology, NASA's TIROS-1 (launched 1960), we have been accustomed to seeing clouds as a dynamical 2D map projected onto the Earth's surface. However, meteorologists and atmospheric scientists in general yearn for knowledge of clouds in the vertical dimension where complex processes in cloud physics unfold, from nucleation to precipitation. This unsatiable thirst for knowledge of the vertical distribution of clouds persists to this day. In fact it permeates NASA's 2017 Decadal Survey (National Academies of Sciences, Engineering, and Medicine, 2018) not only in the Designated Observables

from the Aerosol/Cloud-Convection-Precipitation (ACCP) arena but also in the more experimental Planetary Boundary Layer (PBL) Incubator program.

The earliest known publications on the potential use of molecular absorption to determine cloud height are in a discussion initiated by Hanel (1961), just a year after TIROS-1's launch. He was indeed promptly engaged by Yamamoto and Wark (1961) and Chapman (1962) who suggest using the oxygen A-band (759–769 nm) because O_2 is a dominant constituent with a well-characterized pressure profile. Thus started the idea of using differential Oxygen absorption spectroscopy (DO_2AS), a special case of differential optical absorption spectroscopy (DOAS), to probe clouds from space.

In the following Section 2, we survey the history and geography of DO_2AS-based sensing of scattering particulates in the Earth's atmosphere from space. We focus on the period ending in 2010 because that is more-or-less when theory-dominated research is superseded by data-driven work since, by then, several satellites with O_2 A-band coverage were in orbit. To balance the theory-heavy literature survey, we describe more-or-less chronologically the core technological aspects of satellite missions so far with DO_2AS capability, underscoring EPIC/DSCOVR's uniqueness. Finally, we gaze into what lies ahead for O_2 absorption in satellite missions to be launched in the foreseeable future.

This leads to the lessons-learned from investigating the cloud information content of EPIC's (764 ± 0.2 nm) and B-band (687.75 ± 0.2 nm) channels using both physics and statistics in Section 3. From there, we connect the implicit dependence of EPIC's O_2 absorption channel responses on the mean pathlength of sunlight in the cloudy medium to recent advances in statistical physics. In turn, that deep dive into the fundamental physics of O_2 absorption in scattering media such as clouds reveals a new path toward the inference of cloud optical thickness (COT) for very opaque clouds from DO_2AS, not just through radiance levels in continuum channels that are soon saturated as COT increases.

We summarize in Section 4, and contemplate the future of DO_2AS observation of clouds from space.

2 BRIEF HISTORY OF SPACE-BASED DO_2AS, A LOOK INTO THE NEAR-FUTURE AND THE SPECIAL ROLE OF EPIC/DSCOVR

Soon after the first suggestion of using DO_2AS in cloud sensing (Yamamoto and Wark, 1961; Chapman, 1962), the mathematical connection between the *distribution* of light paths in scattering media and the detailed shape of the absorption spectrum was rigorously established (Irvine, 1964) This key development was followed by the physically-correct analogy with non-stationary radiation transport (Katsev, 1969; Katsev and Zege, 1974). Astrophysical theoreticians made important early contributions (e.g., Ivanov and Sabashvili, 1972; Nagirner, 1974). The earliest known observations of clouds from space in the O_2 A-band are from 1965, using a handheld camera operated aboard Gemini-5 (Saiedy et al., 1965; Saiedy et al., 1967; Wu, 1985). It seems that the first non-astronaut counterparts were performed by a sensor aboard Kosmos 320 in 1970 (Gorodetskiy et al., 1971; Syachinov and Kozlov, 1974), and possibly as early as 1967 with the near-identical Kosmos 149 (Malkevich, 1974).

At any rate, a considerable amount of research on cloud remote sensing using overhead DO_2AS was performed in the Former Soviet Union in the 1970s (Dianov-Klokov et al., 1970; Dianov-Klokov and Krasnokutskaya, 1972; Kargin et al., 1972; Malkevich et al., 1975; Dianov-Klokov, 1976; Grechko et al., 1976; Dianov-Klokov et al., 1977; Grechko, 1978), including observations from an aircraft (Grechko et al., 1973) and a satellite (Gorodetskiy et al., 1971; Syachinov and Kozlov, 1974), and into the 1980s (Badayev and Kozlov, 1980; Grechko et al., 1982; Romanova and Ustinov, 1982; Skorinov and Titov, 1984; Gusev and Dvoryashin, 1990). In the West, there was a fast-growing interest in O_2 absorption as a means of probing clouds during the 1990s (Fisher et al., 1991; Fisher and Grassl, 1991; O'Brien and Mitchell, 1992; Kuze and Chance, 1994; Asano et al., 1995; Hayazaka et al., 1995; O'Brien et al., 1999) and into the 2000s (Heidinger and Stephens, 2000; Partain et al., 2000; Stephens and Heidinger, 2000; Kokhanovsky et al., 2004; Kokhanovsky and Rozanov, 2004; Rozanov and Kokhanovsky, 2004), with an increasing emphasis on 3D RT signatures (e.g., Heidinger and Stephens, 2002; Kokhanovsky et al., 2007; Davis et al., 2009).

The above extensive but non-exhaustive literature survey of cloud-focused space-based DO_2AS ends in 2010. Indeed, by the end of the first decade of the 21st century, there were already several satellites in orbit collecting real DO_2AS data on clouds, as we will document in the following (Table 1). We therefore view 2010, somewhat arbitrarily, as the end of an era

of theory-dominated research on space-based cloud remote sensing using DO_2AS and the beginning of data-driven research. Since then, activity in this field has of course continued to grow steadily. In view of this sustained growth, a Workshop on "Remote sensing in the O2 A-band" was convened at KNMI in de Bilt, Nederlands, in 2016. A Second Workshop on "Remote Sensing in Oxygen Absorption Bands" was planned to happen in Berlin, Germany, in 2020, but has been postponed because of the COVID-19 pandemic to a future date in 2022. At any rate, this shows that there is a well-defined scientific community engaged in DO_2AS, for clouds and from space in particular.

TABLE 1 | Compendium of satellite missions with DOAS capability ordered chronologically and clustering sensors with similar characteristics. To the best of our knowledge, SCIAMACHY is the first instrument with an operational DO_2AS-based cloud product (Kokhanovsky et al., 2005), followed by the POLDER series (Buriez et al., 1997; Vanbauce et al., 1998) and EPIC (Yang et al., 2019). Research cloud property retrievals have been developed for these missions, e.g., MOS-A (Preusker et al., 2007), POLDER-3 (Ferlay et al., 2010), and others, most recently, OCO-2/3 (Richardson et al., 2017; Richardson and Stephens, 2018; Richardson et al., 2019; Richardson et al., 2020). Such experimental retrievals can and have been transitioned into fully operational elements in the data processing pipeline.

Sensor Name	Developed by ...	Platform	Agency	Dates	Spatial resolution	Spectral Sampling	Multi-view?	Reference
GOME	DLR	ERS-2	ESA	**1995**–2011	VL	M	n	Burrows et al. (1999)
MOS-A	DLR	IRS-3	ISRO	1996–2004	M	M	n	Thyagarajan et al. (1996)
SCIAMACHY	SRON	Envisat	ESA	2002–2012	VL	M	n	Bovensmann et al. (1999
GOME-2	DLR	MetOp-A/-B/-C	EUMETSAT	2006-/2012-/2018-	VL	M	n	Callies et al. (2000)
MERIS	ALCATEL	Envisat	ESA	**2002**–2012	M	2C	n	Rast et al. (1999)
POLDER	CNES	ADEOS I	NASDA	1996–1997	L	2C	y	Deschamps et al. (1994)
POLDER-2	CNES	ADEOS II	NASDA	2002–2003	L	2C	y	
POLDER-3	CNES	PARASOL	ESA	**2004**–2013	L	2C	y	
OCO-2	JPL		NASA	**2014**-	M	VH	n	Crisp et al. (2008)
OCO-3	JPL	ISS	NASA	2019-	M	VH	n	Eldering et al. (2019)
OLCI	ACRI-ST	Sentinel-3A/B	ESA	2016-/2018-	M	M	n	Nieke et al. (2012)
EPIC	GSFC	DSCOVR	NASA + NOAA	**2015**-	L	2C (A,B)	n	Marshak et al. (2018)

We can now take a more-or-less chronological stroll through satellite missions with imaging DO_2AS capability, whether or not implemented with clouds in mind.[1] We see five clusters emerge, with spectral sampling and spatial resolution being distinguishing factors. We distinguish between moderate and low spatial resolution based on the implicit definition of "moderate" (M) resolution used by MODIS (MODerate resolution Imaging Spectro-radiometer), namely, pixels that are on the order of 1 km in scale. By this standard, sensors with "low" (L) resolution have pixels on the order of

10 km in scale, and "very low" (VL) resolution sensors have pixels that are several 10s of km. We also distinguish "low," "moderate" and "very high" (VH) spectral resolutions: respectively, ~2-to-5, ~10s, ~1000s of spectral samples across the (~10 nm wide) A-band, all of which are useful. Alternatively, there is the "two-channel" (2C) strategy, typically in-band and out-of-band channels from which a single DOAS ratio can be formed; however, it can also be implemented with a narrow/in and broad/in-and-out pair of channels, as was done for POLDER (POLarization and Directionality of the Earth's Reflectances). Either way, in the 2C scenario, it is important to know if there are single or multiple views. Table 1 displays satellite missions with DOAS capability that we have identified over the past two-and-a-half decades,[2] with some key defining characteristics and a reference for more information. Five clusters emerge.

EPIC's DO_2AS capability is new and unique in at least two respects in the realm of technology. First, it has an extreme standoff distance of ~1.5 10^6 km to the Lagrange-1 point. From there, the sensor sees almost all of the sunlit hemisphere all the time, i.e., there is no down-time. Additionally, EPIC uses a special spectral sampling strategy based on both the A- and B-bands of the di-oxygen molecule. The advantage in this is not, as we will see in the next section, that these bands have different absorption strengths. Rather, the surface albedo is low, hence less confounding for cloud probing, in at least one of these bands: over water, in both; over vegetated land, in the B-band.

The future of DO_2AS in space is bright, especially in Low-Earth Orbit (LEO). There will be two more OLCI/Sentinel-3 launches in the late 2020s, followed by ESA's TROPOMI/Sentinel-5 series (Veefkind et al., 2012)—with a precursor mission already launched in 2017. EUMETSAT will have a multi-angle/multi-spectral/multi-polarization imager (3MI) (Manolis et al., 2013), with POLDER (hence A-band) legacy, on all of its future MetOp second-generation satellites, starting in 2024. Moreover, EUMETSAT's Sentinel-4 series (Meteosat Third Generation, MTG), due to be launched in 2023 and 2030, will carry the S4 UVN Multispectral Spectrometer (Riedl et al., 2019) to Geostationary orbit (GEO), with the O_2 A-band covered at 0.12 nm resolution. Back in LEO, NASA/JPL's Multi-Angle Imager for Aerosols (MAIA) mission (Diner et al., 2018) will have a 2C/multi-angle take on the A-band at moderate spatial resolution. NASA's Plankton, Aerosol, Cloud ocean Ecosystem (PACE) mission (Werdell et al., 2019) will

cover the A-band with two of its three sensors at relatively low spectral resolution:

- GSFC's Ocean Color Instrument (OCI) (Meister et al., 2019), with a moderate spatial resolution, and
- SRON's SPEXone (Rietjens et al., 2019), with a somewhat lower spatial resolution but offering multiple views and polarization across all wavelengths.

MAIA and PACE are scheduled to launch in the October 2024 – March 2025 timeframe. Last but not least, as part of NASA's next generation of Earth observing satellites, the Atmospheric Observing System (AOS) implements the 2017 Decadal Survey's ACCP element; it will include a UV-VIS imaging spectrometer in polar orbit that covers the O_2 A-band at low spectral and moderate spatial resolutions, with a launch date in the late 2020s.

3 INFORMATION CONTENT OF THE PATHLENGTH DISTRIBUTION

We contend that EPIC not only blazed a new path into the observational technology of DO_2AS from space, but also in the associated remote sensing science, which we view as enabling Earth system science via remote sensing. To make this point, we briefly revisit a series of papers motivated by EPIC's two pairs of DOAS channels for the A- and B-bands.

Even before the DSCOVR launch, Yang et al. (2013) devised a method for extracting two cloud properties from EPIC's two DO_2AS ratios, namely, cloud top height (CTH) and cloud geometric thickness (CGT). Specifically, the authors used the sum and difference *apparent* cloud heights from both ratios, where "apparent" refers to the fact that in-cloud propagation and scattering are not accounted for. However, the fact that they are different is precisely because of the finite pathlength cumulated inside the cloud and the different strengths of the A- and B-bands. Two-entry (CTH,CGT) look-up tables (LUTs) were therefore generated to retrieve the two cloud properties, much like how the Nakajima and King (1990) algorithm delivers cloud optical thickness (COT) and cloud particle effective radius given two reflected radiances, one VIS (with dominant sensitivity to COT) and one SWIR (with dominant sensitivity to particle size).

After the DSCOVR launch and EPIC's first light, it became clear to the cloud product team that it is important to factor into their algorithms the sensor's finite radiometric signal-to-noise ratio (SNR). Davis et al. (2018b) therefore followed the well-beaten path of optimal estimation (OE) theory (Rodgers, 2000) to do that. OE is, in essence, a formalism grounded in probabilistic information theory and linear algebra that relates measurement (Level 1) error and any prior/Baysian knowledge to retrieval (Level 2) error. OE has, at its core, a forward RT model that is either linearized or run at sufficient numerical precision to compute accurate Jacobian matrices by finite differencing. However, once implemented in code, the mathematical expressions of OE feel like a "black box" procedure that just has to be trusted. The authors concluded from their formal OE-based cloud information content analysis of EPIC's two DO_2AS ratios that CHT can be inferred with useful accuracy, but not CGT.

It is rare to have a second opinion on the assessment of geophysical information content of some set of measurements that is more transparent in nature, but this did occur for EPIC's two DO_2AS ratios. Indeed, Davis et al. (2018a) derived from first principles a model simple enough to be expressed in closed form, yet realistic enough to capture the main radiative processes unfolding from source to sensor. The authors used this physics-based approach to assess the sensitivities of EPICs DO_2AS ratios to CTH and CGT, bearing in mind the finite amplitude of the sensor noise, and they again found a strong response to CTH and a weak one to CGT.

In hindsight, the series of three papers published in the *Journal of Quantitative Spectroscopy and Radiative Transfer* weave a story about adjusting expectations to sensor and algorithm realities. In the case, it is about EPIC's ability to probe clouds: cloud top from O_2 absorption channel ratios and COT from the radiometrically-calibrated continuum channels, assuming either liquid or ice particles (cf. Yang et al., 2019), but unfortunately not cloud base height via CTH.

That is not however the end of EPIC's influence on the remote sensing science of O_2 absorption observations in application to cloud profiling. By happenstance, EPIC's DO_2AS research team was alerted by N. Ferlay, an expert in POLDER's A-band information content, about a powerful invariance property of mean pathlength $\langle L \rangle$ cumulated *inside* a scattering optical medium of arbitrary shape and internal structure: $\langle L \rangle = 4V/S$, where V

is the volume of the medium and S is its surface (Blanco and Fournier, 2003). This remarkable result is predicated on uniform and isotropic illumination of the medium, which clashes with the cloud-illuminated-by-the-sun scenario, and integration over all possible escape positions and directions, which conflicts with single direction sampled in remote sensing. There is nonetheless a strong message: once reduced to just in-cloud paths, $\langle L \rangle$ informs us directly about the size of the medium. For plane-parallel media, where V and S are infinite, $\langle L \rangle = 2H$, with H being the geometrical thickness of the slab.[3]

This begs the question about what pathlength variance $\mathrm{Var}[L] = \langle (L - \langle L \rangle)^2 \rangle = \langle L^2 \rangle - \langle L \rangle^2$ brings to the table in terms of cloud information. Blanco and Fournier (2006) show that, unlike the mean, higher-order statistical moments of L depend on the opacity of the medium: if σ is the mean extinction coefficient, then $\langle L^q \rangle \propto \langle L \rangle / \sigma^{q-1}$, $q = 1,2,3,\cdots$, as $\sigma \to \infty$ (i.e., RT diffusion limit). The cloud remote sensing implication is that knowledge of both $\langle L \rangle$ and $\mathrm{Var}[L]$ for in-cloud pathlength L can be used to infer both the bulk size and mean opacity of the cloud;. In plane-parallel cloud geometry, that translates to both CGT H and COT $\tau = \sigma H$, irrespective of the value of the latter. In other words, we are no longer limited to the range of COT where there is enough sensitivity in (continuum) reflected radiance to distinguish a change in COT from a fluctuation in the noise, i.e., up to a few 10s.[4] Moreover, while the use of reflected radiance calls for absolute radiometric calibration, inference of moments of L, being based on $\mathrm{DO_2AS}$, only requires a relative calibration across spectral channels.

Figure 1 is adapted from a forthcoming paper by Davis et al. (2021) where a new derivation of the invariance law for $\langle L \rangle$ is presented along with a specific prediction for $\mathrm{Var}[L](\tau)$ in the diffusion limit for plane-parallel geometry. Numerical validation of the diffusion-theoretical predictions for $\langle L \rangle$ and $\mathrm{Var}[L](\tau)$ is performed. Figure 1 shows both moments as a function of τ for both isotropic and Henyey and Greenstein (1941) phase functions, assuming that asymmetry factor $g = 0.85$ in the latter case. As anticipated, the agreement is exact for $\langle L \rangle$ across all COTs, and the diffusion-based prediction for $\mathrm{Var}[L](\tau)$ becomes excellent as the *scaled* COT $\tau_t = (1 - g)\tau$ exceeds ~4 ($\tau \gtrsim 25$). At any rate, given $\langle L \rangle$ and $\mathrm{Var}[L](\tau)$, one can infer H and τ at any value above ~ $1/(1 - g)$, which is precisely when cloud reflectivity in the continuum starts to loose sensitivity to τ.

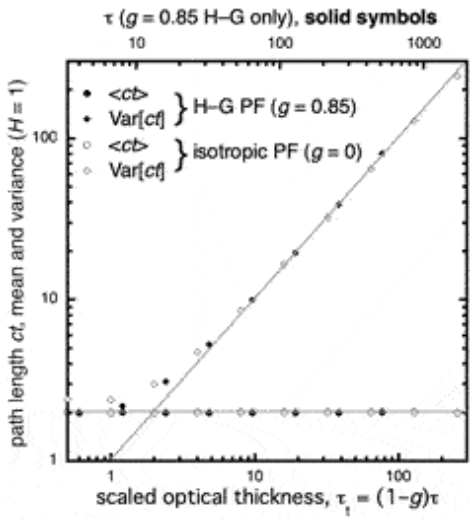

FIGURE 1 | Pathlength moments $\langle L \rangle$ and Var[L](τ) are plotted versus τ in log-log axes. Symbols mark the Monte Carlo simulation results, while diffusion model outcomes are solid lines. The invariance of $\langle L \rangle$ is verified exactly. Furthermore, the diffusion-theoretical prediction that Var[L](τ) = $(1 - g)\tau/2\chi$ (with extrapolation scale factor χ set to 2/3) becomes very accurate at $\tau_t = (1 - g)\tau \sim 4$. Two phase functions were investigated: $g = 0$ (isotropic scattering) and $g = 0.85$ (forward-peaked Henyey and Greenstein (1941) scattering). Adapted from Davis et al. (2021), where $\langle L \rangle$ is denoted $\langle ct \rangle$.

In-cloud pathlength L is a random variable, and its moments are emerging here as key intermediate quantities in DO_2AS that can be inferred from spectroscopic data at sufficiently high resolution (Davis et al., 2021). Figure 1 indeed shows that, given $\langle L \rangle(H)$ and Var[L](H, $(1 - g)\tau$), we can infer H and τ, knowing that g hardly deviates from 0.85 in liquid clouds. MUltiple Scattering Cloud Lidar (MUSCL) (Davis et al., 1999a; Davis A. B. et al., 1999b; Davis et al., 2009) is another emerging technology in cloud remote sensing from above or below (Cahalan et al., 2005; Polonsky et al., 2005; Davis, 2008) where the whole distribution of in-cloud pathlengths is measured directly. This is done by temporal binning the return times (i.e., L/c) of photons injected into a cloud using a pulsed laser beam. Now, the signal in each time bin can be noisy, but the statistical moments $\langle L \rangle$ and Var[L] are robust. As different as are their instrumental implementations, it is clear that DOxAs and MUSCL share the same fundamental signal physics grounded in time-dependent RT. Interestingly, DO_2AS is an inherently daytime observation while MUSCL operates strictly at nighttime since the steady sunlight diffusely reflected or transmitted by the cloud would

overwhelm the laser light in every time-bin (Davis, 2008). DO_2AS and MUSCL are therefore the ideal pair of instruments for a satellite mission for pathlength-based cloud observation that would deliver CTH, CGT, COT and possibly a measure of internal variability from turbulence (Davis et al., 2009).

4 SUMMARY AND DISCUSSION

In this PERSPECTIVE article, we above all celebrate space-based remote sensing using O_2 absorption to track clouds in the vertical dimension above every pixel. To that effect, we survey the relevant literature emphasizing theory up to 2010, which is roughly when there were enough space assets delivering O_2 A-band observations of clouds to see the research become predominantly data-driven. We hope to see others write the important literature review about post-2010 studies of clouds from space-borne O_2 absorption observations. Another worthwhile review would focus on ground-based cloud studies with O_2 absorption spectroscopy, and yet another should focus on using O_2 absorption spectroscopy from above or below to locate aerosol layers in the vertical dimension.

Building on our limited-scope literature survey, we support the viewpoint that EPIC/DSCOVR has been a pathfinder in O_2 absorption-based cloud remote sensing. Several other satellites carry sensors with O_2 absorption capability, EPIC however has by far the largest standoff distance and is also unique in its spectral sampling strategy: "in-band" and "continuum" pairs of channels each for the A- and B-bands. Another hallmark of EPIC's use of O_2 absorption to probe clouds is the impetus it has generated for progress in the associated remote sensing science that is centered on the concept of pathlength cumulated by sunlight, from source to sensor, between every scattering event along the way. To substantiate this claim, we revisited three papers in the *Journal of Quantitative Spectroscopy and Radiative Transfer* that directly address EPIC's characterization of clouds using O_2 absorption, and previewed a key result from a forthcoming one.

Determination of cloud structure in the third dimension is a goal shared by O_2 absorption spectroscopy and other emerging techniques in cloud remote sensing, for instance, 3D computational cloud tomography (CCT). CCT has, so far, been demonstrated on data with small pixel scales that are

readily achievable with airborne multi-view sensors, whether imaging (Levis et al., 2015; Levis et al., 2017; Levis et al., 2020; Levis et al., 2021) or not (Alexandrov et al., 2021). When dealing with such fine pixels, in the 10s of meters, there are necessarily significant radiative fluxes crossing pixel boundaries, thus requiring 3D RT forward modeling. There has been recent progress toward 3D CCT from space using moderate (~100s of meters) resolution multi-angle data from the likes of MODIS and MISR/Terra. On top of the 3D RT effects, this effort has to deal with complications from the larger pixels (optically thick, potentially with high internal heterogeneity) and accordingly larger clouds (Forster et al., 2021).

Looking ahead, we know that O_2 absorption observation is typically implemented in spectroscopy, and the more channels in the absorption band the better since the diversity in absorption coefficient ensures probing different depths into the cloud. However, this key ability can also be obtained using a single absorption channel, as for either of EPIC's O_2 absorption bands, in a multi-view angle collection. POLDER (2004–2013) pioneered the multi-view O_2 absorption observation strategy, and that path will be followed in short order by MAIA, SPEXone/PACE and 3MI. Spectroscopy-based O_2 absorption is also heading into a bright future, starting with OCI/PACE and NASA's upcoming Atmospheric Observing System (AOS). Someday, we may see the deployment of DSCOVR follow-on missions at Lagrange-1 and Lagrange-2 (Valero et al., 2021). At any rate, it will be interesting to see how future synergistic retrievals will blend O_2 absorption spectroscopy with other passive sensing modalities, such as multi-view imaging and CCT, thus enabling robust 3D cloud property retrievals on a global scale.

DATA AVAILABILITY STATEMENT

Inquiries about data used in Figure 1 can be directed to the corresponding author.

AUTHOR CONTRIBUTIONS

AD proposed and wrote this article for the Special Issue on "DSCOVR EPIC/NISTAR: Five Years of Observing Earth from the First Lagrangian Point." YY is the DSCOVR Science Team PI responsible for operational EPIC cloud products, including cloud heights from O_2 A- and B-band

channels; AM is Deputy Project Scientist for the DSCOVR mission. They both provided substantive feedback on the manuscript.

FUNDING

YY acknowledges sustained funding from the DSCOVR Science Team program. AD is supported by NASA's SMD/ESD DSCOVR mission (EPIC CLOUD ALGORITHMS, Project: 105357, Task: 239702.04.32.01.13, HQs PM Richard S. Eckman). This work was carried out at the Jet Propulsion Laboratory, California Institute of Technology, under a contract with the National Aeronautics and Space Administration (80NM0018D0004).

PUBLISHER'S NOTE

ACKNOWLEDGMENTS

We thank Mark Richardson, Quentin Libois, Nicolas Ferlay, Qilong Min, Jay Hermann, Dennis O'Brien, and Andy Sayer for many fruitful discussions about the science and history of probing clouds from space with DO_2AS techniques.

FOOTNOTES

[1]We pass on the Sea-viewing Wide Field-of-view Sensor (SeaWiFS) on the OrbView-2 (a.k.a. SeaStar) satellite mission, from 1997 to 2010. Its channel 7 (745–785 nm) covers the O_2 A-band but it was never exploited for atmospheric scattering. In fact, the O_2 absorption was a minor impediment for the targeted ocean color sensitivity that was eventually "corrected" out of the signal (Wang, 1999).

[2]At first glance, Table 1 seems to show that NASA was the last space agency to develop and launch satellite missions with DO_2AS capability as late as the mid-2010s. That is, however, far from true. Both NASA/JPL's CloudSat and the joint NASA/LaRC - CNES CALIPSO (co-launched into the A-train in 2006) were originally planned to have A-band imagers that were later descoped. With their inherent sensitivity to CTH, these A-band cameras would have extended at least CTH detection from the actively-probed sub-track "curtain" into the across-track direction.

[3]Picture a finite cylinder with radius R and thickness H: $V = H\times(\pi R^2)$ and $S = 2\times\pi R^2 + H\times(2\pi R)$. As $R \to \infty$, $\langle L \rangle = 4V/S \to 2H$.

[4]Indeed, an opaque cloud's reflectivity $R(\tau)$ can be approximated by $1/(1 + 2\chi/(1 - g)\tau)$, with $\chi = 2/3$. Maximum sensitivity to τ on a %-scale is realized when $(\mathrm{d}/\mathrm{d}\log\ \tau)^2\ R = 0$, which occurs in the above diffusion approximation at $\tau = 2\chi/(1 - g) \approx 9$ for the canonical value of $g = 0.85$ for liquid clouds.

REFERENCES

Alexandrov, M. D., Emde, C., Van Diedenhoven, B., and Cairns, B. (2021). Application of Radon Transform to Multi-Angle Measurements Made by the Research Scanning Polarimeter: A New Approach to Cloud Tomography. Part I: Theory and Tests on Simulated Data. *Front. Remote Sens.* 2, 791130. doi:10.3389/frsen.2021.791130

Asano, S., Shiobara, M., and Uchiyama, A. (1995). Estimation of Cloud Physical Parameters from Airborne Solar Spectral Reflectance Measurements for Stratocumulus Clouds. *J. Atmos. Sci.* 52, 3556–3576. doi:10.1175/1520-0469(1995)052<3556:eocppf>2.0.co;2

Badayev, V., and Kozlov, Y. (1980). On a Determination of the Optical Parameters of the Atmosphere from Reflected Radiation Measurements in the 0.76 μm Oxygen Absorption Band. *Izv. Acad. Sci. Ussr, Atmos. Oceanic Phys.* 16, 375–377.

Blanco, S., and Fournier, R. (2003). An Invariance Property of Diffusive Random Walks. *Europhys. Lett.* 61, 168–173. doi:10.1209/epl/i2003-00208-x

Blanco, S., and Fournier, R. (2006). Short-Path Statistics and the Diffusion Approximation. *Phys. Rev. Lett.* 97 (23), 230604. doi:10.1103/physrevlett.97.230604

Bovensmann, H., Burrows, J. P., Buchwitz, M., Frerick, J., Noël, S., Rozanov, V. V., et al. (1999). SCIAMACHY: Mission Objectives and Measurement Modes. *J. Atmos. Sci.* 56 (2), 127–150. doi:10.1175/1520-0469(1999)056<0127:smoamm>2.0.co;2

Buriez, J. C., Vanbauce, C., Parol, F., Goloub, P., Herman, M., Bonnel, B., et al. (1997). Cloud Detection and Derivation of Cloud Properties from POLDER. *Int. J. Remote Sensing* 18 (13), 2785–2813. doi:10.1080/014311697217332

Burrows, J. P., Weber, M., Buchwitz, M., Rozanov, V., Ladstätter-Weißenmayer, A., Richter, A., et al. (1999). The Global Ozone Monitoring Experiment (GOME): Mission Concept and First Scientific Results. *J. Atmos. Sci.* 56 (2), 151–175. doi:10.1175/1520-0469(1999)056<0151:tgomeg>2.0.co;2

Cahalan, R. F., McGill, M., Kolasinski, J., Várnai, T., and Yetzer, K. (2005). THOR-Cloud Thickness from Offbeam Lidar Returns. *J. Atmos. Oceanic Tech.* 22 (6), 605–627. doi:10.1175/jtech1740.1

Callies, J., Corpaccioli, E., Eisinger, M., Hahne, A., and Lefebvre, A. (2000). GOME-2-Metop's Second-Generation Sensor for Operational Ozone Monitoring. *ESA Bull.* 102, 28–36.

Chapman, R. M. (1962). Cloud Distributions and Altitude Profiles from a Satellite. *Planet. Space Sci.* 9, 70–71. doi:10.1016/0032-0633(62)90074-0

Crisp, D., Miller, C. E., and DeCola, P. L. (2008). NASA Orbiting Carbon Observatory: Measuring the Column Averaged Carbon Dioxide Mole Fraction from Space. *J. Appl. Remote Sens.* 2 (1), 023508. doi:10.1117/1.2898457

Davis, A. B., Cahalan, R. F., Spinehirne, J. D., McGill, M. J., and Love, S. P. (1999a). Off-Beam Lidar: An Emerging Technique in Cloud Remote Sensing Based on Radiative Green-Function Theory in the Diffusion Domain (Erratum). *Phys. Chem. Earth* B24, 757–765. doi:10.1016/S1464-1909(99)00077-5

Davis, A. B., Cahalan, R. F., Spinehirne, D., McGill, M. J., and Love, S. P. (1999b). Off-beam Lidar: An Emerging Technique in Cloud Remote Sensing Based on Radiative Green-Function Theory in the Diffusion Domain. *Phys. Chem. Earth, B: Hydrol. Oceans Atmosphere* 24, 177–185. doi:10.1016/s1464-1909(98)00034-3

Davis, A. B., Ferlay, N., Libois, Q., Marshak, A., Yang, Y., and Min, Q. (2018a). Cloud Information Content in EPIC/DSCOVR's Oxygen A- and B-Band Channels: A Physics-Based Approach. *J. Quantitative Spectrosc. Radiative Transfer* 220, 84–96. doi:10.1016/j.jqsrt.2018.09.006

Davis, A. B., Libois, Q., Ferlay, N., and Marshak, A. (2021). Moments of Sunlight Pathlength in Water and Aerosol Clouds from O_2 Spectroscopy: Exploitable Parameter Sensitivities. *J. Quant. Spectrosc. Rad. Transf.* (in preparation). Available at: https://arxiv.org/abs/2110.07231.

Davis, A. B., Merlin, G., Cornet, C., Labonnote, L. C., Riédi, J., Ferlay, N., et al. (2018b). Cloud Information Content in EPIC/DSCOVR's Oxygen A- and B-Band Channels: An Optimal Estimation Approach. *J. Quantitative Spectrosc. Radiative Transfer* 216, 6–16. doi:10.1016/j.jqsrt.2018.05.007

Davis, A. B. (2008). Multiple-Scattering Lidar from Both Sides of the Clouds: Addressing Internal Structure. *J. Geophys. Res.* 113, D14S10–14S25. doi:10.1029/2007jd009666

Davis, A. B., Polonsky, I. N., and Marshak, A. (2009). "Space-Time Green Functions for Diffusive Radiation Transport, in Application to Active and Passive Cloud Probing," in *Light Scattering Reviews* ed . Editor A. Kokhanovsky (Heidelberg (Germany): Springer-Praxis), 4, 169–292. doi:10.1007/978-3-540-74276-0_5

Deschamps, P.-Y., Bréon, F.-M., Leroy, M., Podaire, A., Bricaud, A., Buriez, J.-C., et al. (1994). The POLDER Mission: Instrument Characteristics and Scientific Objectives. *IEEE Trans. Geosci. Remote Sensing* 32, 598–615. doi:10.1109/36.297978

Dianov-Klokov, V. (1976). Determination of Effective Photon Path Lengths from the Spectral Brightness of Clouds. *Izv. Acad. Sci. Ussr, Atmos. Oceanic Phys.* 12, 221–224.

Dianov-Klokov, V., and Krasnokutskaya, L. (1972). Comparison of Observed and Calculated Effective Photon Path Length in Clouds. *Izv. Acad. Sci. Ussr, Atmos. Oceanic Phys.* 8, 487–492.

Dianov-Klokov, V., Kropotkina, E., Malkov, I., and Matveyeva, O. (1970). Absorption-band Deformation and the Effective Path Length of Light in Clouds. *Izv. Acad. Sci. Ussr, Atmos. Oceanic Phys.* 6, 458–463.

Dianov-Klokov, V., Yevstratov, N., and Ozerenskiy, A. (1977). Calculation of Radiant Energy Density and Equivalent Photon Paths for Certain Cloud Models. *Izv. Acad. Sci. Ussr, Atmos. Oceanic Phys.* 13, 217–221.

Diner, D. J., Boland, S. W., Brauer, M., Bruegge, C., Burke, K. A., Chipman, R., et al. (2018). Advances in Multiangle Satellite Remote Sensing of Speciated Airborne Particulate Matter and Association with Adverse Health Effects: From MISR to MAIA. *J. Appl. Remote Sensing* 12, 042603. doi:10.1117/1.jrs.12.042603

Eldering, A., Taylor, T. E., O'Dell, C. W., and Pavlick, R. (2019). The OCO-3 Mission: Measurement Objectives and Expected Performance Based on 1 Year of Simulated Data. *Atmos. Meas. Tech.* 12, 2341–2370. doi:10.5194/amt-12-2341-2019

Ferlay, N., Thieuleux, F., Cornet, C., Davis, A. B., Dubuisson, P., Ducos, F., et al. (2010). Toward New Inferences about Cloud Structures from Multidirectional Measurements in the Oxygen A Band: Middle-Of-Cloud Pressure and Cloud Geometrical Thickness from POLDER-3/PARASOL. *J. Appl. Meteorol. Climatology* 49, 2492–2507. doi:10.1175/2010jamc2550.1

Fisher, J., Cordes, W., Schmitz-Pfeiffer, A., Renger, W., and Mörl, P. (1991). Detection of Cloud-Top Height from Backscattered Radiances within the Oxygen A Band, 2, Measurements. *J. Appl. Meteorol.* 30, 1245–1259.

Fisher, J., and Grassl, H. (1991). Detection of Cloud-Top Height from Backscattered Radiances within the Oxygen A Band, 1, Theory. *J. Appl. Meteorol.* 30, 1260–1267.

Forster, L., Davis, A. B., Diner, D. J., and Mayer, B. (2021). Toward Cloud Tomography from Space Using MISR and MODIS: Locating the "Veiled Core" in Opaque Convective Clouds. *J. Atmos. Sci.* 78, 155–166. doi:10.1175/jas-d-19-0262.1

Gorodetskiy, A., Malkevich, M., and Syachinov, V. (1971). Determination of Cloud Height from Radiation Measurements from the "Cosmos-320" Artificial Earth Satellite. *Dokl. Akad. Nauk SSSR* 200 (3), 588–590. (Available in Russian at http://mi.mathnet.ru/dan36441.

Grechko, Y., Dianov-Klokov, V., and Malkov, I. (1973). Aircraft Measurements of Photon Paths in Reflection and Transmission of Light by Clouds in the 0.76 μm Oxygen Band. *Izv. Acad. Sci. Ussr, Atmos. Oceanic Phys.* 9, 262–269.

Grechko, Y., Dianov-Klokov, V., Yevstratov, N., and Ozerenskiy, A. (1976). Calculation of Mean and Effective Photon Paths for a Two-Layer Cloud Model with Consideration of Reflection from the Underlying Surface. *Izv. Acad. Sci. Ussr, Atmos. Oceanic Phys.* 12, 20–24.

Grechko, Y., Dvoryashin, S., and Red'ko, A. (1982). Evaluation of Effect of Scattering Indicatrix on the Mean Photon Ranges in Clouds. *Izv. Acad. Sci. Ussr, Atmos. Oceanic Phys.* 18, 854–856.

Grechko, Y. (1978). Measuring the Difference in Effective Paths at Two Wavelenghts in the Presence of Reflection of Light by Clouds. *Izv. Acad. Sci. Ussr, Atmos. Oceanic Phys.* 14, 479–481.

Gusev, I., and Dvoryashin, S. (1990). Recovery of the Effective Photon Path Length in Cloud from its Spectral Brightness. *Izv. Acad. Sci. Ussr, Atmos. Oceanic Phys.* 26, 536–539.

Hanel, R. A. (1961). Determination of Cloud Altitude from a Satellite. *J. Geophys. Res.* 66, 1300. doi:10.1029/jz066i004p01300

Hayazaka, A., Nakajima, T., Fujiyoshi, Y., Ishikaza, Y., Takeda, T., and Tanaka, M. (1995). Geometrical Thickness, Liquid Water Content, and Radiative Properties of Stratocumulus Over the Western North Pacific. *J. Appl. Meteorol.* 34, 460–470.

Heidinger, A. K., and Stephens, G. L. (2000). Molecular Line Absorption in a Scattering Atmosphere. Part II: Application to Remote Sensing in the O2A Band. *J. Atmos. Sci.* 57, 1615–1634. doi:10.1175/1520-0469(2000)057<1615:mlaias>2.0.co;2

Heidinger, A. K., and Stephens, G. L. (2002). Molecular Line Absorption in a Scattering Atmosphere. Part III: Pathlength Characteristics and Effects of Spatially Heterogeneous Clouds. *J. Atmos. Sci.* 59, 1641–1654. doi:10.1175/1520-0469(2002)059<1641:mlaias>2.0.co;2

Henyey, L. C., and Greenstein, J. L. (1941). Diffuse Radiation in the Galaxy. *ApJ* 93, 70–83. doi:10.1086/144246

Irvine, W. (1964). The Formation of Absorption Bands and the Distribution of Photon Optical Paths in a Scattering Atmosphere. *Bull. Astron. Inst. Neth.* 17, 226–279.

Ivanov, V. V., and Sabashvili, S. A. (1972). Transfer of Resonance Radiation and Photon Random Walks. *Astrophys Space Sci.* 17, 13–22. doi:10.1007/bf00642537

Kargin, B., Krasnokutskaya, L., and Feygel'son, Y. M. (1972). Reflection and Absorption of Solar Radiant Energy by Cloud Layers. *Izv. Acad. Sci. Ussr, Atmos. Oceanic Phys.* 8, 287–293.

Katsev, I. (1969). The Study of Some Characteristics of a Transient Field of Light. *Zhurnal Prikladnoi Spektroskopii* 11, 85–91. [in Russian]. doi:10.1007/bf00612535

Katsev, I., and Zege, E. (1974). On the Connection between Nonstationary Radiation fields in Absorbing and Nonabsorbing media. *Astrofizika* 10, 219–225. [in Russian].

Kokhanovsky, A. A., Mayer, B., Rozanov, V. V., Wapler, K., Burrows, J. P., and Schumann, U. (2007). The Influence of Broken Cloudiness on Cloud Top Height Retrievals Using Nadir Observations of Backscattered Solar Radiation in the Oxygen A-Band. *J. Quantitative Spectrosc. Radiative Transfer* 103, 460–477. doi:10.1016/j.jqsrt.2006.06.003

Kokhanovsky, A. A., Rozanov, V. V., Burrows, J. P., Eichmann, K.-U., Lotz, W., and Vountas, M. (2005). The SCIAMACHY Cloud Products: Algorithms and Examples from ENVISAT. *Adv. Space Res.* 36, 789–799. doi:10.1016/j.asr.2005.03.026

Kokhanovsky, A. A., and Rozanov, V. V. (2004). The Physical Parameterization of the Top-Of-Atmosphere Reflection Function for a Cloudy Atmosphere-Underlying Surface System: the Oxygen A-Band Case Study. *J. Quantitative Spectrosc. Radiative Transfer* 85, 35–55. doi:10.1016/s0022-4073(03)00193-6

Kokhanovsky, A. A., Rozanov, V. V., von Hoyningen-Huene, W., Bovensmann, H., Burrows, J. P., and Baltink, H. K. (2004). The Determination of Cloud Altitudes Using SCIAMACHY Onboard ENVISAT. *IEEE Geosci. Remote Sensing Lett.* 1, 211–214. doi:10.1109/lgrs.2004.830123

Kuze, A., and Chance, K. (1994). Analysis of Cloud Top Height and Cloud Coverage from the O_2 A and B Bands. *J. Geophys. Res.* 99 (14), 481–491. doi:10.1029/94jd01152

Levis, A., Davis, A. B., Loveridge, J. R., and Schechner, Y. Y. (2021). "3d Cloud Tomography and Droplet Size Retrieval from Multi-Angle Polarimetric Imaging of Scattered Sunlight from above," in *Polarization Science and Remote Sensing X* (Bellingham, WA: International Society for Optics and Photonics), 11833–05. doi:10.1117/12.2593369

Levis, A., Schechner, Y. Y., Aides, A., and Davis, A. B. (2015). "Airborne Three-Dimensional Cloud Tomography," in *Proceedings of the IEEE International Conference on Computer Vision*, *(Cambridge, MA, USA*, *20-23 June 1995)*, 3379–3387. doi:10.1109/iccv.2015.386

Levis, A., Schechner, Y. Y., Davis, A. B., and Loveridge, J. (2020). Multi-View Polarimetric Scattering Cloud Tomography and Retrieval of Droplet Size. *Remote Sensing* 12, 2831. doi:10.3390/rs12172831

Levis, A., Schechner, Y. Y., and Davis, A. B. (2017). "Multiple-Scattering Microphysics Tomography," in *Proceedings of the IEEE Conference on Computer Vision and Pattern Recognition*, *(San Juan, PR, USA*, *17-19 June 1997)*, 6740–6749. doi:10.1109/cvpr.2017.614

Malkevich, M., Chagar, L., and Shukurov, A. (1975). Corrections for Scattering of Radiation in Clouds in Photometric Cloud-Height Determination. *Izv. Acad. Sci. Ussr, Atmos. Oceanic Phys.* 11, 561–564.

Malkevich, M. (1974). "*Optical Investigations of the Atmosphere Using Artificial Satellites*. NASA Technical Translation NASA TT F-15186, National Aeronautics and Space Administration, Washington, D.C," in *Translation of "Opticheskiye Issledovaniya Atmosfery So Sputnikov,"* (Moscow: Nauka Press) 1973, 303 pp.

Manolis, I., Grabarnik, S., Caron, J., Bézy, J.-L., Loiselet, M., Betto, M., et al. (2013). "The MetOp Second Generation 3MI Instrument," in *Sensors, Systems, and Next-Generation Satellites XVII* (Bellingham, WA: International Society for Optics and Photonics), 88890J. doi:10.1117/12.2028662

Marshak, A., Herman, J., Adam, S., Karin, B., Carn, S., Cede, A., et al. (2018). Earth Observations from DSCOVR EPIC Instrument. *Bull. Am. Meteorol. Soc.* 99, 1829–1850. doi:10.1175/bams-d-17-0223.1

Meister, G., Knuble, J. J., Cook, W. B., Gorman, E. T., and Werdell, P. J. (2019). "Calibration Plan for the Ocean Color Instrument (Oci) Engineering Test Unit," in *Sensors, Systems, and Next-Generation Satellites XXIII* (Bellingham, WA: International Society for Optics and Photonics), 11151, 111511W. doi:10.1117/12.2550820

Nagirner, D. (1974). Theory of Nonstationary Transfer of Radiation. *Astrofizika (Engl. Transl.: Astrophysics)* 10, 274–289.

Nakajima, T., and King, M. D. (1990). Determination of the Optical Thickness and Effective Particle Radius of Clouds from Reflected Solar Radiation Measurements. Part I: Theory. *J. Atmos. Sci.* 47, 1878–1893. doi:10.1175/1520-0469(1990)047<1878:dotota>2.0.co;2

National Academies of Sciences, Engineering, and Medicine (2018). *Thriving on Our Changing Planet, A Decadal Strategy for Earth Observation from Space*. Washington (DC): The National Academies Press.

Nieke, J., Borde, F., Mavrocordatos, C., Berruti, B., Delclaud, Y., Riti, J. B., et al. (2012). "The Ocean and Land Colour Imager (OLCI) for the Sentinel 3 GMES Mission: Status and First Test Results," in *Earth Observing Missions and Sensors: Development, Implementation, and Characterization II* (Bellingham, WA: International Society for Optics and Photonics), 8528, 85280C. doi:10.1117/12.977247

O'Brien, D., Mitchell, R., English, S., and Da Costa, G. (1999). Airborne Measurements of Air Mass from O_2 A-Band Absorption Spectra. *J. Atmos. Oceanic Tech.* 15, 1272–1286.

O'Brien, D., and Mitchell, R. (1992). Error Estimates for the Retrieval of Cloud Top Pressure Using Absorption in the A-Band of Oxygen. *J. Appl. Meteorol.* 31, 1179–1192.

Partain, P. T., Heidinger, A. K., and Stephens, G. L. (2000). High Spectral Resolution Atmospheric Radiative Transfer: Application of the Equivalence Theorem. *J. Geophys. Res.* 105, 2163–2177. doi:10.1029/1999jd900328

Polonsky, I. N., Love, S. P., and Davis, A. B. (2005). Wide-angle Imaging Lidar Deployment at the Arm Southern Great plains Site: Intercomparison of Cloud Property Retrievals. *J. Atmos. Oceanic Tech.* 22, 628–648. doi:10.1175/jtech1741.1

Preusker, R., Fischer, J., Albert, P., Bennartz, R., and Schüller, L. (2007). Cloud-Top Pressure Retrieval Using the Oxygen A-Band in the IRS-3 MOS Instrument. *Int. J. Remote Sensing* 28, 1957–1967. doi:10.1080/01431160600641632

Rast, M., Bezy, J. L., and Bruzzi, S. (1999). The ESA Medium Resolution Imaging Spectrometer MERIS a Review of the Instrument and its mission. *Int. J. Remote Sensing* 20, 1681–1702. doi:10.1080/014311699212416

Richardson, M., Lebsock, M. D., McDuffie, J., and Stephens, G. L. (2020). A New Orbiting Carbon Observatory 2 Cloud Flagging Method and Rapid Retrieval of marine Boundary Layer Cloud Properties. *Atmos. Meas. Tech.* 13, 4947–4961. doi:10.5194/amt-13-4947-2020

Richardson, M., Leinonen, J., Cronk, H. Q., McDuffie, J., Lebsock, M. D., and Stephens, G. L. (2019). Marine Liquid Cloud Geometric Thickness Retrieved from OCO-2's Oxygen A-Band Spectrometer. *Atmos. Meas. Techn* . 12, 1717–1737. doi:10.5194/amt-12-1717-2019

Richardson, M., McDuffie, J., Stephens, G. L., Cronk, H. Q., and Taylor, T. E. (2017). The OCO-2 Oxygen A-Band Response to Liquid marine Cloud Properties from CALIPSO and MODIS. *J. Geophys. Res. Atmos.* 122, 8255–8275. doi:10.1002/2017jd026561

Richardson, M., and Stephens, G. L. (2018). Information Content of OCO-2 Oxygen A-Band Channels for Retrieving marine Liquid Cloud Properties. *Atmos. Meas. Tech.* 11, 1515–1528. doi:10.5194/amt-11-1515-2018

Riedl, S., Harlander, M., Schlosser, C., Kolm, M., Maurer, R., Courrèges-Lacoste, G. B., et al. (2019). "Sentinel 4 UVN, a Geostationary Imaging UVN Spectrometer for Air Quality Monitoring: Performance, Measurement Modes and Model Philosophy," in *International Conference on Space Optics—ICSO 2018*, *Chania, Greece* (Bellingham, WA: International Society for Optics and Photonics) 11180–11205. doi:10.1117/12.2535924

Rietjens, J., Campo, J., Chanumolu, A., Smit, M., Nalla, R., Fernandez, C., et al. (2019). "Expected Performance and Error Analysis for SPEXone, a Multi-Angle Channeled Spectropolarimeter for the NASA PACE mission," in *Polarization Science and Remote Sensing IX* (International Society for Optics and Photonics), 11132–08. doi:10.1117/12.2530729

Rodgers, C. D. (2000). *Inverse Methods for Atmospheric Sounding: Theory and Practice*. Singapore: World Scientific.

Romanova, L., and Ustinov, Y. (1982). The Generalized Transfer Equation for the Distribution of Photon Paths and the Problem of Vertically Inhomogeneous Gas Absorption in the Atmosphere. *Izv. Acad. Sci. Ussr, Atmos. Oceanic Phys.* 18, 186–192.

Rozanov, V., and Kokhanovsky, A. (2004). Semi-analytical Cloud Retrieval Algorithm as Applied to the Cloud Top Altitude and the Cloud Geometrical Thickness Determination from Top-Of-Atmosphere Reflectance Measurements in the Oxygen A-Band. *J. Geophys. Res.* D109, 5202. doi:10.1029/2003jd004104

Saiedy, F., Hilleary, D. T., and Morgan, W. A. (1965). Cloud-Top Altitude Measurements from Satellites. *Appl. Opt.* 4, 495–500. doi:10.1364/ao.4.000495

Saiedy, F., Jacobowitz, H., and Wark, D. Q. (1967). On Cloud-Top Determination from Gemini-5. *J. Atmos. Sci.* 24, 63–69. doi:10.1175/1520-0469(1967)024<0063:octdfg>2.0.co;2

Skorinov, V., and Titov, G. (1984). Mean Photon Path Lengths for Broken Clouds. *Izv. Acad. Sci. Ussr, Atmos. Oceanic Phys.* 20, 377–381.

Stephens, G. L., and Heidinger, A. (2000). Molecular Line Absorption in a Scattering Atmosphere. Part I: Theory. *J. Atmos. Sci.* 57, 1599–1614. doi:10.1175/1520-0469(2000)057<1599:mlaias>2.0.co;2

Syachinov, V., and Kozlov, Y. (1974). Determination of Cloud-Top Altitude from the Cosmos-320 Satellite. *Izv. Acad. Sci. Ussr, Atmos. Oceanic Phys.* 10, 582–586.

Thyagarajan, K., Neumann, A., and Zimmermann, G. (1996). The IRS-P3 Remote Sensing Mission. *Acta Astronautica* 39, 711–716. doi:10.1016/s0094-5765(97)00053-2

Valero, F. P. J., Marshak, A., and Minnis, P. (2021). Lagrange Point Missions: The Key to Next Generation Integrated Earth Observations. DSCOVR Innovation. *Front. Remote Sens.* 2. doi:10.3389/frsen.2021.745938

Vanbauce, C., Buriez, J. C., Parol, F., Bonnel, B., Sèze, G., and Couvert, P. (1998). Apparent Pressure Derived from ADEOS-POLDER Observations in the Oxygen A-Band over Ocean. *Geophys. Res. Lett.* 25, 3159–3162. doi:10.1029/98gl02324

Veefkind, J. P., Aben, I., McMullan, K., Förster, H., De Vries, J., Otter, G., et al. (2012). TROPOMI on the ESA Sentinel-5 Precursor: A GMES Mission for Global Observations of the Atmospheric Composition for Climate, Air Quality and Ozone Layer Applications. *Remote Sensing Environ.* 120, 70–83. doi:10.1016/j.rse.2011.09.027

Wang, M. (1999). Validation Study of the SeaWiFS Oxygen A-Band Absorption Correction: Comparing the Retrieved Cloud Optical Thicknesses from SeaWiFS Measurements. *Appl. Opt.* 38, 937–944. doi:10.1364/ao.38.000937

Werdell, P. J., Behrenfeld, M. J., Bontempi, P. S., Boss, E., Cairns, B., Davis, G. T., et al. (2019). The Plankton, Aerosol, Cloud, Ocean Ecosystem mission: Status, Science, Advances. *Bull. Am. Meteorol. Soc.* 100, 1775–1794. doi:10.1175/bams-d-18-0056.1

Wu, M.-L. C. (1985). Remote Sensing of Cloud-Top Pressure Using Reflected Solar Radiation in the Oxygen A-Band. *J. Clim. Appl. Meteorol.* 24, 539–546. doi:10.1175/1520-0450(1985)024<0539:rsoctp>2.0.co;2

Yamamoto, G., and Wark, D. Q. (1961). Discussion of the Letter by R. A. Hanel, “Determination of Cloud Altitude from a Satellite”. *J. Geophys. Res.* 66, 3596. doi:10.1029/jz066i010p03596

Yang, Y., Marshak, A., Mao, J., Lyapustin, A., and Herman, J. (2013). A Method of Retrieving Cloud Top Height and Cloud Geometrical Thickness with Oxygen A and B Bands for the Deep Space Climate Observatory (DSCOVR) Mission: Radiative Transfer Simulations. *J. Quantitative Spectrosc. Radiative Transfer* 122, 141–149. doi:10.1016/j.jqsrt.2012.09.017

Yang, Y., Meyer, K., Wind, G., Zhou, Y., Marshak, A., Platnick, S., et al. (2019). Cloud Products from the Earth Polychromatic Imaging Camera (EPIC): Algorithms and Initial Evaluation. *Atmos. Meas. Tech.* 12, 2019–2031. doi:10.5194/amt-12-2019-2019

Conflict of Interest: The authors declare that the research was conducted in the absence of any commercial or financial relationships that could be construed as a potential conflict of interest.

ORIGINAL RESEARCH
published: 12 April 2022
doi: 10.3389/frsen.2022.833340

The NASA EPIC/DSCOVR Ocean PAR Product

Robert Frouin[1*], Jing Tan[1], Mathieu Compiègne[2], Didier Ramon[2], Marshall Sutton[3], Hiroshi Murakami[4], David Antoine[5,6], Uwe Send[1], Jeff Sevadjian[1] and Vincenzo Vellucci[6]

[1] *Scripps Institution of Oceanography, University of California San Diego, La Jolla, CA, United States*
[2] *HYGEOS, Euratechnologies, Lille, France*
[3] *NASA Goddard Space Flight Center, Greenbelt, MD, United States*
[4] *Earth Observation Research Center, Japan Aerospace Exploration Agency, Ibaraki, Japan*
[5] *Remote Sensing and Satellite Research Group, School of Earth and Planetary Sciences, Curtin University, Perth, WA, Australia*
[6] *Laboratoire d'Océanographie de Villefranche, CNRS, Sorbonne Université, Institut de la Mer de Villefranche, Villefranche-sur-Mer, France*

Edited by:
Gregory Schuster, National Aeronautics and Space Administration (NASA), United States

Reviewed by:
Chuanfeng Zhao, Beijing Normal University, China
Tamas Varnai, University of Maryland, Baltimore County, United States

**** Correspondence:*** *Robert Frouin, rfrouin@ucsd.edu*

Specialty section: *This article was submitted to Satellite Missions, a section of the journal Frontiers in Remote Sensing*

Received: *11 December 2021*
Accepted: *02 March 2022*
Published: *12 April 2022*

Citation: *Frouin R, Tan J, Compiègne M, Ramon D, Sutton M, Murakami H, Antoine D, Send U, Sevadjian J and Vellucci V (2022) The NASA EPIC/DSCOVR Ocean PAR Product. Front.*

Remote Sens. 3:833340. doi: 10.3389/frsen.2022.833340

The EPIC/DSCOVR observations of the Earth's surface lit by the Sun made from the first Lagrange point several times during the day in spectral bands centered on 443, 551, and 680 nm are used to estimate daily mean photosynthetically available radiation (PAR) at the ice-free ocean surface. The PAR algorithm uses a budget approach, in which the solar irradiance reaching the surface is obtained by subtracting from the irradiance arriving at the top of the atmosphere (known), the irradiance reflected to space (estimated from the EPIC Level 1b radiance data), taking account of atmospheric transmission and surface albedo (modeled). Clear and cloudy regions within a pixel do not need to be distinguished, which dismisses the need for often-arbitrary assumptions about cloudiness distribution within a pixel and is therefore adapted to the relatively large EPIC pixels. A daily mean PAR is estimated on the source grid for each EPIC instantaneous daytime observation, assuming no cloudiness changes during the day, and the individual estimates are remapped and weight-averaged using the cosine of the Sun zenith angle. In the computations, wind speed, surface pressure, and water vapor amount are extracted from NCEP Reanalysis 2 data, aerosol optical thickness and Angström coefficient from MERRA-2 data, and ozone amount from EPIC Level 2 data. Areas contaminated by Sun glint are excluded using a threshold on Sun glint reflectance calculated using wind data. Ice masking is based on NSIDC near-real-time ice fraction data. The product is evaluated against *in situ* measurements at various locations and compared with estimates from sensors in polar and geostationary orbits (MODIS, AHI). Unlike with MODIS, the EPIC PAR product does not exhibit gaps at low and middle latitudes. Accuracy is satisfactory for long-term studies of aquatic photosynthesis, especially given the much larger uncertainties on the fraction of PAR absorbed by live algae and the quantum yield of carbon fixation. The EPIC daily mean PAR product is generated operationally on a Plate Carrée (equal-angle) grid with 18.4 km resolution at the equator and on an 18.4 km equal-area grid, i.e., it is fully compatible with the NASA Greenbelt OBPG ocean-color products. Data are available since the beginning of the DSCOVR mission (i.e., June 2015) from the NASA Langley ASDC website.

Keywords: photosynthetically available radiation, satellite remote sensing, Lagrange L1 orbit, EPIC sensor, DSCOVR mission, light

absorption and scattering, ocean biogeochemistry

1 INTRODUCTION

The solar energy flux reaching the ocean surface in the spectral range 400–700 nm, referred to as photosynthetically available (or active) solar radiation (PAR), controls the rate of photosynthesis by phytoplankton and therefore the development of crustaceans, fish, and other consumers (e.g., Ryther, 1956; Platt et al., 1977; Kirk, 1994; Falkowski and Raven, 1997). It ultimately regulates the composition of marine ecosystems. Sunlight absorbed differentially by the upper ocean affects mixed-layer dynamics and oceanic currents (e.g., Nakamoto et al., 2000, 2001; Murtugudde et al., 2002; Sweeney et al., 2005; Ballabrera-Poy et al., 2007), with local and remote consequences on atmospheric temperature and circulation (e.g., Miller et al., 2003; Shell et al., 2003). Absorption by phytoplankton and other water constituents tend to reduce the planetary albedo, i.e., warm the planet (Frouin and Iacobellis, 2002). Knowing the spatiotemporal distribution of PAR over the oceans is critical to understanding biogeochemical cycles of carbon, nutrients, and oxygen and biological-physical interactions (a major uncertainty in coupled climate models) and, therefore, to addressing important global change issues such as the fate of anthropogenic atmospheric carbon dioxide and making accurate projections of future climate (e.g., Frouin et al., 2018a).

Regional and global maps of PAR at the ocean surface can be obtained from a variety of passive Earth-viewing satellite optical sensors. The sensors operating from geostationary altitude provide adequate temporal sampling to deal with cloud diurnal variability but have degraded spatial resolution at high latitudes, and they only cover part of the oceans, i.e., several sensors, optimally positioned are necessary to provide global coverage. Sensors in polar orbits provide the same spatial resolution at all latitudes but pass less frequently over the same target at middle and low latitudes. For ocean primary productivity computations, it is convenient to estimate both PAR and bio-optical variables (phytoplankton chlorophyll abundance, absorption coefficients) from the same sensor. Ocean-color sensors offer this capability, even though they are principally designed to retrieve water reflectance if they do not saturate over clouds. The same data preprocessing is required, i.e., PAR can be produced with little extra effort as part of the same processing line. In this way, the key variables in primary production modeling are

provided together at the same resolution, facilitating studies of photosynthesis and ecosystem dynamics.

In this context, a simple yet efficient and fairly accurate algorithm has been developed to estimate the daily mean PAR at the ocean surface from Sea-viewing Wide Field-of-view Sensor (SeaWiFS) data (Frouin et al., 2003) and adapted for application to MODerate resolution Imaging Spectroradiometer (MODIS) data (Frouin et al., 2012), GLobal Imager (GLI) data (Frouin and Murakami, 2007), GOCI data (Frouin and McPherson, 2013; Kim et al., 2016), Medium Resolution Imaging Spectrometer (MERIS) data, Visible Infrared Imaging Radiometer Suite (VIIRS) data, Second-generation Global Imager (SGLI) data, and Advanced Hiwamari Imager (AHI) data with plans for an extension to future ocean color sensors. Daily mean PAR refers to the 24-h averaged planar quantum energy flux from the Sun in the spectral range 400–700 nm. It is expressed in units of Einstein per meter squared per day, i.e., $Em^{-2}d^{-1}$. The global daily mean PAR products from SeaWiFS, MODIS, VIIRS, and MERIS data have been routinely generated by the National Aeronautics and Space Administration (NASA) Ocean Biology Processing Group (OBPG) and made available to the user community from their website (https://oceancolor.gsfc.nasa.gov). Estimated uncertainty, based on comparisons against *in situ* measurements, expressed in relative root-mean-square (RMS) difference and bias, is typically 10-30% and 4-9%, respectively, depending on satellite sensor and atmospheric conditions (Frouin et al., 2003; Frouin et al., 2012; Laliberté et al., 2016; Ramon et al., 2016; Somayajula et al., 2018). Somayajula et al. (2018) compared satellite-based PAR algorithms used in primary production studies; they concluded that the best overall performance was obtained with the NASA OBPG algorithm. This uncertainty is reasonable for large-scale studies of aquatic photosynthesis (e.g., Frouin et al., 2012; Frouin et al., 2018a), but better accuracy is desirable. Note, in this respect, that primary productivity models depend not only on PAR but also on efficiency factors that are difficult to estimate with uncertainty comparable to (i.e., as low as) that of PAR.

The standard Level-2 and -3 PAR products generated by the NASA OBPG have been used extensively in the science community for a variety of applications. In primary productivity calculations, they have replaced PAR estimates obtained from a clear sky model corrected for cloudiness using fractional cloud coverage or deduced from satellite estimates of total solar

irradiance, the treatment applied in Longhurst et al. (1995), Antoine et al. (1996), and Behrenfeld and Falkowski (1997) to obtain the first global maps of seasonal and/or annual oceanic primary productivity from space. Such treatment is limited, because the effect of clouds on PAR does not depend only on fractional coverage, but also on optical thickness, and the relation between total solar irradiance and PAR, rather constant under clear skies (Baker and Frouin, 1987), varies strongly with water vapor and cloud liquid water content (Frouin and Pinker, 1995). Studies using the NASA OBPG PAR products have addressed a variety of topics, including biosphere productivity during an El Niño transition (Behrenfeld et al., 2001), chlorophyll-a and carbon-based ocean productivity modeling (Behrenfeld et al., 2005; Platt et al., 2008), climate-driven trends in productivity (Behrenfeld et al., 2006; Kahru et al., 2009; Henson et al., 2010), phytoplankton class-specific productivity (Uitz et al., 2010), inter-comparison of productivity algorithms (Carr et al., 2006; Lee et al., 2015), and the relation between primary productivity, vertical mixing, and atmospheric input (Tang and Shi, 2012). They have also been used to check the stability of CERES measurements (Loeb et al., 2006).

The parameters governing PAR variability are essentially the Sun zenith angle and the cloud transmittance. Aerosol properties and surface albedo have a smaller impact. Since the Sun zenith angle can be computed precisely, estimating daily PAR from data collected by a single sensor aboard a Sun-synchronous satellite is chiefly limited, in terms of accuracy, by the lack of information about diurnal variability of cloud properties, especially at low and middle latitudes. This variability may be large in some regions, as evidenced by the International Cloud Climatology Project (ISCCP) cloud analyses (Bergman and Salby, 1996; Rossow and Shiffer, 1999) and other studies (e.g., Wang and Zhao, 2017; Zhao et al., 2019; Yang et al., 2020). Consequently, the PAR products from individual polar-orbiting sensors exhibit biases, not only with respect to ground truth but also between themselves, as evidenced in inter-comparison and evaluation studies (Frouin et al., 2003, 2012; Tan and Frouin, 2019). Merging data from several sensors with different overpass times may significantly improve the quality of daily PAR estimates, as demonstrated with MODIS-Terra, SeaWiFS, and MODIS-Aqua, which cross the equator at approximately 10:30, 12:00, and 13:30 local time (Frouin et al., 2012). In generating a long-term PAR time series, however, one must deal with various sensor combinations, and there is a need, for ocean biogeochemistry studies related to climate change to reduce

the individual biases against *in situ* measurements and make the PAR estimates consistent across individual sensors (Frouin et al., 2018a).

The Earth Polychromatic Imaging Camera (EPIC) onboard DSCOVR, operating from the first Sun-Earth Lagrange point (L1) one million miles from Earth (Marshak et al., 2018; https://avdc.gsfc.nasa.gov/pub/DSCOVR/Web_EPIC/), provides a great opportunity to generate accurate PAR products and address issues associated with polar-orbiting sensors. By frequently observing the sunlit part of the Earth, EPIC inherently allows one to account properly for diurnal cloud variability, while maximizing spatial coverage. In other words, EPIC with respect to PAR can do the job of several geostationary sensors with the further advantage that spatial resolution at high latitudes is less of an issue (the L1 orbit is much farther from Earth than the geostationary orbit). The spectral bands centered on 443, 551, and 680 nm, the non-saturation of measured radiance over clouds, and the spatial resolution of 10 km at nadir are adequate for PAR calculations, especially using the NASA OBPG algorithm, which does not require knowing whether the pixel is clear or cloudy, i.e., is applicable to large pixels.

In view of the above, the current NASA OBPG daily mean PAR algorithm has been modified/adapted for application to EPIC data. Algorithm uncertainties have been associated with EPIC PAR estimates on a pixel-by-pixel basis. A full processing line has been created and implemented to generate operationally daily mean EPIC PAR products at the NASA Center for Climate Simulation (NCCS). The data are archived at and distributed by the Langley Atmospheric Science Data Center (ASDC). In Section 2, the methodology to estimate daily mean PAR from EPIC data is presented and the various steps to obtain the surface flux values are detailed. The tasks include integrating atmospheric functions spectrally and temporally during the day (the number of observations in a day varies depending on geographic location), eliminating data contaminated by Sun glint, incorporating ancillary information such as ozone content, sea ice extent (for masking), and aerosol optical properties, and remapping the data to a common grid. In Section 3, a procedure is described to associate algorithm uncertainties (i.e., bias and standard deviation) to each EPIC daily mean PAR estimate as a function of parameters readily available from applying the algorithm, i.e., daily mean clear sky PAR and cloud factor (characterizes the effect of clouds on daily mean PAR). In Section 4, EPIC PAR estimates are compared to *in situ*

measurements routinely collected from long-term fixed buoys. Experimental performance is also compared to that of MODIS PAR estimates. In Section 5, examples of global daily mean PAR products are displayed and examined in view of corresponding MODIS and AHI products, and PAR time series at contrasted locations are presented to illustrate the capability of EPIC to describe PAR seasonal to interannual variability. In Section 6, finally, the EPIC PAR algorithm and its performance against field data and other satellite estimates are summarized, advantages and limitations of using observations from the L1 orbit are pointed out, the significance of the new ocean PAR product in complementing existing PAR time series for a wide range of research applications is emphasized, and a perspective for future work to estimate variables used more directly in primary productivity or water reflectance models, such as scalar PAR, spectral PAR, and average cosine of the light field just below the surface, as well as ultraviolet fluxes, is provided.

2 ALGORITHM DESCRIPTION

The algorithm estimates daily mean PAR reaching the ice-free ocean surface, as defined above. Following Frouin et al. (2003), a budget approach is used, in which the solar flux reaching the surface is obtained by subtracting from the flux arriving at the top of the atmosphere (know) the flux reflected to space (estimated from the EPIC measurements) accounting for atmospheric transmission and surface albedo (modeled). Clear and cloudy regions within a pixel do not need to be distinguished, which is appropriate to the relatively large (i.e., 10 km at nadir) EPIC pixels. This approach was shown to be valid by Dedieu et al. (1987) and Frouin and Chertock (1992).

Based on the previous work, the PAR model assumes that the effects of clouds and other atmospheric constituents are decoupled. The planetary atmosphere is therefore modeled as a clear sky layer that contains molecules and aerosols positioned above a cloud/surface layer, and surface PAR is expressed as the product of a clear-sky component and a transmittance that accounts for cloudiness and surface optical effects. Under solar incidence (zenith angle) θ_s, the incoming spectral solar flux at the top of the atmosphere, $E_{TOA}cos(\theta_s)$, is reduced by a factor $T_a(\theta_s)T_g(\theta_s)[1 - S_aA(\theta_s)]^{-1}$ by the time it enters the cloud/surface system, where T_a is the clear-sky transmittance (due to scattering by molecules and aerosols), T_g is the gaseous transmittance (essentially due to absorption by ozone), S_a is the spherical

albedo of the clear atmosphere, and A is the cloud/surface system albedo. As the transmitted flux, $E_{TOA}cos(\theta_s)T_a(\theta_s)T_g(\theta_s)[1-S_aA(\theta_s)]^{-1}$, passes through the cloud/surface system, it is further reduced by a factor 1—A. The instantaneous planar flux reaching the ocean surface at any wavelength in the PAR spectral range, E, is then given by:

$$E(\theta_s) = E_0(\theta_s)[1-A(\theta_s)][1-A_s(\theta_s)]^{-1}[1-S_aA(\theta_s)]^{-1}, \quad (1)$$

where A_s is the albedo of the ocean (surface and water body) and $E_0(\theta_s) = E_{TOA}cos(\theta_s)T_a(\theta_s)T_g(\theta_s)$ is the solar flux that would reach the surface if the cloud layer and the surface were non-reflecting. In clear sky conditions, A reduces to A_s and E to $E_{clear} = E_0(1-S_aA_s)^{-1}$. The term $[1-S_aA(\theta_s)]^{-1}$ in Eq. 1 represents interactions between the cloud/surface layer and the clear atmosphere.

To compute E, A is expressed as a function of the radiance measured by EPIC in bands centered on 443, 551, and 680 nm, and this for each observation collected during the day (i.e., between sunrise and sunset). These bands do not saturate over clouds, and they sample sufficiently the PAR spectral range. In this range, the scattering properties of molecules and aerosols vary smoothly with wavelength, gaseous absorption is relatively weak, and A is quite constant spectrally. The algorithm works on a pixel-by-pixel basis, i.e., a daily mean PAR estimate is obtained for each pixel of the satellite imagery. The various processing steps and procedures are detailed in the following.

First the bidirectional reflectance of the cloud/surface layer, ρ, is determined from the instantaneous EPIC Level 1b reflectance data at source resolution. This is only accomplished for pixels that are not contaminated by sea ice or Sun glint. For sea ice masking, fractional ice coverage at 25 km resolution from the National Snow and Ice Data Center (NSIDC) is used. If the fractional coverage is greater than 0.1, then the pixel is discarded. For Sun glint masking, the Fresnel signal at the wavy interface surface is calculated from the wind speed according to Cox and Munk (1954), and all pixels with a glint reflectance above 0.05 at 780 nm are eliminated. National Centers for Environmental Prediction (NCEP) Reanalysis-2 wind data at 1° and 6-h resolution is used after interpolation to the EPIC observation time. Both ancillary data sets are remapped to the source grid prior to masking. Since in the modeling the clear atmosphere is located above the

cloud/surface layer, ρ is obtained from the top-of-atmosphere (TOA) reflectance, ρ_{TOA} by inverting the following equation (Tanré et al., 1979):

$$\rho_{TOA}(\theta_s, \theta_v, \phi) = T_g(\theta_s, \theta_v)\left[\rho_a(\theta_s, \theta_v, \phi) + \rho T_a(\theta_s, \theta_v)(1 - S_a\rho)^{-1}\right], \quad (2)$$

where ρ_a is atmospheric reflectance and θ_v and ϕ are view zenith and relative azimuth angles, respectively. In Eq. 2 T_g and T_a are transmittances along the Sun-to-surface and surface-to-sensor path. This expression is strictly valid for an isotropic target of reflectance ρ, which is not the case for the cloud/surface layer, but a good approximation for many geometries, except when θ_s is large and clouds are optically thin, i.e., when the albedo of that layer, A, is relatively close to ρ (Zege, et al., 1991). At large θ_s, however, E becomes small since modulated directly by $cos(\theta_s)$, and when clouds are thin their impact on $(1 - A)$ in Eq. 1 is also small, which tends to minimize effects on daily mean surface fluxes. A better treatment would be to use the following equation (Tanré et al., 1979; Deschamps et al., 1983):

$$\rho_{TOA}(\theta_s, \theta_v, \phi) = T_g(\theta_s, \theta_v)\{\rho_a + [\rho(\theta_s, \theta_v, \phi) - A(\theta_s)]e^{-\tau_a m} + A(\theta_s)T_a(\theta_s, \theta_v)[1 - S_a A(\theta_s)]^{-1}\}, \quad (3)$$

where τ_a is the optical thickness of the clear atmosphere and m is airmass, i.e., $m = 1/\cos(\theta_s) + 1/\cos(\theta_v)$. Eq. 3 reduces to Eq. 2 when ρ is isotropic. The retrieval of ρ would be accomplished through iteration. This would require a first estimate of A, which can be obtained as described below for isotropic ρ.

To compute the atmospheric functions T_g, T_a, and ρ_a, the surface pressure and water vapor amount are extracted from NCEP Reanalysis 2 data, aerosol optical thickness at 550 nm, Angström coefficient, and single scattering albedo at 550 nm from MERRA-2 data at 0.625° × 0.5° (Gelaro et al., 2017), and ozone amount from EPIC Level 2 data at source resolution (Herman et al., 2018). Single scattering albedo is assumed constant over the PAR spectral range. For ρ_a, the quasi-single scattering approximation (Q-SSA) used in Frouin et al. (2003), which gives too high values at large zenith angles, is replaced by a parameterization that combines Q-SSA and exact single-scattering approximation (SSA):

$$\rho_a = f_{SSA}(m, \tau_{aer})\rho_a(SSA) + f_{Q\text{-}SSA}(m, \tau_{aer})\rho_a(Q\text{-}SSA), \quad (4)$$

where f_{SSA} and f_{Q-SSA} depend on m and aerosol optical thickness, τ_{aer}, but are independent of the aerosol model. These functions were obtained from

the simulations with the 6S code (Kotchenova et al., 2006, 2007) for atmospheres containing various mixtures of maritime and continental aerosols and angular geometries. Figure 1 displays ρ_a at 443, 551, and 680 nm as a function of θ_v for θ_s = 70°. Scattering angle, quasi constant with EPIC, is fixed at 171.5°. The aerosols are of maritime type and τ_{aer} at 550 nm is 0.2 and 0.4 (top and bottom panels, respectively). The parameterization works well yielding ρ_a values very close to the 6S values except in the blue, where τ_{aer} is large (0.4) and the molecular scattering is effective. At 443 nm the coupling between aerosol and molecule scattering is relatively important and the 6S ρ_a is substantially smaller than ρ_a (Q–SSA), even at θ_v < 65°, which is partly explained by the fact that in Q-SSA the molecule and aerosol contributions to atmospheric reflectance correspond to the atmosphere containing only molecules or aerosols, i.e., the neglected aerosol-coupling term is negative (Deschamps et al., 1983). The 6S and SSA values are quite similar at that wavelength, a consequence of the SSA formulation that also assumes either molecules or aerosols, i.e., the probability of encountering one type of scatterer is enhanced (SSA values are expected to be lower in the presence of both molecules and aerosols). As wavelength increases, this effect is less prominent because the atmosphere is less thick optically contributing to larger differences between 6S and SSA values.

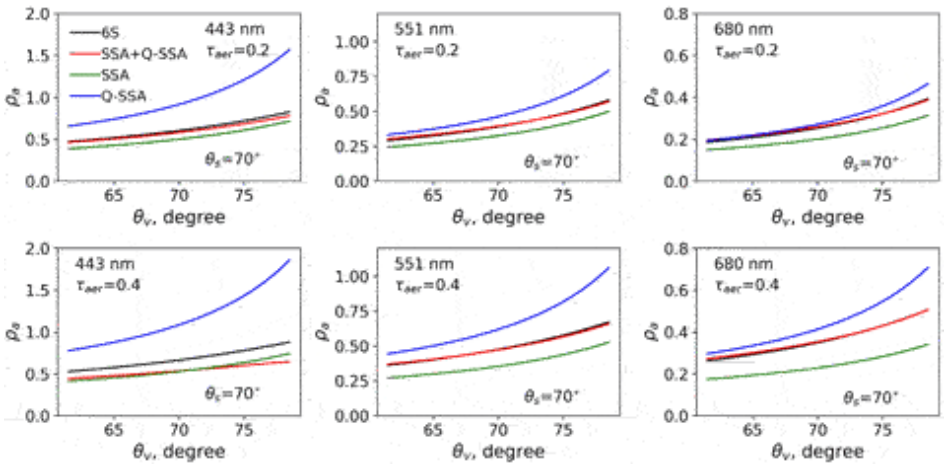

FIGURE 1 | Atmospheric reflectance ρ_a parameterization using SSA, Q-SSA, and a combination of SSA and Q-SSA (green, blue, and black dots, respectively). 6S calculations (RT) are displayed as red curves. Sun zenith angle is 70 deg., scattering angle is 171.5 deg., aerosols are of maritime type with optical thickness of 0.2 and 0.4 at 550 nm, and wavelengths are 388, 551, and 680 nm.

Once the reflectance of the cloud/surface layer, ρ, is determined, it is converted into albedo A. This is accomplished for each observation during daytime and the three spectral bands by applying a cloud bidirectional correction factor F (independent of wavelength) to $\rho - A_s$ since $A \approx NAc + A_s$ where Ac is cloud albedo and N is fractional cloud cover (see Frouin and Chertock, 1992; Frouin et al., 2003), i.e.,

$$A = F(\rho - A_s) + A_s, \qquad (5)$$

Analytical formulas developed by Zege et al. (1991) for optically thick scattering layers in the non-absorbing medium are used for F. The parameterization depends on the asymmetry coefficient of the cloud indicatrix, g, and the cloud optical thickness, τ_c, which are fixed at 0.853 and 15, respectively. Sensitivity of F on g and τ_c is an issue, especially when τ_c is relatively small (ρ exhibits more directionality), but since E depends on $(1 - A)$ the relative impact on E computed from Eq. 1 is reduced in such situations (A is also small). The g and τ_c variables can be viewed as tuning parameters, e.g., to reduce biases in estimated fluxes. The surface albedo A_s is parameterized as a function of the Sun zenith angle, aerosol optical thickness at 500 nm, and wind speed following Jin et al. (2004). In the A_s calculation, the chlorophyll-a concentration is fixed at 0.1 mgm^{-3}, and the wind speed is from NCEP Reanalysis-2 data.

Next, the daily mean PAR, $< E_{PAR} >$, is computed by integrating over the PAR spectral range, i.e., 400 to 700 nm, and the length of the day:

$$< E_{PAR} > = \left(\frac{1}{24}\right) \int_t [\cos(\theta_s(t)) G(t)] dt$$
$$\text{with } G = \int_\lambda \left[E_{TOA} T_g T_a (1 - A)(1 - A_s)^{-1} (1 - S_a A)^{-1} \right] d\lambda, \qquad (6)$$

where E_{TOA} is the extraterrestrial spectral solar flux per unit of wavelength corrected for Earth-Sun distance variation during the year and time t is expressed in hour. The integral is calculated for each EPIC observation during the day. In other words, if after masking a surface target (pixel) is observed n times during the day, the algorithm generates n daily mean PAR values. The dependence of A and A_s on θ_s is accounted for in the time integration, but assuming that the characteristics of the atmosphere and surface are unchanged during the day. This is a crude assumption, especially

for cloudiness, but diurnal variability of the atmosphere is considered implicitly in the final step of the algorithm (see below).

In the final step, the individual daily mean estimates obtained on the source grid (number varies from 1 to 13 depending on geographical location, the time during the year, and data availability) are first remapped to an 18.4 km equal-area grid and weight-averaged using the cosine of the Sun zenith angle and then remapped to a Plate Carrée (equal-angle) grid with 18.4 km resolution at the equator. The remapping algorithm is exactly the one used by NASA OBPG to generate a Level 3 binned ocean color products (https://oceancolor.gsfc.bnasa/gov/docs/format/l3bins). Triangular-based linear interpolation is used to fill missing pixels at the edges.

The weighting procedure to obtain the final $< E_{PAR} >$ estimates is accurate, except when only one or two EPIC observations per day is available. Such situations are infrequent; they are due to instrument problems and mission activities (e.g., sensor calibration, spacecraft maneuvers). The accuracy of the weighting procedure was checked from radiative transfer calculations with hourly MERRA-2 data for cloud and aerosol properties and ozone and water vapor contents. In the calculations, E_{PAR} was expressed as $E_{PAR} = E_{clearPAR}(1 - NA_c)$, where A_c is obtained from τ_c according to Fitzpatrick et al. (2004) and $E_{clearPAR}$ is simulated with the 6S code assuming a chlorophyll-a concentration of 0.5 mgm^{-3} and a wind speed of 5 ms^{-1}. Two dates, i.e., January 1 and July 1, 2018, and ocean locations evenly distributed in the spatial domain within 60°S to 40°N and 180°W to 180°E, i.e., every 5° along latitude, and every 6.25° along longitude, were selected. Table 1 displays the comparison statistics of $\cos(\theta_s)$-weighed $< E_{PAR} >$ obtained from 1, 2, 3, 6, 9, and 12 individual $< E_{PAR} >$ estimates during the day versus the $< E_{PAR} >$ value obtained by trapezoidal integration of all the hourly E_{PAR} values at the time of the MERRA-2 observations (referred to as actual or theoretical$< E_{PAR} >$). The individual estimates correspond to hourly observations randomly distributed between sunrise and sunset. In estimating $< E_{PAR} >$ for each observation, the aerosol and cloud properties and gaseous absorber amounts are assumed unchanged during the day, but the dependence of A_c and A_s on θ_s are accounted for in the time integration, as in the EPIC daily mean PAR algorithm. The $\cos(\theta_s)$-weighted $< E_{PAR} >$ values agree well with the theoretical ones when 3 and more observations per day are used, with biases less than 0.10 (0.4%) $Em^{-2}d^{-1}$ in magnitude and root-mean-square difference (RMSD) less than 3.83 (14.2%) $Em^{-2}d^{-1}$. RMSD is reduced

to 1.34 (4.5%) and 1.07 (3%) $Em^{-2}d^{-1}$ with 9 and 12 observations per day. The biases are small because of the random sampling of times during the day and the large number of locations considered in the data ensemble. RMSD is noticeably larger when 1 or 2 $< E_{PAR} >$ estimates are used, i.e., 7.00 (25.9%) and 4.86 (18.0%) $Em^{-2}d^{-1}$, respectively. In such situations, the alternative procedure to obtain $< E_{PAR} >$, i.e., trapezoidal integration of hourly E_{PAR} values, would also give inaccurate results.

TABLE 1 | Statistics of comparing $cos(\theta_s)$-weighted $< E_{PAR} >$ with actual (theoretical) $< E_{PAR} >$ using different number of observations at randomly distributed hourly times during the day on January 1 and July 1, 2018, at ocean locations within 60°S to 40°N and 180°W to 180°E. The number of data points (N) is slightly different when six and more hourly observations per day are used, because such number of observations may not be available for some locations during some days of the year.

No. of observations	R^2	Bias ($Em^{-2}d^{-1}$)	RMSD ($Em^{-2}d^{-1}$)	N
1	0.859	−0.07 (−0.3%)	7.00 (25.9%)	1,874
2	0.929	0.04 (0.1%)	4.86 (18.0%)	1,874
3	0.955	−0.10 (−0.4%)	3.83 (14.2%)	1,874
6	0.987	0.06 (0.2%)	2.04 (7.4%)	1,851
9	0.993	−0.02 (−0.1%)	1.34 (4.5%)	1,682
12	0.996	−0.06 (−0.2%)	1.07 (3.0%)	1,095

A way to reduce the sampling biases in such situations, not yet implemented in the algorithm, is to use MERRA-2 hourly cloud products for the very day of the EPIC observations, as proposed by Tan et al. (2020). If τ_{cMERRA} and N_{MERRA} denote the MERRA-2 cloud optical thickness and fractional coverage, A is replaced by A' in Eq. 5 as follows:

$$A' = (A - A_s)[N_{MERRA}(t)A_c(\tau_{cMERRA}(t))] / \times [N_{MERRA}(t_i)A_c(\tau_{cMERRA}(t_i))] + A_s, \quad (7)$$

where t_i is the time of satellite observation and A_c is computed from τ_{cMERRA} at time t and t_i. Basically, the quantity $A - A_s$ is adjusted by the ratio of NA_c computed from MERRA-2 products at times t and t_i In Eq. 6 A, determined at t_i, is corrected for variations with θ_s, but assuming that cloud properties are unchanged. Figure 2 illustrates the potential improvement expected using Eq. 6. It displays scatter plots of OBPG MODIS-A $< E_{PAR} >$ estimates at source resolution (about 1 km) versus *in situ* measurements at the Chesapeake Bay CERES Ocean Validation Experiment (COVE) site (36.9°N, 75.7°W) in the Western Atlantic during 2003–2014 (see Tan et al., 2020, for details about the *in situ* data collected at that site). Bias is reduced from 1.72 (5.3%) to

−0.05 (-0.1%) $Em^{-2}d^{-1}$, i.e., practically eliminated on average, but RMSD is marginally improved, i.e., 7.02 (21.4%) instead of 7.37 (22.5%) $Em^{-2}d^{-1}$, when using the hourly MERRA-2 cloud products.

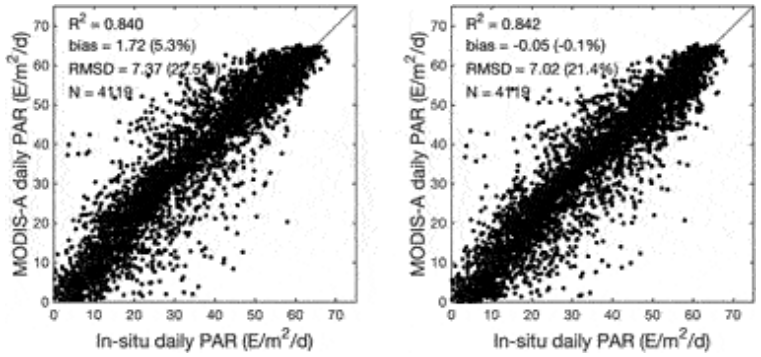

FIGURE 2 | MODIS-A <E_{PAR}> estimate vs. *in situ* data collected at the COVE site in the Western Atlantic. Left: No correction for cloud diurnal variability. Right: Using MERRA-2 hourly cloud products.

3 UNCERTAINTY ASSIGNMENT

Associating uncertainty to each $< E_{PAR} >$ estimate is necessary to use properly the information provided by the estimate. It allows one to verify that variability and trends are actual to merge different datasets optimally, and to constrain adequately model predictions (Frouin et al., 2018a; IOCCG, 2019). Comparisons with contemporaneous and collocated *in situ* measurements at a few sites, the current approach to quantify experimental performance may not be sufficient to describe uncertainty in the wide range of conditions expected to be encountered. Representing uncertainty on a pixel-by-pixel basis requires modeling the measurement, identifying all possible error sources (e.g., noise in the input variables, imperfect or incomplete mathematical model), and determining the combined uncertainty (JGCM-100, 2008; Povey and Grainger, 2015; IOCCG, 2019). Algorithm uncertainty is due to model approximations and parameter errors (e.g., using plane-parallel atmosphere, decoupling effects of clouds and clear atmosphere, neglecting diurnal variability of clouds, fixing cloud optical thickness to a constant in bidirectional correction) if the input variables (EPIC TOA reflectance at wavelengths in the PAR spectral range) are known perfectly. A complete pixel-by-pixel uncertainty budget should include, not only algorithm uncertainty, but also uncertainty due to measurement noise,

radiometric calibration, and preprocessing to Level 1b, a component that is difficult to determine accurately.

The procedure described in Frouin et al. (2018a, b) is used to estimate and provide, for each pixel of the daily mean PAR product, the algorithm uncertainty component of the total uncertainty budget, which is expected to dominate. The bias and standard deviation portions are calculated as a function of clear sky daily mean PAR, $< E_{clearPAR} >$, and cloud factor, $< CF_{PAR} > = < E_{PAR} > / < E_{clearPAR} >$ (characterizes the effect of clouds on PAR and varies from 0 to 1), by simulating for many situations the satellite measurements and corresponding $< E_{PAR} >$ and comparing the latter to the $< E_{PAR} >$ estimated from the TOA reflectance. The simulations were performed with the Atmospheric Radiative Transfer Database for Earth and Climate Observation (ARTDECO) code (Dubuisson et al., 2016; https://www.icare.univ-lille.fr/artdeco/) using as input several years (2003 to 2012) of MERRA-2 hourly data (aerosol and cloud properties). The large number of data points allows one to sample a wide range of geometric configurations for the satellite data and atmospheric variability, in particular many situations of daytime nebulosity for all latitudes. At this stage, the resulting look-up-tables (LUTs) only depend on $< E_{clearPAR} >$ and $< CF_{PAR} >$, but other parameters, e.g., angular geometry and latitude, will be considered in the future. Since the final $< E_{PAR} >$ is a $\cos(\theta_s)$-weighted average of individual $< E_{PAR} >$ estimates during the day, the uncertainty on the final $< E_{PAR} >$ is obtained by weighting the individual uncertainties in the same way.

Figure 3 displays the resulting uncertainty (bias and standard deviation) on individual $<E_{PAR}>$ estimates as a function of $< CF_{PAR} >$ for several $< E_{clearPAR} >$ levels, i.e., 12, 35, and 58 $Em^{-2}d^{-1}$. The bias between estimated and simulated $< E_{PAR} >$ values (Figure 3A) is small (mostly within 1 $Em^{-2}d^{-1}$ in magnitude) and does not vary much with $< CF_{PAR} >$ at low and moderate $< E_{clearPAR} >$ values (blue and red curves) but reaches 3 $Em^{-2}d^{-1}$ at high $< E_{clearPAR} >$ values when $< CF_{PAR} >$ is small (black curve). The standard deviation (Figure 3B) is peaked toward intermediate cloud factors (the risk or probability that cloudiness at the time of satellite measurement may not be representative of the conditions at other times during the day is larger), increasing from about 2.2 to 8.7 $Em^{-2}d^{-1}$ when $< E_{clearPAR} >$ increases from 12 to 58 $Em^{-2}d^{-1}$ and $< CF_{PAR} > = 0.5$, i.e., about 15% relatively.

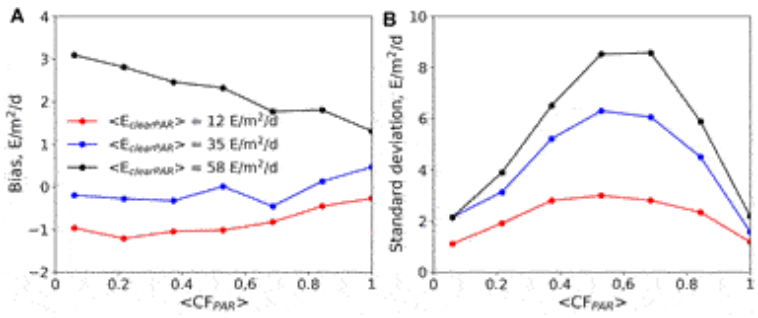

FIGURE 3 | Algorithm uncertainity on individual $<E_{PAR}>$ estimates (i.e., using one observation per day) as a function of $<CF_{PAR}>$ for several values of $<E_{clearPAR}>$. **(A)** Bias (estimated minus simulated values); **(B)** standard deviation. The theoritical uncertainity was obtained from simulations of the TOA reflectance and $<E_{PAR}>$ for a wide range of situations using 10 years of MERRA-2 aerosol and cloud data (see text for details).

As mentioned above, a complete per-pixel uncertainty budget must include errors in the Level 1b data, which may require estimating the sensitivity of $< E_{PAR} >$ to input reflectance and the covariance in the various spectral bands (JGCM-100, 2008). Noise in the input data is difficult to estimate, especially spectral correlations, but this can be attempted by analyzing the Level 1b imagery using structure functions or variograms (e.g., Curran and Dungan, 1989; Wald, 1989) and considering information gleaned from inflight calibration studies. The approach, therefore, would be to establish the uncertainty LUTs using noisy TOA reflectance simulations. Note, however, that in the case of MERIS comparisons with match-up data at the COVE site have revealed that experimental uncertainties are similar to algorithm uncertainties obtained from modeled data without noise (Frouin et al., 2018b). Similar results are expected for EPIC $< E_{PAR} >$ uncertainties.

4 EVALUATION AGAINST *IN SITU* MEASUREMENTS

4.1 Datasets

The EPIC $<E_{PAR}>$ product has been evaluated against *in situ* measurements at three mid-latitude oceanic sites (Figure 4), where long-term E measurements are routinely acquired from moored buoys i.e., BOUée pour l'acquiSition d'une Série Optique à Long termE (BOUSSOLE) and California Current Ecosystem (CCE) buoys 1 and 2 (hereafter denoted CCE-1 and CCE-2). Table 2 lists the main characteristics of the data sets. Although situations for which Sun zenith angles stay large during the day

(such as in polar regions) were not sampled, the atmospheric conditions at the three sites exhibited large variability in cloud and aerosol properties making the datasets appropriate for statistically quantifying uncertainties in the $< E_{PAR} >$ estimates.

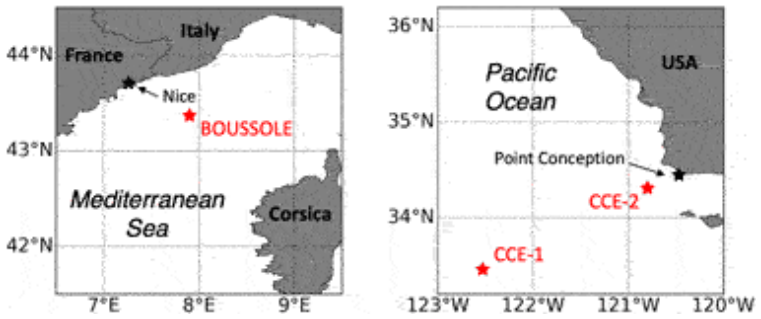

FIGURE 4 | Location of the three *in situ* sites (BOUSSOLE in the Western Mediterranean Sea and CCE-1 and -2 in the Northeast Pacific Ocean) used to evaluate EPIC $<E_{PAR}>$ estimates.

TABLE 2 | I Characteristics of the *in situ* above surface downward solar irradiance datasets used in the evaluation of the EPIC $< E_{PAR} >$ estimates.

Sites	Geographic location	Platform type	Sensor type	Time period	Measurement frequency (min)
BOUSSOLE	43.3667°N, 7.9°E	Moored buoy	PAR (400-700 nm)	5/29/2015–7/28/2019	15
CCE-1	33.462°N, 122.526°W	Moored buoy	Multispectral (412 nm, 443 nm, 490 nm, 510 nm, 555 nm, 620 nm, 669 nm)	10/18/2018–6/9/2020	30
CCE-2	34.309°N, 120.804°W	Moored buoy	Multispectral (412 nm, 443 nm, 490 nm, 510 nm, 555 nm, 620 nm, 669 nm)	8/15/2017–9/8/2020	30

The BOUSSOLE above-surface downward solar irradiance dataset (http://www.obs-vlfr.fr/Boussole/html/project/boussole.php; Antoine et al., 2008) consists of high frequency E_{PAR} measurements (every 15 min) collected from the long-term mooring located at 43.37°N and 7.90°E in the Western Mediterranean Sea about 60 km off the coast (between Nice and Corsica, France). The E_{PAR} measurements were made by Satlantic cosine radiometers installed on top of the immerged part of the buoy during May 29, 2015-July 28, 2019 (i.e., corresponding to the EPIC operational phase). Four deployments were made during this period, but there was a large data gap between December 11, 2017 and February 16, 2019. Before conversion into geophysical quantities, the raw data were calibrated using coefficients provided by the manufacturer and checked for outliers. The E_{PAR}

measurements were corrected for tilt effects according to Antoine et al. (2008). To obtain daily mean values, i.e., $< E_{PAR} >$, instantaneous E_{PAR} with tilt angles less than 20° was integrated over time from sunrise to sunset.

The CCE-1 and -2 datasets were collected at two surface moorings in the California Current (http://mooring.ucsd.edu/cce/). Multiple deployments are available and for this study we used the CCE-1 deployments from October 23, 2017 to June 9, 2020, and the CCE-2 deployments from August 15, 2017 to May 7, 2019. CCE-1 is located at 33.46°N, 122.53°W in the core of California Current, approximately 220 km off Point Conception, California. The CCE-2 mooring is operated at 34.31°N and 120.80°W and closer to the shore, approximately 35 km off Point Conception. For both mooring locations, the E measurements were made every 30 min at 412 nm, 443 nm, 490 nm, 510 nm, 555 nm, 620 nm, and 669 nm by Sea-Bird OCR-507 sensors. The raw data were calibrated to actual E using radiative transfer (RT) simulations. First, clear sky days were identified by carefully examining the shape of raw data as a function of time each day. Only those following strictly the cosine function $E_{PAR} = a\cos(\theta_s)e^{-\beta/\cos(\theta_s)}$ with limited error (Tan et al., 2020, Section 4.1) were selected. Second, the theoretical E for these clear days were simulated using the 6S code with aerosol properties, water vapor, and ozone, wind speed, and chlorophyll-a concentration from NASA OBPG MODerate resolution Imaging Spectroradiometer (MODIS) and Visible Infrared Imaging Radiometer Suite (VIIRS) Level 2 products. Only days with τ_{aer} less than 0.1 at 550 nm were retained and θ_s was limited to 60°. For those τ_{aer} and θ_s conditions the aerosol transmittance, about $1 - 0.16\tau_{aer}/cos(\theta_s)$ according to Tanré et al. (1979), is above 0.97, i.e., aerosols affect minimally *E*. Third, linear relations $y = ax$ were determined by comparing the simulated E and raw data yielding the calibration coefficients to be applied to the raw counts. This was done for each deployment since instruments were switched for different deployments and it is expected that the calibration coefficients are different. The raw data corresponding to tilt larger than 10° were not used in this process and dark subtraction was performed before running the linear regression. Figure 5 displays calibration results at wavelengths 443, 555, and 669 nm for selected deployments. Uncertainty of the calibration gain a (expressed in 10^{-6}/Count) associated with the least-squares fit varies from ± 0.25% to ±0.68% depending on wavelength. Finally, the calibrated spectral E data were first integrated over wavelength and then over time during the day to generate $< E_{PAR} >$.

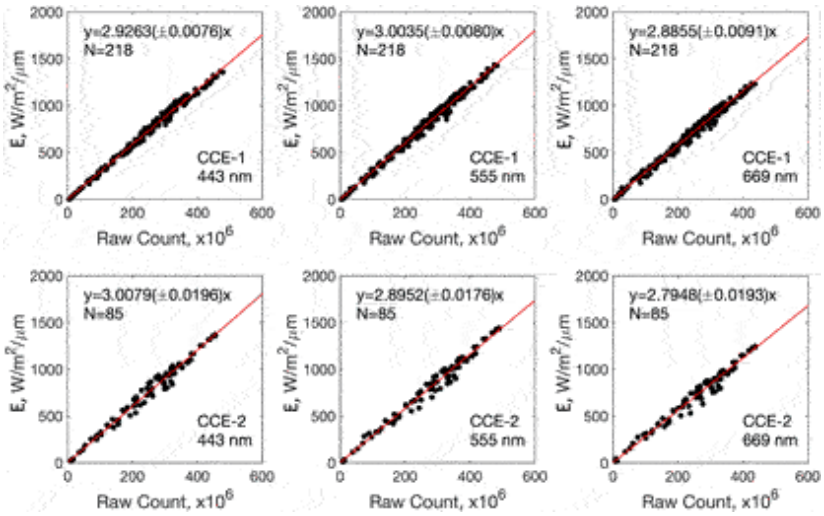

FIGURE 5 | Examples of derived calibration coefficients for CCE-1 (deployment #13) and CCE-2 (deployment #9) datasets at 443, 559, and 669 nm. Raw counts are compared with *E* simulation in conditions of clear sky with small aerosol optical thickness (see text for details).

4.2 Calibration and Adjustment

The calibrated datasets need to be checked and eventual biases removed before evaluating the EPIC $< E_{PAR} >$ estimates. This is important because laboratory calibration errors and other errors (e.g., due to exposure to the marine environment and data processing) may significantly affect the quality of the *in situ* measurement. An independent check-of-calibration can be performed, as indicated above, by comparing the calibrated measurements to RT simulations in clear sky conditions that allow accurate computations of the atmospheric transmittance. Since the CCE-1 and -2 datasets were already calibrated using such RT simulations, as described in the previous sub-section, no further bias adjustment is necessary for those datasets.

The BOUSSOLE dataset, however, was checked against 6S simulations. The same procedure as described for CCE-1 and -2 datasets, including the selection of clear sky days with small aerosol content and θ_s less than 60°, was used. Only five suitable clear sky days were identified during deployments #3 (June 29, 2016—May 24, 2017) and #5 (February 16, 2019—July 28, 2019); the processing, therefore, was limited to those deployments. Corrections were then applied to the *in situ* data based on the best linear fits ($y = ax$) obtained by regressing, for each deployment separately, instantaneous E simulations against corresponding *in situ* measurements.

Figure 6 displays scatter plots of 6S-simulated versus measured E for the two BOUSSOLE deployments before and after correction. The overall bias before correction (Figure 6, left) decreased from 0.55 Em^{-2} d^{-1} (0.4%) to -0.14 Em^{-2} d^{-1} (−0.1%) after correction (Figure 6, right) and RMSD from 2.07 Em^{-2} d^{-1} (1.6%) to 1.69 Em^{-2} d^{-1} (1.3%). The small bias and RMSD in the BOUSSOLE data before correction indicate that the BOUSSOLE data are well-calibrated for those deployments and suggests that one may use with confidence the data from other deployments, even without adjustment. Examination of those deployments, however, revealed abnormal E values. Therefore, only data from deployments 3 and 5 were used, and for consistency with the CCE-1 and -2 datasets the small bias adjustment was still applied to the data.

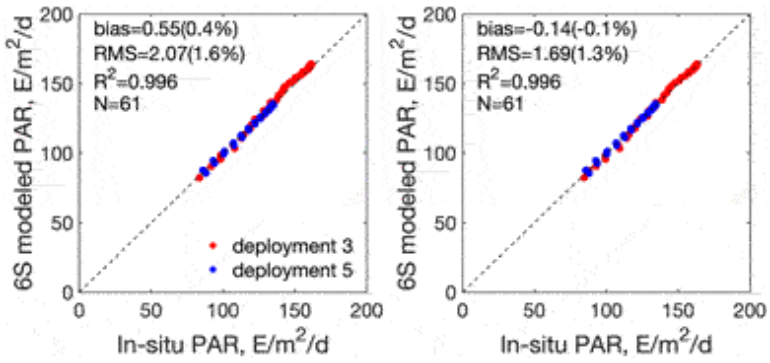

FIGURE 6 | Comparison between 6S-modeled and field-measured instantaneous <E_{PAR}> in very clear sky conditions at the BOUSSOLE site using hourly data: (Left) before any correction; (Right) after adjustment of the measured values to the 6S value *via* linear regression.

4.3 Match-Up Comparison

EPIC $< E_{PAR} >$ estimates remapped at 18.4 km spatial resolution (equal-area grid) were matched with *in situ* measurements at the three evaluation sites. The EPIC pixel with center closest to the site was selected. One may wonder whether, due to the size of the EPIC $< E_{PAR} >$ pixel, satellite estimates are mismatched with the local *in situ* measurements. Comparisons of MODIS-Aqua and -Terra $< E_{PAR} >$ estimates at 4.6, 9.2, and 18.4 km resolution during June 13, 2015 (beginning of the EPIC dataset), to June 23, 2021, indicated practically no biases at the BOUSSOLE and CCE-1 sites and a slight overestimation by about 0.5–0.7% at 18.4 km resolution with respect to 9.2 and 4.6 km resolution, respectively, at the CCE-2 site. RMSD was 3.9–4.7%

between estimates at 9.2 and 18.4 km resolution depending on site and sensor, increasing to 5.6–6.8% between estimates at 4.6 and 18.4 km resolution. In other words, the relatively large spatial resolution of the EPIC pixels is expected to minimally affect statistical performance in terms of bias at the three sites, but RMSD might be significantly underestimated.

Figure 7 displays for each site scatter plots of EPIC, MODIS-Aqua, and MODIS-Terra PAR estimates versus *in situ* measurements. In the comparisons, MODIS values at 9.2 km resolution were averaged to the 18.4 km resolution. The satellite estimates agree with the measurements, but statistical performance is better using EPIC, with bias and RMSD of 0.12 $Em^{-2}d^{-1}$ (0.4%) and 3.93 $Em^{-2}d^{-1}$ (12.0%) for BOUSSOLE, -0.5 $Em^{-2}d^{-1}$ (−1.5%) and 3.4 $Em^{-2}d^{-1}$ (10.2%) for CCE-1, and 0.8 $Em^{-2}d^{-1}$ (2.2%) and 4.6 $Em^{-2}d^{-1}$ (13.3%) for CCE-2. The MODIS-Aqua and -Terra estimates are more biased and exhibit more scatter, reflecting the points made above about using one instead of multiple observations during the day. In particular, the positive bias obtained with MODIS data is likely due to a higher probability of having clear skies at the time of satellite overpass, i.e., late morning or early afternoon, yielding higher than actual daily mean values. Such overestimation was documented in many studies (Section 1) and recently reported by Tan et al. (2020), who compared Medium Resolution Imaging Spectrometer (MERIS) $< E_{PAR} >$ estimates against *in situ* measurements when the satellite observation was made under clear skies. In many instances, the MERIS-derived values were too high, resulting in an overall positive bias, which was explained by the presence of clouds at other times during the day.

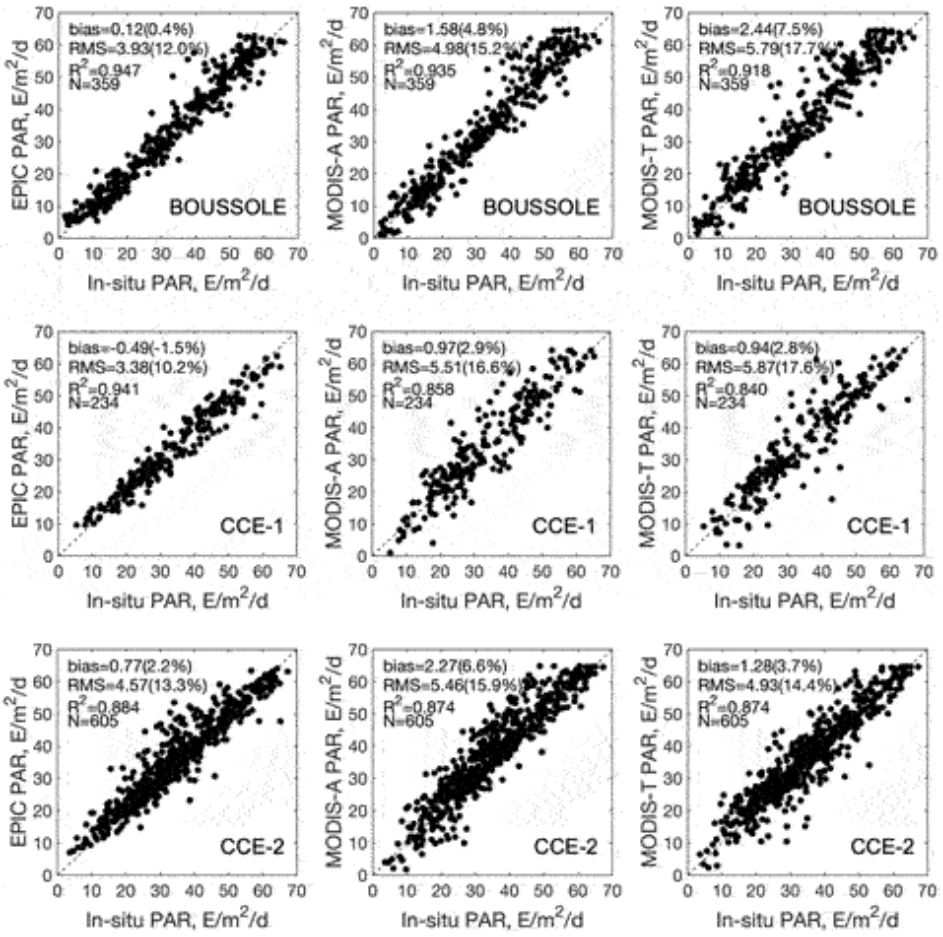

FIGURE 7 | Comparison of EPIC, MODIS-T, $<E_{PAR}>$ estimates against *in situ* data collected at the three evaluation sites (BOUSSOLE, CCE-1, and CCE-2). Left columns are for EPIC, middle columns for MODIS-A, and right columns for MODIS-T.

Algorithm uncertainty was calculated for each $< E_{PAR} >$ estimate of the match-up data set, as described in Section 3, but is not displayed in Figure 7. The resulting average bias and RMSD uncertainty (includes bias and standard deviation components) are respectively 0.49 and 3.63 $Em^{-2}d^{-1}$ at BOUSSOLE, 0.70 and 4.73 $Em^{-2}d^{-1}$ at CCE-1, and 0.77 and 4.28 $Em^{-2}d^{-1}$ at CCE-2. These values resemble those obtained experimentally, i.e., 0.12 and 3.93 $Em^{-2}d^{-1}$ at BOUSSOLE, −0.49 and 3.38 $Em^{-2}d^{-1}$ at CCE-1, and 0.57 and 4.77 $Em^{-2}d^{-1}$ at CCE-2, see Figure 7, suggesting that the procedure to associate uncertainty is adequate and that it might not be necessary to include EPIC imagery noise in the theoretical uncertainty budget.

5 APPLICATION TO SATELLITE IMAGERY

Figures 8A–C displays an example of an EPIC $< E_{PAR} >$ product with associated uncertainties. The date is March 20, 2018 (equinox); the land is in black and the sea ice is in white. The values range from a few $Em^{-2}d^{-1}$ at high latitudes to about 58 E $m^{-2}d^{-1}$ at equatorial and tropical latitudes with atmospheric disturbances modulating the $< E_{PAR} >$ field, especially at middle latitudes (Figure 8A). The bias uncertainty tends to be positive when $< E_{PAR} >$ values are high (overestimation by up to 2 $Em^{-2}d^{-1}$) and slightly negative when $< E_{PAR} >$ values are low (underestimation by up to 1 $Em^{-2}d^{-1}$). The overestimation is relatively larger when $< E_{clearPAR} >$ is high and cloud factor is low, which occurs at low and middle latitudes (Figure 8B). The standard deviation uncertainty is more variable spatially, ranging from 2 to 8 $Em^{-2}d^{-1}$, with highest values obtained at moderate cloud factors and high $< E_{clearPAR} >$ values, as expected from Figure 3, for example off the coast of Chile and Peru at about 25°S and 80°W where cloud factor is about 0.5 (Figure 8C).

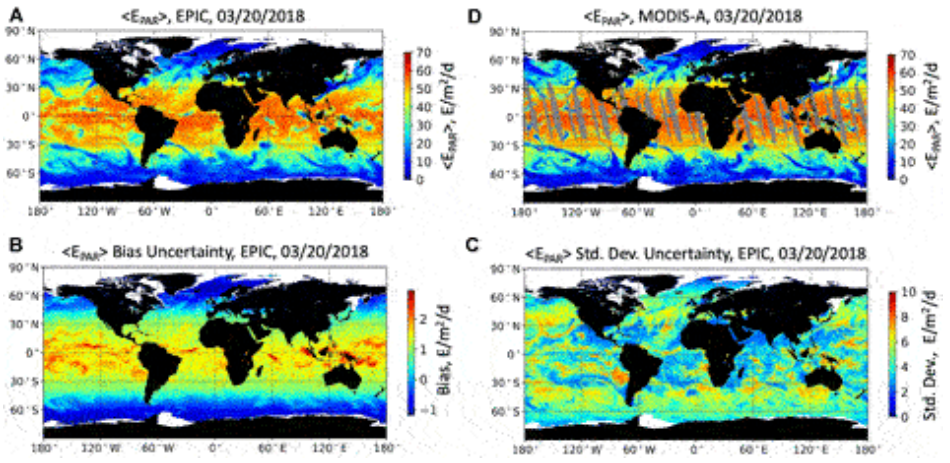

FIGURE 8 | (A) $<E_{PAR}>$ derived from EPIC imagery of March 20, 2018; **(B,C)** Algorithm uncertainity (bias, standard deviation) associated to EPIC $<E_{PAR}>$ estimates; **(D)** $<E_{PAR}>$ derived from MODIS-Aqua imagery of March 20, 2018.

Compared with the MODIS-Aqua $< E_{PAR} >$ product (Figure 8D), the EPIC product (Figure 8A) is less noisy due to multiple observations during the day and does not have any spatial gaps at low/middle latitudes (gray color). The difference map between the two products (Figure 9A) shows good agreement, with higher differences generally encountered in middle to high latitude regions affected by storm activity. The MODIS-Aqua values cover a slightly larger range, which is expected because more extreme values are likely to be encountered with only one observation per day (Figure 9B).

The frequency of values between 15 and 30 $Em^{-2}d^{-1}$ is higher for EPIC reflecting the lower probability of having very low values when several observations during the day are used in estimating $< E_{PAR} >$ in cloudy conditions. The difference histogram indicates that the EPIC $< E_{PAR} >$ values are slightly lower than the MODIS-Aqua values, by 0.7 $Em^{-2}d^{-1}$ on average (Figure 9C). This may result from MODIS-Aqua observing at about 1:30:pm local time, i.e., when cloudiness is usually reduced (e.g., Bergman and Salby, 1996).

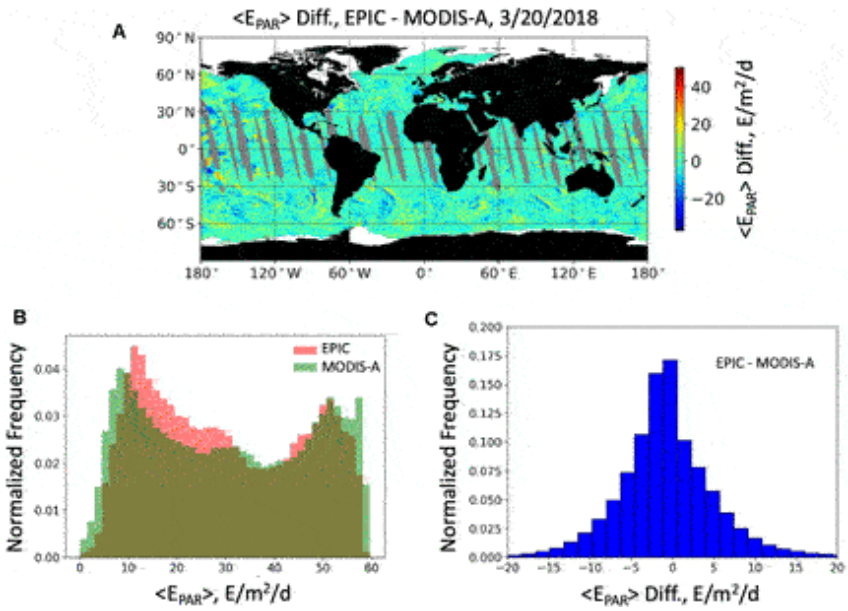

FIGURE 9 | (A) Map of the difference between EPIC and MODIS-A $<E_{PAR}>$ estimates for March, 20, 2018; **(B)** histogram of the EPIC and MODIS-A $<E_{PAR}>$ values; **(C)** histogram of the EPIC difference between EPIC and MODIS-A $<E_{PAR}>$ estimates.

The EPIC $< E_{PAR} >$ imagery of March 20, 2018, was also compared with corresponding imagery from AHI onboard Hiwamari-8 (operated by the Japanese Meteorological Agency) over the oceans and seas surrounding East and Southeast Asia and Australia (Figure 10). The AHI $< E_{PAR} >$ product, available at 5 km resolution on the equal latitude-longitude grid from the Japanese Aerospace Exploration Agency (JAXA) was generated from geostationary observations acquired every 10 min using an adapted version of the algorithm described in Frouin and Murakami (2007). It was remapped to the equal-angle grid (18.4 km at the equator) for comparison to the EPIC $< E_{PAR} >$ product. The spatial features are very similar in both products (Figure 10A,B), and differences do not exhibit a distinct pattern, although

there is some evidence that larger differences often occur near the edges of low-pressure systems (Figure 10C). This may be due to the different temporal resolution of the two products with AHI capturing more accurately the daily variability of moving disturbances. The range of $< E_{PAR} >$ values is practically the same for EPIC and AHI, but the AHI histogram exhibits a small number of higher values between 5 and 25 $Em^{-2}d^{-1}$ and lower values above 55 $Em^{-2}d^{-1}$ (Figure 10D). Again, this is plausibly attributed to using more observations during the day in the AHI $< E_{PAR} >$ estimation. The $< E_{PAR} >$ differences are generally small (i.e., mostly between -5 and 5 $Em^{-2}d^{-1}$) but may be as large in magnitude as 20 $Em^{-2}d^{-1}$, resulting in an overall bias (higher EPIC values) of 1.34 $Em^{-2}d^{-1}$ or 3.6% (Figure 10E). Of course, this bias is only valid for the date and area considered in the comparison—it is expected to differ depending on region and period, yet it corresponds to a wide range of atmospheric conditions.

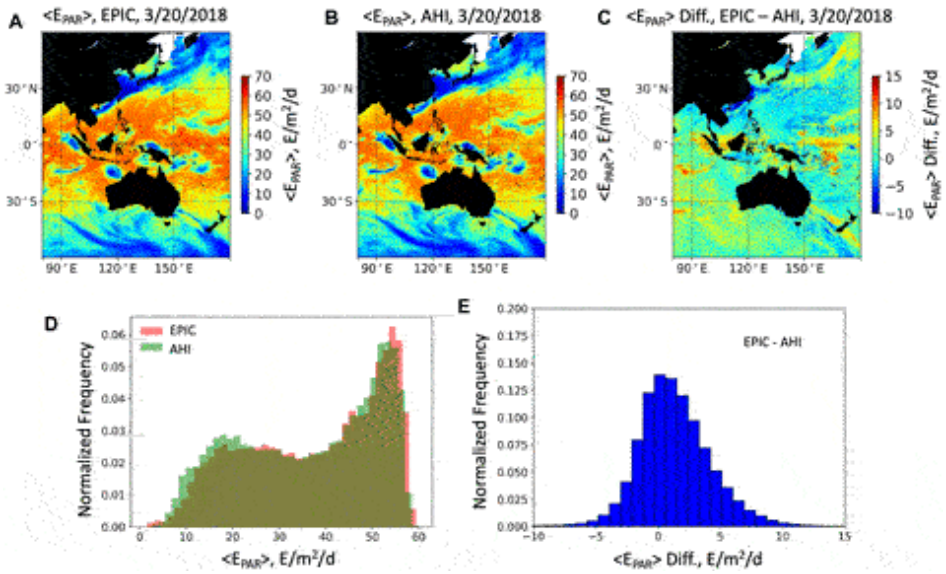

FIGURE 10 | (A) <E_{PAR}> derived from EPIC imagery of March, 20, 2018; **(B)** same as **(A)**, but AHI imagery; **(C)** map of the difference between EPIC and AHI <E_{PAR}> estimates; **(D)** histogram of the EPIC and AHI <E_{PAR}> values; **(E)** histogram of the difference between EPIC and AHI <E_{PAR}> estimates.

Figure 11 displays the time series of EPIC and MODIS daily and monthly mean E_{PAR} during the entire DSCOVR mission until August 2021 at 50°N and 30°W (North Atlantic) and 0° and 30°W (Equatorial Atlantic). The MODIS values are averages of MODIS-Aqua and -Terra estimates. The seasonal cycle and day-to-day variability are large at 50°N, while short-term

variability dominates at the Equator. Seasonal E_{PAR} changes are depicted in the same way by EPIC and MODIS, but the MODIS values tend to be slightly higher, as expected. These examples of time series, and the good performance against *in situ* measurements (Figure 7), illustrate the potential of the EPIC $< E_{PAR} >$ product in ocean biogeochemistry studies.

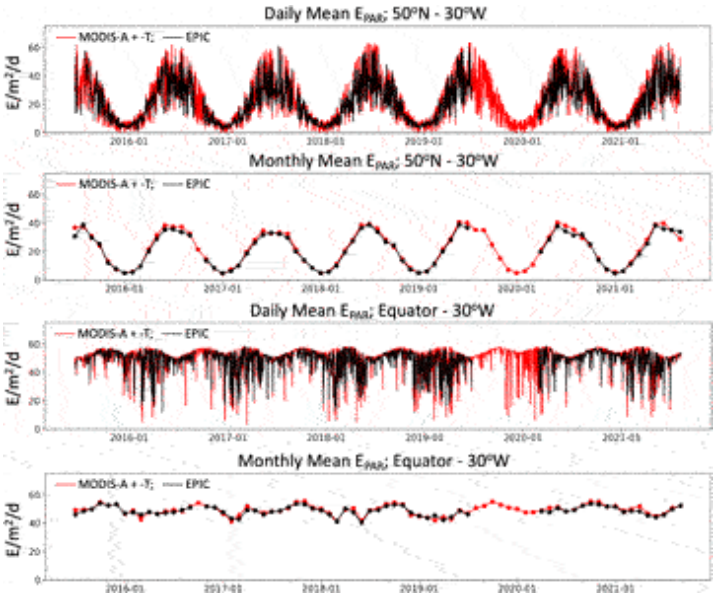

FIGURE 11 | Time series of EPIC and MODIS-A and -T daily and monthly mean E_{PAR} at 50°N and 30°W (North Atlantic) and 0° and 30°W (Equatorial Atlantic). Seasonal cycle is pronounced at 50 N and small at equator; short term variability dominates at the equator.

6 CONCLUSION

An algorithm was developed to estimate daily mean PAR at the ice-free ocean surface, E_{PAR}, from EPIC observations in spectral bands centered on 443, 551, and 680 nm. The algorithm, based on Frouin et al. (2003), uses a budget approach that does not require distinguishing whether a pixel is clear or cloudy, which is appropriate for the coarse EPIC pixels. Algorithm uncertainties (bias and standard deviation) were associated to each $< E_{PAR} >$ estimate using LUTs established from RT simulations. A preliminary evaluation showed good agreement with $< E_{PAR} >$ estimates from other satellite sensors (polar-orbiting MODIS and geostationary AHI) and *in situ* measurements at ocean moorings. Match-up data analysis indicated that the EPIC-derived $< E_{PAR} >$ was less biased than the MODIS $< E_{PAR} >$, and the EPIC $< E_{PAR} >$ imagery was less noisy, which was explained by using multiple observations during the day with EPIC instead of only one

observation with MODIS. The uncertainty of the EPIC $< E_{PAR} >$ product, with biases of −1.5 to 2.2% and RMSDs of 10.0–13.3% depending on the site is lower than the uncertainty of other parameters coming into play in primary production modeling (e.g., phytoplankton absorption and quantum yield). The $< E_{PAR} >$ 2015–2021 time series at selected oceanic locations demonstrated the algorithm ability to capture monthly to interannual variability for investigating the ocean response to temporal changes in available light over a wide range of scales.

The EPIC $< E_{PAR} >$ product is generated routinely by the NASA Center for Climate Simulation (NCCS) and distributed by the Langley ASDC. The data (with documentation) are archived since the beginning of the DSCOVR mission, i.e., June 13, 2015, at https://asdc.larc.nasa.gov/project/DSCOVR/DSCOVR_EPIC_L3_PAR_01. They are available on equidistant cylindrical Plate Carrée grid with 18.4 km resolution at the equator and in 18.4 km equal-area sinusoidal projection, i.e., on spatial grids that are compatible with MODIS and VIIRS Level 3 NASA OBPG ocean-color products.

The current algorithm can be improved in several ways, i.e., by calculating atmospheric reflectance more accurately at large zenith angles (LUTs may be used instead of approximate analytical representation), by relaxing the Lambertian assumption in the retrieval of the cloud/surface layer reflectance, by improving the parameterization of cloud bidirectional effects, and by including from reanalysis data information about cloud variability, which would provide better accuracy when only a few EPIC observations are available to estimate the daily means. Uncertainty may also be specified as a function of angular geometry and latitude, even region, instead of using an average estimate for all latitudes over several years of MERRA-2 data, and they can be fitted by a generalized additive model with proper auxiliary variables.

Other $< E_{PAR} >$ datasets exist (e.g., OBPG MODIS and VIIRS products), but the EPIC time series is uniquely valuable for several reasons. First, the daily mean PAR estimates, which exploit the multiple EPIC observations from sunrise to sunset (i.e., consider diurnal cloud variability), are more accurate than those from sensors in polar orbit (i.e., typically use one observation per day). Second, coverage is global on a daily time scale at low and middle latitudes, which is currently not achieved with instruments onboard polar orbiters (due to Sun glint, limited swath). Sensors operating from geostationary orbit have limited coverage and reduced spatial resolution

at high latitudes, a smaller problem with EPIC. Third, and particularly important, comparisons between daily $< E_{PAR} >$ estimates from EPIC and concurrent polar-orbiting sensors (e.g., MODIS and VIIRS) would determine biases associated with estimates from these sensors, allowing for a consistent $< E_{PAR} >$ time series across sensors, not only during the overlap period, but before and after, i.e., for a long-term (over several decades) science quality $< E_{PAR} >$ record.

The EPIC $< E_{PAR} >$ product is useful to a wide range of research applications, such as primary production and carbon export modeling, ecosystem dynamics and mixed-layer physics, photochemical transformations of dissolved organic matter, and control of stable soluble iron in marine waters. It complements existing $< E_{PAR} >$ datasets and, as mentioned above, may bring about consistency across sensors, allowing a better description of biological phenomena that could lead to new information about temporal variability of biological processes.

The methodology can be easily extended to estimating ultraviolet (UV) surface irradiance using the EPIC spectral bands centered on 317, 325, 340, and 388 nm, especially since ozone content, a key variable governing atmospheric transmittance in the UV, is a standard EPIC product. Furthermore, planar and scalar fluxes below the surface, as well as average cosine for total light (a measure of the angular structure of the light field), variables more directly relevant to addressing science questions pertaining to biogeochemical cycling of carbon, nutrients, and oxygen can also be estimated without major difficulty from the above-surface quantities. Approaches have been identified and procedures devised (Frouin et al., 2018a); they are based on LUTs of clear sky and overcast situations and the derived cloud factor, $< CF >$ ($< CF_{PAR} >$ for the PAR spectral range), from the EPIC observations (Frouin et al., 2018a). Following Mobley and Boss (2012), the LUTs may only depend on a reduced set of parameters, the most important ones being the location and date, which control the day length and mean Sun zenith angle, then the influence of the clouds which is between null (clear sky) and maximum (100% cloud cover), and finally the wind speed. In other words, the observed $< CF >$ may be used as a proxy for the actual cloud factor in linearly interpolating between clear sky and overcast LUTs as a function of $< CF >$. The prospects are promising for ocean biogeochemistry applications.

DATA AVAILABILITY STATEMENT

The raw data supporting the conclusion of this article will be made available by the authors, without undue reservation.

AUTHOR CONTRIBUTIONS

All the authors participated in the conception and organization of the study, the interpretation of the results, and the writing of the findings. RF and JT arranged the contents of the sections and wrote the first version of the manuscript. RF developed the algorithm to estimate ocean surface PAR. MC and DR created LUTs to associate uncertainties. JT coded the algorithms and performed the statistical analyses. MS implemented the processing line at the NASA Center for Climate Simulation and organized data archival at the Atmospheric Science Data Center. HM provided information about the AHI PAR product. DA, US, JS, and VV were involved in the field data collection and processing at the mooring sites. Everyone critically revised the manuscript.

FUNDING

The work effort to accomplish the study was funded by the National Aeronautics and Space Administration (NASA) under DSCOVR Grant 80NSSC19K0764 (Program Manager: R. S. Eckman) and by the Japan Aerospace Exploration Agency (JAXA) under GCOM-C Contract JX-PSPC-515384. The CCE moorings are funded by National Oceanic and Atmospheric Administration (NOAA) GOMO and OAP under Grant OAR4320278 Award# 304593. The BOUSSOLE data used in this work were collected when the project was funded by the European Space Agency, the Centre National d'Etudes Spatiales (CNES) and JAXA.

PUBLISHER'S NOTE

ACKNOWLEDGMENTS

The authors gratefully acknowledge the various teams that produced and quality-controlled the EPIC data used in the study, the NASA OBPG for

generating and making available the MODIS and VIIRS products, and JAXA for providing the AHI imagery *via* the P-Trees System. They also thank everyone involved in servicing the field instruments and collecting, processing, and archiving the BOUSSOLE, CCE-1 and CCE-2, and COVE solar irradiance data, and the MERRA-2 Science Team for the reanalysis data. The CCE-1 and CCE-2 moorings are part of the global OceanSITES program.

REFERENCES

Antoine, D., André, J.-M., and Morel, A. (1996). Oceanic Primary Production: 2. Estimation at Global Scale from Satellite (Coastal Zone Color Scanner) Chlorophyll. *Glob. Biogeochem. Cycles* 10, 57–69. doi:10.1029/95GB02832

Antoine, D., Guevel, P., Desté, J.-F., Bécu, G., Louis, F., Scott, A. J., et al. (2008). The "BOUSSOLE" Buoy-A New Transparent-To-Swell Taut Mooring Dedicated to Marine Optics: Design, Tests, and Performance at Sea. *J. Atmos. Ocean. Technol.* 25, 968–989. doi:10.1175/2007jtecho563.1

Baker, K. S., and Frouin, R. (1987). Relation between Photosynthetically Available Radiation and Total Insolation at the Ocean Surface under clear Skies1. *Limnol. Oceanogr.* 32, 1370–1377. doi:10.4319/lo.1987.32.6.1370

Ballabrera-Poy, J., Murtugudde, R., Zhang, R.-H., and Busalacchi, A. J. (2007). Coupled Ocean-Atmosphere Response to Seasonal Modulation of Ocean Color: Impact on Interannual Climate Simulations in the Tropical Pacific. *Am. Meteorol. Soc.* 20, 353–374. doi:10.1175/JCLI3958.1

Behrenfeld, M. J., Boss, E., Siegel, D. A., and Shea, D. M. (2005). Carbon-based Ocean Productivity and Phytoplankton Physiology from Space. *Glob. Biogeochem. Cycles* 19, GB1006. doi:10.1029/2004GB002299

Behrenfeld, M. J., and Falkowski, P. G. (1997). Photosynthetic Rates Derived from Satellite-Based Chlorophyll Concentration. *Limnol. Oceanogr.* 42, 1–20. doi:10.4319/lo.1997.42.1.0001

Behrenfeld, M. J., O'Malley, R. T., Siegel, D. A., McClain, C. R., Sarmiento, J. L., Feldman, G. C., et al. (2006). Climate-driven Trends in Contemporary Ocean Productivity. *Nature* 444, 752–755. doi:10.1038/nature05317

Behrenfeld, M. J., Randerson, J. T., McClain, C. R., Feldman, G. C., Los, S. O., Tucker, C. J., et al. (2001). Biospheric Primary Production during an ENSO Transition. *Science* 291, 2594–2597. doi:10.1126/science.1055071

Bergman, J. W., and Salby, M. L. (1996). Diurnal Variations of Cloud Cover and Their Relationship to Climatological Conditions. *J. Clim.* 9, 2802–2820. doi:10.1175/1520-0442(1996)009<2802:dvocca>2.0.co;2

Carr, M.-E., Friedrichs, M. A. M., Schmeltz, M., Noguchi Aita, M., Antoine, D., Arrigo, K. R., et al. (2006). A Comparison of Global Estimates of marine Primary Production from Ocean Color. *Deep Sea Res. Part Topical Stud. Oceanography* 53, 741–770. doi:10.1016/j.dsr2.2006.01.028

Cox, C., and Munk, W. (1954). Measurement of the Roughness of the Sea Surface from Photographs of the Sun's Glitter. *J. Opt. Soc. Am.* 44, 838–850. doi:10.1364/JOSA.44.000838

Curran, P. J., and Dungan, J. L. (1989). Estimation of Signal-To-Noise: a New Procedure Applied to AVIRIS Data. *IEEE Trans. Geosci. Remote Sensing* 27, 620–628. doi:10.1109/tgrs.1989.35945

Dedieu, G., Deschamps, P. Y., and Kerr, Y. H. (1987). Satellite Estimation of Solar Irradiance at the Surface of the Earth and of Surface Albedo Using a Physical Model Applied to Metcosat Data. *J. Clim. Appl. Meteorol.* 26, 79–87. doi:10.1175/1520-0450(1987)026<0079:seosia>2.0.co;2

Deschamps, P.-Y., Herman, M., and Tanré, D. (1983). *Modélisation du rayonnement réfléchi par l'atmosphère et la terre entre 0.35 and 4 μm*. France: ESA contract report

4393/8C/F/DO(SC)University of Lille, 155

Dubuisson, P., Labonnote, L.-C., Riedi, J., Compiègne, M., and Winiarek, V. (2016). "ARTDECO: Atmopsheric Radiative Transfer Data Base for Earth and Climate Observation," in *Proc. International Radiation Symposium* (Auckland, New Zealand, 16–22. April 2016.

Falkowski, P. G., and Raven, J. A. (1997). *Aquatic Photosynthesis*. Oxford: Blackwell.

Fitzpatrick, M. F., Brandt, R. E., and Warren, S. G. (2004). Transmission of Solar Radiation by Clouds over Snow and Ice Surfaces: A Parameterization in Terms of Optical Depth, Solar Zenith Angle, and Surface Albedo. *J. Clim.* 17, 266–275. doi:10.1175/1520-0442(2004)017<0266:tosrbc>2.0.co;2

IOCCG (2019). *Uncertainties in Ocean Colour Remote Sensing* ed . Editor F. Mélin (Dartmouth, Canada: IOCCG Report Series, No. 18, International Ocean Colour Coordinating Group). doi:10.25607/OBP-696

Frouin, R., and Chertock, B. (1992). A Technique for Global Monitoring of Net Solar Irradiance at the Ocean Surface. Part I: Model. *J. Appl. Meteorol.* 31, 1056–1066. doi:10.1175/1520-0450(1992)031<1056:atfgmo>2.0.co;2

Frouin, R., Franz, B. A., and Werdell, P. J. (2003). "The SeaWiFS PAR Product," in *Algorithm Updates for the Fourth SeaWiFS Data Reprocessing, NASA Tech. Memo. 2003-206892,* ed . Editors S. B. Hooker, and E. R. Firestone (Greenbelt, Maryland: NASA Goddard Space Flight Center), Vol. 22, 46–50.

Frouin, R., and Iacobellis, S. F. (2002). Influence of Phytoplankton on the Global Radiation Budget. *J. Geophys. Res.* 107, 5–10. doi:10.1029/2001JD000562

Frouin, R., Ramon, D., Jolivet, D., and Compiègne, M. (2018b). Specifying Algorithm Uncertainties in Satellite-Derived PAR Products. *Proc. SPIE* 8525, 107780W. doi:10.1117/12.2501681

Frouin, R., and McPherson, J. (2012). Estimating Photosynthetically Available Radiation at the Ocean Surface from GOCI Data. *Ocean Sci. J.* 47, 313–321. doi:10.1007/s12601-012-0030-6

Frouin, R., McPherson, J., Ueyoshi, K., and Franz, B. A. (2012). A Time Series of Photosynthetically Available Radiation at the Ocean Surface from SeaWiFS and MODIS Data. *Remote Sensing Mar. Environ.* , 19–12. doi:10.1117/12.981264

Frouin, R., and Murakami, H. (2007). Estimating Photosynthetically Available Radiation at the Ocean Surface from ADEOS-II Global Imager Data. *J. Oceanogr.* 63, 493–503. doi:10.1007/s10872-007-0044-3

Frouin, R., and Pinker, R. T. (1995). Estimating Photosynthetically Active Radiation (PAR) at the Earth's Surface from Satellite Observations. *Remote Sensing Environ.* 51, 98–107. doi:10.1016/0034-4257(94)00068-x

Frouin, R., Ramon, D., Boss, E., Jolivet, D., Compiègne, M., Tan, J., et al. (2018a). Satellite Radiation Products for Ocean Biology and Biogeochemistry: Needs, State-Of-The-Art, Gaps, Development Priorities, and Opportunities. *Front. Mar. Sci.* 510778, 3. doi:10.3389/fmars.2018.00003

Gelaro, R., McCarty, W., Suárez, M. J., Todling, R., Molod, A., Takacs, L., et al. (2017). The Modern-Era Retrospective Analysis for Research and Applications, Version 2 (MERRA-2). *J. Clim.* 30, 5419–5454. doi:10.1175/jcli-d-16-0758.1

Henson, S. A., Sarmiento, J. L., Dunne, J. P., Bopp, L., Lima, I., Doney, S. C., et al. (2010). Detection of Anthropogenic Climate Change in Satellite Records of Ocean Chlorophyll and Productivity. *Biogeosciences* 7, 621–640. doi:10.5194/bg-7-621-2010

Herman, J., HuangMcPeters, L. R., McPeters, R., Ziemke, J., Cede, A., and Blank, K. (2018). Synoptic Ozone, Cloud Reflectivity, and Erythemal Irradiance from Sunrise to sunset for the Whole Earth as Viewed by the DSCOVR Spacecraft from the Earth-Sun Lagrange 1 Orbit. *Atmos. Meas. Tech.* 11, 177–194. doi:10.5194/amt-11-177-2018

JGCM-100 (2008). *Evaluation of Measurement Data—Guide to the Expression of Uncertainty in Measurement, Document Produced by Working Group 1 of the Joint Committee for Guides in Metrology (Jcgm/Wg 1), Published by the JCGM Member Organizations*, 134. Sèvres: BIPM, IEC, IFCC, ILAC, ISO, IUPAC, IUPAP and OIML.

Jin, Z., Charlock, T. P., Smith, W. L., and Rutledge, K. (2004). A Parameterization of Ocean Surface Albedo. *Geophys. Res. Lett.* 31. 1180.doi:10.1029/2004GL021180

Kahru, M., Kudela, R., Manzano-SarabiaSarabia, M., and Mitchell, B. G. (2009). Trends in Primary Production in the California Current Detected with Satellite Data. *J. Geophys. Res.* 114, C02004. doi:10.1029/2008JC004979

Kim, J., Yang, H., Choi, J.-K., Moon, J.-E., and Frouin, R. (2016). Estimating Photosynthetically Available Radiation from Geostationary Ocean Color Imager (GOCI) Data. *Korean J. Remote Sensing* 32, 253–262. doi:10.7780/kjrs.2016.32.3.5

Kirk, J. T. O. (1994). *Light and Photosynthesis in Aquatic Ecosystems*. Bristol: Cambridge University Press.

Kotchenova, S. Y., Vermote, E. F., and Frouin, E. F. (2007). Validation of a Vector Version of the 6S Radiative Transfer Code for Atmospheric Correction of Satellite Data. Part II: Homogeneous Lambertian and Anisotropic Surfaces. *Appl. Opt.* 46, 4455. doi:10.1364/ao.46.004455,

Kotchenova, S. Y., Vermote, E. F., Matarrese, R., and Klemm, (2006). Validation of a Vector Version of the 6S Radiative Transfer Code for Atmospheric Correction of Satellite Data. Part I: Path Radiance. *Appl. Opt.* 45, 6762. doi:10.1364/ao.45.006762

Laliberté, J., Bélanger, S., and Frouin, R. (2016). Evaluation of Satellite-Based Algorithms to Estimate Photosynthetically Available Radiation (PAR) Reaching the Ocean Surface at High Northern Latitudes. *Remote Sensing Environ.* 184, 199–211. doi:10.1016/j.rse.2016.06.014

Lee, Y. J., Matrai, P. A., Friedrichs, M. A. M., Saba, V. S., Antoine, D., Ardyna, M., et al. (2015). An Assessment of Phytoplankton Primary Productivity in the Arctic Ocean from Satellite Ocean Color/*In Situ* Chlorophyll- a Based Models. *J. Geophys. Res. Oceans* 120, 6508–6541. doi:10.1002/2015JC011018

Loeb, N. G., Wielicki, B. A., Su, W., Loukachine, K., Sun, W., Wong, T., et al. (2007). Multi-instrument Comparison of Top-Of-Atmosphere Reflected Solar Radiation. *Am. Meteorol. Soc.* 20, 575–591. doi:10.1175/JCLI4018.1

Longhurst, A., Sathyendranath, S., Platt, T., and Caverhill, C. (1995). An Estimate of Global Primary Production in the Ocean from Satellite Radiometer Data. *J. Plankton Res.* 17, 1245–1271. doi:10.1093/plankt/17.6.1245

Marshak, A., Herman, J., Adam, S., Karin, B., Carn, S., Cede, A., et al. (2018). Earth Observations from DSCOVR EPIC Instrument. *Bull. Amer. Meteorol. Soc.* 99, 1829–1850. doi:10.1175/BAMS-D-17-0223.1

Miller, A. J., Alexander, M. A., Boer, G. J., Chai, F., Denman, K., Erickson, D. J., et al. (2003). Potential Feedbacks between Pacific Ocean Ecosystems and Interdecadal Climate Variations. *Bull. Amer. Meteorol. Soc.* 84, 617–634. doi:10.1175/BAMS-84-5-617

Mobley, C. D., and Boss, E. S. (2012). Improved Irradiances for Use in Ocean Heating, Primary Production, and Photo-Oxidation Calculations. *Appl. Opt.* 51, 6549–6560. doi:10.1364/AO.51.006549

Murtugudde, R., Beauchamp, J., McClain, C. R., Lewis, M., and Busalacchi, A. J. (2002). Effect of Penetrative Radiation on the Upper Tropical Ocean Circulation. *J. Clim.* 15, 470486. doi:10.1175/1520-0442(2002)015<0470:eoprot>2.0.co;2

Nakamoto, S., Kumar, S. P., Oberhuber, J. M., Ishizaka, J., Muneyama, K., and Frouin, R. (2001). Response of the Equatorial Pacific to Chlorophyll Pigment in a Mixed Layer Isopycnal Ocean General Circulation Model. *Geophys. Res. Lett.* 28, 2021–2024. doi:10.1029/2000GL012494

Nakamoto, S., Kumar, S. P., Oberhuber, J. M., Muneyama, K., and Frouin, R. (2000). Chlorophyll Modulation of Sea Surface Temperature in the Arabian Sea in a Mixed-Layer Isopycnal General Circulation Model. *Geophys. Res. Lett.* 27, 747–750. doi:10.1029/1999GL002371

Platt, T., Denman, K. L., and Jassby, A. D. (1977). “Modeling the Productivity of Phytoplankton,” in *The Sea: Ideas and Observations on Progress in the Study of the Seas* ed . Editor E. D. Goldberg (New York, NY: John Wiley, 807–856.

Platt, T., Forget, M.-H., White, G. N., Caverhill, C., Bouman, H., Devred, E., et al. (2008). Operational Estimation of Primary Production at Large Geographical Scales. *Remote Sensing Environ.* 112, 3437–3448. doi:10.1016/j.rse.2007.11.018

Povey, A. C., and Grainger, R. G. (2015). Known and Unknown Unknowns: Uncertainty Estimation in Satellite Remote Sensing. *Atmos. Meas. Tech.* 8, 4699–4718. doi:10.5194/amt-8-4699-2015

Ramon, D., Jolivet, D., Tan, J., and Frouin, R. (2016). "Estimating Photosynthetically Available Radiation at the Ocean Surface for Primary Production (3P Project): Modeling, Evaluation, and Application to Global MERIS Imagery," in *Proc. SPIE 9878" in Remote Sensing of the Oceans and Inland Waters: Techniques, Applications, and Challenges* , 98780D. doi:10.1117/12.2229892

Rossow, W. B., and Schiffer, R. A. (1999). Advances in Understanding Clouds from ISCCP. *Bull. Amer. Meteorol. Soc.* 80, 2261–2287. doi:10.1175/1520-0477(1999)080<2261:aiucfi>2.0.co;2

Ryther, J. H. (1956). Photosynthesis in the Ocean as a Function of Light Intensity1. *Limnol. Oceanogr.* 1, 61–70. doi:10.4319/lo.1956.1.1.0061

Shell, K. M., Frouin, R., Nakamoto, S., and Somerville, R. C. J. (2003). Atmospheric Response to Solar Radiation Absorbed by Phytoplankton. *J. Geophys. Res.* 108, 4445. doi:10.1029/2003JD003440

Somayajula, S. A., Devred, E., Bélanger, S., Antoine, D., Vellucci, V., and Babin, M. (2018). Evaluation of Sea-Surface Photosynthetically Available Radiation Algorithms under Various Sky Conditions and Solar Elevations. *Appl. Opt.* 57, 3088–3105. doi:10.1364/ao.57.003088

Sweeney, C., Gnanadesikan, A., Griffies, S. M., Harrison, M. J., Rosati, A. J., and Samuels, B. L. (2005). Impacts of Shortwave Penetration Depth on Large-Scale Ocean Circulation and Heat Transport. *J. Phys. Oceanogr.* 35, 1103–1119. doi:10.1175/jpo2740.1

Tan, J., and Frouin, R. (2019). Seasonal and Interannual Variability of Satellite-Derived Photosynthetically Available Radiation over the Tropical Oceans. *J. Geophys. Res. Oceans* 124, 3073–3088. doi:10.1029/2019JC014942

Tan, J., FrouinJolivet, R. D., Jolivet, D., Compiègne, M., and Ramon, D. (2020). Evaluation of the NASA OBPG MERIS Ocean Surface PAR Product in clear Sky Conditions. *Opt. Express* 28, 33157. doi:10.1364/OE.3960610.1364/oe.396066

Tan, S.-C., and Shi, G.-Y. (2012). The Relationship between Satellite-Derived Primary Production and Vertical Mixing and Atmospheric Inputs in the Yellow Sea Cold Water Mass. *Continental Shelf Res.* 48, 138–145. doi:10.1016/j.csr.2012.07.015

Tanré, D., Herman, M., Deschamps, P. Y., and De Leffe, A. (1979). Atmospheric Modeling for Space Measurements of Ground Reflectances, Including Bidirectional Properties. *Appl. Opt.* 18, 3587–3594. doi:10.1364/ao.18.003587

Uitz, J., Claustre, H., Gentili, B., and Stramski, D. (2010). Phytoplankton Class-specific Primary Production in the World's Oceans: Seasonal and Interannual Variability from Satellite Observations. *Glob. Biogeochem. Cycles* 24, a–n. doi:10.1029/2009GB003680

Wald, L. (1989). Some Examples of the Use of Structure Functions in the Analysis of Satellite Images of the Ocean. *Photogramm. Eng. Rem. Sen.* 55, 1487–1490.

Wang, Y., and Zhao, C. (2017). Can MODIS Cloud Fraction Fully Represent the Diurnal and Seasonal Variations at DOE ARM SGP and Manus Sites?*J. Geophys. Res. Atmos.* 122, 329–343. doi:10.1002/2016JD025954

Yang, Y., Zhao, C., and Fan, H. (2020). Spatiotemporal Distributions of Cloud Properties over China Based on Himawari-8 Advanced Himawari Imager Data. *Atmos. Res.* 240, 104927. doi:10.1016/j.atmosres.2020.104927

Zege, E. P., Ivanov, A. P., and Katsev, I. L. (1991). *Image Transfer through a Scattering Medium*. New York: Springer-Verlag, 349.

Zhao, C., Chen, Y., Li, J., Letu, H., Su, Y., Chen, T., et al. (2019). Fifteen-year Statistical Analysis of Cloud Characteristics over China Using Terra and Aqua Moderate Resolution Imaging

Spectroradiometer Observations. *Int. J. Climatol.* 39 (5), 2612–2629. doi:10.1002/joc.5975

Conflict of Interest: Authors DR and MC are employed by HYGEOS. The remaining authors declare that the research was conducted in the absence of any commercial or financial relationships that could be construed as a potential conflict of interest.

ORIGINAL RESEARCH
published: 12 April 2022
doi: 10.3389/frsen.2021.788525

Unique Observational Constraints on the Seasonal and Longitudinal Variability of the Earth's Planetary Albedo and Cloud Distribution Inferred From EPIC Measurements

Barbara E. Carlson[1*], Andrew A. Lacis[1], Gary L. Russell[1], Alexander Marshak[2] and Wenying Su[3]

[1] *NASA Goddard Institute for Space Studies, New York, NY, United States*
[2] *NASA Goddard Space Flight Center, Greenbelt, MD, United States*
[3] *NASA Langley Research Center, Hampton, VA, United States*

Edited by:
Benjamin Torres, Université de Lille, France

Reviewed by:
Chao Liu, Nanjing University of Information Science and Technology, China
Tim Kane, The Pennsylvania State University, United States

**** Correspondence:** Barbara E. Carlson, Barbara.E.Carlson@nasa.gov*

***Specialty section:** This article was submitted to Satellite Missions, a section of the journal Frontiers in Remote Sensing*

***Received:** 02 October 2021*
***Accepted:** 06 December 2021*
***Published:** 12 April 2022*

***Citation:** Carlson BE, Lacis AA, Russell GL, Marshak A and Su W (2022) Unique Observational Constraints on the Seasonal and Longitudinal Variability of the Earth's*

Planetary Albedo and Cloud Distribution Inferred From EPIC Measurements. Front. Remote Sens. 2:788525. doi: 10.3389/frsen.2021.788525

Thorough comparison to observations is key to developing a credible climate model forecasting capability. Deep Space Climate Observatory (DSCOVR) measurements of Earth's reflected solar and emitted thermal radiation provide a unique observational perspective that permits a more reliable model/data comparison than is possible with the otherwise available satellite data. The uniqueness is in the DSCOVR satellite's viewing geometry, which enables continuous viewing of the Earth's sunlit hemisphere from its Lissajous orbit around the Lagrangian L1 point. The key instrument is the Earth Polychromatic Imaging Camera (EPIC), which views the Earth's sunlit hemisphere with 1024-by-1024-pixel imagery in 10 narrow spectral bands from 317 to 780 nm, acquiring up to 22 high spatial resolution images per day. The additional feature is that the frequency of EPIC image acquisition is nearly identical to that of the climate GCM data generation scheme where climate data for the entire globe are 'instantaneously' calculated at 1-h radiation time-step intervals. Implementation of the SHS (Sunlit Hemisphere Sampling) EPIC-view geometry for the in-line GCM output data sampling establishes a precise self-consistency in the space-time data sampling between EPIC observational and GCM output data generation and sampling. The remaining problem is that the GCM generated data are radiative fluxes, while the EPIC measurements are backscatter-dependent radiances. Radiance to flux conversion is a complex problem with no simple way to convert GCM radiative fluxes into spectral radiances. The more expedient approach is to convert the EPIC spectral radiances into broadband radiances by MODIS/CERES-based regression relationships and then into solar radiative fluxes using the CERES angular distribution models. Averaging over the sunlit hemisphere suppresses the meteorological weather noise, but preserves the intra-seasonal larger scale variability. Longitudinal slicing by the Earth's rotation permits a self-consistent model/data comparison of the longitudinal model/data differences in the variability of the reflected solar radiation. Ancillary EPIC Composite data provide additional cloud property information for climate model diagnostics. Comparison of EPIC-derived seasonal and longitudinal variability of the Earth's planetary albedo with the GISS ModelE2 results shows systematic overestimate of cloud reflectivity over the Pacific Ocean with corresponding underestimates over continental land areas.

Keywords: DSCOVR, deep space climate observatory, self-consistent space/time data sampling, longitudinal slicing, sunlit hemisphere observations, climate diagnostic data, EPIC

INTRODUCTION

Model/data comparisons are essential for improved understanding of the Earth's climate system. But, as illustrated in Figure 1, this seemingly straightforward task is not simple. Climate GCMs and the real world are quasi-chaotic in behavior. So, there is no reason to expect agreement except for averages taken over sufficiently large space and time scales. Moreover, most climate system variables exhibit strong diurnal variability (e.g., Eastman and Warren, 2014). Whereas GCM output data are computed uniformly over the globe at uniform time-steps, and uniformly averaged into monthly-mean latitude-longitude tables such as the planetary albedo and total cloud cover in Figure 1 (Left panels), the observational data typically use sequential space-time sampling from a sun-synchronous satellite track, such as the CERES planetary albedo data (Top Right), with considerable uncertainty as to how the diurnal cycle might have been averaged or referenced. The European Centre for Medium-Range Weather Forecasts Reanalysis Interim (ECMWFs ERAI) total cloud cover, which is a global re-analysis product of observations acquired over the past 3.5 decades. These data comparisons show qualitative similarity, but with substantial small-scale differences. Even for monthly-mean averages, considerable meteorological weather noise remains. By averaging data over the entire globe, the weather noise can be minimized, as in Figure 1 Bottom. The seasonal CERES Energy Balanced and Filled (EBAF) planetary albedo for 2003 to 2019 (Loeb et al., 2009, Loeb et al., 2018) is the reference. The GISS ModelE2 planetary albedo seasonal change shown by the black squares. There is a close similarity, but the off-sets are difficult to interpret quantitatively. All data comparisons are useful, but they focus on different aspects of the climate variables. The longitudinal slicing methodology used here describes an approach that averages out the weather noise, but retains important intra-seasonal and longitudinal variability that is not simple to extract from conventional data.

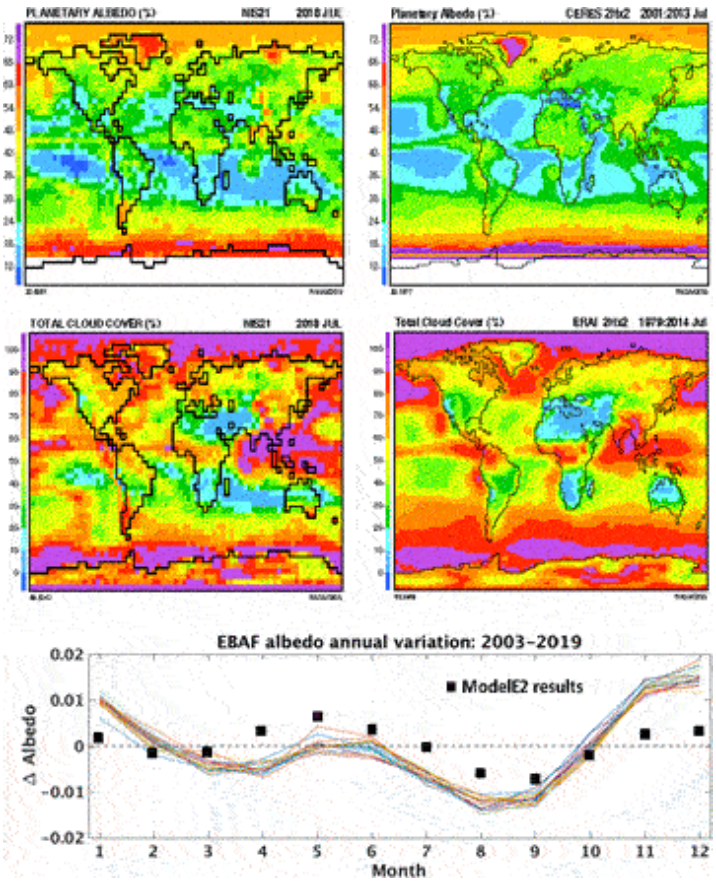

FIGURE 1 | ModelE2 4 × 5 degree horizontal resolution monthly-mean planetary albedo **(Upper Left)** and total cloud cover **(Middle Left)** computed for July 2018. The corresponding observational counterparts are the CERES planetary albedo **(Upper Right)** on a 2 × 2.5 degree grid averaged over the years 2001–2013, and the ECMWF Re-Analysis-Interim (ERAI) total cloud cover **(Middle Right)** also on a 2 × 2.5 degree grid averaged over the years 1979–2014. Seasonal CERES EBAF planetary albedo **(Bottom)** for 2003–2019 (Loeb et al., 2009; 2018) with the ensemble annual mean subtracted. For comparison, the black squares depict the ModelE2 decadal-mean seasonal variability of the global planetary albedo for years 2000–2010 with the annual mean subtracted.

EPIC-DERIVED CLIMATE CONSTRAINT

EPIC makes full-disk images of the Earth's sunlit hemisphere in 10 narrow spectral band channels with a 1024 × 1024 (download) spatial resolution. Depending on telemetry rate, 13 to 22 images per day are acquired from the Lissajous orbit at the Lagrangian L1 point 1.4 to 1.6 × 10^6 km from the Earth in the direction of the Sun. The procedure for converting the EPIC spectral radiances into EPIC reflected SW fluxes is described by Su et al., 2018; Su et al., 2020. Using MODIS/CERES-based regression relationships, the spectral radiances are first converted into broadband SW radiances. They are then

transformed into radiative fluxes using the CERES angular distribution models. All these tasks are performed at the pixel level, then integrated over the entire sunlit hemisphere (as viewed from the Lagrangian L1 point) to convert each EPIC image into a single climate-style data point for the sunlit hemisphere-mean reflected SW flux. Without loss in precision, these reflected SW fluxes are normalized relative to CERES global annual-mean SW radiative flux (Loeb et al., 2018), and divided by the Total Solar Irradiance (TSI) (Kopp and Lean, 2011) to obtain the planetary albedo.

For each day's-worth of 13–22 images, the EPIC derived SW fluxes are interpolated to their nearest Greenwich-Mean (GMT) hour to align the data points in longitude. Thus, the 5,000 to 6000 EPIC images per year are transformed into 12 × 24 monthly-mean tables of planetary albedo points, plotted in Figure 2 (Upper). The color-coded longitudes cover the full rotation of the Earth in 1-h time-steps (24 h of GMT, and 15^{o} steps in longitude). The data are grouped into five broad longitude ranges color-coded as follows: Pacific Ocean (dark blue), East-Asia (green), Africa-Asia (magenta), Atlantic Ocean (light blue), and North America (orange). Key meridians of the five longitude ranges are further identified by their heavier solid color and black dots that depict their monthly-mean value at their mid-month position, which also include the sub-satellite latitude listed at the bottom of the figure. The group members are further identified by a different line-style. Each color-coded meridian is identified by its Greenwich-Mean time (GMT) of noon-time sun. Thus, the international Date Line is identified by its 0 GMT. In addition to the GMT designation, each meridian is also identified by a geographic reference to help identify its relative location.

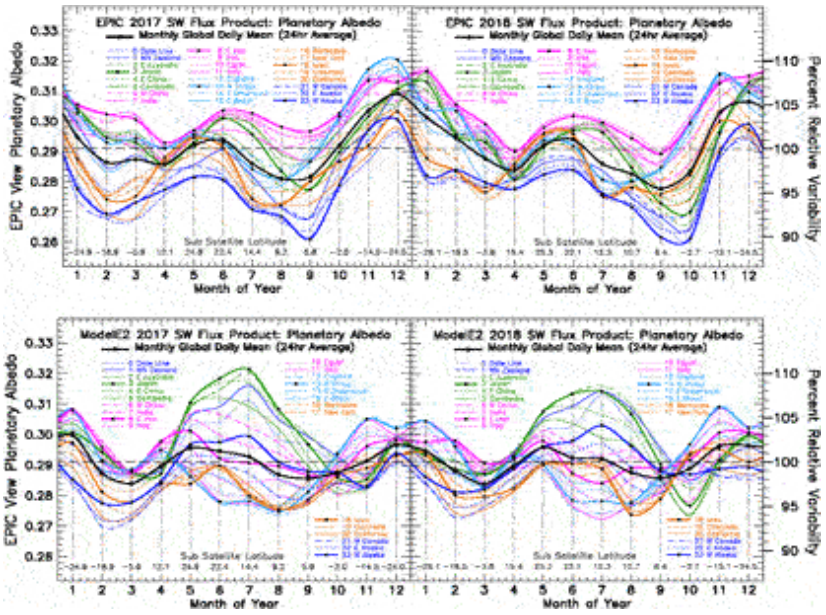

FIGURE 2 | Planetary albedo from EPIC reflected SW flux for 2017 and 2018 **(Upper Left** and **Upper Right)**, normalized by the CERES global annual-mean SW radiative flux (Loeb et al., 2018), and divided by the seasonal Total Solar Irradiance (Kopp and Lean, 2011). The longitudinal slicing is depicted by the colored lines, which represent longitudinally contiguous regions, and which correspond to Greenwich-mean time of high-noon meridians that are also tagged with the geographic location of the illuminated hemisphere-center meridian. The representative members of each colored longitude grouping is identified by its designated black dot monthly-mean position. Geographically, the colored lines proceed westward from the international date line at 1-**hourly** intervals (15° of longitude). The heavy black line is the daily-mean average over a full rotation of the Earth. The mid-month DSCOVR sub-satellite latitude is depicted at figure bottom. **Bottom Left** and **Bottom Right** are the corresponding planetary albedo results for 2017 and 2018 obtained from GISS ModelE2 simulations running with prescribed current-climate sea surface temperatures, and using in-line sampling of the GCM output data using SHS sampling in accord with the DSCOVR Ephemeris viewing geometry.

The key takeaway from Figure 2 Bottom panels is that, over the East-Asia area (3 GMT, black-dot green), ModelE2 overestimates clouds during the NH summer season (since clouds are the principal contributors to Earth's planetary albedo, e.g., Stephens et al., 2015). Meanwhile, the cloud reflectivity over the continental Africa-Asia land areas (8 GMT, black-dot magenta) is strongly underestimated. By comparison, the EPIC results in the Figure 2 Top panel show planetary albedo to be highest over the Africa-Asia region, in strong contrast to the ModelE2 longitudinal dependence.

A likely explanation for this striking model/data difference is the use of a globally uniform relative humidity criteria for the onset of cloud

condensation in the ModelE2 cloud scheme, which involves utilizing a critical (less than 100%) relative humidity criteria for the statistical overlap of water vapor and temperature probability distributions, becoming sufficient to achieve the relative humidity threshold for cloud condensation over some fraction of the grid box. Due to the broader water vapor and temperature probability distributions that exist over land compared to ocean, conditions are more favorable for cloud formation over land compared to the ocean. Thus, using a globally uniform cloud condensation onset will overestimate clouds over the ocean and underestimate clouds over land. Using land/ocean dependent relative humidity criteria to make it more difficult to form clouds over ocean, and easier over land, would lead to improved agreement with observations by reducing the cloud radiative effect over the ocean while increasing the cloud contribution to planetary albedo over land.

Other significant differences are the daily-mean of the seasonal variability depicted by the heavy black line, which resembles the general EPIC data variability, but has less than half of seasonal amplitude of the EPIC planetary albedo, and the ModelE2 planetary albedo during NH summer months, which has little resemblance to the EPIC planetary albedo. However, there is some similarity in that ModelE2 planetary albedo exhibits similar longitudinal ordering and slope during the winter months, from January to March and also from October to December.

The Figure 2 "spaghetti-line" planetary albedo data is shown in Figure 3 in Hovmöller format with the EPIC planetary albedo at figure Left, and corresponding ModelE2 results at figure Right. The Hovmöller format has specific value for displaying space-time variability, whereas the line format provides a more quantitative comparison for the amplitude of the seasonal and longitudinal variability. In the Hovmöller (1949) format, the Y-scale has time increasing upward (with some implicit latitudinal perspective). The X-scale depicts the longitudinal dependence (including the noon-time GMT of EPIC image acquisition). To help locate GMT and longitude points in their geographic perspective, world maps in 4^{o} x 5^{o} GCM resolution are displayed in Figure 4.

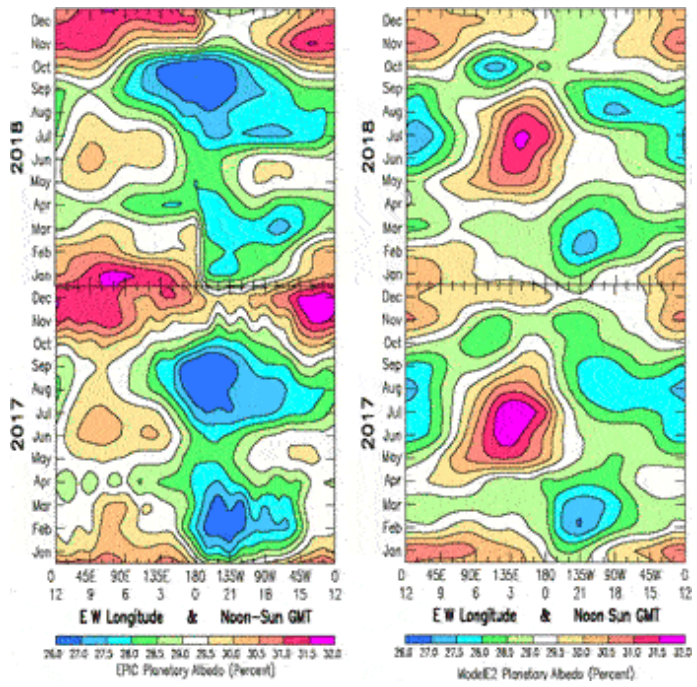

FIGURE 3 | Hovmöller plots of the EPIC **(Left)** and ModelE2 **(Right)** planetary albedo for 2017 and 2018 for the same data presented in Figure 2. The Y-scale has time running upward starting with January 2017 at the bottom through December 2018 at the top. The X-scale is longitude running from 0° E longitude at the left and 0° W longitude at the right. The X-scale references the GMT of the noon-time Sum, starting at GMT = 0 at the Date Line at the center, proceeding westward toward the left as the Earth rotates. The input data for the Hovmöller plots is precisely the same 12 × 24 tables of monthly-mean sunlit hemisphere averages for the 24 uniformly spaced GMT for both EPIC and ModelE2, respectively. In the color bar, magenta identifies the highest planetary albedos, deep blue the lowest.

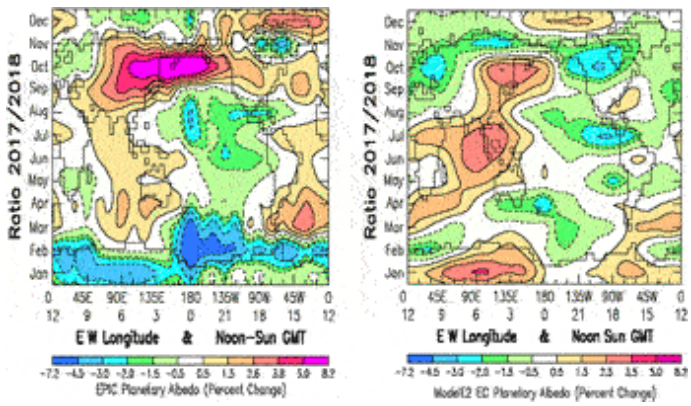

FIGURE 4 | Hovmöller-style ratio plot of year 2017 divided by year 2018 of the EPIC **(Left)** and ModelE2 **(Right)** planetary albedo plotted in Figure 3. The Y-scale has time running upward starting with January at the bottom through December at the top. As in Figure 3, the X-scale is longitude running from 0° E longitude at the left to 0° W longitude at the right. GMT references the location of high-noon Sun. The world map is included for geographic reference.

Year 2017 has been identified as a La Niña year (Zhang et al., 2019). Presumably related to this, there is the significantly greater space-time variability evident in 2017 than in 2018. Most notable is the sharp decrease in planetary albedo (Figure 3, Bottom Left) over the Central Pacific region during February-March of 2017.

Also remarkable are the enigmatic oscillations (with a peak-to-peak periodicity spanning ~ 30° in longitude) that appear over the Eastern Pacific in February and November, and over the Indian Ocean in April. In contrast, year 2018 appears to be a uniformly quiescent year having apparently reverted back to ENSO-neutral conditions. As for identifying the geographic epicenter and its spatial extent of the features responsible, that is not within reach, based just on the hemisphere-averaged longitudinal variability information that is available. These features appear to be of limited extent in size and duration in time. Yet their radiative impact is clearly evident on the hemisphere-mean EPIC derived planetary albedo. La Niña activity is identified by fluctuations in sea surface temperature that then induce the atmospheric response in cloud cover. It may be that the space-time variability of the EPIC planetary albedo can serve as an indicator of La Niña/ENSO activity.

The 2017 April oscillations over what is likely the Indian Ocean, are unique in that they are limited in their time duration as well as in spatial

extent. Like the February and October-November oscillations in this area, they have peak-to-peak ~ 30° extent in longitude, but have a time duration that is only about a month. Their location in longitude extends basically from South Africa to Australia. It is unclear whether these Indian Ocean oscillations might be related to the La Niña phenomenon, or if they are just simply a different member of the ubiquitous climate system oscillations.

Interestingly, there are several longitudes that exhibit extended periods of steady monotonic change in planetary albedo. One such example is the 2017 (and 2018) Atlantic Ocean region, represented by West Africa (13 GMT, black-dot light blue) in Figure 2 Top, and in Figure 3 Left along the GMT = 13 longitude, which has its season minimum planetary albedo in August that keeps increasing steadily through December.

The Figure 3 Right Hovmöller comparison of ModelE2 results to EPIC shows little resemblance, due largely to the overestimated northern hemisphere (NH) summer cloudiness over the East-Asia and Western Pacific, which appear as the isolated large regions high albedo near left-center of the annual panels. Perhaps the most disappointing is the absence in the ModelE2 results of the strong decrease in planetary albedo over the Central Pacific in February is the Figure 3 Bottom Left EPIC results. It is plausible that this might be an artifact due to initialization issues of switching on the prescribed current-climate SSTs for 2017 and 2018 from their climatological spin-up versions, and not allowing sufficient time for the atmosphere and clouds to adjust to the prescribed SSTs. Otherwise, there are only modest perceptible differences between the ModelE2 results for the 2017 La Niña year and 2018. There is little evidence of the persistent oscillations that are so prominent in the EPIC results in Figure 3 Bottom Left.

Figure 4 is a ratio plot of the 2017 and 2018 Hovmöller maps in Figure 3. With 2018 as the reference year, ratioing isolates the La Niña atmospheric (and cloud) response by removing the large seasonal climatological variability. Except for the still glaring absence of the February La Niña signature in the ModelE2 results, there is otherwise substantial agreement in the ModelE2 response to the 2017 La Niña SST changes that are seen in the EPIC results, such as decreased planetary albedo across the Central and Eastern Pacific and increased planetary albedo over the East-Asia region.

Overall, ModelE2 does not reproduce the strong EPIC February decrease in planetary albedo, or the sharp increase in October, which appears to be caused by a shift in the seasonal increase planetary albedo between 2017 and

2018. Also, assuming 2018 to be a ENSO-neutral year, there would appear to be a possible La Niña precursor occurring over the Indian Ocean during January 2017 with a strong decrease in the EPIC planetary albedo.

The "spaghetti" line plots in Figure 2 and the Hovmöller contour maps in Figure 3 are two very different ways to represent and compare precisely the same data, in this case, the tabulated data of longitudinally sliced EPIC planetary albedo and the similarly sampled ModelE2 GCM output data. The data have been strongly averaged, thus making small differences of a percent or less to be meaningful. The Figure 2 line plots provide the more quantitative representation of the differences in the seasonal variability between neighboring longitudes or longitude groups, showing quantitatively the GCM deficiencies in longitudinal cloud distribution.

Clearly, the Figure 3 Hovmöller maps are best in displaying the patterns of variability, showing convincingly the La Niña signature in the EPIC planetary albedo data. And the Hovmöller ratio plots of years 2017 and 2018 in Figure 4, by removing the largest common variability, could readily identify the similarities between the EPIC and ModelE2 planetary albedo results that were not apparent from the Figure 2 or Figure 3 comparisons. This same approach is applicable for examining the patterns of variability of cloud properties to see how they contribute to the planetary albedo.

EPIC HEMISPHERIC COMPOSITE DATA

Since clouds are the principal contributors to planetary albedo, the next step is to access the changes in cloud properties and the cloud distribution that produce the observed variability in planetary albedo. For this purpose, the necessary cloud property data are conveniently available in the form of the EPIC Composite data.

In the process of generating the EPIC-based radiative SW fluxes, Su et al. (2018) constructed the 5-km resolution EPIC composite database, which includes detailed cloud properties such as cloud fraction, cloud-top altitude, and cloud optical depth, water/ice phase, and particle size, compiled from multiple imagers in low earth orbit (LEO) and geostationary (GEO) satellites, with the data selection tuned to closely match the EPIC observations in time and viewing geometry. Monthly-mean and sunlit hemisphere averages are thus available for longitudinal slicing analyses that match those for the radiative fluxes. With the EPIC composite data, it

becomes possible to see the actual causes that lead to the radiative climate symptoms.

The key component of this transformation is the 5-km resolution global composite data product with its optimally merged together cloud properties from Low Earth Orbit (LEO) satellites, and from geostationary (GEO) satellites, based on cloud property retrievals using a common set of retrieval algorithms (Minnis et al., 2008; Minnis et al., 2011). The 5-km composite data product is aggregated from LEO/GEO data for closeness in time and viewing geometry to the EPIC observation time, then convolved to the EPIC grid.

Ancillary data, such as surface type, snow/ice, skin temperature, and precipitable water, are also included in the EPIC composite data (Khlopenkov et al., 2017). CERES Edition4 angular distribution models (Su et al., 2015) are then used to compute SW anisotropic factors for converting EPIC broadband radiances into reflected SW fluxes, which are integrated over the sunlit hemisphere to provide a basic calibration reference for NISTAR measurements, and serve as reference for climate GCM longitudinal slicing comparisons.

Figure 5 Top Panel shows the seasonal variability for the EPIC derived all-cloud sky fraction for 2017 and 2018. The highest cloud fractions are found over the Pacific Ocean (22 GM, black-dot blue) and over the East-Asia region (3 GMT, black dot-green), except for the large dip in September-October of 2018 when North America (18 GMT, orange) is surging to its top value in October-November. The lowest cloud fractions are seen over the Atlantic West Africa region (13 GMT, black-dot light blue). We use the term “dayurnal” here to refer to the variability seen at the Lissajous orbital vantage point during a full day’s rotation of the Earth, and “dayurnal mean”, for the average over all 24 longitude views (heavy black line), which is a *global* dawn-to-dusk diurnal average, given that each longitude view incorporates a range of diurnal samples from the neighboring longitudes, but *its* viewing locality is at the Lissajous orbit. This is to differentiate this from the term “diurnal mean”, which already has an established meaning of referring to a *local* 24-h average. The saving grace for using this term, is that the dayurnal mean is identically reproduced for both EPIC and GCM data sampling.

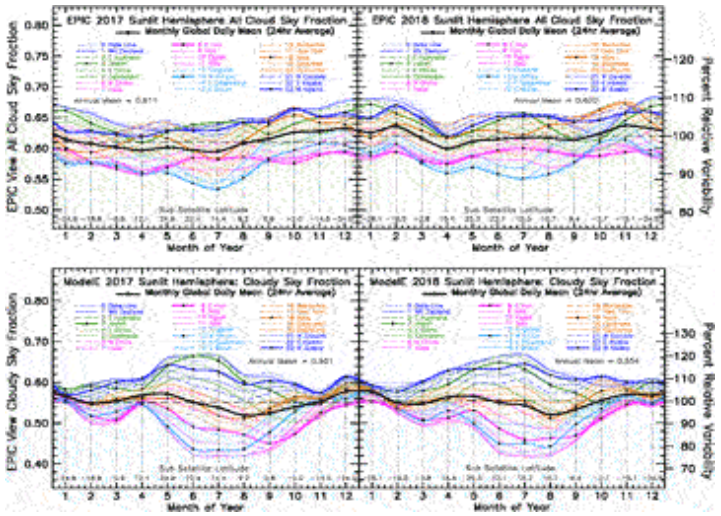

FIGURE 5 | All-cloud cloudy sky fraction **(Top Panel)** from EPIC Composite analysis results for the year 2017 **(Top Left)** and 2018 **(Top Right)**. **(Bottom Panel)**: All-cloud cloudy sky fraction from GISS ModelE2 SHS in-line sampling results for the year 2017 **(Bottom Left)** and 2018 **(Bottom Right)**.

The Figure 5 Bottom Panel depicts the seasonal variability of the ModelE2 cloudy sky fraction for the years 2017 and 2018, which corresponds to the EPIC all-cloud sky fraction that is shown in the Figure 5 Top Panel. Here again, the one redeeming feature of the ModelE2 all-cloud sky fraction is that ModelE2 tends to reproduce the overall longitudinal ordering of the EPIC all-cloud sky fraction results, at least in the NH summer months. For ModelE2 and EPIC, the highest cloud fractions occur over East-Asia (3 GMT, black-dot green) and Pacific Ocean (23 GMT, black-dot dark blue) regions, while the lowest occur over Atlantic (13 GMT, black-dot light blue) and Africa-Asia (8 GMT, black-dot magenta) regions. The North America (18 GMT, black-dot orange) meridians are in between, exhibiting a biannual variability with maxima occurring in April-May and in October-November. For ModelE2, the dayurnal amplitude of the seasonal cloud fraction amplitude is at maximum and also at minimum during the NH summer months, with strong constriction of the cloud fraction amplitude, during the NH winter months. Both EPIC and ModelE2 show a small increase in cloud fraction going from 2017 to 2018, with the EPIC cloud fraction increasing by about 1.5%, and ModelE2 by about 0.5%.

Figure 6 displays the cloudy sky fraction data from Figure 5 in Hovmöller format with the EPIC cloud fraction at Figure 6 Left, and the ModelE2 results at Figure 6 Right. The Hovmöller results basically echo the

spaghetti line plot results in showing the highest cloud fractions over the Pacific Ocean region with the lowest over the Atlantic, including also much of Europe and Africa and the eastern parts of North and South America.

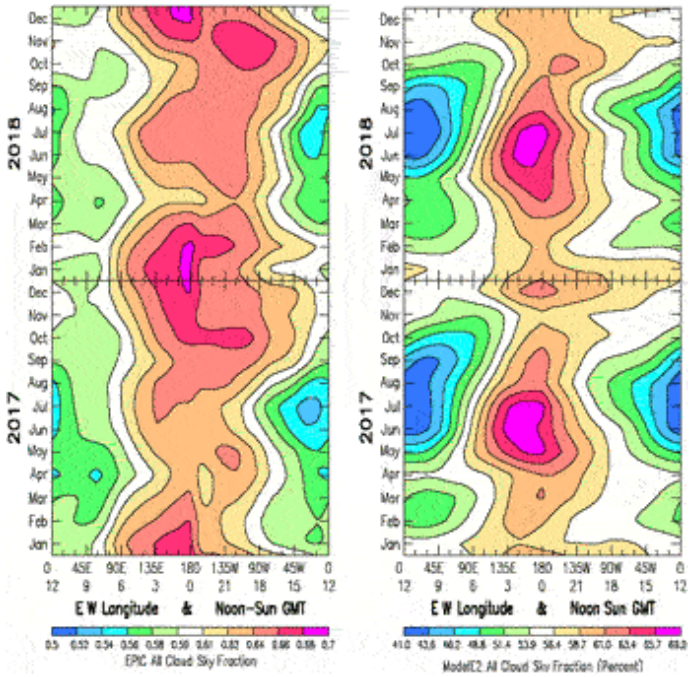

FIGURE 6 | Hovmöller plots of the EPIC **(Left)** and ModelE2 **(Right)** cloudy sky fraction for 2017 and 2018. The Y-scale has time running upward starting with January 2017 at the bottom through December 2018 at the top. The X-scale is longitude running from 0° E longitude at the left and 0° W longitude at the right. The X-scale references the GMT of the noon-time Sum, starting at GMT = 0 at the Date Line at the center, proceeding westward to the left as the Earth rotates. In the color bar, magenta identifies the highest cloud fractions, deep blue the lowest.

In comparing the EPIC cloud fraction variability between the year 2017 (La Niña) and 2018, there are no significant differences in small-scale fluctuations between the 2 years. Except perhaps for a couple of points in April 2017 that appear to be coincident with similar isolated small-scale points occurring in April 2017 of the EPIC planetary albedo fluctuations in Figure 3, the 2 years are similarly quiescent. Given the totally different nature of these two measurements, it is not necessarily surprising. The EPIC planetary albedo is derived directly from a single set of observed spectral radiances. On the other hand, cloud changes involve more options. For example, with favorable meteorological conditions for cloud condensation, clouds can increase vertically in optical depth, rather than spreading out

horizontally. Moreover, for the EPIC cloudy sky fraction, thresholds are involved in deciding whether a given pixel is declared to be mostly clear, or mostly cloudy, and that for some threshold, optically thin clouds might be missed altogether.

For ModelE2, cloud fraction is defined in a still different way. Based on grid-box-mean meteorological conditions, a cloud fraction is determined at each grid box. A random number is then used to decide whether radiative calculations are to be performed for either a totally clear or totally cloudy grid box. Thus, as a computing time saving device, ModelE2 clouds are treated as being fractional in time rather than being fractional in space. Radiatively, for monthly-mean averages, it all averages out. Perhaps it is remarkable that the EPIC and ModelE2 cloud fractions agree as well as they do. As for the strong constrictions in dayurnal amplitude of ModelE2 cloud-top altitude during winter months, there appears to be no explanation.

While changes in cloud-top altitude have only minimal impact on the planetary albedo, they have a profound effect on the outgoing LW radiation due to the direct temperature dependence of thermal radiation that is emitted to space from the cloud-top region. As a result, cloud-top altitude is an important climate variable that is directly involved in defining the Earth's radiative energy balance, but on the thermal outgoing LW radiation side. Thermal LW radiation is not currently included in the EPIC Composite data collection, so comparing cloud altitude and its LW radiative effects is beyond the scope of this model/data comparison.

Nevertheless, cloud-top altitude is one of the key cloud properties that are tabulated as part of the EPIC Composite Data (Su et al., 2018). The cloud property information is retrieved from multiple imagers in low Earth orbit (LEO) satellites that include MODIS, VIIRS, and AVHRR, and also geostationary (GEO) satellites such as GOES-13, GOES-15, METEOSAT-7, METEOSAT-10, MTSAT-2, Himawari-8. Cloud properties were deduced using a common set of algorithms based on the CERES cloud detection and retrieval system (e.g., Minnis et al., 2008; Minnis et al., 2011). Cloud properties from the LEO/GEO imagers are merged together to provide a global composite data product with 5-km resolution by using an aggregated rating system that optimizes the space-time viewing geometry characteristics to provide the best match with EPIC observations. The global composite data are then remapped into the EPIC grid so as not to degrade the EPIC Composite cloud fraction information (Khlopenkov, et al., 2017).

The Figure 7 Top Panels display the seasonal and longitudinal variability of the EPIC Composite cloud-top altitude. Interestingly, both the highest and lowest cloud altitudes occur in July, and more broadly, during the NH summer months for both 2017 and 2018, when the dayurnal cloud-top amplitude has its largest variability. The highest cloud-top altitudes are experienced over the West China continental region (6 GMT, dot-dash magenta), while simultaneously, the lowest cloud-top altitudes occur over the North America region epitomized by the Iowa (18 GMT, black-dot orange) meridian. The cloud-top minima in the dayurnal amplitude are seen in April and October in 2017, with a somewhat deeper minimum occurring in October-November of 2018. The annual-mean cloud-top altitude remains basically unchanged between 2017 and 2018 (registering a small 1.3% increase).

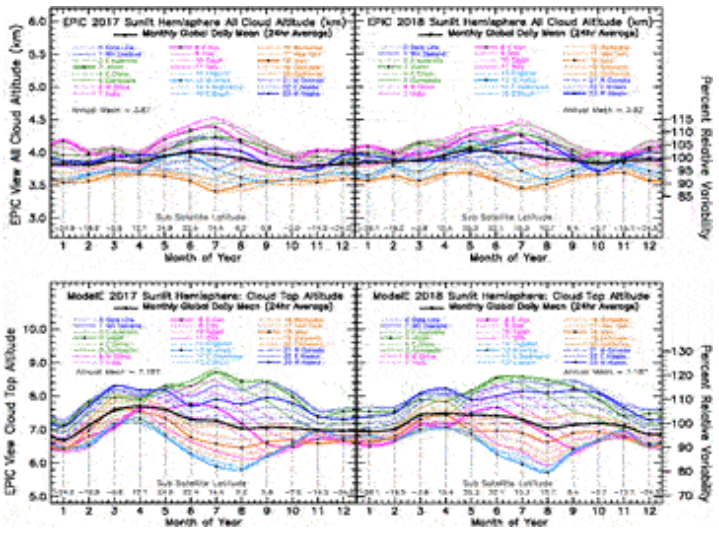

FIGURE 7 | Top Panel: All-cloud cloud-top altitude from EPIC Composite analysis results for the year 2017 **(Top Left)** and for the year 2018 **(Top Right)**. **Bottom Panel**: All-cloud cloud-top altitude (km) from GISS ModelE2 climate simulations for the year 2017 **(Bottom Left)** and 2018 **(Bottom Right)** sampled using the Sunlit Hemisphere Sampling (SHS) simulator and employing the DSCOVR Ephemeris viewing geometry.

The Figure 7 Bottom Panel shows the seasonal and longitudinal variability of the GISS ModelE2 cloud-top altitude. There are some similarities in the overall shape of the seasonal variability of the cloud-top altitude between the EPIC and the ModelE2 results, in that the GCM also has a July centered NH summer maximum, with a mirror minimum, in the cloud-top dayurnal amplitude, but with a more extended (January to May) spring

minimum, and a shortened (December) winter minimum. Moreover, there is substantial ramp-up in the dayurnal-mean of the cloud-top altitude from January to April, (heavy black line) followed by a steady deline. The same behavior is seen in the EPIC dayurnal-mean (Top Panel), but with a greatly reduced amplitude. However, the one big difference between the EPIC and ModelE2 cloud-top altitude variability is the difference in the longitudinal ordering. For EPIC, cloud-top altitude maxima are centered over West China (6 GMT, dot-dash magenta), whereas the ModelE2 cloud-top altitude maxima are centered over East-Asia (3 GMT, black-dot green). Similarly, the EPIC, cloud-top altitude minima are centered over North America region epitomized by Iowa (18 GMT, black-dot orange), whereas the ModelE2 cloud-top altitude minima are centered more over the Atlantic Ocean region (13 GMT, black-dot light blue).

The apparent shift in longitude between the cloud-top altitude location between the EPIC observational data and the ModelE2 climate simulation is made far more clearly evident in the Hovmöller representation of the cloud-top altitude variability, as demonstrated in Figure 8. The Hovmöller format shows both the maxima and the minima to be longitudinally aligned, and that his holds for both EPIC (Left) and ModelE2 (Right). For EPIC, the ridge of cloud-top altitude maxima for 2017 and 2018 are persistently located along the 6 GMT (90° E longitude) meridian running through central Asia (W China). Similarly, a broad valley of cloud-top altitude minima for years 2017 and 2018 are persistently located along the 17 GMT (-75° W longitude) meridian that runs through New York of the North America longitude group. Extremes in cloud-top maximum and minimum altitudes both occur during the NH summer season centered on July.

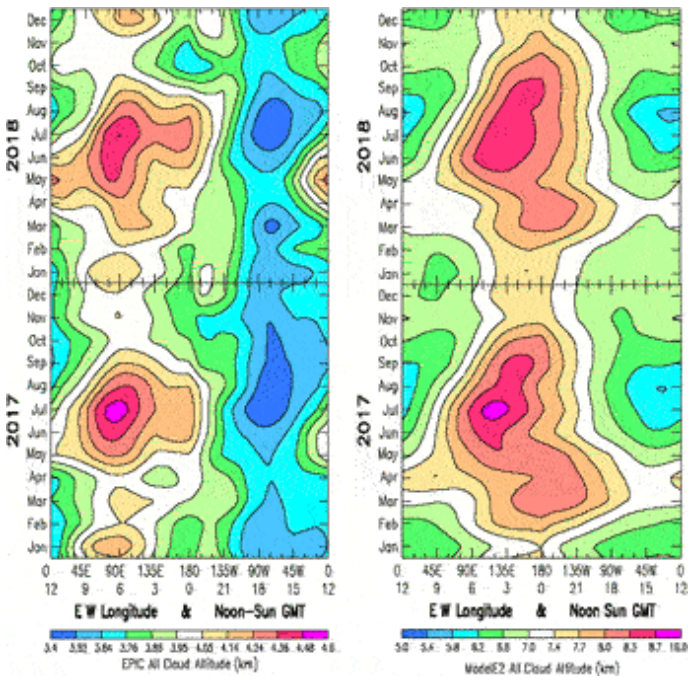

FIGURE 8 | Hovmöller plots of the EPIC **(Left)** all-cloud cloud-top altitude from EPIC Composite analysis results for 2017 and 2018, and ModelE2 **(Right)** from GISS ModelE2 climate simulations for the years 2017 and 2018, for the corresponding line plots of cloud-top altitude in Figure 7.

A similar pattern in the seasonal and longitudinal variability of cloud-top altitude appears also to hold for ModelE2, as shown in Figure 8 Right. The principal difference is a general eastward shift by about 45˚ in longitude of the ridge of cloud-top maxima, and an eastward shift by about 60˚ in longitude for the cloud-top minima.

Another difference between EPIC and ModelE2 cloud-top altitude variability is the more limited range of variability for the ModelE2 cloud-top maximum altitudes, and a larger range of variability for the cloud-top minimum altitudes, compared to EPIC.

Perhaps the biggest difference, but also one of less significance, is the large difference in the cloud-top altitude depicted in Figure 7, which shows the mean cloud-top altitude for EPIC to be about 4 km, while the average cloud-top altitude for ModelE2 clouds is about 8 km. The reasons for this difference arise from the limited ability of satellite remote sensing measurements to detect optically thin clouds, and also the retrieved, or inferred, cloud-top altitude refers to the optical depth $\tau = 1.0$ level. For ModelE2 clouds, cloud-top pressure is known precisely for all of the model

generated clouds, which includes significant numbers of optically thin ($\tau < 0.1$) high altitude cirrus clouds (that automatically constitute the grid-box cloud-top). Also, since the ModelE2 diagnostics assign the cloud layer's top edge as the cloud-top, this is setting the ModelE2 cloud top at the optical depth $\tau = 0$ level, which further biases higher the ModelE2 cloud-top results. Since all of the ModelE2 cloud optical depth information is available at the SHS diagnostic data sampling aggregation, it should be possible to establish a thin-cloud threshold, compute the optical depth $\tau = 1.0$ level, and re-define the ModelE2 cloud-top altitude to more closely coincide with the observational cloud-top data.

Also of interest, because the EPIC Composite LE/GEO cloud products are retrieved separately for liquid water and ice clouds (Minnis et al., 2021), the differences in the seasonal and longitudinal variability for the ice cloud the water cloud altitude can thereby be also examined separately, as done in Figures 9, 10.

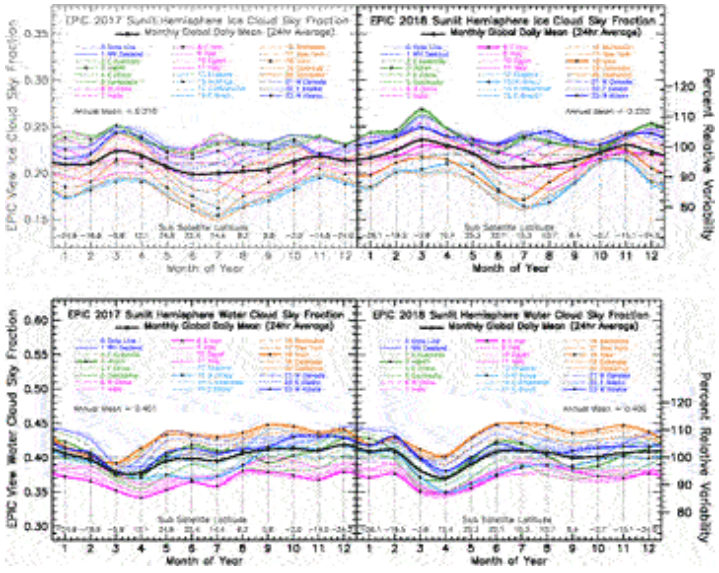

FIGURE 9 | Top Left: Ice cloud sky fraction from EPIC Composite analysis results for year 2017, and **Top Right**: ice cloud sky fraction for year 2018. **Bottom Panel Left**: Water cloud sky fraction from EPIC Composite analysis results for year 2017, and **Bottom Right**: water cloud sky fraction for 2018.

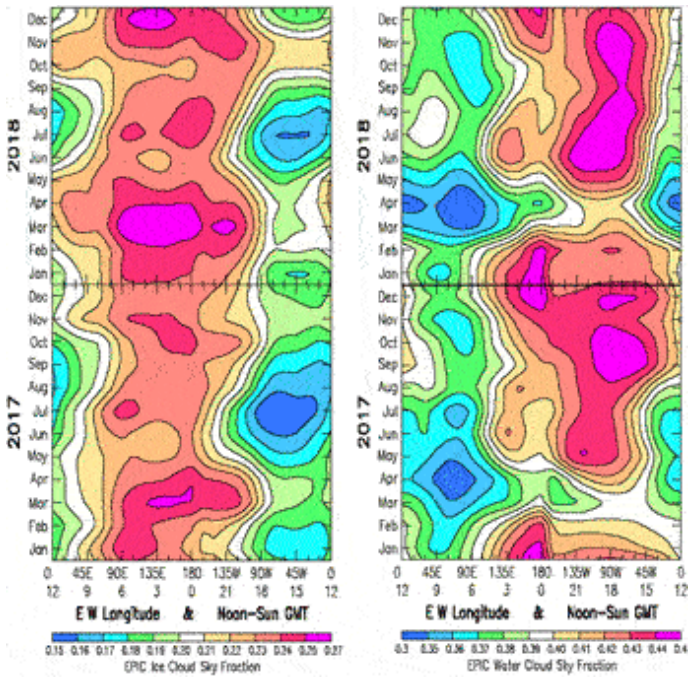

FIGURE 10 | Left: Hovmöller format ice cloud sky fraction from EPIC Composite analysis results for the year 2018 **(Upper Left)** and 2017 **(Lower Left)**. **Right Panel**: Water cloud sky fraction from EPIC Composite analysis results for the year 2018 **(Upper Right)**, and for year 2017 **(Lower Right)**.

EPIC COMPOSITE: ICE AND WATER CLOUDS

In addition to the all-cloud category, the EPIC Composite database also separates clouds into ice cloud and water cloud categories. The GISS ModelE2 also generates ice and water clouds, with precise internal knowledge of the ice and water cloud radiative properties and distribution. But due to unbridgeable differences in definition, direct comparison of the EPIC and ModelE2 ice and water cloud properties is not warranted, as this could lead to false conclusions. The EPIC Composite ice/water cloud differentiation is tied to the Minnis et al. (2021) retrieval algorithms that are used in CERES and MODIS retrievals, and this differentiation would be difficult to reproduce from within the GCM output data. Accordingly, the EPIC/ModelE2 cloud property comparisons have been limited just to the more physically based all-cloud sky fraction and cloud altitude.

Thus, it makes good sense to intercompare the EPIC Composite ice cloud and water cloud properties against each other, with the caveat that an increase in ice cloud fraction could have come at the expense of a decrease in water cloud fraction, and vice versa. The same algorithms have been applied

uniformly for years 2017 and 2018, so the relative changes should be meaningful. Clearly, the La Niña event has significantly disrupted the cloud distribution, so it is of interest to see how the clouds have changed between 2017 and 2018, even if just from the EPIC Composite data. Bender et al.

(2017) have demonstrated the existence of a convincingly strong positive relationship between cloud albedo and cloud fraction, i.e., that cloud albedo increases with increasing cloud fraction, and that the increase in cloud albedo becomes increasingly greater as the cloud fraction approaches unity, although this relationship does not have an explicit dependence on cloud optical depth.

Figure 9 Top shows the seasonal variability of the EPIC ice cloud fraction, with Figure 9 Bottom showing the corresponding water cloud variability. Compared to the roughly uniform all-cloud sky fraction in Figure 5 Top, counter-acting changes are seen during January-March with the ice cloud fraction increasing and the water cloud fraction decreasing in both 2017 and 2018. Interestingly, the longitudinal ordering of the ice cloud dayurnal variability exhibits similarity to the ModelE2 all-cloud fraction longitudinal variability (Figure 5 Bottom) with the East-Asia (3 GMT, black-dot green) and Central Pacific (23 GMT, black-dot blue) regions near the top, and the Atlantic region (13 GMT, black-dot light blue) near the bottom. Also, there is some tendency for the dayurnal range of the EPIC ice cloud fraction variability to 'bulge' in the NH summer months, like the ModelE2 results, with both the maximum and minimum occurring in July. Perhaps most notable is the strong constriction in the ice cloud dayurnal amplitude in November 2018, which again shows some similarity to the ModelE2 results.

A broad range of longitudes from the Date Line 0 GMT, blue dot line) to India (7 GMT, long dash magenta line) appear near the top of the ice cloud sky fraction in Figure 9 Top. It is of interest that the East-Asia (3 GMT, black-dot green line) and Central Pacific (23 GMT, black-dot blue) regions also exhibit some of the sporadic small-amplitude 60-days oscillations during January-March of 2017 and 2018, and from August to December of 2017. Longer periods of 4-to-6-months duration, are also evident in this longitude region. More specifically, the Date Line longitude (0 GMT, blue dot line) appears to be aliasing the changing land/ocean fraction, which is being sampled on 1-h intervals as the Earth rotates (described in more detail in Figure 15). Also prominent in Figure 9 Top is the long period ice fraction variability over the West Africa region (13 GMT, black-dot light blue line), which exhibits the lowest cloud fractions, and is interrupted by some low-

amplitude shorter-period 60–90-days oscillations from November 2017 to April 2018.

On the other hand, for the water cloud sky fraction in Figure 9 Bottom, shows that for the most part, the North America region Iowa (18GMT, black-dot orange line) exhibits the largest water cloud sky fraction from 2017 through 2018, and that similarly the Africa-Asia, East Iran region (8 GMT, black-dot magenta line) displays the lowest water cloud sky fractions. Both of these regions also exhibit a couple of the low-amplitude 60-days oscillations from October 2017 to April 2018, with the Date Line longitude (0 GMT, blue dot line) also popping up to the top during this time period. Figure 9 Bottom shows a strong decrease in the water cloud sky fraction centered on March in 2017 for essentially all longitudes, broadening toward April in 2018. The EPIC water cloud fraction accounts for ~ 2/3 of the all-cloud sky fractions.

Figure 10 shows the seasonal and longitudinal variability of the ice cloud (Left) and water cloud (Right) sky fraction expressed in Hovmöller format. The Hovmöller plots show a clear separation in longitude of the ice cloud and water cloud sky fraction regions of maximum concentration, with the ice cloud sky fraction favoring the longitudes spanning the Indian Ocean, East-Asia, and Central Pacific Ocean, from roughly 45E to 135W. The water cloud sky fraction dominates from the Eastern Pacific (135W to the North and South America continent longitude (45W). The maximum in ice cloud sky fraction occurs in March, with March 2018 being considerably more intense than March 2017. Consistent with the counteractive nature of the ice/water cloud phase determination, the ice cloud maxima coincide with the prominent breaks in the column of the water cloud sky fraction in March 2017 and again in March 2018. As noted in Figure 9 Top, the ice cloud sky fraction increased by nearly 5% from 2017 to 2018, In contrast, Figure 9 Bottom shows essentially no change in the annual mean of the water cloud sky fraction from 2017 to 2018, though there are substantial changes in the longitudinal distribution of the water cloud sky fraction. There is the appearance of a parallel longitudinal column along the Central Pacific Date Line (0 GMT) with less intensity but greater seasonal variability than along the principal water cloud longitudinal column along 90W (18 GMT). Also of note is the relative minimum in the ice cloud longitudinal column occurring in May of 2017 and 2018 when the DSCOVR Spacecraft is at its northern-most position viewing the maximum in land fraction. During December-

January, when the Spacecraft is viewing maximum ocean fraction (at 0 GMT), the water cloud sky fraction appears to have a local maximum.

Figure 11 Top shows the seasonal variability in ice cloud altitude for the years 2017 and 2018. There is an overall smoothness and symmetry in the seasonal cloud-top altitude change with a broad NH summer maximum occurring in July and a small secondary SH summer maximum in January, with remarkably little change between 2017 and 2018. The Africa-Asia region, as epitomized by India (7 GMT, long-dash magenta) and East Iran (8 GMT, black-dot magenta), has the highest ice cloud altitude. This is followed by East-Asia (3 GMT, green), Pacific (22 GMT, blue), and Atlantic (13 GMT, light blue), with the North America (18 GM, orange) exhibiting the lowest cloud-top altitude. The same longitudinal order holds for 2018, but with some distortion in the winter months.

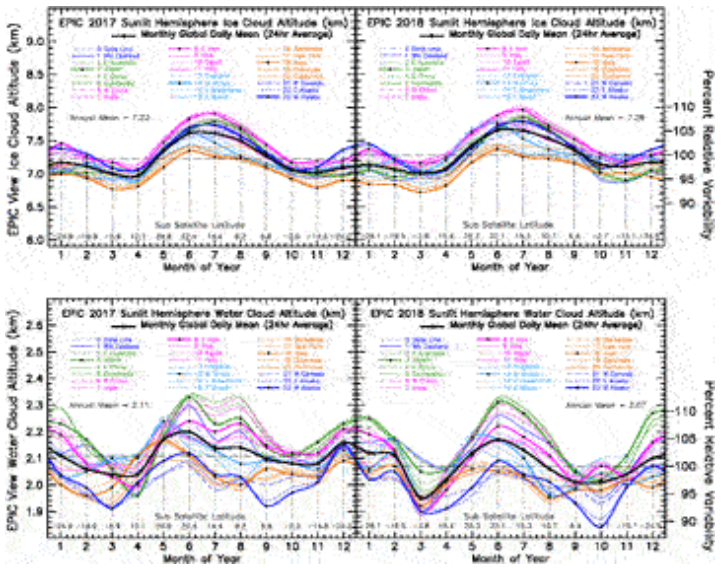

FIGURE 11 | Top Left: Ice cloud altitude from EPIC Composite analysis results for the year 2017, and **Top Right**: ice cloud altitude for the year 2018. **Bottom Panel Left**: Water cloud altitude from EPIC Composite analysis results for the year 2017, and **Bottom Right**: water cloud altitude for 2018.

Figure 11 Bottom shows the corresponding seasonal variability of the water cloud-top altitude, which, in contrast to the ice cloud altitude, exhibits more chaotic variability, especially for year 2017, which has been identified as the La Niña year. The water cloud altitude has a broad NH summer maximum with a secondary SH summer maximum in January, thus exhibiting what appears to be a biannual oscillation in global cloud structure.

The minima in the water cloud-top altitude occur in March-April and in October, which is the same as the ice cloud seasonal pattern. In 2018, the water cloud summer maximum narrows, and the minima become deeper and broader.

The longitudinal ordering of the water cloud-top maximum has East-Asia region as represented by Cambodia (5 GMT, green) and East China (4 GMT, dash green), at top, followed by neighboring West China (6 GMT, dot-dash magenta) and India (7 GMT, dash magenta), with the minima in water cloud altitude occurring over the East Pacific region, as represented by West Alaska (23 GMT, black-dot blue). The raggedness in the 2017 water cloud altitude variability might be indicative of potential La Niña related activity that is not present in 2018, but the ice cloud shows no such change.

Figure 11 shows some traces of low-amplitude 60-days oscillations in ice cloud altitude, at a number of longitudes from October 2017 to April 2018, with many being 180° out of phase with each other. Perhaps the most persistent are the low-amplitude oscillations over the North America region (18 GM, black-dot orange) beginning in April 2017 and continuing through 2018. Figure 11 Bottom shows similar 60-days oscillations at multiple longitudes, but with a somewhat larger amplitude, the most prominent of those being over the longitude range from New Zealand (1 GMT, solid blue) to India (7 GMT, long dash magenta) from June to August of 2017. There are also oscillations in the January-March time period that might be related to the EPIC La Niña planetary albedo variability. In any case, there are far more of the low-amplitude 60-days oscillations in the 2017 water cloud altitude variability than in non-La Niña 2018.

Nevertheless, representing the water cloud altitude variability in Hovmöller format in Figure 12 does not significantly enhance its discrimination capability to distinguish between the 2017 La Niña conditions and the 2018 non-La Niña conditions the same way that the Hovmöller format could enhance the EPIC planetary albedo in Figure 3 relative to Figure 2. The purported La Niña discrimination in Figure 12 Bottom Right panel does exhibit more variability in 2017 than in 2018, but that variability occurs more along the time dimension than in longitude.

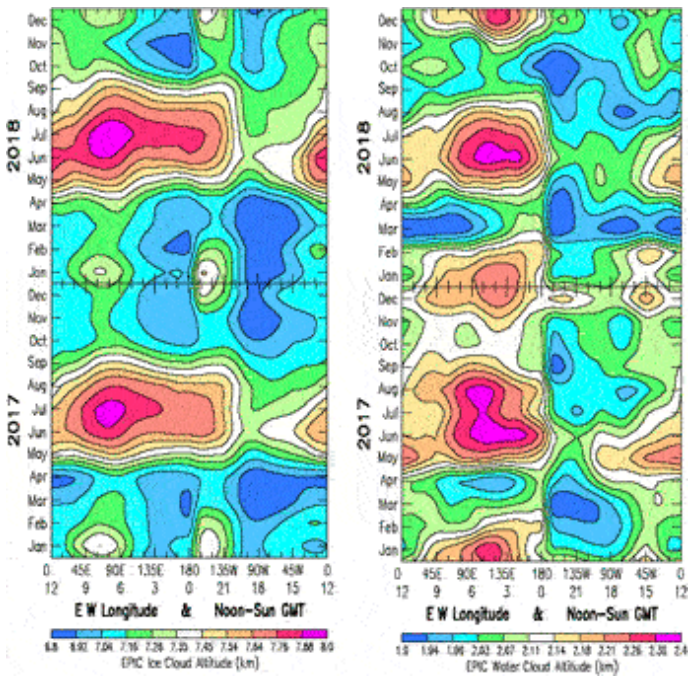

FIGURE 12 | Left: Hovmöller format ice cloud altitude from EPIC Composite analysis results for the year 2018 **(Upper Left)** and 2017 **(Lower Left)**. **Right Panel**: Water cloud altitude from EPIC Composite analysis results for the year 2018 **(Upper Right)**, and for year 2017 **(Lower Right)**.

However, what does seem to be more unusual about Figure 12, is the near-vertical alignment along longitude lines, as well as also the strong seasonal alignment. The ice cloud altitude in Figure 12 Left shows islands of secondary cloud altitude maxima occurring in December-January along the 7-to-8 GMT and the 22-to-23 GMT longitudes. December-January is the time when the EPIC-view is focused most strongly on Antarctica. The 7-to-8 GMT and the 22-to-23 GMT time periods correspond to the longitudes of maximum and minimum planetary albedo in Figure 2 Top, respectively. The seasonal islands of the strong NH summer maxima in 2017 and 2018 both exhibit a steep rise to maximum in May, and an equally steep decline in August-September. There is a similarly steep longitudinal gradient for these NH summer maxima the extends from May on to September at their eastern edge at 120° W longitude, while tapering off more gradually at their western edge, after spanning nearly the entire globe. Broad regions of ice cloud minimum altitude extend from October to April of the following year. They appear to be offset from the longitude of ice cloud maxima by essentially

180°. The ice cloud altitude variability shows little change between 2017 and 2018, except for the increase in June over England (0 GMT).

On the other hand, it is the water cloud altitude (Figure 12 Right) that exhibits the more significant features that differentiate the La Niña year 2017 from 2018. Most noticeable are the 60-days (time dependent) oscillations that occur during March to August of 2017 over a broad swath of longitudes reaching from the Central Pacific to the Indian Ocean (0–9 GMT). These are the same time dependent oscillations that were readily identifiable in the line plot in Figure 11 Bottom. There appears to be some degree of correlation of this time dependent variability of the water cloud altitude with the water cloud sky fraction variability in Figure 9 Bottom Left, and in Figure 10 Bottom Right, but not with the EPIC planetary albedo variability in Figure 3 Bottom Left. Also, the prominent February-March longitudinal variability feature in the EPIC planetary albedo, is absent in the water cloud altitude plot, but still coinciding the overall space-time location of this feature.

There is the additional June-July longitudinal wave feature in Figure 9 Bottom Right, appearing over the Eastern Pacific Ocean with peak-to-peak variability (17–21 GMT) extending over 7,000 km. Similar variability in water cloud altitude also appears in the year 2018 in March-April, also over the Eastern Pacific Ocean region.

However, the most curious feature of the water cloud altitude variability is the apparent longitudinal discontinuity at the 0 GMT Date Line, with the water cloud altitudes rising steeply to the west, and decreasing steeply to the east. If this were really real, it would require an explanation as to the underlying cause. It is also possible that this demarcation might be a selection criteria artifact in the EPIC Composite data matching process that switches between the different LEO/GEO data sources to select the closest match to the EPIC image time and viewing geometry.

The artificial-looking demarcation and longitudinal alignment along the 0 GMT meridian that stands out prominently in Figure 12 Right, is evident, a least to some extent, in previous Hovmöller plots of EPIC data, such as the sharp longitudinal gradient in the planetary albedo near the 0 GMT meridian during January-March of 2018 in Figure 3 Left**,** but is not reproduced in the Hovmöller ratio plot in Figure 4 Left. This appears to be an interpolation bias that arises from interpolating EPIC image data points to a uniform GMT grid. Due to telemetry limitations, there are only 13 EPIC images on some days, instead of the normal 22 images per day, which creates wider data gaps

in the 0 GMT vicinity that need to be bridged. This interpolation bias persists from year to year and appears to be more pronounced for larger gradients near 0 GMT.

The basic objective of the Hovmöller ratio plots is to isolate the atmospheric and cloud property changes that take place between the 2017 (La Niña) and 2018, by removing the common seasonal and longitudinal variability due to the Lissajous orbital perspective, as well as the surface contributions from Antarctica and continental boundaries that undergo little change. In the process, data artifacts common to both years are also eliminated.

The Hovmöller ratio plots in Figure 13 show little evidence of longitudinal demarcation for the EPIC Composite ice cloud and water cloud sky fraction and cloud altitude results from Figures 10, 12. Figure 10, with cloud fraction uniformity near 0 GMT, had little evidence of longitudinal artifacts from the start. The presence of strong cloud fraction gradients and longitudinal artifacts near 0 GMT in Figure 12, and their elimination by the Hovmöller ratioing tends to confirm their nature as interpolation biases.

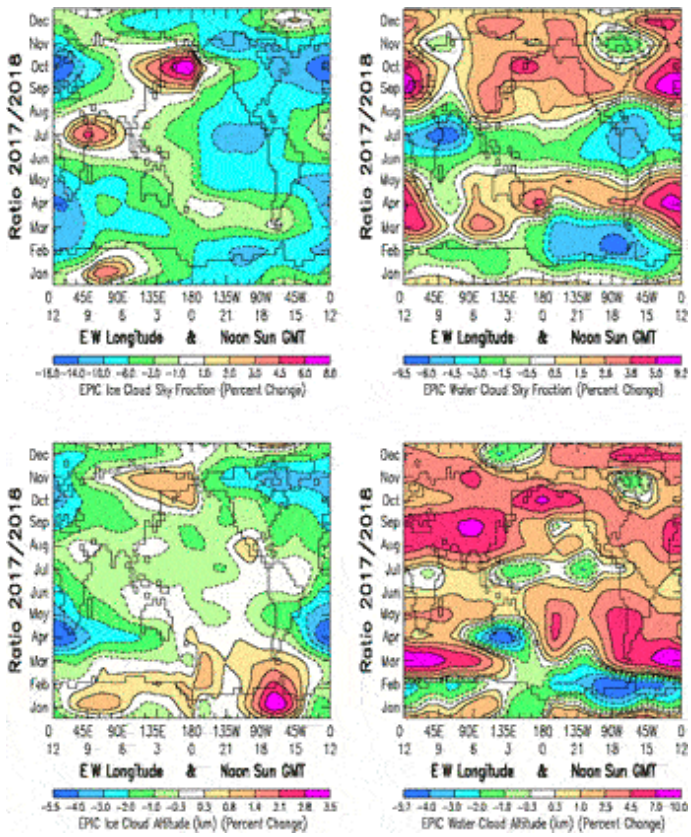

FIGURE 13 | Hovmöller ratio contour plots of the percent change for year 2017 relative to reference year 2018 of the EPIC Composite cloud property data for: **Upper Left**: the ice cloud sky fraction for years 2017/2018 from Figure 10 left; **Upper Right**: the water cloud sky fraction for 2017/2018 from Figure 10 right; **Lower Left**: the ice cloud altitude (km) for years 2017/2018 from Figure 12 left; **Lower Right**: the water cloud altitude (km) for 2017/2018 from Figure 12 right.

The Hovmöller ratio plots for the individual EPIC Composite ice cloud sky fraction and altitude (Figure 13 Left, Top and Bottom), and the water cloud sky fraction and altitude (Figure 13 Right, Top and Bottom), are directly comparable to the Figure 3 EPIC planetary albedo Hovmöller ratio. These four individual cloud components show significant variability and have only several features that coincide with the EPIC planetary albedo features. Moreover, they have but a few features that coincide with each other, and show nothing that might resemble a La Niña signature. Yet, acting together, they must reproduce the space-time variability of the planetary albedo, demonstrating convincingly that independent component comparisons are no substitute for a wholistic quantity.

The Hovmöller ratio plot in Figure 14 Left is the 2017/2018 ratio of the all-cloud EPIC Composite sky fraction from Figure 6 Left, which is also the combined result of the individual ice cloud and water cloud sky fraction components from Figure 13 Top. The EPIC Composite database contains only the all-cloud and the ice cloud components. Given that it is a binary choice for database clouds to be either ice or water cloud, the water cloud variable is defined as a separate entity by the difference between the all-cloud and the ice cloud categories.

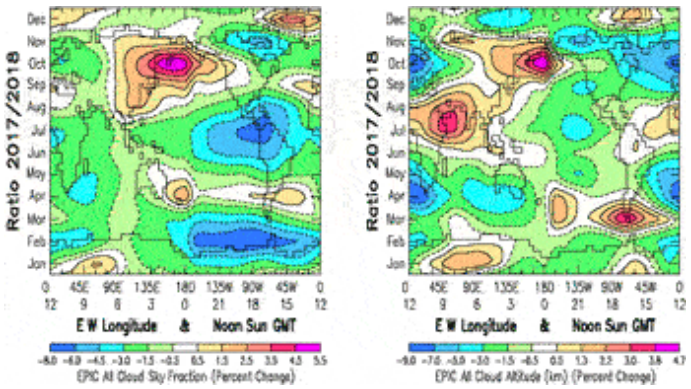

FIGURE 14 | Left: Hovmöller ratio plot of the percent change for year 2017 relative to reference year 2018 for the all-cloud sky fraction, combining the results of the separate ice cloud and water cloud sky fractions in Figure 13, top left and top right, respectively. **Right**: All-cloud sky fraction, combining the results of the separate ice cloud and water cloud altitude in Figure 13, bottom left and bottom right, respectively.

Interestingly, the all-cloud sky fraction ratio in Figure 14 Left compares far more favorably with the EPIC planetary albedo ratio (Figure 3 Left) than the ice cloud and water cloud sky fraction ratios considered separately as in Figure 13 Top. The two most prominent features of the EPIC planetary albedo ratio are the strong February albedo decrease stretching from 180° W to 0° W longitude, and the strong October increase in albedo that stretches from 90° E to 135° W longitude. Both of these year-2017 "La Niña" features are reproduced in the all-cloud sky fraction ratio plot, especially the February strong decrease in sky fraction, also stretching from 180° W to 0° W longitude. Since cloud fraction correlates well with cloud albedo (Bender et al., 2017), these changes in cloud fraction are consistent with the space-time changes in the EPIC planetary albedo variability. However, there is an additional "strong decrease in all-cloud sky fraction" occurring in July from

135° W to 45° W longitude in the all-cloud fraction ratio, which has no similar feature in the EPIC planetary albedo ratio.

Similarly, the all-cloud altitude ratio in Figure 14 Right also compares far better with the EPIC planetary albedo ratio pattern of variability than the separate ice cloud and water cloud altitude ratios shown in Figure 13 Bottom. The improved agreement is not specifically in achieving a closer match-up for the principal features, but rather in a more general alignment of the peripheral pattern of variability surrounding a more or less quiescent Pacific Ocean region during the April to September time period. Since the cloud altitude change by itself has only minimal impact on the planetary albedo, the actual improvements in agreement with the planetary albedo variability patterns must originate from radiative effects that arise from changes in the other accompanying cloud properties. The cloud altitude changes would more directly affect the outgoing LW thermal radiation, which may potentially have its own unique "La Niña" response signature.

Despite the apparent agreement of the all-cloud sky fraction in reproducing the principal February decrease in planetary albedo, there is a potentially significant difference in that the prominent 30° period longitudinal oscillations in the EPIC planetary albedo variability, which, except for the interval from 45° E to 180° E, effectively span the entire globe, but which are not reproduced in the all-cloud sky fraction variability. It may be that the reason for this is due to differences in data resolution. The EPIC planetary albedo, or rather the reflected solar SW radiance measurements at the pixel level are unitary wholistic measurements that record and tabulate the reflected radiances at a high digital resolution. Cloud cover, on the other hand, is the result of a binary decision of clear of cloudy, depending on some arbitrary threshold. There is no way for the retrieval algorithm to know if at the sub-pixel level, the entire pixel is filled with an optically thin cloud, or if it is only a small fraction of the pixel that may contain an optically thick cloud. Thus, it may be that for reflected solar SW radiation, as a unitary wholistic measurement, tiny changes that contain the global-scale oscillation signal can be reliably tabulated and recorded across the entire sunlit hemisphere, whereas such tiny changes that might be present in the different cloud properties, never get a chance to be tabulated by getting wiped out by the clear/cloudy threshold.

From the foregoing, it appears that it may be the unitary wholistic nature of the EPIC radiance measurements that enable the planetary albedo data to

provide the best representation for comparing the year-to-year space-time variability that may be contained within the sunlit hemisphere EPIC measurements. Such comparisons of year-to-year changes in the EPIC data planetary albedo are being examined here to see if characteristic differences can be identified between 2 years of data, such as the 2017 La Niña year and 2018, which is representative of more ENSO-neutral conditions. While cloud radiative properties may be the fundamental building blocks of the planetary albedo, cloud properties do not vary lockstep as clouds change in the climate system. Thus, selection of a cloud property to serve as an indicator in the year-to-year comparisons does not lead to greater clarity in interpretating the comparison results, but rather serves to magnify the diversity of the different cloud property radiative effects. Knowing quantitatively how the different cloud properties contribute toward the planetary albedo is important in itself, but the planetary albedo is also robust as a measure of the Earth's global energy balance.

The changing DSCOVR-view Lissajous orbital perspective of the EPIC data is a significant contributing factor to the seasonal and longitudinal variability that is seen in the longitudinal slicing comparisons of EPIC and ModelE2 data. Averaging data over the Earth's sunlit hemisphere averages out meteorological weather noise as well as the latitudinal and longitudinal information. The rotation of the Earth retrieves the longitudinal component of the planetary scale variability via longitudinal slicing. Likewise, some significant fraction of the latitude dependent information is retained by the combined change in solar declination and the Lissajous orbital motion of the DSCOVR Satellite as depicted by the sub-satellite latitude at figure bottom (Figure 15 Top) that is varying from its southern extreme position in January, to its northern extreme in May, and then back to its southern extreme in December.

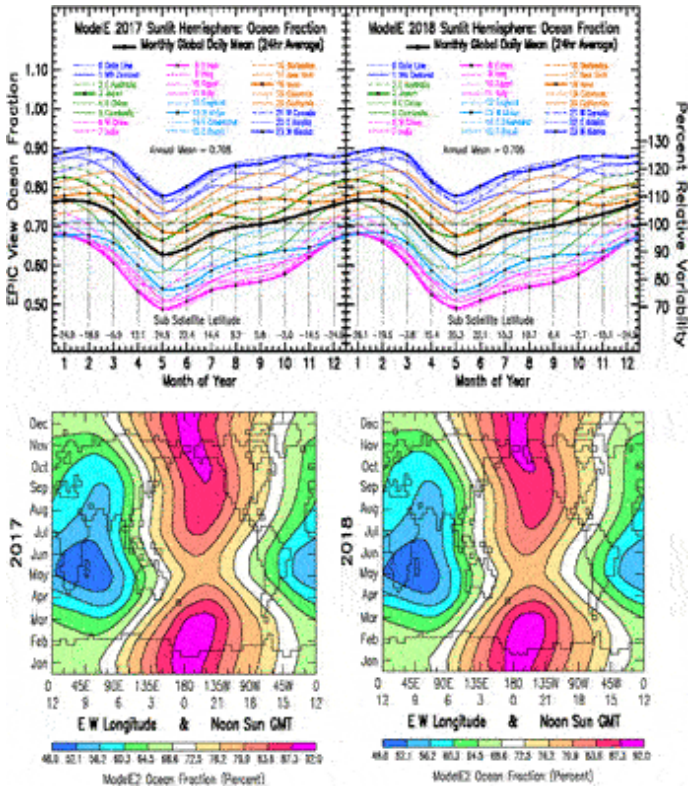

FIGURE 15 | Upper Left: Line plot of the ModelE2 ocean fraction for the year 2017. **Upper Right**: Line plot of the ModelE2 ocean fraction for the year 2018. **Lower Left**: Hovmöller contour map of the ModelE2 ocean fraction for year 2017. **Lower Right**: Hovmöller contour map of the ModelE2 ocean fraction for year 2017. The seasonal change in ocean fraction is due to the DSCOVR Spacecraft Lissajous orbital motion as denoted by the Sub-Satellite latitude at figure bottom. The tiny differences in the line and Hovmöller plots between years 2017 and 2018 arise from the slow orbital drift of the DSCOVR Spacecraft in its Lissajous orbit.

The land/ocean fraction is another significant contributor to the seasonal and longitudinal variability in the longitudinal slicing comparisons of EPIC and ModelE2 data. Except for a small seasonal change in sea ice, the ocean fraction is static in time. Hereby, we identify and quantify the net effect that these otherwise invariant contributors have on the line format and Hovmöller contour map comparisons between the EPIC observational, and the ModelE2 climate GCM results for planetary albedo and cloud properties.

Figure 15 Top is the line plot of the (static) ocean fraction for years 2017 and 2018. As to be expected, the Pacific Ocean region (black-dot blue) corresponds to the largest ocean fraction, and the Africa-Asia region (black-dot magenta) the smallest with the Atlantic region (black-dot light blue) nearby. The East Asia (green) and the North and South America regions

(orange) undergo significant seasonal variability, showing time dependent oscillations of 4-to-6 months duration, in particular during the July to November time frame. More importantly, the dayurnal and seasonal variability of the ocean fraction does not generate the higher frequency 60–90 days oscillations that are abundantly present in the EPIC planetary albedo and cloud property data.

Figure 15 Bottom shows the Hovmöller contour map of the (static) ocean fraction for year 2017 (Left) and for 2018 (Right). The objective of these plots is to show that while the seasonal effects of the Lissajous orbital and solar declination motion are significant, the effect of the year-to-year Lissajous orbital shift is practically imperceptible. The minimum ocean fraction occurs in May over Iraq (9 GMT). With world map superimposed, the time dependent oscillations in the line plot are visible in the East Asia region from May to September, as is the constriction in ocean fraction near the 0 GMT Date Line. No longitudinal oscillations are discernable.

DISCUSSION

The current model/data comparison study arose from a brute-force effort to calibrate the NISTAR Band-B full-disk sunlit hemisphere measurements. Fully calibrated; with the ability to reliably convert near-backscattered radiances into SW fluxes, NISTAR data would, on their own, be able to reproduce the EPIC planetary albedo results in Figures 2, 3. To this end, Su et al. (2018) converted the EPIC image 1024 × 1024 narrow-band, backscattered radiances into the 12 × 24 tables of monthly-mean, SW reflected hemisphere-mean fluxes for years 2017 and 2018, that constitute the planetary albedo comparisons of this study.

Spectral radiances from 5388 EPIC images for 2017, and 5,351 for the year 2018 were processed and converted into the 12 × 24 (monthly-mean, GMT-hourly) tables of reflected SW fluxes. The EPIC-viewable sunlit-hemisphere fractions generated annual-means of 204.63 and 202.90 Wm^{-2}, respectively, with ~ 1.0 Wm^{-2} standard deviation. The EPIC Composite cloud properties have similar data reliability out to the third decimal. Because of Lissajous orbital motion, the EPIC-viewable fraction of the sunlit disk varies from ~ 92 to ~ 97 percent of the full disk, introducing some uncertainty as to the total full disk reflected radiation. Accordingly, both the EPIC and the ModelE2 annual-mean planetary albedo have been normalized to the 29.1%

CERES value (Loeb et al., 2018) to focus more on comparing the space-time patterns of variability rather than interannual change.

Moreover, it is important to note that planetary albedo contains both atmospheric and surface contributions. The DSCOVR vantage point combined with the seasonal change in the tilt of the Earth's rotational access results in a time changing contribution from the polar regions which maybe further enhanced in the EPIC observations due to the backscatter viewing geometry. Explicit treatment of the scattering enhancement at near back-scattering angles introduces an uncertainty in both the calculation of the shortwave flux from the EPIC observations and the model. Thus, while the signature of these surface contributions is apparent in the figures shown in this paper, quantitative evaluation of these surface driven model/observation differences requires additional research and is beyond the scope of this investigation. To ensure that we are not mixing this type of surface contribution into our analysis, we examine the ratios two individual years since orbital and surface contributions will be minimized allowing us to focus on the atmospheric changes.

With quasi-chaotic meteorological weather-scale noise averaged out, the EPIC and the similarly sampled ModeE2 data are uniquely positioned for a climate-style model/data comparison with excellent space-time data sampling self-consistency. EPIC image acquisition on the near-hourly basis coincides closely with the climate GCM (GISS ModelE2) 1-h radiation time-step radiation calculations that are performed 'instantaneously' for all GCM grid boxes.

The only real requirement on the part of the GCM in the sunlit hemisphere averaging of output data, is to use Solar and DSCOVR Satellite Ephemeris information to impose Lissajous orbital viewing geometry and projected area weighting of the individual grid box contributions to the sunlit hemisphere average. All this ensures that the diurnal cycle is sampled the same way by the GCM as by EPIC, with high noon sub-satellite meridian, and sliding noon-to-dusk, and noon-to-dawn, diurnal contributions from neighboring longitudes to east and to the west, properly aggregated.

In this way, weather noise and the latitudinal and longitudinal dependence in the sunlit hemisphere are averaged out. Differences in spatial resolution between the EPIC and GCM data are similarly side-stepped. Remaining in the data is the seasonal and planetary scale variability. Longitudinal dependence is made accessible by the rotation of the Earth.

Some latitudinal dependence is captured by the seasonal change in solar declination and also as a result of the Lissajous orbital motion of the DSCOVR Satellite.

The Figure 2 line plots are the first longitudinal slicing EPIC and ModelE2 planetary albedo comparisons, showing the seasonal change in dayurnal variability of the planetary albedo in 1-hourly time-steps as the Earth rotates. The immediate take away of this comparison is that while the overall envelope of planetary albedo variability is comparable, the ModelE2 dayurnal amplitude is too large during the northern hemisphere (NH) summer months and too small during the winter months, and it is only during the winter months that the longitudinal ordering of the dayurnal variability matches that of EPIC.

The biggest mismatch is that during the NH summer months, ModelE2 significantly overestimates the planetary albedo, hence clouds, over the ocean areas, and underestimates clouds over the continental land areas. This was a problem stemming from the use of a globally uniform relative humidity threshold in ModelE2 that the GISS GCM modeling group had been aware of, and have already implemented a rigorous physics-based cloud treatment for the GISS ModelE3 version. The Figure 2 comparison makes this a quantitative climate GCM performance diagnostic showing the largest overestimate to be over the East-Asia region (3 GMT, black-dot green line), while the EPIC data show t the maximum NH summer planetary albedo to be occurring instead over the continental Africa-Asia region (8 GMT, black-dot magenta line).

The model used in this study was the GISS coarse-grid coupled atmosphere-ocean 4° x 5° ModelE2 version (Schmidt et al., 2014), utilizing a mass-flux cumulus parameterization that is based on a cloud base neutral buoyancy flux closure originally described by Del Genio and Yao (1993), with stratiform clouds based on a Sundqvist-type prognostic cloud water approach, with diagnostic cloud fraction (Del Genio et al., 1996). Tuning is used to bring the empirical parameterizations of physical processes in acceptable agreement with observations (Schmidt et al., 2017). This involves establishing a critical relative humidity criteria for the onset of cloud condensation in a GCM grid box, based on the statistical overlap of water vapor and temperature probability distributions to achieve relative humidity conditions for cloud condensation.

Replotting the planetary albedo data in Hovmöller format in Figure 3 Left produced an unexpected result by bringing out detail in the EPIC planetary albedo variability that was not apparent in the Figure 2 line plots. It turns out that there is far more of the characteristic (monthly, and 30° longitude) variability in planetary albedo in year 2017, compared to the more quiescent appearance in 2018. Most notable it the strong decrease in planetary albedo during February 2017 over the Central Pacific Ocean longitudes.

This difference in planetary albedo variability between the years 2017 and 2018 is further enhanced and isolated to atmospheric changes by the 2017/2018 Hovmöller ratio plot in Figure 4 Left, by canceling out the seasonal variability patterns that are common to both years (e.g., the surface contribution from Antarctica shown by the magenta areas in Dec/Jan evident in the upper left of the two right panels of Figure 3). The sharp February decrease in the EPIC planetary albedo stretches from 180° W to 0° W longitude, which exhibits superimposed (30° extent) longitudinal oscillations. There is also a strong October increase in the planetary albedo that stretches from 90° E to 135° W longitude.

Year 2017 has been identified as a La Niña year (Zhang et al., 2019), which is typically associated by the appearance of colder sea surface temperatures (SSTs) in Central and Eastern Pacific, with strong winds blowing ripples of warm water westward. Thus, there is reason to associate the increased variability in the EPIC planetary albedo occurring in the year 2017 relative to 2018 with ongoing La Niña activity. Since clouds are principal contributors to planetary albedo, it then becomes pertinent to investigate is there are characteristic cloud changes that might be associated with La Niña conditions. This is where the EPIC Composite database of cloud properties generated in the Sue et al. (2018) conversion of the EPIC spectral radiances into radiative SW fluxes, provide the essential context of how the cloud radiative properties might have changed between the 2017 La Niña year and 2018.

Figure 5 Top shows a 1.5% increase in the EPIC all-cloud sky fraction, with most of it occurring in March of 2018, and some in December of 2018. Also, Figure 7 Top shows the corresponding increase by 1.3% in the all-cloud cloud-top altitude. The EPIC Composite database breaks down of the cloud properties into ice and water cloud categories. Thus, Figure 9 shows the ice and water cloud changes in cloud fraction to be a 4.8% increase for

the ice cloud fraction, and a 0.25% decrease for the water cloud fraction in going from 2017 to 2018. Similarly, Figure 11 shows the ice cloud altitude increasing by 0.7%, and the water cloud altitude decreasing by 1.9% from 2017 to 2018.

Hovmöller contour plots of the EPIC cloud property variability for years 2017 and 2018, along with the corresponding ModelE2 cloud property variability, are shown in Figure 6 and Figure 8 for the all-cloud sky fraction and the all-cloud altitude, respectively. There is general agreement between the EPIC and ModelE2 cloud fraction variability, although impacted by the ModelE2 longitudinal land/ocean cloud distribution differences relative to the EPIC data. However, the all-cloud altitude comparison in Figure 8 shows an eastward shift by ~ 45° in longitude of the longitudinally aligned all-cloud altitude maximum and minimum all-cloud altitude ridges in the ModelE2 data compared to EPIC. It is possible that this might also be related to the ModelE2 land/ocean cloud distribution problem.

However, the apparent shift by nearly 90° between the EPIC ice cloud and water cloud longitudinal sky fraction distribution maxims and minima locations in the Figure 10 Hovmöller plots could well be real, since the cloud ice and water phase separation in the EPIC Composite database is a binary differentiation. On the other hand, the apparent longitudinal demarcations in the Figure 12 Hovmöller plots along the 0 GMT meridian for the ice and water cloud altitude, in both 2017 and 2018, appear to be interpolation artifacts arising from interpolation between sparse EPIC data points in the 0 GMT vicinity where wider data gaps exist due to telemetry limitations. The fact that these longitudinal discontinuities are all eliminated in the Figure 13 by the Hovmöller 2017/2018 ratio plots, which cancel out any variability that is common to both years.

The Hovmöller ratio plots in Figure 13 for the ice and water clouds properties and Figure 14 for the all-cloud cases, of year 2017 relative to 2018, are designed to extract changes in cloud properties of the 2017 La Niña year relative to 2018 ENSO-neutral conditions. These Hovmöller ratio plots, along with the Figure 4 Left Hovmöller ratio plot of the EPIC planetary albedo, describe the relationship of planetary albedo, and the La Niña impact, with respect to variability changes in Earth's global energy balance, where the planetary albedo has a unitary wholistic relationship to the global energy balance, and so apparently does the La Niña impact. This makes the planetary albedo an adequate representative of the La Niña

impact, and thus a convenient indicator of La Niña activity. Individually, cloud properties are only partial contributors to the planetary albedo, and thus can only account for a part of the La Niña impact on planetary albedo, and in proportion to their contribution.

Thus, the all-cloud sky fraction Hovmöller ratio in Figure 14 Left shows remarkable similarity to the EPIC Hovmöller ratio in Figure 4 Left, in agreement with the Bender et al. (2017) results that show a close relationship between cloud fraction and cloud albedo. The all-cloud altitude Hovmöller ratio in Figure 14 Right also shows some similarity to the EPIC Hovmöller ratio results, even though the cloud altitude, by itself, makes no significant contribution to the planetary albedo. The cloud altitude is however a principal contributor to the outgoing LW thermal radiation. Hence, the reason for the similarity of cloud altitude Hovmöller ratio to the planetary albedo variability must be implicit though its LW thermal impacts, which are not addressed in this study.

On the other hand, the Hovmöller ratio plots in Figure 13 show little resemblance to the EPIC Hovmöller ratio in Figure 4 Left, thus confirming their role as minor independent contributors to the EPIC planetary albedo, or as indicators of La Niña activity. Still, like the planetary albedo, they continue to have their unique role as observational constraints in climate GCM diagnostic comparisons. But even in this role, the contributing constituents are not equal. Having precise self-consistent space-time sampling is not enough. There must also exist a close agreement in the physical definition of the climate variables that are being compared in the longitudinal slicing comparisons between the observational retrieval results and their corresponding climate GCM equivalents.

Cloud fraction and cloud-top altitude are undoubtedly the most robust of the cloud properties, as has also been corroborated by the intercomparison of the principal satellite and ground-based cloud datasets using comprehensive spectral analysis techniques (Li et al., 2015). Yet even for these cloud properties, there are substantial issues regarding the self-consistency of the operational definition of these quantities between observational limitations and climate GCM representations. For example, in observational retrievals, arbitrary thresholds are involved in deciding whether a given pixel might be mostly clear or cloudy, or if some optically thin atmospheric layer is really a cloud, or an aerosol.

Thus, the EPIC/ModelE2 cloud fraction and cloud altitude comparisons are only partially successful due to threshold and physical definition differences that still persist in the comparisons. The large difference in cloud-top altitude in Figure 7, where the ModelE2 mean cloud altitude is ~ 7 km, compared to ~4 km for the EPIC results, is one such example. The cloud-top altitude in satellite retrievals is typically determined by the pressure level where the cloud optical depth is unity. In ModelE2, the pressure level of the top-most cloud is known precisely. But that top-most cloud is often an optically thin cirrus cloud that might not even be recognized as a cloud in satellite retrievals. Knowing whether the cloud altitude is being defined relative to sea level, or to the surface topography is another source of uncertainty.

The cloud water/ice phase is another important cloud property in tracking the dynamically active storm regions that are typically accompanied by the presence of ice clouds. However, the ice cloud identification, by means of cloud-top temperature, or other means, refers only to the cloud-top region, with no information available on the rest of the cloud structure. Thus, whatever is inferred at the top-cloud level, is what is used to separate the all-cloud sky fraction into its ice cloud and water cloud components. Differentiating clouds from aerosol also impacts the cloud fraction definition.

In ModelE2, differentiating between clouds and aerosols is no problem. However, as for the ModelE2 cloud fraction, clear and cloudy grid-boxes are accurately tabulated. But, ModelE2 uses a fractional-in-time *vs* fractional-in-space cloud radiative fraction definition that go back to the early days of GCM development (Hansen et al., 1983) whereby (to save computing time) grid-box level fractional clouds are interpreted as being fractional-in-time with a random number selection deciding when to perform radiative calculations (with 100% cloud cover). On a monthly-mean basis, the fractional-in-time approach achieves the same effective cloud fraction as the fractional-in-space approach, but at a significantly reduced computing cost.

The cloud optical depth and cloud particle size are the more difficult cloud properties to determine by remote sensing. Optical depths for ice clouds in particular are difficult to retrieve from remote sensing radiance measurements. The radiative transfer calculations are tractable only for plane-parallel geometry and for homogenous clouds, thus requiring numerous approximations and assumptions. Also, ice clouds come in many shapes and sizes that range from rosettes to columns to oriented flat plates.

The cloud properties from EPIC cloud composite data are compiled from multiple GEO and LEO imagers (Minnis et al., 2008, Minnis et al., 2021), and are dominated by GEO contributions because they are most closely matched to the EPIC image time especially within 60°S-60°N. Thus, the cloud properties within EPIC cloud composite data are subject to changes in GEO imagers that occur from year-to-year, as in early 2018, when Meteosat-10 switched to Meteosat-11, and GOES-13 switched to GOES-16. Since these changes in GEO imagers also involve retrieval algorithms, some of the changes in cloud properties between 2017 and 2018 could be due to changes in GEO imagers and algorithms.

The EPIC Composite cloud optical depths and particle sizes show suspiciously large discontinuous decreases between 2017 and 2018. Also, the physical definition of the cloud optical depths and particle sizes between the EPIC Composite cloud data and ModelE2 results differ significantly. Accordingly, we have not included these cloud properties in the EPIC/ModelE2 comparisons.

We have examined this type of problem previously by using empirical orthogonal function spectral analysis techniques (e.g., Li et al., 2015 for cloud properties; and Li et al., 2014a, Li et al., 2014b for aerosol space-time variability), which are specifically designed to quantitatively establish correlations, and to identify and quantify data artifacts in global datasets that may arise from calibration and algorithm changes. The Li et al. (2015) study verified that cloud fraction and cloud-top altitude variability was robust among the different cloud property determinations, but that the cloud optical depth and cloud particle size determinations were problematic. Such spectral analysis techniques should also be applied to the EPIC composite cloud property data, especially since they are all independently retrieved, to identify possible data artifacts.

Also relevant to the 2017 La Niña is the finding by Loeb et al. (2021) of a decrease in the Earth's absorbed solar radiation by about 0.8 Wm^{-2} going from 2017 to 2018 (which translates to a global-mean planetary albedo increase by about 0.23% in going from 2017 to 2018). Loeb et al. attribute most of the global decrease in absorbed solar radiation to clouds, noting that the Niño 3.4 SST index was decreasing in 2017, and increasing during 2018. The EPIC Composite all-cloud sky fraction increase by 1.5% is fully consistent with an increase in planetary albedo. The increase in all-cloud altitude by 1.3 % would have no significant impact on the planetary albedo.

But the possible decrease in the cloud optical depth, if true, would imply a planetary albedo contribution in the downward direction.

On the climate GCM side of the ledger, a basic closure exists naturally since the GCM planetary albedo automatically includes the radiative contributions from all contributors from the ground on up. Moreover, the GCM explicit radiation modeling capability would make attribution calculations possible, which would make the model/data comparisons a two-way street. But there too many missing pieces of information from the observation side to make reliable closure calculations a reality.

For successful longitudinal slicing comparison, the key factors that assure self-consistent space-time sampling are to replicate the viewing geometry of the DSCOVR/EPIC imaging of the Earth's sunlit hemisphere in the GCM output data sampling, and to align the timing of the model/data comparison for the same identical GMT longitudinal sequencing. Also, the closer the match between the model and data of the physical definition of the variable that is being compared, the more effective the comparison. But there is also a more subtle factor, and that is a numerical detail in how the integration over the sunlit hemisphere is performed. As a case in point, there is a large difference in planetary albedo between EPIC and ModelE2 during December-January when the DSCOVR view is turned most strongly toward the Antarctic ice cap. Both Figures 2, 3 show the ModelE2 albedo in this region to be significantly lower than that of EPIC. Does this mean that the surface albedo of Antarctica in ModelE2 is much too low, or is EPIC overstating the Antarctic contribution? The Hovmöller ratio plot in Figure 4 does not show any interannual variability, suggesting either a surface contribution, or artifact in the model, or data processing, common to both years, that cancels out in the Hovmöller ratio.

The most plausible explanation is some mismatch in the sunlit hemisphere integration. Once the EPIC image pixels and GCM grid boxes corresponding to the DSCOVR-view geometry are determined, how specifically the integration over the viewable area is performed is not a sensitive issue, as long as it is the same for both EPIC and ModelE2. This may not be the case and could be further investigated by comparing the EPIC sunlit hemisphere-mean to the NISTAR full-disk measurements, since NISTAR sees the sunlit hemisphere as a projected area. Still further, there is also a small correction to the viewable fraction of the sunlit hemisphere due to the changing Earth-Satellite distance because of the radial component of

the Lissajous orbital motion. Being beyond the scope of this investigation, these details will be examined in future studies of EPIC and NISTAR data comparisons.

LOOKING AT DATA: WHAT IS THERE TO SEE?

Different views of data stem from different capabilities and point to different objectives to extract information that may be submerged. The relatively coarse (4° x 5°) resolution planetary albedo and cloud cover maps of the GISS ModelE2 in Figure 1, and of the corresponding observational data, illustrate the qualitative nature of these comparisons. Nevertheless, they demonstrate the fact that climate GCMs, like the real world, operate in quasi-chaotic fashion. Not shown are the 1024 × 1024 higher resolution full-disk EPIC images of the sunlit hemisphere of the Earth, which are all readily available on the internet at https://epic.gsfc.nasa.gov.

No two EPIC images are alike. They show the evolving quasi-chaotic nature of the climate system. Figure 1 Bottom addresses the energy balance of the climate system in response to the seasonal changes in solar radiative forcing, but only in a global-mean sense. This is where the unique DSCOVR Mission viewing perspective makes significant improvement in model/data comparison possible.

For Figures 2, 3, the input data are identical, i.e., the same 12 × 24 monthly-mean tables of the longitudinally sliced, climate-quality planetary albedo with the weather noise averaged out. The plotted results look very different, but are complementary. They show different aspects of the climate system variability with optimized focus directed to isolating these different aspects.

The important feature in the Figure 2 line plots is the quantitative nature of comparison for the seasonal dependence of the dayurnal amplitude variability. In Figure 2, there are 24 color-coded curves, one for each hour of GMT, or every 15° of longitude (far beyond the canonical line limit that can be counted on the fingers of one hand). These longitude curves are grouped into five contiguous regions, with individual liens further differentiated by their line structure, and tagged by a geographic location in addition to their GMT tag. The results show that the highest planetary albedos occur over the Western China to Egypt (6–10 GMT, magenta) region during NH summer months, while the GISS ModelE2 has the highest planetary albedos occurring over the East Asia and Western Pacific (2–5 GMT, green) region,

implying unequivocally that MoelE2 overestimates clouds over the ocean areas, while underestimating clouds over the continental land areas.

The Figure 5 EPIC cloud fraction line plot shows low amplitude oscillations for virtually the entire year of 2017 to February 2018 over the Central Pacific (23 GMT, black-dot blue line), and perhaps also over the Indian Ocean (8 GMT, black-dot magenta line). Also noticeable are the October 2017 to October 2018 cloud fraction oscillations over the North America longitudes (18 GMT, black-dot orange line). The EPIC cloud altitude plot in Figure 7 also exhibits low amplitude oscillations from roughly October 2017 to June 2018 at nearly all of the longitudes. Most prominent are the December 2017 to April 2018 oscillations over Japan (3 GMT, black-dot green line) and West Africa (13 GMT, black-dot light blue line) that are virtually 180° out of phase.

This is where the Hovmöller (1949) contour maps demonstrate their worth. They are designed to display and study the principal patterns of the climate system variability by averaging out the latitudinal dimension over its range, and plotting the results as contour maps with time running downward along the *Y*-axis, and with the *X*-axis displaying the longitudinal dependence. The EPIC data also get averaged over the longitudinal dimension in the sunlit hemisphere averaging (which eliminates the weather noise). But the rotation of the Earth preserves the longitudinal dependence of the large intra-seasonal changes that occur in the climate system. By accounting explicitly for the longitudinal location of the same 12 × 24 data points used in the Figure 2 line plots, a remarkably different picture emerges in the Figure 3 Hovmöller contour maps for the 2017 and 2018 planetary albedo variability. There is now a much more structured difference in the EPIC seasonal variability of planetary albedo that clearly differentiates the 2017 La Niña year from the more quiescent variability that is the characteristic norm for 2018.

The Hovmöller ratio plots in Figure 4 cancel out the basic seasonal climatological variability to further isolate the La Niña signature. This clearly identifies February over the Central Pacific (21–24 GMT), and October over the Western Pacific Ocean (0–5 GMT), as the months exhibiting the largest change in planetary albedo based on the EPIC data.

The EPIC data are unique in several important ways. First, the EPIC measurements from the DSCOVR mission vantage point at the Lagrangian L1 point provide a clear view of the Earth's sunlit hemisphere, including a

full view of the daytime diurnal cycle of cloud changes across the entire sunlit hemisphere. Second, the EPIC backscattered spectral radiance measurements are highly leveraged against other more specialized satellite data sources. The internal information content of the EPIC spectral radiances is not sufficient to deduce full-spectrum radiative fluxes and cloud properties from just the internal information, but it has been more than sufficient to successfully select and incorporate the ancillary satellite data to generate a physically more complete EPIC data product. As a result, it makes sense to analyze together the EPIC planetary albedo and the EPIC composite cloud products since they are intimately related, though not on a closure basis, as would be the case for the MoelE2 counterparts.

SOME FUTURE CONSIDERATIONS

It has been known since the early days of satellite measurements that, on an annual basis, the reflected solar SW radiation from the Northern and Southern hemispheres is nearly identical despite the large difference in the hemispheric land-ocean distribution (Vonder Haar and Suomi, 1971). Given the major differences in land-ocean surface albedo, this implies significant compensation by the climate system in order to achieve the hemispheric symmetry in reflected solar SW radiation. This SH-NH hemispheric conundrum has been further analyzed and quantified (e.g., Voigt et al., 2013, Voigt et al., 2014; Stephens et al., 2015). The Bender et al. (2017) analysis, based on 13 years of CERES and MODIS data, finds differences in tropical, subtropical, and midlatitude cloud fraction, as well as cloud albedo distributions that exhibit zonal dependence.

As amply demonstrated, the longitudinal slicing of the EPIC cloud fraction and planetary albedo data retains the longitudinal and intra-seasonal variability. Integration over the sunlit hemisphere to suppress the weather noise, has also averaged out latitudinal information. However, much of that latitudinal information can be retained by piecewise integration over the sunlit hemisphere, setting up, as a minimum, longitudinal slicing over the southern and northern hemispheres, and preferably, with even higher zonal resolution.

The sunlit hemisphere data sampling could also be conducted separately over specified land and ocean regions for a more precise characterization of the differing cloud property and radiative flux correlations over land and ocean areas noted by Stephens et al. (2015). With such coordinated data

sampling between EPIC and the GCM, the self-consistent space-time sampling will provide a more quantitative assessment of cloud interactions in the climate system.

As another significant topic, ice clouds tend to have a bi-modal distribution in optical depth, given that they are associated both with the dynamic meteorological activity, and also with fair-weather conditions. This typically involves large optical depths in the former case, and small optical depths in the latter. Since all-cloud optical depths are available at the EPIC Composite data level, separating the ice clouds into their small optical depth ($\tau < 1.0$) fair-weather cirrus categories, and large ($\tau > 1.0$) optical depths characteristic of storm systems, should be feasible. Such considerations are equally applicable for separating ice cloud optical depth categories in the climate GCM output data.

From the GCM perspective, virtually all of the climate diagnostic variables are available for sunlit hemisphere sampling. The sunlit hemisphere averaging and longitudinal slicing offer a unique and quantitative way to compare directly the space-time variability of climate system variables with their observational counterparts on regional and planetary spatial-scales, as well as intra-seasonal and inter-annual time scales.

Longitudinal data slicing provides a convenient platform with a uniform perspective for a broad range of climate GCM performance assessments, including model numerics. Would ModelE2, using a higher horizontal resolution of 1° x 1°, fare better than the current 5° x 4° version? Or the GISS ModelE2.2 version, with more than double the vertical resolution, that is optimized for middle atmosphere simulations (Rind et al., 2020)? For the rectangular grid, polar grid-boxes become smaller than those along the equator, with undesirable dynamic consequences. As a potential remedy, there is also the GISS icosahedral grid (Russell et al., 2018), which utilizes equal-sized triangular grid-boxes. Basically, the SHS DSCOVR-view sampling can be implemented in any climate GCM setting to accumulate a year's worth of longitudinal slicing data.

CONCLUSIONS

This paper describes a new model/data comparison technique that uses sunlit hemisphere averaging to average out the weather-scale noise, and longitudinal slicing by the rotation of the Earth, to conduct self-consistent space-time sampling of observational and model-generated data. For

observational data this comparison technique uses EPIC images of the sunlit hemisphere of the Earth collected by the DSCOVER Mission spacecraft from its Lissajous orbit around the Lagrangian L1 point. The climate GCM comparison data are similarly compiled, using identical space-time sampling, based on DSCOVR-view viewing geometry, to aggregate GCM diagnostic output data over the Earth's sunlit hemisphere for the longitudinal slicing comparison. The standard line plots and Hovmöller contour maps bring out the different aspects of variability that are present in the same hemisphere averaged input data.

Comparison of the seasonal and dayurnal variability of Earth's planetary albedo derived from EPIC measurements with the GISS ModelE2 generated planetary albedo shows unequivocally that the GCM results are significantly overestimating cloudiness over ocean areas, while underestimating clouds over the continental land areas. The longitudinal slicing comparison also shows that the overall seasonal dayurnal amplitude of the daily-mean planetary albedo of ModelE2 is less than half of the EPIC planetary albedo, but that during the northern hemisphere winter months, the GCM does reproduce the longitudinal ordering and the seasonal slope of the EPIC planetary albedo variability.

With the weather-scale noise averaged out, seasonal line plots and Hovmöller contour and ratio maps of the EPIC longitudinal slicing data for the years 2017 and 2018 appear to detect 60–90 days Madden-Julian-type (MJO) oscillations within the planetary albedo variability patterns. The most notable in the 2017/2018 Hovmöller ratio map is the stand-alone feature of a sharp decrease in planetary albedo that appears in February-March 2017 over Central Pacific longitudes, exhibiting longitudinal oscillations that are 30° in extent, spanning ~ 3,000 km peak-to-peak, in strong support of identifying 2017 as an active La Niña year.

EPIC planetary albedo data, augmented by the EPIC Composite database, form a solid foundation for a unique type of model/data comparison. Sunlit hemisphere-averaging removes weather-scale noise, allowing model/data comparisons to target planetary-scale variability. Currently, the EPIC Composite database contains cloud property information for cloud fraction, altitude, optical depth, and particle size, as well as water/ice phase, which can be compared to climate GCM equivalents in longitudinal slicing comparisons with self-consistent space-time and diurnal sampling.

In the current configuration, the longitudinal slicing is applied to data that have been averaged over the entire sunlit hemisphere. Aside from averaging out the weather-scale noise, the hemispheric averaging also averages out the latitude and longitude dependent information. The longitudinal slicing approach is able to retrieve not only the longitudinal dependence of climate system variability, but it also has the flexibility to accommodate conducting the sunlit hemisphere averaging with specified latitudinal resolution to retain separately the seasonal variability information over the northern and southern hemispheres.

Furthermore, the sunlit hemisphere sampling is also flexible enough to sample data separately over continental land and ocean regions, enabling self-consistent space-time characterization of global-scale cloud properties separately over land and ocean regions. Including these improvements, as well as adding additional climate system variables to compare, will greatly enhance the utility of the longitudinal slicing approach as a new model/data comparison tool for climate system analysis.

DATA AVAILABILITY STATEMENT

The EPIC data used here are available from the Langley DAAC.

AUTHOR CONTRIBUTIONS

BC and AL developed the concept for the longitudinal slicing of hemisphere-mean data and the Hovmöller representation of EPIC cloud products. AL and GR developed the Sunlit Hemisphere Sampling (SHS) coding. GR coded and ran the ModelE2 SHS simulations. WS converted EPIC spectral radiances into radiative fluxes and produced the hemisphere-mean tables of EPIC SW flux and the composite cloud properties. AM assisted with DSCOVR Ephemeris data, and provided insight on topical emphasis and relevance to DSCOVR Mission objectives. BC, AL, GR, WS, and AM wrote and edited the text. AL made most of the figures.

FUNDING

Funding for this investigation has been provided by the NASA DSCOVR Project through WBS grant 437949.02.07.01.13.

PUBLISHER'S NOTE

All claims expressed in this article are solely those of the authors and do not necessarily represent those of their affiliated organizations, or those of the publisher, the editors and the reviewers. Any product that may be evaluated in this article, orclaim that may be made by its manufacturer, is not guaranteed or endorsed by the publisher.

ACKNOWLEDGMENTS

We thank the NASA Earth Science Research Division managed by Jack Kaye, and the DSCOVR Program managed by Richard Eckman for support.

REFERENCES

Bender, F. A.-M., Engström, A., Wood, R., and Charlson, R. J. (2017). Evaluation of Hemispheric Asymmetries in marine Cloud Radiative Properties. *J. Clim.* 30, 4131–4147. doi:10.1175/jcli-d-16-0263.1

Del Genio, A. D., Yao, M.-S., Kovari, W., and Lo, K. K.-W. (1996). A Prognostic Cloud Water Parameterization for Global Climate Models. *J. Clim.* 9, 270–304. doi:10.1175/1520-0442(1996)009<0270:apcwpf>2.0.co;2

DelGenio, A. D., and Yao, M.-S. (1993). "Efficient Cumulus Parameterization for Long-Term Climate Studies: The GISS Scheme," in *The Representation of Cumulus Convection in Numerical Models* ed . Editors K. A. Emanuel, and D. A. Raymond (Boston, MA: American Meteorological Society), 181–184. doi:10.1007/978-1-935704-13-3_18

Eastman, R., and Warren, S. G. (2014). Diurnal Cycles of Cumulus, Cumulonimbus, Stratus, Stratocumulus, and Fog from Surface Observations over Land and Ocean. *J. Clim.* 27, 2386–2404. doi:10.1175/jcli-d-13-00352.1

Hansen, J., Russell, G., Rind, D., Stone, P., Lacis, A., Lebedeff, S., et al. (1983). Efficient Three-Dimensional Global Models for Climate Studies: Models I and II. *Mon. Wea. Rev.* 111, 609–662. doi:10.1175/1520-0493(1983)111<0609:etdgmf>2.0.co;2

Hovmöller, E. (1949). The Trough-And-ridge Diagram. *Tellus* 1 (2), 62–66. doi:10.3402/tellusa.v1i2.8498

Kopp, G., and Lean, J. (2011). A New, Lower Value of Total Solar Irradiance: Evidence and Climate Significance. *Geophys. Res. Lett.* 38, L01706. doi:10.1029/2010gl045777

Li, J., Carlson, B. E., and Lacis, A. A. (2014b). Application of Spectral Analysis Techniques in the Intercomparison of Aerosol Data: Part III. Using Combined PCA to Compare Spatiotemporal Variability of MODIS, MISR, and OMI Aerosol Optical Depth. *J. Geophys. Res. Atmos.* 119 (7), 4017–4042. doi:10.1002/2013JD020538

Li, J., Carlson, B. E., and Lacis, A. A. (2014a). Application of Spectral Analysis Techniques in the Intercomparison of Aerosol Data. Part II: Using Maximum Covariance Analysis to Effectively Compare Spatiotemporal Variability of Satellite and AERONET Measured Aerosol Optical Depth. *J. Geophys. Res. Atmos.* 119 (1), 153–166. doi:10.1002/2013JD020537

Li, J., Carlson, B. E., Rossow, W. B., Lacis, A. A., and Zhang, Y. (2015). An Intercomparison of the Spatiotemporal Variability of Satellite- and Ground-Based Cloud Datasets Using Spectral Analysis Techniques. *J. Clim.* 28 (14), 5716–5736. doi:10.1175/JCLI-D-14-00537.1

Loeb, N. G., Doelling, D. R., Wang, H., Su, W., Nguyen, C., Corbett, J. G., et al. (2018). Clouds and the Earth's Radiant Energy System (CERES) Energy Balanced and Filled (EBAF) Top-Of-Atmosphere (TOA) Edition-4.0 Data Product. *J. Clim.* 31, 895–918. doi:10.1175/jcli-d-17-0208.1

Loeb, N. G., Wielicki, B. A., Doelling, D. R., Smith, G. L., Keyes, D. F., Kato, S., et al. (2009). Toward Optimal Closure of the Earth's Top-Of-Atmosphere Radiation Budget. *J. Clim.* 22, 748–766. doi:10.1175/2008JCLI2637.1

Minnis, P., Nguyen, L., Palikonda, R., Heck, P. W., Spangenberg, D. A., Doelling, D. R., et al. (2008). "Near-real Time Cloud Retrievals from Operational and Research Meteorological Satellites," in *Proc. SPIE 7108, Remote Sens. Clouds Atmos. XIII*, *(Cardiff, Wales, UK*, *September 15-18, 2008)*, 710703. doi:10.1117/12.800344

Minnis, P., Sun-Mack, S., Chen, Y., Chang, F.-L., Yost, C. R., Smith, W. L., et al. (2021). CERES MODIS Cloud Product Retrievals for Edition 4-Part I: Algorithm Changes. *IEEE Trans. Geosci. Remote Sensing* 59 (4), 2744–2780. doi:10.1109/tgrs.2020.3008866

Minnis, P., Sun-Mack, S., Young, D. F., Heck, P. W., Garber, D. P., Chen, Y., et al. (2011). CERES Edition-2 Cloud Property Retrievals Using TRMM VIRS and Terra and Aqua MODIS Data-Part I: Algorithms. *IEEE Trans. Geosci. Remote Sensing* 49 (11), 4374–4400. doi:10.1109/TGRS.2011.2144601

Rind, D., Orbe, C., Jonas, J., Nazarenko, L., Zhou, T., Kelley, M., et al. (2020). GISS Model E2.2: A Climate Model Optimized for the Middle Atmosphere-Model Structure, Climatology, Variability, and Climate Sensitivity. *J. Geophys. Res. Atmos.* 125 (10), e2019JD032204. doi:10.1029/2019JD032204

Russell, G. L., Rind, D. H., and Jonas, J. (2018). Symmetric Equations on the Surface of a Sphere as Used by Model GISS:IB. *Geosci. Model. Dev.* 11, 4637–4656. doi:10.5194/gmd-11-4637-2018

Schmidt, G. A., Bader, D., Donner, L. J., Elsaesser, G. S., Golaz, J.-C., Hannay, C., et al. (2017). Practice and Philosophy of Climate Model Tuning across Six US Modeling Centers. *Geosci. Model. Dev.* 10, 3207–3223. doi:10.5194/gmd-10-3207-2017

Schmidt, G. A., Kelley, M., Nazarenko, L., Ruedy, R., Russell, G. L., Aleinov, I., et al. (2014). Configuration and Assessment of the GISS ModelE2 Contributions to the CMIP5 Archive. *J. Adv. Model. Earth Syst.* 6, 141–184. doi:10.1002/2013MS000265

Stephens, G. L., O'Brien, D., Webster, P. J., Pilewski, P., Kato, S., and Li, J.-l. (2015). The Albedo of Earth. *Rev. Geophys.* 53, 141–163. doi:10.1002/2014RG000449

Su, W., Liang, L., Doelling, D. R., Minnins, P., Duda, D. P., Khopenkov, K., et al. (2018). Determining the Shortwave Radiative Flux from Earth Polychromatic Imaging Camera. *J. Geophys. Res.* 123, 11479–11491. doi:10.1029/2018JD029390

Su, W., Minnis, P., Liang, L., Duda, D. P., Khlopenkov, K., and Thieman, M. M. (2020). Determining the Daytime Earth Radiative Flux from National Institute of Standards and Technology Advanced Radiometer (NISTAR) Measurements. *Atmos. Meas. Tech.* 13, 429–443. doi:10.5194/amt-13-429-2020

Su, W., Corbett, J., Eitzen, Z. A., and Liang, L. (2015). Next-generation Distribution Models for Top-Of-The-Atmosphere Radiative Flux Calculation from the CERES Instruments: Methodology. *Atmos. Meas. Tech.* 8, 611–632. doi:10.5194/amt-8-611-2015

Su, W., Khlopenkov, K. V., Duda, D. P., Minnis, P., Bedka, K. M., and Thieman, M. (2017). "Development of Multi-Sensor Global Cloud and Radiance Composites for Earth Radiation Budget Monitoring from DSCOVR," in *Proceedings of SPIE 10424, Remote Sensing of Clouds and the Atmosphere*, *(Warsaw, Poland*, *2 October 2017)*, 104240K. doi:10.1117/12.2278645

Voigt, A., Stevens, B., Bader, J., and Mauritsen, T. (2014). Compensation of Hemispheric Albedo Asymmetries by Shifts of the ITCZ and Tropical Clouds. *J. Clim.* 27, 1029–1045. doi:10.1175/JCLI-D-13-00205.1

Voigt, A., Stevens, B., Bader, J., and Mauritsen, T. (2013). The Observed Hemispheric Symmetry in Reflected Shortwave Irradiances. *J. Clim.* 26, 468–477. doi:10.1175/jcli-d-12-00132.1

Vonder Haar, T. H., and Suomi, V. E. (1971). Measurements of the Earth's Radiation Budget from Satellite during a Five-Year Period. Part I: Extended Time and Space Means. *J. Atmos. Sci.* 28, 305–314. doi:10.1175/1520-0469(1971)028<0305:moterb>2.0.co;2

Zhang, C., Luo, J.-J., and Li, S. (2019). Impacts of Tropical Indian and Atlantic Ocean Warming on the Occurrence of the 2017/2018 La Niña. *Geophys. Res. Lett.* 46, 3435–3445. doi:10.1029/2019GL082280

Conflict of Interest: The authors declare that the research was conducted in the absence of any commercial or financial relationships that could be construed as a potential conflict of interest.

ORIGINAL RESEARCH
published: 02 May 2022
doi: 10.3389/frsen.2022.777314

Reduction of Spectral Radiance Reflectance During the Annular Solar Eclipse of 21 June 2020 Observed by EPIC

Guoyong Wen[1,2*], Alexander Marshak[1], Jay Herman[1,3] and Dong Wu[1]

[1] *NASA Goddard Space Flight Center, Greenbelt, MD, United States*
[2] *Goddard Earth Sciences Technology Research, Morgan State University, Baltimore, MD, United States*
[3] *Joint Center for Earth Systems Technology, University of Maryland Baltimore County, Baltimore, MD, United States*

Edited by:
Hartmut Boesch, University of Leicester, United Kingdom

Reviewed by:
Yolanda Shea, Langley Research Center, United States
Xiuqing Hu, China Meteorological Administration, China

**** Correspondence:** Guoyong Wen, Guoyong.Wen@nasa.gov*

***Specialty section:** This article was submitted to Satellite Missions, a section of the journal Frontiers in Remote Sensing*

***Received:** 15 September 2021*
***Accepted:** 08 April 2022*
***Published:** 02 May 2022*

***Citation:** Wen G, Marshak A, Herman J and Wu D (2022) Reduction of Spectral Radiance Reflectance During the Annular Solar Eclipse of 21 June 2020 Observed by EPIC. Front. Remote Sens. 3:777314. doi: 10.3389/frsen.2022.777314*

The annular solar eclipse on 21 June 2020 passed over desert areas (parts of Central and Eastern Africa, the southern Arabian Peninsula), partly cloudy regions (parts of South Asia and the Himalayas), and the mostly cloudy region in East Asia. Moving around the Earth-Sun Lagrange point 1 (L_1), the Earth Polychromatic Imaging Camera (EPIC) instrument on the Deep Space Climate Observatory (DSCOVR) spacecraft captured three sets of images of the sunlit Earth during the eclipse, allowing us to study the impact of the solar eclipse on reflected solar radiation when the underlying surface and/or cloudy conditions in the Moon's shadow are quite different. We analyzed EPIC images acquired during the 21 June 2020 and 21 August 2017 eclipses. We found that (1) EPIC-observed average spectral as well as spectrally averaged reflectance reductions of the entire sunlit Earth during the 21 June 2020 solar eclipse are distinctly different from those during the total solar eclipse of 21 August 2017; (2) the reduction of spectral reflectance depends strongly on underlying reflector properties, including the brightness, the area coverage of each reflector in the penumbra and the average distance to the center of the Moon's shadow.

Keywords: eclipse, DSCOVR/EPIC, solar radiation, cloud, surface

INTRODUCTION

A rare but spectacular event in the Sun-Earth-Moon system, a solar eclipse occurs when the Moon moves between the Sun and Earth, casting a shadow on Earth and resulting in the reduction of the incident solar irradiance at the top-of-atmosphere (TOA). The Moon's shadow consists of two parts: umbra and penumbra. The umbra is the Moon's dark inner shadow, from where total solar eclipse is visible; the penumbra is the Moon's faint outer shadow, from where partial solar eclipses are visible. Typically, the umbra is 100–160 km wide, while the penumbra diameter can be greater than 6,400 km. Thus, a solar eclipse has a strong impact on local solar radiation budget, particularly in and near umbra regions, and significant impact on global average solar radiation budget.

Over the past several decades, researchers have studied the impact of an eclipse on surface solar radiation from ground-based radiometer observations and radiative transfer simulations. Several ground-based radiation experiments and modeling activities have been carried out to understand radiation in solar eclipse conditions in the past. Sharp et al. (1971) reported

that the sky light may be considered as attenuated sunlight up to at least 99.8% obscuration and the effect of multiple scattering from outside the umbral region dominates the sky brightness close to and during totality (e.g., Mikhalev et al., 1999; Zerefos et al., 2000). Shaw (1978) developed a model to compute sky radiance during a total solar eclipse by including first- and second-order scattering processes that would compute the diffused light scattered into the umbra. Koepke et al. (2001) studied surface spectral variation of the solar radiation during an eclipse, and Emde and Mayer (2007) performed a full 3D radiative transfer simulation of surface spectral solar radiance and irradiance change for cloudless atmosphere during a total eclipse on 29 March 2006, providing a benchmark for studying radiative transfer under solar eclipse conditions.

During the recent total eclipse on 21 August 2017, Bernhard and Petkov (2019) made surface spectral solar irradiance observations and performed 3D radiative transfer simulations; Ockenfuβ et al. (2020) further used 3D radiative transfer simulations for understanding the impact of surface spectral albedo, ozone vertical distribution and surrounding mountains on surface spectral irradiance observed by Bernhard and Petkov (2019); Wen et al. (2020) used ground-based pyranometer observations to estimate the impact of solar eclipse on surface broadband irradiance reduction; Calamas et al. (2018) studied the impact of the eclipse on surface irradiance and ambient temperature; and Eshelman et al. (2020) studied impact of total solar eclipse on all-sky polarization images. Gedzelman (2020) showed that the sunlit tops of cloud layers and arctic sea ice near the umbra appeared salmon-brown when viewed from airplanes or satellite during the 21 August 2017 as well as 2 July 2019 eclipse. Sarid et al. (2021) demonstrated the radiance reduction observed by Terra MODIS for several eclipse events. Madhavan and Venkat Ratnam (2021) studied the impact of a solar eclipse on surface radiation and photovoltaic energy.

One major impact of a solar eclipse is the reduction of the TOA input solar radiation, resulting in global and local reduction in incident and reflected solar radiation. Although the distribution of incoming solar radiation can be calculated with high accuracy, the global reduction of reflected solar radiation remained unknown until the 2015 launch of the Deep Space Climate Observatory (DSCOVR) satellite. For the first time, Herman et al. (2018a) used observations from the Earth Polychromatic Imaging Camera (EPIC) instrument to estimate the average reflectance

reduction of the sunlit Earth disk. Flying onboard the DSCOVR satellite located near the Earth-Sun Lagrange point 1 (L_1), about 1.5 million kilometers from the Earth and with a spacecraft-Earth-Sun angle varying from 2° to 12° (Marshak et al., 2018; Marshak et al., 2021), the EPIC instrument views the entire sunlit side of the Earth including the shadow of the Moon during a solar eclipse. Herman et al. (2018a) showed that the day-to-day variability of the disk average reflectance from EPIC image at similar UTC times is very small. Thus, the EPIC images taken at a similar UTC time from the day before or after can be used as a reference to estimate the eclipse-induced disk reflectance reduction.

Evidence shows that the brighter the atmosphere-surface under the Moon's shadow, the larger the solar eclipse impact on the reflected solar radiation. Since the TOA reflectance depends on wavelength and underlying surface type and cloud amount, it is necessary to study the eclipse induced reflectance when the Moon's shadow is over different atmosphere-surface conditions.

In this study, we use three sets of EPIC images acquired during the 21 June 2020 annular eclipse when the center of the Moon's shadow was in the Arabian Peninsula, Himalayas, and Southwest China to quantify and understand the impact of the eclipse on the average reflectance reduction over the sunlit disk. We further compare the reflectance reductions during the 2020 eclipse with two sets of EPIC images acquired during the 2017 Great American eclipse over Casper, Wyoming and Columbia, Missouri where the surface reflective properties and cloud fraction differ significantly. In Section 2, we describe the EPIC data and methodology used in this study. The results are presented in Section 3 followed by the summary in Section 4.

DATA AND METHODS

We use EPIC observations to estimate the reduction of spectral solar irradiances during solar eclipses. EPIC is a 10-channel spectroradiometer onboard the DSCOVR spacecraft flying in a Lissajous orbit around the L_1 point, where the combined gravitational pull of the Sun and Earth equals the centripetal force required for the spacecraft to move with them. The DSCOVR orbit has a period of 6 months, resulting in a spacecraft-Earth-Sun angle varying from 2° to 12°. This allows EPIC to view the Moon's shadow in the sunlit disk of the Earth under eclipse conditions. EPIC consists of a 30-cm aperture Cassegrain telescope with a 0.62° field of view (FOV)

encompassing the Earth that has a nominal size of 0.5° at the L_1 point. EPIC provides 10 narrowband spectral images of the entire sunlit side of Earth using a 2048 × 2048 pixel charge-coupled device (CCD) detector every 65 min (in the Northern Hemisphere summer) to 111 min (in the Northern Hemisphere winter). The wavelengths range from ultraviolet (UV), to visible, to near infrared (NIR). The sampling size on the Earth is nominally ~8 × 8 km^2 at the center of the image with an effective spatial resolution of 12 × 12 km^2 for the 443 nm channel when EPIC's point spread function is considered. To reduce the downlink transmission time, the images for all wavelengths, except 443 nm, have been reduced to 1,024 × 1,024 pixels. A more detailed description of EPIC is given in Herman et al. (2018b) and Marshak et al. (2018).

In this study, we use EPIC level 1B (L1B) version 3 data distributed by the Atmospheric Science Data Center of NASA Langley Research Center (https://eosweb.larc.nasa.gov). The L1B digital counts multiplied by the after-launch wavelength dependent calibration coefficient (Geogdzhayev and Marshak, 2018; Herman et al., 2018b; Doelling et al., 2019; Geogdzhaev et al., 2021) yield TOA reflectance. While the EPIC images are geolocation processed (Blank et al., 2021), the L1B algorithm produces images in which all wavelengths are regridded to the same common grid, i.e., every pixel has the same geolocation (latitude and longitude) for all 10 wavelength channels.

Three sets of images were acquired by EPIC on 21 June 2020 when the center of the Moon's shadow eclipse was in the Arabian Peninsula, Himalayas, and East Asia (Southwest of China). The surface and/or cloudy conditions in the Moon's shadow are quite different. The Arabian Peninsula is a vast desert wilderness in Western Asia; the Himalayas are a mountain range in South and East Asia; and most of the surface in Southwest China is covered by vegetation. Most of the Arabian Peninsula was cloud free; the Himalayas were mostly; and Southwest China was mostly cloudy. Two sets of images were taken by EPIC during the 2017 eclipse when the totality was in Casper, Wyoming and Columbia, Missouri. The surrounding areas of the Casper site are mostly covered by grasslands; while the surrounding areas of the Columbia site are mostly covered by croplands. EPIC images during the 21 June 2020 and 21 August 2017 solar eclipses are presented in Figure 1. Information about EPIC images acquired during the two eclipses are described in Table 1. In this study, we analyze images at five nonabsorbing wavelengths at 388, 443, 551, 680, and 780 nm.

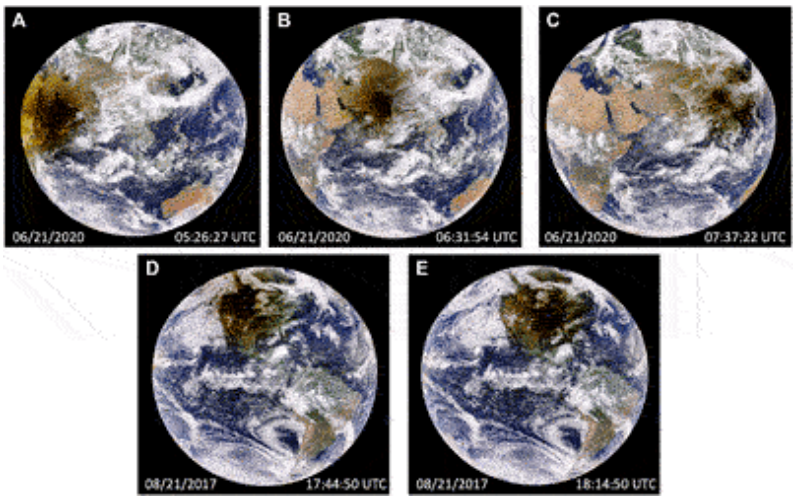

FIGURE 1 | Three EPIC images taken during 21 June 2020 solar eclipse when the center of the Moon's shadow was in **(A)** Arabian Peninsula, **(B)** Himalayas, and **(C)** Southwest China. Two EPIC images taken during 21 August 2017 when the center of the Moon's shadow was in **(D)** Casper, Wyoming and **(E)** Columbia, Missouri.

TABLE 1 | Eclipse measurement time and location of the center of the Moon's shadow of five sets of EPIC images.

	YY/MM/DD	UTC	Latitude	Longitude
Casper, WY	2017/08/21	17:44:50	42.8666°N	106.3131°W
Columbia, MO	2017/08/21	17:54:36	38.9517°N	92.3341°W
Arabian Peninsula	2020/06/21	05:26:27	20.5115°N	53.7671°E
Himalayas	2020/06/21	06:31:54	30.0267°N	76.9467°E
Southwest China	2020/06/21	07:37:22	29.7300°N	101.1630°E

To understand the average reflectance reduction over the sunlit disk we need to quantify the contribution of different reflectors to the average reflectance reduction. Thus, we need to recover the image under hypothetical non-eclipse conditions from the image acquired during the eclipse. Initially, one needs to know the true input spectral solar irradiance for each EPIC image pixel when the part of the solar disk is covered by the Moon.

We know the brightness of the Sun's disk decreases from its center to its edge, i.e., limb darkening. Here, we use the limb darkening function from Neckel (2005) based on McMath Solar Telescope and the large vertical spectrograph observations at the National Solar Observatory on Kitt Peak

(Neckel and Labs, 1994) to compute the normalized solar irradiance relative to the irradiance at the center of the solar disk as a function of the radius of the Sun (Figure 2). Then, we follow Koepke et al. (2001) to compute the brightness of the Sun as a function of apparent Moon-Sun distance X, where X = 0 when the centers of the Moon and the Sun coincide, $X = 1$ when the Moon first contacts the Sun, $X = -1$ when the disk of the Moon leaves the Sun again. On the reference plane passing through the center of the Moon's shadow on Earth and perpendicular to the incident sunlight at a given time, the distance between a point to the center of the Moon's shadow (upper scale of Figure 3) is linearly related to X as demonstrated by Emde and Mayer (2007). Thus, one can calculate the normalized solar irradiance during an eclipse, defined as the TOA spectral solar irradiance for solar disk covered by the Moon normalized by the irradiance of the uncovered solar disk, as a function of the Sun-Moon distance (Koepke et al., 2001) or a function of the distance from the center of the Moon's shadow on the reference plane (Figure 3). The reference plane almost coincides with the EPIC image plane that is perpendicular to Earth-spacecraft direction since the DSCOVR spacecraft is slightly off the Sun-Moon-Earth line during an eclipse (about 3° for the 21 June 2020 and 7.7° for the 21 August 2017).

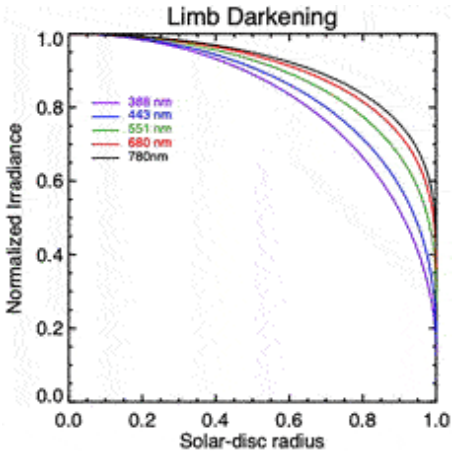

FIGURE 2 | Limb darkening function based on Neckel (2005).

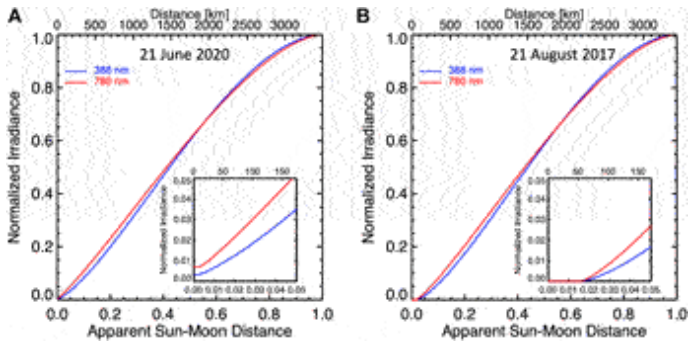

FIGURE 3 | (A) Normalized solar irradiance as a function of apparent Sun-Moon distance in lower X-axis and the distance to the center of the Moon's shadow in upper X-axis on the Earth for the 21 June 2020 eclipse; **(B)** similar to **(A)** but for the 21 August 2017 eclipse. The insets show details of the irradiance variation near the center of the eclipse.

Note the difference between the two normalized irradiances in Figure 3, due to different eclipse magnitudes of the two eclipses. Although the apparent sizes of the Sun and Moon as viewed from Earth are both about 0.5°, both vary because the Earth-Moon and Earth-Sun distances vary. The angular diameter of the Moon is about 3.1% larger than that of the Sun during the 21 August 2017 total eclipse, while the angular diameter of the Moon is about 0.6% smaller than that of the Sun during the 21 June 2020 annular eclipse. Thus, the normalized irradiances are greater than zero when the Sun and Moon coincide with apparent Sun-Moon distance of zero for the 2020 eclipse.

The distance between a pixel to the center of the Moon's shadow can be estimated in an EPIC image. First, we need to estimate the pixel size in EPIC images. These are projections of the sunlit face of the Earth onto the focal plane of the 2048 × 2048 CCD array. With a 20-km altitude of atmosphere at the edge of the Earth, the Earth's disk diameter in EPIC images is 12,782 km. The pixel size of an EPIC image is estimated by dividing the disk diameter by number of pixels across the diameter in the image. Second, the center of the Moon's shadow changes a little from one image to another because the images are taken at slightly different times. We use the locations (latitude and longitude) of the center of Moon's shadow at specific times as the first estimates (Table 1). Then, we search the images around the estimated locations to find the minimum value of reflectance to locate the center of the Moon's shadow for each image. With both pixel size and the center of the Moon's shadow available, the distance between a pixel in the penumbra and

the center of the Moon's shadow can be easily calculated. The distance is further multiplied by cosine of Sun-Earth-Vehicle (SEV) angle (Vehicle refers here to the DSCOVR spacecraft) to obtain the corresponding distance in the reference plane from which we calculate the normalized solar irradiance (Figure 3) for estimating the reflectance of the pixel under non-eclipse conditions as explained in the following paragraph. The SEV angle for each EPIC image is available at the DSCOVR/EPIC website (https://epic.gsfc.nasa.gov).

Within the Moon's shadow, the digital counts multiplied by the calibration coefficient yields apparent reflectance ($R_{e,\lambda}$, *e* stands for eclipse and λ for wavelength)

$$R_{e,\lambda}(i,j) = \frac{\pi I_\lambda(i,j)}{I_{0,\lambda}}, \qquad (1a)$$

where $I_\lambda(i,j)$ is the reflected radiance of pixel (i,j), $I_{0,\lambda}$ is the incident spectral solar irradiance at wavelength λ for normal conditions (or uncovered solar disk). For the same TOA reflected radiance $I_\lambda(i,j)$, the true reflectance ($R_{ne,\lambda}$, *ne* stands for non-eclipse) is

$$R_{ne,\lambda}(i,j) = \frac{\pi I_\lambda(i,j)}{I'_{0,\lambda}(i,j)}, \qquad (1b)$$

where $I'_{0,\lambda}(i,j)$ is the incident spectral solar irradiance when the solar disk is partially covered by the Moon. Thus, the reflectance for a hypothetical non-eclipse condition can be recovered using the relationship

$$R_{ne,\lambda}(i,j) \approx \frac{R_{e,\lambda}(i,j)}{I_{norm,\lambda}(i,j)} \qquad (1c)$$

and

$$I_{norm,\lambda}(i,j) \approx \frac{I'_{0,\lambda}(i,j)}{I_{0,\lambda}} \qquad (1d)$$

where $I_{norm,\lambda}(i,j)$ is the normalized irradiance (Figure 3) for pixel (i,j) in an EPIC image. Koepke et al. (2001) used this method to compute photolysis frequencies while Trees et al. (2021) applied it to estimate UV absorbing aerosol index for hypothetical non-eclipse conditions.

Examples of the original and recovered images for the 2020 eclipse in the Arabian Peninsula and the 2017 eclipse in Casper, Wyoming are presented in Figures 4, 5, respectively. $I_{norm,\lambda}$ is very small near the center of the Moon's

shadow and $I_{norm,\lambda} = 0$ for pixels in the totality. The radiation in this area is strongly influenced by the 3D radiative effects (Emde and Mayer, 2007). The reflectance cannot be calculated using the simple relationship of Eq.1c. Here, we neglect the area within a radius of ~170 km from the center of the shadow for both eclipse and corresponding non-eclipse images in computing eclipse-induced reflectance reduction. Since the area neglected is ~0.3% of the total area penumbra of ~3,000 km in radius (see Figure 3), neglecting this small area would introduce a negligible error, slightly underestimating the disk-averaged reflectance reduction. Using the normalized TOA solar irradiance, typical disk-averaged spectral reflectance, and reflectance for different reflector types for the center of the Moon's shadow, we found that the errors in reflectance reduction due to neglecting the small area are very small, depending on underlying reflector conditions of the area. For wavelengths from 388 to 780 nm, the error in the reflectance reduction estimate ranges from −0.5% to −0.1% for clear ocean; −0.6% to −0.8% for clear land; −0.5% to −1.6% for clear vegetation; −1.5% to −1.6% for cloudy ocean; −1.5% to −1.8% for cloudy land; and −1.5 to −2.0% for cloudy vegetation.

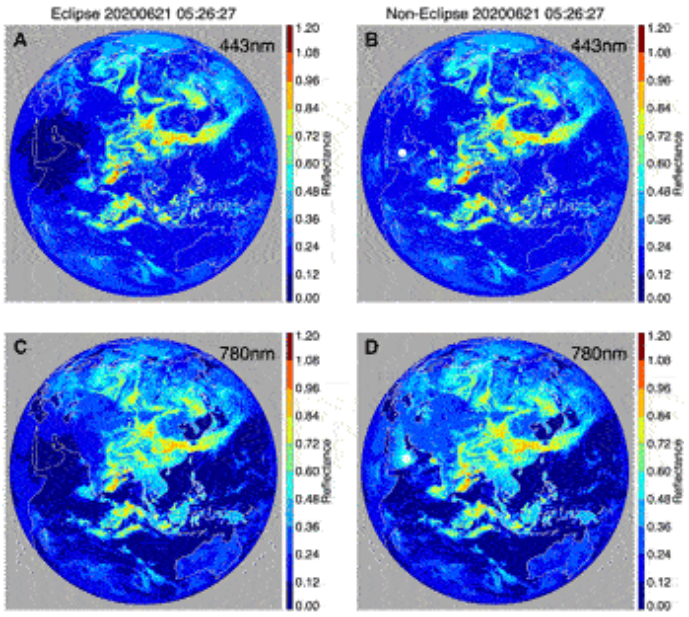

FIGURE 4 | (A) EPIC image at 443 nm acquired during the 21 June 2020 eclipse when the center of the Moon's shadow was in Arabian Peninsula; **(B)** the recovered image for hypothetical non-eclipse conditions for image in **(A)**; **(C)** similar to **(A)** but for 780 nm; **(D)** similar to **(B)** but for 780 nm. The white circles in **(B)** and **(D)** are the center of the Moon's shadow with a radius of about 170 km.

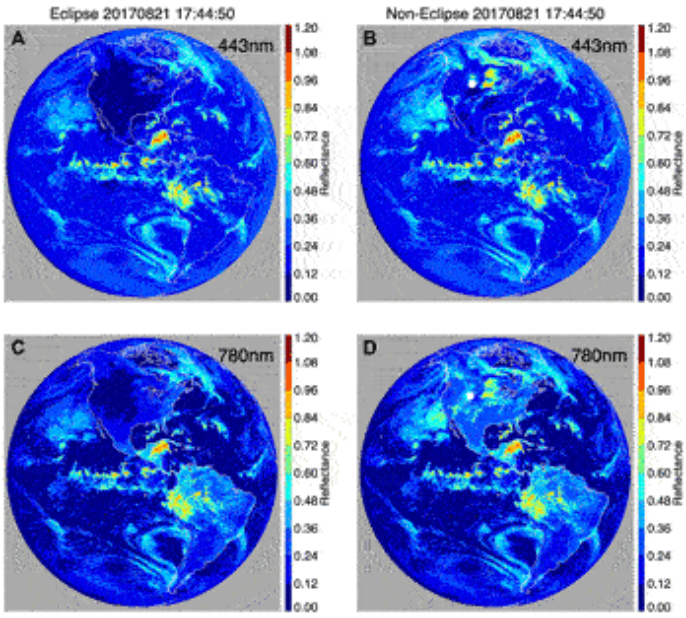

FIGURE 5 | Similar to Figure 4 but for the 21 August 2017 solar eclipse when the center of the Moon's shadow was in Casper, Wyoming.

From its center, the Moon's shadow can extend large distances (~3,000 km in radius). For that scale, both surface albedo and cloud cover can vary significantly. Thus, to understand the impact of a solar eclipse on the disk average reflectance, one needs to quantify the reflectance reduction from different reflector types. With the recovered image for non-eclipse conditions, we further apply Earth Reflector Type Index (ERTI) developed by Song et al. (2018) for classifying EPIC pixels into four dominant reflector types: clear ocean, clear land, clear green vegetation, and cloud. This method was used to study the blue and near-IR global spectral reflectance relationship as well as the response of global average reflectance to the change in cloud cover from EPIC observations (Wen et al., 2019). We do not separate clouds over land from clouds over ocean, though there are some differences in spectral reflectance between the two types of cloud. On average, cloud is the brightest of all wavelengths among the four dominant reflectors. Thus, dividing the image into four reflector types is sufficient for this study.

An important point is that the ERTI is sensitive to the presence of green leaves in a pixel and attributes the pixel to vegetation if the leaf area index (LAI) is larger than ~0.5 (Song et al., 2018). The area of green leaves can exhibit strong seasonal variation from its maximum to a very low value

(Samanta et al., 2012); therefore, one should distinguish between vegetated land according to a land cover classification map and actual presence of green leaves in the scene. For example, the ERTI classifies savannas in the southern part of Africa as vegetated land during wet season (mean LAI~2.4 in March), and it attributes this land cover type as bare land during dry season (LAI can drop to ~0.4 in August). We emphasize that the clear vegetation refers to cloud-free green vegetation, clear land includes dry vegetation and bare soil. In this study, we do not distinguish clouds over different surface types since the wavelength dependence of reflectance of cloud over ocean is similar to that over land (Figure 6). Though the reflectance from clouds over green vegetation has a very different wavelength-dependent signature, the coverage of green vegetation is quite small, less than 5% coverage of any EPIC images (Wen et al., 2019).

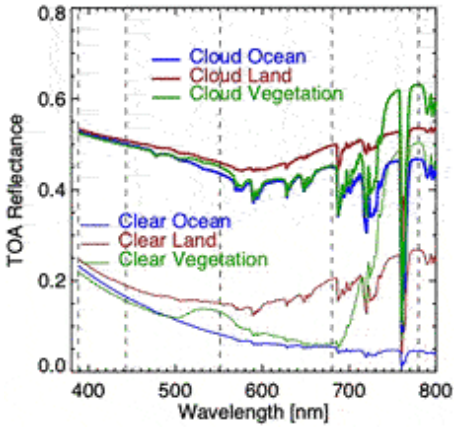

FIGURE 6 | TOA spectral reflectance simulated using SBDART (Ricchiazzi et al., 1998) for clear and cloudy atmospheric conditions over ocean, land, and vegetation. The cloud optical depth is 10, and solar zenith angle is 30°. The vertical dashed lines indicate the EPIC wavelengths.

RESULTS

Recovering EPIC images for non-eclipse conditions is critical for understanding the reduction of spectral reflectance during a solar eclipse. Figures 4, 5 present original and recovered images for the blue-band at 443 nm and the near-IR band at 780 nm for the Arabian Peninsula and Casper, Wyoming during the 2020 and 2017 solar eclipses, respectively. Since both land surface and ocean are dark at 443 nm, the blue-band image can be used to examine the recovered cloud structure. For the Arabian

Peninsula case, the clouds that were not visible in the eclipse image (Sudanian savanna to the west of the center of the Moon's shadow) or less bright (to the east and southeast of the center of the Moon's shadow) (Figure 4A) become visible and evidently brighter after the correction (Figure 4B). Comparing the recovered non-eclipse image with the RGB composite image (Figure 1A), we can see that the non-eclipse image has indeed recovered cloud features and enhanced the cloud visibility.

Since land surfaces are bright at 780 nm, the non-eclipse image can be used to examine the recovery of land surface as well as clouds. Under eclipse conditions, the entire Arabian Peninsula and the Sahara Desert in North Africa and part of West Asia were under the Moon's shadow, thereby dark or even invisible in 780 nm image (Figure 4C). After the corrections, the Arabian Peninsula is clearly recovered, the Sahara Desert in North Africa and West Asia are recovered, and the coastlines and water bodies next to land (e.g., the Red Sea, the Persian Gulf, the Gulf of Oman, the Arabian Sea, and the Indian Ocean) are clearly visible in the non-eclipse image (Figure 4D). Similar to the blue-band, cloud structure in the near-IR image has been recovered or enhanced. Again, one can compare the non-eclipse image with the RGB composite image (Figure 1A) to see the recovery of land.

The original eclipse and non-eclipse images during the 2017 solar eclipse over Casper, Wyoming show the recovery of clouds and land after the corrections (Figure 5). It is interesting to see the cloud deck off the coast of California and the clouds in North America are much brighter in the non-eclipse images at both 443 and 780 nm bands (Figures 5B,D) compared to the eclipse images (Figures 5A,C). Clouds to the east of Casper that not clearly visible in the eclipse image are evidently recovered after the correction. In addition to clouds, the land of all North America is brighter at 780 nm in the corrected image compared to the original image.

With both eclipse and non-eclipse images, we estimate the eclipse-induced global reflectance reduction. The global average reflectance can be expressed as a sum of reflectance from each reflector component. Assuming there are N pixels and N_1, N_2, N_3, … pixels for type *1*, *2*, *3*, … reflector component ($N = \sum_i N_i$) in the whole EPIC image, then the global average reflectance can be expressed as

$$\langle R \rangle = \frac{1}{N}\left[\sum_{i=1}^{N_1} R_1(i) + \sum_{i=1}^{N_2} R_2(i) + \sum_{i=1}^{N_3} R_3(i) + \dots\right] \quad (2a)$$

where $R_j(i)$ is the reflectance of reflector type *j* at pixel *i* (the wavelength dependence is omitted for simplicity). The global reflectance reduction is the difference between the reflectance for non-eclipse $\langle R_{ne} \rangle$ and eclipse conditions $\langle R_e \rangle$

$$\Delta R = \langle R_{ne} \rangle - \langle R_e \rangle = \sum_j \Delta R_j, \qquad (2b)$$

where ΔR_j is the reflectance reduction from j^{th} reflector. We consider pixels in the Moon's shadow only because there is no reflectance reduction outside of the shadow. For j^{th} reflector with n_j pixels in the Moon's shadow in an EPIC image ($n_j < N_j$), the reflectance reduction is

$$\Delta R_j = \frac{1}{N} \sum_{i=1}^{n_j} \left(R_{ne,j}(i) - R_{e,j}(i) \right). \qquad (2c)$$

or

$$\Delta R_j = \frac{1}{N} \sum_{i=1}^{n_j} \left(1 - I_{norm,j}(i) \right) R_{ne,j}(i) \qquad (2d)$$

or

$$\Delta R_j = \eta_j \frac{\sum_{i=1}^{n_j} R_{ne,j}(i)}{n_j} = \eta_j \bar{R}_{ne,j} \qquad (2e)$$

where $\eta_j = \frac{n_j}{N} (1 - \bar{I}_{norm,j})$ and $\bar{I}_{norm,j}$ is the mean value of the normalized solar irradiance for all j^{th} reflector pixels. Thus, the reduction from j^{th} reflector depends on three competing factors, i.e. the average reflectance ($\bar{R}_{ne,j}$), the number of pixels (n_j) in the Moon's shadow or the ratio ($\frac{n_j}{N}$), and average normalized solar irradiance ($\bar{I}_{norm,j}$) of j^{th} reflector in the Moon's shadow. Radiative transfer model-simulated TOA reflectances for clear and cloudy atmospheric conditions over different surface types are presented in Figure 6 for interpreting observed reflectance reduction.

The average reflectance ($\bar{R}_{ne,j}$) determines the brightness of the reflector. The brighter the reflector, the larger the associated reduction. The more pixels in the Moon's shadow, the larger the ratio $\frac{n_j}{N}$, the larger the reduction. $\bar{I}_{norm,j}$ is a measure of the average radial distance of the pixels to the center of the Moon's shadow. Near the center of the Moon's shadow, $\bar{I}_{norm,j}$ is small and $1 - \bar{I}_{norm,j}$ is large, resulting in large reflectance reduction; conversely, far from the center of the Moon's shadow, $\bar{I}_{norm,j}$ approaches 1 and η_j approaches 0, resulting in small reflectance reduction. Thus, the reflectance reduction

from j^{th} reflector is proportional to the average reflectance of the reflector within the Moon's shadow. However, the associated reflectance reduction (ΔR_j) can be very small if the number of pixels is nominal or the pixels are near the edges of the Moon's shadow ($\bar{I}_{norm,j}$ approaches 1) even if the reflector is very bright. We call η_j the contribution factor that accounts for the effects of both number of pixels in the Moon's shadow and average distance of pixels to the center of the Moon's shadow for j^{th} reflector.

Figure 7 shows the disk average spectral reflectance reduction and associated contribution from different reflector types when the center of the 21 June 2020 solar eclipse was in the Arabian Peninsula, the Himalayas, and Southwest China, respectively. For the Arabian Peninsula case (Figure 7A), the total disk reflectance reduction decreases from 388 to 551 nm followed by an increase to 780 nm. This feature is explained by the contribution from each reflector type. The land makes the largest contribution to the total reflectance reduction, followed by cloud and then ocean. Green vegetation makes little contribution to the disk average reflectance reduction.

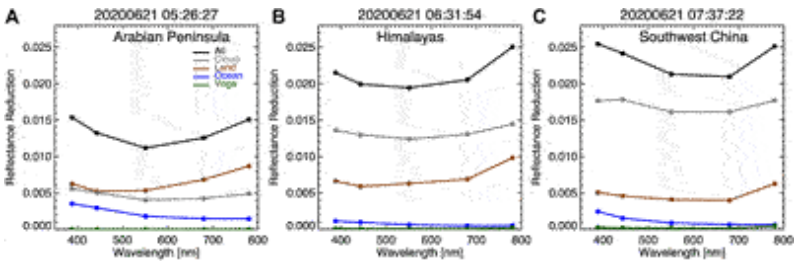

FIGURE 7 | Disk average reflectance reduction with contributions from different reflector types for the 2020 solar eclipse when the center of the Moon's shadow was in **(A)** Arabian Peninsula, **(B)** Himalayas, **(C)** Southwest China.

For the Himalayas case (Figure 7B), there is a small decrease in the average reflectance reduction from 388 to 551 nm followed by a larger increase in the reduction from 551 to 780 nm compared to the Arabian Peninsula case. Here, clouds make the largest contribution, about two thirds, to the disk average reflectance reduction. Land is the second largest contributor, and, though it is small, clear ocean contributes significantly at shorter wavelengths, and the associated reduction decreases rather quickly with wavelength. Again, green vegetation makes a minimal contribution to the average reflectance reduction.

For the Southwest China case (Figure 7C), the total reduction decreases with wavelength from 388 to 551 nm followed by a small decrease from 551 to 680 nm and a large increase from 680 to 780 nm. It is evident that clouds contribute the most, more than 70%, of the total reflectance reduction because a large area near the center of the Moon's shadow is cloudy. Clear land contribution makes the second largest contribution to the total reflectance reduction since the clear land is less reflective than cloud over land and the clear land pixels being farther from the center of the Moon's shadow contribute to the reflectance reduction. Clear ocean makes a significant contribution to the reflectance reduction. In all three 2020 eclipse cases, the contributions from green vegetation are small. The contribution from different reflector types explains the global reflectance reduction for three cases of EPIC-observed global reflectance reductions.

To interpret the reduction from each reflector, we present $\bar{R}_{ne,j}$, $1-\bar{I}_{norm,j}$, and $\frac{n_j}{N}$ (see Eq.2e) for each reflector in Figure 8. First, we examine the average reflectance of each reflector for the three cases from 2020. It is clear that the reflectance reduction for each reflector (Figure 7) is proportional to the average reflectance in the Moon's shadow (Figures 8a1–a3). The spectral dependence of EPIC-observed average spectral reflectances are similar to the model simulations (Figure 6). For all three cases, on average, cloud is the brightest reflector followed by land. Additionally, green vegetation compared to ocean is darker in UV and blue channels at 388 and 443 nm, similar in visible channels at 551 and 680 nm, and much brighter at near-IR channel at 780 nm. The observed reflectance has large variability for clouds and less variable for clear land, clear ocean, and green vegetations reflectors. The average cloud reflectances for the Himalayas and Southwest China cases are larger than the Arabian Peninsula case: clouds for the Himalayas and Southwest China cases are mostly over land compared to a large fraction of clouds over the Indian Ocean for the Arabian Peninsula case, and, on average, optical depth of water cloud over land is significantly thicker than clouds over ocean while ice clouds over land and ocean have similar optical depth (King et al., 2013). In addition, land is brighter than ocean, especially at near-IR wavelength, resulting in a larger TOA reflectance for the same cloud optical depth. The average reflectance of land, ocean, and green vegetation has a similar wavelength dependence feature for three cases.

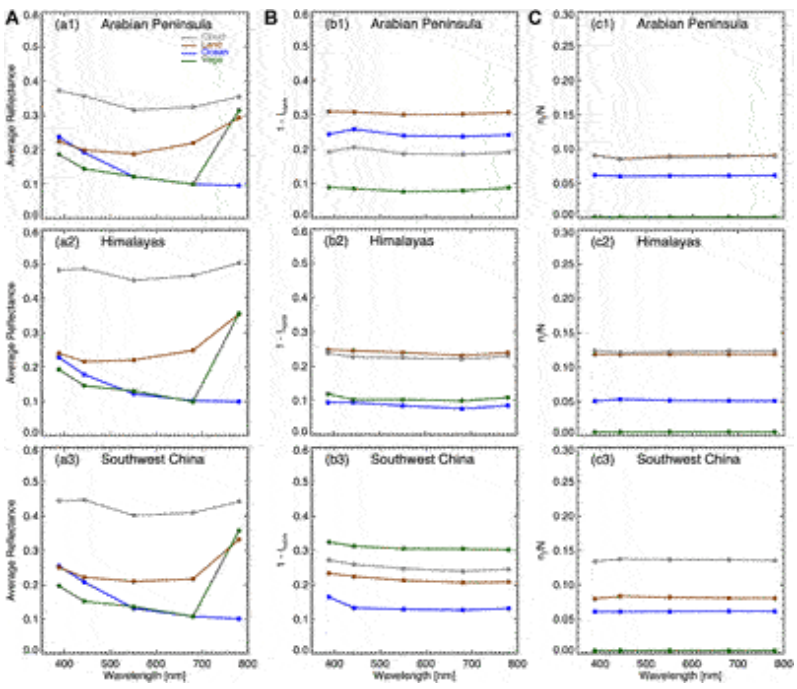

FIGURE 8 | (a1–a3) the average reflectance; **(b1–b3)** $1 - \bar{I}_{norm,j}$; **(c1–c3)** $\frac{n_j}{N}$ (the ratio of number of pixels in the Moon's shadow to total number of pixels in the EPIC image) for each reflector *j* in the penumbra for the three cases during the 2020 solar eclipse.

Now, we examine $1 - \bar{I}_{norm,j}$ (Figures 8b1–b3), and $\frac{n_j}{N}$ (Figures 8c1–c3). We found that both $1 - \bar{I}_{norm,j}$ and $\frac{n_j}{N}$ slightly depend on wavelength. In fact, $\frac{n_j}{N}$ for each reflector would be the same for all 10-wavelength images if they were taken concurrently. In reality, each of the 10-wavelength set of EPIC images is obtained at slightly different times and the Moon's shadow moves a little during the time intervals, resulting in a slightly different Moon's shadow and $\frac{n_j}{N}$ from one wavelength image to another. For randomly distributed reflector pixels in a complete circular Moon's shadow on the reference plane, we found that the average normalized solar irradiance ($\bar{I}_{norm,j}$) is almost independent of wavelength for the five EPIC wavelengths concerned. For the areas close to the umbra, the normalized irradiance for longer wavelength is larger than that for shorter wavelength; farther from the umbra, the normalized irradiance for longer wavelength is smaller than that for shorter wavelength (Figure 4); and, averaging over the whole penumbra yields similar $\bar{I}_{norm,j}$ for each wavelength. In reality, the pixel for a given reflector is not randomly distributed in the penumbra, resulting in a slight wavelength dependence in $\bar{I}_{norm,j}$.

For the Arabian Peninsula case, the factor of (Figure 8b1) is the largest for land followed by ocean, cloud, and green vegetation, respectively. The average normalized solar irradiance is about 0.69, 0.77, 0.81, and 0.92 for land, ocean, cloud, and green vegetation, respectively. Since the normalized solar irradiance monotonically increases with the distance from the center of the Moon's shadow (see Figure 4), the smaller normalized solar irradiance corresponds to a closer distance from a reflector to the center of the Moon's shadow. Thus, on average, land pixels, including desert and bare soil, are closest to the center of the Moon's shadow followed by ocean, cloud, and green vegetation. In addition to the average solar irradiance, the number of pixels determines the collective contribution from each individual reflector type. Figure 8c1 shows that the ratio ($\frac{n_j}{N}$) is about 0.09, 0.09, 0.06, and 0.001 for land, cloud, ocean, and green vegetation, respectively. Multiplying $1 - \bar{I}_{norm,j}$ by $\frac{n_j}{N}$ yields the contribution factor. As a result, the contribution factor (η_j) is the largest for land (~0.027) followed by cloud (~0.017), ocean (~0.015), and green vegetation (~0.0001). Therefore, the reflectance reduction of each reflector can be explained by the average reflectance, the average distance to the center of Moon's shadow plus the area coverage of the reflector in the Moon's shadow.

Indeed, from Figure 1, one could visualize the area size of each reflector and the average distance to the center of the Moon's shadow for the 21 June 2020 eclipse. For the Arabian Peninsula case, the Arabian Desert in the Arabian Peninsula, the Sahara Desert in Northern Africa, and the Ogaden Desert in Eastern Africa occupy the largest areas close to the center of the Moon's shadow. The Red Sea, the Persian Gulf, the Gulf of Oman, and the Arabian Sea are close to the center of the Moon's shadow; however, those areas are much smaller than the deserts. The clear area of the Indian Ocean is large, but farther from the center of the Moon's shadow. As a result, the average radial distance for land pixels to the center of the Moon's shadow is smaller (smaller $\bar{I}_{norm,j}$ or larger $1 - \bar{I}_{norm,j}$) than clear ocean. Although some clouds are close to the center of the Moon's shadow in the Sudanian savanna, the Gulf of Oman, and the Arabian Sea, more clouds are farther away over the Indian Ocean, India, Southwest China, and Europe, resulting in a larger average radial distance for cloudy pixels to the center of the Moon's shadow (larger $\bar{I}_{norm,j}$ or smaller $1 - \bar{I}_{norm,j}$) compared to clear land and clear ocean. The fractional coverage of green vegetation is small and contributes a little to the disk average reflectance (Wen et al., 2019). In this case, a small area of

green vegetation coverage in Europe is visible and the green vegetation region is farther away from the center of the Moon's shadow with negligible area compared to land, ocean, and cloud (Figure 8c1).

For the Himalayas case (Figures 8b2,c2), the similar values of the factor $1 - \bar{I}_{norm,j}$ (~0.23) and $\frac{n_j}{N}$ (~0.12) for land and cloud, indicates similar average distance to the center of the Moon's shadow and area coverage of the two reflectors, which can be seen in Figure 1. To the east and southeast of the center of the Moon's shadow, it is mostly cloudy; to the west and northwest of the center of Moon's shadow, it is mostly clear, resulting in similar average radial distance and area in the penumbra. The green vegetation in Europe and clear oceans (the Indian Ocean and the Pacific Ocean) are rather far away compared to land and cloud reflectors, resulting in a smaller and similar value of $1 - \bar{I}_{norm,j}$ (~0.1) for both green vegetation and clear ocean. The area of green vegetation is evidently smaller than clear ocean; and $\frac{n_j}{N}$ is ~0.006 and ~0.05 for green vegetation and ocean, respectively. The contribution factor (η_j) is ~0.028 for both land and cloud, ~0.005 for ocean, and ~0.0006 for green vegetation, respectively. Again, the reflectance reduction of each reflector can be explained as the result of the brightness, the average distance from the center of Moon's shadow, and the area coverage of the reflector in the Moon's shadow.

For the Southwest China case (Figures 8b3, c3), the factor $1 - \bar{I}_{norm,j}$ is the largest for green vegetation followed by cloud, land, and ocean, respectively; $\frac{n_j}{N}$ is the largest for cloud followed by land, ocean, and green vegetation respectively. The largest factor ($1 - \bar{I}_{norm,j}$) of about 0.3 is for vegetation, which is mainly associated with green vegetation pixels in Mainland Southeast Asia or Indochinese Peninsula, including Cambodia, Laos, Myanmar, Vietnam, and China's Hainan Island. On average, those green vegetation pixels are much closer to the center of the Moon's shadow compared to cloud, land, and ocean although the area coverage of green vegetation is smallest with $\frac{n_j}{N}$ about 0.004 more than one order smaller than other reflectors. The second largest factor ($1 - \bar{I}_{norm,j}$) of about 0.25 is for cloud, mainly due to large bright clouds to the east and north and broken clouds to the south and west of the umbra (see Figure 1). In fact, the area coverage of cloud with $\frac{n_j}{N}$ about 0.14 is the largest among the four reflectors. The third largest factor ($1 - \bar{I}_{norm,j}$) of about 0.22 is for land. The area coverage with $\frac{n_j}{N}$ about 0.08 ranks second. On average, clear ocean pixels are

farthest among all four reflectors and fractional coverage with $\frac{n_j}{N}$ about 0.06 smaller than that for clouds.

The contribution factor (η_j) is ~0.035 for cloud, 0.018 for land, ~0.008 for ocean, and ~0.001 for green vegetation, respectively. Thus, clouds contribute the most to the average reflectance reduction followed by land and ocean. With the larger contribution factor for green vegetation compared to both the Arabian Peninsula and Himalayas cases, the reflectance reduction from green vegetation is noticeable (Figure 7C), particularly for the near-IR wavelength at 780 nm, at which green vegetation is extremely reflective (see Figure 6, Figure 8a3).

It is important to note that the reflectance reduction for Arabian Peninsula case is significantly smaller compared to the Himalayas and Southwest China cases, mainly because part of the Moon's shadow falls outside of the Earth's disk. The Moon's shadow covers about 24% of the whole Earth disk, but a significant portion of the shadow falls outside of the Earth's disk, compared to ~28–30% for Himalayas and Southwest China cases (Table 2).

TABLE 2 | The average fraction of area covered by different reflectors in the whole EPIC image (n_j/N) and associated standard deviation for selected five wavelengths.

	Casper	Columbia	Arabian pen	Himalayas	SW China
Ocean	0.053 (2.e-3)	0.065 (3.e-3)	0.061 (6.e-4)	0.051 (1.e-3)	0.061 (3.e-4
Land	0.056 (4.e-4)	0.056 (1.e-4)	0.090 (2.e-3)	0.119 (2.e-4)	0.081 (1.e-3
Cloud	0.137 (1.e-3)	0.145 (1.e-3)	0.089 (2.e-3)	0.123 (1.e-3)	0.136 (1.e-3
Vege	0.020 (5.e-5)	0.022 (4.e-5)	0.001 (9.e-5)	0.006 (4.e-5)	0.004 (5.e-5
Total	0.267	0.289	0.241	0.299	0.282

For the two cases of the 2017 eclipse (Figure 9), the average reflectance reductions are similar except for a decrease from 551 to 680 nm and a larger increase from 680 to 780 nm in reflectance reduction for the Columbia, Missouri case compared to the Casper, Wyoming case. Clouds contribute about 60 and 50% to the global spectral reflectance reduction, depending on wavelength, for the Casper and Columbia case, respectively. Clear land contributes about 30% to the global spectral reflectance reduction depending on wavelength for both cases. Clear ocean contribution for the Columbia case is larger than that for the Casper case since most clear ocean area is in the Atlantic Ocean to the east of the totality of the two eclipses (Figure 1). With the clear Atlantic Ocean areas are closer to Columbia than Casper, the

contribution from clear ocean to the total reflectance reduction for the Columbia case is larger than Casper. Green vegetation makes a similar contribution to the reflectance for the two cases and a significant contribution to the disk reflectance reduction for the 2017 eclipse compared to the 2020 eclipse.

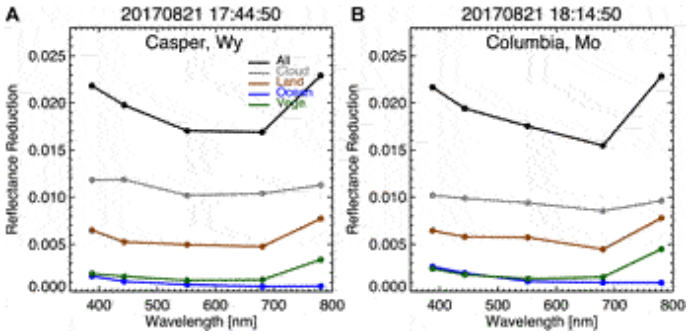

FIGURE 9 | Similar to Figure 7 but the two cases during the 2017 solar eclipse.

As demonstrated in the 2020 eclipse, the reduction of spectral reflectance of each reflector for the 2017 eclipse is proportional to the average spectral reflectance in the Moon's shadow (Figures 10a1,a2). The proportionality factor, or the contribution factor, is the product of $1 - \bar{I}_{norm,j}$ and $\frac{n_j}{N}$ for each reflector. $1 - \bar{I}_{norm,j}$ is largest (~0.55) for green vegetation followed by land (~0.45) for both the Casper and Columbia cases, because of relatively small average pixel to the center of shadow distance compared to ocean and cloud (Figures 10b1,b2). For cloud, $1 - \bar{I}_{norm,j}$ is ~0.22 and ~0.18 for the Casper and Columbia case, respectively, because the major stratocumulus cloud system off the California coast is closer to Casper, Wyoming than Columbia, Missouri. For ocean, $1 - \bar{I}_{norm,j}$ is smaller for the Casper case (~0.12) than that for the Columbia case (~0.18); the major body of water, the Atlantic Ocean, is relatively closer to Columbia than Casper. This is consistent with the larger ocean coverage for the Columbia case than the Casper case (Figures 10c1,c2), i.e., $\frac{n_j}{N}$ for ocean is ~0.007 for the Columbia case compared to ~0.005 for the Casper case. $\frac{n_j}{N}$ for cloud (~0.15), land (~0.05) and green vegetation (~0.02) is similar for the Casper and Columbia case, respectively. One can determine the contribution factor for each reflector for the two cases. For the Casper case, η_j is ~0.029 for cloud, 0.025 for land, ~0.011 for green vegetation, and ~0.007 for ocean, respectively. For the Columbia case,

η_j is ~0.024 for cloud and land, ~0.012 for green vegetation and ocean, respectively. By combining the average reflectance and associated contribution factor, one obtains the average reflectance reduction.

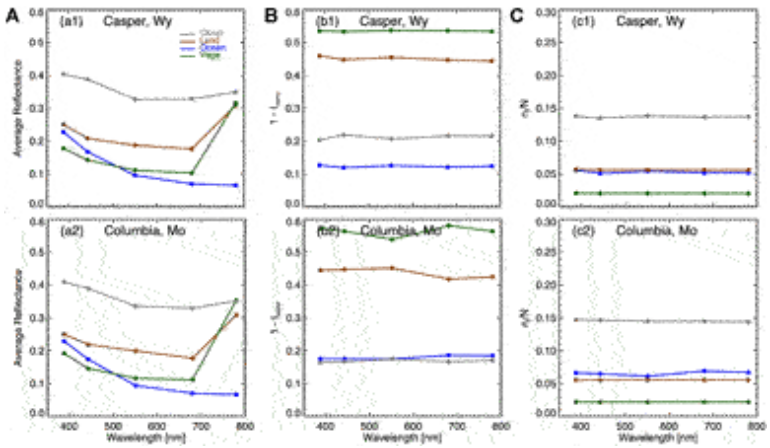

FIGURE 10 | Similar to Figure 8 but for the two cases during the 2017 solar eclipse.

The relative spectral reflectance reductions (defined as the difference between non-eclipse and eclipse reflectance divided by the eclipse reflectance) and associated components from different reflectors are presented in Figure 11 and Figure 12 for the 2020 and 2017 eclipse cases, respectively. For the Arabian Peninsula case, the average percent reflectance reduction increases with wavelength with an average of ~5.5%. The wavelength dependence of the percent reduction is mainly due to the increase of the reflectance from land compensated to some extent by the decrease of the reduction from clear ocean. For the Himalayas case, the average percent global reflectance reduction increases with wavelength with an average of ~9%. The wavelength dependence of the percent reduction is due to the increase of the reduction with wavelength from cloud and clear land. Green vegetation contributes little to the average relative reflectance reduction for both the Arabian Peninsula and Himalayas cases. For the Southwest China case, the reflectance reduction increases from 388 to 551 nm followed by a slight decrease from 551 to 680 nm and small increase to 780 nm. The wavelength dependence of the relative reduction can be explained by the contribution from each individual reflector. The total average reduction of ~9.5%, where cloud contributes over 7%, clear land contributes about 2%, and clear ocean contributes significantly at shorter wavelengths (~1% at

388 nm) and decreases toward longer wavelengths. The contribution from green vegetation is visible particularly at 780 nm wavelength.

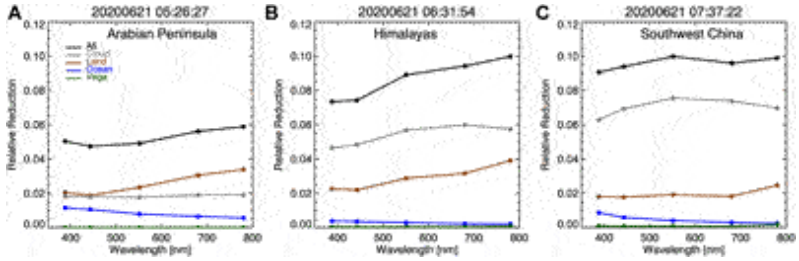

FIGURE 11 | Relative global average reflectance reduction with contributions from different reflector types for 2020 eclipse when the center of the Moon's shadow was in **(A)** Arabian Peninsula, **(B)** Himalayas, **(C)** Southwest China.

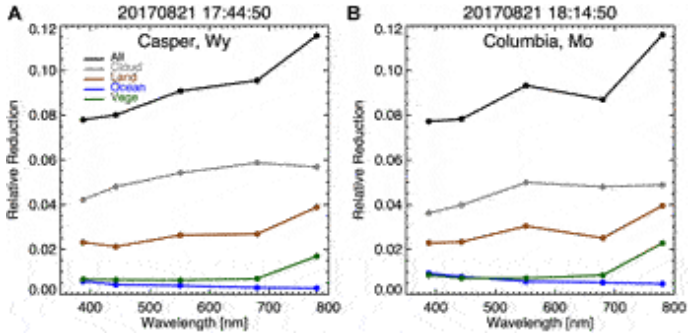

FIGURE 12 | Relative disk average reflectance reduction with contributions from different reflector types for 2017 eclipse when the center of the Moon's shadow was in **(A)** Casper, Wyoming, **(B)** Columbia, Missouri.

For the 2017 eclipse, the wavelength dependence of the average reflectance reduction for the Casper case is similar to that for the Columbia case and can be explained by the contribution from each reflector (Figure 12). Similar to the absolute reductions, for the Casper case, cloud makes the larger contributions compared to the Columbia case; land makes similar percent reduction for the two cases; ocean and green vegetation contributes slightly more percentage reductions for the Columbia case compared to the Casper case. The total average reduction is ~9% for both cases.

The contribution from each reflector type to the disk and spectrally averaged percent reflectance reduction is summarized in Figure 13. For 2020 solar eclipse over Arabian Peninsula, clear land (mostly desert) makes the largest contribution to the reduction, followed by clouds and clear ocean. For

both the Himalayas and Southwest China cases, clouds contribute the most to the reduction, followed by clear land and clear ocean. Green vegetation makes little contribution to the reflectance reduction. For 2017 solar eclipse, clouds make the largest contribution to the total reduction, followed by clear land, clear ocean, and green vegetation.

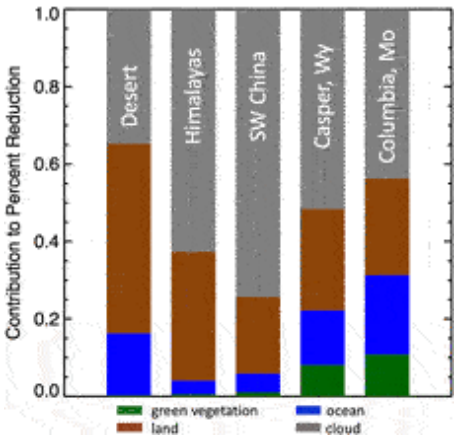

FIGURE 13 | Summary of percentage contribution from different reflectors for the three cases during 2020 solar eclipse and two cases during 2017 solar eclipse.

SUMMARY AND DISCUSSION

We have analysed EPIC images to quantify and understand eclipse-induced disk spectral reflectance reduction. Radiative transfer calculations showed that different reflector types of the Earth have different spectral reflectance that affects the amount of eclipse radiances at TOA. The global reflectance reduction is the sum of the contribution from different reflectors. We showed that the reduction from each reflector is proportional to the average reflectance, the area coverage in the penumbra, and the average distance from the center of the Moon's shadow.

Using calculated reduced brightness during eclipses, we recovered the EPIC images under hypothetical non-eclipse conditions from eclipse images. We further classified dominant reflector types based on the recovered non-eclipse images. We found that the average spectral reflectance reductions for the three cases during the 2020 eclipse differ significantly from each other and two cases during 2017 eclipse. The differences were explained by the difference in the brightness of underlying reflectors, the associated radial distances to the center of the Moon's shadow as well as the area coverages in the Moon's shadow.

We also quantified the percentage reductions. For the 2020 eclipse, the spectrally averaged relative reflectance reduction is ~5.5%, ~9%, and ~9.5% for the Arabian Desert, Himalayas, Southwest China case, respectively, compared to ~9% for the two cases for 2017 eclipse. The reflectance reductions from different reflectors were used to interpret the disk average spectral reflectance reduction.

Note that the global reflectance reduction for the Arabian Peninsula case is about 5%, significantly smaller than the other cases. This difference is mainly due to a large portion of the Moon's shadow being outside of the Earth. Another factor is that desert is almost cloud-free and bright clouds farther away from the center of the Moon's shadow do not contribute effectively to the average reflectance reduction compared to the other cases.

DATA AVAILABILITY STATEMENT

Publicly available datasets were analyzed in this study. This data can be found here: https://search.earthdata.nasa.gov/.

AUTHOR CONTRIBUTIONS

GW composed the majority of this manuscript with assistance from AM, JH, and DW. GW performed most of the analyses with the help from AM. This is a follow-up paper of our earlier work led by JH (Herman et al., 2018a).

FUNDING

The DSCOVR EPIC project is funded by NASA Earth Science Division. GW and JH research was supported by the DSCOVR Science Management Project.

PUBLISHER'S NOTE

ACKNOWLEDGMENTS

AM acknowledges support from the NASA's DSCOVR Project. DW acknowledges support from the NASA's TSIS Project.

REFERENCES

Bernhard, G., and Petkov, B. (2019). Measurements of Spectral Irradiance during the Solar Eclipse of 21 August 2017: Reassessment of the Effect of Solar Limb Darkening and of Changes in Total Ozone. *Atmos. Chem. Phys.* 19, 4703–4719. doi:10.5194/acp-19-4703-2019

Blank, K., Huang, L.-K., Herman, J., and Marshak, A. A. (2021). Earth Polychromatic Imaging Camera Geolocation; Strategies to Reduce Uncertainty. *Front. Remote Sens.* 2, 715296. doi:10.3389/frsen.2021.715296

Calamas, D. M., Nutter, C., and Guajardo, D. N. (2018). Effect of 21 August 2017 Solar Eclipse on Surface-Level Irradiance and Ambient Temperature. *Int. J. Energ. Environ. Eng.* 10, 147–165. doi:10.1007/s40095-018-0290-8

Doelling, D., Haney, C., Bhatt, R., Scarino, B., and Gopalan, A. (2019). The Inter-calibration of the DSCOVR EPIC Imager with Aqua-MODIS and NPP-VIIRS. *Remote Sens.* 11, 1609. doi:10.3390/rs11131609

Emde, C., and Mayer, B. (2007). Simulation of Solar Radiation during a Total Eclipse: a challenge for Radiative Transfer. *Atmos. Chem. Phys.* 7, 2259–2270. doi:10.5194/acp-7-2259-2007

Eshelman, L. M., Tauc, M. J., Hashimoto, T., Gillis, K., Weiss, W., Stanley, B., et al. (2020). Digital All-Sky Polarization Imaging of the Total Solar Eclipse on 21 August 2017 in Rexburg, Idaho, USA. *Appl. Opt.* 59 (No. 21), F41–F52. doi:10.1364/AO/391736

Gedzelman, S. D. (2020). Solar Eclipse Skies and Limb Reddening. *Appl. Opt.* 59 (No. 21), F78–F84. doi:10.1364/AO.396964

Geogdzhaev, I. V., Marshak, A., and Alexandrov, M. (2021). Calibration of the DSCOVR EPIC Visible and NIR Channels Using Multiple LEO Radiometers. *Front. Remote Sens* 2. doi:10.3389/frsen.2021.671933

Geogdzhayev, I. V., and Marshak, A. (2018). Calibration of the DSCOVR EPIC Visible and NIR Channels Using MODIS Terra and Aqua Data and EPIC Lunar Observations. *Atmos. Meas. Tech.* 11, 359–368. doi:10.5194/amt-11-359-2018

Herman, J., Huang, L., McPeters, R., Ziemke, J., Cede, A., and Blank, K. (2018b). Synoptic Ozone, Cloud Reflectivity, and Erythemal Irradiance from Sunrise to sunset for the Whole Earth as Viewed by the DSCOVR Spacecraft from the Earth-Sun Lagrange 1 Orbit. *Atmos. Meas. Tech.* 11, 177–194. doi:10.5194/amt-11-177-2018

Herman, J., Wen, G., Marshak, A., Blank, K., Huang, L., Cede, A., et al. (2018a). Reduction in Earth Reflected Radiance during the Eclipse of 21 August 2017. *Atmos. Meas. Tech.* 11, 4373–4388. doi:10.5194/amt-11-4373-2018

King, M. D., Platnick, S., Menzel, W. P., Ackerman, S. A., and Hubanks, P. A. (2013). Spatial and Temporal Distribution of Clouds Observed by MODIS Onboard the Terra and Aqua Satellites. *IEEE Trans. Geosci. Remote Sens.* 51, 3826–3852. doi:10.1109/TGRS.2012.2227333

Koepke, P., Reuder, J., and Schween, J. (2001). Spectral Variation of the Solar Radiation during an Eclipse. *metz* 10, 179–186. doi:10.1127/0941-2948/2001/0010-0179

Madhavan, B. L., and Venkat Ratnam, M. (2021). Impact of a Solar Eclipse on Surface Radiation and Photovoltaic Energy. *Solar Energy* 223 (2021), 351–366. doi:10.1016/j.solener.2021.05.062

Marshak, A., Delgado-Bonal, A., and Knyazikhin, Y. (2021). The Effect of Scattering Angle on Earth Reflectance. *Front. Remote Sens.* 2. doi:10.3389/frsen.2021719610

Marshak, A., Herman, J., Adam, S., Karin, B., Carn, S., Cede, A., et al. (2018). Earth Observations from DSCOVR EPIC Instrument. *Bull. Amer. Meteorol. Soc. (Bams)* 99, 1829–1850. doi:10.1175/bams-d-17-0223.1

Mikhalev, A. V., Chernigovskaya, M. A., Beletsky, A. B., Kazimirovsky, E. S., and Pirog, O. M. (1999). Variations of the Ground-Measured Solar Ultraviolet Radiation during the Solar Eclipse on March 9, 1997. *Adv. Space Res.* 24 (5), 657–660. doi:10.1016/s0273-1177(99)00209-4

Neckel, H. (2005). Analytical Reference Functions F(λ) for the Sun's Limb Darkening and its Absolute Continuum Intensities (λ 300 to 1100 Nm). *Sol. Phys.* 229, 13–33. doi:10.1007/s11207-005-4081-z

Neckel, H., and Labs, D. (1994). *Solar Limb Darkening 1986–1990 (Lambda 303–1099 nm)*153, 1–2, 91–114. doi:10.1007/BF00712494

Ockenfuß, P., Emde, C., Mayer, B., and Bernhard, G. (2020). Accurate 3D Radiative Transfer Simulation of Spectral Solar Irradiance during the Total Solar Eclipse of August 21, 2017. *Atmos. Chem. Phys.* 20, 1961–1976. doi:10.5194/acp-20-1961-2020

Ricchiazzi, P., Yang, S., Gautier, C., and Sowle, D. (1998). SBDART: A Research and Teaching Software Tool for Plane-Parallel Radiative Transfer in the Earth's Atmosphere. *Bull. Amer. Meteorol. Soc.* 79 (10), 2101–2114. doi:10.1175/1520-0477(1998)079<2101:sarats>2.0.co;2

Samanta, A., Knyazikhin, Y., Xu, L., Dickinson, R. E., Fu, R., Costa, M. H., et al. (2012). Seasonal Changes in Leaf Area of Amazon Forests from Leaf flushing and Abscission. *J. Geophys. Res. Biogeosciences* 117 (G1). doi:10.1029/2011jg001818

Sarid, G., Twedt, K. A., and Xiong, X. (2021). "Terra MODIS Sees Solar Eclipses: Analysis of Reflective Solar Band Response at Multiple Radiance Levels," in *Proceedings of the SPIE 11727, Algorithms, Technologies, and Applications for Multispectral and Hyperspectral imaging XXVII*, *(online only, United States*, *April 12–16, 2021)*, 1172701. doi:10.1117/12.2586219

Sharp, W. E., Silverman, S. M., and Lloyd, J. W. (1971). Summary of Sky Brightness Measurements during Eclipses of the Sun. *Appl. Opt.* 10, 1207–1210. doi:10.1364/AO.10.001207

Shaw, G. E. (1978). Sky Radiance during a Total Solar Eclipse: a Theoretical Model. *Appl. Opt.* 17, 272–278. doi:10.1364/ao.17.000272

Song, W., Knyazikhin, Y., Wen, G., Marshak, A., Mõttus, M., Yan, G., et al. (2018). Implications of Whole-Disc DSCOVR EPIC Spectral Observations for Estimating Earth's Spectral Reflectivity Based on Low-Earth-Orbiting and Geostationary Observations. *Remote Sens.* 10, 1594. doi:10.3390/rs10101594

Trees, V., Wang, P., and Stammes, P. (2021). Restoring the Top-Of-Atmosphere Reflectance during Solar Eclipses: a Proof of Concept with the UV Absorbing Aerosol index Measured by TROPOMI. *Atmos. Chem. Phys.* 21, 8593–8614. doi:10.5194/acp-21-8593-2021

Wen, G., Marshak, A., Song, W., Knyazikhin, Y., Mõttus, M., and Wu, D. (2019). A Relationship between Blue and Near-IR Global Spectral Reflectance and the Response of Global Average Reflectance to Change in Cloud Cover Observed from EPIC. *Earth Space Sci.* 6, 1416–1429. doi:10.1029/2019ea000664

Wen, G., Marshak, A., Tsay, S.-C., Herman, J., Jeong, U., Abuhassan, N., et al. (2020). Changes in the Surface Broadband Shortwave Radiation Budget during the 2017 Eclipse. *Atmos. Chem. Phys.* 20, 10477–10491. doi:10.5194/acp-20-10477-2020

Zerefos, C. S., Bali, D. S., Meleti, C., Bais, A. F., Tourpali, K., Kourtidis, K., et al. (2000). Changes in Surface UV Solar Irradiance and Ozone over the Balkans during the Eclipse of August 11, 1999. *J. Geophys. Res.* 105 (26), 463473. doi:10.1016/S0273-1177(01)00279-4

Conflict of Interest: The authors declare that the research was conducted in the absence of any commercial or financial relationships that could be construed as a potential conflict of interest.

Frontiers in
Remote Sensing

Highlights innovation in remote sensing science and its applications

An exciting journal which focuses on physical and quantitative approaches to remote sensing of the land, oceans, biosphere, atmosphere and space at local and global levels.

Discover the latest Research Topics

See more →

Frontiers

Avenue du Tribunal-Fédéral 34
1005 Lausanne, Swizerland
frontiersin.org

Contact us

+41 (0)21 510 17 00
frontiersin.org/about/contact